UNIVERSITY OF SOUTHAMPTON

FACULTY OF ENGINEERING AND THE ENVIRONMENT

Institute of Sound and Vibration Research

Loudspeaker Compression-Driver Phase-Plug Design

by

Jack Oclee-Brown

Thesis for the degree of Doctor of Philosophy

November 2012

UNIVERSITY OF SOUTHAMPTON

ABSTRACT

FACULTY OF ENGINEERING AND THE ENVIRONMENT

Institute of Sound and Vibration Research

Doctor of Philosophy

LOUDSPEAKER COMPRESSION-DRIVER PHASE-PLUG DESIGN

by Jack Oclee-Brown

This thesis is concerned with the linear acoustical performance of compression-driver loudspeakers. The general principles of operation of electromagnetic loudspeakers are thoroughly introduced and a number of acoustical analysis methods are then presented that form the basis for modern loudspeaker behavioural simulation. The acoustical behaviour of the compression-driver phase plug and compression cavity is discussed and targets are determined for the ideal behaviour. The Smith guidelines for the design of annular-channel compression drivers are outlined. It is demonstrated that, for realistic geometries, the Smith guidelines do not lead to optimum performance. A new channel-positioning method is outlined that is based on a more realistic representation of the compression driver. This approach is further developed into a general channel-positioning methodology that may be applied using numerical techniques to compression drivers of arbitrary geometry. It is shown that the performance of a compression driver may be improved by careful shaping of the compression cavity. A number of methods for designing optimally shaped compression cavities are described. A Smith-type approach to the design of radial-channel compression drivers is outlined, including methods specifically intended to ease the manufacture of such devices. A prototype driver using one of these methods is described and measurements of the performance of this prototype are compared with predictions of the driver performance. The behaviour of compression drivers with non-rigid radiating diaphragms is considered. It is shown that, if the mechanical diaphragm modes and acoustical cavity modes meet a certain condition, then the diaphragm non-rigidity is not a factor that limits the linear driver response. An attempt is made to find geometries that meet this condition.

for Helen

Contents

Author's declaration

I, Jack Oclee-Brown, declare that the thesis entitled Loudspeaker Compression-Driver Phase-Plug Design and the work presented in the thesis are both my own, and have been generated by me as the result of my own original research. I confirm that:

- this work was done wholly or mainly while in candidature for a research degree at this University;
- where any part of this thesis has previously been submitted for a degree or any other qualification at this University or any other institution, this has been clearly stated;
- where I have consulted the published work of others, this is always clearly attributed;
- where I have quoted from the work of others, the source is always given. With the exception of such quotations, this thesis is entirely my own work;
- I have acknowledged all main sources of help;
- where the thesis is based on work done by myself jointly with others, I have made clear exactly what was done by others and what I have contributed myself;
- parts of this work have been published as:
    - M. Dodd and J. Oclee-Brown, "A New Methodology for the Acoustic Design of Compression Driver Phase Plugs with Concentric Annular Channels," presented at The 123rd Convention of the AES, preprint 7258, Oct 2007. [1]
    - M. Dodd and J. Oclee-Brown, "A New Methodology For The Acoustic Design Of Compression Driver Phase Plugs With Concentric Annular Channels," presented at The Institute of Acoustics, Reproduced Sound 24, Nov 2008. [2]
    - M. Dodd and J. Oclee-Brown, "A New Methodology for the Acoustic Design of Compression Driver Phase Plugs with Radial Channels," presented at The 125th Convention of the AES, preprint 7532, Oct 2008. [3]
    - M. Dodd and J. Oclee-Brown, "New Methodology for the Acoustic Design of Compression Driver Phase Plugs with Concentric Annular Channels," *Journal of the Audio Engineering Society*, vol. 57, no. 10, pp. 771-787, Oct 2009. [4]
    - M. Dodd and J. Oclee-Brown, "Design of a Coincident Source Driver Array with a Radial Channel Phase Plug and Novel Rigid Body Diaphragms," presented at Audio Engineering Society Convention 127, Oct 2009. [5]

Signed: Date:

Acknowledgements

There is no doubt that the completion of my doctoral training has been an extremely hard personal challenge. Without the support and encouragement of my colleagues, friends and family, I can say with absolute certainty I would have failed this challenge a number of years ago. I would like to thank them all. There are a number of individuals who I would like to mention in person.

I would like to sincerely thank my supervisor Prof. Philip Nelson. It is largely down to Philip's encouragement and belief that I decided to begin my doctoral training. Throughout my studies he has offered his support and advice. I am very grateful for the renewed motivation I felt after each of our meetings. His scientific guidance is the foundation to this work.

I would like to thank Mark Dodd, my colleague, mentor and friend. Much of the work in this thesis has sprung from conversations, or work, with Mark. I greatly admire his focus and his fastidiousness when it comes to loudspeakers of all types. He continually challenges me to do better. I am indebted to him for his support of my doctoral training.

I am very grateful to Patrck Macey of PACSYS, in particular for his advice and guidance on BEM, FEM and continuum mechanics.

Many thanks to Dr Keith Holland for his enthusiasm for my research. His encouragement, expertise and advice has been greatly appreciated.

Many thanks to Dr Takashi Takeuchi and Dr Filipo Fazi both of whom have inspired me with their research. Our conversations have been a great source of encouragement and motivation.

Many thanks to all my colleagues at GP Acoustics for their support and friendship, in particular to my colleagues in the KEF Audio R&D department.

I am extremely grateful for the support of GP Acoustics in both allowing me to embark on my doctoral training, in parallel with my employment with them, and also for their sponsorship.

On a personal level, I am grateful for the love and support of my family. To my wife Helen, thank you for your patience during the many hours I have dedicated to my work and thesis. And thank you for your help in casting your eyes over the text. To my mother and father Caroline and Gavin, to my sister and brother Claire and Guy, to my grandparents, Vera, Mac, Jeanne, Brian and Susan, to Lorenz, Hannah and Beatrix. My deepest gratitude.

1 Introduction

This thesis is concerned with loudspeakers and specifically with the design of compression drivers for horn loudspeakers. Compression drivers are widely used for professional sound reproduction applications because of their extremely high efficiencies. However, they present a unique acoustical design challenge as the compression-driver arrangement, with coupled phase plug and compression cavity, results in a complex acoustical structure that is typically several times larger than the maximum wavelength to be radiated. Additionally, there is little dissipation in the acoustical structure other than the radiated energy. As a result, the performance of a compression driver is highly dependent upon the precise details of the geometry. Despite this interesting acoustical problem, there is relatively little published work on how to design the geometry of compression drivers. In this thesis the behaviour of the various parts of the compression driver are analysed. The presented analyses are illustrated with numerically-modelled examples and measured data from prototype drivers. Several new approaches to compression-driver design have resulted that, particularly if used in combination with one another, greatly improve the state of the art of compression-driver design. In summary, the new contributions in the field of compression driver design are:

- the improvement of the channel-entrance geometry guidelines from those suggested by Smith in 1952, which are universally used in the loudspeaker industry. This improvement is based on the realisation that the Smith geometry is not as effective if the radiating diaphragm has a curved surface. The new guidelines are based on a more accurate geometric representation of the compression driver, including this curvature;
- the development of a general approach to determining compression-driver channel-entrance geometry, independent of the specific geometry of the compression-driver radiating diaphragm and compression cavity;
- the concept of compression-driver cavity shaping to improve the suppression of the compression driver cavity modes;
- the application of a Smith-type approach to the design of radial-channel compression drivers;
- the development of methods to allow optimal radial-channel phase plugs to be designed within the practical constraints of current fabrication methods; and
- a detailed analysis of the behaviour of compression drivers with non-rigid radiating diaphragms and the description of an approach for designing non-rigid diaphragm and cavity combinations that result in improved acoustical performance.

This thesis was completed over a period from 2006. During this period the author was employed full time by the GP Acoustics group as a Research Engineer. The GP Acoustics group includes the loudspeaker brands KEF Audio and Celestion and, consequently, much of the work presented here has been used in the design of KEF Audio and Celestion products launched at various times in this period. Additionally, this thesis has resulted in a number of publications as outlined in the Author's declaration.

1.1 Outline of the thesis

This section contains a brief outline of the contents of this thesis. Three preliminary chapters are included in order to familiarise the reader with the concepts discussed and the analysis methods used. The four chapters following these describe new analyses and approaches to the design of compression drivers.

1.1.1 Chapter 2

Chapter 2 is concerned with the acoustical behaviour of loudspeakers and describes the general principles of operation of electromagnetic loudspeakers. Following this, the behaviour of direct-radiating loudspeakers is considered. Finally, the behaviour of horn-loaded and compression-loaded loudspeakers is covered.

1.1.2 Chapter 3

In chapter 3, a number of acoustical analysis approaches are introduced that form the basis for the analysis of compression-driver behaviour in the following chapters. The first section in the chapter considers the solution to the homogeneous acoustical wave equation in a rigid-walled enclosure. It is demonstrated that this type of analysis provides rigid-walled eigenfrequencies and eigenfunctions that are unique to the enclosure geometry and these are extremely valuable for subsequent driven-cavity behaviour analysis.

The second section outlines the general Green-function approach to the solution of the inhomogeneous wave equation. This technique is the foundation of many types of acoustical analysis. Following this outline, a specific case of the Green-function approach is described: the driven sound field in a lightly-damped enclosure. Using the assumption that the Green function within the acoustical enclosure may be described in terms of the rigid-walled eigenfunctions, an expression for the acoustical pressure in the cavity is found in terms of the rigid-walled eigensolution and the distribution of acoustical volume velocity within, and on the bounding surface of, the enclosure. This technique is particularly relevant to the thesis as

it is the basis that was used by Smith to derive his phase-plug guidelines and it is also the basis that is repeatedly used herein to derive the outlined new phase-plug design methods.

Following this section, the external acoustical problem is considered with particular reference to loudspeakers where the acoustical radiation into infinite and semi-infinite spaces is a very important consideration.

Finally, the last three sections are concerned with numerical solution techniques of both the homogeneous and inhomogeneous wave equation. Firstly, the Rayleigh-Ritz method is outlined as an introduction to the subsequent section that describes the Finite-Element Method (FEM). The Rayleigh-Ritz method is also of particular relevance to the following chapters as it forms the basis for the cavity-shaping techniques presented in chapter 6. The last section of this chapter describes the Boundary-Element Method (BEM) and uses concepts introduced in both section 3.5 and 3.7 to outline a method that allows acoustical radiation problems from arbitrary radiator geometries to be numerically considered. The FEM and BEM approaches are widely used in this thesis as a means of evaluating the performance of various compression-driver phase-plug arrangements and also as a tool for performing acoustical experiments that would conventionally be very difficult to perform.

1.1.3 Chapter 4

The detailed behaviour of compression drivers, and specifically of the phase plug, is outlined in this section. The introduction presents numerically calculated examples that show various different aspects of compression-driver and horn-loaded loudspeaker behaviour. Following this discussion, the Smith method for the positioning of the compression channel entrances is described. The performance of the Smith geometry is demonstrated, compared to another channel positioning method, using FEM analysed examples. The desired behaviour of the phase-plug structure is then outlined based on a simplified 1-D duct model and the acoustics of the compression-driver phase plug as a whole is discussed, including its effect on the suppression methods outlined by Smith.

1.1.4 Chapter 5

In chapter 5, a new method for the positioning of the phase-plug channels entrances of annular-channel compression drivers is outlined. The compression cavity is considered as a narrow spherical-cap acoustical cavity whose driven behaviour may be accurately described in terms of its rigid-walled eigenfrequencies and eigenfunctions, as was outlined in section 3.4. Using this representation, it is possible to derive locations at which the annular channels

should be attached to the compression cavity to avoid excitation of acoustical modes in the cavity in the driven case.

This approach is the exact parallel to the technique outlined by Smith. The difference compared to the Smith case is the geometry of the problem. Smith considers that the compression-driver geometry is approximated with little error in a cylindrical geometry, in which case the radiating diaphragm is approximated as a rigid-plane circular piston. However, this approximation has the effect that the radiating diaphragm does not excite any of the compression-cavity modes. It is shown that when a more realistic geometry is used for the compression cavity and diaphragm, the Smith phase-plug geometry does not prevent the excitation of the acoustical modes of the compression cavity because the radiating diaphragm does contribute to the excitation of the acoustical cavity modes. The new analysis, using a more representative geometry, results in a different set of guidelines for the phase-plug channel-entrance geometry. The performance of these new guidelines is compared to the original Smith guidelines using numerical theoretical models. A commercial compression driver based on these new guidelines is briefly described and measurements of this new compression driver are shown compared to FEM/BEM predictions.

The final part of the chapter describes a general approach to the positioning of the phase-plug channels, independent of the geometry to be considered. This technique is a generalisation of both the Smith method and the new method. By using FEM techniques to provide the cavity eigenfrequencies and eigenfunctions, the consideration of compression-cavity geometries that are thin acoustical cavities with otherwise arbitrary geometry are permitted. As an example of the generalised method, a common compression-cavity geometry is considered, that of an axially extruded spherical cap, and the phase-plug channel positions are derived for this example. The performance of this theoretical compression driver is evaluated using a FEM model. This model interestingly demonstrates a much improved modal suppression performance compared to the spherical-cap compression cavity despite the fact that the derived phase-plug channel positions are extremely similar. The reasons for this performance improvement are considered in the next chapter.

1.1.5 Chapter 6

The final result from chapter 5 serves as a motivation for more detailed consideration of the effect of the cavity geometry on the compression driver performance. Using the orthogonality of the compression-cavity modes, the ideal compression cavity shape is derived for a rigid-radiating diaphragm and the performance of this ideal cavity shape is

shown using an idealised compression-driver FEM model. However, there are often some other practical constraints on the shape of the compression cavity that means that in many situations the derived ideal shape cannot be used, particularly because it is normally necessary to have a little extra space at the outside diameter of the compression cavity for the driver surround or voice coil to be positioned. This problem is considered in section 6.2 and it is demonstrated that by controlling the cavity shape in terms of only a few eigenfunctions, compared to a conventional constant-width compression cavity, it is possible to make significant improvements in the modal suppression performance while still allowing a little additional space for these extra features. Ultimately, however, the conclusion of this section is that the cavity-shaping techniques are difficult to usefully implement as it is very hard to control the derived cavity shape. It is also inevitable that the resulting shaped cavity is of larger acoustical volume than the ideal cavity design method presented at the start of the chapter.

1.1.6 Chapter 7

The radial-channel compression-driver arrangement uses a number of radially extending channels, as opposed to the annular channels that have been considered up until this point. In chapter 7, the modal suppression problem is considered for the radial case and it is shown that a similar approach to the annular case is possible. An ideal geometry for the radial channels is derived based on a spherical-cap compression cavity. The cavity-shaping method introduced in chapter 6 for the annular case is then also applied to the radial-channel case and results in a marked performance improvement.

The ideal radial geometry suffers from a practical problem. The derived geometry requires that the channels meet at the central axis of the phase plug with each channel covering an equal angular segment of the radiating diaphragm. This situation cannot be realised in practice as it requires the channels to be arbitrarily narrow in the centre. Due to the manufacturing constraints on the phase-plug moulding, this is clearly not possible. In a similar analysis to that which was presented in chapter 6.2, a less restrictive method for deriving the channel geometry is outlined based on controlling only the modal excitation for a few of the compression cavity modes. The design of a commercial loudspeaker driver using this approach is described in detail and culminates with measurements that shown the performance of the final produced driver.

1.1.7 Chapter 8

Throughout the previous chapters, to simplify the analyses, the assumption has been made that the radiating diaphragm of the compression driver moves rigidly. It is firstly demonstrated that this is a poor assumption for many common compression-driver designs. To discover the theoretical performance limits of compression drivers with a non-rigid radiating diaphragm, the vibration of the diaphragm is expanded in terms of the mechanical eigenfunctions and eigenfrequencies. Using this description of the diaphragm motion along with the figures of merit introduced in the previous chapters, it is demonstrated that if the mechanical and acoustical eigenfunctions meet a specific set of conditions then the performance of the compression driver is not restricted by the diaphragm's non-rigidity. An attempt is made to find diaphragm and cavity geometries that approximately meet the outlined conditions for the acoustical and mechanical eigenfunctions. FEM models are used to assess the performance of the resulting driver geometries. The geometries that more closely meet the eigenfunction conditions have an improved acoustical performance. This is a very exciting result as it provides a clear approach to the design of the diaphragm, an area which is currently not well understood. The developments in this chapter works in harmony with the phase-plug design methods of the previous sections, and the more accurately the eigenfunction condition is met, the better the performance of the approaches outlined in chapters 5 and 7. Additionally, as it discussed in this chapter, the eigenfunction criterion approach is also quite closely linked to the cavity-shaping methods of chapter 6.

1.2 Notation and nomenclature

Complex phasors

Loudspeakers designed for audio are concerned with the transduction of signals with frequency content in the audio bandwidth, commonly estimated as between 20Hz and 20kHz. The linear behaviour of loudspeakers is most readily and helpfully considered in the steady-state frequency domain. The complex exponential notation is used in this thesis as it allows concise formulation of the behavioural equations. The time dependence of oscillatory functions is defined to be $e^{j\omega t}$, where $j=\sqrt{-1}$, ω is the frequency in radians per second and t is the temporal variable. Thus, a harmonic function $x(t)$ can be defined as

$$x(t)=\Re\left(A e^{j\omega t}\right) \qquad 1.1.$$

where A is the complex amplitude of the function and ω is the frequency of oscillation. As indicated, in this thesis the implicit convention that the real part of the complex phasor

represents the physical solution is assumed: this is not be stated explicitly with each result. Additionally, the oscillatory function $e^{j\omega t}$ is generally omitted from expressions for clarity. Note that the complex amplitude is not written with a bold typeface: bold typeface is reserved for vectors (in lower-case) and matrices (in upper-case).

It should be noted that this convention defines complex amplitude, A, to be a peak amplitude. When calculating power transfer and dissipation, it is important that this is taken into account and these peak amplitudes are first converted into root mean square (RMS) amplitudes. For a sinusoidal signal, as are considered in this case, this relationship is simple: $A_{peak} = A_{rms}\sqrt{2}$. As power is proportional to the square of the circuit flux or potential, this $\sqrt{2}$ term results in an additional division by 2. Thus, for example, the power dissipated in a resistor is calculated as

$$P = \frac{|V|^2}{2R} \qquad 1.2.$$

where V is the peak-voltage amplitude across the terminals of the resistor of resistance R, and P is the power dissipated in the resistor. Similar care must also be taken when calculating decibels. The decibel scale is generally intended to be a comparable to power or intensity. Strictly only RMS amplitudes should be used when calculating decibel levels from harmonic signal amplitudes.

Eigenfrequencies, eigenfunctions, natural frequencies and modes

The physical behaviour of oscillating fluid and mechanical structures is described by differential equations. For acoustical analysis, the full governing equations are approximated using linear partial differential equations that omit the higher-order non-linear terms, resulting in a description that is valid at small amplitudes. The homogeneous boundary-value acoustical problem is readily dealt with using eigenanalysis that provides a solution to the differential equations in terms of a characteristic set of eigenfunctions and eigenfrequencies. When the governing differential equations are formed directly in terms of physically observable dependent variables, such as acoustical pressure or mechanical displacement, then the solution to the mathematical description is indistinguishable from the behaviour of the physical system itself. Consequently, in this thesis, it is considered that the physical system *itself* has characteristic eigenfrequencies and eigenfunctions and also that these are equivalent to the natural frequencies and modes of vibration of the physical system. The two sets of terminology are used equivalently and interchangeably when referring to the characteristic behaviour of a physical system.

2 The acoustics of loudspeakers

2.1 Introduction

In this thesis many aspects of loudspeaker acoustics are considered. This chapter is provided as a review of the relevant fundamentals of loudspeaker behaviour. Most generally, a loudspeaker is a transducer that converts energy between electrical and acoustical forms. This thesis exclusively considers electromagnetic loudspeakers and, in this case, the magnetic and mechanical domains act as an intermediary in the energy chain from electrical to acoustical. Although other types of loudspeaker, such as piezoelectrical, eletrostatic and magnetostrictive are occasionally seen, electromagnetic loudspeakers are by far the most common type of loudspeaker. This is due to the fact that they can be relatively cheaply manufactured, they are easily designed for many different bandwidths, powers and efficiencies and they require only moderate partnering electronics.

The next section begins by looking in detail at the transduction path of an electromagnetic loudspeaker before then considering more specific types of loudspeaker. Firstly, the direct-radiating loudspeaker is considered, followed by the horn-loaded loudspeaker and, finally the compression-loaded loudspeaker. Special attention is paid to the efficiency, bandwidth and size trade-offs in each case.

Initial suffix	Domain
e	electrical
m	mechanical
a	acoustical

Table 2.1: Variable initial suffix reference table.

The analysis of loudspeakers using lumped components can be very confusing for the reader because of the great number of variables that are used to represent the various impedances and components in the different domains. In order to aid the reader, a simple convention has been adopted for the variable suffixes. The initial suffix denotes to which domain the variable refers, according to table 2.1.

The second suffix denotes to what component the variable refers according to table 2.2 below.

Second suffix	Component
d	diaphragm
r	radiation
s	Infinite-baffle mounted loudspeaker

Table 2.2: Variable second suffix reference table.

Thus, the impedance Z_{ms} is the mechanical impedance of the infinite-baffle mounted system.

2.2 The electromagnetic transduction mechanism

The path of energy flow in an electromagnetic loudspeaker is always the same. Firstly, the drive signal for the loudspeaker is provided in the electrical domain. This drive signal is used to provide a mechanical force by arranging for electrical current to flow in a region of high magnetic-field strength. The force generated is used to drive a mechanical system that incorporates one, or possibly multiple, acoustical diaphragms that transfer energy as acoustical pressure waves into an adjacent medium. For a loudspeaker this is most commonly air. Indeed, two transduction processes are present in the transducer: the energy that begins in the electromagnetic domain is then transferred to the mechanical domain and then finally to the acoustical domain[1]. It is useful to summarise the transduction path into a circuit model as shown in figure 2.1.

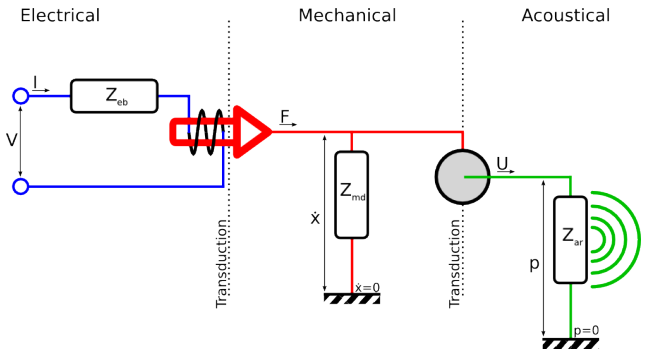

Figure 2.1.Lumped circuit representation of a generic electromagnetic loudspeaker.

In each domain two physical quantities describe the state of the components. While other conventions are sometimes used, see Beranek [6], in the opinion of the author it is most clear

1 Strictly, one could consider that a third transduction process is present and the electrical energy is transferred into the magnetic domain and then subsequently to the mechanical domain. For the purpose of this thesis, this is only considered as a single transduction step although the reader should note that it is useful to make this separation when considering non-linearities in the electromagnetic motor system.

when the circuit directly represents the geometry of the physical situation under consideration. The key to this is that the node connection rule follows the physical behaviour that one would expect when connecting real components. This approach results in the equivalence shown in table 2.3.

	Electrical	**Mechanical**	**Acoustical**
Node connection rule	Kirchhoff's current law $\sum_{\text{node}} I = 0$ The sum of all currents entering a node is zero.	D'Alembert's principle $\sum_{\text{node}} F = 0$ The sum of all forces applied to a node is zero	Continuity Equation $\sum_{\text{node}} U = 0$ The sum of volume velocities entering a node is zero
Circuit Potential	V – voltage - volts	$\dot{x}$ - velocity - ms^{-1}	p - pressure - Pa
Circuit Flux	I - current - amps	F - force - newtons	U - volume velocity - $m^3 s^{-1}$
	Electrical admittance $\frac{I}{V} = Y_e$	Mechanical impedance $\frac{F}{\dot{x}} = Z_m$	Acoustical admittance $\frac{U}{p} = Y_a$
	Electrical impedance $\frac{V}{I} = Z_e$	Mechanical admittance $\frac{\dot{x}}{F} = Y_m$	Acoustical Impedance $\frac{p}{U} = Z_a$

Table 2.3 Table of equivalence for circuit analysis in different domains.

In the circuit shown in figure 2.1, there are two transducing elements that interconnect the different domains. These are:

1. The loudspeaker motor system
    - This is usually a coil of wire located in a magnetic field. The element obeys the transduction law $F = BLI$. This law describes how the flux of the mechanical side, F, is related to the flux of the electrical side, I, by the transduction coefficient BL;
    - At frequencies in the audio band, BL can be considered as constant and is a physically meaningful parameter. It is the length of the coil wire, L, multiplied by the magnetic field strength in which the coil is located, B;
    - The transduction law can be equivalently written as $V = BL\dot{x}$ in terms of the mechanical potential, $\dot{x}$, and the electrical potential, V. This relationship between velocity and voltage is familiar as a electromagnetic induction process;
    - Taking the ratio of these two laws provides an expression that describes how an impedance on one side of the transduction appears from the

other, $B^2L^2/Z_m = Z_e$. The transduction in this case is said to be anti-reciprocal as impedance in one domain is transferred to admittance in the other. For example, if the circuit on the mechanical side is a damper to ground with resistance R_m, the electrical impedance at the terminals of the electromechanical transduction component is B^2L^2/R_m.

2. The diaphragm
    - This is usually a lightweight rigid mechanical surface adjacent to the acoustical medium to which energy is to be transduced. The element obeys the transduction law $U = S_d\dot{x}$. This law describes how the flux of the acoustical side, U, is related to the potential of the mechanical side, $\dot{x}$, by the transduction coefficient S_d;
    - Physically S_d is the radiating area of the diaphragm that may be considered constant only at low frequencies while the diaphragm moves rigidly;
    - The law can be equivalently written in terms of the acoustical potential, p, and the mechanical flux, F, as $F = S_d p$;
    - Taking the ratio of these two laws provides an expression that describes how an impedance on one side of the transduction appears from the other, $S_d^2 Z_a = Z_m$. The transduction in this case is said to be reciprocal as impedance in one domain is transferred to impedance in the other. For example, if the circuit on the acoustical side is composed of an acoustical mass, M_a, the mechanical impedance of the transduction component is $S_d^2 M_a$.

Also included in the circuit shown in figure 2.1 are three impedances, one in each of the domains. The positions of these impedances are typical for the majority of loudspeakers; however, for certain special cases the arrangement may be slightly different. In the electrical domain, the impedance Z_{eb} is shown in series with the input to the electromechanical transaction component.

This electrical impedance is commonly called the blocked electrical impedance and is the electrical impedance of the voice coil when the mechanical side of the transducer is blocked and the voice coil is held stationary, defined as

$$Z_{eb} = \left. \frac{V}{I} \right|_{\dot{x}=0} \qquad 2.1.$$

In the mechanical domain, the impedance Z_{md} is shown as a parallel branch connecting the both the electromechanical and mechanoacoustical transaction steps to ground. Implicit to this topology is that the voice coil and diaphragm are mechanically rigidly coupled and move with the same velocity, $\dot{x}$. At high frequencies, where some non-rigid motion may occur between or in the voice coil and diaphragm, or for the rare case of a loudspeaker designed with a compliant mechanical link between voice coil and diaphragm, a more complex mechanical model is required including some mechanical impedance in series between the electromechanical and mechanoacoustical transduction steps. The mechanical impedance as shown is commonly called the open-circuit mechanical impedance and is the mechanical impedance of the moving parts of the loudspeaker without any loading from the electrical or acoustical parts of the circuit, defined as

$$Z_{md} = \left. \frac{F}{\dot{x}} \right|_{I=0,\, p=0} \qquad 2.2.$$

In the acoustical domain, the impedance Z_{ar} is shown between the mechanoacoustical transduction stage and ground. This acoustical impedance is commonly called the acoustical radiation impedance and is the acoustical impedance of the acoustical part of the circuit when there is no loading from the mechanical domain, defined as

$$Z_{ar} = \left. \frac{p}{U} \right|_{F=0} \qquad 2.3.$$

It is very common practice to transform the acoustical radiation impedance into an equivalent mechanical impedance using the transformation

$$Z_{mr} = Z_{ar} S_d^2 \qquad 2.4.$$

where Z_{mr} is referred to as the mechanical radiation impedance. This transformation allows the simpler circuit shown in figure 2.2 to be used.

More generally, this transformation can be considered in a different way using a new mechanical impedance, Z_{ms}, the system mechanical impedance, defined as

$$Z_{ms} = \left. \frac{F}{\dot{x}} \right|_{I=0} \qquad 2.5.$$

Note that, compared to the expression for Z_{md}, p is not defined to be zero.

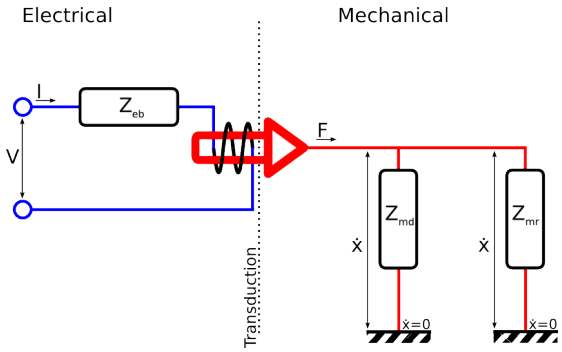

Figure 2.2. Simplified circuit representation of a generic electromagnetic loudspeaker after transformation of the acoustical radiation impedance into the mechanical domain.

Whereas Z_{md} is the mechanical impedance of the mechanical parts alone without the influence of the acoustical domain, Z_{ms} includes the acoustical effects. This is a useful generalisation as it encourages one to think of the mechanoacoustical system as intimately coupled rather than as two separate domains. The definition of Z_{ms} in this way allows the easy extension of the lumped parameter approach to more complex mechanical and acoustical systems.

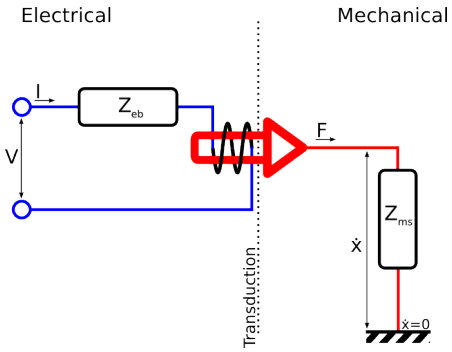

Figure 2.3. Further simplified circuit representation of a generic electromagnetic loudspeaker using the system mechanical impedance Z_{ms} .

For the simple diaphragm transducer model it is possible to write the system mechanical impedance as

$$Z_{ms} = Z_{md} + Z_{mr} \qquad 2.6.$$

Traditional analysis of loudspeaker lumped model, such a that by Olsen [7] and in the works of Thiele [8,9] and Small [10,11,12,13,14,15,16], commonly take the impedance transformation approach a step further and transform all components into the electrical domain. The relevance of this is primarily historical: much of the early analysis of loudspeakers was performed on behalf of radio-set manufacturers by electrical engineers who were most used to working in the electrical domain. Additionally, the transformed

electrical circuit could be built using the transformed component values and could then be analysed using electrical circuit equipment such as signal generators and oscilloscopes. At the time, well before computers were available to calculate the lumped model behaviour, this was the simplest means of generating bode response graphs for specific lumped systems. This approach is not encouraged by the author as it is not useful to think of the whole loudspeaker system in terms of isolated lumped electrical components: while this is a reasonably good approximation for the components that exist in the electrical domain it is a poor starting point for considering the mechanical and acoustical parts of the loudspeaker that act in a more complex manner in all but most rudimentary of models. The presence of the electromechanical transduction usefully demarcates where the lumped component approach drops significantly in accuracy.

2.2.1 Loudspeaker electrical input impedance

The electrical part of the circuit in figure 2.3, above, consists of two components connected in series, the blocked electrical impedance, Z_{eb}, and the electromechanical transduction component. The system input voltage can be described as the sum of the two voltages across each of these components, using the expressions above, as

$$V_{\text{in}} = Z_{eb} I + BL \dot{x} \qquad 2.7.$$

The force on the mechanical part of the system exerted by the electromechanical transduction component is equal to

$$F = BL I \qquad 2.8.$$

The velocity with which the mechanical system reacts when this force is applied to it is described using the system mechanical impedance

$$\dot{x} = \frac{BL I}{Z_{ms}} \qquad 2.9.$$

Inserting this expression into the description of the input voltage above, 2.7, results in an expression for the electrical input impedance of the loudspeaker,

$$Z_{es} = Z_{eb} + \frac{B^2 L^2}{Z_{ms}} \qquad 2.10.$$

2.2.2 Voltage driven loudspeaker voice coil velocity

The velocity of the mechanical side of the electromechanical transduction component as a function of the electrical current flowing in the electrical side of the circuit is given by

expression 2.9. However, the majority of loudspeakers are driven by low output impedance voltage amplifiers. In this case, it is more useful to write the mechanical drive point velocity in terms of the loudspeaker input voltage. This is relatively straightforward as the electrical input impedance that was outlined above, expression 2.10, can be used to determine the electrical current, I, flowing in the voice coil due to the input voltage, V. Substituting this into expression 2.9 provides an expression for the mechanical drive point velocity in terms of the loudspeaker input voltage as

$$\frac{\dot{x}}{V}=\frac{BL}{Z_{ms}Z_{eb}+B^2L^2} \qquad 2.11.$$

It is instructive to extract the Z_{eb} term in the denominator, using the blocked electrical admittance $Y_{eb}=Z_{eb}^{-1}$ for conciseness, this results in the expression

$$\frac{\dot{x}}{V}=\frac{BLY_{eb}}{Z_{ms}+B^2L^2Y_{eb}} \qquad 2.12.$$

This expression is quite revealing. When a voltage source is applied to the loudspeaker terminals it can be considered that the mechanical parts are driven with a force equal to $VBLY_{eb}$ and, assuming that the blocked electrical impedance Z_{eb} is predominantly resistive, that there is an effective additional mechanical damper fixed between the mechanical drive point and mechanical ground of magnitude $B^2L^2Y_{eb}$. Physically this is due to the induced electromotive force (EMF) that is generated by the motion of the voice coil in the magnetic gap. This induction is often called the “back EMF”.

2.2.3 Loudspeaker efficiency

The efficiency of a loudspeaker is defined as the useful power output as a proportion of the total power input. The input impedance of a loudspeaker was given in expression 2.10, expanding the Z_{ms} term as the sum of the open-circuit mechanical impedance of the diaphragm, Z_{md}, and the mechanical radiation impedance, Z_{mr}, results in

$$Z_{es}=Z_{eb}+\frac{B^2L^2}{Z_{md}+Z_{mr}} \qquad 2.13.$$

The dissipative part of the electrical impedance is represented by the real part of this complex expression, given by

$$\Re\left(Z_{es}\right)=\Re\left(Z_{eb}\right)+\frac{B^2L^2\Re\left(Z_{md}\right)}{\left|Z_{md}+Z_{mr}\right|^2}+\frac{B^2L^2\Re\left(Z_{mr}\right)}{\left|Z_{md}+Z_{mr}\right|^2} \qquad 2.14.$$

As the purpose of the loudspeaker is to convert energy into an acoustical form it shall be assumed that all of the power that is dissipated into the acoustical domain is useful power output. This may not always be the case. For example, acoustical output that is subsequently dissipated by absorbent material inside the loudspeaker cabinet may not be considered to be useful. However, in this case, the $\Re\left(Z_{mr}\right)$ term represents the useful power output and the efficiency, η, can be written as

$$\eta = \frac{\Re\left(Z_{mr}\right)}{\frac{\Re\left(Z_{eb}\right)}{B^2 L^2}\left|Z_{md}+Z_{mr}\right|^2+\Re\left(Z_{md}\right)+\Re\left(Z_{mr}\right)} \qquad 2.15.$$

or slightly more compactly as

$$\eta = \frac{\Re\left(Z_{mr}\right)}{\frac{\Re\left(Z_{eb}\right)}{B^2 L^2}\left|Z_{ms}\right|^2+\Re\left(Z_{ms}\right)} \qquad 2.16.$$

This expression for transducer efficiency, written in terms of electrical impedance, has been widely used [7,p.126][17][18,p.405].

2.2.4 Nominal efficiency

In addition to the true efficiency described above, it is sometimes common to use “nominal efficiency” defined as the useful power output as a proportion of the power dissipated by a resistor of the same magnitude as the voice-coil resistance. The power output of the loudspeaker, with the same assumptions regarding Z_{mr} that were made above, is given by

$$P_{out} = \frac{\Re\left(Z_{mr}\right)}{2}\left|\dot{x}\right|^2 \qquad 2.17.$$

In terms of the input voltage, the power output is given as

$$P_{out} = \frac{\Re\left(Z_{mr}\right)}{2}\left|\frac{V\,BL}{Z_{ms}Z_{eb}+B^2L^2}\right|^2 \qquad 2.18.$$

The power dissipated by a resistance equal to $\Re\left(Z_{eb}\right)$ is

$$P_{nom} = \frac{\left|V\right|^2}{2\Re\left(Z_{eb}\right)} \qquad 2.19.$$

Dividing the output power by this “nominal input power” results in the definition for the nominal loudspeaker efficiency

$$\eta_{nom} = \frac{B^2 L^2 \Re\left(Z_{mr}\right) \Re\left(Z_{eb}\right)}{\left|Z_{eb}\right|^2} \left| \frac{1}{Z_{ms} + B^2 L^2 / Z_{eb}} \right|^2 \qquad 2.20.$$

“Nominal efficiency” was popularised, although not first used [6], by Small in his seminal papers on loudspeaker efficiency and alignment. He outlines this definition in the first of the series [10]. The motivation for this alternative method of considering the efficiency is that it is normal for a loudspeaker to be driven with an electrical voltage source. The true efficiency, η, of a loudspeaker is extremely high at any resonance of the mechanical system because the system mechanical impedance, Z_{ms}, becomes very small. However, when driven with a voltage source, this high efficiency does not result in an increased output power, but rather a decreased power input: the damping effect of the back EMF manifests itself as a large peak in the electrical input impedance. The efficiency at this peak is of little significance to designs intended for use with voltage sources. The nominal efficiency definition ignores the motional part of the electrical impedance and, as a result, the nominal efficiency has the same response shape as the power output of the voltage-driven loudspeaker. The nominal efficiency expression, equation 2.20, naturally falls into the product of a response magnitude function, on the right hand side, and an efficiency term, on the left. For most loudspeakers the efficiency term on the left is approximately invariant of frequency. This was an important step in Theile and Small's work in using filter theory to describe loudspeaker behaviour and alignment: the efficiency term is a parallel concept to sensitivity ratio as used in filter analysis.

2.2.5 Standard low-frequency impedance models

The loudspeaker behavioural equations have been derived hitherto in terms of three abstract circuit impedances, Z_{eb}, Z_{md} and Z_{mr}. The standard lumped parameter models that are commonly used to mimic the behaviour of a conventional electromagnetic loudspeaker at low frequencies are outlined in this section. The third of these impedances, Z_{mr}, is discussed in the following chapters as its nature depends on the type of loudspeaker under consideration.

Figure 2.4 shows a cross section through a generic paper cone low-frequency driver, the type of loudspeaker shown is very common in high-fidelity and professional applications. Although other shapes of diaphragm, magnet system arrangements and suspension locations are commonly found, for the vast majority of loudspeakers, the general arrangement of parts

is the same as shown in the figure below. Thus, for the vast majority of electromagnetic loudspeakers, the same low-frequency approximations for Z_{eb} and Z_{md} can be used.

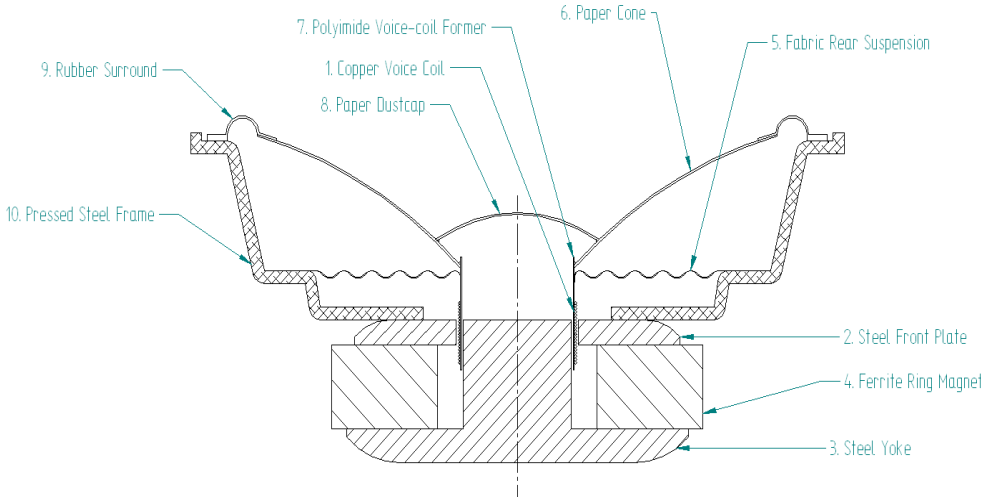

Figure 2.4. Cross section of a paper-cone low-frequency electromagnetic loudspeaker.

Blocked electrical impedance models

Referring to figure 2.4, the motor system of the loudspeaker consists of one or more permanent magnets that are glued to accompanying steel parts to form a magnetic circuit between the poles of the magnets. This circuit is broken only at a very narrow annular gap where the loudspeaker voice coil is located. This arrangement results in a concentrated magnetic field passing radially through the voice-coil wire such that when a current passess through the voice-coil wire, a mechanical force equal to BLI is generated on the voice coil. Typically, with a high-quality loudspeaker, the magnet system and voice coil are designed so that for moderate displacements the transduction coefficient, BL, does not change with too much severity. The arrangement shown in figure 2.4 is referred to as a short-gap, long-coil layout. Only part of the voice coil is positioned in the area of highest magnetic flux such that when some of the windings move axially out of the gap, others move into the other end of the gap and the BL remains approximately constant. The voice coil itself is a closely wound coil of wire supported on a cylindrical member known as the former. The very simplest model used for the blocked electrical impedance, Z_{eb}, uses only a lumped resistance equal to the resistance of the wire in the coil windings, R_e, and is written as

$$Z_{eb} = R_e \qquad 2.21.$$

Although extremely simple, this model is regularly used, particularly because it is simple to estimate the voice-coil resistance when designing the voice coil and it is a reasonably accurate approximation for loudspeakers that are only to be used at low frequencies. In

reality, the blocked impedance also has a significant inductive contribution because of the turns of the voice coil and the surrounding magnetically permeable media. In its simplest form this is approximated, in the impedance Z_{eb}, as the series combination of a resistor, R_e equal to the wire resistance of the coil, and an inductance, L_e, written as

$$Z_{eb} = R_e + j\omega L_e \qquad 2.22.$$

The inductive characteristic of the blocked electrical impedance reduces the loudspeaker output at high frequencies. For some designs, this output reduction is problematic and is one of the factors that necessitates the use of small diameter voice coils, with few turns, on designs intended to work to the top end of the audio bandwidth.

However, in reality the inductive rise of the voice coil does not follow the exact $j\omega L_e$ form of the ideal inductor, but instead has a somewhat slower rise and hence it is often called a semi-inductance. This semi-inductance results from the electromagnetic interaction between the voice coil and the magnet system. Some of the magnet system regions, such as the steel, are electrically conductive and, consequently, as the electrical current flows in the voice-coil electrical current is induced in these regions. These induced currents are commonly called eddy currents. The eddy current flow direction naturally opposes the flow of the voice coil and thus tends to reduce the apparent inductance of the voice coil. The induction of the eddy currents occurs by electromagnetic coupling, in the same way as an electrical transformer operates. The various magnet system regions have different magnetic permeabilities, depending on their material and magnetic saturation, and this alters the effectiveness of the eddy current coupling and also the direct inductance of the voice coil itself. Additionally, as the various regions lie at different distances from the voice coil and the depth to which the eddy currents are induced is frequency dependent, the corresponding voice-coil impedance characteristic can be quite complex. There are many lumped models for the blocked electrical impedance that are used as a better fit to this semi-inductance [19,20,21]. However, few of these are based on the physical situation and, consequently, the parameters of these models have no physical significance. The most established of these is the “LR2” model that includes an additional resistor and inductor as shown in figure 2.5.

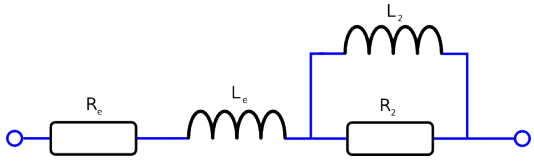

Figure 2.5. LR2 blocked electrical impedance.

The electrical impedance of the LR2 model is given by the expression

$$Z_{eb} = R_e + j\omega L_e + \frac{j\omega L_2 R_2}{R_2 + j\omega L_2} \qquad 2.23.$$

Despite not giving the best match with real measurements compared to other Z_{eb} models, the LR2 model is widely used as it is easy to implement in circuit simulation software and, because it can be written in the time domain, it may be used in non-linear lumped modelling [22].

Diaphragm mechanical impedance models

The diaphragm mechanical impedance, Z_{md}, describes the mechanical behaviour of the moving parts of the loudspeaker when there is no coupling from either the electrical transduction step nor the acoustical transduction. Referring to figure 2.4, the mechanical system is composed of parts that are intended to remain rigid and move together, such as the diaphragm itself, the voice coil and the former, and parts that are intended to allow the rigid parts to move axially when a force is applied, but to prevent them from moving in other directions, such as the suspension and surround. The standard lumped model that is used to mimic this arrangement is a mass supported by a stiffness and resistance as depicted in figure 2.6.

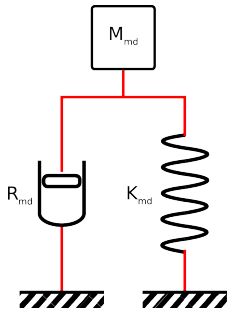

Figure 2.6. Simple lumped model of the driver mechanical parts.

The diaphragm mechanical impedance, Z_{md}, for this standard representation is given by the expression

$$Z_{md} = j\omega M_{md} + R_{md} + \frac{K_{md}}{j\omega} \qquad 2.24.$$

The lumped mass of the system, M_{md}, is the summed mass of all the rigid parts. Similarly, the lumped stiffness, K_{md}, and lumped resistance, R_{md}, is the sum of the stiffness and resistance of all the supporting parts. In practice, the M_{md} appears to be slightly higher than the combined mass of the rigid parts because there is a small, but significant, mass

contribution from the flexible parts, such as the suspension and surround. If this is accounted for, by estimation, the lumped M_{md} can be predicted relatively accurately from the loudspeaker part masses (from measurement or drawings). The stiffness, K_{md}, and resistance, R_{md}, are more difficult to predict without more detailed modelling. It is common in loudspeaker engineering to use the mechanical compliance, the inverse stiffness. This is primarily historical and due to the fact that if using a force-current analogous circuit the stiffness transforms into a reciprocal inductance.

2.3 Direct-radiating loudspeakers

Direct-radiating loudspeakers use the diaphragm to radiate directly into the environment where the listener is located without any other acoustical devices in the radiation path. The majority of loudspeakers designed for use in domestic environments are direct radiating. To illustrate the typical behaviour of a direct-radiating loudspeaker, a rigid piston in an infinite baffle is used to model the radiating behaviour. This infinite-baffle mounted piston is a common model for the mechanical radiation impedance, Z_{mr}, of a loudspeaker which can be expressed as

$$Z_{mr}=\rho_0 c_0 \pi a^2\left[R_1(2ka)+ jX_1(2\mathrm{ka})\right] \qquad 2.25.$$

where

$$R_1(x)=1-\frac{2J_1(x)}{x} \qquad 2.26.$$

and

$$X_1(x)=\frac{2H_1(x)}{x} \qquad 2.27.$$

In this expression ρ_o is the equilibrium density of the acoustical medium, c_0 is the speed of sound in the acoustical medium, a the piston radius and k the wavenumber. $J_1(x)$ is a Bessel function of the first kind [23, p.27] and $H_1(x)$ the first-order Struve function [24, §12.1]. This expression was first given by Rayleigh [25, Vol.2 p162]. In a previous publication, he mentions that the calculation technique was suggested to him by Maxwell [26, p. 102]. The derivation of this expression is described in this notation by Kinsler and Frey [18, pp.185-187].

At low frequencies ($ka \ll 1$), the radiation impedance of the baffle mounted piston can be approximated by the expression

$$Z_{mr}\approx\rho_0 c\pi a^2\left[\frac{(ka)^2}{2}+ j\frac{8ka}{3\pi}\right] \qquad 2.28.$$

The imaginary part of this expression is equivalent to the impedance of a mass of magnitude

$$M_{mr} = \rho_0 S_d \frac{8a}{3\pi} \qquad 2.29.$$

and the radiation resistance is

$$R_{mr} = \rho_0 S_d^2 \frac{\omega^2}{2\pi c} \qquad 2.30.$$

Combining these low frequency approximations with the standard mechanical diaphragm impedance model, described in section 2.2.5, provides an expression for the system mechanical impedance, Z_{ms}, which can be written as

$$Z_{ms} = j\omega M_{ms} + R_{ms} + \frac{K_{ms}}{j\omega} \qquad 2.31.$$

where

$$M_{ms} = M_{md} + M_{mr} \qquad 2.32.$$

$$R_{ms} = R_{md} + R_{mr} \qquad 2.33.$$

and

$$K_{ms} = K_{md} \qquad 2.34.$$

This approximation of the acoustical load on the mechanical system is reasonable because in the case of a direct-radiating loudspeaker the mechanical radiation impedance is typically a factor of ten smaller than the diaphragm mechanical impedance.

The system mechanical impedance, Z_{ms}, can also be written in terms of two normalised parameters: the mechanical system natural frequency, ω_s, and the mechanical system Q-factor, Q_{ms}, defined as

$$\omega_s^2 = \frac{K_{ms}}{M_{ms}} \quad \text{and} \quad Q_{ms} = \omega_s \frac{M_{ms}}{R_{ms}} \qquad 2.35.$$

Using these two parameters, the system mechanical impedance is

$$Z_{ms} = \omega_s^2 M_{ms} \left[\frac{j\omega}{\omega_s^2} + \frac{1}{Q_{ms}\omega_s} + \frac{1}{j\omega} \right] \qquad 2.36.$$

Pressure response

The far-field complex pressure radiated by a rigid axially moving piston mounted in an infinite baffle is given by the expression [18, p. 182]

$$p_{far}(r,\theta) = j\omega \dot{x} \frac{\rho_0 S_d}{2\pi r} \left[\frac{2J_1(ka\sin\theta)}{ka\sin\theta} \right] e^{-jkr} \qquad 2.37.$$

The term in the square brackets describes the directivity of the piston source, which is dependent upon the angle of observation from the piston axis, θ. This directivity term is unity on-axis with the piston. From this it is clear that if the piston moves with a constant acceleration amplitude the axially radiated pressure response is even at all frequencies. The axial pressure response of the direct-radiating loudspeaker based on this radiation model may be written, with the help of expression 2.12, as

$$p_{ax}(r) = BL\,S_d \frac{\rho_0}{2\pi r}\left[\frac{j\omega V}{Z_{ms}Z_{eb} + B^2L^2}\right]e^{-jkr} \qquad 2.38.$$

Choosing a simplified resistive blocked impedance, $Z_{eb} = R_e$, as described in section 2.2.5, and inserting the system mechanical impedance outlined above, the pressure response of the loudspeaker is

$$p_{ax}(r) = \frac{\rho_0}{2\pi r}\frac{S_d}{M_{ms}}\frac{BL}{R_e}\left[V.\frac{\dfrac{\omega^2}{\omega_s^2}}{\dfrac{\omega^2}{\omega_s^2} - \dfrac{j\omega}{Q_{ms}\omega_s} - \dfrac{j\omega B^2L^2}{R_e\omega_s^2 M_{ms}} - 1}\right] \qquad 2.39.$$

The damping effect of the back emf can, similarly to the mechanical damping effect, be written as a Q-factor, Q_{es}, defined as

$$Q_{es} = \omega_s \frac{M_{ms}R_e}{B^2L^2} \qquad 2.40.$$

Using this parameter, the axial pressure response of the direct radiating loudspeaker can be written

$$p_{ax}(r) = \frac{\rho_0}{2\pi r}\frac{S_d}{M_{ms}}\frac{BL}{R_e}\left[V.G\left(\frac{j\omega}{\omega_s}\right)\right] \qquad 2.41.$$

where

$$G(s) = \frac{s^2}{1 + s/Q_{ts} + s^2} \qquad 2.42.$$

and

$$Q_{ts} = \frac{Q_{es}Q_{ms}}{Q_{es} + Q_{ms}} \qquad 2.43.$$

The expression for the pressure response of the direct-radiating loudspeaker in equation 2.41 is in a very useful form, the shape of the frequency response is described by the second order

high pass function $G(s)$ and the voltage sensitivity is given by the other terms on the left of the expression. This reveals the useful observation that, above the natural frequency of the system mechanical impedance, the direct-radiating loudspeaker has an approximately flat response. Figure 2.7 shows the magnitude of the response function plotted for several different values of Q_{ts}. From the figure it is observed that a very low value of Q_{ts} results in a reduction in the output close to the loudspeaker natural frequency whereas an overly high value of Q_{ts} results in a peaking in the response close to the loudspeaker natural frequency. A Q_{ts} of $1/\sqrt{2}$ gives a high-pass frequency response that has the maximum low-frequency extension without any peaking, this type of response is known as a Butterworth alignment [27].

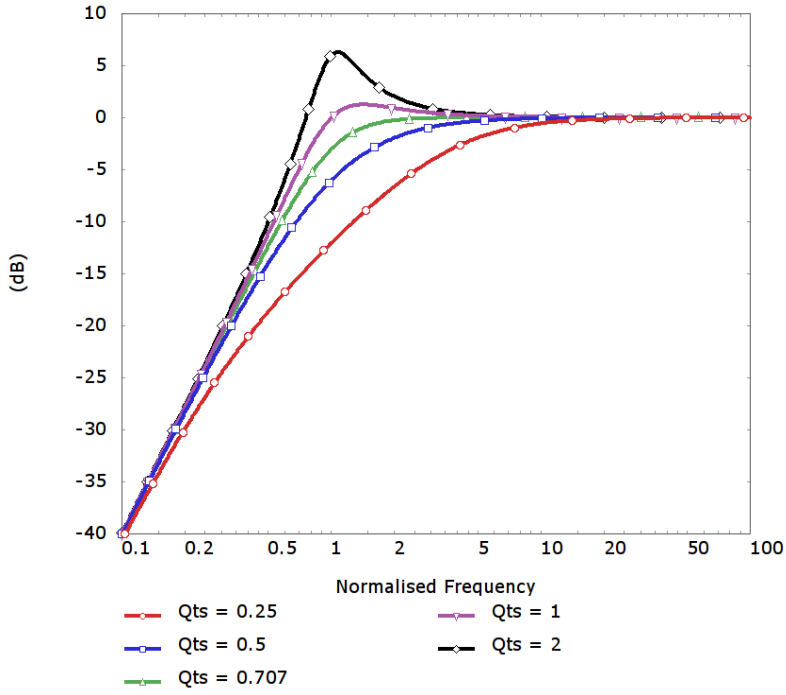

Figure 2.7. Direct-radiating loudspeaker response function $|G(jx)|$ *plotted for different values of* Q_{ts}.

The voltage sensitivity term is also instructive. From this it is clear to see that if the ratio S_d/M_{ms} can be increased then the loudspeaker sensitivity is improved. Similarly, an increase in the ratio BL/R_e results in an increase in the voltage sensitivity. However, changes to these ratios have other effects. In practice, it becomes very difficult to maximise the ratio S_d/M_{ms} as this requires that the mass per unit area of the diaphragm be minimised, a goal that at some point compromises the structural rigidity of the diaphragm. An increase of the ratio BL/R_e not only necessitates a larger, more expensive magnet system, but also inevitably results in a decrease in the Q_{es}, as defined in 2.40, and correspondingly a decrease in the Q_{ts}

that ultimately leads to an undesirable over-damped response function. Thus, in practice, these constraints restrict the voltage sensitivity achievable with direct-radiating designs.

Power response

As previously outlined in section 2.2.4, the power output of the loudspeaker can be described in terms of the input voltage using the expression

$$P_{out} = \frac{\Re(Z_{mr})}{2} \left| \frac{V\,BL}{Z_{ms} Z_{eb} + B^2 L^2} \right|^2 \qquad 2.44.$$

Note that the factor 2 in the denominator of this expression is present because the complex amplitudes in the circuit are defined to be peak amplitudes. Using the same model for Z_{eb} and Z_{ms} as was used above to describe the axial pressure response, the power output can be written

$$P_{out} = \frac{\Re(Z_{mr})}{2\omega^2} \frac{1}{M_{ms}^2} \frac{B^2 L^2}{R_e^2} \left| V\,G\left(\frac{j\omega}{\omega_s}\right) \right|^2 \qquad 2.45.$$

The real part of the mechanical radiation impedance, the mechanical radiation resistance $\Re(Z_{mr})$, of the baffle mounted piston was given in expression 2.25. Using this mechanical radiation resistance, after a little manipulation, the power response expression can be written in terms of the far field axial pressure response, as defined in expression 2.41, as

$$P_{out} = \frac{2\pi R_1(2ka)}{\rho_0 c k^2 a^2} \left| r\, p_{ax}(r) \right|^2 \qquad 2.46.$$

In this expression the function R_1 was defined in equation 2.26. Figure 2.8 shows a logarithmic plot of the function $2R_1(2ka)k^{-2}a^{-2}$, taken from the first term of the power output expression above. From this it is clearly seen that at frequencies greater than $ka = 1$, compared to the axial pressure response of the loudspeaker, the power response falls. This fall in power tends to an asymptotic rate of -6dB per octave. By implication, this means that, while the axial pressure response of the direct radiating loudspeaker may be approximately flat over a wide bandwidth, the response drops off in other directions once frequency is above $ka = 1$.

The directional response of a infinite baffle mounted rigidly moving piston in the far field relative to the axial pressure is given given by the expression [18, p.182]

$$H(\theta) = \frac{2J_1(ka\sin\phi)}{ka\sin\phi} \qquad 2.47.$$

This directivity function is plotted at increments of 15 degrees from the piston axis in figure 2.9. The increasing directivity is clearly seen with the responses furthest off axis dropping most rapidly as *ka* increases. In addition there are clear nulls visible in the off-axis responses indicating lobeing behaviour in the polar response at high frequencies.

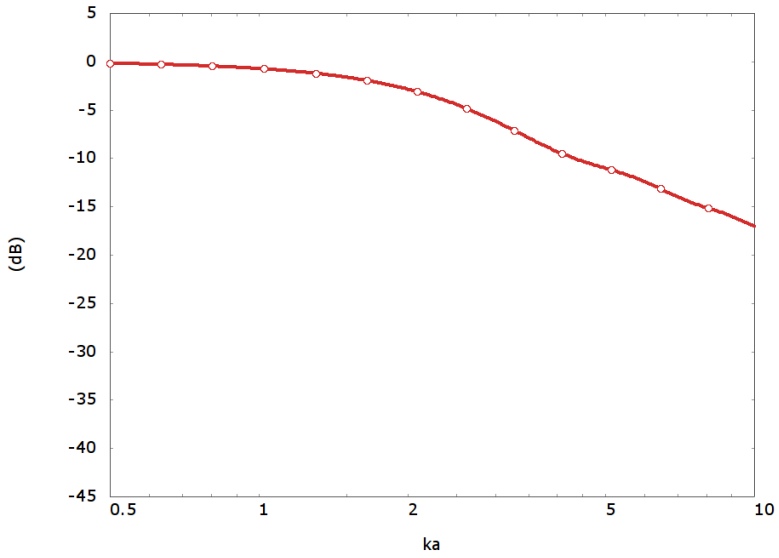

Figure 2.8. Bode response plot of the function $2R_1(2ka)k^{-2}a^{-2}$*, plotted in dB power relative to unity versus normalised frequency, ka.*

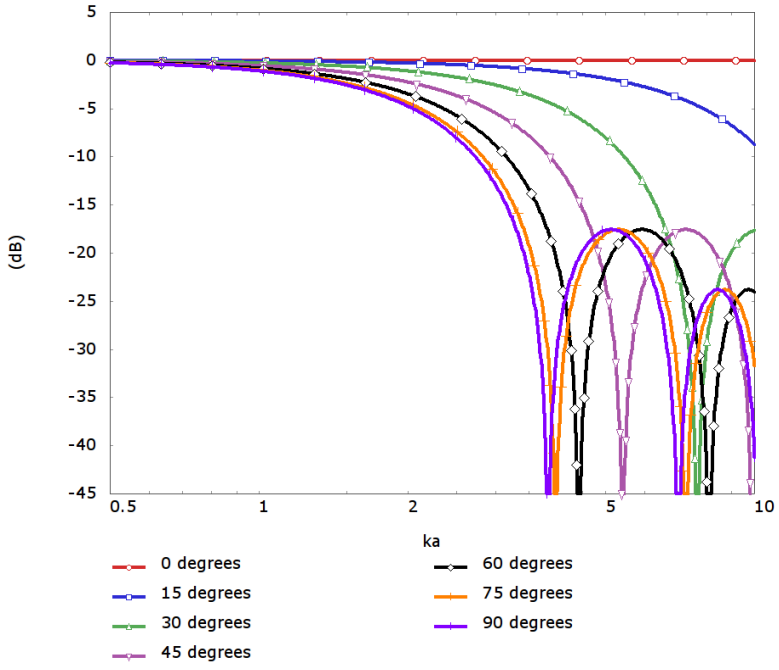

Figure 2.9. Infinite baffle mounted piston far-field response magnitude relative to axial pressure.

Diaphragm excursion

The diaphragm peak motion, or excursion, is a important consideration when designing a loudspeaker driver as the mechanical parts must allow enough motion to produce the required acoustical radiation levels while remaining intact and hopefully reasonably linear. The excursion of the diaphragm is easily derived using the expressions outlined above as

$$x = \frac{1}{M_{ms}} \frac{BL}{R_e} \left[V . \frac{G(j\omega/\omega_s)}{-\omega^2} \right] \qquad 2.48.$$

This reveals that, unlike the pressure response, which exhibits a high-pass characteristic, the diaphragm excursion has a low pass characteristic, with the diaphragm moving most at low frequencies and reducing above the natural frequency of the system mechanical impedance. Additionally, it is observed that the magnitude of the excursion is to a first approximation invariant to the diaphragm radiating area. More precisely, there is a slight dependence as the mechanical system moving mass, M_{ms}, has a small dependence upon the diaphragm surface area, S_d, as demonstrated at the beginning of this section. Figure 2.10 shows the variation of diaphragm excursion with frequency for loudspeakers with various values of Q_{ts}. In this figure the displacement amplitude is normalised by $BLM_{ms}^{-1}\omega_s^{-2}R_e^{-1}$ and ω/ω_s is set as the abscissa.

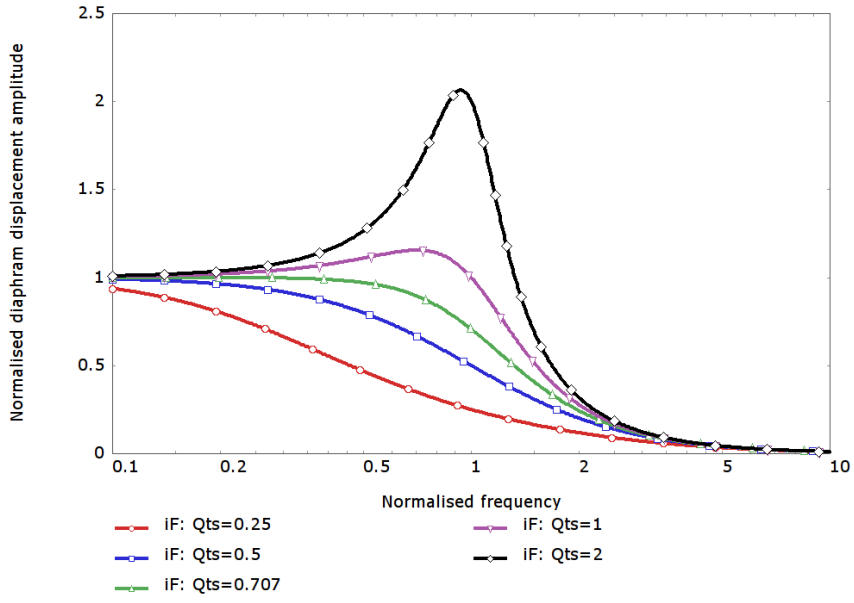

Figure 2.10. Diaphragm normalised displacement amplitude versus normalised frequency.

Sensitivity and efficiency

A well-designed direct-radiating loudspeaker frequency response has an approximately flat pass-band axial pressure and power response below $ka=1$. In this region the pressure voltage-sensitivity of the loudspeaker, given by the first few terms of expression 2.41, is

$$p_{sens}=\frac{\rho_0}{2\pi}\frac{S_d}{M_{ms}}\frac{BL}{R_e} \qquad 2.49.$$

This sensitivity value determines the pass-band pressure amplitude measured at 1m on axis with the loudspeaker when a voltage signal of amplitude 1v is applied to the loudspeaker terminals. Similarly the power voltage-sensitivity can be similarly written as

$$P_{sens}=\frac{\rho_0}{2c_0 2\pi}\frac{S_d^2}{M_{ms}^2}\frac{B^2L^2}{R_e^2} \qquad 2.50.$$

This sensitivity value determines the pass band power output when a voltage signal of 1v is applied to the loudspeaker terminals. Note that there is an additional factor of 2 in the denominator compared to the definition given by Small [10, p. 187] that is present as, with the convention outlined in section 2.1, voltage amplitude is a peak amplitude.

As discussed in section 2.2.3, there are several different definitions of efficiency that are commonly used for loudspeakers. In the pass band of the loudspeaker the input power is approximately

$$P_{\text{in}}=\frac{|V|^2}{2R_e} \qquad 2.51.$$

and the pass-band efficiency is simply

$$\eta_{pass}=\frac{\rho_0}{2\pi c}\frac{S_d^2}{M_{ms}^2}\frac{B^2L^2}{R_e} \qquad 2.52.$$

Assuming that the system natural frequency is somewhat below $ka=1$ and the Q_{ts} is close to $1/\sqrt{2}$, this is a meaningful single value that describes the useful efficiency of the loudspeaker in the pass band. As was discussed in section 2.2.4, nominal efficiency is commonly used: ratio of the power output compared to the power input to a resistor of resistance R_e. Small uses this definition in his paper on direct-radiating loudspeakers [10] and, using the low frequency approximation for $\Re(Z_{mr})$ given in equation 2.28, he provides an expression for efficiency that includes the high-pass response shape that was introduced in equation 2.42

$$\eta_{small}=\frac{\rho_0}{2\pi c}\frac{S_d^2}{M_{ms}^2}\frac{B^2L^2}{R_e}\left|G\left(\frac{j\omega}{\omega_s}\right)\right|^2 \qquad 2.53.$$

Slightly more accurately, the nominal efficiency can be written without the low-frequency approximation of $\Re(Z_{mr})$ as

$$\eta_{nom}=\frac{2R_1(2ka)}{k^2a^2}\frac{\rho_0}{2\pi c}\frac{S_d^2}{M_{ms}^2}\frac{B^2L^2}{R_e}\left|G\left(\frac{j\omega}{\omega_s}\right)\right|^2 \qquad 2.54.$$

Finally the full efficiency for the loudspeaker considered here, including the reduction in the input power at the loudspeaker system resonance, ignored by the preceding definitions, is

$$\eta=\frac{2R_1(2ka)}{k^2a^2}\frac{\rho_0}{2\pi c}\frac{S_d^2}{M_{ms}^2}\frac{B^2L^2}{R_e}\left|G\left(\frac{j\omega}{\omega_s}\right)\right|^2\left(1+\frac{1}{\omega_s Q_{es}}\frac{1}{\left|1+Q_{ms}\left(j\omega/\omega_s+\omega_s/j\omega\right)\right|^2}\right) \qquad 2.55.$$

Figure 2.11 shows the differences between these four efficiency definitions on an example loudspeaker system with $\omega_s=0.1c/a$ ($ka=0.1$), $Q_{ts}=0.707$ and $Q_{ms}=7.07$. The plotted efficiencies are normalised by the pass-band efficiency as defined in equation 2.52. The pass band efficiency calculation, shown in red, has no frequency variation in the efficiency but does agree with the other calculations in the centre of the pass band region for this loudspeaker, between $ka=0.2$ and $ka=0.5$. Small's nominal efficiency definition, shown in blue, includes the high-pass characteristic that was seen in the power and pressure responses derived in the previous sections. The nominal efficiency calculation including the piston directivity effects, shown in green, also includes a reduction in the efficiency at $ka>1$ as the radiation beams on axis.

The full efficiency including the reduction in the power input because of the peak in the electrical input impedance, shown in purple, additionally shows a very large peak in the efficiency close to the mechanical system natural frequency. While the nominal efficiency definition is useful as it has the same response shape as the voltage-driven loudspeaker, it is important that this is not confused with the true efficiency, which is, as can be seen from figure 2.11, significantly different near the system natural frequency.

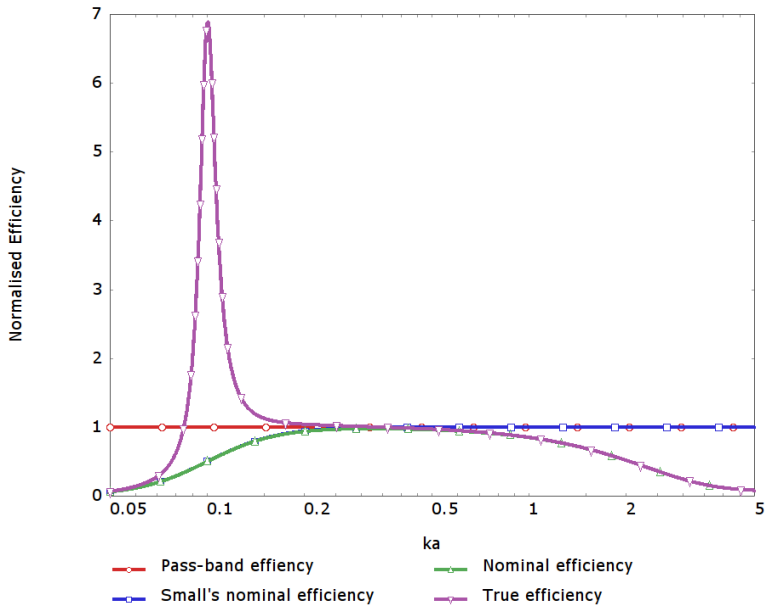

Figure 2.11. Comparison of different approximations of direct-radiating loudspeaker efficiency.

Maximum pass-band efficiency

The pass-band efficiency of the loudspeaker was above shown to be described by the expression

$$\eta_{pass} = \frac{\rho_0}{2\pi c} \frac{S_d^2}{M_{ms}^2} \frac{B^2 L^2}{R_e} \qquad 2.56.$$

This expression is composed of two ratios of physical parameters. The first is the ratio of the diaphragm area squared, S_d^2, to the diaphragm effective moving mass squared, M_{ms}^2. This ratio is determined by the physical construction of the loudspeaker mechanical parts. Loudspeakers commonly use cone- or dome-shaped diaphragms in an effort to maximise this ratio by enabling very thin materials to be formed into a reasonably stiff diaphragm. The cone and dome shapes attain their rigidity without relying on bending stiffness: resistance to deformation comes primarily from tensile and compressive stiffness in the material surface. This means that if the diameter of a diaphragm is increased in practice, it is not necessary to increase the thickness of the cone or dome by as great a proportion. Additionally, a significant part of the moving mass of the loudspeaker driver is in the voice coil and former – and the size of these parts are set by other considerations such as power handling, the BL requirement and the excursion requirement. These two effects mean that, in practice, the ratio S_d^2/M_{ms}^2 is almost invariant to driver size and is primarily a function of the motor-system design and the material and shape of the diaphragm. In practice, it is extremely

difficult to achieve a value of S_d^2/M_{ms}^2 greater than unity without seriously compromising the driver design in other areas. Similarly, the ratio B^2L^2/R_e is limited by practical constraints. An increase in the coil resistance requires the use of thinner wire that results a greater number of turns in the motor-system gap and hence a higher value of BL. Conversely, a lower coil resistance requires a larger diameter wire with fewer turns in the gap and a lower *BL*. Because of this effect, for any particular motor design and winding height, the ratio B^2L^2/R_e is almost invariant of the coil resistance. In practice, without an overly large, and heavy, voice coil and motor system the maximum attainable value of B^2L^2/R_e is approximately 30. Thus, it is very rare to find direct-radiating loudspeakers with a pass-band efficiency greater than 1%, indeed the majority of direct-radiating loudspeakers have significantly lower pass-band efficiencies, particularly, since to achieve this efficiency would almost certainly necessitate compromise in other areas of the design.

Maximum bandwidth

The pass-band efficiency expression can be equivalently written as

$$\eta_{pass} = \frac{V_{as}}{2\pi c^3}\frac{\omega_s^3}{Q_{es}} \qquad 2.57.$$

where

$$V_{as} = \rho_0 c^2 \frac{S_d^2}{K_{ms}} \qquad 2.58.$$

The parameter V_{as} represents the volume of air that, when coupled to a piston of area S_d, has the same compliance as the mechanical parts of the loudspeaker driver. The electrical Q-factor, Q_{es}, is normally dominant to the extent that $Q_{ts} \approx Q_{es}$. Thus, if the designer is aiming for an overall high-pass alignment, such as one of those shown in figure 2.7, the target for Q_{es} can be readily set. For the bandwidth of the direct-radiating loudspeaker system to be as large as possible, the natural frequency of the mechanical system, ω_s, must be as low as possible. The form of the efficiency shown in expression 2.4 highlights that in effect this requirement has a negative effect on the efficiency of the system. Effectively, this is because of the dependence of ω_s on M_{ms}. The only way that this effect can be countered for a given alignment, and corresponding value of Q_{es}, is by maximising V_{as}, making the stiffness of the mechanical system as low as possible. Obviously, there is a practical limit to how low it is possible to push the value of K_{ms} and still maintain a structurally stable mechanical system. This bandwidth trade-off is not withstanding the practical constraints on B^2L^2/R_e and S_d^2/M_{ms}^2 discussed above.

Above a frequency of $ka=1$ the power output from a direct radiating loudspeaker decreases due to the axial narrowing of the radiated pressure. Thus, a small diaphragm is preferable for reproducing high frequencies. However, the mechanical parts of the loudspeaker have a finite excursion capability and, as the axially radiated sound pressure is directly proportional to the volume *acceleration* generated by the loudspeaker, the displacement-limited maximum output capability falls with the square of decreasing frequency as

$$p_{ax,max}=S_d x_{max}\frac{-\omega^2\rho_0}{2\pi r} \qquad 2.59.$$

Thus, for maximum output at low frequencies, a large diaphragm is preferable. In effect, there is a trade-off between the maximum output capability that the loudspeaker is required to have close to ω_{ms}, where driver excursion is a maximum, and the upper limit to the driver bandwidth at $ka=1$. By increasing the maximum excursion capability of the loudspeaker, x_{max}, it is possible to offset this trade-off to some extent; however, designs with a particularly high x_{max} are inevitably expensive as they require a motor capable of driving the coil with a approximately constant *BL* over a large distance. Because of this trade-off, it is very difficult to design a single loudspeaker driver that is able to reproduce the whole audio bandwidth with sufficient output power for high-quality reproduction. For this reason, the vast majority of high-quality loudspeakers use multiple drivers of various sizes each operating in distinct bands.

2.4 Horn-loaded loudspeakers

In section 2.2.3 it was demonstrated that the efficiency of a general loudspeaker can be written in the form

$$\eta=\frac{\Re\left(Z_{mr}\right)}{\frac{\Re\left(Z_{eb}\right)}{B^2L^2}\left|Z_{ms}\right|^2+\Re\left(Z_{ms}\right)} \qquad 2.60.$$

The most effective way to increase the efficiency is by increasing the term in the numerator of this expression, $\Re\left(Z_{mr}\right)$, which is the real part of the acoustical radiation impedance or the radiation resistance. In the previous sections, direct-radiating loudspeakers have been considered and, as was outlined in section 2.3, the practical upper limit of achievable efficiency for a direct-radiating loudspeakers is roughly 1%. If higher efficiencies are required a different type of approach must be used.

Since the advent of electroacoustics, horns have been used to improve the efficiency of transducers. The physical principles of horn behaviour have been well understood for some time, with Webster's key work on the topic being published in 1919 [28]. Horn loading of the radiating diaphragm results in a significant increase in the radiation resistance at low frequencies, which, in turn, allows higher efficiencies to be achieved. In their 1924 paper [29], Hanna and Seplian were possibly the first to analyse thoroughly the behaviour of a horn loaded loudspeaker. They drew attention to the significance of the increased motional resistance experienced by the radiating diaphragm due to the presence of the horn.

The radiation from simple sources, such as the direct-radiating diaphragm, is hampered by the large volume velocities required to generate acoustical pressure change. This can be explained by considering the expansion of the wave front: the action of the source causes the acoustical particles to move outward away from the source. The movement of these particles for the simple source at low frequencies is spherical or hemispherical in nature, depending upon whether a mounting baffle is present, and the particles are moved away from the source such that they momentarily occupy a larger volume. This increase in volume is accompanied by a corresponding drop in pressure that counters the pressure associated with the propagated sound. These two pressures – the hydrodynamic, occurring because of the change in the volume occupied by the immediate acoustical particles, and the propagating pressure, associated with the sound propagation – are different in nature. The hydrodynamic pressure change is in phase with the source volume displacement; the propagating pressure is in phase with the source volume velocity. Thus, it is only the propagating pressure that carries energy away from the source. For the case of a plane-propagating wave, or a spherical wave in the far field, the hydrodynamic effect is zero because the motion of acoustical particles does not result in a change in the volume that they occupy. For example, considering the case of a pulsating spherical source of radius a, or indeed a conical horn with a pulsating spherical segment at the throat, the complex acoustical radial particle velocity, $u(r)$ at a distance r from the centre of the sphere [18, p.171] is given by the expression

$$u(r) = p(a)\frac{1}{\rho_0 c_0}\frac{a}{r}e^{-jk(r-a)} - p(a)\frac{j}{\rho_0 c_0}\frac{a}{kr^2}e^{-jk(r-a)} \qquad 2.61.$$

where $p(a)$ is the pressure at the surface of the sphere. The first of these two terms is the propagating wave and the second, the hydrodynamic effect. In the far field, when $kr \gg 1$, the first term is dominant and the second term tends to zero as the wave-front rate of expansion tends to zero. When $kr \ll 1$, the second term is dominant. The transition from the near field

to the far field may be characterised by distance at which the hydrodynamic and propagating particle velocity magnitude are equal. For the spherical source this situation occurs at

$$kr=1 \tag{2.62.}$$

At the radiator surface, $r=a$, this expression indicates the frequency above which the radiation efficiency is maximal and the majority of source volume velocity results in propagated pressure, and the minority, hydrodynamic pressure. In the context of a horn, the frequency corresponding to this condition is called the cut-on frequency, f_c. For the case of a conical horn

$$f_c=\frac{c_0}{2\pi a} \tag{2.63.}$$

However, with the conical horn the transition from hydrodynamic to propagation is very gentle.

The acoustical horn functions by controlling the wave front expansion in order to reduce the hydrodynamic pressure compared to the propagating pressure, thus allowing more energy to be radiated for a given volume velocity. The behaviour of horns for loudspeakers is very nicely covered by Holland in [30, p.30].

Horns are commonly characterised by their flare rate, $m(x)$, which is defined as

$$m(x)=\frac{1}{S(x)}\frac{dS(x)}{dx} \tag{2.64.}$$

where $S(x)$ is the horn sectional area at axial position x. The flare rate is a measure of the rate of expansion along the length of the horn. For example, the flare rate of a conical horn is given by

$$m(x)=\frac{2}{x} \tag{2.65.}$$

The exponential horn shape is commonly used and is characterised by the sectional area law

$$S(x)=S(0)e^{mx} \tag{2.66.}$$

Unlike the conical horn, the exponential horn has a constant flare rate irrespective of the radiator size. The cut-on frequency of a horn is related to the flare rate at the horn throat by the expression

$$f_c=\frac{mc_0}{4\pi} \tag{2.67.}$$

The exponential horn, with its constant flare rate, has a very sudden frequency transition from hydrodynamic dominated behaviour below f_c and propagation dominated behaviour above f_c. This transition is very sudden because above f_c the propagated pressure becomes dominant over the entire length of the horn at once.

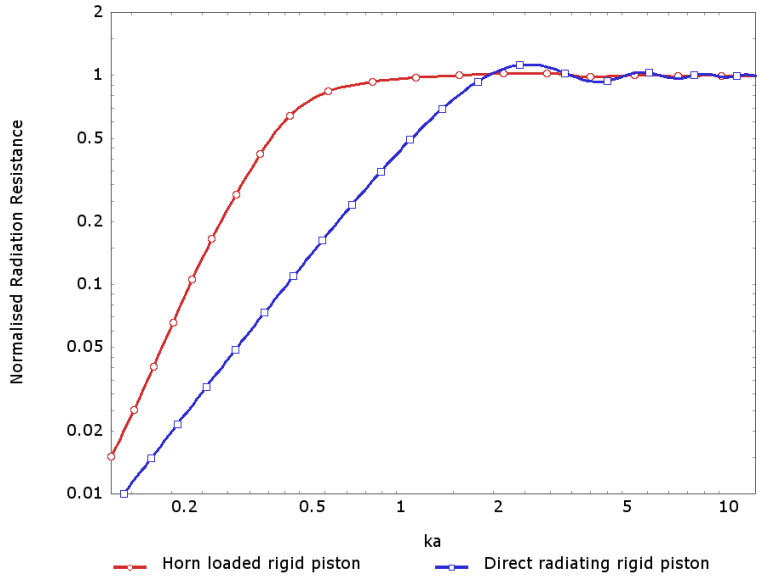

Figure 2.12. Comparison of the radiation resistance of a direct-radiating rigid circular piston with a horn loaded rigid circular piston.

Figure 2.12 shows the normalised radiation resistance of a direct-radiating rigid circular piston compared to the radiation resistance of the same diaphragm placed at the throat of a finite exponential horn. In this case, the horn is exponential, with flare rate giving a cut-on frequency of $ka=0.35$, and terminates smoothly into an infinite baffle. The radiation resistance is shown normalised to the radiation resistance of a pipe loaded rigid circular piston. An area of increased radiation resistance is clearly seen between the cut-on frequency of the horn, $ka=0.35$, and $ka=2$ where the radiation resistance of the direct radiator reaches a maximum.

The cut-on frequency of the horn is directly related to the flare rate. A low flare rate results in a low cut-on frequency, f_c. In order to create a horn with a low flare rate, it is inevitably necessary to have a physically large horn. The flare rate of an exponential horn may be equivalently written as

$$m=\frac{1}{L}\ln\left(\frac{S(L)}{S(0)}\right) \qquad 2.68.$$

where L is the physical length of the horn.

Additionally, in order to avoid reflections from the acoustical transition to the radiating environment as the propagated wave leaves the horn at the mouth, it is necessary for the horn mouth to have a circumference comparable in length to the lowest frequency to be radiated [31,32]. The result of these two requirements is that horn loudspeakers designed for low-frequency sound reproduction must be physically large. As a result of this, they are seldom used over the full audio band except in professional installations.

Horns are also useful in controlling the directivity and power output of loudspeakers. As was outlined in section 2.3, the directivity of a plane circular piston radiator is wide at low frequencies and then becomes very narrow at high frequencies. This gives the loudspeaker an uneven power response: the power output is high at lower frequencies and then falls above $ka = 2$. The directivity of a horn loudspeaker is controlled, to a great degree, by the shape of the horn walls, which may be designed to achieve the required dispersion pattern and power output. For example, the constant-dispersion type horn design is frequently used [33] and provides a near constant angle of dispersion and an approximately flat power response over a wide bandwidth, albeit with compromises in other areas, such as response smoothness.

2.4.1 Compression loading

It is possible to increase the radiation resistance of a horn-loaded loudspeaker significantly by reducing the size of the horn throat while keeping the diaphragm diameter constant. In this case, the acoustical impedance at the horn throat is increased but the transduction coefficient between the mechanical and acoustical systems, the diaphragm area, is not affected. This results in an increase of the radiation resistance by the ratio of the diaphragm area to the horn throat area. In practice, this can be achieved by joining a large diaphragm to a small horn throat using a small acoustic volume, as depicted in figure 2.13. This concept is first suggested by Hanna and Slepian, who outline and analyse the benefits of using a large diaphragm and small horn throat to increase efficiency in their 1924 paper [29]. At low frequencies, the air chamber is effectively incompressible and the volume velocity on the input side, imparted by the diaphragm, is equal to the volume velocity on the exit side, at the horn throat. As a result, compared to coupling the same diaphragm directly into an equivalent horn with larger throat diameter, the radiation resistance is increased by the ratio of the diaphragm area to the throat area. This arrangement is often referred to as a “compression driver”, the acoustical volume as the “compression chamber” and the ratio of the areas the “compression ratio”, which is denoted by α in this thesis (precisely defined in Appendix X). The caveat to this approach is that the boost in radiation resistance is only seen while the compression cavity is of insignificant volume and behaves as a simple compliance.

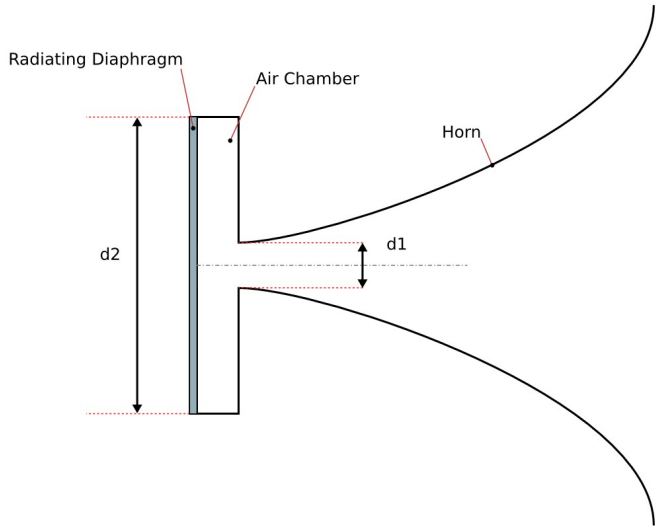

Figure 2.13. Schematic layout of a horn driver having a large diaphragm, of diameter d2, and small horn throat, of diameter d2, joined by a small acoustical volume.

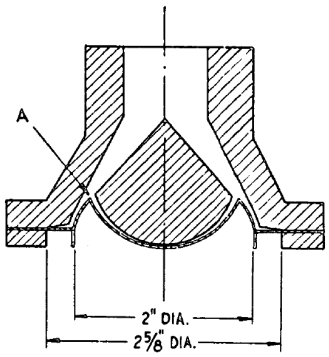

Figure 2.14. The Wente and Thuras phase plug [17] "The throat of the horn is flared annularly to the point A", note that this figure is rotated by 90 degrees anticlockwise compared with the orientation of figure 2.13.

In order to increase the frequency range of operation of the compression driver, Wente and Thuras [17] devised a "plug" to be placed in front of the radiating diaphragm. The plug keeps the effective volume of the compression cavity to a minimum. Furthermore it provides additional geometric parameters such that the design might be "tuned" in order to avoid some of the high-frequency irregularities that are encountered with the simple example above. In an appendix of the same work they describe a criterion for the design of compression drivers, relating the highest frequency of operation to the maximum difference in acoustical path from diaphragm to horn throat. This type of phase-plug design approach is commonly known as "path-length" based. The "phase plug" was subsequently patented by Wente in 1936 [34]. Significantly, with the introduction of a phase plug, the point of coupling between the horn and the cavity is moved away from the axis of rotation: the eigenfunctions of the cavity all have a maximum at the axis of rotation.

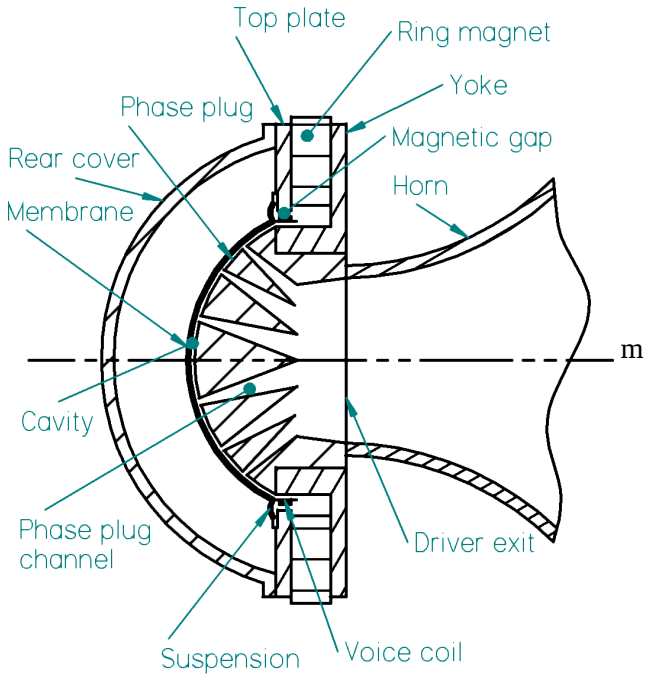

Figure 2.15. Illustration of a typical modern compression driver with three annular channels in the phase plug.

The phase plug of a modern compression driver is a complex acoustical structure. Typically, the phase plug has between two and five annular channels that lead from the compression cavity to the horn throat. The positions at which the channels meet the cavity and the arrangement of the annular channels as they are joined at the horn throat are key design factors in achieving a smooth overall driver output. In 1953, Smith [35] published a paper describing how the phase-plug channels entrances can be positioned such that the modes in the compression cavity are suppressed. This is an important piece of work in compression driver development, but, surprisingly, it was largely ignored for a number of years before becoming popularised primarily through compression drivers produced by JBL with designs using Smith's method [36]. Most modern compression drivers, by design or inheritance, are based on Smith's channel position guidelines. The majority of subsequent work on compression drivers has concentrated on the analysis and modelling of the acoustical non-linearities that occur due to the very high sound pressure levels in the compression cavity and channels during use [37][38][39]. There are some publications that outline the design of particular commercial compression drivers [40], the most recent of these with the assistance of FEM and BEM analysis [41][42][43]. However, there are no publications, subsequent to Smith, that consider the methodology for the geometric design of the phase plug.

2.4.2 Non-linearity in horn- and compression-loaded loudspeakers

For a given acoustical output in the far field, the horn-loaded and compression-loaded arrangements result in higher acoustical pressures in the regions adjacent to the driver diaphragm when compared to direct-radiating designs. The regions of high acoustical pressure are typically the compression cavity, the phase-plug channels and the horn throat. Additionally, due the their high efficiencies and directivity control, horn- and compression-loaded loudspeakers are most commonly used for high sound pressure level applications. During normal operation the acoustical pressure within the driver and horn structures can reach sufficiently high levels that acoustical non-linearity is significant and, as a result, acoustically generated non-linear distortion is observable in the output of the device. The non-linear behaviour of acoustical horns and compression drivers has been widely studied [37][38][39]. In terms of the audio performance of a loudspeaker, significant non-linearity results in an audible deterioration in the reproduction quality.

With a linear time invariant system (LTI), the system response, $y(t)$, to a sinusoidal input signal $x(t)$ with frequency of oscillation ω and complex amplitude X will take the general form

$$y(t)=Y e^{j\omega t} \qquad 2.69.$$

Id est the system response is only at the same frequency as the input signal. Y is the complex amplitude of the sinusoidal response. For a non-linear system, the response to the same single frequency input signal will result in a more complex output signal taking the general form

$$y(t)=\sum_{n=0}^{\infty} Y_n e^{jn\omega t} \qquad 2.70.$$

The system response is not a single frequency signal but will also have harmonic frequency components at integer multiples of the input frequency. Y_n is the complex amplitude of the n^{th} harmonic. The levels of the generated harmonics $Y_n(\omega)$ are commonly used to characterise the degree of distortion of the audio signal.

Loudspeakers are specifically designed to produce audio signals with reasonably low levels of non-linear distortion. This is achieved by such precautions as ensuring that the diaphragm area is sufficient that the motion is not excessively large, ensuring that the motor and mechanical parameters are approximately invariant of diaphragm position, the use of multiple drivers for different frequency bands and, for particularly high pressure level systems, the use of arrays of drivers. As a result, though significant distortion products are

generated to be of concern in term of fidelity, during normal operation the linear response of the loudspeaker is dominant.

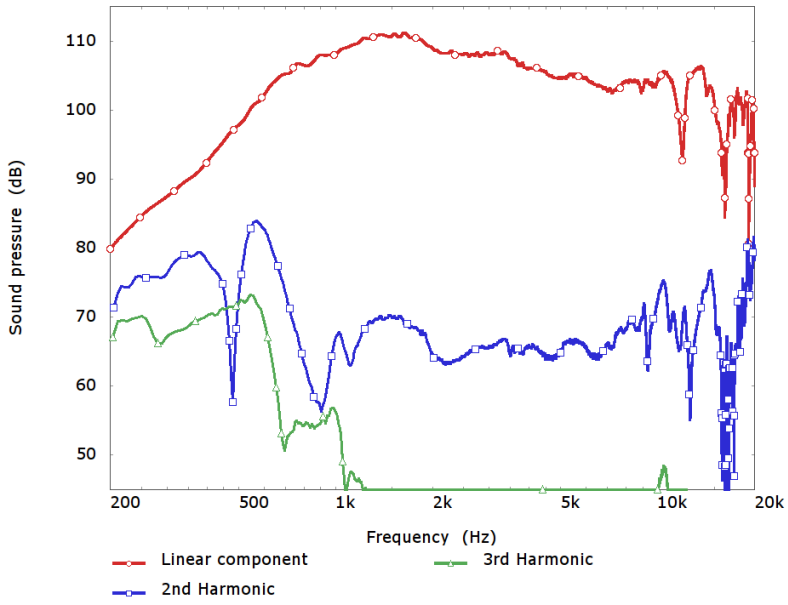

Figure 2.16. Linear, 2nd and 3rd harmonic distortion pressure level response measurement of a Celestion CDX1.4 compression driver connected to B&C ME10 horn measured 1m on-axis at 1watt (2.83V RMS).

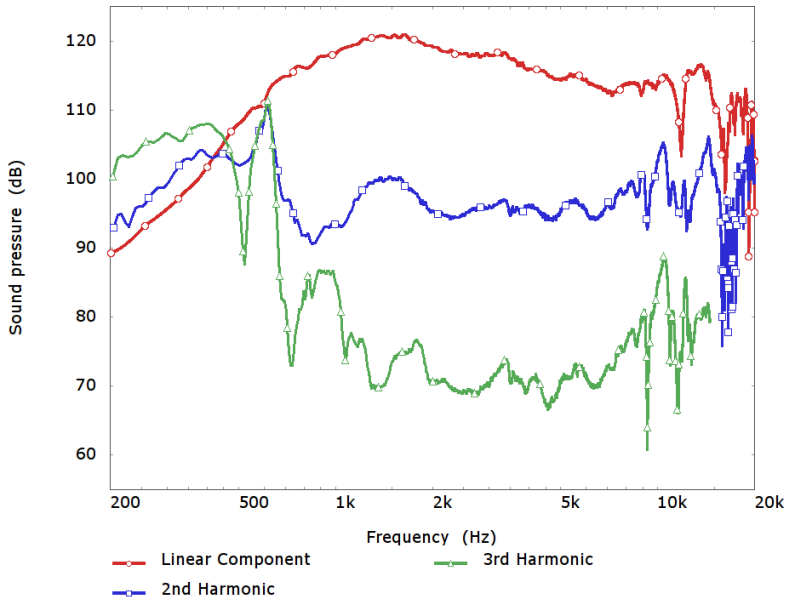

Figure 2.17. Linear, 2nd and 3rd harmonic distortion pressure level response measurement of a Celestion CDX1.4 compression driver connected to B&C ME10 horn measured 1m on-axis at 10watts (8.94V RMS).

Figures 2.16 and 2.17 show linear, 2nd and 3rd harmonic pressure level response measurements of a Celestion CDX1.4 compression driver connected to a B&C ME10 horn. The measurements are taken at a distance of 1m directly on-axis with the horn at a input signal level of 1watt and 10 watts respectively. At 10watts, high levels of distortion are observed however, in the passband of the driver (in this case between approximately 2kHz and 20kHz) the linear response is dominant.

Figure 2.18 shows the 1watt and 10watt linear response plotted on the same chart, the 10watt curve is reduced in level by 10dB to allow easy comparison of the response shape. Both responses are extremely similar even in the region below the passband, where extremely high distortion levels were seen in the 10watt measurements shown in figure 2.17.

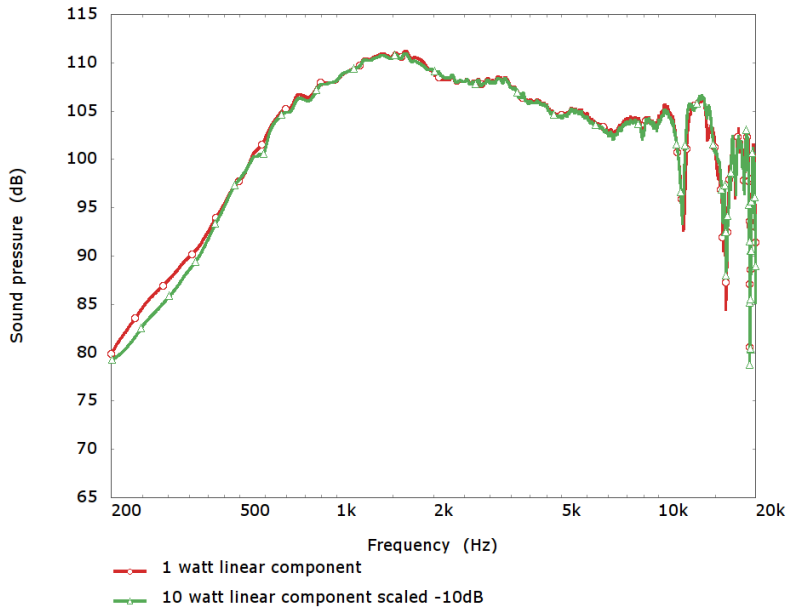

Figure 2.18. Comparison of the linear response of of a Celestion CDX1.4 compression driver connected to B&C ME10 horn measured 1m on-axis at 1watt and 10watts (10 watt shifted -10dB).

In this thesis the acoustical behaviour of compression drivers is modelled exclusively using linear theory. Consequently the models are unable to predict the level of non-linear distortion generated by the driver. However, these LTI models are able to accurately approximate the linear, $Y_0(\omega)$, response even when the real devices exhibit moderate levels of non-linearity (For example see figure 5.23). Indeed, even under extreme levels of excitation, with significant non-linearity, the linear model is still a useful first approximation to the $Y_0(\omega)$ behaviour.

2.5 Conclusions

The principles of operation of the electrodynamic loudspeaker are introduced in this chapter in order to prepare the reader for the main body of this thesis, where compression drivers are considered in more detail. Particular reference was made to the underlying efficiency limitations as the raison d'etre of the compression-driver arrangement is to improve this aspect of the loudspeaker performance.

3 Acoustical analysis techniques

3.1 Introduction

The methods of acoustical analysis used in this thesis are introduced in this chapter. The contents is loosely divided in two halves: the first concerned with analytical methods and the second, with numerical methods. The chapter begins by considering the solution of the homogeneous wave equation in a rigid-walled enclosure. The Green-function approach to solution of the inhomogeneous wave equation is then outlined. The two subsequent chapters look at specific implementations of the general Green-function approach, firstly, for the case of a lightly damped acoustical enclosure and, secondly, for the problem of radiation from bodies of arbitrary shape into infinite and semi-infinite spaces. The first three topics provide the foundation that is required for Smith's phase-plug geometry derivation, which is outlined in chapter 4. The fourth topic provides the foundation required for understanding of the Boundary-Element Method (BEM).

By means of an introduction to numerically based methods, section 3.6 outlines the Rayleigh-Ritz method for a simple acoustical pipe. This is followed by two sections that describe the Finite Element and Boundary-Element Methods for acoustical problem respectively.

These first four sections follow, somewhat less comprehensively, the detailed description given by Nelson and Elliot [44] and Williams [45]. The forth, fifth and sixth section are based on the presentation given by Fahy and Gardonio [46].

3.2 The eigenfunctions and eigenfrequencies of an enclosure

The pressure field in a rigid-walled acoustical enclosure, with no sources or dissipation present inside the walls, must obey the homogeneous Helmholtz equation, such that

$$\nabla^2 p(\boldsymbol{x}) + k^2 p(\boldsymbol{x}) = 0 \qquad 3.1.$$

where $p(\boldsymbol{x})$ is the pressure at the position $\boldsymbol{x}$ in the enclosure, k is the acoustical wavenumber and ∇^2 is the Laplacian operator [23]. The spatial pressure function must also satisfy the rigid-walled boundary condition

$$\nabla p(\boldsymbol{x}) . \boldsymbol{n} = 0 \qquad 3.2.$$

where $\boldsymbol{n}$ is a unit vector normal to the enclosure boundary and ∇ is the gradient operator [47, p. 598]. Solution of this expression for the sound field, conventionally performed by finding a form for ∇^2 that fits nicely into the geometry of the enclosure in consideration such

that the boundary consideration is easy to apply, provides an infinite set of solutions to the pressure field

$$p(\boldsymbol{x}) = \Psi_n(\boldsymbol{x}) \tag{3.3.}$$

The functions $\Psi_n(\boldsymbol{x})$ are the eigenfunctions of the homogeneous Helmholtz equation and are associated with a set of eigenvalues, k_n, such that

$$\nabla^2 \Psi_n(\boldsymbol{x}) + k_n^2 \Psi_n(\boldsymbol{x}) = 0 \tag{3.4.}$$

The eigenfunctions correspond to the mode shapes of the acoustical enclosure. The eigenfunctions satisfy the orthogonality relationship

$$\int_V \Psi_n(\boldsymbol{x}) \Psi_m(\boldsymbol{x}) dV = 0 \Big|_{n \neq m} \tag{3.5.}$$

As the Helmholtz equation is linear, and the eigenfunctions are solutions to the Helmholtz equation, the magnitude of the eigenfunctions is arbitrary. Commonly the normalisation of the eigenfunctions is chosen to be

$$\int_V \Psi_n^2(\boldsymbol{x}) dV = V \tag{3.6.}$$

where the volume integral of the squared eigenfunction is equal to the enclosure volume. The above two conditions are neatly summarised by the expression

$$\int_V \Psi_n(\boldsymbol{x}) \Psi_m(\boldsymbol{x}) dV = V \delta_{nm} \tag{3.7.}$$

where δ_{nm} is the Kronecker delta function [47, p.692], which has the property that

$$\delta_{nm} = \begin{cases} 0, & m \neq n \\ 1, & m = n \end{cases} \tag{3.8.}$$

3.3 Green-function solution of the inhomogeneous wave equation

In order to derive the driven behaviour of a sound field, it is necessary to formulate a solution to the inhomogeneous Helmholtz equation. The inhomogeneous Helmholtz equation is defined to be

$$\left(\nabla_y^2 + k^2\right) p(\boldsymbol{y}) = -Q_{vol}(\boldsymbol{y}) \tag{3.9.}$$

where $\boldsymbol{y}$ is a vector position within the enclosure and the function $Q_{vol}(\boldsymbol{y})$ describes source-strength distribution within the acoustical medium. This section outlines the Green-function based approach to the solution of the inhomogeneous wave equation. This is a powerful

technique that forms the basis for many different methods of acoustical analysis. Unlike the case considered above for the homogeneous Helmholtz equation used to derive the eigenfrequencies and functions, the right-hand side of the equation is non-zero. The right-hand term, Q_{vol}, defines source-strength distribution within the acoustical medium. For example, it could consist of a combination of monopole and dipole sources where

$$Q_{vol} = j\omega\rho_0 q_{vol}(\boldsymbol{y}) - \nabla . \boldsymbol{f}_{vol}(\boldsymbol{y}) \qquad 3.10.$$

with $q_{vol}(\boldsymbol{y})$ the complex volume velocity distribution per unit volume, $f_{vol}(\boldsymbol{y})$ the complex force distribution per unit volume applied to the medium and $\nabla .$ is the divergence operator. For example in Cartesian coordinates operating on a vector $\boldsymbol{s}$

$$\nabla . \boldsymbol{s} = \frac{\partial s_x}{\partial x} + \frac{\partial s_y}{\partial y} + \frac{\partial s_z}{\partial z} \qquad 3.11.$$

The general solution of the inhomogeneous Helmholtz equation can be readily dealt with using a Green-function approach. The Green function, $G(\boldsymbol{y}|\boldsymbol{x})$, satisfies the equation

$$(\nabla^2 + k^2) G(\boldsymbol{y}|\boldsymbol{x}) = -\delta(\boldsymbol{y} - \boldsymbol{x}) \qquad 3.12.$$

where $\delta(\boldsymbol{y} - \boldsymbol{x})$ is the Dirac delta function. In other words, the Green function is proportional to the complex pressure field at a point $\boldsymbol{y}$ produced by a harmonic point-monopole source at position $\boldsymbol{x}$. Indeed, the complex pressure at a point $\boldsymbol{y}$ in the medium due to a point monopole at a position $\boldsymbol{x}$ is given by $p(\boldsymbol{y}) = j\omega\rho_0 G(\boldsymbol{y}|\boldsymbol{x})$. An important property of the Green function is the principle of reciprocity. That is to say that for all possible functions satisfying equation 3.12 the relation $G(\boldsymbol{x}|\boldsymbol{y}) = G(\boldsymbol{y}|\boldsymbol{x})$ is true. The interested reader is directed to Nelson and Elliot for proof of this property [44, pp.277-279].

The inhomogeneous Helmholtz equation, expression 3.9, is first multiplied by $G(\boldsymbol{y}|\boldsymbol{x})$ and expression 3.12 multiplied by $p(\boldsymbol{y})$ is then subtracted, this gives

$$G(\boldsymbol{y}|\boldsymbol{x})\nabla_y^2 p(\boldsymbol{y}) - p(\boldsymbol{y})\nabla_y^2 G(\boldsymbol{y}|\boldsymbol{x}) = -Q_{vol}(\boldsymbol{y}) G(\boldsymbol{y}|\boldsymbol{x}) + p(\boldsymbol{y})\delta(\boldsymbol{y} - \boldsymbol{x}) \qquad 3.13.$$

Performing a volume integration over both sides and using the sifting property of the delta function, results in the expression

$$\int_V G(\boldsymbol{y}|\boldsymbol{x})\nabla_y^2 p(\boldsymbol{y}) - p(\boldsymbol{y})\nabla_y^2 G(\boldsymbol{y}|\boldsymbol{x})\,dV + \int_V Q_{vol}(\boldsymbol{y}) G(\boldsymbol{y}|\boldsymbol{x})\,dV = \begin{Bmatrix} p(\boldsymbol{x}), & \boldsymbol{x}\ within V \\ 0, & \boldsymbol{x}\ outside V \end{Bmatrix} \qquad 3.14.$$

Green's theorem states that if S is the surface that encloses the volume V, and a and b are scalar functions then

$$\int_V \left(a\nabla^2 b - b\nabla^2 a\right) dV = \int_S \left(a\nabla b - b\nabla a\right).\boldsymbol{n}\, dS \qquad 3.15.$$

where $\boldsymbol{n}$ is the unit vector pointing out of the volume V.

This allows the first volume integral in equation 3.14 to be converted to a surface integral and, with the additional substitution of $G(\boldsymbol{x}|\boldsymbol{y}) = G(\boldsymbol{y}|\boldsymbol{x})$, allows the pressure at a point $\boldsymbol{x}$ within the acoustical volume V to be expressed as

$$p(\boldsymbol{x}) = \int_V Q_{vol}(\boldsymbol{y})\, G(\boldsymbol{x}|\boldsymbol{y})\, dV + \int_S \left[G(\boldsymbol{x}|\boldsymbol{y})\nabla_y p(\boldsymbol{y}) - p(\boldsymbol{y})\nabla_y G(\boldsymbol{x}|\boldsymbol{y})\right].\boldsymbol{n}\, dS \qquad 3.16.$$

The pressure in the volume V is found by the sum of two integrals. The first of these is an integration over the whole volume for all acoustical sources inside the volume. The second is an integral over the bounding surface of the volume and is dependent upon the pressure and pressure gradient, $\nabla_y p(\boldsymbol{y})$, at the surface. Both integrals include the Green function $G(\boldsymbol{x}|\boldsymbol{y})$. However, the only requirement for the Green function is that it is well defined inside the entire volume V and that it satisfies equation 3.12. This makes the expression particularly powerful, especially if one considers that in some cases it may be feasible to choose Green functions that satisfy the condition $\nabla_y G(\boldsymbol{x}|\boldsymbol{y}) = 0$, which permits further simplification of expression 3.16.

3.4 The sound field in a lightly-damped enclosure

Much of this thesis is concerned with controlling the acoustical behaviour of lightly-damped acoustical cavities or enclosures. There are several different approaches for the analysis of the acoustical behaviour of a lightly-damped enclosure. For example, the image and ray methods [48] or the direct inhomogeneous Finite-Element Method described in section 3.7. However, the modal description is particularly useful when considering the low frequencies of an enclosure. The behaviour of the acoustical enclosure over the first few modes may be written concisely with only a few parameters. The modal description is especially powerful when the aim is some type of control of the global sound field because it clearly illustrates how the presence of sources at various positions in the enclosure effects the sound field over the entire acoustical interior.

The rigid-walled enclosure eigenfunctions form a complete orthonormal set [49, p. 267] and so any well-behaved function of enclosure position $\boldsymbol{x}$ can, within the bounds of the enclosure volume V, be approximated by a linear combination of the eigenfunctions.

Thus, the Green function used to determine the solution of the inhomogeneous Helmholtz equation and determine the sound field in the enclosure is constructed from a linear summation of the eigenfunctions

$$G(\boldsymbol{x}|\boldsymbol{y}) = \sum_{m=0}^{\infty} b_m \Psi_m(\boldsymbol{x}) \tag{3.17.}$$

To determine the complex coefficients, b_m, this expression for the Green function is substituted into expression 3.12, along with the relation $\nabla^2 \Psi_m(\boldsymbol{x}) = -k_m^2 \Psi_m(\boldsymbol{x})$, resulting in

$$\sum_{m=0}^{\infty} b_m \left(k^2 - k_m^2\right) \Psi_m(\boldsymbol{x}) = -\delta(\boldsymbol{x} - \boldsymbol{y}) \tag{3.18.}$$

Multiplying this by $\Psi_n(\boldsymbol{x})$ and integrating over the volume, V, results in

$$\sum_{m=0}^{\infty} b_m \left(k^2 - k_m^2\right) \int_V \Psi_m(\boldsymbol{x}) \Psi_n(\boldsymbol{x}) dV = \int_V -\delta(\boldsymbol{x} - \boldsymbol{y}) \Psi_n(\boldsymbol{x}) dV \tag{3.19.}$$

Recalling the sifting property of the delta function and the orthogonality of the eigenfunctions, expressed in 3.7, this simplifies to

$$\sum_{m=0}^{\infty} b_m \left(k^2 - k_m^2\right) V \delta_{mn} = -\Psi_n(\boldsymbol{y}) \tag{3.20.}$$

and reveals that $b_n = \Psi_n(\boldsymbol{y}) / \left(V\left(k_n^2 - k^2\right)\right)$. Consequently the Green function can be written as

$$G(\boldsymbol{x}|\boldsymbol{y}) = \sum_{n=0}^{\infty} \frac{\Psi_n(\boldsymbol{x}) \Psi_n(\boldsymbol{y})}{V\left(k_n^2 - k^2\right)} \tag{3.21.}$$

This Green function is now used in the general solution to the inhomogeneous Helmholtz equation, expression 3.16 in the previous section. Assuming that the pressure in the enclosure is only generated by the motion of the enclosure walls, and not because of any acoustical sources within the enclosure, the term $Q_{vol}(\boldsymbol{y})$ is zero. Additionally, as the boundary condition for the initial calculation of the eigenfunctions was that of a rigid boundary, the spatial derivative of the Green function at the enclosure surface, $\nabla_y G(\boldsymbol{x}|\boldsymbol{y})$, is also zero. This results in a simplified expression for the acoustical pressure in the enclosure given by

$$p(\boldsymbol{x}) = \int_S G(\boldsymbol{x}|\boldsymbol{y}) \nabla_y p(\boldsymbol{y}) . \boldsymbol{n} \, dS \tag{3.22.}$$

The pressure gradient term $\nabla_y p(\boldsymbol{y})$ can only arise because of some normal surface velocity, $\boldsymbol{u}_i(\boldsymbol{y}) . \boldsymbol{n}$ at the enclosure boundaries. The momentum equation [44, p. 23] allows the surface

velocity to be related to the pressure gradient and the expression for pressure in the enclosure to be written as

$$p(\boldsymbol{x}) = \int_S G(\boldsymbol{x}\,|\,\boldsymbol{y})\, j\omega\rho_0 \boldsymbol{u}_i(\boldsymbol{y}).\boldsymbol{n}\, dS \qquad 3.23.$$

or in full including the Green-function summation derived above as

$$p(\boldsymbol{x}) = \sum_{n=0}^{\infty} \frac{j\omega\rho_0 \Psi_n(\boldsymbol{x})}{V\left[k_n^2 - k^2\right]} \int_s \Psi_n(\boldsymbol{y}) \boldsymbol{u}_i(\boldsymbol{y}).\boldsymbol{n}\, dS \qquad 3.24.$$

For situations where the acoustical medium within an enclosure is approximately lossless this is a very useful description. It is used in many places in this thesis. It forms the basis of the Smith phase-plug geometry derivation, outlined in chapter 4, and also the basis of the new phase-plug geometry derivations.

3.5 Radiation of sound from sources of arbitrary geometry

The radiation of sound is a key topic in loudspeaker analysis. In section 2.3, the simple model of a rigid planar-circular piston mounted in an infinite baffle was used to approximate the radiation behaviour of a loudspeaker. While this is a useful model to use to outline the radiation characteristics of the direct-radiating loudspeaker, few real loudspeakers have exactly this geometry and it is thus useful to have an analysis method that allows the radiation from an arbitrary geometry to be considered. The acoustical problem can be generally formulated as the sound field radiated into an unbounded infinite region V_a from a surface of arbitrary shape, S_a, as shown in figure 3.1.

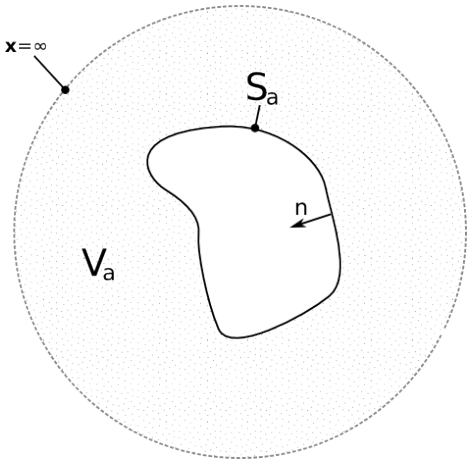

Figure 3.1. Schematic representation of the exterior problem.

In section 3.3, the Green-function method of solution of the inhomogeneous Helmholtz equation for a point $\boldsymbol{x}$ in the acoustical field was found to be

$$p(\boldsymbol{x}) = \int_{V_a} Q_{vol}(\boldsymbol{y})\, G(\boldsymbol{x}|\boldsymbol{y})\, dV + \int_{S_a} \left[G(\boldsymbol{x}|\boldsymbol{y}) \nabla_y p(\boldsymbol{y}) - p(\boldsymbol{y}) \nabla_y G(\boldsymbol{x}|\boldsymbol{y}) \right] . \boldsymbol{n}\, dS \qquad 3.25.$$

This approach is equally valid for the situation at hand where the bounding surface defines an exterior volume within which the behaviour is described by either the homogeneous or inhomogeneous Helmholtz equation. Considering the first the case, when the bounded region, V_a, is described by the homogeneous Helmholtz equation, with no sources within the volume and excitation only applied via the boundary conditions at the surface S_a, the volume integral is zero and the simplified integral equation is

$$p(\boldsymbol{x}) = \int_{S_a} \left[G(\boldsymbol{x}|\boldsymbol{y}) \nabla_y p(\boldsymbol{y}) - p(\boldsymbol{y}) \nabla_y G(\boldsymbol{x}|\boldsymbol{y}) \right] . \boldsymbol{n}\, dS \qquad 3.26.$$

The Green functions must be carefully chosen so that there is a well-defined single solution. Only outward-travelling acoustical waves are allowed. This requirement can be met by ensuring that at an infinite distance from S_a the acoustic pressure $p(x)$ tends to zero,

$$\lim_{|\boldsymbol{x}| \to \infty} |\boldsymbol{x}| \left(\frac{\partial p(\boldsymbol{x})}{\partial |\boldsymbol{x}|} + j k p(\boldsymbol{x}) \right) = 0 \qquad 3.27.$$

This requirement can be reposed as a condition on the Green function as

$$\lim_{|\boldsymbol{x}-\boldsymbol{y}| \to \infty} |\boldsymbol{x}-\boldsymbol{y}| \left(\frac{\partial G(\boldsymbol{x}|\boldsymbol{y})}{\partial |\boldsymbol{x}-\boldsymbol{y}|} + j k G(\boldsymbol{x}|\boldsymbol{y}) \right) = 0 \qquad 3.28.$$

This condition guarantees that the integral over the surface at infinity, which bounds the volume V_a, is zero and need not be included in the integral over the bounding surface. For the consideration of radiation problems, it is common to define $G(\boldsymbol{x}|\boldsymbol{y})$ as the “free space” Green function,

$$G(\boldsymbol{x}|\boldsymbol{y}) = \frac{e^{-jk|\boldsymbol{x}-\boldsymbol{y}|}}{4\pi|\boldsymbol{x}-\boldsymbol{y}|} \qquad 3.29.$$

However, this choice must be treated with some caution as at the point $\boldsymbol{x}=\boldsymbol{y}$ the free space Green function is undefined. This problem is managed by ensuring that an infinitesimally small region around the point $\boldsymbol{x}=\boldsymbol{y}$ is excluded from the fluid region. This is diagrammatically shown in figure 3.2. The surface, S_a, bounding the volume has been extended with a narrow canal to include a small spherical surface, S_x, surrounding the evaluation point $\boldsymbol{x}$. The canal joining the main part of the surface S_a to S_x is vanishingly

narrow and, as the normal along one side of the canal is the exact opposite of the normal on the other side of the canal, it effectively disappears from the surface integrals.

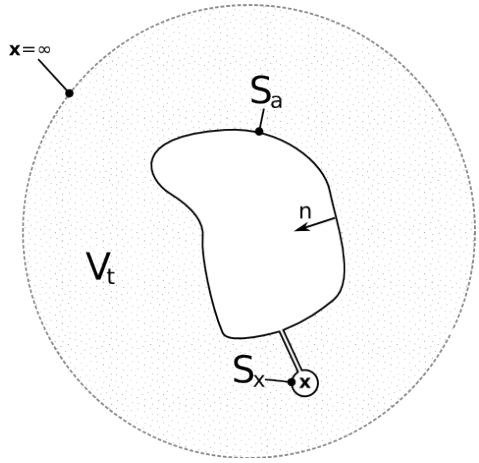

Figure 3.2. Schematic representation of the exterior problem with infinitesimal excluded region at evaluation point $\boldsymbol{x}$.

The new system has a total surface of $S_t = S_a \cup S_x$ and the pressure in the new volume V_t, which excludes the sphere around $\boldsymbol{x}$, bounded by this surface may be described by the same integral expression discussed above as

$$p(\boldsymbol{x}) = \int_{S_t} \left[G(\boldsymbol{x}|\boldsymbol{y}) \nabla_y p(\boldsymbol{y}) - p(\boldsymbol{y}) \nabla_y G(\boldsymbol{x}|\boldsymbol{y}) \right] . \boldsymbol{n}\, dS \qquad 3.30.$$

The surface integral over the new surface S_t is simply the sum of the integrals over the two bounding surfaces S_a and S_x,

$$\begin{aligned} p(\boldsymbol{x}) = & \int_{S_a} \left[G(\boldsymbol{x}|\boldsymbol{y}) \nabla_y p(\boldsymbol{y}) - p(\boldsymbol{y}) \nabla_y G(\boldsymbol{x}|\boldsymbol{y}) \right] . \boldsymbol{n}\, dS \\ & + \int_{S_x} \left[G(\boldsymbol{x}|\boldsymbol{y}) \nabla_y p(\boldsymbol{y}) - p(\boldsymbol{y}) \nabla_y G(\boldsymbol{x}|\boldsymbol{y}) \right] . \boldsymbol{n}\, dS \end{aligned} \qquad 3.31.$$

The pressure evaluation point $\boldsymbol{x}$ lies outside of the volume V_t bounded by the new surface S_t and, thus, as defined in section 3.3 equation 3.14, the integral over S_t is equal to zero. Accordingly the sum of the integrals over S_a and S_x must also be zero and

$$\begin{aligned} \int_{S_a} \left[G(\boldsymbol{x}|\boldsymbol{y}) \nabla_y p(\boldsymbol{y}) - p(\boldsymbol{y}) \nabla_y G(\boldsymbol{x}|\boldsymbol{y}) \right] . \boldsymbol{n}\, dS = \\ - \int_{S_x} \left[G(\boldsymbol{x}|\boldsymbol{y}) \nabla_y p(\boldsymbol{y}) - p(\boldsymbol{y}) \nabla_y G(\boldsymbol{x}|\boldsymbol{y}) \right] . \boldsymbol{n}\, dS \end{aligned} \qquad 3.32.$$

Considering the integral over the excluded spherical surface S_x, the point bold x lies at the centre of the sphere and it is simple to calculate the integral over the spherical surface to be,

$$\int_{S_x}\left[G(\boldsymbol{x}|\boldsymbol{y})\nabla_y p(\boldsymbol{y})-p(\boldsymbol{y})\nabla_y G(\boldsymbol{x}|\boldsymbol{y})\right].\boldsymbol{n}\,dS$$

$$=-\int_0^{2\pi}\int_0^{\pi}\left[R_1\frac{e^{-jkR_x}}{4\pi}\nabla_y p(\boldsymbol{y}).\boldsymbol{n}+\ p(\boldsymbol{y})\left(1+\ jkR_x\right)\frac{e^{-jkR_1}}{4\pi}\right]\sin\theta\,d\theta\,d\phi \qquad 3.33.$$

in the limiting case as the sphere radius $R_x \to 0$, the pressure at the surface of the sphere $p(\boldsymbol{y}) \to p(\boldsymbol{x})$, and the integral

$$\lim_{R_x\to 0}\int_{S_x}\left[G(\boldsymbol{x}|\boldsymbol{y})\nabla_y p(\boldsymbol{y})-p(\boldsymbol{y})\nabla_y G(\boldsymbol{x}|\boldsymbol{y})\right].\boldsymbol{n}\,dS$$

$$=-\int_0^{2\pi}\int_0^{\pi}p(\boldsymbol{x})\frac{\sin\theta}{4\pi}d\theta\,d\phi=-p(\boldsymbol{x}) \qquad 3.34.$$

This means that for the case where the sphere lies completely in the volume V_a, as the radius of the sphere tends to zero the pressure in the volume is again given by the original integral expression,

$$p(\boldsymbol{x})=\int_{S_a}\left[G(\boldsymbol{x}|\boldsymbol{y})\nabla_y p(\boldsymbol{y})-p(\boldsymbol{y})\nabla_y G(\boldsymbol{x}|\boldsymbol{y})\right].\boldsymbol{n}\,dS \qquad 3.35.$$

The situation when $\boldsymbol{x}$ lies on the surface S_a must also be considered. In this case, it is not possible to use an entire sphere surrounding $\boldsymbol{x}$ to exclude the point $\boldsymbol{x}=\boldsymbol{y}$ from the volume. If the surface is S_a is smooth then as the radius, R_x, of the spherical surface S_x tends to zero, S_x becomes a hemispherical region as depicted in figure 3.3.

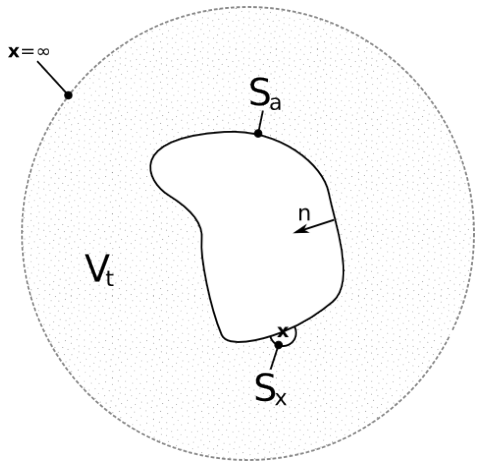

Figure 3.3. Schematic representation of the exterior problem with infinitesimal excluded region at evaluation point $\boldsymbol{x}$ *when* $\boldsymbol{x}$ *lies on the surface* S_a.

Again, the behaviour in the new volume V_t is given by the same integral expression, expression 3.30, which excludes this hemispherical region around $\boldsymbol{x}$, and the surface integral of expression 3.30 is zero, because $\boldsymbol{x}$ lies outside of the volume bounded by $S_t = S_a \cup S_x$. Thus, the sum of the integral over S_a and the integral over S_x must equal zero.

In the limiting case, as the hemisphere radius R_x tends to zero, the pressure at the surface of the hemisphere $p(\boldsymbol{y})$ tends to $p(\boldsymbol{x})$, and the integral

$$\lim_{R_x \to 0} \int_{S_x} \left[G(\boldsymbol{x}|\boldsymbol{y}) \nabla_y p(\boldsymbol{y}) - p(\boldsymbol{y}) \nabla_y G(\boldsymbol{x}|\boldsymbol{y}) \right] . \boldsymbol{n} \, dS$$

$$= -\int_0^{2\pi} \int_0^{\pi/2} p(\boldsymbol{x}) \frac{\sin\theta}{4\pi} d\theta \, d\phi = -\frac{1}{2} p(\boldsymbol{x}) \qquad 3.36.$$

Note that the limits of the integral in θ are now from 0 to $\pi/2$. This result indicates that, in this case, the original integral expression over S_a returns half of the actual pressure at the point $\boldsymbol{x}$,

$$\frac{1}{2} p(\boldsymbol{x}) = \int_{S_a} \left[G(\boldsymbol{x}|\boldsymbol{y}) \nabla_y p(\boldsymbol{y}) - p(\boldsymbol{y}) \nabla_y G(\boldsymbol{x}|\boldsymbol{y}) \right] . \boldsymbol{n} \, dS \qquad 3.37.$$

The surface-normal complex acoustical-particle-velocity, $\boldsymbol{u}(\boldsymbol{y}_{S_a}) . \boldsymbol{n}$, is related to the surface normal gradient of the pressure by the expression

$$\nabla_y p(\boldsymbol{y}) . \boldsymbol{n} = -j\omega\rho_0 \boldsymbol{u}(\boldsymbol{y}_{S_a}) . \boldsymbol{n} \qquad 3.38.$$

This, along with the other outcomes above, results in an overall description of the pressure in the volume, V_a, of

$$c(\boldsymbol{x}) \, p(\boldsymbol{x}) = \int_{S_a} \left[G(\boldsymbol{x}|\boldsymbol{y}) \, j\omega \boldsymbol{u}(\boldsymbol{y}) \rho_0 + p(\boldsymbol{y}) \nabla_y G(\boldsymbol{x}|\boldsymbol{y}) \right] . \boldsymbol{n} \, dS \qquad 3.39.$$

where $c(\boldsymbol{x})$ is defined to be

$$c(\boldsymbol{x}) = \begin{cases} -1 & x \in V_a \\ 0 & x \notin V_a \\ -1/2 & x \in S_a \end{cases} \qquad 3.40.$$

This expression is commonly known as the Kirchoff-Helmholtz integral equation that states for any sound field that satisfies the homogeneous Helmholtz equation and the Sommerfeld radiation condition, the sound field at any point $\boldsymbol{x}$ is determined by the pressure and normal velocity of the bounding surface. Note also that if the bounding surface S_a is not smooth then as $R_x \to 0$ the excluded region S_x may not necessarily become a hemisphere when $\boldsymbol{x}$ lies on

the surface S_a. For example, if $\boldsymbol{x}$ lies on an exterior 90 degree apex of the surface then $c(\boldsymbol{x})=-3/4$.

The inhomogeneous solution is found by an extension of the above to allow sources within the volume V_a resulting in the integral expression

$$p(\boldsymbol{x})=\int_{V_a} Q_{vol}(\boldsymbol{y})\,G(\boldsymbol{x}|\boldsymbol{y})\,dV+\frac{1}{c(\boldsymbol{x})}\int_{S_a}\left[G(\boldsymbol{x}|\boldsymbol{y})\,j\omega\,\boldsymbol{u}(\boldsymbol{y})\rho_0+p(\boldsymbol{y})\nabla_y G(\boldsymbol{x}|\boldsymbol{y})\right].\boldsymbol{n}\,dS \qquad 3.41.$$

This expression is commonly called the "direct boundary integral formulation". Although in this case, the exterior problem was considered, the derivation is equally valid for an interior region. Indeed, the treatment above is simply a special case of the more general Green-function approach to the solution of the Helmholtz equation as described in section 3.3. The additional considerations required here occur as a result of the choice of Green function.

3.6 The Rayleigh-Ritz method

The Rayleigh-Ritz method is illustrated through a simple example: the acoustical behaviour of the one-dimensional acoustical pipe shown in figure 3.4.

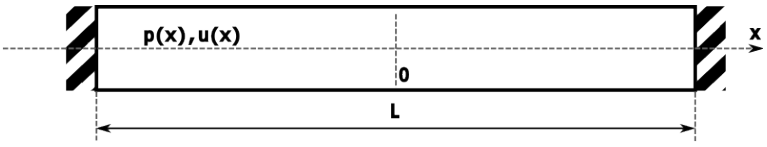

Figure 3.4. Acoustical pipe with closed ends.

It is assumed that the pipe only carries plane waves and that the ends of the pipe are perfectly rigid walled. The Rayleigh-Ritz method makes the assumption that the solution may be approximated by a finite series expansion. In this case, it is assumed that the solution can be written as

$$\phi(x,t)=\sum_{i=1}^{n} d_i(x)\phi_i(t) \qquad 3.42.$$

where $\phi(x,t)$ is the velocity potential and x is the axial position in the pipe, $d_i(x)$ are a set of prescribed functions that describe the spatial variation of ϕ, and $\phi_i(t)$ are unknown coefficients that must be determined. For plane-wave propagation, the velocity potential is related to the acoustical pressure, $p(x,t)$, and acoustical particle velocity, $u(x,t)$, by the expressions

$$p(x,t)=-\rho_0\frac{d\phi(x,t)}{dt} \quad \text{and} \quad u(x,t)=\frac{d\phi(x,t)}{dx} \qquad 3.43.$$

In assuming that the solution is accurately described by the summation in expression 3.42, the continuous acoustical system has been reduced to an equivalent discrete system with n degrees of freedom. The discrete system approximately describes the solution to the continuous original up to a certain point where there are insufficient degrees of freedom for an accurate representation.

The unknown coefficients, $\phi_i(t)$, are determined using Hamilton's principle [50], which for this problem can be stated as

$$\int_{t_1}^{t_2} \left[\delta(T+U)+\delta W\right] dt = 0 \qquad 3.44.$$

where T is the kinetic energy of the system, U is the potential energy of the system, δW is the virtual work performed by external forces on the system and t_1 and t_2 are the closed time interval over which the system is considered. With the closed-pipe system currently under consideration, there is no external excitation and thus δW is equal to zero. The kinetic- and potential-energy densities for small-amplitude oscillations in fluids are given by the two expressions

$$\frac{T}{dV} = \frac{1}{2}\rho_0 |u|^2 \quad \text{and} \quad \frac{U}{dV} = \frac{1}{2}\frac{1}{\rho_0 c_0^2} p^2 \qquad 3.45.$$

The system kinetic and potential energy can be found by integrating these densities over the length of the pipe, resulting in the expressions

$$T = \int_0^L \frac{1}{2}\rho_0 u^2(x,t) A\, dx \qquad 3.46.$$

and

$$U = \int_0^L \frac{1}{2}\frac{1}{\rho_0 c_0^2} p^2(x,t) A\, dx \qquad 3.47.$$

These can both be written in terms of the velocity potential, ϕ, as

$$T = \int_0^L \frac{1}{2}\rho_0 \left(\frac{\partial \phi(x,t)}{\partial x}\right)^2 A\, dx \qquad 3.48.$$

and

$$U = \int_0^L \frac{1}{2}\frac{\rho_0}{c_0^2} \left(\frac{\partial \phi(x,t)}{\partial t}\right)^2 A\, dx \qquad 3.49.$$

The set of prescribed functions $d_i(x)$ must be carefully chosen to satisfy the following four conditions [51,52]:

1. they are linearly independent;
2. they are compatible with the governing equations, i.e. if the governing equations require the pth differential then it must be possible to differentiate $d_i(x)$ at least p times;
3. they satisfy the system's geometric boundary conditions;
4. they form a complete series such that

$$\lim_{n\to\infty} \int_0^L \left[\phi(x,t) - \sum_{i=1}^{n} d_i(x)\,\phi_i(t)\right]^2 dx = 0 \qquad 3.50.$$

Several common function families are complete series including polynomials in the power of *x*, trigonometric functions, Legendre polynomials [53, p.233] and Tchebycheff polynomials [53, p.270]. For the acoustical pipe under consideration, the prescribed functions are chosen to be

$$d_i(x) = x^i \qquad 3.51.$$

with $i \geq 0$. This is a suitable choice[2] as it allows evaluation of the derivative in equation 3.49 and also satisfies the boundary conditions, which are

$$p(-L/2) \neq 0 \text{ and } p(L/2) \neq 0 \qquad 3.52.$$

or in terms of velocity potential

$$\phi(-L/2) \neq 0 \text{ and } \phi(L/2) \neq 0 \qquad 3.53.$$

This choice of the prescribed functions means that the velocity potential for the system as a whole is approximated as a n-th order polynomial with coefficients $\phi_i(t)$. The finite summation for ϕ is compactly written as the product of two vectors as

$$\phi(x,t) = \boldsymbol{d}(x)^T \boldsymbol{\phi}(t) = \begin{bmatrix} d_1(x) \\ d_2(x) \\ \vdots \\ d_n(x) \end{bmatrix}^T \begin{bmatrix} \phi_1(t) \\ \phi_2(t) \\ \vdots \\ \phi_n(t) \end{bmatrix} \qquad 3.54.$$

2 In [46] the set of prescribed functions for this example is chosen with $i \geq 1$. However, this restriction prevents any velocity potential occurring at $x = 0$ and subsequently is unable to correctly predict the odd order eigensolution. Nonetheless, in including the $i = 0$ term in the set extra care must be taken in calculating the matrix $\boldsymbol{H}$, according to expression 3.59, as zeros appear in both the numerator and denominator.

The expressions for the system kinetic and potential energy can now be rewritten in terms of the discrete $\phi(x,t)$ as

$$T=\frac{1}{2}\rho_0\boldsymbol{\phi}(t)^T\boldsymbol{H}\ \boldsymbol{\phi}(t) \qquad 3.55.$$

and

$$U=\frac{1}{2}\rho_0\dot{\boldsymbol{\phi}}(t)^T\boldsymbol{Q}\ \dot{\boldsymbol{\phi}}(t) \qquad 3.56.$$

where

$$\boldsymbol{H}=A\int_{-L/2}^{L/2}\frac{\partial\boldsymbol{d}(x)}{\partial x}\frac{\partial\boldsymbol{d}(x)^T}{\partial x}dx \qquad 3.57.$$

and

$$\boldsymbol{Q}=\frac{A}{c_0^2}\int_{-L/2}^{L/2}\boldsymbol{d}(x)\boldsymbol{d}(x)^T dx \qquad 3.58.$$

The vector $\dot{\boldsymbol{\phi}}(t)$is used to indicate the time derivative of each element of the vector $\boldsymbol{\phi}(t)$. The integrals in the two matrix definitions are readily evaluated for the choice of prescribed function, $d_i(x)=x^i$, to give the elemental matrix components as

$$H_{k,s}=A\frac{ks}{k+s-1}\left[\left(\frac{L}{2}\right)^{k+s-1}-\left(-\frac{L}{2}\right)^{k+s-1}\right] \qquad 3.59.$$

and

$$Q_{k,s}=\frac{A}{c_0^2}\frac{1}{k+s+1}\left[\left(\frac{L}{2}\right)^{k+s+1}-\left(-\frac{L}{2}\right)^{k+s+1}\right] \qquad 3.60.$$

Using these definitions of the system kinetic and potential energy, Hamilton's principle gives

$$\int_{t_1}^{t_2}\delta\left(\frac{1}{2}\rho_0\boldsymbol{\phi}(t)^T\boldsymbol{H}\ \boldsymbol{\phi}(t)+\frac{1}{2}\rho_0\dot{\boldsymbol{\phi}}(t)^T\boldsymbol{Q}\ \dot{\boldsymbol{\phi}}(t)\right)dt=0 \qquad 3.61.$$

After integration by parts, this can be written

$$\int_{t_1}^{t_2}\delta\boldsymbol{\phi}(t)^T\left(\rho_0\boldsymbol{H}\boldsymbol{\phi}(t)+\rho_0\boldsymbol{Q}\ddot{\boldsymbol{\phi}}(t)\right)dt=0 \qquad 3.62.$$

The term in brackets must be zero to satisfy this expression. The system behaviour can thus be given by

$$\rho_0\boldsymbol{H}\boldsymbol{\phi}(t)+\rho_0\boldsymbol{Q}\ddot{\boldsymbol{\phi}}(t)=\boldsymbol{0} \qquad 3.63.$$

or, using the relation $p_i = -\rho_0 \partial \phi / \partial t$, equivalently as

$$\boldsymbol{H}\,\boldsymbol{p}(t) + \boldsymbol{Q}\,\ddot{\boldsymbol{p}}(t) = \boldsymbol{0} \qquad 3.64.$$

The vector $\boldsymbol{p}(t)$ directly describes the pressure in the pipe in terms of the prescribed functions and, combining expressions 3.54 and 3.43, the pressure at any point in the pipe can be calculated from

$$p(x,t) = \begin{bmatrix} d_1(x) \\ d_2(x) \\ \vdots \\ d_n(x) \end{bmatrix}^T \begin{bmatrix} p_1(t) \\ p_2(t) \\ \vdots \\ p_n(t) \end{bmatrix} \qquad 3.65.$$

The equations of motion have been derived in a homogeneous form, considering only harmonic variation of the pressure in the pipe such that $\boldsymbol{p}(t) = \Re\left(\boldsymbol{a}\, e^{j\omega t}\right)$. By rearranging the system equations into the form

$$[\boldsymbol{H} - \omega^2 \boldsymbol{Q}]\,\boldsymbol{p}(t) = \boldsymbol{0} \qquad 3.66.$$

the system eigenfrequencies can be found and occur at the values of ω at which the matrix within the square braces has a determinant of zero [47, p.427]. Once the system eigenfrequencies have been found, the corresponding eigenvectors are identified by reinserting the eigenfrequency values in to the expression [47, p.461]. The eigenfrequencies and eigenfunctions are shown in figure 3.5 for a 0.5-meter-long closed pipe calculated using the Rayleigh-Ritz method with 4 and 6 prescribed functions alongside the exact eigensolution. The Matlab [54] code to calculate these results is given in Appendix II.

The accuracy of the Rayleigh-Ritz method depends upon the ability of the set of prescribed functions to describe the pressure variation of the exact solution. At low frequencies, where the pressure variation is spatially slow, both the $n=4$ and $n=6$ results can predict the eigenfrequencies and eigenfunctions with good accuracy. At higher frequencies, where there is greater spatial variation in pressure in the pipe, the eigensolution prediction is worse. It may also be observed that the Rayleigh-Ritz prediction always overestimates the exact eigenfrequency. This is because the continuous acoustical system has been approximated by a stiffer discrete system with a finite number of degrees of freedom.

Unfortunately, practical uses of the Rayleigh Ritz method are limited as, despite the fact that it provides a straightforward means of creating an approximate equivalent discrete system equivalent without the use of a Green function or calculation of the Laplacian, it is nevertheless difficult to apply the method to a problem with arbitrary geometry because of the restrictions placed on the prescribed functions. Indeed, the prescribed functions must

obey the enclosure's boundary conditions make the method extremely hard to implement for anything but simple geometries and boundary conditions.

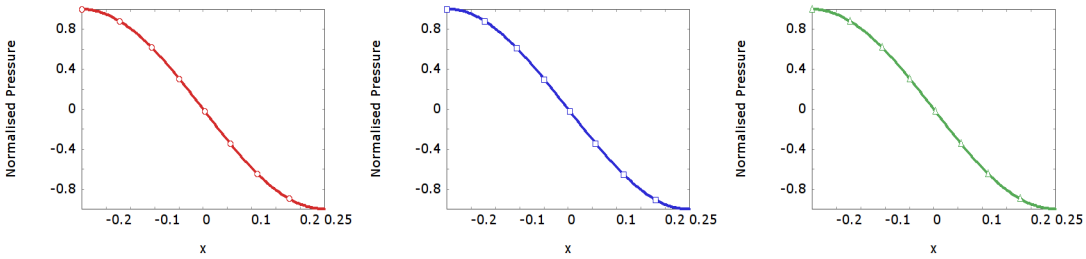

Mode 1: Exact solution, 343Hz. *Rayleigh-Ritz, n=4, 343.094Hz* *Rayleigh-Ritz, n=6, 343.000Hz*

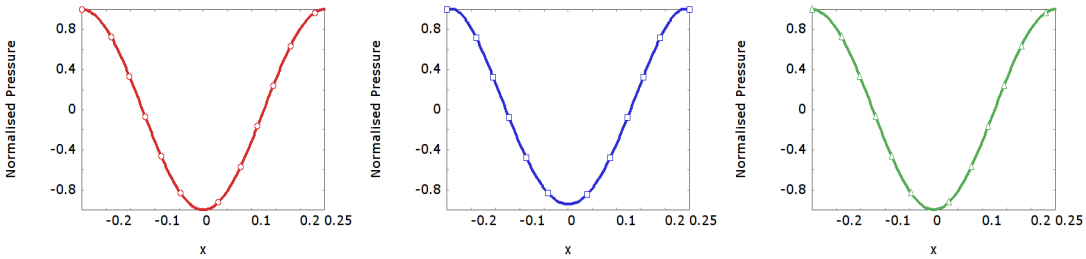

Mode 2: Exact solution, 686Hz. *Rayleigh-Ritz, n=4, 688.484Hz* *Rayleigh-Ritz, n=6, 686.012Hz*

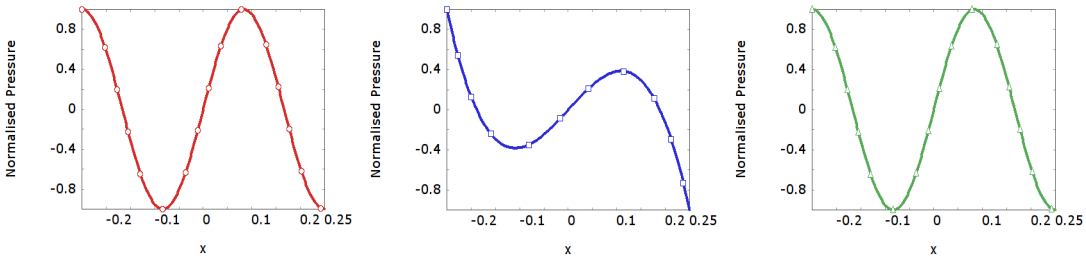

Mode 3: Exact solution, 1029Hz *Rayleigh-Ritz, n=4, 1424.060Hz* *Rayleigh-Ritz, n=6, 1042.803Hz*

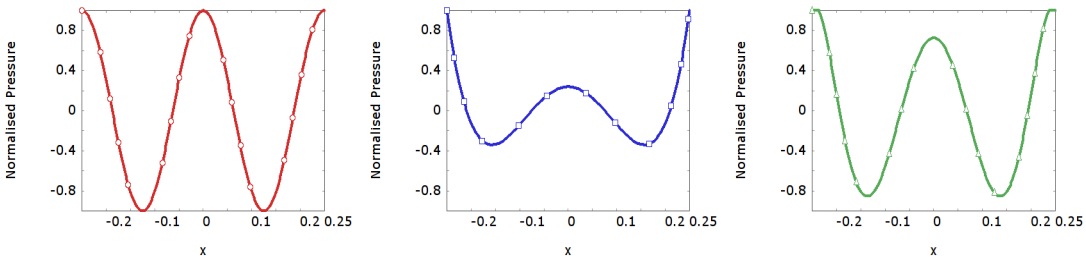

Mode 4: Exact solution, 1372Hz *Rayleigh-Ritz, n=4, 2128.974Hz* *Rayleigh-Ritz, n=6, 1414.790Hz*

Figure 3.5. The first four modes of the exact eigenfunction and eigenfrequencies of a closed 0.5m long pipe compared to the Rayleigh-Ritz approximate solution using 4 and 6 prescribed functions.

3.7 The Finite-Element Method

The Finite-Element Method (FEM) allows the analysis of systems with complex and arbitrary shape by geometric discretisation into small regions or elements. The global prescribed functions required in the Rayleigh-Ritz method are automatically generated as a series of elemental shape functions. The Finite Element (FE) approach follows a well defined algorithmic method that makes it ideally suited for implementation on a computer.

The FE method is illustrated in this section using the same acoustical pipe that was considered in the previous section where the Rayleigh-Ritz method was used.

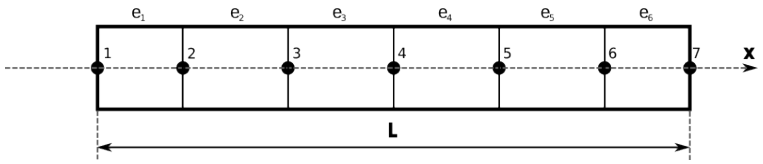

Figure 3.6. FEM discretised acoustical pipe.

The geometry of the pipe is first broken up into a finite number of elements as depicted in figure 3.6. In this case, the elements are one dimensional, they allow pressure variation in only one direction, and each element has two nodes, one at either end. The elements are joined to one another at the nodes. Interconnected elements share the node along the coincident edge.

Within each element the velocity potential $\phi(x,t)$ is given by a first order polynomial that is described in terms of a local element normalised coordinate axis ζ_1. The coordinates ζ_1 are normalised for each element so that $\zeta_1=-1$ at the left-hand node of the element and $\zeta_1=1$ at the right-hand node.

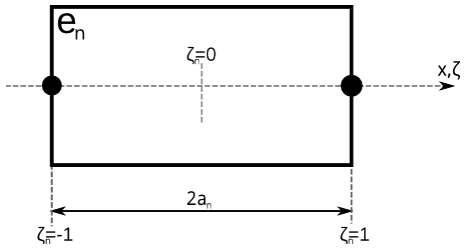

Figure 3.7. Diagram showing the local coordinate system within a single 1D element.

The velocity potential within element e is then described by the expression

$$\phi(\zeta_1,t)=\frac{1}{2}(1-\zeta_1)\phi_1(t)+\frac{1}{2}(\zeta_1+1)\phi_2(t) \qquad 3.67.$$

where $\Phi_1(t)$ is the velocity potential at the node on the left-hand side of the nth element and $\Phi_2(t)$ is the velocity potential at the node on the right-hand side of the nth element. This function is known as a shape function. Globally, these functions compose the equivalent prescribed functions used in the Rayleigh-Ritz method. The equivalent prescribed functions may be found as the combination of all the element shape functions when all nodes have zero velocity potential with the exception of a single node with unity velocity potential. Thus, this defines N_n prescribed functions where N_n is the number of nodes in the approximated discrete system. In the same way as the prescribed functions for the Rayleigh-Ritz method must be carefully constructed to meet specific conditions, similar constraints apply to the choice of the element shape-functions. Most importantly that they are compatible with the governing equations. For the case of the acoustical situation at hand, a first order polynomial is sufficient to permit the single spatial derivative required to calculate the acoustical kinetic energy.

The shape function in expression 3.67 can equivalently be written in matrix form as

$$\phi(\zeta_1,t)=\begin{bmatrix}G_1(\zeta_1) & G_2(\zeta_1)\end{bmatrix}\begin{bmatrix}\Phi_1(t)\\ \Phi_2(t)\end{bmatrix}=\boldsymbol{g}(\zeta_1)^T\boldsymbol{\Phi}_e(t) \qquad 3.68.$$

where the coefficients *G* are defined to be

$$G_1(\zeta_1)=\frac{1}{2}(1-\zeta_1)\ ,\ G_2(\zeta_1)=\frac{1}{2}(1+\zeta_1) \qquad 3.69.$$

For each element, the kinetic energy, T_e, can be calculated using the same integral expression as was used in the Rayleigh-Ritz method with the alteration that the limits are adjusted to be from x_s, the left-hand limit of the element, to x_e, the right-hand limit of the element,

$$T_e=\int_{xs}^{xe}\frac{1}{2}\rho_0\left(\frac{\partial\phi(x,t)}{\partial x}\right)^2 A\,dx \qquad 3.70.$$

By substitution this can be rewritten in terms of the local coordinates, ζ_1, as

$$T_e=\int_{-1}^{1}\frac{1}{2}\rho_0\left(\frac{\partial\phi(\zeta_1,t)}{\partial\zeta_1}\right)^2\frac{A}{a_1}d\zeta_1 \qquad 3.71.$$

Similarly, the potential energy for each element can be written as

$$U_e=\int_{-1}^{1}\frac{1}{2}\rho_0\left(\frac{\partial\phi(\zeta_1,t)}{\partial\zeta_1}\right)^2\frac{A}{c_0^2}a_1\,d\zeta_1 \qquad 3.72.$$

In both these expressions, A is the cross-sectional area of the pipe. Using the matrix expression for the velocity potential, given in equation 3.68, the kinetic and potential energies can be written

$$T_e = \frac{1}{2}\rho_0 \boldsymbol{\phi}_e(t)^T \boldsymbol{H}_e \boldsymbol{\phi}_e(t) \qquad 3.73.$$

and

$$U_e = \frac{1}{2}\rho_0 \dot{\boldsymbol{\phi}}_e(t)^T \boldsymbol{Q}_e \dot{\boldsymbol{\phi}}_e(t) \qquad 3.74.$$

where

$$\boldsymbol{H}_e = \frac{A}{a_1}\int_{-1}^{1} \frac{\partial \boldsymbol{g}(\zeta_1)}{\partial \zeta_1}\frac{\partial \boldsymbol{g}(\zeta_1)^T}{\partial \zeta_1} d\zeta_1 = \frac{A}{a_1}\begin{bmatrix} 1/2 & -1/2 \\ -1/2 & 1/2 \end{bmatrix} \qquad 3.75.$$

and

$$\boldsymbol{Q}_e = \frac{A a_1}{c_0^2}\int_{-1}^{1} \boldsymbol{g}(\zeta_1)\boldsymbol{g}(\zeta_1)^T d\zeta_1 = \frac{A a_1}{c_0^2}\begin{bmatrix} 2/3 & 1/3 \\ 1/3 & 2/3 \end{bmatrix} \qquad 3.76.$$

These two matrices, $\boldsymbol{H}_e$ and $\boldsymbol{Q}_e$, are known as the element-stiffness and element-inertia matrices respectively. As the elemental velocity-potential prescribed functions are defined in terms of the nodal velocity potentials, consequently, the elemental potential and kinetic energy is also described in terms of the nodal velocity potential. The integration is only performed once when formulating the element, thereafter expressions 3.73 and 3.74 along with the element-stiffness and element-inertia matrices may be used to very easily find the element energies for an element of any size and shape.

The velocity potentials at all nodes in the whole system are defined to be members of a vector $\bar{\boldsymbol{\phi}}(t)$,

$$\bar{\boldsymbol{\phi}}(t) = \begin{bmatrix} \phi_1(t) & \phi_2(t) & \phi_3(t) & \dots & \phi_{N_n}(t) \end{bmatrix}^T \qquad 3.77.$$

The velocity potential vectors for each element, $\boldsymbol{\phi}_e(t)$, can be retrieved from this vector with an indexing matrix, $\boldsymbol{A}_e$. For example, considering the first element, the elemental velocity potential vector is

$$\boldsymbol{\phi}_1(t) = \begin{bmatrix} \phi_1(t) \\ \phi_2(t) \end{bmatrix} \qquad 3.78.$$

which may be retrieved from the system velocity potential vector using the indexing matrix $\boldsymbol{A}_1$ as

$$\boldsymbol{\phi}_1(t)=\boldsymbol{A}_1\bar{\boldsymbol{\phi}}(t) \qquad 3.79.$$

where

$$\boldsymbol{A}_1=\begin{bmatrix}1 & 0 & 0 & ... & 0\\ 0 & 1 & 0 & ... & 0\end{bmatrix} \qquad 3.80.$$

The system kinetic and potential energy is approximated as the sum of the individual elemental kinetic- and potential-energies as were defined above. This summation is neatly expressed by defining global acoustical stiffness and acoustical inertia matrices, which are constructed from the elemental-stiffness and elemental-inertia matrices using the indexing matrices, $\boldsymbol{A}_e$, as

$$\bar{\boldsymbol{H}}=\sum_{e=1}^{N_e}\boldsymbol{A}_e^T\boldsymbol{H}_e\boldsymbol{A}_e \quad \text{and} \quad \bar{\boldsymbol{Q}}=\sum_{e=1}^{N_e}\boldsymbol{A}_e^T\boldsymbol{Q}_e\boldsymbol{A}_e \qquad 3.81.$$

where N_e is the number of elements in the system. Effectively, the multiplication $\boldsymbol{A}_e^T\boldsymbol{H}_e\boldsymbol{A}_e$ simply sums the elemental matrices consecutively into the global matrix, $\bar{\boldsymbol{H}}$, such that their rows and columns are located according to the global indexing of their nodes. In practice, the matrices $\boldsymbol{A}_e$ need not be formed. It is generally computationally more efficient to directly add the elemental terms directly to the global matrices by row and column index. Once the global acoustical stiffness and acoustical inertia matrices are formed, the system kinetic and potential energy are given by the expressions

$$T=\frac{1}{2}\rho_0\dot{\bar{\boldsymbol{\phi}}}(t)^T\bar{\boldsymbol{H}}\,\dot{\bar{\boldsymbol{\phi}}}(t) \qquad 3.82.$$

and

$$U=\frac{1}{2}\rho_0\bar{\boldsymbol{\phi}}(t)^T\bar{\boldsymbol{Q}}\,\bar{\boldsymbol{\phi}}(t) \qquad 3.83.$$

The system is now expressed in the same form as expressions 3.55 and 3.56 in the previous section and the last few steps to generate the system equations of motion follow. From this point, the same path as the Rayleigh-Ritz method. This results in the equations of motion for the system

$$\boldsymbol{H}\,\boldsymbol{p}(t)+\boldsymbol{Q}\,\ddot{\boldsymbol{p}}(t)=\boldsymbol{0} \qquad 3.84.$$

where $\boldsymbol{p}(t)=-\rho_0\partial\boldsymbol{\phi}(t)/\partial t$. As in the previous section, the FE method is demonstrated for a 0.5m-long closed pipe. The calculated and exact eigenfrequencies and eigenfunctions for pipe discretised into 10 and 20 elements, creating systems with 11 and 21 nodes,

respectively, are shown below. The Matlab code to calculate these results is given in Appendix III.

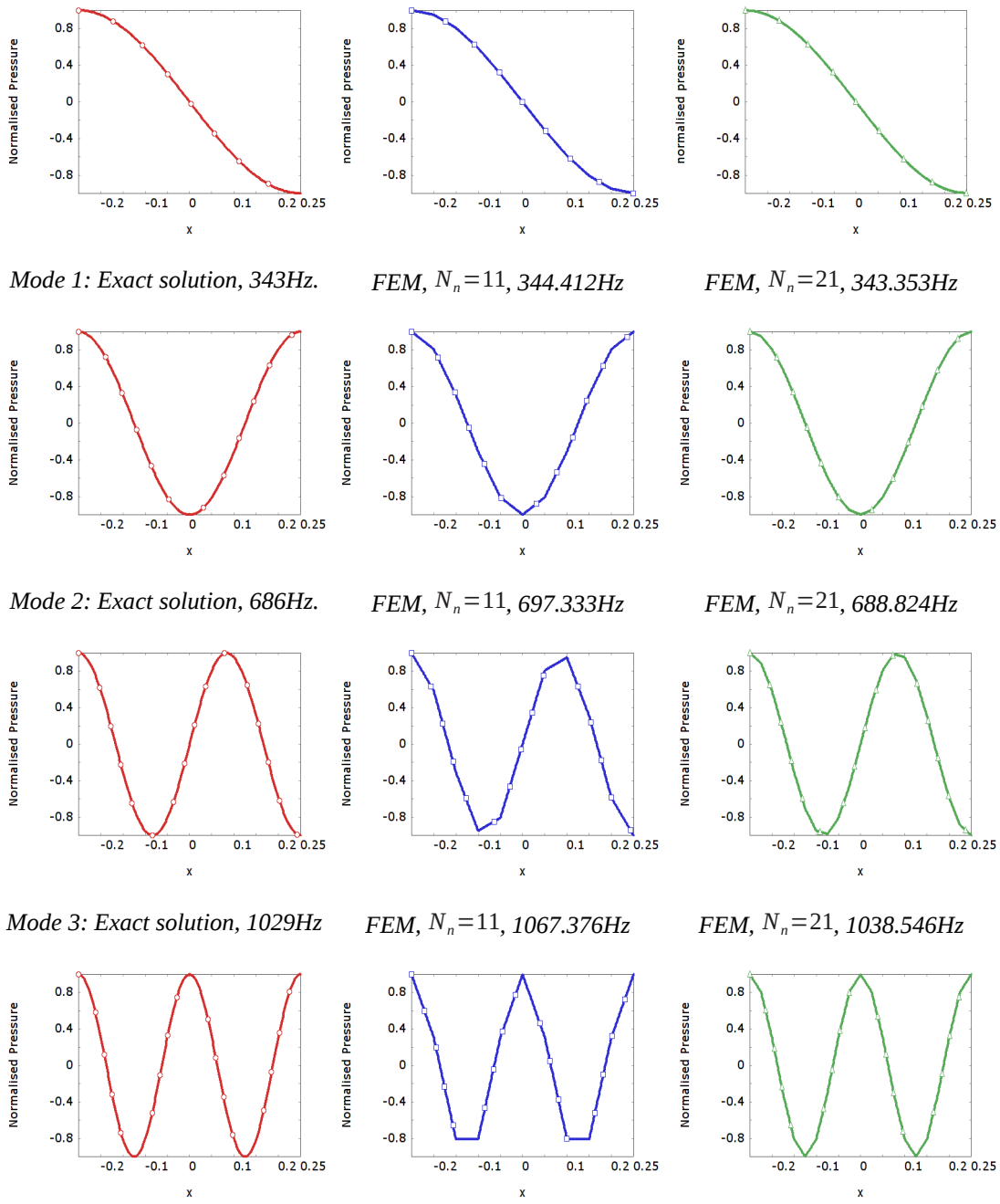

Mode 1: Exact solution, 343Hz. *FEM, $N_n=11$, 344.412Hz* *FEM, $N_n=21$, 343.353Hz*

Mode 2: Exact solution, 686Hz. *FEM, $N_n=11$, 697.333Hz* *FEM, $N_n=21$, 688.824Hz*

Mode 3: Exact solution, 1029Hz *FEM, $N_n=11$, 1067.376Hz* *FEM, $N_n=21$, 1038.546Hz*

Mode 4: Exact solution, 1372Hz *FEM, $N_n=11$, 1462.985Hz* *FEM, $N_n=21$, 1394.665Hz*

Figure 3.8. The first four modes of the exact eigenfunction and eigenfrequencies of a closed 0.5m long pipe compared to the FEM approximate solution using 10 and 20 linear finite elements.

As was seen with the Rayleigh-Ritz method, the accuracy of the solution decreases if the prescribed functions are unable to describe the pressure variation. This means that the FE method is most accurate at low frequencies, where the spatial variation in pressure is low,

and that it becomes increasingly less accurate with increasing frequency. Increasing the number of elements has the effect of increasing the number of prescribed functions that are used and makes the FE method more accurate as the variation in pressure is more easily imitated by the element shape functions. The shape functions that have been used for these simple elements allows only a linear variation in pressure within each element. With the Rayleigh-Ritz method in the previous section, for the first few eigenfunctions only a few prescribed functions were required for a good match with the exact solution. For example, for a good approximation of the fourth mode (at 686Hz), it was only necessary to use 6 prescribed functions, whereas, with the FEM solution more prescribed functions are required. The fourth mode is predicted less accurately even when 20 elements are used (which is equivalent to 21 prescribed functions, one per node). The reason for this is that the exact eigenfunction solution in this case is a sinusoid, which is a function with continuous curvature and no linear regions, the linear shape functions of the simple elements are very poor at approximating this solution and hence many elements are required for a good convergence.

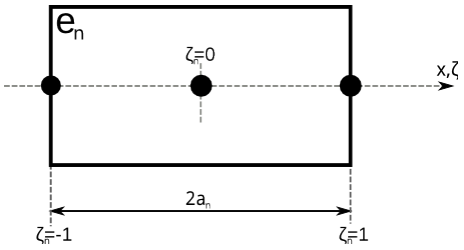

Figure 3.9. 1D three-noded element function.

This problem can be overcome by using finite elements with a higher order shape function and a greater number of nodes. For example, consider the three-noded element shown in figure 3.9. For this element, a quadratic shape function is defined as

$$\phi(\zeta_1,t)=\frac{\zeta_1}{2}(1-\zeta_1)\phi_1(t)+(1-\zeta_1^2)\phi_2(t)+\frac{\zeta_1}{2}(\zeta_1+1)\phi_3(t) \qquad 3.85.$$

This can be written in terms of the multiplication of two vectors

$$\phi(\zeta_1,t)=\begin{bmatrix}G_1(\zeta_1)\\G_2(\zeta_1)\\G_3(\zeta_1)\end{bmatrix}^T\begin{bmatrix}\phi_1(t)\\\phi_2(t)\\\phi_3(t)\end{bmatrix}=\boldsymbol{g}(\zeta_1)^T\boldsymbol{\Phi}_e(t) \qquad 3.86.$$

where the coefficients *G* are defined to be

$$G_1(\zeta_1)=\frac{\zeta_1}{2}(\zeta_1-1)\ ,\ G_2(\zeta_1)=(1-\zeta_1^2)\ ,\ G_3(\zeta_1)=\frac{\zeta_1}{2}(1+\zeta_1) \qquad 3.87.$$

The elemental-stiffness and elemental-inertial matrices are then calculated as

$$\boldsymbol{H}_e = \frac{A}{a_1}\int_{-1}^{1} \frac{\partial \boldsymbol{g}(\zeta_1)}{\partial \zeta_1}\frac{\partial \boldsymbol{g}(\zeta_1)^T}{\partial \zeta_1} d\zeta_1 = \frac{A}{a_1}\begin{bmatrix} 7/6 & -4/3 & 1/6 \\ -4/3 & 8/3 & -4/3 \\ 1/6 & -4/3 & 7/6 \end{bmatrix} \qquad 3.88.$$

and

$$\boldsymbol{Q}_e = \frac{A a_1}{c_0^2}\int_{-1}^{1} \boldsymbol{g}(\zeta_1)\boldsymbol{g}(\zeta_1)^T d\zeta_1 = \frac{A a_1}{c_0^2}\begin{bmatrix} 4/15 & 2/15 & -1/15 \\ 2/15 & 16/15 & 2/15 \\ -1/15 & 2/15 & 4/15 \end{bmatrix} \qquad 3.89.$$

Using these matrices to analyse the same 0.5m pipe results in the eigenfrequency and eigenfunction approximations shown in figure 3.10. The Matlab code to calculate these results is given in Appendix III.

The results are shown for the pipe discretised into 5 and 10 quadratic elements resulting in systems with 11 and 21 nodes. Compared to the two FEM systems shown in figure 3.8, with the linear shape function elements but the same number of nodes, the results are closer to the exact solution in all cases. As before, the same trend is observed that for eigenfunctions that vary slowly with respect to x the FEM-approximated solution is most accurate. At high frequencies, where the variation of the eigenfunction with respect to x is high, the FEM approximated system diverges from the exact solution and the approximated eigenfrequencies overestimate the exact solution. The choice of geometric discretisation is very important when using the finite element and care must be taken that enough elements are used so that the discrete-system solution converges with the exact solution. The type of element is an important consideration. As a general guideline for elements with linear shape functions, at least 20 elements per acoustical wavelength are required and for elements with a quadratic shape function, at least 6 elements per acoustical wavelength are required.

The Finite-Element Method is outlined for a one dimensional acoustical system. However, the approach is applicable to two-dimensional and three-dimensional cases and, additionally, for many other physical domains including mechanical and magnetic. The details of these applications are not described in this thesis. The interested reader is referred to Fahy for a description of three-dimensional acoustical and mechanical FEM formulations [46].

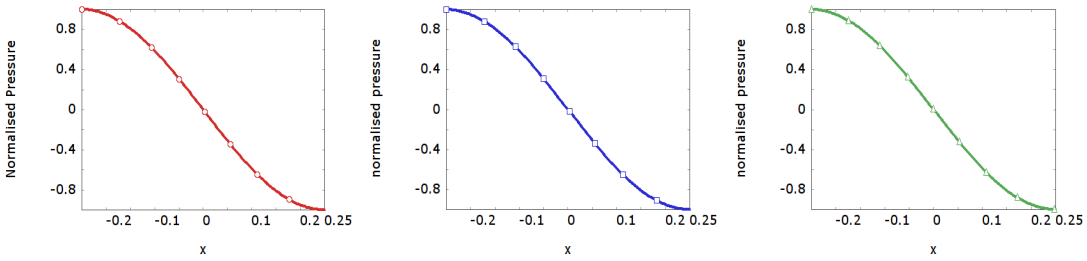

Mode 1: Exact solution, 343Hz. *FEM, N_n=11, 343.036Hz* *FEM, N_n=21, 343.002Hz*

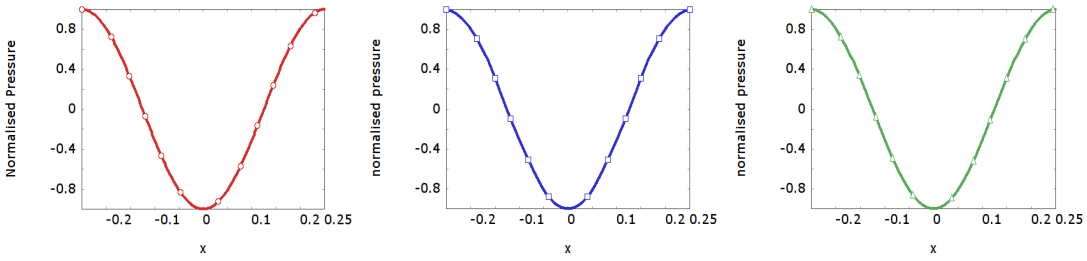

Mode 2: Exact solution, 686Hz. *FEM, N_n=11, 687.099Hz* *FEM, N_n=21, 686.073Hz*

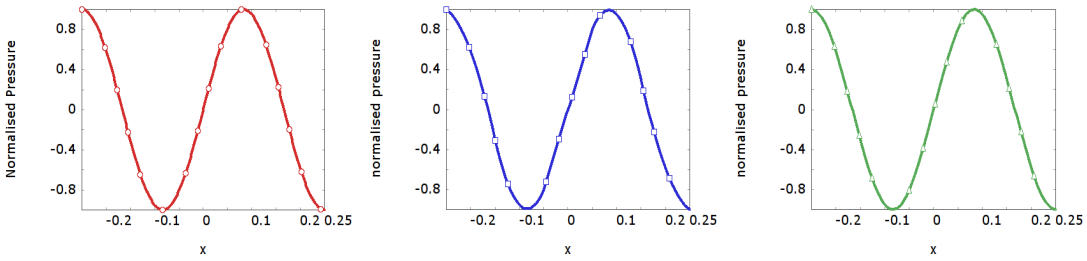

Mode 3: Exact solution, 1029Hz *FEM, N_n=11, 1036.632Hz* *FEM, N_n=21, 1029.539Hz*

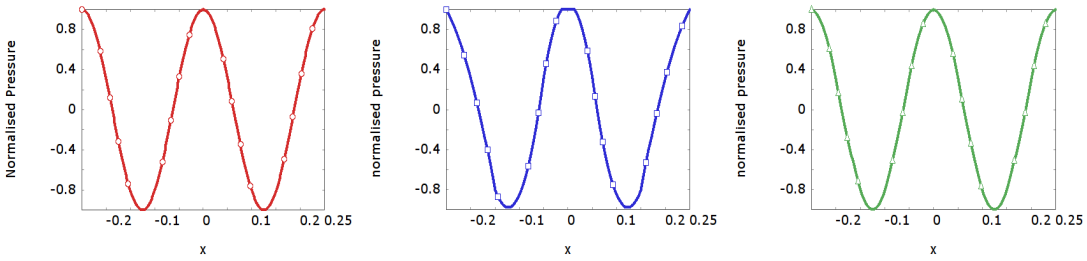

Mode 4: Exact solution, 1372Hz *FEM, N_n=11, 1400.148Hz* *FEM, N_n=21, 1374.197Hz*

Figure 3.10. The first four modes of the exact eigenfunction and eigenfrequencies of a closed 0.5m long pipe compared to the FEM approximate solution using 5 and 10 quadratic finite elements.

The Finite-Element Method is a powerful tool for analysis of real-world engineering problems and it is used extensively in this thesis to provide approximate solutions for the behaviour of various parts of loudspeakers. While it is instructive to work through the FEM formulation for simple cases, for the analysis of full acoustical and mechanical systems, the author has chosen to use a commercially available FEM package. PAFEC-FE [55] is used

throughout this thesis for the solution of mechanoacoustical FEM problems. PAFEC-FE provides many element types including 2D linear and quadratic plane and shell mechanical elements, 2D mechanical and acoustical axisymmetric elements, and 3D linear and quadratic mechanical and acoustical elements. Additionally, several material models are permitted including acoustical materials with complex sound speed and mechanical viscoelastic materials. PAFEC also permits fully-coupled mechanoacoustical models that include full approximation of the fluid-structure interaction. As was outlined in section 2.2.5, the acoustic loading of the mechanical parts of the loudspeaker is an important consideration.

Figure 3.11 shows the PAFEC calculated eigenfrequencies and eigenfunctions for the same closed-acoustical-pipe problem posed above. This FEM model was defined by hand directly into the PAFEC dat file, which is provided in Appendix IV. Ten 2D axisymmetric quadratic elements were used and the pipe was given a diameter of 10mm. Comparison of these results with figure 3.10 show that they are extremely close to the Matlab FEM results.

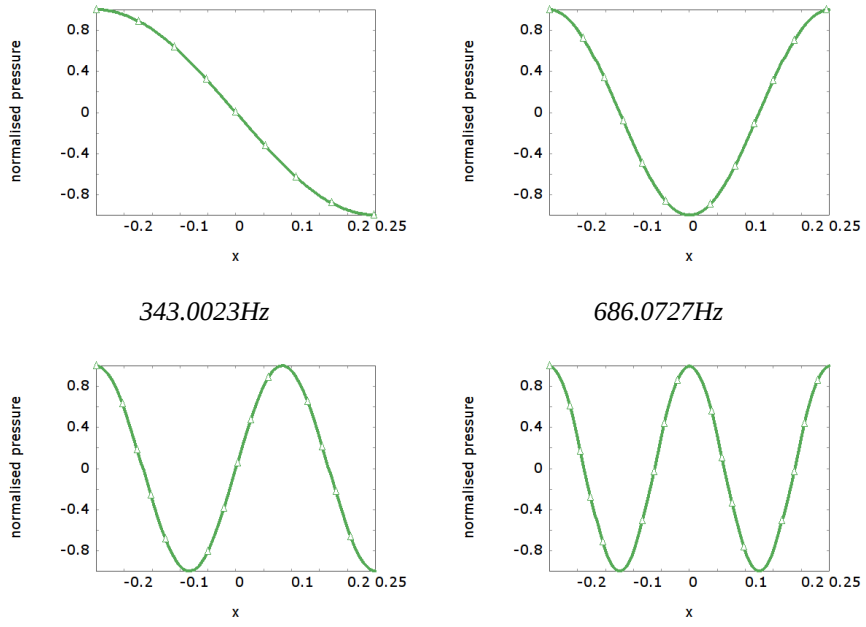

Figure 3.11. PAFEC-FE calculated eigenfrequencies and eigenfunctions of a 0.5m closed narrow acoustical pipe using 10 2D axisymmetric quadratic elements.

3.8 The Boundary-Element Method

The Boundary-Element Method (BEM) is a numerical approach to solving the boundary integral formulation that was introduced in section 3.5. The BEM approach is similar to the FEM approach in that the geometry is approximated by discretisation. However, compared to the FEM, which requires the acoustical volume to be discretised into finite elements joined at nodes, the BEM requires the bounding surface of the geometry to be discretised into boundary element “patches” joined at nodes. Like the boundary integral formulation, the acoustical field in the bounded volume is completely characterised by the acoustical behaviour on the bounding surface. Although it is possible to apply the BEM to both interior and exterior problems, generally the BE method is less efficient than the FE method for interior problems. As is outlined below, formation of the BEM matrices requires the patch pressure and normal velocity to be numerically integrated several times for each patch in the boundary element. The FEM-system matrices, by comparison, are constructed directly from predetermined element matrices that require only minimal processing before inclusion in the system. Additionally, the FEM-system matrices only hold non-zero values either at locations on the diagonals or at locations that correspond to nodes shared by two or more elements. Consequently, the FEM matrices are sparse and this characteristic can be used to improve the memory consumption and speed of matrix manipulations. The BEM-system matrices are not sparse, every location is non-zero, and such performance optimisations cannot be applied. In most cases, as BEM only requires the bounding surface to be discretised, it is simpler to generate a mesh for BEM analysis than FEM analysis. However, the real advantage of the BEM compared to the FEM is that it allows an infinite, or semi-infinite regions to be considered.

The first stage of the method is to discretise the bounding surface of the geometry into boundary element “patches”, that are joined at nodes. The term “patch” is used in a BEM context to refer to an individual discretised region; whereas, in the FEM these regions were called elements. For the BEM case, the entire set of patches forms a single boundary element which defines the complete bounding surface. The reason for this distinction is that the boundary element formulation is valid only for the complete set of patches. This is not like the FEM case where an additional element is easily added to extend the geometry without requiring complete recalculation of the behavioural equations for rest of the geometry.

Within each patch the acoustical parameters, pressure p and surface normal particle velocity $\boldsymbol{u}.\boldsymbol{n}$, are described using shape functions in a similar way as was used for the FE method. Unlike the FE method, the boundary integral formulation, equation 3.41, does not require the

computation of any spatial pressure derivatives (in directions perpendicular to the surface normal) and hence the simplest possible shape function that could be used is a uniform function. The uniform function results in a so-called “constant-pressure Boundary-Element patch” and, in this case, each patch has a single degree of freedom. However, the constant-pressure patch is infrequently used as it requires a great number of patches for an accurate approximation to the solution.

In this case a four-noded planar patch using linear shape functions is formulated, as illustrated in figure 3.12.

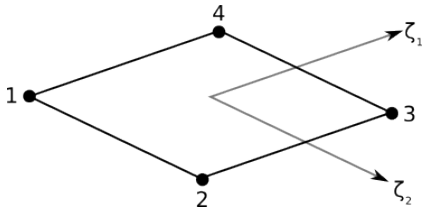

Figure 3.12. Four-noded planar-rectangular Boundary-Element patch.

The surface of the patch is geometrically parametrised by the two normalised local coordinate variables ζ_1 and ζ_2. These are normalised so that the nodal positions correspond to the locations $\zeta_1 = \pm 1$ and $\zeta_2 = \pm 1$.

The surface pressure on the patch is described in terms of the four nodal pressures as

$$\begin{aligned} p(t,\zeta_1,\zeta_2) = & \\ & \frac{1}{4} p_1(t)(1-\zeta_1)(1-\zeta_2) + \\ & \frac{1}{4} p_2(t)(1-\zeta_1)(1+\zeta_2) + \\ & \frac{1}{4} p_3(t)(1+\zeta_1)(1+\zeta_2) + \\ & \frac{1}{4} p_4(t)(1+\zeta_1)(1-\zeta_2) \end{aligned} \qquad 3.90.$$

where $p_i(t)$ is the pressure at the i-th node. Similarly the surface normal velocity is written in terms of the four nodal normal velocities as

$$\begin{aligned} u_n(t,\zeta_1,\zeta_2) = & \\ & \frac{1}{4} u_{n1}(t)(1-\zeta_1)(1-\zeta_2) + \\ & \frac{1}{4} u_{n2}(t)(1-\zeta_1)(1+\zeta_2) + \\ & \frac{1}{4} u_{n3}(t)(1+\zeta_1)(1+\zeta_2) + \\ & \frac{1}{4} u_{n4}(t)(1+\zeta_1)(1-\zeta_2) \end{aligned} \qquad 3.91.$$

where u_{ni} is the normal velocity, $\boldsymbol{u}.\boldsymbol{n}$, at the i-th node.

These two expressions can be written as the multiplication of two vectors as

$$p(t,\zeta_1,\zeta_2)=\begin{bmatrix}B_1(\zeta_1,\zeta_2)\\B_2(\zeta_1,\zeta_2)\\B_3(\zeta_1,\zeta_2)\\B_4(\zeta_1,\zeta_2)\end{bmatrix}^T\begin{bmatrix}p_1(t)\\p_2(t)\\p_3(t)\\p_4(t)\end{bmatrix}=\boldsymbol{b}(\zeta_1,\zeta_2)^T\,\boldsymbol{p}_p(t) \tag{3.92.}$$

and

$$u_n(t,\zeta_1,\zeta_2)=\begin{bmatrix}B_1(\zeta_1,\zeta_2)\\B_2(\zeta_1,\zeta_2)\\B_3(\zeta_1,\zeta_2)\\B_4(\zeta_1,\zeta_2)\end{bmatrix}^T\begin{bmatrix}u_{n1}(t)\\u_{n2}(t)\\u_{n3}(t)\\u_{n4}(t)\end{bmatrix}=\boldsymbol{b}(\zeta_1,\zeta_2)^T\,\boldsymbol{u}_{np}(t) \tag{3.93.}$$

where the coefficients of the vector $\boldsymbol{b}(\zeta_1,\zeta_2)$ are

$$\begin{aligned}B_1(\zeta_1,\zeta_2)&=\frac{1}{4}(1-\zeta_1)(1-\zeta_2),\quad B_2(\zeta_1,\zeta_2)=\frac{1}{4}(1-\zeta_1)(1+\zeta_2)\\B_3(\zeta_1,\zeta_2)&=\frac{1}{4}(1+\zeta_1)(1+\zeta_2),\quad B_4(\zeta_1,\zeta_2)=\frac{1}{4}(1+\zeta_1)(1-\zeta_2)\end{aligned} \tag{3.94.}$$

At this stage, the pressure at any point in the acoustical volume may be approximated with the expression

$$c(\boldsymbol{x})\,p(\boldsymbol{x})=\sum_{p=1}^{N_p}\boldsymbol{h}_p(\boldsymbol{x})^T\,\boldsymbol{p}_p+j\omega\rho_0\,\boldsymbol{g}_p(\boldsymbol{x})^T\boldsymbol{u}_{np} \tag{3.95.}$$

which is a discrete equivalent to the Kirchoff Helmholtz integral, given in expression 3.39. The summation is performed over each patch with the vectors $\boldsymbol{h}_p(\boldsymbol{x})$ and $\boldsymbol{g}_p(\boldsymbol{x})$ uniquely defined for each patch. Each element of these vectors correspond to a node on the p-th patch and are calculated from the integrals

$$h_{pj}(\boldsymbol{x})=\int_{-1}^{1}\int_{-1}^{1}\nabla_{\boldsymbol{x}_{pj}}G(\boldsymbol{x}\,|\,\boldsymbol{x}_{pj}).\boldsymbol{n}\,B_j(\zeta_1,\zeta_2)\,d\zeta_1\,d\zeta_2 \tag{3.96.}$$

and

$$g_{pj}(\boldsymbol{x})=\int_{-1}^{1}\int_{-1}^{1}G(\boldsymbol{x}\,|\,\boldsymbol{x}_{pj})\,B_j(\zeta_1,\zeta_2)\,d\zeta_1 d\zeta_2 \tag{3.97.}$$

The coefficient $c(\boldsymbol{x})$ was encountered in the boundary integral formulation and is the correction factor resulting from the proportion of the excluded geometry that lies in the

acoustical volume V_b. If the pressure sampling location, $\boldsymbol{x}$, lies in the fluid region then $c(\boldsymbol{x})=-1$. If the pressure sampling location lies on the boundary element surface then $c(\boldsymbol{x})$ must be calculated and is defined by the expression

$$c(\boldsymbol{x})=1+\frac{1}{4\pi}\sum_{p=1}^{N_p}\int_{-1}^{1}\int_{-1}^{1}\nabla_{\boldsymbol{x}_{pj}}\left[\frac{1}{|\boldsymbol{x}-\boldsymbol{x}_{pj}|}\right].\boldsymbol{n}\,d\zeta_1\,d\zeta_2 \qquad 3.98.$$

However, rather than directly evaluating this expression, $c(\boldsymbol{x})$ is commonly interpreted geometrically as minus the proportion of the solid angle at $\boldsymbol{x}$ that lies within the modelled region. Using this definition, $c(\boldsymbol{x})$ may be calculated quickly by inspection of the meshed geometry.

Typically, the two integrals in the calculation of the members of $\boldsymbol{h}_p(\boldsymbol{x})$ and $\boldsymbol{g}_p(\boldsymbol{x})$ are evaluated using Gauss-Legendre quadrature [47, p.571]. The patch face-normal, $\boldsymbol{n}$, must point out of the fluid volume. As is described in more detail below, in order to form the system equations for the boundary element these integrals are evaluated $4N_nN_p$ times, where N_n is the number of system nodes, N_p is the number of patches and the 4 occurs as each patch has four nodes. This means that this integration step is a critical stage in the BE computation and typically has the most significant impact on the run time in formulating the full behavioural equations. Gauss-Legendre quadrature is an appropriate method as it provides an optimal accuracy of integral approximation for a given number of integrand evaluations [56]. In this form it is relatively difficult to handle the equations of motion of the system because the individual node pressures and normal velocities appearing in the patch pressure and normal velocity vectors, $\boldsymbol{p}_p$ and $\boldsymbol{u}_{np}$, appear four times in the summation as each node should be used by four different patches. The pressures and normal velocities at all nodes in the whole system are defined to be members of the vectors $\boldsymbol{p}$ and $\boldsymbol{u}_n$,

$$\boldsymbol{p}^T=\begin{bmatrix}p_1(t) & p_2(t) & p_3(t) & \ldots & p_{N_n}(t)\end{bmatrix} \qquad 3.99.$$

and

$$\boldsymbol{u}_n^T=\begin{bmatrix}u_{n1}(t) & u_{n2}(t) & u_{n3}(t) & \ldots & u_{nN_n}(t)\end{bmatrix} \qquad 3.100.$$

The patch pressure and normal velocity vectors, $\boldsymbol{p}_p$ and $\boldsymbol{u}_{np}$, may be retrieved from the global pressure and normal velocity vectors by use of an indexing matrix $\boldsymbol{A}_p$.

For example, considering a patch that uses the first four global nodes in descending order the patch pressure vector is

$$\boldsymbol{p}_1 = \begin{bmatrix} p_4(t) \\ p_3(t) \\ p_2(t) \\ p_1(t) \end{bmatrix} \qquad 3.101.$$

that may be retrieved from the global pressure matrix using the indexing matrix matrix $\boldsymbol{A}_1$ as

$$\boldsymbol{p}_1 = \boldsymbol{A}_1 \boldsymbol{p} \qquad 3.102.$$

where

$$\boldsymbol{A}_1 = \begin{bmatrix} 0 & 0 & 0 & 1 & \dots & 0 \\ 0 & 0 & 1 & 0 & \dots & 0 \\ 0 & 1 & 0 & 0 & \dots & 0 \\ 1 & 0 & 0 & 0 & \dots & 0 \end{bmatrix} \qquad 3.103.$$

Similarly the patch normal velocity vector may be retrieved from the global normal velocity matrix using the same indexing matrix as

$$\boldsymbol{u}_{n1} = \boldsymbol{A}_1 \boldsymbol{u}_n \qquad 3.104.$$

Using these indexing matrices it is easy to form global vectors containing the appropriate coefficients from $\boldsymbol{h}_p(\boldsymbol{x})$ and $\boldsymbol{g}_p(\boldsymbol{x})$ resulting in

$$c(\boldsymbol{x})\, p(\boldsymbol{x}) = \boldsymbol{h}(\boldsymbol{x})^T \boldsymbol{p} + j\omega\rho_0 \boldsymbol{g}(\boldsymbol{x})^T \boldsymbol{u}_n \qquad 3.105.$$

where

$$\boldsymbol{h}(\boldsymbol{x}) = \sum_{p=1}^{N_p} \boldsymbol{A}_p^T \boldsymbol{h}_p(\boldsymbol{x}) \qquad 3.106.$$

and

$$\boldsymbol{g}(\boldsymbol{x}) = \sum_{p=1}^{N_p} \boldsymbol{A}_p^T \boldsymbol{g}_p(\boldsymbol{x}) \qquad 3.107.$$

As with the FEM case, although the indexing matrices, $\boldsymbol{A}_p$, are useful for the precise definition of the mapping from $\boldsymbol{g}_p(\boldsymbol{x})$ and $\boldsymbol{h}_p(\boldsymbol{x})$ to $\boldsymbol{g}(\boldsymbol{x})$ and $\boldsymbol{h}(\boldsymbol{x})$, in practice this stage is commonly implemented by indexing the patch vectors directly into the global vectors, which is generally a more computationally efficient approach.

Before expression 3.105 can be used to approximate the acoustical pressure within the bounded volume, it is first necessary to solve for the acoustical fields at the nodes themselves so that the vectors $\boldsymbol{u}_{np}$ and $\boldsymbol{p}_p$ are known. By evaluating expression 3.105 at the

location of each node in turn, the field pressure $p(\boldsymbol{x})$ is eliminated and the resulting expression relates the node pressures, $\boldsymbol{p}_p$, to the node normal velocities, $\boldsymbol{u}_{np}$, as

$$\boldsymbol{C}\,\boldsymbol{p} = \boldsymbol{H}\,\boldsymbol{p} + j\omega\rho_0\boldsymbol{G}\,\boldsymbol{u}_n \qquad 3.108.$$

This stage is commonly called collocation. The rows of the N_n by N_n matrix, $\boldsymbol{H}$, are given by the vector $\boldsymbol{h}(\boldsymbol{x}_i)$, as defined above, where $\boldsymbol{x}_i$ is the location of the i-th node such that

$$\boldsymbol{H} = \begin{bmatrix} \boldsymbol{h}(\boldsymbol{x}_1)^T \\ \boldsymbol{h}(\boldsymbol{x}_2)^T \\ \vdots \\ \boldsymbol{h}(\boldsymbol{x}_{N_n})^T \end{bmatrix} \qquad 3.109.$$

Similarly the rows of the N_n by N_n matrix, $\boldsymbol{G}$, are given by the vector $\boldsymbol{g}(\boldsymbol{x}_i)$, as defined above, such that

$$\boldsymbol{G} = \begin{bmatrix} \boldsymbol{g}(\boldsymbol{x}_1)^T \\ \boldsymbol{g}(\boldsymbol{x}_2)^T \\ \vdots \\ \boldsymbol{g}(\boldsymbol{x}_{N_n})^T \end{bmatrix} \qquad 3.110.$$

The matrix $\boldsymbol{C}$ is N_n by N_n and diagonal holding the correction factors for each node,

$$\boldsymbol{C} = \begin{bmatrix} c(\boldsymbol{x}_1) & 0 & \cdots & 0 \\ 0 & c(\boldsymbol{x}_2) & \cdots & 0 \\ \vdots & \vdots & \ddots & \vdots \\ 0 & 0 & \cdots & c(\boldsymbol{x}_{N_n}) \end{bmatrix} \qquad 3.111.$$

It is quite common for this expression to be rearranged slightly to give

$$\boldsymbol{A}\,\boldsymbol{p} = j\omega\rho_0\boldsymbol{G}\,\boldsymbol{u}_n \qquad 3.112.$$

where

$$\boldsymbol{A} = \boldsymbol{C} - \boldsymbol{H} \qquad 3.113.$$

Typically, either the surface pressures, $\boldsymbol{p}$, or the surface velocities, $\boldsymbol{u}_n$, are prescribed and, by evaluation of expression 3.112, the other acoustical surface quantity is easily determined. It is common for the FEM and BEM to be combined so that the FEM approach can be used to model finite regions or interior regions of the geometry and the BEM method can be used for infinite regions. Despite this common combination, it is relatively rare to find commercial solvers that allow complete FEM to BEM coupling. For many applications this lack of complete coupling is not a significant problem. In many industries the acoustical load on the

mechanical structure is insignificant. However for loudspeakers where the mechanical radiation impedance is a significant proportion of the mechanical moving mass, it is critical that the BEM is fully coupled to the FEM.

The BEM formulation for interior modelling is approached in exactly the same manner as the method above, which was assumed to be for the exterior case, with the exception that the normal direction must be adjusted accordingly. The result of this is that if the exterior case is considered, then the governing equations for the interior case are identical save for a change in sign of the elements of $\boldsymbol{H}_i = -\boldsymbol{H}$ and a reversal of the solid angle proportions $c_i(\boldsymbol{x}) = 1 - c(\boldsymbol{x})$. Consequently, both the internal and the external matrix equations are singular at the acoustical modes of the interior problem. As a result, the standard exterior BEM formulation suffers from the so called “characteristic-frequency problem” where the solution cannot be determined close to the interior modal frequencies. There are two commonly used methods to remove the characteristic-frequency problem. Burton and Miller [57] reformulated the standard boundary integral equation taking its derivative with respect to $\boldsymbol{n}$. This alternative formulation can still be used for both interior and exterior problems; however, the interior modes are present at different frequencies compared to the standard formulation. By also formulating the standard BEM equations, it is possible to find a solution at a given frequency by choosing the most well conditioned of the two sets of equations. Another method used to remove the characteristic frequency problem is described by [58] in which N_c additional points are included in the collocation stage. The additional points should lie outside of the fluid region where evaluation of expression 3.95 should return zero. This condition is enforced on the solution by the addition of N_c rows in the system matrices defined by

$$0 = \boldsymbol{h}(\boldsymbol{x}_{ci})\boldsymbol{p} + j\omega\rho_0 \boldsymbol{g}(\boldsymbol{x}_{ci})\boldsymbol{u}_n \qquad 3.114.$$

where $\boldsymbol{x}_{ci}$ is the position of the i-th additional collocation point. This results in an over-determined problem where the dimensions of $\boldsymbol{H}$ and $\boldsymbol{G}$ are $N_n + N_c$ by N_n. Consequently, the solution cannot be computed using a matrix inverse; however, a other methods can be used, for example, the Moore-Penrose pseudoinverse [59]. This technique is commonly known as the Combined Helmholtz Integral Equation Formulation, or CHIEF method. The position and number of the additional collocation points is a critical consideration for the performance of the CHIEF method. Ideally, they should not coincide with the nodes of the internal modes, as otherwise they are ineffective at damping the interior normal modes, but rather be placed at location where the interior solution has a pressure maximum.

Included in Appendix V is a simple Matlab [54] based BEM formulation that has been used to calculate the exterior boundary element solution to a simple acoustical problem by means of an illustration. The Matlab BEM code was developed based on the description above in conjunction with the very clear Matlab BEM implementation provided in the Masters dissertation of Holmström [60]. The formulation uses planar, quadrilateral patches with linear shape-functions, the integrals required to form the vectors $\boldsymbol{h}_p(\boldsymbol{x})$ and $\boldsymbol{g}_p(\boldsymbol{x})$ are calculated using a Gauss-Legendre quadrature with 2 Gauss points in each local coordinate direction. The formulation allows the inclusion of additional interior collocation points as required by the CHIEF method described above.

Using this BEM formulation a simple example problem is considered, the acoustical pressure field generated by a pulsating sphere is considered. This acoustical problem has been selected as the radiated acoustical field from a pulsating sphere is easily solved analytically, this makes it easy to assess the accuracy of the BEM solutions.

The sphere considered has a radius of 100mm, all points on the surface of the sphere move with equal normal velocity such that the sphere approximately pulsates. The total volume velocity of the sphere surface is unity. The radiated pressure field is evaluated at a point 1m from the centre of the sphere. The analytical solution to this acoustical problem is well known [18, p.171] and is given by the expression

$$p(r) = u_n \rho_0 c_0 \left[\frac{(kr)^2}{1+(kr)^2} + j\frac{kr}{1+(kr)^2} \right] \frac{a}{r} e^{-jk(r-a)} \qquad 3.115.$$

where a is the radius of the sphere, r is the observation distance from the sphere. The mesh used to analyse the problem using the Boundary-Element Method is shown in figure 3.13.

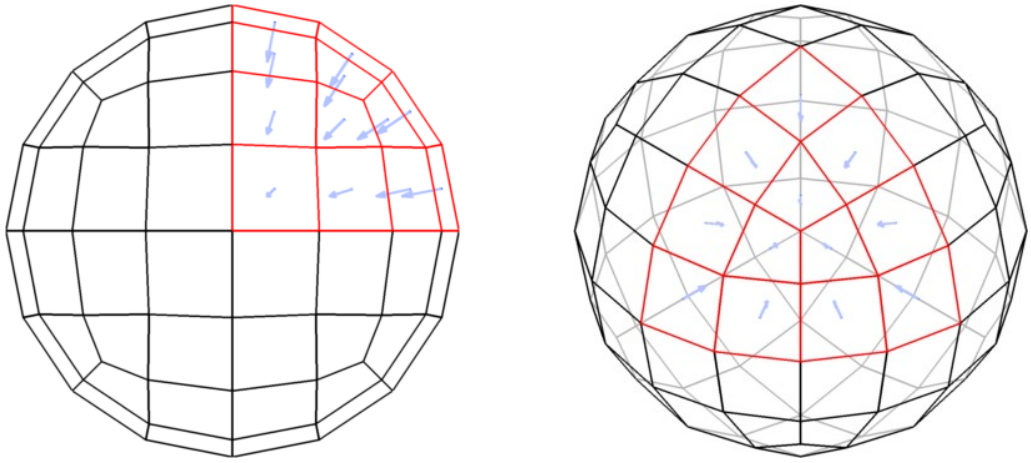

Figure 3.13. BEM mesh used to approximate the pulsating sphere. Black mesh shows the full mirrored geometry, red mesh shows the symmetry reduced mesh that is modelled. Face normals of the red mesh patches are shown.

As the sphere is a symmetrical geometry, and the prescribed velocity is also symmetrical, it is not necessary to form the full BEM matrices for the entire sphere as pressure field solution shares the same symmetry. Consequently the BEM matrices are only formed for the portion of the sphere shown in red. This has a significant effect on the efficiency and stability of the solution. The figures also show the patch normals for the red region. The total number of patches in the entire sphere is 96. Figure 3.14 shows the calculated pressure at 1m from the sphere versus frequency for the analytical solution and two BEM approximations.

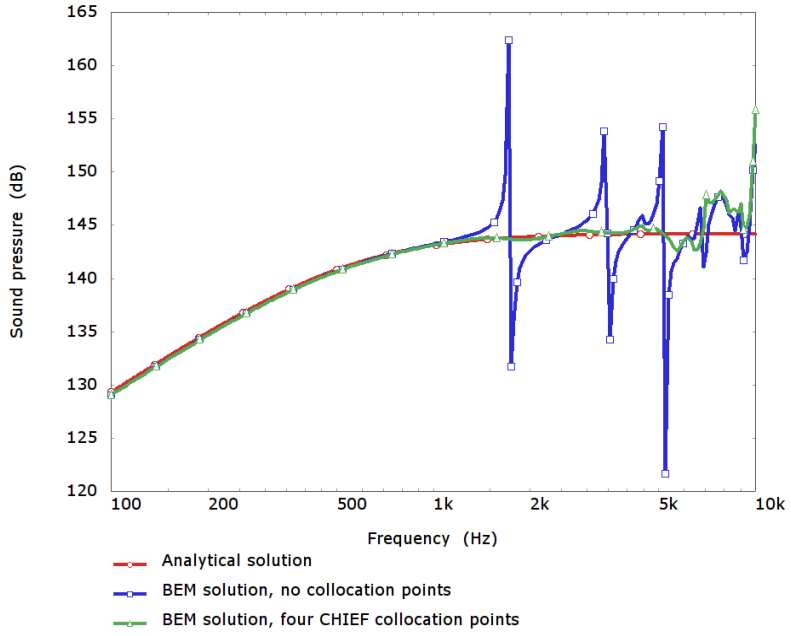

Figure 3.14. 100mm pulsating sphere radiation at 1m, analytical solution and BEM approximations.

The first BEM approximation is for the standard BEM formulation without any consideration for the characteristic frequency problem. It is observed that at low frequencies the agreement between this approximation and the analytical solution is good. However there are clear problem frequencies in the solution where the BEM approximation is very inaccurate. This is the characteristic frequency problem and the frequencies of the large response deviations coincide with the modal frequencies of the internal spherical acoustical cavity. It should also be observed that the frequency area affected by the characteristic frequency problem is relatively wide.

The second BEM approximation is for the same geometry, but the solution method includes four additional collocation points in the interior of the sphere, as required by the CHIEF method. It can be seen that this approximation is much improved and the characteristic frequency problem is almost completely, although not totally, eliminated. However, at very

high frequencies the BEM approximation fails to accurately describe the analytical solution. This occurs as the discretised geometry and patch shape-functions are unable to accurately describe the acoustical solution. For a more accurate solution either more elements, elements with a higher order shape function or higher degrees of quadrature for the element integrations should be used.

A second example, computed with the same Matlab BEM formulation, is also provided in Appendix VII.

3.8.1 BEM illustration: calculation of radiation impedance using BEM

In section 2.3, the radiation impedance of an infinite-baffle-mounted planar circular piston was used in the discussion of the efficiency of direct-radiating loudspeakers. There are only few arrangements of radiator for which the radiation impedance can be explicitly described [61]. For rigid infinite-baffle mounted radiators of other shapes, there are a number of publications that describe methods of calculating the radiation impedance typically using a numerical integration to perform the last step in the calculation [62,63,64]. However, in order to more generally calculate the radiation impedance, with arbitrary radiator geometry, arbitrary radiation environment and more complex radiator-surface velocities, a different approach is required. It is possible to use the BEM to calculate the radiation impedance of radiators of arbitrary shape, arbitrary motion and in an arbitrary environment. To demonstrate this, the simple case of a circular piston in an infinite baffle is considered using the commercial FEM and BEM package PAFEC-FE [55]. The analytical solution to this acoustical problem was described in section 2.3.

PAFEC-FE FEM and BEM analyses are defined in a single text file that is then passed to the PAFEC-FE software for processing and solution. This text file, hereafter the dat file, irrespective of the type of analysis, always outlines the same information for the solver to process:

1. a definition of the type of problem to be solved;
2. a description of the meshed geometry to be considered. Achieved by definition firstly of nodal coordinates and secondly element topology and type;
3. the prescription of boundary conditions.

This three stage outline will be familiar to readers with experience of FEM and BEM analysis. PAFEC-FE is a very versatile software tool and allows many different solution types, and several different methods to outline the geometry. When complex geometries are

involved, it is common to use an external program, such as [65,66,67], to provide nodal coordinates and element topology directly into the PAFEC-FE dat file. It is feasible to use an alternative method of defining the geometry in the dat file by hand for simple geometries. The full, commented text of the dat file for this problem definition is given in Appendix VIII. Figure 3.15 illustrates the layout of the PAFEC-FE model.

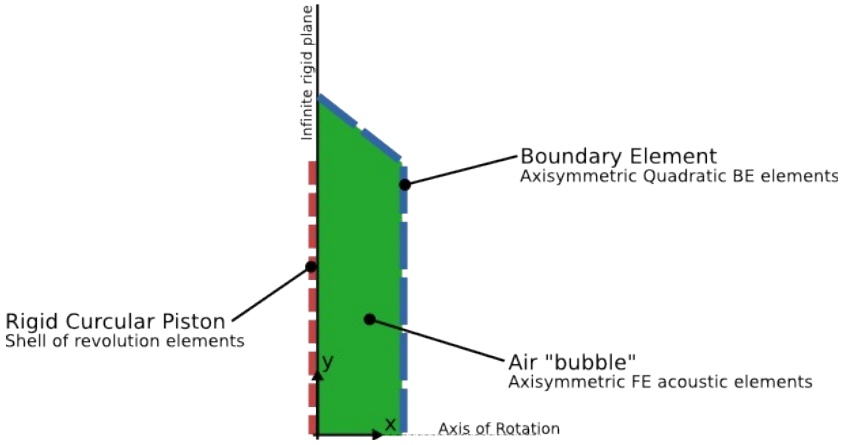

Figure 3.15. Geometry of PAFEC-FE model: rigid piston in an infinite baffle.

The problem under consideration is rotationally symmetric (axisymmetric). Because of this symmetry, it is not necessary to create a full, three-dimensional meshed representation of the geometry, but instead an axisymmetric modelling approach may be used. PAFEC-FE provides element formulations of one- and two-dimensional finite and boundary elements that have rotational symmetry mathematically defined. Using these elements, only a half section through the model need be defined. When using an axisymmetric solution type, the PAFEC-FE convention is for the x axis to be the axis of rotation. The infinite baffle is included in the formulation by using a plane of symmetry defined in the dat file and applied to the BE. Because of this symmetry condition, the modelling approach must be slightly adjusted. The BE in combination with any planes of symmetry must form a complete enclosed surface. PAFEC-FE does not allow BE patches to lie directly on planes of symmetry. This means that the BE region must extend away from the infinite baffle. The cavity left between the rigid mechanical piston and the BE is bridged using a region of axisymmetric FE acoustic elements. The piston is constructed from one-dimensional thin shell-of-revolution elements. The formulation of these finite elements includes both thickness and mechanical rotation. They are only valid for use when the region to be modelled is of minimal thickness. In the case of the piston, which is constrained to move rigidly, the validity of this approximation is not of concern. The rigidity of the piston is applied by instructing PAFEC-FE to consider the x-direction motion of all the nodes on the

piston to be the same variable: in PAFEC-FE terminology “repeating the freedoms”. The PAFEC-FE solver is sufficiently advanced so that it is able to fully model each of the three regions: structural FE piston, acoustical FE air “bubble” and acoustical BE, and, additionally, the coupling between the regions. The piston is set to move with harmonic velocity of unit amplitude. Once solved, the total mechanical impedance may be calculated by extracting the PAFEC-FE result for the force, F, applied to the driving point on the piston: this force is equal to the mechanical impedance because the piston is driven with unit velocity, u. This impedance is equal to the sum of mechanical impedance of the piston itself, Z_m, and the mechanical impedance due to the presence of the acoustical load, Z_r,

$$Z_m + Z_r = \frac{F}{u} \qquad 3.116.$$

The mechanical impedance of the piston is, in this case, simply the impedance due to the piston mass, M.

$$Z_m = j\,\omega\,M \qquad 3.117.$$

As the piston mechanical impedance, Z_m, is purely imaginary, it follows that the radiation resistance, R_r, is equal to the real part of the force applied to the piston.

$$R_r = \Re\left(F\right) \qquad 3.118.$$

In this way, the radiation resistance of a circular piston mounted in an infinite baffle can be numerically calculated using PAFEC-FE. Indeed, there is no restriction to this simple case; it is clear that a similar approach can be taken to analyse radiators of other geometries.

Figure 3.16 shows the PAFEC-FE calculated radiation resistance compared to the analytical solution. The plotted radiation resistances are normalised in magnitude by the radiation resistance of a tube mounted piston,

$$R_r = \rho_0\,c\,\pi\,a^2 \qquad 3.119.$$

The frequency axis of the plotted results is given in normalised wavenumber, $k\,a$. The PAFEC-FE approximation of the radiation resistance is very good. There is a very small deviation that occurs at $ka = 12$. Other than this slight error, the two results are extremely close.

Clearly, the major advantage of the numerical BEM approach is that it is possible to analyse radiators of arbitrary shape. For example, figure 3.18 shows the PAFEC-FE calculated radiation resistance of an infinite-baffle mounted rigid spherical-cap diaphragm (as depicted in figure 3.17) along with the analytical calculation of the rigid circular piston previously

shown. The spherical-cap diaphragm is a common geometry for high-frequency loudspeaker drivers given its mechanical rigidity. No analytical formulation for the radiation resistance of a rigid spherical-cap diaphragm in an infinite baffle exists. PAFEC-FE is used throughout this thesis for numerical solutions to acoustical problems.

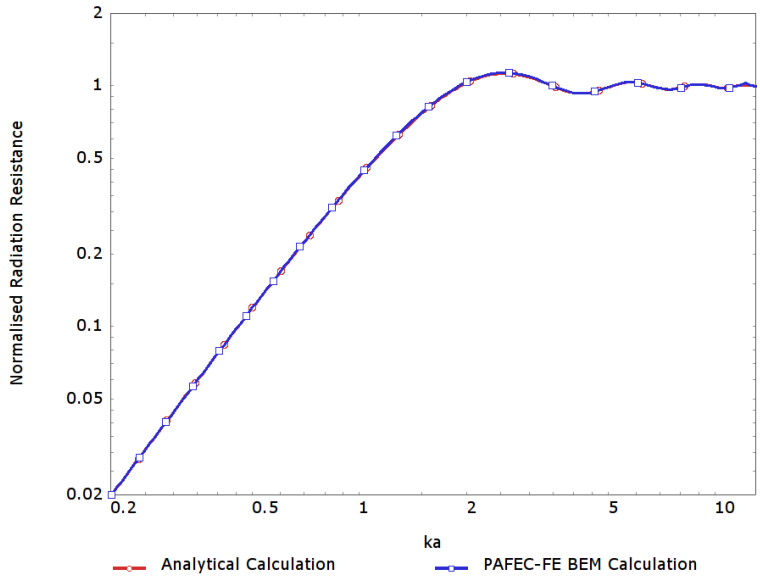

Figure 3.16. Radiation resistance of a circular piston mounted in an infinite baffle calculated by analytical method and FE/BE using PAFEC-FE.

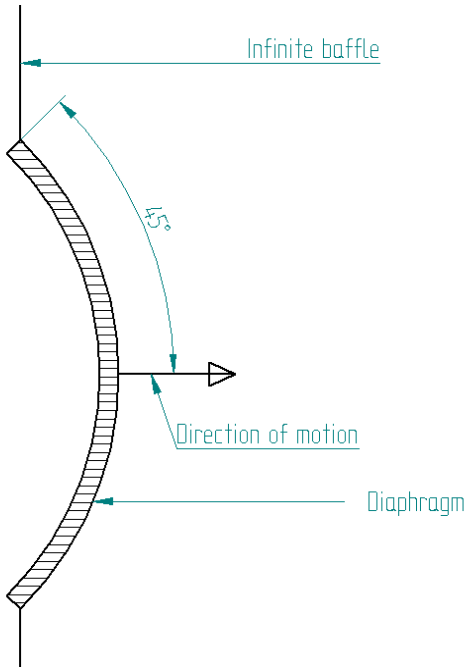

Figure 3.17. Illustration showing an infinite-baffle mounted rigid spherical-cap diaphragm.

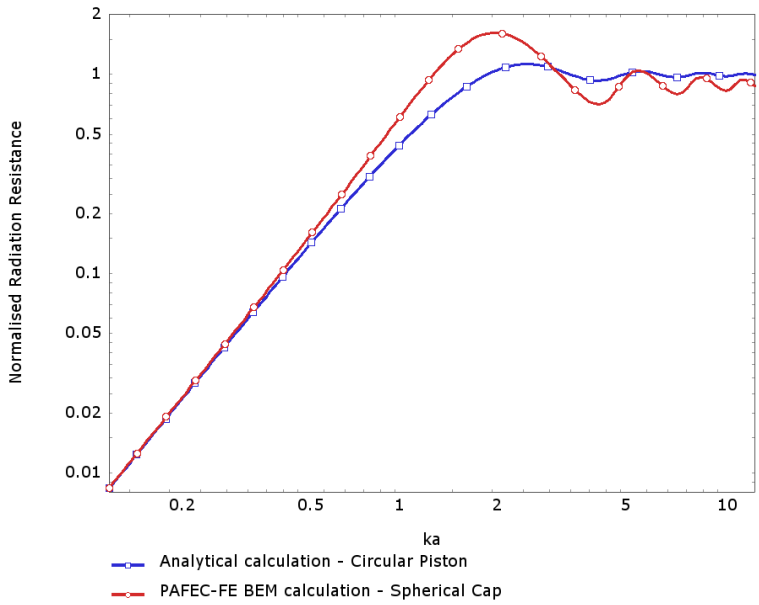

Figure 3.18. Radiation resistance of a rigid circular piston mounted in an infinite baffle analytically calculated and 45 degree rigid spherical-cap diaphragm mounted in an infinite baffle calculated using PAFEC-FE.

3.9 Conclusions

In this chapter a number of methods for the analysis and modelling of acoustical behaviour of various situations were outlined. The various techniques form the theoretical basis for the work in subsequent chapters which consider the specific problem of compression-driver design in more detail.

4 The acoustics of compression-driver phase plugs

4.1 Introduction

The basic compression driver principle is illustrated in figure 4.1. The radiating diaphragm is connected to one face of a narrow acoustical cavity and on the opposite face the loudspeaker horn is connected to the cavity via a small hole. At low frequencies, the compression cavity is effectively incompressible and unit volume-displacement applied to the cavity by the diaphragm results in unit volume-displacement leaving the compression cavity through the hole to the horn. As the diaphragm area is larger than the hole area, unit displacement of the radiating diaphragm causes a much greater than unit displacement of the acoustical particles at the entrance to the horn. The compression arrangement behaves like a transformer converting relatively low displacements or velocities at the diaphragm into larger acoustical velocities at the horn throat.

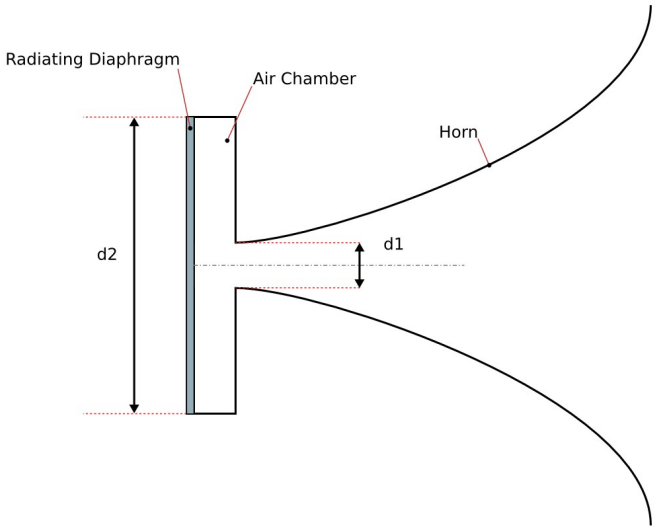

Figure 4.1. Schematic layout of a horn driver with a large diaphragm, of diameter d2, and small horn throat, of diameter d2, joined by a small acoustical volume.

Using the numerical methods outlined in chapter 3, it is possible to determine the performance of a few different compression-driver arrangements in order to highlight some of the caveats of the approach and the issues encountered during the design. Figure 4.2 shows the radiation resistance of an axially-driven dome-diaphragm placed directly at the throat of a truncated exponential horn in comparison to the same dome diaphragm driving a narrow acoustical cavity, which is then connected via a central hole to an exponential horn. This is very similar to the situation depicted in figure 4.1. Both of these horn radiators are modelled using PAFEC-FE. The mechanical diaphragm and the air in the horn are modelled using finite elements and the FE horn region is coupled to a boundary element at the horn mouth to permit the horn to radiate into a 2π space.

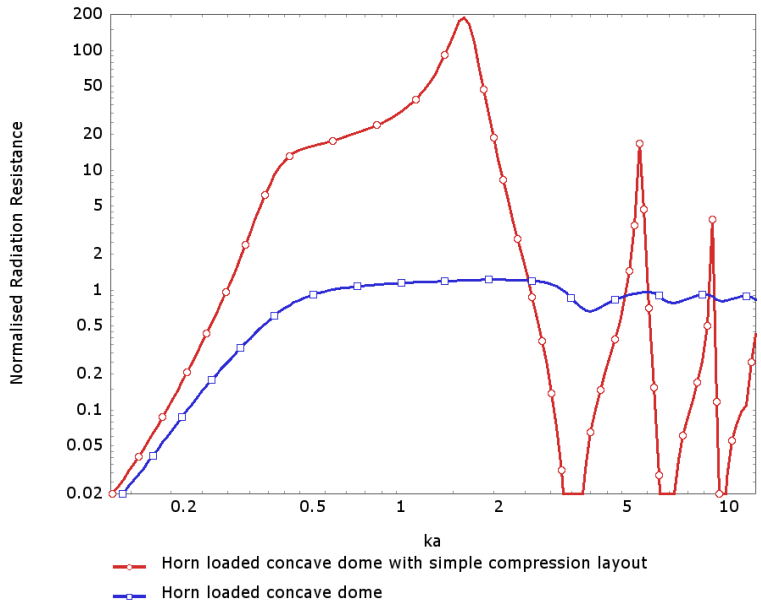

Figure 4.2. Comparison of the radiation resistance of a horn-loaded rigid spherical-cap diaphragm with and without a simple compression chamber. The cap surface is 45 degrees from axis to edge in cross section. The horns are truncated exponential with cut-on frequency $ka \approx 0.35$. *For the case with compression* $\alpha = 10$.

Both horns have the same flare rate and termination. Above the horn cut-on frequency of $ka = 0.35$, the driver with the compression cavity shows an area of significantly increased radiation resistance. However, at frequencies $ka > 1.5$, the radiation resistance of the compression loaded driver is very erratic. This is because at these frequencies the compression cavity is not behaving as a simple acoustical compliance. Consequently this compression driver arrangement is of little practical use.

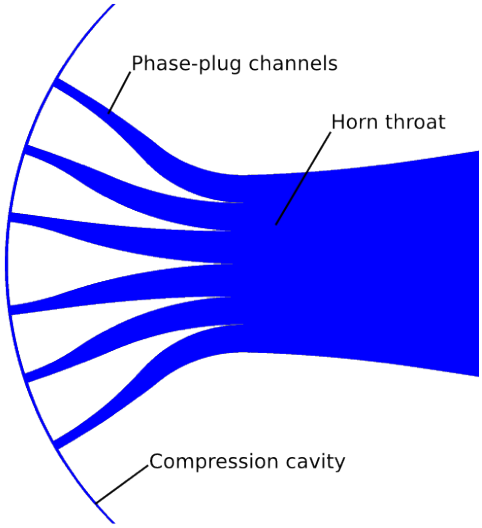

Figure 4.3. Simple unoptimised phase-plug geometry using evenly spaced phase-plug channels..

The performance of the compression driver may be improved by introducing a simple phase plug. The phase plug is positioned between the compression cavity and the horn throat, and carries a number of acoustical channels between the two. The design of the channels is critical to the performance of the driver. A very simple phase plug was constructed with three evenly positioned annular channels of unoptimised length and shape, as shown in figure 4.3. The FEM/BEM analysed result for this simple phase-plugged compression driver is shown in figure 4.4 in comparison to the compression driver with the single exit hole (as shown in figure 4.2). As with the previous comparison, both drivers have the same dome-shaped diaphragm, the same compression ratio and the same truncated exponential horn. Even with this very approximate phase-plug design, the radiation resistance is improved. In particular, the area of increased radiation resistance is extended to higher frequency and the magnitude of the response deviations have been significantly reduced, albeit not completely eliminated.

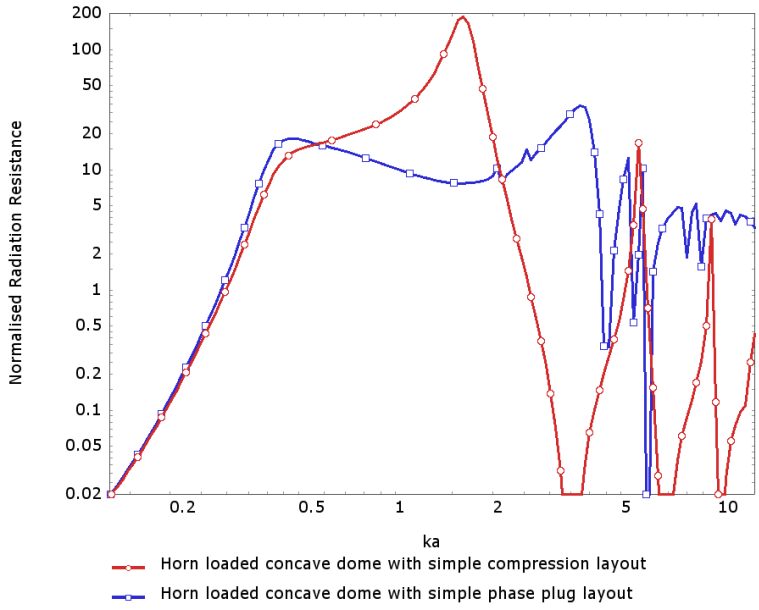

Figure 4.4. Comparison of the radiation resistance of a horn-loaded rigid spherical-cap diaphragm with and without a simple phase plug. The cap surface is 45 degrees from axis to edge in cross section.

This type of annular phase plug is widely used. The cross section of a typical compression driver is shown in figure 4.5. In this illustration, there are three annular channels, each of which leads from the compression cavity to the horn throat. With this arrangement, there is plenty of scope for adjusting the exact geometry of the channels to try to optimise the compression-driver response. The channel geometry has a critical effect on the compression-driver performance. The cavity and the channels are typically several times larger than the highest wavelength to be radiated and there is little acoustical damping in the system.

Consequently, there is great potential for acoustical resonance in this complex acoustical structure. During operation, the pressure in the phase-plug structure is extremely large, sound pressure levels exceeding 120dB are common. The non-linearity of the acoustical system is a significant cause of audible distortion in the driver. This non-linearity problem is significantly worsened by the presence of acoustical resonance in the phase-plug structure, which can typically cause pressure peaks in the channels 20 to 25dB higher than the horn throat pressure.

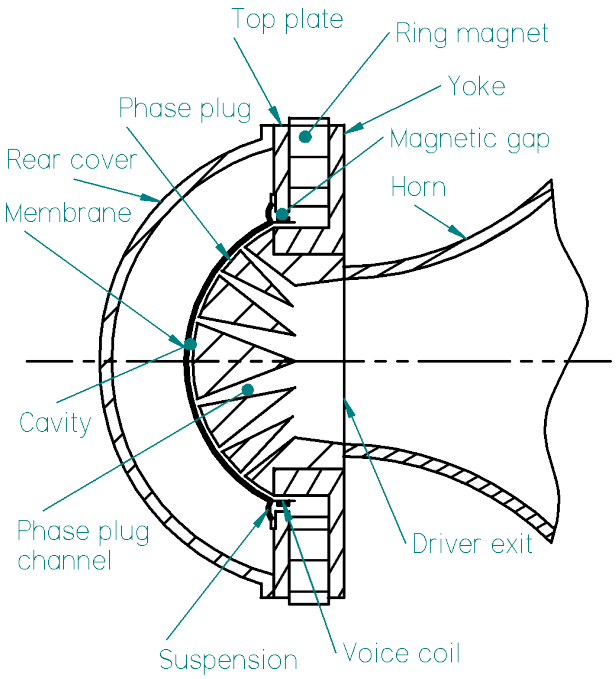

Figure 4.5. Illustration of a typical modern compression driver with three annular channels in the phase plug.

The desired behaviour of the phase plug is relatively simple to outline. Motion of the radiating diaphragm causes air to leave the compression cavity with equal velocity through each of the exit channels. This motion of air causes an acoustical wave to propagate down each of the annular channels. The propagated acoustical wave in each channel arrives at the horn throat at the same time and with the same strength such that the individual propagated waves merge, without reflection, to form a single coherent wave. This wave continues into the horn and is propagated to the listener. Realising this simple behaviour is not straightforward.

Smith's analysis is a critical piece of work that leads towards the ideal behaviour. Figure 4.6 shows the radiation resistance of two phase-plugged compression drivers loaded by the same truncated exponential horn and with the same domed radiating diaphragm. The first of these drivers is the simple unoptimised design already shown in figure 4.4. The other, has channel

entrance geometry in accordance with Smith's guidelines, as shown in figure 4.7. It can be observed that the irregularity in the radiation resistance is greatly reduced by the Smith design and the potential output bandwidth is extended significantly. Smith's analysis of the compression cavity, based on the modal description of the acoustics, showed that, by careful choice of the geometry at the phase-plug entrance, it is possible in principle to generate equal acoustical velocities at the channels. Smith's analysis method is outlined in the next section.

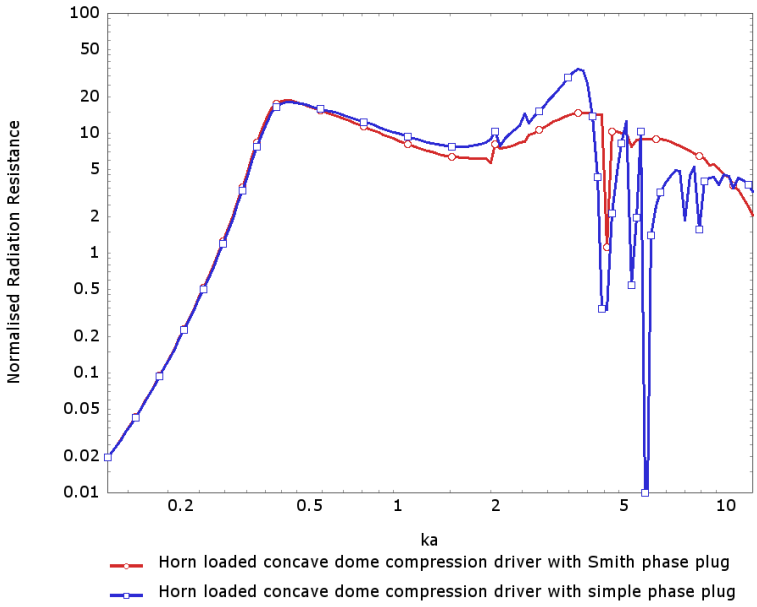

Figure 4.6. Comparison of the radiation resistance of a horn-loaded rigid spherical-cap diaphragm with two designs of phase plug: one based on an equal path-length approach, the other designed according to Smith's guidelines.

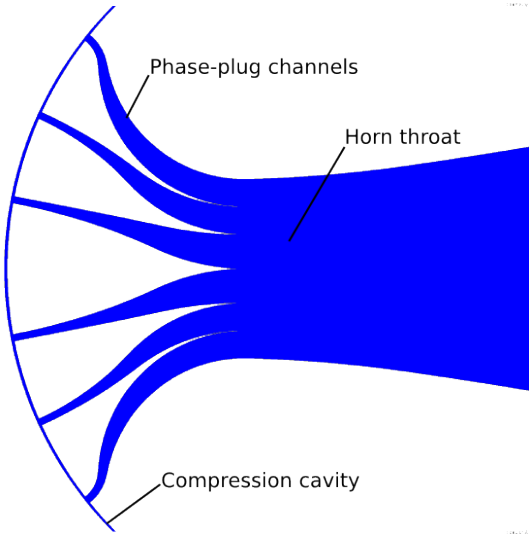

Figure 4.7. Simple unoptimised phase-plug geometry using Bob Smith's channel entrance geometry.

4.2 Smith's channel-positioning methodology

In this section, Smith's optimum phase-plug geometry derivation is outlined, as described in his 1953 paper [35]. Smith describes the behaviour of the compression driver cavity as a boundary value problem. The presentation and notation used by Smith is not consistent with modern acoustics texts. Additionally he presents little derivation or background to the expressions that he uses. The terminology and notation used in this section, although ultimately equivalent to that presented by Smith, should hopefully be more familiar to the reader. The analysis also forms a foundation for much of the work in the following chapters.

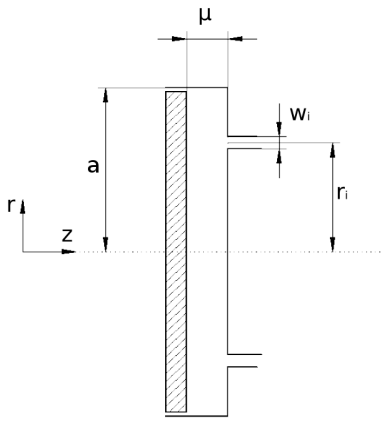

Figure 4.8. A cross section through the cylindrical representation of the compression cavity used by Smith.

Smith suggests that “the compression cavity, being only slightly curved, may be analysed, with only small error, in a cylindrical coordinate system”. Figure 4.8 shows the approximated cavity in cylindrical coordinates with a single exit channel, *i*.

The cylindrical coordinate system in this thesis is given in the notation of Beyer [68] as depicted in Figure 4.9.

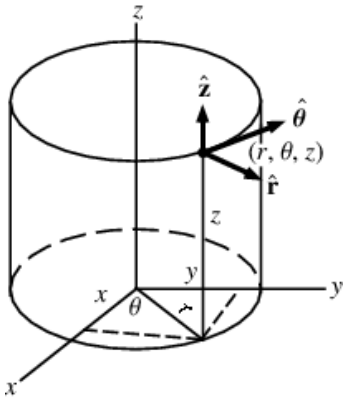

Figure 4.9. The cylindrical coordinate system.

The first stage of the analysis is to derive the rigid-walled eigenfrequencies and eigenfunctions of the compression cavity. These are found as the solution to the homogeneous Helmholtz equation, which is given by the expression

$$\nabla^2 p + \frac{\omega^2}{c_o^2} p = 0 \qquad 4.1.$$

In cylindrical coordinates, the Laplacian can be written in the form [23, p.12]

$$\nabla^2 = \frac{\partial^2}{\partial r^2} + \frac{1}{r}\frac{\partial}{\partial r} + \frac{1}{r^2}\frac{\partial^2}{\partial \theta^2} + \frac{\partial^2}{\partial z^2} \qquad 4.2.$$

Solutions can be found using the method of separation of variables [45 p.116]. Thus in this case it is assumed that the pressure in the cavity may be described as

$$p(r,\theta,z,t) = R(r)\Theta(\theta)Z(z)T(t) \qquad 4.3.$$

with temporal dependence given by

$$T(t) = T_1 e^{-j\omega t} + T_2 e^{j\omega t} \qquad 4.4.$$

the dependence on the circumferential-angular coordinate, θ, given by

$$\Theta(\theta) = \Theta_1 e^{-jm\theta} + \Theta_2 e^{jm\theta} \qquad 4.5.$$

the dependence on the radial coordinate, r, given by

$$R(r) = R_1 J_m(k_r r) + R_2 Y_m(k_r r) \qquad 4.6.$$

and the dependence on the axial coordinate, z, given by

$$Z(z) = Z_1 e^{-jk_z z} + Z_2 e^{jk_z z} \qquad 4.7.$$

In these equations, $T_1, T_2, Z_1, Z_2, \Theta_1, \Theta_2, R_1$ and R_2 are arbitrary constants. The functions J_m and Y_m appearing in equation 4.6 are Bessel functions of the first and second kind, respectively [23, p.27]. To effectively apply this general solution of the wave equation to the situation at hand some simplifications are made. Selecting a convention for time dependence, T_1 is set to be zero. The compression cavity is small in z and in the frequency band of interest only trivial behaviour is observed in this direction. It is therefore assumed that $k_z = 0$ and $Z_1 + Z_2 = 1$. The Bessel function of the second kind, $Y_m(k_r r)$, appearing in the radial function, is singular at $k_r r = 0$. Consequently, to ensure the solution is finite in the cavity, R_2 is set to be zero.

The simplified solution of the wave equation in the rigid-walled compression cavity is therefore given by

$$p(r,\theta,t)=A_1 J_m(k_r r)\left(e^{-jm\theta}+e^{jm\theta}\right)e^{j\omega t} \qquad 4.8.$$

The pressure must obey the rigid wall boundary condition (Neumann [46, p.228]), at the diameter of the compression cavity, given by

$$\frac{dp}{dr}=0\Big|_{r=a} \qquad 4.9.$$

Inserting the solution to the wave equation into to this condition results in

$$\frac{dJ_m(j_{mn})}{dr}=0\Big|_{r=a} \qquad \text{where} \qquad k_{mn}=\frac{j_{mn}}{r_0} \qquad 4.10.$$

Values of j_{mn} that satisfy equation 4.10 are available from mathematical tables [68, pp. 370-374]. The homogeneous wave equation in the rigid-walled compression cavity has solutions only at district values of k. These values of k_{nm} give the eigenfrequencies of the system

$$\omega_{nm}=k_{nm}c_0 \qquad 4.11.$$

The indices n and m refer to the radial and circumferential order of the eigenfunctions respectively. The eigenfunctions of the cavity are found by inserting the values of k_{nm} in to the expression for the spatial pressure variation in the cavity, given in equation 4.8. This results in

$$\Psi_{mn}(r,\theta)=A_{nm}J_m(k_{mn}r)\left(e^{-jm\theta}+e^{jm\theta}\right) \qquad 4.12.$$

The normalisation constant, A_{nm} in equation 4.12 is chosen to satisfy the condition

$$\int_V \Psi_{nm}^2(r,\theta)\,dV=V \qquad 4.13.$$

where V is the volume of the compression cavity.

4.2.1 Analysis of the driven behaviour of the cavity

As outlined in section 3.4, the pressure in a lightly-damped acoustical cavity excited by motion of its walls can be described in terms of the rigid-walled eigenfunctions and eigenfrequencies

$$p(\boldsymbol{x},\omega)=\sum_{n=0}^{\infty}\frac{j\omega\rho_0\Psi_n(\boldsymbol{x})}{V\left[k_n^2-k^2\right]}\int_s \Psi_n(\boldsymbol{y})\boldsymbol{u}(\boldsymbol{y}).\boldsymbol{n}\,dS \qquad 4.14.$$

In this expression, $\boldsymbol{u}(\boldsymbol{y}).\boldsymbol{n}$ is the surface-normal velocity of the cavity wall at vector position $\boldsymbol{y}$ and ρ_0 is the ambient fluid density. In the case of the compression cavity, the eigenfunctions and eigenfrequencies are indexed by two indices, *m* and *n*. As a result a slightly adapted expression must be used

$$p(\boldsymbol{x},\omega)=\sum_{n=0}^{\infty}\sum_{m=0}^{\infty}\frac{j\omega\rho_0\Psi_{nm}(\boldsymbol{x})}{V\left[k_{nm}^2-k^2\right]}\int_s\Psi_{nm}(\boldsymbol{y})\boldsymbol{u}(\boldsymbol{y}).\boldsymbol{n}\,dS \qquad 4.15.$$

The summation is thus performed over all calculated eigenfunctions.

For this application, the integral on the right of this expression can be written as the sum of three integrals each over a separate regions of the cavity surface, as shown in equation 4.16.

$$\int_{r=0}^{a}\int_{\theta=0}^{2\pi}\Psi_{nm}(r,\theta)u_d(r,\theta)r\,d\theta\,dr+\int_{r=0}^{a}\int_{\theta=0}^{2\pi}\Psi_{nm}(r,\theta)u_e(r,\theta)r\,d\theta\,dr + \int_{z=0}^{\mu}\int_{\theta=0}^{2\pi}\Psi_{nm}(r,\theta)u_z(z,\theta)a\,d\theta\,dz \qquad 4.16.$$

The first double integral is performed over the diaphragm side of the compression-cavity surface, the function $u_d(r,\theta)$ describes the normal velocity of this surface. The second double integral is performed over the exit side of the compression-cavity surface, the function $u_e(r,\theta)$ describes the normal velocity of this surface. Finally, the third integral is performed over the small cylindrical surface at the outside diameter of the compression cavity, the function $u_z(z,\theta)$ describes the normal velocity of this surface. Conventional annular-channel compression-driver and phase-plug geometries, including that considered in this case, are completely rotationally symmetrical about the *z* axis. Additionally, the mechanical parts that form and support the radiating diaphragm are also rotationally symmetrical about the *z* axis. The result of this "axisymmetry" is that the three surface normal-velocity functions introduced above are invariant to circumferential angle, θ, and can be written

$$u_d(r,\theta)=u_d(r) \qquad 4.17.$$

$$u_e(r,\theta)=u_e(r) \qquad 4.18.$$

and

$$u_z(r,\theta)=u_z(r) \qquad 4.19.$$

These simplifications to the velocity functions allow the three integrals in equation 4.16 to be rewritten

$$\int_{r=0}^{a} u_d(r) r \int_{\theta=0}^{2\pi} \Psi_{nm}(r,\theta)\, d\theta\, dr + \int_{r=0}^{a} u_e(r) r \int_{\theta=0}^{2\pi} \Psi_{nm}(r,\theta)\, d\theta\, dr + \int_{z=0}^{\mu} u_z(z) a \int_{\theta=0}^{2\pi} \Psi_{nm}(r,\theta)\, d\theta\, dz \qquad 4.20.$$

with all the velocity functions now appearing outside of the second circumferential angle integral. The same integral

$$\int_{\theta=0}^{2\pi} \Psi_{nm}(r,\theta)\, d\theta \qquad 4.21.$$

appears three times, once in each of the double integrals. Inserting the calculated eigenfunctions, $\Psi_{nm}(r,\theta)$, into this integral gives

$$\int_{\theta=0}^{2\pi} \Psi_{nm}(r,\theta)\, d\theta = A_{nm} J_m(k_{mn} r) \int_{\theta=0}^{2\pi} \left(e^{-jm\theta} + e^{jm\theta}\right) d\theta \qquad 4.22.$$

From this expression, it is immediately clear that the integral is only non-zero for the case $m=0$. Effectively, this means that a reduced set of eigenfrequencies and eigenfunctions may be used,

$$\Psi_n(r) = A_n J_0(k_n r) \qquad 4.23.$$

4.2.2 Cavity behaviour without exit channels

First, the behaviour of the compression cavity is considered for the case when there are no exit channels and the cavity is only excited by the radiating diaphragm. The surface velocity is zero at all locations on the enclosure walls except for the surface occupied by the diaphragm. Consequently, it is only necessary to perform the integral on the right-hand side of equation 4.15. This can be written as

$$\int_{r=0}^{a} \int_{\theta=0}^{2\pi} \Psi_n(r) u_d(r) r\, d\theta\, dr \qquad 4.24.$$

where $u_d(r)$ is a function describing the normal velocity of the circular diaphragm. The diaphragm is rigid and the surface of integration is perpendicular to the diaphragm direction of motion, hence the normal velocity function is simply

$$u_d(r) = u_0 \qquad 4.25.$$

The eigenfunctions form an orthonormal set that obey the orthogonality relationship

$$\int_V \Psi_n(\boldsymbol{y})\,\Psi_m(\boldsymbol{y})\,dV = V\,\delta_{nm} \tag{4.26.}$$

In the case of this compression cavity the orthogonality relationship can be written as

$$\int_{r=0}^{a}\int_{\theta=0}^{2\pi}\int_{z=0}^{\mu} \Psi_n(r)\,\Psi_m(r)\,r\,dr\,d\theta\,dz = V\,\delta_{nm} \tag{4.27.}$$

which, performing the integration in z, becomes

$$\int_{r=0}^{a}\int_{\theta=0}^{2\pi} \Psi_n(r)\Psi_m(r)\,r\,dr\,d\theta = \frac{V}{\mu}\,\delta_{nm} \equiv \pi a^2\,\delta_{nm} \tag{4.28.}$$

Within the limits of the integrals in this expression, the diaphragm normal-velocity function $u_d(r)$ can be described in terms of the zeroth eigenfunction as

$$u_d(r) = u_0 \equiv u_0\,\Psi_0(r) \tag{4.29.}$$

After inserting this expression into equation 4.24, comparison with equation 4.28 reveals that the solution to the surface-velocity integral is

$$\int_{r=0}^{a}\int_{\theta=0}^{2\pi} \Psi_n(r)\,u_0\,\Psi_0(r)\,r\,d\theta\,dr = u_0\,\pi a^2\,\delta_{n0} \tag{4.30.}$$

The integral is only non-trivial for the case $n=0$. The pressure in the cavity in this case is, from equation 4.15, simply

$$p_d = u_0\,\pi a^2\,\frac{\rho_0 c_0^2}{j\omega V} \tag{4.31.}$$

The pressure in the cavity is the same as an ideal acoustical compliance. This result has an interesting implication. Using this geometric representation, excitation of the acoustical modes in the compression cavity only occurs due to the presence of the channels, and specifically because of the motion of air at their entrances.

4.2.3 Cavity behaviour with exit channels

The arrangement of the compression driver, as shown in figure 4.8, is to have not only a radiating diaphragm on one face of the cavity, but also a number of exit channels on the opposite face through which sound is radiated. It is most common for these exit paths to be annular channels, having the same rotationally symmetry about the z axis as the radiating diaphragm and the compression cavity. The modal description of the behaviour in the compression cavity, given in equation 4.15, is used to analyse this situation. As the same

rotational symmetry is present, the same reduced set of eigenfunctions and eigenfrequencies, given in equation 4.23, is again used.

It is not necessary to reanalyse the effect of the radiating diaphragm. Instead, it is assumed that the pressure in the cavity can be described as the linear superposition of two pressure contributions: one occurring because of the velocity of the diaphragm, p_d, and the other because of the velocity of air entering and leaving the cavity at the exit channels, p_e,

$$p = p_d + p_e \tag{4.32.}$$

From the analysis above, the pressure due to the diaphragm motion, p_d, is given by

$$p_d = \frac{\rho_0 c_0^2}{V} \frac{u_0 \pi a^2}{j\omega} \tag{4.33.}$$

The exit-surface normal velocity is described by the function $u_e(r)$. The pressure in the compression cavity due to this velocity can, making use of equation 4.15, be written as

$$p_e(r,\omega) = \sum_{n=0}^{\infty} \frac{j\omega\rho_0 \Psi_n(r)}{V\left[k_n^2 - k^2\right]} \int_{\acute{r}=0}^{a} \Psi_n(\acute{r}) u_e(\acute{r}) 2\pi \acute{r}\, d\acute{r} \tag{4.34.}$$

The exit-surface normal velocity is zero except for the locations where a channel exit is positioned. The channel exits are narrow in r and, in the frequency range of operation, the surface normal velocity exiting the compression cavity into the channels may be accurately considered as constant over each channel entrance. To simplify the integral in equation 4.34, the approximation is made that each channel acts on the cavity at one distinct point. This behaviour is defined using the Dirac delta function [69, pp.144-148],

$$u_e(r) = w_1 u_1 \delta(r - r_1) + w_2 u_2 \delta(r - r_2) + \ldots + w_N u_N \delta(r - r_N) \tag{4.35.}$$

where w_i is the width of the i^{th} channel entrance, r_i is the radial position of the i^{th} channel entrance and u_1 is the cavity-surface normal velocity at the entrance to the i^{th} channel. On initial inspection, this expression may appear dimensionally inconsistent because of the w_i terms. However, the integral of the normal velocity over the cavity surface

$$\int_{r=0}^{a} u_e(r) 2\pi r\, dr = q_e \tag{4.36.}$$

is equal to the volume velocity entering the cavity, q_e. Considering this integral for a single thin annular channel, the channel-entrance volume velocity is approximately equal to

$$q_i = u_i A_i \approx u_i w_i 2\pi r_i \tag{4.37.}$$

where A_i is the entrance area of the i^{th} channel.

Using the Dirac delta function to define the channel position, it follows that

$$\int_{r=0}^{a} K_i \delta(r-r_i) 2\pi r\, dr = q_i \approx u_i w_i 2\pi r_i \tag{4.38.}$$

which, recalling the sifting property of the delta function [69, p.146, eq.8], indicates that

$$K_i \approx u_i w_i \tag{4.39.}$$

Using the approximate expression for $u_e(r)$, in equation 4.35, the integral in equation 4.34 is easily evaluated using the sifting property of the Dirac delta. This results in

$$\int_{r=0}^{a} \Psi_n(r) u_e(r) 2\pi r\, dr = \sum_{i=1}^{N} \Psi_n(r_i) A_i u_i \tag{4.40.}$$

where N is the total number of channel entrances on the exit side of the compression cavity. The expression for the cavity pressure due to the velocity of air in the channel entrances is then given by

$$p_e(r) = \sum_{n=0}^{\infty} \left[\frac{j\omega\rho_o \Psi_n(r)}{V\left[k_n^2 - k^2\right]} \sum_{i=1}^{N} \Psi_n(r_i) A_i u_i \right] \tag{4.41.}$$

The total cavity pressure, both due to the velocity of the diaphragm and the velocity of air in the channels, is thus given by

$$p(r) = \frac{\rho_0 c_0^2}{V} \frac{u_0 \pi a^2}{j\omega} + \sum_{n=0}^{\infty} \left[\frac{j\omega\rho_0 \Psi_n(r)}{V\left[k_n^2 - k^2\right]} \sum_{i=1}^{N} \Psi_n(r_i) A_i u_i \right] \tag{4.42.}$$

4.2.4 Suppression of modal excitation by channel arrangement

Equation 4.42 is used as a starting point to derive a channel geometry which minimises the excitation of the compression-cavity modes. Extracting the $n=0$ term from the summation in 4.42, the excitation of the zeroth mode is separated from the other modes, giving

$$p(r) = \frac{\rho_0 c_0^2}{j\omega V} \left(u_0 \pi a^2 + \sum_{i=1}^{N} A_i u_i \right) + \sum_{n=1}^{\infty} \left[\frac{j\omega\rho_0 \Psi_n(r)}{V\left[k_n^2 - k^2\right]} \sum_{i=1}^{N} \Psi_n(r_i) A_i u_i \right] \tag{4.43.}$$

This is a very useful manipulation as it separates the desired lumped behaviour from the undesirable higher order behaviour. From this expression, it is clear that in order to suppress excitation of the nth mode it is required that

$$\sum_{i=1}^{N} \Psi_n(r_i) A_i u_i = 0 \tag{4.44.}$$

The approach taken by Smith is to make the assumption that the velocities in the channel entrances are identical. This simplifies the condition to

$$\sum_{i=1}^{N} \Psi_n(r_i) A_i = 0 \qquad 4.45.$$

This is a fair simplification and can be justified as follows. Firstly, assuming that the final design provides good suppression of the modes in the compression cavity, the compression-driver behaviour is described by the zeroth mode terms in equation 4.43. In this case, the pressure in the cavity is simply related to the total volume velocity at the chamber walls,

$$p = \frac{\rho_0 c_0^2}{j\omega V}\left(u_0 \pi a^2 + \sum_{i=1}^{N} A_i u_i\right) \qquad 4.46.$$

The channel-entrance velocities can be related to the channel-entrance pressure by the acoustic impedance of the channels, z_i,

$$u_i = \frac{p}{z_i} \qquad 4.47.$$

By implication, in order to assume that the channel-entrance velocities are identical, Smith assumes that the acoustical impedance of each of the channels is identical. The condition set in equation 4.45 can be met for specific modes by careful selection of the channel positions, r_i, and entrance areas, A_i. If there are N channels, it is possible to meet the condition for N modes. Logically, the lowest N modes of the compression chamber are chosen for two reasons: firstly, to extend the bandwidth of the driver as high as possible in frequency and, secondly, because the suppression is only effective if simple lumped behaviour of the compression driver results.

The condition outlined in equation 4.45 can be written in matrix form as

$$\begin{bmatrix} \Psi_0(r_1) & \Psi_0(r_2) & \cdots & \Psi_0(r_N) \\ \Psi_1(r_1) & \Psi_1(r_2) & \cdots & \Psi_1(r_N) \\ \Psi_2(r_1) & \Psi_2(r_2) & \cdots & \Psi_2(r_N) \\ \vdots & \vdots & \ddots & \vdots \\ \Psi_N(r_1) & \Psi_N(r_2) & \cdots & \Psi_N(r_N) \end{bmatrix} \begin{bmatrix} A_1/A_T \\ A_2/A_T \\ \vdots \\ A_N/A_T \end{bmatrix} = \begin{bmatrix} 1 \\ 0 \\ 0 \\ \vdots \\ 0 \end{bmatrix} \qquad 4.48.$$

The first equation of this set is trivial, but must be present to ensure that the sum of the area ratios is equal to unity. The matrix on the left of the expression containing the eigenfunction terms is of dimensions N by $N+1$ and thus not invertible in this form. Additionally, there are two sets of unknowns, r_i and A_i. To solve this problem the variables r_i are set so that they

make one row of the matrix trivial, which results in a square and invertible matrix. This can be achieved by setting the values of r_i to meet the condition

$$\Psi_N(r_i)=0 \tag{4.49.}$$

In other words, the channel positions are set to coincide with the nodes of the Nth eigenfunction. This results in a slightly different set of equations given by

$$\begin{bmatrix} \Psi_0(r_1) & \Psi_0(r_2) & \cdots & \Psi_0(r_N) \\ \Psi_1(r_1) & \Psi_1(r_2) & \cdots & \Psi_1(r_N) \\ \Psi_2(r_1) & \Psi_2(r_2) & \cdots & \Psi_2(r_N) \\ \vdots & \vdots & \ddots & \vdots \\ \Psi_{N-1}(r_1) & \Psi_{N-1}(r_2) & \cdots & \Psi_{N-1}(r_N) \end{bmatrix} \begin{bmatrix} A_1/A_T \\ A_2/A_T \\ \vdots \\ A_N/A_T \end{bmatrix} = \begin{bmatrix} 1 \\ 0 \\ 0 \\ \vdots \\ 0 \end{bmatrix} \tag{4.50.}$$

The matrix on the left is now determined and invertible. The set of equations can be solved to find a vector of channel area ratios. For example, for the case $N=3$, the nodes of the 3rd mode of the are located at

$$r=0.238\text{a} \quad , \quad r=0.543\text{a} \quad , \quad r=0.853\text{a} \tag{4.51.}$$

Thus, the channel positions are set to be

$$r_1=0.238\,a \quad , \quad r_2=0.543\,a \quad , \quad r_3=0.853\,a \tag{4.52.}$$

Solving the simultaneous equations, as described above, gives the channel area ratios

$$\begin{bmatrix} A_1/A_T \\ A_2/A_T \\ A_3/A_T \end{bmatrix} = \begin{bmatrix} 0.13975 \\ 0.32682 \\ 0.53343 \end{bmatrix} \tag{4.53.}$$

The areas can be equivalently written as width ratios, using the approximation

$$A_i \approx w_i 2\pi r_i \tag{4.54.}$$

This gives us approximate width ratios of

$$\frac{w_3}{w_1} \approx 1.065 \quad , \quad \frac{w_2}{w_1} \approx 1.025 \tag{4.55.}$$

Smith thus shows that the N channels should be located at the nodes of the Nth radial mode of the compression cavity and that the channels should all have approximately the same width.

4.2.5 Discussion

In his paper, Smith graphically illustrated the suppression technique for a three-channel phase plug using two plots reproduced below.

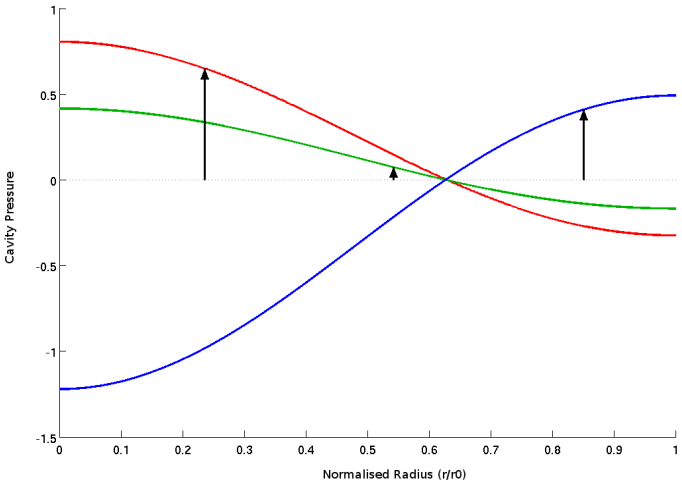

Figure 4.10. Reproduction of Smith's illustration of his suppression technique for the eigenfunction n=1.

Figure 4.10 shows the excitation of the first eigenfunction resulting from the velocity in each channel entrance separately. The vector locations indicate the position of the channels and the vector magnitude indicates the strength of the excitation from that channel, given by

$$\Psi_n^2(r_i)A_i \qquad 4.56.$$

It can be easily appreciated from these illustrations that the contributions from the individual channels sum to zero, which indeed was the condition set in equation 4.45.

The same type of illustration is shown for the second eigenfunction in figure 4.11. No illustration is given by Smith for the third eigenfunction because, for a the three-channel phase plug, none of the channels excite the third eigenfunction as

$$\Psi_3(r_i)A_i=0 \qquad 4.57.$$

There have been few further published works on the details of compression-driver phase-plug design since Smith. Indeed there are a number of subsequent papers and patents that ignore Smith's work and incorrectly interpret the behaviour of the compression cavity, most choosing instead to use the Wente and Thuras path-length interpretation [70][71][40][72]. The reason for the lack of publications is possibly attributable to commercial interests, with manufacturers unwilling to share the secrets of their designs. Additionally, numerical methods, such as FEM and BEM, allow the designer to simply draw the shape of phase plug

and see the simulated results without having to worry about whether the fundamental design approach is correct. However, although the numerical simulation process has many benefits, for a complex acoustical structure with many design parameters, it can be extremely difficult to disseminate the underlying physical behaviour using FEM and BEM data.

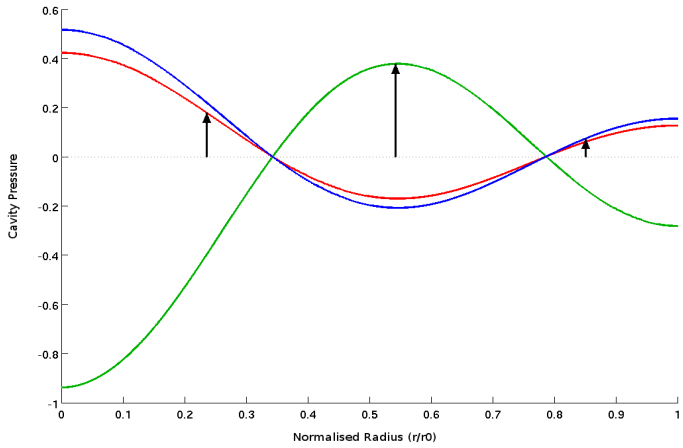

Figure 4.11. Reproduction of Smith's illustration of his suppression technique for the eigenfunction n=2.

Using Smith's approach, modes above the Nth may still be excited in the final driver. Commonly the number of channels is chosen so that the Nth eigenfrequency is above the intended bandwidth of operation of the driver. However, as can be seen from equation 4.14, the pressure contribution from an individual mode decreases at a relatively gentle 6dB per octave on either side of the associated eigenfrequency. Consequently, modes having eigenfrequencies above the intended bandwidth of the driver may still effect the in-band behaviour if they are heavily excited. In chapters 6 and 8 this problem is encountered. For idealised situations, such as the rigid-body diaphragm motion that is considered in this section, the modal excitation tends to decrease with increasing mode number. As will be shown in the next section, under these ideal conditions, the final driver pressure response remains smooth even above the Nth eigenfrequency. However, for real designs it is often not easy to determine what number of channels is optimal other than by trial and error.

4.3 Numerical modelling of Smith's phase plug

A simple FEM model was constructed to confirm Smith's compression-driver phase-plug analysis. The geometry of this model is illustrated in figure 4.12. It simply consists of a cylindrical compression cavity, driven by a rigid diaphragm on the left-hand side, with three exit channels located on the right-hand side. The exit channels are kept very narrow and are terminated at their right-hand end with a $\rho_0 c_0$ specific acoustical impedance. This ensures

that there are no reflections from these terminations provided that plane waves alone propagate in the channels. As the channels are narrow, only plane-wave propagation occurs within them in the frequency range of interest. This arrangement satisfies Smith's assumption that the channels all have the same specific acoustical impedance.

This model was geometrically constructed in Cedrat's Flux2D Preprocessor [73] and the mesh was exported to PAFEC-FE [55] for solution using two-dimensional quadratic axisymmetric acoustic finite elements. Flux2D allows the geometry of the model to be parametrised. Using this feature it is very easy to move the positions and adjust the areas of the channels as desired. The pressure-magnitude response was extracted from the model in each of the three channels. As the narrow channels only carry a plane wave the precise location at which the pressure is sampled within each channel is not critical.

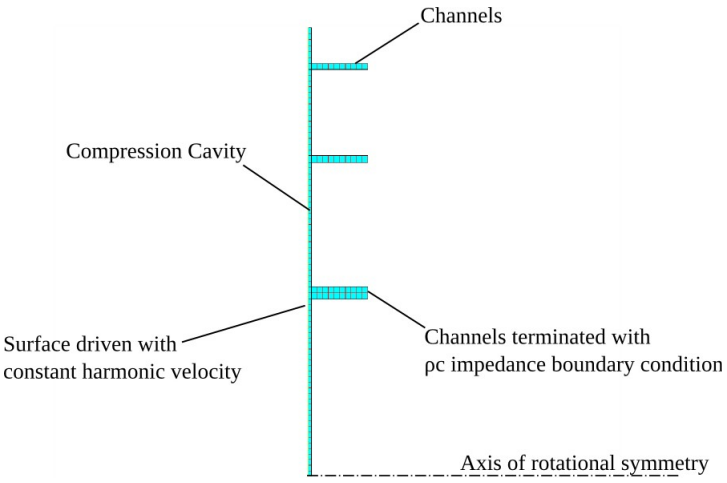

Figure 4.12. Cross section of the geometry used in simple equal area compression-driver FEM model.

The geometry shown in figure 4.12 is based on an equal-area approach to the channel geometry. This is a methodology that has previously been suggested for compression-driver phase-plug design [72]. All three channel entrances are of area $\pi a^2/45$, giving a total compression ratio of 15. The outer channels, being at a larger diameter, are of a narrower width to maintain this equal area. The position of the channels is also based on equal area. The circular cross section of the compression cavity is divided into three equal area parts and the channels are positioned to be at the areal centroid of each. The left-hand surface of the compression cavity is driven harmonically with a unit velocity as if excited by a rigid piston. The calculated pressure response in each of the channels is shown in figure 4.13. The pressure is sampled halfway between the start of the channel and the impedance termination at the right hand channel end.

The pressure levels shown are normalised by the specific acoustical impedance of a tube,

$$L_{norm} = 20\log_{10}\left|\frac{p}{\rho_0 c_0}\right| \qquad 4.58.$$

such that at low frequencies a normalised pressure level of 23.5dB is seen in all three channels. This level corresponds directly to the compression ratio of 15. Above $ka \approx 3.3$, the pressure in the channels is very dissimilar from one another.

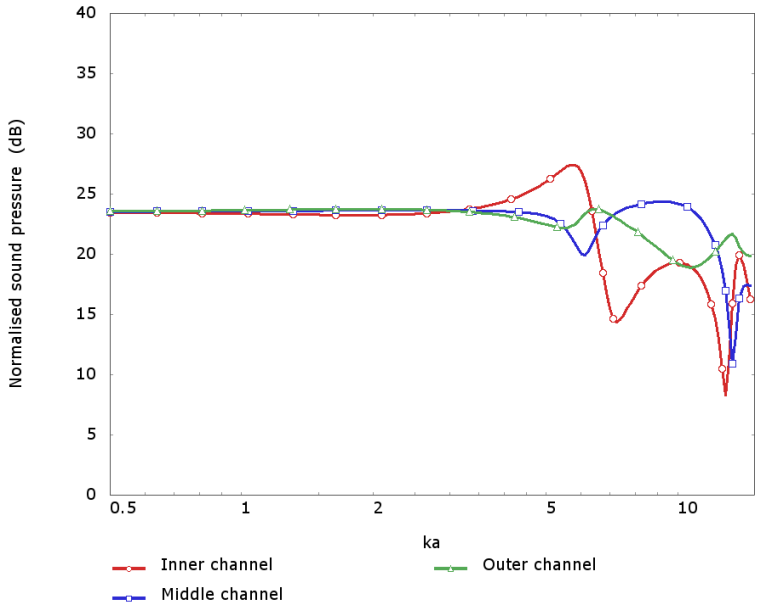

Figure 4.13. Normalised channel-pressure level response for simple compression driver arrangement based on equal area design methodology.

Figure 4.14 shows the sectional geometry of a similar FEM model, again constructed using Cedrat's Flux2D software and solved using PAFEC-FE. This time the channel positions and sizes are arranged according to Smith's methodology.

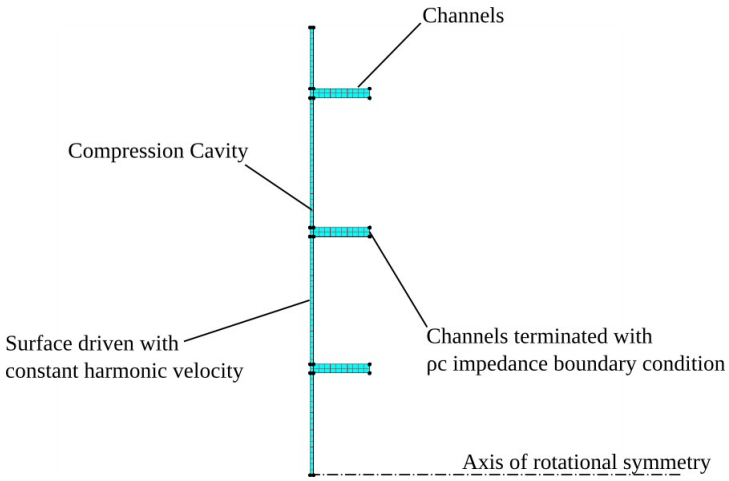

Figure 4.14. Sectional geometry used in simple Smith methodology compression driver FEM model.

The normalised channel pressure-level responses are plotted in figure 4.15, again normalised by the specific acoustical impedance of a plane wave. This time the channel pressures remain at 23.5dB until $ka \approx 8$ and even above this frequency the three channel pressures are very similar to one another. It is clear that Smith's guidelines are working as he anticipated.

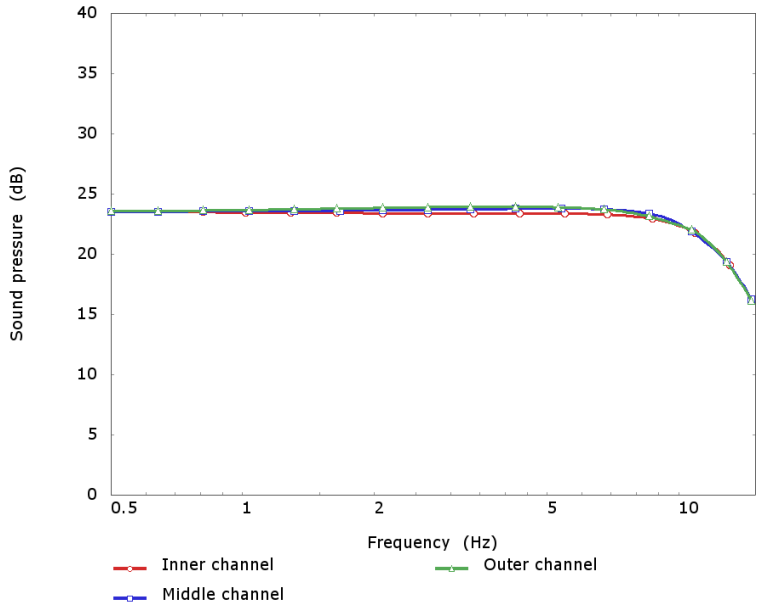

Figure 4.15. Normalised cavity-pressure level response for simple compression driver arrangement based on Smith design methodology.

The analysis presented by Smith concentrates on controlling the acoustical modes of the compression cavity itself, as opposed to resonances occurring in the entire acoustical structure. In a complete driver the problematic acoustical modes occur in the full acoustical structure, including the cavity, the phase-plug and horn throat. Indeed, they cannot be simply separated into those occurring in the cavity and those occurring in the phase plug. The two parts of the driver are well coupled and combined modes are observed. However, the results of the FEM analysis above indicate that if the channels all have the same specific acoustical impedance then it is possible to derive a channel-entrance arrangement that causes the same acoustical velocity to be generated at the entrance to each channel over a wide range of frequencies. The remaining design challenge is then to find a geometry for the result of the phase plug that gives the same specific acoustical impedance at each channel entrance. This is a problem that is outlined in the next section.

4.4 The phase-plug channel behaviour

The phase-plug channels are very narrow and, consequently, it may be considered that, in the bandwidth of operation, each carry a single parameter propagating wave. The channels must be routed from their entrance positions to meet at the horn throat. This normally means that they must follow a somewhat curved path. It is also sometimes the case that the sectional area of the channels is not constant, but instead increases along the length of the channel. However, for simplicity of analysis, it is assumed that each channel may be represented as a one dimensional narrow duct of constant sectional area. Within each narrow duct, the complex acoustical pressure is described by the expression

$$p(x)=A\,e^{-jkx}+B\,e^{jkx} \qquad 4.59.$$

where x is the position in the duct measured from one end. This expression defines that the pressure in the duct is composed of two plane waves propagating in opposite directions with complex amplitudes A and B. The acoustical pressure is related to the acoustical particle velocity by the linear Euler equation

$$\rho_0 \frac{\partial \boldsymbol{u}}{\partial t} - \nabla p = 0 \qquad 4.60.$$

As p is only a function of the spatial coordinate x, in this case the relationship is simply

$$u(x)=\frac{-1}{\rho_0}\int \frac{\partial p}{\partial x}\,dt \qquad 4.61.$$

Consequently, the acoustical particle velocity in the duct can be described in terms of the same two complex wave amplitudes as

$$u(x)=\frac{A\,e^{-jkx}-B\,e^{jkx}}{\rho_0 c_0} \qquad 4.62.$$

The narrow ducts are of constant sectional area, S, and the volume velocity at any position along the duct length is related to the acoustical particle velocity by the expression

$$U(x)=S\,u(x) \qquad 4.63.$$

A three-channel phase plug may be approximately represented using four of these one-dimensional ducts, connected as shown in figure 4.16. Three ducts represent the channels and a fourth represents the throat of the horn. The four ducts are connected at the end of the phase plug. The opposite end of each of the phase-plug channel ducts are driven by a volume velocity that represents the excitation from the compression cavity. This simple model allows

the behaviour of the phase plug to be considered in terms of these three excitation volume velocities. From this, one can deduce the situation required for an acoustical wave to be propagated into the horn throat without any other disturbance occurring.

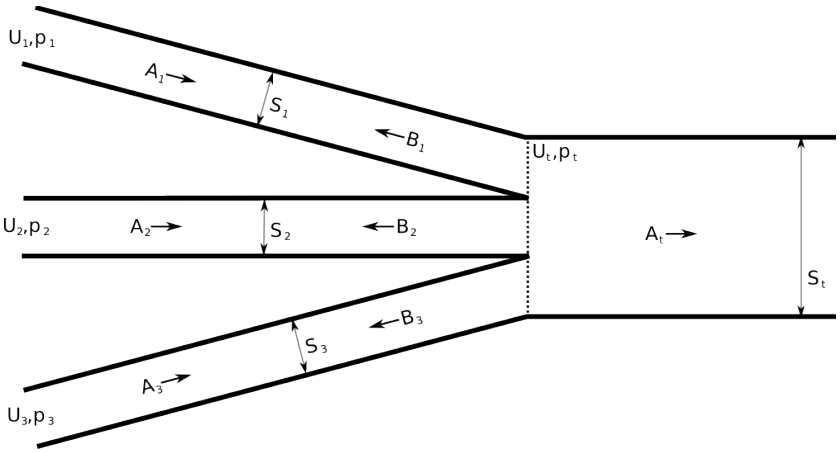

Figure 4.16. Simplified 1-D duct representation of a compression driver phase plug.

The acoustical pressures in each duct are described by the expressions

$$p_1(x) = A_1 e^{-jk(x+L_1)} + B_1 e^{jk(x+L_1)} \quad 4.64.$$

$$p_2(x) = A_2 e^{-jk(x+L_2)} + B_2 e^{jk(x+L_2)} \quad 4.65.$$

$$p_3(x) = A_3 e^{-jk(x+L_3)} + B_3 e^{jk(x+L_3)} \quad 4.66.$$

and

$$p_t(x) = A_t e^{-jkx} \quad 4.67.$$

The coordinate system is arranged so that $x = 0$ is the junction where the four ducts meet. L_1, L_2 and L_3 are the lengths of the first, second and third channel respectively. The fourth of these expressions, that for the pressure in the horn throat duct, only includes a term for a forward-propagating acoustical wave. This is because, for simplicity, the throat duct is considered to be semi-infinite and, consequently, no wave propagation is allowed in the reverse direction. The volume velocities within the ducts are written as

$$U_1(x) = S_1 \frac{A_1 e^{-jk(x+L_1)} - B_1 e^{jk(x+L_1)}}{\rho_0 c_0} \quad 4.68.$$

$$U_2(x) = S_2 \frac{A_2 e^{-jk(x+L_2)} - B_2 e^{jk(x+L_2)}}{\rho_0 c_0} \quad 4.69.$$

$$U_3(x) = S_3 \frac{A_3 e^{-jk(x+L_3)} - B_3 e^{jk(x+L_3)}}{\rho_0 c_0} \quad 4.70.$$

and

$$U_t(x)=S_t\frac{A_t e^{-jkx}}{\rho_0 c_0} \qquad 4.71.$$

where S_1, S_2 and S_3 are the sectional areas of each of the channel ducts and S_t is the sectional area of the horn throat duct.

The solution to the duct system is derived in terms of the volume velocities at the compression cavity end of each of the three channel ducts, which are given the notation

$$U_1(-L_1)=q_1 \qquad 4.72.$$

$$U_2(-L_2)=q_2 \qquad 4.73.$$

and

$$U_3(-L_3)=q_3 \qquad 4.74.$$

Equating these volume velocities at the starts of the ducts to the expressions for the volume velocity over the length of the ducts results in the conditions,

$$q_1=\frac{S_1}{\rho_0 c_0}\left(A_1-B_1\right) \qquad 4.75.$$

$$q_2=\frac{S_2}{\rho_0 c_0}\left(A_2-B_2\right) \qquad 4.76.$$

and

$$q_3=\frac{S_3}{\rho_0 c_0}\left(A_3-B_3\right) \qquad 4.77.$$

At the junction of the four ducts, the principle of continuity of volume velocity applies. In this case this results in the relationship

$$U_1(0)+U_2(0)+U_3(0)=U_t(0) \qquad 4.78.$$

In terms of the wave amplitudes, this is written

$$S_1\left(A_1 e^{-jkL_1}-B_1 e^{jkL_1}\right)+S_2\left(A_2 e^{-jkL_2}-B_2 e^{jkL_2}\right)+S_3\left(A_3 e^{-jkL_3}-B_2 e^{jkL_3}\right)-S_t A_t=0 \qquad 4.79.$$

Additionally, at the junction, the principle of continuity of pressure is applied resulting in the relationship

$$p_1(0)=p_2(0)=p_3(0)=p_t(0) \qquad 4.80.$$

In terms of the wave amplitudes this is written as

$$A_1 e^{-jk L_1} + B_1 e^{jk L_1} = A_t \qquad 4.81.$$

$$A_2 e^{-jk L_2} + B_2 e^{jk L_2} = A_t \qquad 4.82.$$

and

$$A_3 e^{-jk L_3} + B_3 e^{jk L_3} = A_t \qquad 4.83.$$

Combining these expressions, the pressure amplitude in the throat duct can be written in terms of the three entrance volume velocities as

$$A_t = \rho_0 c_0 \frac{\frac{q_1}{\cos k L_1} + \frac{q_2}{\cos k L_2} + \frac{q_3}{\cos k L_3}}{S_t + j S_1 \frac{\sin k L_1}{\cos k L_1} + j S_2 \frac{\sin k L_2}{\cos k L_2} + j S_3 \frac{\sin k L_3}{\cos k L_3}} \qquad 4.84.$$

It is clear from this expression that there is plenty of opportunity for irregularity in the throat pressure. However, if the lengths of the channels are equal then this simplifies to

$$A_t = \frac{(q_1 + q_2 + q_3)\rho_0 c_0}{S_t \cos k L + (S_1 + S_2 + S_3) j \sin k L} \qquad 4.85.$$

Further to this, if the area of the horn throat is set to be the same as the sum of the channel areas, $S_t = S_1 + S_2 + S_3$, the expression further simplifies to

$$A_t = (q_1 + q_2 + q_3) \frac{\rho_0 c_0}{S_t} e^{-jkL} \qquad 4.86.$$

Which, recalling expression 4.71, is equivalent to

$$U_t(0) = (q_1 + q_2 + q_3) e^{-jkL} \qquad 4.87.$$

This indicates that, if the channels have the same length and the horn throat area is equal to the combined area of the individual channels then, the volume velocity at the horn throat is equal to the summed volume velocity at the channel entrances delayed by the propagation distance along the channels. This is a very well-behaved situation. Clearly this simple model provides a target for the ideal behaviour of the phase-plug channels. However, it also highlights that if the target is not met, then the acoustical behaviour of the phase-plug channels is complex and potentially the horn throat pressure will be very irregular.

The specific acoustical impedance at the entrance to the nth channel is given by the expression

$$Z_n = S_n \frac{p_n(-L_n)}{U_n(-L_n)} \qquad 4.88.$$

Considering the first channel, the entrance volume velocity, $U_1(-L_1)$, is known to be q_1 and so to determine the specific acoustical impedance it is necessary to determine the pressure at the entrance to the channel. The pressure at the entrance of the first channel is given by the expression

$$p_1(-L_1) = A_1 + B_1 \qquad 4.89.$$

Using the relationships in expressions 4.75, 4.68 and 4.80, the coefficients A_1 and B_1 may be defined in terms of the horn throat pressure, $p_t(0) = A_t$, and the channel entrance pressure as

$$p_1(0) = \frac{A_t}{\cos k L_1} + \rho_0 c_0 \frac{q_1}{S_1} \frac{j \sin k L_1}{\cos k L_1} \qquad 4.90.$$

For the case when the channels are equal length and the throat area is equal to the sum of the channel areas, the channel entrance pressure becomes

$$p_1(0) = \rho_0 c_0 \left[\frac{q_1 + q_2 + q_3}{S_1 + S_2 + S_3} \left(1 - \frac{j \sin k L}{\cos k L} \right) + \frac{q_1}{S_1} \frac{j \sin k L}{\cos k L} \right] \qquad 4.91.$$

and, consequently, the channel entrance specific acoustical impedance is

$$Z_1 = S_1 \frac{\rho_0 c_0}{q_1} \left[\frac{q_1 + q_2 + q_3}{S_1 + S_2 + S_3} \left(1 - \frac{j \sin k L}{\cos k L} \right) + \frac{q_1}{S_1} \frac{j \sin k L}{\cos k L} \right] \qquad 4.92.$$

The other channels may be analysed in a similar manner resulting in expressions for the channel-entrance specific acoustical impedance at all three channels,

$$Z_2 = S_2 \frac{\rho_0 c_0}{q_2} \left[\frac{q_1 + q_2 + q_3}{S_1 + S_2 + S_3} \left(1 - \frac{j \sin k L}{\cos k L} \right) + \frac{q_2}{S_2} \frac{j \sin k L}{\cos k L} \right] \qquad 4.93.$$

and

$$Z_3 = S_3 \frac{\rho_0 c_0}{q_3} \left[\frac{q_1 + q_2 + q_3}{S_1 + S_2 + S_3} \left(1 - \frac{j \sin k L}{\cos k L} \right) + \frac{q_3}{S_3} \frac{j \sin k L}{\cos k L} \right] \qquad 4.94.$$

In order to derive the optimum channel geometry, Smith makes the assumption that the channel entrance specific acoustical impedances are identical. The three expressions reveal that even when the phase plug is designed perfectly it is not necessarily the case that the channel entrance specific acoustical impedances are the same. However, if the channel-

entrance acoustical particle velocities are all identical and equal to u, then the source volume velocities are $q_1 = uS_1$, $q_2 = uS_2$ and $q_3 = uS_3$, and the channel-entrance specific acoustical impedances all simplify to

$$Z_n = \rho_0 c_0 \qquad 4.95.$$

i.e., they have the same specific acoustical impedance as the horn throat, which was, in this case, simply assumed to be the plane-wave impedance.

This results in an interesting situation. Smith's suppression method assumes that the compression channels all present the same specific acoustical impedance to the compression cavity. However this is only the case when, firstly, the phase plug is correctly designed and, secondly, the channel entrance acoustical velocities are all identical. However, the channel entrance acoustical velocities are only identical when the cavity modal suppression is working perfectly. Altogether, in order the realise the ideal compression driver behaviour, it is necessary for both the phase-plug design and the channel entrance geometry to be correct. If one of these two aspects is not correct the performance of the other suffers, for example using Smith's exact geometry along with a poorly designed phase plug will not provide modal suppression in the compression cavity.

4.5 Conclusions

The target behaviour for the compression driver is relatively simple. However, as the geometry is typically several times larger than the shortest wavelength to be radiated, it is quite a challenge to meet the simple target behaviour in practice. To separate the design problem into two parts that may be analysed effectively, it is useful to consider the cavity modal suppression problem separately from the phase-plug design problem. For example, the results shown in figure 4.15, with all three channel pressures identical when terminated into $\rho_0 c_0$ specific acoustical impedances, are an indication that the channel-entrance acoustical velocities are identical. A design exhibiting this behaviour has the possibility that, provided a correctly designed phase plug is used with it, the final compression driver may be free from acoustical resonance. However, should this type of analysis result in even a moderate dissimilarity in the channel pressures, then it should be kept in mind that the performance in the full compression driver is likely to be significantly worse because the overall design cannot meet the assumption that the channel specific acoustical impedances are identical. In order for the final driver to function correctly, both the cavity modal suppression and the phase-plug channel design must be correct.

5 A new channel-positioning methodology for annular compression drivers

5.1 The effect of curving the compression cavity

In section 2.4.1, compression drivers were introduced to the reader as an arrangement that allows the efficiency of mid and high-frequency horn loaded loudspeakers to be increased. The Smith phase-plug geometry derivation was then subsequently outlined in chapter 4 along with a series of figures that demonstrate the importance of the compression-driver phase-plug geometry on the smoothness of the radiation resistance, and hence the response.

In these discussions it was implicitly assumed that the mechanical radiating diaphragm was rigid over the whole bandwidth of the transducer. In practice, this is a difficult goal to achieve. Modern compression-driver diaphragms are typically constructed from thin metal foils, commonly of aluminium or titanium. These materials have very high values of specific modulus: the ratio of Young's modulus to density. As specific modulus is proportional to wave speed, a high specific modulus material can be used to push the eigenfrequencies of a structure high in frequency. The radiating diaphragm must be kept as light as possible in order to maximise transducer efficiency and so it is necessary to use a very small amount of material, especially considering the relatively high density of Titanium and Aluminium. The metal foils used in modern radiating diaphragms are very thin indeed, typically 50μm for Aluminium or 30μm for Titanium. These foils are so thin that, despite having high Young's modulus, they have very little mechanical resistance to bending. To make the diaphragm approximately rigid over the bandwidth of the transducer, it must be formed into a shape that does not rely on bending resistance for rigidity. This is achieved by forming the diaphragm surface into a compound curve, and typically a domed geometry is used.

Figure 5.1 shows a cross section of a modern compression driver with a radiating diaphragm shaped as a spherical cap, or dome. The compression cavity follows the curvature of the radiating diaphragm in order to keep the volume of the compression cavity as small as possible. The result is that the geometry of real compression drivers is slightly different from the idealised geometric description that was used by Smith (shown in figure 4.8).

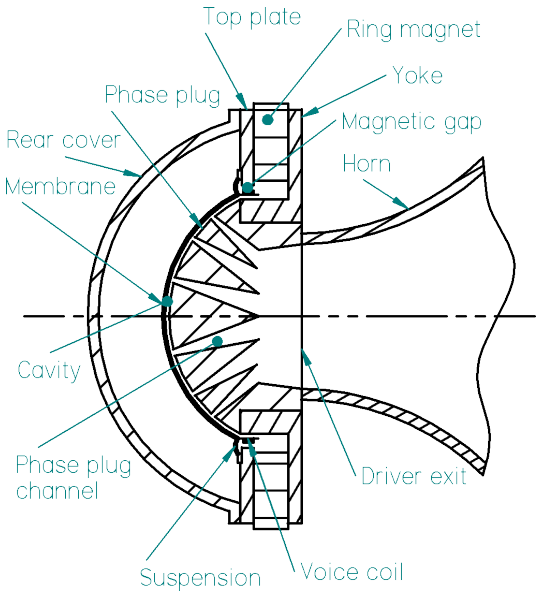

Figure 5.1. Cross-sectional view of a modern compression driver.

The acoustic importance of this departure from Smith's geometry can be demonstrated using a FEM model. Figure 5.2 shows the geometry used to investigate the effect of a curved radiating diaphragm. The channel positions and sizes are set using Smith's criterion. However the radiating diaphragm is not planar, but is domed. The radiating diaphragm curvature is 55 degrees, measured from axis of rotational symmetry to the outside edge. The compression ratio is 15. The channels are gently curved so that the right hand extent of each is a simple annular channel that is terminated with a $\rho_0 c_0$ specific acoustical impedance. The area of each channel is constant along its length to avoid any sudden change of acoustical impedance in the channels.

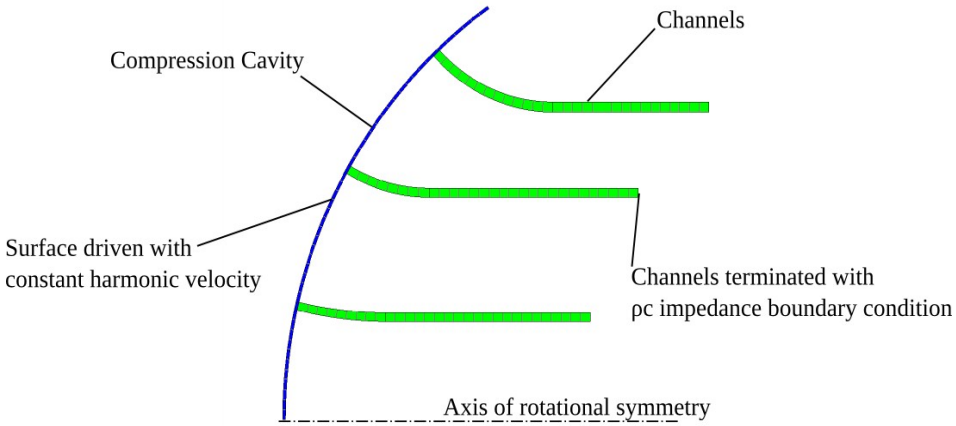

Figure 5.2. Half-section geometry of FE-modelled simplified compression driver using Smith's channel guidelines and a domed diaphragm.

The channel-pressure level responses are plotted in figure 5.3. These are normalised by the specific acoustical impedance of a plane wave (as in equation 4.58). While the three pressures are not as dissimilar as the equal area case, which was considered in figure 4.13, the pressures are significantly more dissimilar than was seen for the idealised Smith geometry (shown in figure 4.15). Despite this divergence, the three responses in figure 5.3 are smooth. However, these simple models do not include the rejoining of the compression channels at the throat of the horn. As was outlined in section 4.4, this rejoining is a critical part of the design, an imbalance in the contributions from each channel is likely to result in large amplitude resonances in the rejoined case.

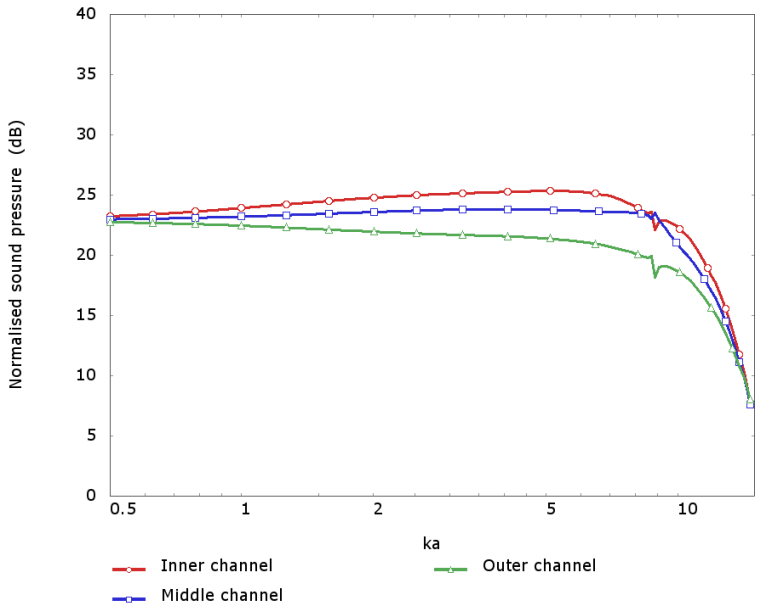

Figure 5.3. Normalised channel pressure-level response of FE-modelled simplified compression driver using Smith's channel guidelines and a domed diaphragm.

To demonstrate the problems that the unequal channel pressures can cause in a full design when the channels are joined at the horn throat, a simple phase plug was designed to join these three channels to a single semi-infinite pipe. The geometry of the FEM model to analyse this situation is shown in figure 5.4. The three channels are routed to a single central pipe that is terminated on the right-hand side using an infinite-pipe impedance condition as implemented by PAFEC-FE [55]. This termination uses a series approximation for the acoustical boundary condition in order to mimic the effect of a semi-infinite pipe. The phase-plug channel design is very basic. The area of the channels as they join to the pipe is the same as the areas of the channels as they leave the compression cavity. The apparent expansion is due to the decreasing radius of the channels as they are routed towards the pipe. The channels are all straight edged and they have been arranged such that the length of each

channel, measured along the centroid from the compression cavity to a point in the pipe, is the same for each channel. The design is very rudimentary, for example, there is no attempt to smooth the channel paths. However, the channels are approximately the same length and the throat area is equal to the sum of the channel areas. This approximately meets the requirements found in section 4.4.

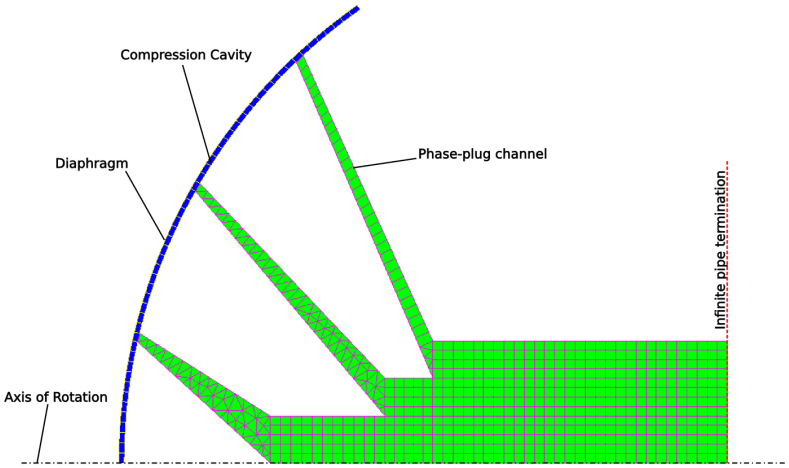

Figure 5.4. Half-section of geometry used in simple Smith methodology compression-driver FEM model with domed diaphragm with channels joined by rudimentary phase plug.

The normalised pressure response in the semi-infinite pipe is shown in figure 5.5. There are several very sharp "glitches" that can be seen on this response curve. In order to consider what is happening at these frequencies, figure 5.6 shows the acoustical intensity pattern at the third of these glitches, occurring at $ka \approx 5.5$. It can be seen from this figure that, rather than all channels carrying acoustical energy from the diaphragm to the pipe, the two inner channels carry acoustical energy in the reverse direction. The behaviour seen here is a standing wave where energy circulates around the phase plug rather than propagating in the pipe. This figure is in contrast to the vectors shown in figure 5.7, which are for a frequency position where there is no glitch on the response curve, in this case, at $ka = 5$. This result shows the desired behaviour with all channels carrying acoustical energy away from the compression cavity and summing in the tube to a plane wave travelling from left to right.

The glitches on the response curve shown in figure 5.5 may, on first consideration, seem relatively benign as they are very narrow in frequency and primarily cause a reduction in the response magnitude. The perceptual consequences may be considered as relatively benign, particularly as Bücklein [74] demonstrates that narrow band notches are particularly difficult to hear. However, what must also be considered is that the acoustical pressure magnitude in the compression driver channels is extremely high under normal operation and the linearity

of the channel acoustics is often a problem even at frequencies where the driver is well behaved [39][38].

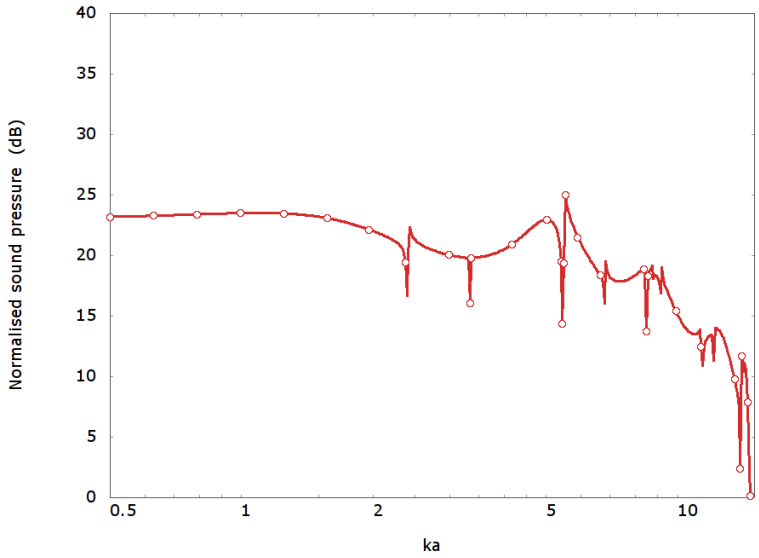

Figure 5.5. Normalised pressure magnitude evaluated at the start of the infinite pipe region.

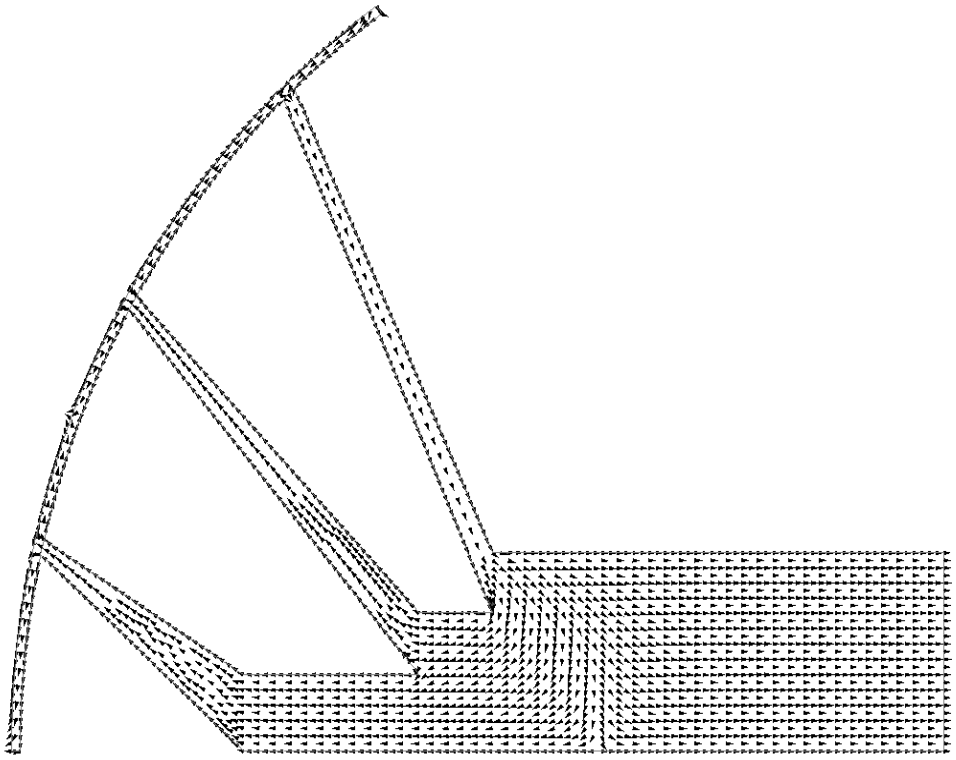

Figure 5.6. Vectors of acoustical intensity direction showing energy movement in simple phase-plugged curved Smith model at 7427Hz.

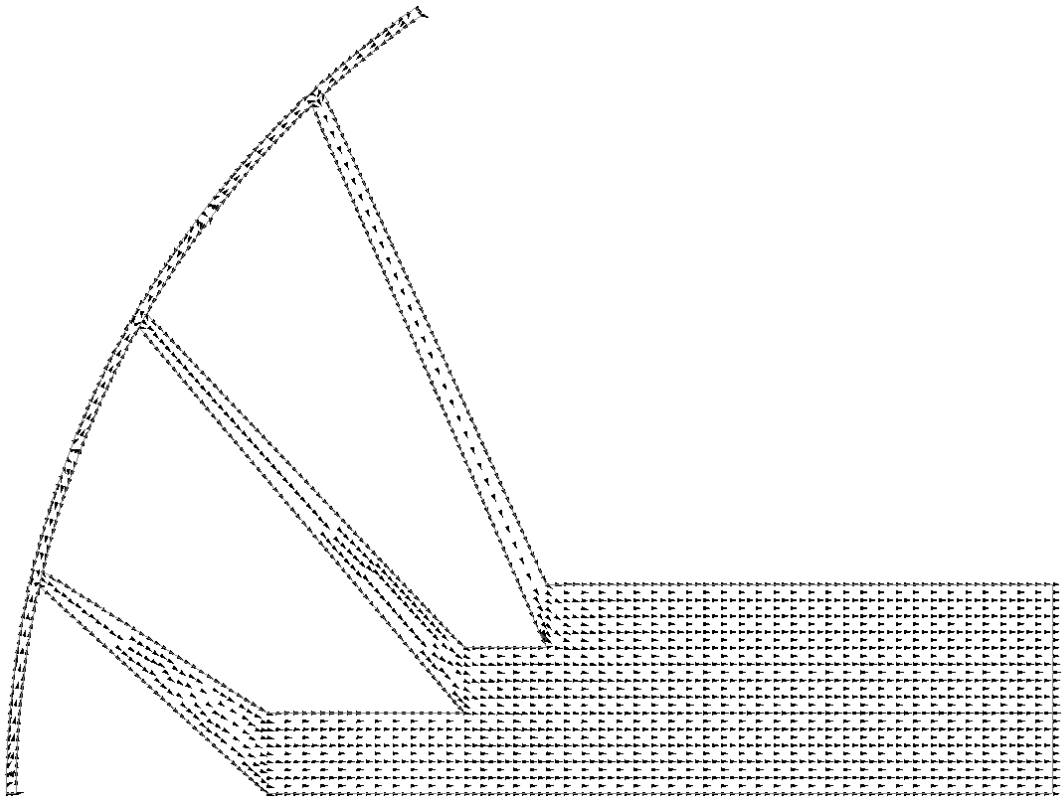

Figure 5.7. Vectors of acoustical intensity direction showing energy movement in simple phase-plugged curved Smith model at 7000Hz.

The linearity problem is severely exacerbated by the presence of the standing waves in the phase plug For example in the FEM model above at $ka = 5.5$, where the third glitch is seen, the pressure in the inner channel is approximately 23dB greater than the pressure propagated in the pipe.

In conclusion, in contradiction to Smith, the velocity of the diaphragm itself does excite the compression cavity modes and, although the channel pressure deviation for the simplified model, without the channels joined, is only a few decibels in the full compression driver geometry this is sufficient to cause severe resonance.

The motivation for searching for an improved channel-positioning method

Modern transducer design relies heavily on the Finite-Element Method and Boundary-Element Method for performance predictions [75]. The application of these techniques to compression-driver phase-plug design is now relatively common [76,43]. Typically the vibroacoustical design is completed with the help of a fully coupled FEM analysis of the moving mechanical parts, the compression chamber, the phase-plug channels, an appropriate horn, the radiating environment and often the air in the rear chamber behind the radiating diaphragm. During such analysis, the technique of parametrisation is frequently used to

allow the geometry to be quickly manipulated and a range of different geometric perturbations investigated. These geometric parameters may be used in conjunction with optimisation techniques [55]. This is a powerful tool and, if used effectively, can result in significant improvements. During the course of the design of a compression driver having a 76.2mm diameter titanium dome diaphragm, it was observed that the optimisation routine would consistently alter the geometry away from the Smith channel arrangement. It was generally observed that the optimiser suggested narrower outer channels than Smith's theory. This observation was the catalyst for this thesis on compression-driver phase-plug design. While the parametrised FEM approach is a very powerful tool, for the compression driver geometry there are a great number of parameters that may be varied and, consequently, it is extremely difficult to assesss when an optimum solution is reached. This work, on deriving an analytical solution to for the optimum geometry, was begun with the goal of fully understanding the limits of what can be achieved with the compression-driver arrangement.

5.2 An improved design methodology

To improve upon Smith's method for setting channel geometry, it is first necessary to analyse the behaviour of the diaphragm, cavity and channels in a spherical coordinate system. This allows a closer geometric representation of a real compression driver. Conceptually, the approach is similar to Smiths. All excitation of the cavity modes is arranged so that the overall pressure variation in the cavity is zero.

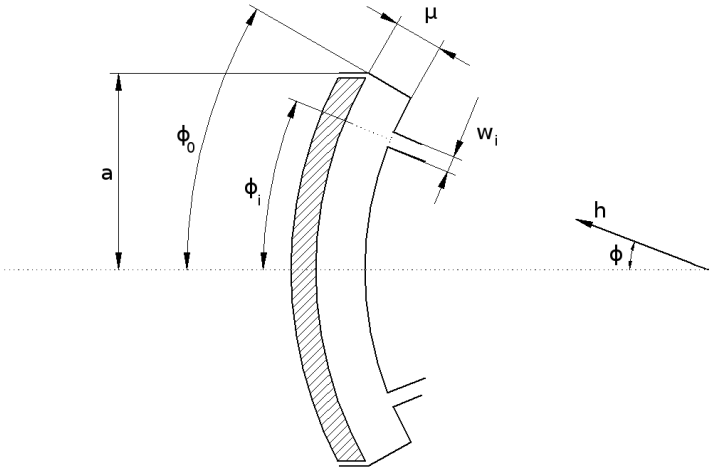

Figure 5.8. A cross section through the spherical representation of the compression cavity used for the analysis.

The geometry of the compression driver is approximated as shown in figure 5.8. The common notation used to describe a spherical coordinate system is that of Zwillinger [77]

[47, p.355], shown in figure 5.9. However, in this thesis the symbol for the radial coordinate *r* is replaced with *h* in order to avoid confusion with the radial coordinate in the cylindrical coordinate system.

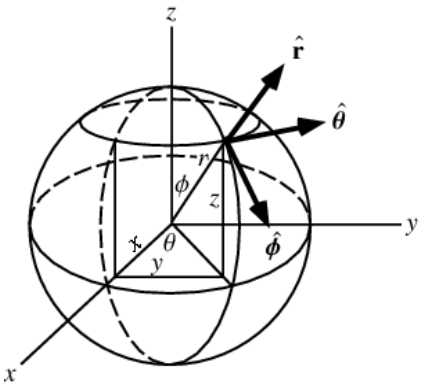

Figure 5.9. Spherical coordinate system notation.

The eigenfunctions and eigenfrequencies of the curved cavity are found by considering the homogeneous Helmholtz equation [45 p.18]

$$\nabla^2 p + \frac{\omega^2}{c_o^2} p = 0 \tag{5.1.}$$

In spherical coordinates, the Laplacian can be written as [23, p.25]

$$\nabla^2 p = \frac{\partial^2 p}{\partial h^2} + \frac{2}{h}\frac{\partial p}{\partial h} + \frac{1}{h^2 \sin^2\phi}\frac{\partial^2 p}{\partial \theta^2} + \frac{1}{h^2}\frac{\partial^2 p}{\partial \phi^2} + \frac{\cos\phi}{h^2 \sin\phi}\frac{\partial p}{\partial \phi} \tag{5.2.}$$

Solutions can be found using the method of separation of variables [45 p.185]. One can thus assume that

$$p(h,\theta,\phi,t) = H(h)\Theta(\theta)\Phi(\phi)T(t) \tag{5.3.}$$

with temporal dependence given by

$$T(t) = T_1 e^{-j\omega t} + T_2 e^{j\omega t} \tag{5.4.}$$

the dependence on the polar angular coordinate, Φ, given by

$$\Phi(\phi) = \Phi_1 P_l^m(\cos\phi) + \Phi_2 Q_l^m(\cos\phi) \tag{5.5.}$$

the dependence on the radial coordinate, *h*, given by

$$H(h) = H_1 j_l(kh) + H_2 y_l(kh) \tag{5.6.}$$

and the dependence on the circumferential angular coordinate, θ, given by

$$\Theta(\theta) = \Theta_1 e^{-jm\theta} + \Theta_2 e^{jm\theta} \tag{5.7.}$$

In these equations T_1, T_2, Φ_2, Φ_2, Θ_1, Θ_2, H_1 and H_2 are arbitrarily constants. P_l^m and Q_l^m, in equation 5.5, are associated Legendre functions of the first and second kinds respectively [23, p.27]. j_l and y_l in equation 5.6 are spherical Bessel functions of the first and second kind respectively [23, p.27]. Selecting a convention for time dependence, T_1 is set to zero. The compression cavity is small in h and, in the frequency band of interest, only trivial behaviour is observed in this direction. It is therefore assumed that $H(h)=1$. The Legendre function of the second kind, Q_l^m, appearing in the polar function, is singular at $\cos\phi=1$. The solution is constrained to be finite by setting $\Phi_2=0$.

The simplified solution of the wave equation in the rigid-walled compression cavity is therefore given by

$$p(\theta,\phi,t)=A_1 P_l^m(\cos\phi)\left(e^{-jm\theta}+e^{jm\theta}\right)e^{-j\omega t} \qquad 5.8.$$

The cavity pressure must obey the rigid-wall boundary condition at the diameter of the cavity as described by equation 5.9.

$$\frac{dp}{d\phi}=0\Big|_{\phi=\phi_0} \qquad 5.9.$$

To resolve this condition, it is required that

$$\frac{dP_l^m(\cos\phi)}{d\phi}=0\Big|_{\phi=\phi_0} \qquad 5.10.$$

This requirement is met by choice of l. It should be noted that these values are, in most circumstances, non-integer. Therefore, it cannot be assumed that the associated Legendre functions, P_l^m, can be simplified to associated Legendre polynomials as is usually the case with spherical harmonic expansions. This is because the angle of the cavity may not be a factor of 2π. Because of this, the eigenfunctions are a little challenging to describe analytically. Hoersch [78] demonstrates that a Legendre function of the first kind may be approximately described as a summation of Bessel functions. Using his expression for the Legendre function it is, in principle, possible to derive analytically an infinite set of values of l_{nm} satisfying equation 5.10 in terms of a summation of Bessel function zeros.

Associated Legendre functions of the first and second kind are the solutions to the associated Legendre differential equation [47, p.676] which can be written

$$\frac{-m^2}{\sin^2\phi}y+\frac{d^2y}{d\phi^2}+\frac{\cos\phi}{\sin\phi}\frac{dy}{d\phi}+l(l+1)y=0 \qquad 5.11.$$

The acoustical wave equation written in spherical coordinates is

$$\frac{\partial^2 p}{\partial h^2}+\frac{2}{h}\frac{\partial p}{\partial h}+\frac{1}{h^2\sin^2\phi}\frac{\partial^2 p}{\partial \theta^2}+\frac{1}{h^2}\frac{\partial^2 p}{\partial \phi^2}+\frac{\cos\phi}{h^2\sin\phi}\frac{\partial p}{\partial \phi}+k^2 p=0 \qquad 5.12.$$

The simplified solution to the wave equation in the compression cavity was described above to be

$$p=A_1 P_l^m(\cos\phi)\left(e^{-jm\theta}+e^{jm\theta}\right)e^{-j\omega t} \qquad 5.13.$$

In order to reduce the complexity of the next few expressions, this solution is abbreviated to

$$p(\phi,\theta,t)=A_1\Phi(\phi)\Theta(\theta)T(t) \qquad 5.14.$$

Inserting the abbreviated solution into the wave equation given in equation 5.12, after a little simplification, this results in the expression

$$\frac{\Phi(\phi)}{\sin^2\phi}\frac{d^2\Theta(\theta)}{d\theta^2}+\Theta(\theta)\left[\frac{d^2\Phi(\phi)}{d\phi^2}+\frac{\cos\phi}{\sin\phi}\frac{d\Phi(\phi)}{d\phi}+h_0^2k^2\Phi(\phi)\right]=0 \qquad 5.15.$$

where h_0 is the radius of curvature of the diaphragm, which can be evaluated from the other geometric parameters as $h_0=\frac{a}{\sin\phi_0}$. The differential of the theta function can be performed

$$\frac{d^2\Theta(\theta)}{d\theta^2}=-m^2\Theta(\theta) \qquad 5.16.$$

This allows further simplification giving

$$\frac{-m^2}{\sin^2\phi}\Phi(\phi)+\frac{d^2\Phi(\phi)}{d\phi^2}+\frac{\cos\phi}{\sin\phi}\frac{d\Phi(\phi)}{d\phi}+h_0^2k^2\Phi(\phi)=0 \qquad 5.17.$$

Comparison of this expression with the associated Legendre differential (equation 5.11) reveals that the eigenvalues of the system are given by

$$\omega_{nm}=k_{nm}c_0 \qquad 5.18.$$

where

$$k_{nm}^2=\frac{1}{h_0^2}l_{nm}(l_{nm}+1) \qquad 5.19.$$

The eigenfunctions of the cavity are found by inserting the values of l_{nm} into the expression for the spatial pressure variation in the cavity, this results in

$$\Psi_{nm}(\phi,\theta)=A_{nm}P_{l_{nm}}^m(\cos\phi)\left(e^{-jm\theta}+e^{jm\theta}\right) \qquad 5.20.$$

The normalisation term, A_{nm}, is chosen to satisfy the condition

$$\int_V \Psi_{nm}(\phi,\theta)^2\,dV=V \qquad 5.21.$$

where V is the volume of the compression cavity.

5.2.1 Numerical calculation of eigenfrequencies and eigenfunctions

Hoerch's Legendre approximation is only valid for a small range of x and l. Therefore, numerically calculated values of ω_{nm} and $\Psi_{nm}(\phi,\theta)$ were used in the derivation of channel position and width. These calculations were performed using the Finite-Element Method, as was described in section 3.7, making use of the PAFEC-FE solver. The approach is described in more detail below.

In section 4.2, the eigenfrequencies and eigenfunctions for an acoustical cavity shaped like a thin disc were derived, and can be exactly expressed as

$$\Psi_{mn}(r,\theta)=A_{nm}J_m(k_{mn}r)\left(e^{-jm\theta}+e^{jm\theta}\right) \qquad 5.22.$$

and

$$\omega_{nm}=j_{mn}\frac{c_0}{r_0} \qquad 5.23.$$

where j_{mn} are the zeros of the Bessel function of the first kind

$$J_{m+1}(j_{mn})=0 \qquad 5.24.$$

This is a useful test case for the numerical approach to determining the eigenfrequencies and eigenfunctions of a rigid-walled acoustical cavity using PAFEC-FE. A thin-disc cavity with outer radius, r_0, of 40mm was meshed using Cedrat's Flux2D Preprocessor [73] and then exported to PAFEC-FE [55] for calculation. This mesh is shown in figure 5.10. The PAFEC .dat file for this analysis is summarised in Appendix IX. Table 5.1 compares the FEM calculated eigenfrequencies to those calculated using the analytical expressions above. The agreement between the two sets of values is very good. Similarly, figure 5.11 shown on page 137, compares the analytically calculated eigenfunctions with those calculated using the FE method. Again, the agreement between the two sets of functions is extremely good.

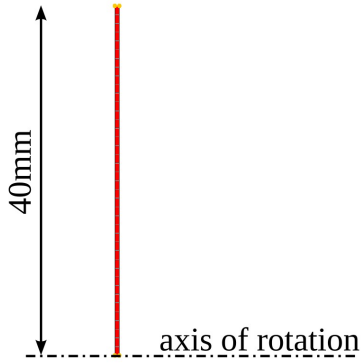

Figure 5.10. FEM Mesh used for the numerical calculation of the eigenfrequencies and eigenfunctions of a thin disc of air.

n	m	Analytically calculated eigenfrequencies	FEM calculated eigenfrequencies
0	0	0 Hz	0.41 Hz
1	0	5229.33 Hz	5229.34 Hz
2	0	9574.57 Hz	9574.61 Hz
3	0	13884.32 Hz	13884.47 Hz
4	0	18183.57 Hz	18184.01 Hz
5	0	22478.31 Hz	22479.27 Hz

Table 5.1: Comparison of FEM calculated eigenfrequencies with analytically calculated eigenfrequencies.

The FEM approach to determining the rigid-walled eigenfrequencies and eigenfunctions is a very useful alternative for situations where the cavity is not of a geometry that allows easy analytical solution.

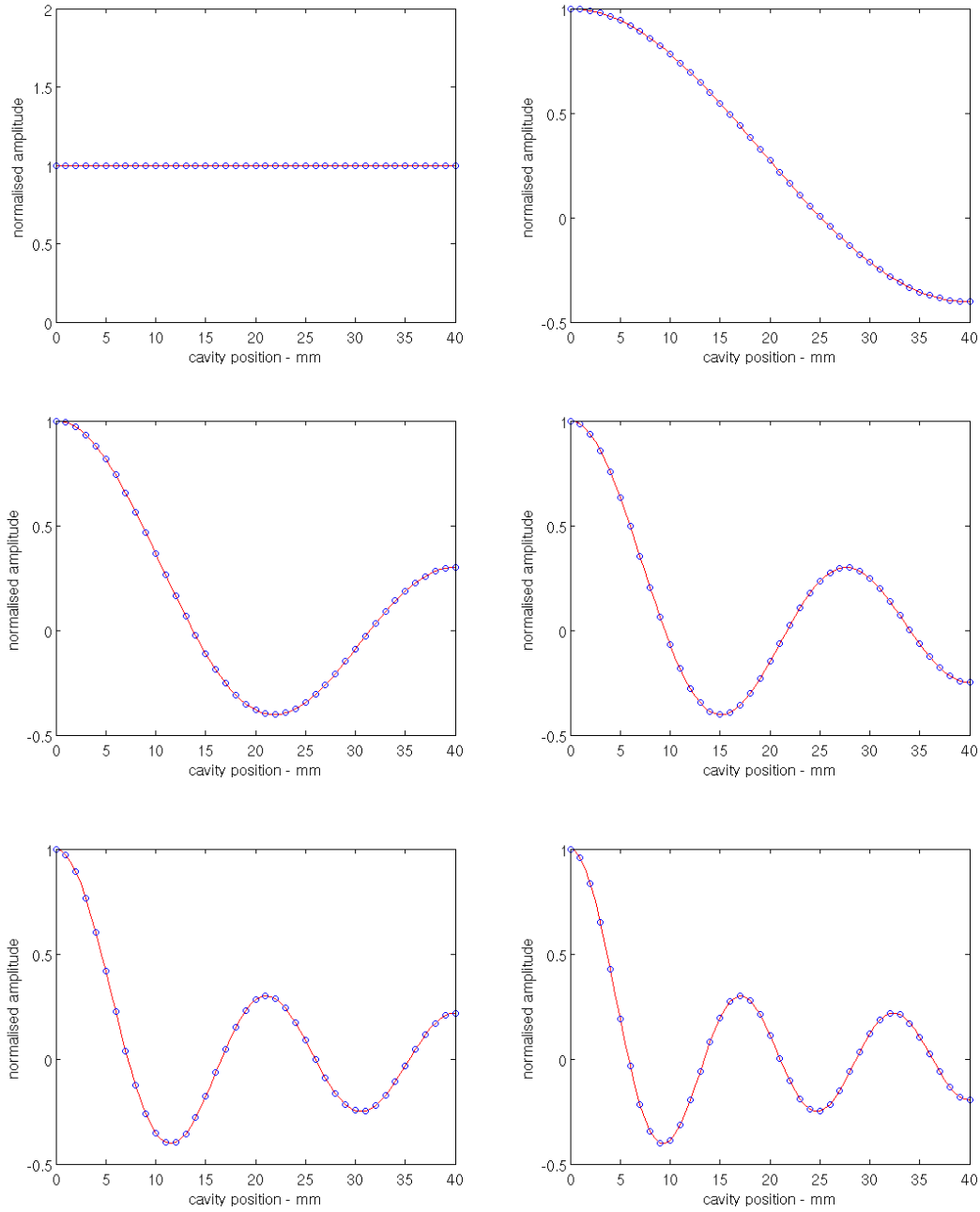

Figure 5.11. Comparison between the analytically calculated eigenfunctions, solid red line, and eigenfunctions calculated numerically using FEM, blue circles. The first six eigenfunctions are shown for m=0 and n=0,1,2,3,4,5 (ordered left to right and from top to bottom).

5.2.2 Analysis of the driven behaviour of the cavity

As outlined in section 3.4, the pressure in a lightly-damped acoustical cavity excited by motion of its walls can be described in terms of the rigid-walled eigenfunctions and eigenfrequencies.

$$p(\boldsymbol{x},\omega)=\sum_{n=0}^{\infty}\frac{j\omega\rho_0\Psi_n(\boldsymbol{x})}{V\left[k_n^2-k^2\right]}\int_S \Psi_n(\boldsymbol{y})\boldsymbol{u}(\boldsymbol{y}).\boldsymbol{n}\,dS \qquad 5.25.$$

In this expression, $\boldsymbol{u}(\boldsymbol{y}).\boldsymbol{n}$ is the surface-normal velocity of the cavity wall at vector position $\boldsymbol{y}$ and ρ_0 is the ambient fluid density. In the case of the compression cavity, the eigenfunctions and eigenfrequencies are indexed by two indices, *m* and *n*. As a result a slightly adapted expression must be used

$$p(\boldsymbol{x},\omega)=\sum_{n=0}^{\infty}\sum_{m=0}^{\infty}\frac{j\omega\rho_0\Psi_{nm}(\boldsymbol{x})}{V\left[k_{n,m}^2-k^2\right]}\int_S \Psi_{nm}(\boldsymbol{y})\boldsymbol{u}(\boldsymbol{y}).\boldsymbol{n}\,dS \qquad 5.26.$$

The summation is thus performed over all calculated eigenfunctions.

For this application, the integral on the right of this expression can be written as the sum of three integrals each over a separate regions of the cavity surface, as shown in equation 5.27.

$$\begin{aligned}\int_S \Psi_{nm}(\boldsymbol{y})\boldsymbol{u}(\boldsymbol{y}).\boldsymbol{n}\,dS=&\int_{\phi=0}^{\phi_0}\int_{\theta=0}^{2\pi}\Psi_{nm}(\phi,\theta)u_d(\phi,\theta)h_0^2\sin\phi\,d\theta\,d\phi\\&+\int_{\phi=0}^{\phi_0}\int_{\theta=0}^{2\pi}\Psi_{nm}(\phi,\theta)u_e(\phi,\theta)(h_0-\mu)^2\sin\phi\,d\theta\,d\phi\\&+\int_{h=h_0}^{h_0+\mu}\int_{\theta=0}^{2\pi}\Psi_{nm}(\phi,\theta)u_h(h,\theta)h^2\sin\phi_0\,d\theta\,dh\end{aligned} \qquad 5.27.$$

The first double integral is performed over the diaphragm region of the compression-cavity surface, the function $u_d(\phi,\theta)$ describes the normal velocity of this surface. The second double integral is performed over the exit side of the compression cavity surface, the function $u_e(\phi,\theta)$ describes the normal velocity of this surface. Finally, the third integral is performed over the small truncated conical surface at the outside diameter of the compression cavity, the function $u_h(h,\theta)$ describes the normal velocity of this surface. Conventional annular-channel compression-driver and phase-plug geometries, including that considered in this case, are completely rotationally symmetrical about the *z* axis. Additionally, the mechanical parts that form and support the radiating diaphragm are also rotationally symmetrical about the *z* axis.

The result of this "axisymmetry" is that the three surface-normal velocity functions introduced above are invariant of circumferential angle, θ, and can be written

$$u_d(\phi,\theta)=u_d(\phi) \tag{5.28.}$$

$$u_e(\phi,\theta)=u_e(\phi) \tag{5.29.}$$

and

$$u_h(h,\theta)=u_h(h) \tag{5.30.}$$

These simplifications allow three integrals in equation 5.27 to be rewritten

$$\begin{aligned}\int_s \Psi_{nm}(\boldsymbol{y})\boldsymbol{u}(\boldsymbol{y}).\boldsymbol{n}\,dS=&\int_{\phi=0}^{\phi_0} u_d(\phi)h_0^2\sin\phi\int_{\theta=0}^{2\pi}\Psi_{nm}(\phi,\theta)d\theta\,d\phi\\&+\int_{\phi=0}^{\phi_0} u_e(\phi)\left(h_0-\mu\right)^2\sin\phi\int_{\theta=0}^{2\pi}\Psi_{nm}(\phi,\theta)d\theta\,d\phi\\&+\int_{h=h_0}^{h_0+\mu} u_h(h)h^2\sin\phi_0\int_{\theta=0}^{2\pi}\Psi_{nm}(\phi,\theta)d\theta\,dh\end{aligned} \tag{5.31.}$$

with all the velocity functions now appearing outside of the second circumferential angle integral. The same integral

$$\int_{\theta=0}^{2\pi}\Psi_{nm}(\phi,\theta)d\theta \tag{5.32.}$$

appears three times, once in each of the double integrals. Inserting the calculated eigenfunctions, $\Psi_{nm}(\phi,\theta)$, into this integral gives

$$\int_{\theta=0}^{2\pi}\Psi_{nm}(\phi,\theta)d\theta=A_{nm}P_{l_{nm}}^m(\cos\phi)\int_{\theta=0}^{2\pi}\left(e^{-jm\theta}+e^{jm\theta}\right)d\theta \tag{5.33.}$$

From this expression, it is immediately clear that the integral is only non-zero for the case $m=0$. Effectively, this means that a reduced set of eigenfrequencies and eigenfunctions may be used,

$$\Psi_n(\phi)=A_nP_{l_n}^0(\cos\phi) \tag{5.34.}$$

The three surface integrals in 5.31 can also be simplified to

$$\begin{aligned}\int_s \Psi_n(\boldsymbol{y})\boldsymbol{u}(\boldsymbol{y}).\boldsymbol{n}\,dS=&\int_{\phi=0}^{\phi_0} 2\pi\Psi_n(\phi)u_d(\phi)h_0^2\sin\phi\,d\phi\\&+\int_{\phi=0}^{\phi_0} 2\pi\Psi_n(\phi)u_e(\phi)\left(h_0-\mu\right)^2\sin\phi\,d\phi+\int_{h=h_0}^{h_0+\mu} 2\pi\Psi_n(\phi)u_h(h)h^2\sin\phi_0\,dh\end{aligned} \tag{5.35.}$$

5.2.3 Cavity behaviour without exit channels

First, the behaviour of the compression cavity is considered for the case when there are no exit channels and the cavity is only excited by the radiating diaphragm. Only the diaphragm normal velocity u_d, appearing in the surface integrals of equation 5.35, is non zero. Assuming that the diaphragm is rigid, the normal velocity can be written as

$$u_d(\phi)=u_0\cos\phi \tag{5.36.}$$

and the surface integral correspondingly as

$$\int_s \Psi_n(\boldsymbol{y})\boldsymbol{u}(\boldsymbol{y}).\boldsymbol{n}\,dS=u_0\frac{\pi a^2}{\sin^2\phi_0}\int_{\phi=0}^{\phi_0}\Psi_n(\phi)\sin(2\phi)\,d\phi \tag{5.37.}$$

For the particular case $n=0$, this integral is easily evaluated since $\Psi_0(\phi)=1$, and therefore

$$u_0\frac{\pi a^2}{\sin^2\phi_0}\int_{\phi=0}^{\phi_0}\Psi_0(\phi)\sin(2\phi)\,d\phi=u_0\pi a^2 \tag{5.38.}$$

Inserting equations 5.38 and 5.37 into 5.25, the cavity pressure is given by

$$p_d(\phi)=u_0\pi a^2\frac{\rho_0 c_0^2}{j\omega V}+\sum_{n=1}^{\infty}\frac{j\omega\rho_0\Psi_n(\phi)}{V\left[k_n^2-k^2\right]}\frac{u_0\pi a^2}{\sin^2\phi_0}\int_{\hat{\phi}=0}^{\hat{\phi}_0}\Psi_n(\hat{\phi})\sin(2\hat{\phi})\,d\hat{\phi} \tag{5.39.}$$

It is useful to separate the zeroth order terms from the summation in this way, as these describe the desired lumped behaviour. Comparison of this expression with the equivalent for the Smith cylindrical geometry, equation 4.31, reveals an important detail. With the cylindrical approximation of the geometry, the diaphragm velocity does not excite any of the cavity modes (with the exception of the desired zeroth mode). In section 4.2.2, the Smith channel-geometry derivation continues assuming that cavity-mode excitation only occurs because of acoustic velocity at the channel entrances. However, this result indicates that in the spherical case the motion of the diaphragm itself also excites the compression cavity modes.

5.2.4 Cavity behaviour with exit channels

In addition to the radiating diaphragm on the entrance face of the compression cavity, there are also a number of exit channels on the opposite face through which sound is radiated. It is most common for these exit paths to be annular channels having the same rotationally symmetry about the z axis as the radiating diaphragm and compression cavity. The modal description of the compression cavity is once again used to represent this situation. As the

same rotational symmetry about the z axis is present, the reduced set of eigenfunctions and eigenfrequencies (given in equation 5.34) may be used.

It is not necessary to re-analyse the effect of the radiating diaphragm. The pressure in the cavity is described as the linear sum of two pressure contributions: one occurring due to the velocity of the diaphragm, p_d, and the other due to the acoustical velocity of air entering and leaving the cavity at the exit channels, p_e

$$p = p_d + p_e \tag{5.40.}$$

The pressure occurring because of the velocity of the diaphragm is given in equation 5.39. The exit surface normal velocity is described by the function $u_e(\phi)$, the pressure in the compression cavity due to this velocity can, making use of equations 5.25 and 5.35, be written as

$$p_e(\phi) = \sum_{n=0}^{\infty} \frac{j\omega\rho_0 \Psi_n(\phi)}{V\left[k_n^2 - k^2\right]} \int_{\hat{\phi}=0}^{\phi_0} 2\pi \Psi_n(\hat{\phi}) u_e(\hat{\phi}) \left(h_0 - \mu\right)^2 \sin\phi \, d\hat{\phi} \tag{5.41.}$$

The exit surface normal velocity is zero except for the locations where a channel exit is positioned. The channel exits are narrow in ϕ and, in the frequency range of operation, the surface-normal acoustical velocity exiting the cavity into the channels may be accurately considered constant across each channel entrance. In order to simplify the integral, the Dirac delta function [47, p.147] is used to define that the cavity surface velocity is only non-zero at an infinitesimal locations where each channel is located. The exit-surface normal velocity function is thus approximated as

$$u_e(\phi) \approx \frac{w_1}{h_0 - \mu} u_1 \delta(\phi - \phi_1) + \frac{w_2}{h_0 - \mu} u_2 \delta(\phi - \phi_2) + \ldots + \frac{w_N}{h_0 - \mu} u_N \delta(\phi - \phi_N) \tag{5.42.}$$

where w_i is the width of the ith channel entrance, Φ_i is the angular position of the ith channel entrance, u_i is the cavity surface normal velocity at the entrance to the ith channel and $\frac{w_i}{h_0 - \mu}$ is the angular width of the ith channel in radians. On initial inspection, this expression may appear dimensionally inconsistent because of the angular width terms. However, the integral of the normal velocity over the cavity surface

$$\int_{\phi=0}^{\phi_0} 2\pi u_e(\phi) \left(h_0 - \mu\right)^2 \sin\phi \, d\phi = q_e \tag{5.43.}$$

is equal to the volume velocity entering the cavity, q_e. Considering this integral for a single thin annular channel, the channel entrance volume velocity is approximately equal to

$$q_i = u_i A_i \approx 2\pi u_i w_i (h_0 - \mu)\sin\phi_i \tag{5.44.}$$

where A_i is the entrance area of the i^{th} channel. Defining the position of the cavity using the Dirac delta function, it follows that

$$\int_{\phi=0}^{\phi_0} 2\pi K_i \delta(\phi - \phi_i)(h_0 - \mu)^2 \sin\phi \, d\phi = q_i \tag{5.45.}$$

which, recalling the sifting property of the delta function, $\int A(\phi)\delta(\phi - a)d\phi = A(a)$, indicates that

$$q_i = 2\pi K_i (h_0 - \mu)^2 \sin\phi \approx 2\pi u_i w_i (h_0 - \mu)\sin\phi_i \tag{5.46.}$$

and

$$K_i \approx u_i \frac{w_i}{h_0 - \mu} \tag{5.47.}$$

Using this approximation of $u_e(\phi)$ the integral in equation 5.41 may be simplified to

$$\int_{\hat{\phi}=0}^{\phi_0} 2\pi \Psi_n(\hat{\phi}) u_e(\hat{\phi})(h_0 - \mu)^2 \sin\phi \, d\hat{\phi} = \sum_{i=1}^{N} \Psi_n(\phi_i) A_i u_i \tag{5.48.}$$

where N is the total number of channel entrances on the exit side of the compression cavity. Inserting 5.48 into 5.41 provides an expression for the pressure in the cavity excited by the motion of air in the channel entrances,

$$p_e(\phi) = \sum_{n=0}^{\infty} \left[\frac{j\omega\rho_0 \Psi_n(\phi)}{V\left[k_n^2 - k^2\right]} \sum_{i=1}^{N} \Psi_n(\phi_i) A_i u_i \right] \tag{5.49.}$$

The full pressure due to the channel air motion and the diaphragm motion is consequently given by

$$p(\phi) = \sum_{n=0}^{\infty} \frac{j\omega\rho_0 \Psi_n(\phi)}{V\left[k_n^2 - k^2\right]} \left[\frac{u_0 \pi a^2}{\sin^2\phi_0} \int_{\hat{\phi}=0}^{\hat{\phi}_0} \Psi_n(\hat{\phi})\sin(2\hat{\phi})\, d\hat{\phi} + \sum_{i=1}^{N} \Psi_n(\phi_i) A_i u_i \right] \tag{5.50.}$$

5.2.5 Suppression of modal excitation by channel arrangement

Equation 5.50 provides a means of deriving a channel geometry that minimises the excitation of the acoustical modes in the compression cavity. From equation 5.50, it is clear that in order to suppress the excitation of the mth mode it is required that

$$\zeta_m^d + \sum_{i=1}^{N} \Psi_m(\phi_i) A_i u_i = 0 \tag{5.51.}$$

where

$$\zeta_m^d = \frac{u_0 \pi a^2}{\sin^2 \phi_0} \int_{\hat{\phi}=0}^{\hat{\phi}_0} \Psi_m(\hat{\phi}) \sin(2\hat{\phi})\, d\hat{\phi} \qquad 5.52.$$

The superscript ^{d} denotes diaphragm. This condition is quite similar to that which was encountered for the case of the cylinder compression cavity (equation 4.44) but with an additional ζ_m^d term. The ζ_m^d term represents the amplitude of excitation of the mth mode that occurs because of the motion of the diaphragm. In the cylindrical case, there was no excitation of the modes, except for the zeroth, and, consequently, this term was not seen. The integral expression giving ζ_m^d can be calculated explicitly for each mode of the cavity. This could be done analytically, using the Hoersch description of the Legendre functions to give $\Psi_m(\phi)$ [78]. Alternatively, the computed eigenfunctions, determined as described in 5.2.1, can be numerically integrated.

Equation 5.51 requires knowledge of both the diaphragm velocity, u_0, and also the channel velocities, u_i. A similar situation was encountered for the Smith derivation and, in this case, it was assumed that the acoustical velocities at the entrance to each channel were identical. It is possible to take a parallel approach and make the assumption that the cavity of the final compression driver behaves like the lumped terms in expression 5.50:

$$p = \frac{\rho_0 c_0^2}{j\omega V} \left[u_0 \pi a^2 + \sum_{i=1}^{N} A_i u_i \right] \qquad 5.53.$$

The channel-entrance velocities can be related to the channel-entrance pressure by the acoustic impedance of the channels, z_i,

$$u_i = \frac{p}{z_i} \qquad 5.54.$$

Unfortunately, unlike the cylindrical case, it is not sufficient to only assume that the channel impedances are all the same. In addition to the assumption that the channel velocities are identical, in order to satisfy the condition in expression 5.51, the ratio of the channel velocity to the diaphragm velocity must be known. Consequently, the channel impedances must be known. This is a little problematic. The channel impedances are dependent upon the horn to which the driver is connected and the precise geometry of the phase plug. However, at this stage of the design the phase-plug and horn geometry is not determined. Nevertheless, while the acoustical impedance of the channel is likely to vary at the lower end of the driver bandwidth, given the cut-on characteristics of an attached horn (see section 2.4), at higher

frequencies, the specific acoustical impedance in the narrow channel is very close to $\rho_0 c_0$. This is a satisfactory approximation as the eigenfrequencies of the cavity are likely to be at the upper end of the driver bandwidth.

Inserting this acoustical impedance assumption into equation 5.53 results in the relationship between the diaphragm and channel entrance velocities

$$u_i\left(\frac{j\omega V}{c_0 \pi a^2}-\frac{A_T}{\pi a^2}\right)=u_0 \qquad 5.55.$$

where

$$A_T=\sum_{i=1}^{N} A_i \qquad 5.56.$$

The real part of the diaphragm- and channel-entrance velocities are related by the compression ratio as might be expected. The imaginary part is a little more problematic. The acoustical modes of the cavity are excited by the motion of the diaphragm and also the acoustical velocity at the channel entrances. The intention is to arrange these velocities such that the modal excitation occurring because of the diaphragm motion is compensated by the excitation occurring because of the channel air motion. This is only feasible when these two velocities are in phase with each other. There is nothing that can be done to suppress excitation from the dome that occurs in quadrature to the excitation from the channels. The quadrature component is a result of the compliance of the air in the compression cavity. This is an effect that is also problematic in other areas. When the compliance becomes significant the channel velocity magnitude is reduced compared to the dome motion and the output of the driver is reduced. Typically, the compliance sets the upper bandwidth limit on the compression driver output. This effect is well known [30]. The practical solution to this problem is to minimise the compression-cavity volume. Equation 5.55 can be approximately written in terms of the width of the compression cavity, μ, as

$$u_i\left(\frac{j\omega\mu}{c_o}-\frac{A_T}{\pi a^2}\right)\approx u_o \qquad 5.57.$$

Modern compression drivers, built with carefully designed and constructed parts, have extremely small cavity widths to keep the acoustical compliance problem to a minimum. Typically, μ is in the range 0.3 - 0.6mm, and, within the bandwidth of the driver, equation 5.55 is dominated by the real term. In this case, the approximation is made that the velocities are related by only the real part,

$$u_i \approx \frac{-\pi a^2 u_o}{A_T} \equiv \frac{\zeta_0^d}{A_T} \tag{5.58.}$$

Substituting this expression into equation 5.51, the condition for suppression of the mth mode can be written as

$$A_T \frac{\zeta_m^d}{\zeta_0^d} - \sum_{i=1}^{N} \Psi_m(\phi_i) A_i = 0 \tag{5.59.}$$

The suppression condition is now in a form where it is only dependent upon geometric parameters of the compression driver. The condition can be met for specific modes by careful selection of the channel positions, ϕ_i, and channel areas, A_i. As with the Smith case, the first N modes should be suppressed to extend the lumped behaviour to a higher frequency. The condition is a set of N simultaneous equations that can be written in matrix form as

$$\begin{bmatrix} \Psi_0(\phi_1) & \Psi_0(\phi_2) & \cdots & \Psi_0(\phi_N) \\ \Psi_1(\phi_1) & \Psi_1(\phi_2) & \cdots & \Psi_1(\phi_N) \\ \Psi_2(\phi_1) & \Psi_2(\phi_2) & \cdots & \Psi_2(\phi_N) \\ \vdots & \vdots & \ddots & \vdots \\ \Psi_N(\phi_1) & \Psi_N(\phi_2) & \cdots & \Psi_N(\phi_N) \end{bmatrix} \begin{bmatrix} A_1/A_T \\ A_2/A_T \\ \vdots \\ A_N/A_T \end{bmatrix} = \begin{bmatrix} \zeta_0^d/\zeta_0^d \\ \zeta_1^d/\zeta_0^d \\ \zeta_2^d/\zeta_0^d \\ \vdots \\ \zeta_N^d/\zeta_0^d \end{bmatrix} \tag{5.60.}$$

The equation in the first row of the matrix is trivial. This is necessary in order to force the sum of the area ratios to equal unity. The matrix on the left of the expression containing the eigenfunction terms is of dimensions N by $N+1$ and thus not invertible in this form. Additionally, there are two sets of unknowns, ϕ_i and A_i. To solve this problem the variables ϕ_i are set so that they make one row of the matrix trivial, resulting in a square and invertible matrix with only the areas unknown. This is achieved by setting the values of ϕ_i to meet the condition

$$\Psi_N(\phi_i) = \zeta_N^d/\zeta_0^d \tag{5.61.}$$

This results in a reduced set of equations given by

$$\begin{bmatrix} \Psi_0(\phi_1) & \Psi_0(\phi_2) & \cdots & \Psi_0(\phi_N) \\ \Psi_1(\phi_1) & \Psi_1(\phi_2) & \cdots & \Psi_1(\phi_N) \\ \Psi_2(\phi_1) & \Psi_2(\phi_2) & \cdots & \Psi_2(\phi_N) \\ \vdots & \vdots & \ddots & \vdots \\ \Psi_{N-1}(\phi_1) & \Psi_{N-1}(\phi_2) & \cdots & \Psi_{N-1}(\phi_N) \end{bmatrix} \begin{bmatrix} A_1/A_T \\ A_2/A_T \\ \vdots \\ A_N/A_T \end{bmatrix} = \begin{bmatrix} \zeta_0^d/\zeta_0^d \\ \zeta_1^d/\zeta_0^d \\ \zeta_2^d/\zeta_0^d \\ \vdots \\ \zeta_{N-1}^d/\zeta_0^d \end{bmatrix} \tag{5.62.}$$

The matrix on the left is now determined and invertible. The set of equations can be solved to find the vector of area ratios.

A worked example

As a demonstration of how to determine the positions and sizes of the channel entrances using this process, a compression driver with a domed diaphragm of $\phi_0 = 55^o$ is considered. Provided that the width of the compression cavity, μ, remains small compared to a wavelength, it is not necessary to specify the dimensions of the compression cavity that is being considered as the results can be simply scaled to suit a driver of any diaphragm radius, a.

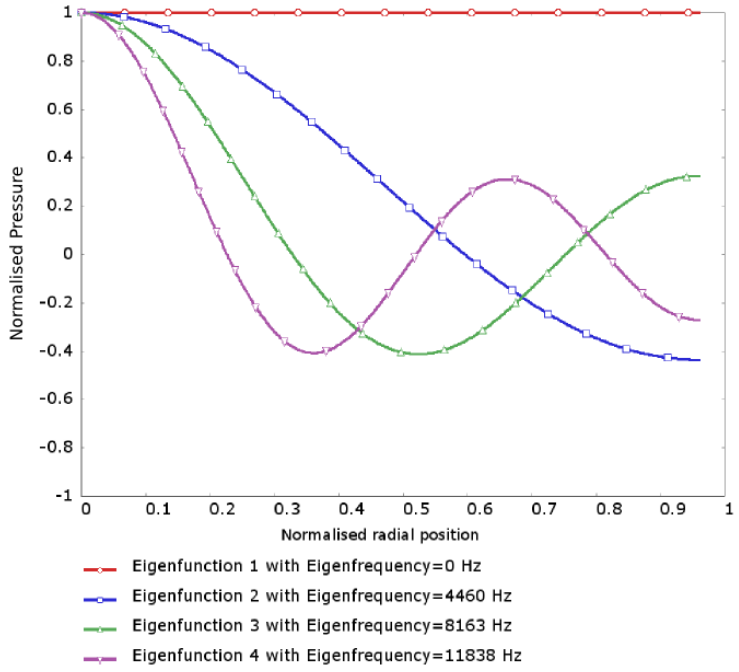

Figure 5.12. PAFEC calculated eigenfrequencies and eigenfunctions for a 55° compression cavity normalised to have maximum value of unity.

The first stage in the process is to determine the eigenfunctions and eigenfrequencies of the compression cavity. The eigenfunctions of the spherical cavity cannot be easily determined analytically, as discussed in section 5.2. It is preferable to determine the eigenfunctions numerically using the method outlined in section 5.2.1. In order to perform this calculation, a simple axisymmetric mesh was constructed in Flux [73] using geometric parameters of $\mu = 0.3\text{mm}$, $a = 40\text{mm}$ and $\phi_0 = 55^o$. The mesh was imported into PAFEC-FE [55] and set up as a "modes and frequencies" analysis. The first four eigenfrequencies and eigenfunctions for this cavity are shown in figure 5.12 as a function of the cavity angle ϕ.

Unfortunately, the convention for the PAFEC solver is to provide the eigenfunctions normalised such that their maximum value is unity, whereas for use in expression 5.25 the eigenfunctions must be normalised according to the expression

$$\int_V \Psi_n(\phi)^2 \, dV = V \tag{5.63.}$$

For the spherical coordinate system in which the compression cavity is described this condition can be re-written as

$$\int_{\phi=0}^{\phi_0} \int_{\theta=0}^{2\pi} \int_{h=h_0-\mu}^{h_0} \Psi_n(\phi)^2 h^2 \sin\phi \, dh \, d\theta \, d\phi = V \tag{5.64.}$$

Performing the integrals with respect to θ and h, this simplifies to

$$2\pi\left(\frac{\mu^3}{3} + h_0^2\mu - h_0\mu^2\right)\int_{\phi=0}^{\phi_0} \Psi_n(\phi)^2 \sin\phi \, d\phi = V \tag{5.65.}$$

The spherical-cap cavity volume can be determined as the difference between the volume of two spherical sectors [47, p.106], which gives the volume to be

$$V = 2\pi(1-\cos\phi_0)\left(\frac{\mu^3}{3} + h_0^2\mu - h_0\mu^2\right) \tag{5.66.}$$

Inserting this into equation 5.65 the correct normalisation for the eigenfunctions with respect to ϕ alone is

$$\int_{\phi=0}^{\phi_0} \Psi_n(\phi)^2 \sin\phi \, d\phi = (1-\cos\phi_0) \tag{5.67.}$$

Matlab [54] was used to numerically integrate the raw PAFEC results and scale the eigenfunctions to correct the normalisation. The resulting functions are shown in figure 5.13. Using these eigenfunctions, the value of the coefficient ζ_n^d can be calculated according to equation 5.52, again using Matlab to perform the numerical integration of the FEM derived eigenfunctions.

The calculated values are

$$\zeta_0^d/\zeta_0^d = 1 \;,\; \zeta_1^d/\zeta_0^d = 0.356271 \;,\; \zeta_2^d/\zeta_0^d = -0.129868 \;,\; \zeta_3^d/\zeta_0^d = 0.0727257 \tag{5.68.}$$

For a three-channel phase-plug design, the channel positions are set according to equation 5.61. This results in channel positions of

$$\phi_1 = 0.2350\,\phi_o \;,\; \phi_2 = 0.5431\,\phi_o \;,\; \phi_3 = 0.8476\,\phi_o \tag{5.69.}$$

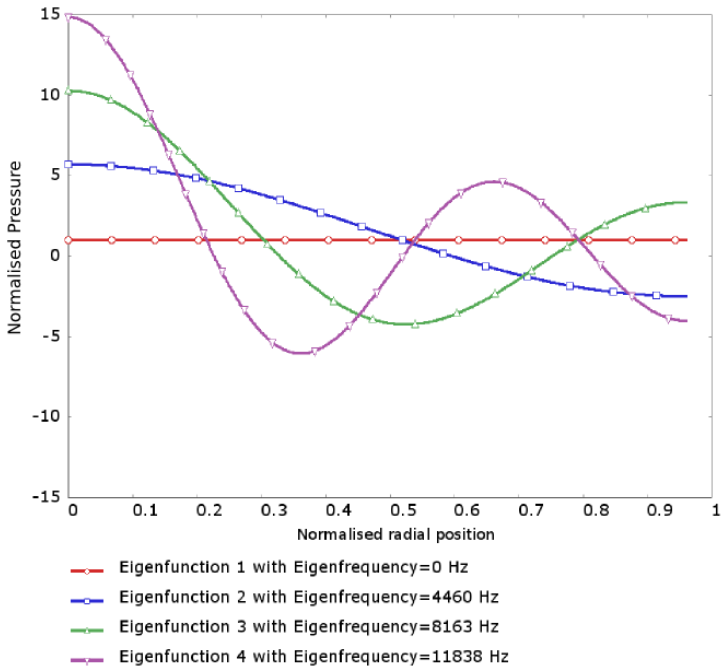

Figure 5.13. PAFEC calculated eigenfrequencies and eigenfunctions for a 55 degree compression cavity. Normalised according to equation 5.67.

Once the channel positions are fixed, the matrix in equation 5.62 can be determined using the values of ζ_n^d above along with the calculated eigenfunctions

$$\begin{bmatrix} 1 & 1 & 1 \\ 4.6023 & 0.9598 & -2.0557 \\ 4.3768 & -4.2344 & 1.5341 \end{bmatrix} \begin{bmatrix} A_1/A_T \\ A_2/A_T \\ A_3/A_T \end{bmatrix} = \begin{bmatrix} 1 \\ 0.356271 \\ -0.129868 \end{bmatrix} \quad 5.70.$$

This expression can be solved by inversion of the matrix which results in the channel area ratios

$$\begin{bmatrix} A_1/A_T \\ A_2/A_T \\ A_3/A_T \end{bmatrix} = \begin{bmatrix} 0.189356 \\ 0.381768 \\ 0.428875 \end{bmatrix} \quad 5.71.$$

Equivalently the area ratios can be written as channel width ratios,

$$\begin{bmatrix} w_2/w_1 \\ w_3/w_1 \end{bmatrix} = \begin{bmatrix} 0.9056 \\ 0.6973 \end{bmatrix} \quad 5.72.$$

5.2.6 Discussion

The results above for the case of the $\phi=55$ degree compression cavity may be directly compared to the results in section 4.2.4 for the simplified cylindrical compression cavity. Tables 5.2 and 5.3 compare the results of two methods.

	Smith Positioning Method	New Positioning Method
ϕ_1 or r_1	0.238a	$0.2350\,\phi_0$
ϕ_2 or r_2	0.543a	$0.5431\,\phi_0$
ϕ_3 or r_3	0.853a	$0.8476\,\phi_0$

Table 5.2: Comparison of channel positioning for the case of a 55 degree compression cavity using two methods, i) Smith method using a cylindrical model of the compression cavity and ii) new method using a spherical cap compression cavity.

It can be seen from table 5.2 that if the r and ϕ coordinates are interpreted to be equivalent, there is very little difference between the new channel positions compared to the Smith method. This is not perhaps surprising as the channels are positioned in both cases close the nodes of the third mode and in both cases and the cavity eigenfunctions are very similar.

	Smith Positioning Method	New Positioning Method
w_2/w_1	1.065	0.9056
w_3/w_1	1.025	0.6973

Table 5.3: Comparison of channel widths a for the case of a 55 degree compression cavity using two methods, i) Smith method using a cylindrical model of the compression cavity and ii) new method using a spherical cap compression cavity.

Table 5.3 shows the difference between the channel widths using the two methods. A distinct difference is seen here: the Smith method results in all channels having approximately the same width; with the new method the channels decrease in width towards the outer diameter of the cavity.

In his paper, Smith graphically illustrated the suppression technique for a three-channel phase plug with plots that were recreated in section 4.2.5. Figure 5.14 shows the excitation of the first eigenfunction resulting from the velocity in each channel entrance separately. The vector locations indicate the position of the channels and the vector magnitude indicates the strength of the excitation from that channel, given by

$$\Psi_n^2(\phi_i)A_i \qquad 5.73.$$

Additionally, unlike figures 4.10 and 4.11, this time there is a fourth black line on the plot without an attached vector that indicates the excitation due to the diaphragm motion, given by

$$-\Psi_n(\phi)A_T\frac{\zeta_n^d}{\zeta_0^d} \qquad 5.74.$$

where A_T is the summed area of the channels as defined in equation 5.56.

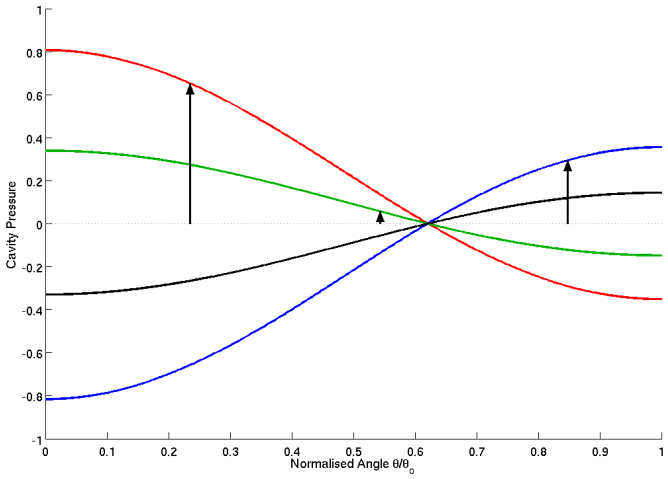

Figure 5.14. Illustrative plot showing new suppression technique for the first mode with compression cavity of $\phi=55$. Red curve is the excitation due to the inner channel, the green curve is the excitation due to the middle channel, the blue curve is the excitation due to the outer channel, the black curve shows the excitation due to the diaphragm motion.

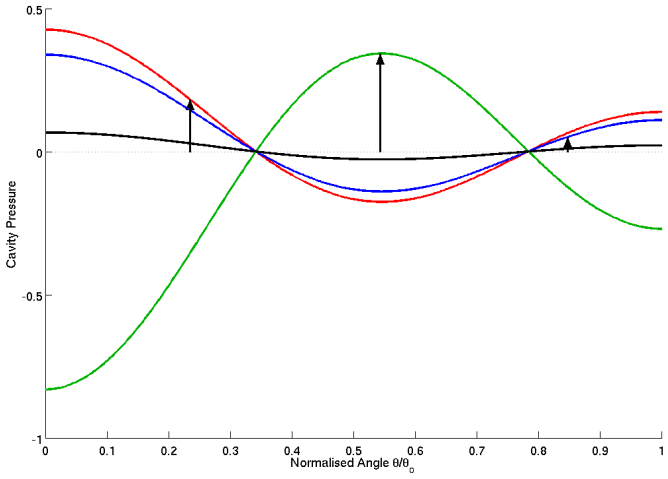

Figure 5.15. Illustrative plot showing new suppression technique for the second mode with compression cavity of $\phi=55$. Red curve is the excitation due to the inner channel, the green curve is the excitation due to the middle channel, the blue curve is the excitation due to the outer channel, the black curve shows the excitation due to the diaphragm motion.

Figures 5.15 and 5.16 show similar plots for the second and third modes respectively. It is easily seen from these illustrations that the contributions from the individual channels, along with the excitation from the diaphragm motion, sum to zero, which indeed was our condition in equation 5.51.

In section 4.2.5, the suppression plot was not shown for the third mode as the result is trivial. In the Smith case, there is no excitation of the third mode as the channels are placed on the nodes. For the analysis with a curved diaphragm and compression cavity, this is not the case. There is excitation of the third mode by the diaphragm and the channels are positioned such that their combined excitation compensates for this.

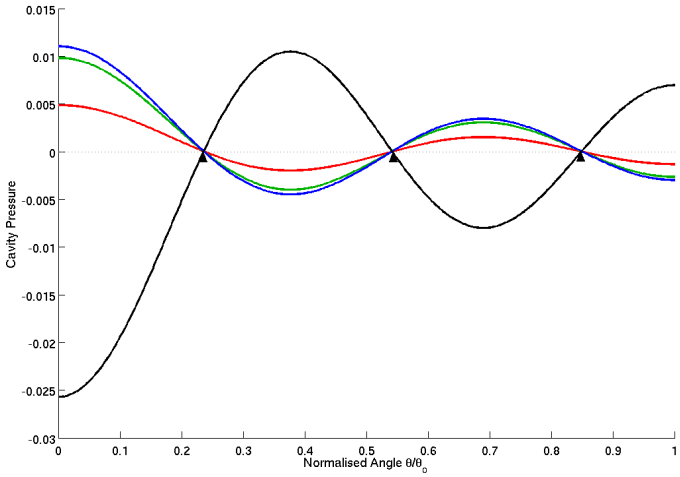

Figure 5.16. Illustrative plot showing new suppression technique for the third mode with compression cavity of $\phi = 55$. *Red curve is the excitation due to the inner channel, the green curve is the excitation due to the middle channel, the blue curve is the excitation due to the outer channel, the black curve shows the excitation due to the diaphragm motion.*

However, the position of the channels is still very close to the nodes of the third mode. This is because, firstly, the value of the coefficient ζ_n^d reduces as the modes increase in order and, secondly, because the modal excitation from all three channels is in the same polarity and only a small excitation from each is enough to compensate for the diaphragm. In practice, it is debatable whether modal suppression is achievable for the Nth mode: the suppression shown in Figure 5.16 is very sensitive to slight errors in the position and area of the channels. An alternative approach is to position the channels of the phase plug exactly at the nodal positions of the Nth mode to attempt to isolate the channels from this mode. The only difference in the process outlined above is that the channel positions Φ_i are set to meet the condition $\Psi_N(\phi_i) = 0$ instead of that outlined in equation 5.61.

The channel areas can be found by forming the matrix equation, 5.62, and then inverting exactly as before. However, this slightly modified derivation results in channel positions and area which are extremely close to those derived using the first positioning method. For example with, the 55-degree compression cavity considered in section 5.2.5, the channel positions and widths derived using both channel positioning methods is shown in tables 5.4 and 5.5. There is a very small change in both the position and a correspondingly small change in the channel widths.

	Original Positioning Method	Nodal Channel Positioning
ϕ_1	$0.2350\,\phi_0$	$0.2360\,\phi_0$
ϕ_2	$0.5431\,\phi_0$	$0.5417\,\phi_0$
ϕ_3	$0.8476\,\phi_0$	$0.8493\,\phi_0$

Table 5.4: Comparison of channel positioning for the case of a 55-degree compression cavity using two methods: i) attempted suppression of the Nth mode and ii) isolation of channels from the Nth mode by positioning at nodes.

	Original Positioning Method	Nodal Channel Positioning
w_2/w_1	0.9056	0.9177
w_3/w_1	0.6973	0.7008

Table 5.5: Comparison of channel width for the case of a 55-degree compression cavity using two positioning methods: i) attempted suppression of the Nth mode and ii) isolation of channels from the Nth mode by positioning at nodes.

This small difference is likely in practice to be swamped by other factors. For example, in the derivation the channels are assumed to connect only at distinct positions, defined using the Dirac delta, whereas this is clearly not the reality with real channels of a definite entrance width.

A simple FEM model was constructed to confirm the derived channel geometry. The geometry of this model is illustrated in figure 5.17. The compression ratio is 15. The channels are terminated with a $\rho_0 c_0$ specific acoustical impedance to avoid reflections. The channels are gently curved so that the termination is a simple annular channel in each case. Throughout the channel, the area is continuous to avoid any sudden change of acoustical impedance.

The normalised channel pressure level responses are plotted in figure 5.18. At low frequencies, a normalised pressure level of 23.5dB is seen in all three channels corresponding directly to the compression ratio of 15. This plot is directly comparable to

figure 5.3, which has exactly the same compression cavity geometry but uses the Smith channel positions and areas. The pressure responses in the three channels are very similar and flat up to approximately $ka=5$. This is a distinct improvement over the responses using the Smith channel geometry. Above $ka=5$, there is some separation of the pressure responses with a maximum spread of 3.6dB.

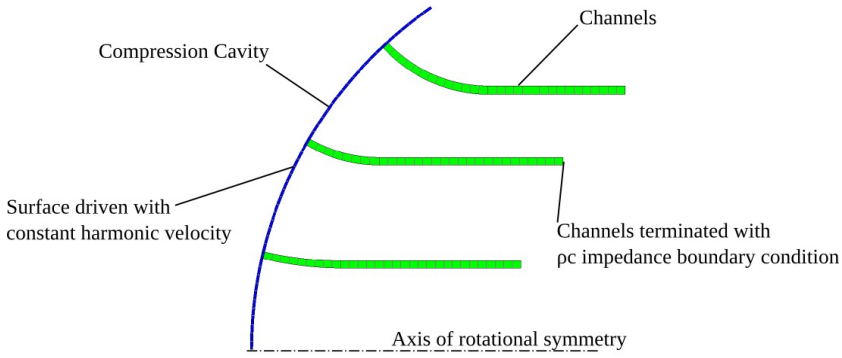

Figure 5.17. Half-section of geometry used in simple compression driver FEM model with domed diaphragm.

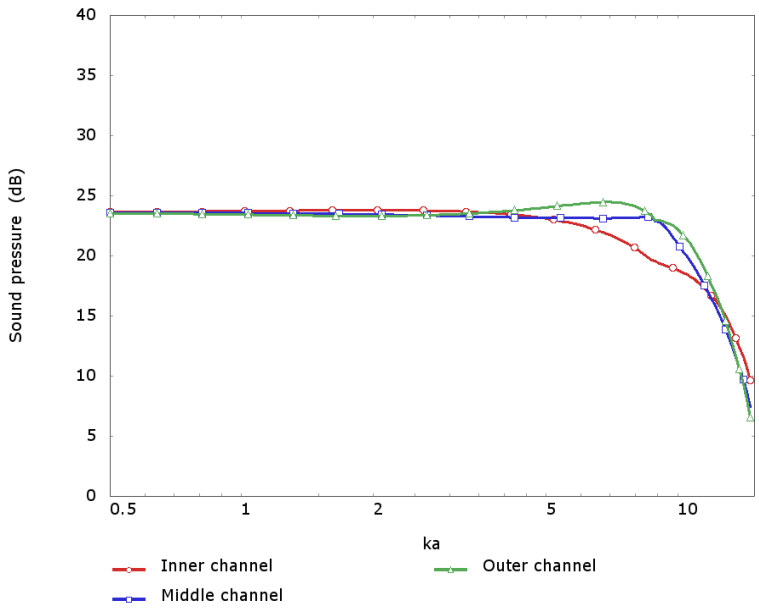

Figure 5.18. Normalised channel-pressure level response for simple compression-driver arrangement having a domed radiating diaphragm using the new channel-geometry design methodology.

The Smith channel arrangement combined with a cylindrical compression cavity, as assumed in the Smith channel derivation, resulted in channel-pressure responses that were virtually identical over the whole analysed range (shown in figure 4.15). However, the pressure results in this case, with the new derivation and spherical cap cavity, do not have the same consistency. This is an interesting difference. It is believed that the spread in the channel-

pressure responses above $ka=5$ is attributable to the imaginary part of the velocity transfer function between the diaphragm motion and the channel-entrance acoustical velocity which it is not possible to suppress. This issue was discussed in detail on page 144.

The variation of the channel derivation with cavity angle

To investigate how the channel geometry varies with cavity angle, 18 FEM models with cavity angle from 5 degrees to 90 degrees in 5-degree increments were set-up in FLUX, and PAFEC-FE was used to determine the eigenfrequencies and functions for each. The channel geometry for a $N=3$ phase plug was then designed for each cavity using the method demonstrated in 5.2.5. The resulting channel geometry variation with compression cavity angle is shown in figures 5.19 and 5.20.

Figure 5.19 indicates that the calculated positions of the phase-plug channels are almost invariant of cavity angle. This is because the target for their location, outlined in equation 5.61, places them close to the nodal positions of the third mode of the cavity. The nodal positions are approximately invariant to the cavity angle.

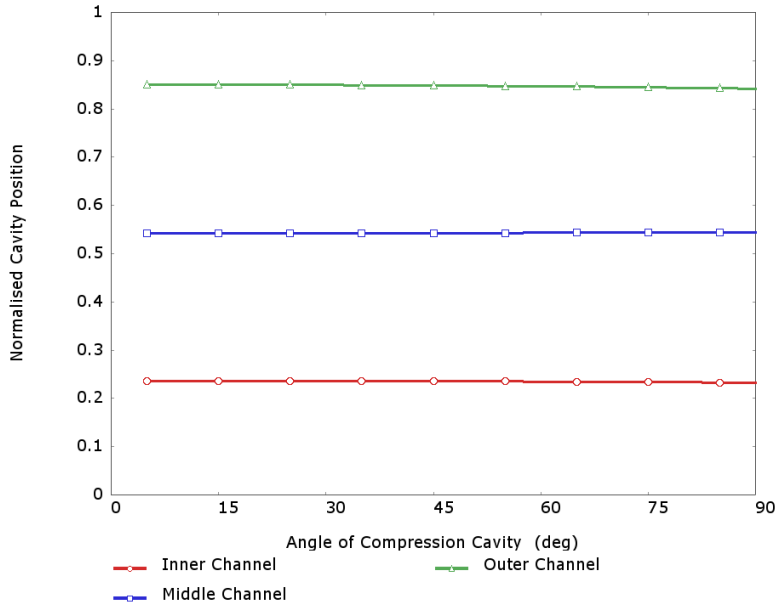

Figure 5.19. Normalised calculated channel position variation with compression-cavity angle Φ_0 for a N=3 channel phase plug. Channel positions are normalised by Φ_0.

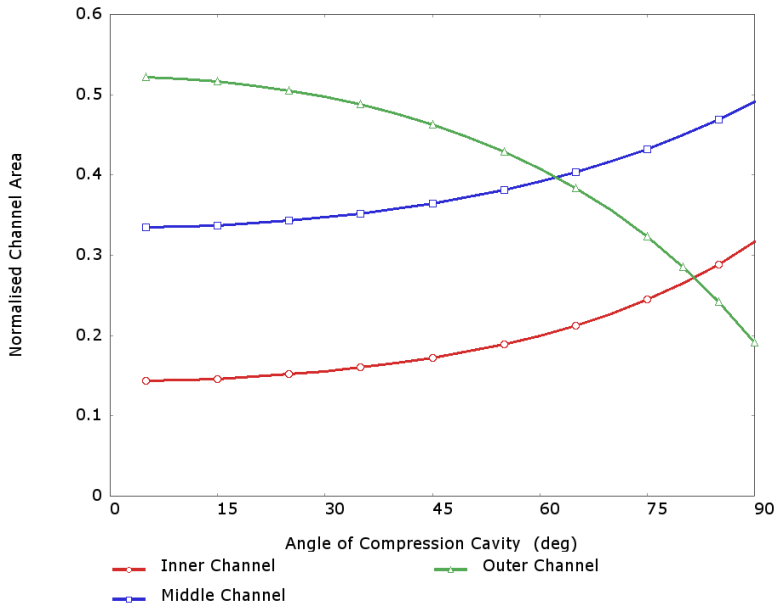

Figure 5.20. Normalised calculated channel area variation with compression-cavity angle Φ_0 for a N=3 channel phase plug. Channel areas are normalised by A_T.

Figure 5.20 reveals that, at low cavity angles, the channel areas tend towards Smith's originally derived results, as given in table 5.5. This is logical because the spherical geometry approaches the cylindrical representation as the cavity angle is decreased to zero. As the cavity angle is increased from zero, the derived channel areas diverge from the Smith values: the outer channel decreases in area while the inner channels both increase in area. It is helpful to plot the same results in terms of the channel widths that can be calculated from the channel positions and areas using the relation

$$w_i = \frac{A_i}{2\pi a}\frac{\sin\phi_0}{\sin\phi_i} \qquad 5.75.$$

The normalised widths calculated for a range of cavity angles are shown in figure 5.21. From this figure, it is easier to recognise the trend that as the dome angle is increased the outer channel narrows while the inner channel widens. This is perhaps a logical result, bearing in mind that the volume velocity of the channels is in the opposite polarity to the diaphragm velocity. The diaphragm normal velocity is lower at the periphery and so correspondingly the outer channels must be smaller, the velocity must also be lower at the periphery on the exit side of the compression cavity in order to suppress undesirable modal excitation.

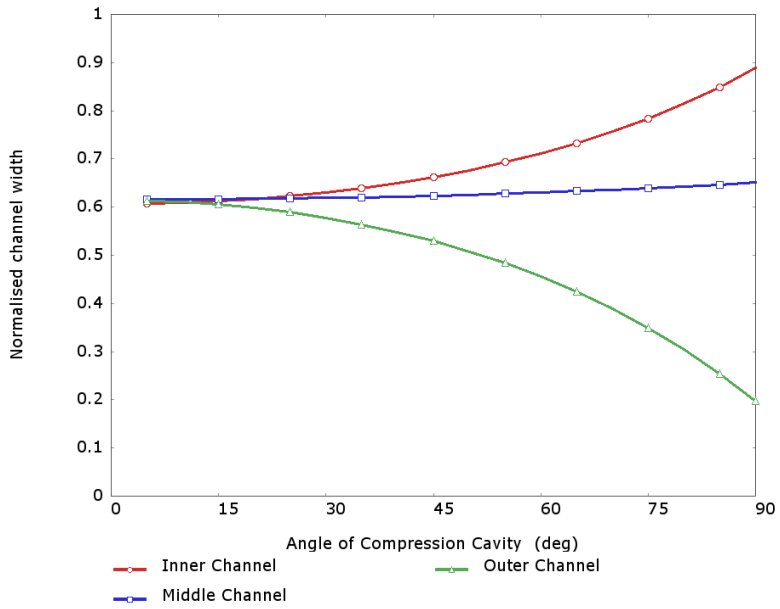

Figure 5.21. Normalised calculated channel-width variation with compression cavity angle Φ_0 *for a N=3 channel phase plug. Channel positions are normalised by* $A_T/2\pi a$.

5.3 A practical design based on the new methodology

The theory outlined above was used as the basis for a commercial compression-driver design, the Celestion CDX1.4. The driver has a 3 inch (76.2mm) diameter titanium dome of 55-degrees curvature and is designed to connect to a horn-throat diameter of 1.4 inches (38.1mm). The design was developed using a great deal of FEM and BEM modelling. The final overall modelling was performed by Mark Dodd, head of research at GP Acoustics.

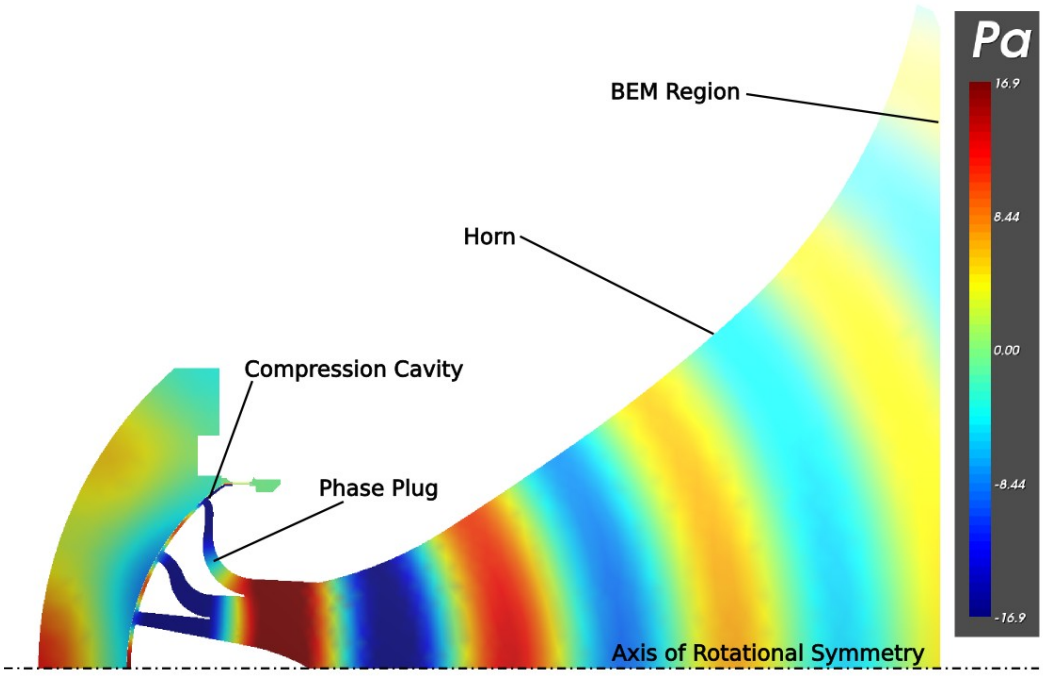

Figure 5.22. FEM/BEM axisymmetric model of the mechanical and acoustical parts of the CDX1.4 with instantaneous acoustical pressure at 7.6kHz indicated by colour shading.

In order to predict the frequency response function of a loudspeaker it is necessary to model the driver behaviour in all the active physical domains: mechanical, acoustical, magnetic and electrical. The strategy commonly used by the Author, and his colleagues at GP Acoustics, is to separate the mechanoacoustical domain from the electrical and the magnetic domain and then to join the results using a single degree of freedom coupling. This approach is outlined in more detail by Dodd [76]. Separation of the domains in this way is quite a useful as it allows models to be developed independently in the various domains and then subsequently linked to mimic the overall behaviour.

The new geometry guidelines were used as a starting point for the design of the CDX1.4 and subsequently FEM simulations were used to fine tune the positions and sizes of the compression driver channel entrances. This process was partly performed using automated optimisation of the FEM geometry with PAFEC's built in optimisation facility. In this case

the gradient descent method was used [47, p.875] and the objective function based upon the maximum deviation in pressure between the three $\rho_0 c_0$ terminated channels. The final positions of the channels are not far from the theoretical ideals. Considering the other significant differences between the very simplified models that were used in the previous section, such as the additional acoustical volume at the outside diameter of the compression cavity where the voice coil gap is located and the non rigid radiating diaphragm, this is encouraging.

	Smith method	New method	CDX1.4 optimised
ϕ_1	0.238a	$0.2350\,\phi_0$	$0.2363\,\phi_0$
ϕ_2	0.543a	$0.5431\,\phi_0$	$0.5454\,\phi_0$
ϕ_3	0.853a	$0.8476\,\phi_0$	$0.8727\,\phi_0$

Table 5.6: Comparison of channel positioning for the case of a 55-degree compression cavity using three methods: i) Smith method using a cylindrical model of the compression cavity; ii) new method using a spherical cap compression cavity; and iii) optimised final positions for the CDX1.4 driver.

	Smith method	New method	CDX1.4 optimised
w_2/w_1	1.065	0.9056	0.8852
w_3/w_1	1.025	0.6973	0.5851

Table 5.7: Comparison of channel widths a for the case of a 55-degree compression cavity using three methods: i) Smith method using a cylindrical model of the compression cavity; ii) new method using a spherical cap compression cavity; and iii) optimised final positions for the CDX1.4 driver.

The final channel geometry is compared to the Smith and the new positioning method in tables 5.6 and 5.7. Indeed, the final positions for the CDX1.4 are even more of a departure from the original Smith geometry than the new positions derived in the previous sections. This may be a result of the additional volume at the outside diameter of the compression cavity of the CDX1.4 where the voice coil gap is located. This region is effectively undriven by the dome diaphragm and, consequently, may require a greater departure from the Smith than suggested by the derived new channel geometry. The large imbalance in the width of the inner and outer cavity is extreme, requiring special attention during both the design of the phase-plug channels and the mechanical construction of the driver.

Figure 5.23 shows a comparison of the FEM/BEM predicted and measured linear frequency response of the final compression driver. The agreement between the two is excellent. The compression driver was able to achieve a smooth response up to a frequency of approximately 10kHz ($ka \approx 6.9$).

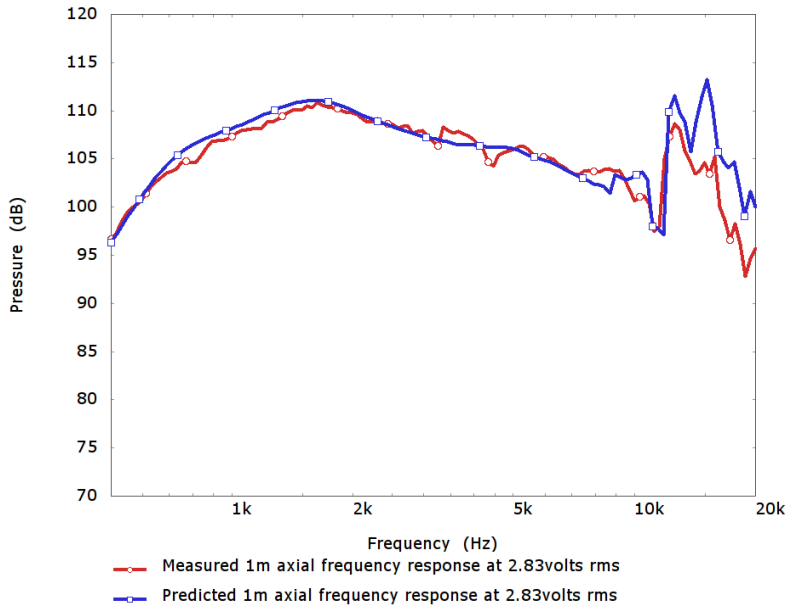

Figure 5.23. Comparison of predicted and measured frequency response function of the CDX1.4 Celestion compression driver on an axisymmetric horn, measured at 1m on-axis at an input level of 2.83V rms.

For easy comparison with the results given in the previous sections, an axisymmetric FEM model was constructed of the final CDX1.4 compression driver geometry, but with the phase plug truncated just before where the channels join. The truncated channels are terminated with a $\rho_0 c_0$ specific acoustical impedance. The geometry of the truncated CDX1.4 FEM model is shown in figure 5.24.

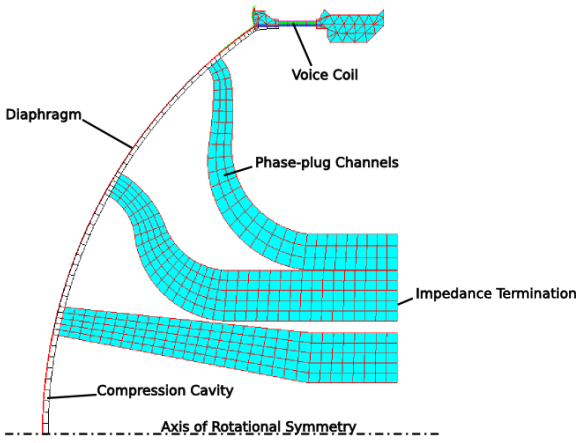

Figure 5.24. FEM axisymmetric model of the mechanical and acoustical parts of the CDX1.4, phase-plug channels truncated into $\rho_0 c_0$ impedance before the channels are joined.

The pressure response at the ends of the three channels are shown in figure 5.25 for the situation when the voice coil moves with unity velocity amplitude at all frequencies. The

pressures levels are normalised by the specific acoustical impedance of a plane wave given by

$$L_{norm} = 20\log_{10}\left|\frac{p}{\rho_0 c_0}\right| \qquad 5.76.$$

At low frequencies a normalised pressure level of approximately 13.5dB is seen in all three channels corresponding directly to the compression ratio of 6.5. The compression ratio of the driver was intentionally kept low for this design in an attempt to reduce the non-linearities resulting from the large pressure levels occurring in the phase-plug channels. This figure is directly comparable to that shown for the idealised compression driver in figure 5.18. The three channel responses are relatively similar up to a frequency of approximately $ka = 4$, above this frequency the pressures diverge. In particular, the outer channel is markedly different from the inner two, which remain quite similar. The region of separation of the three responses occurs at a lower frequency and is much larger than that shown in the idealised compression driver, shown in figure 5.18.

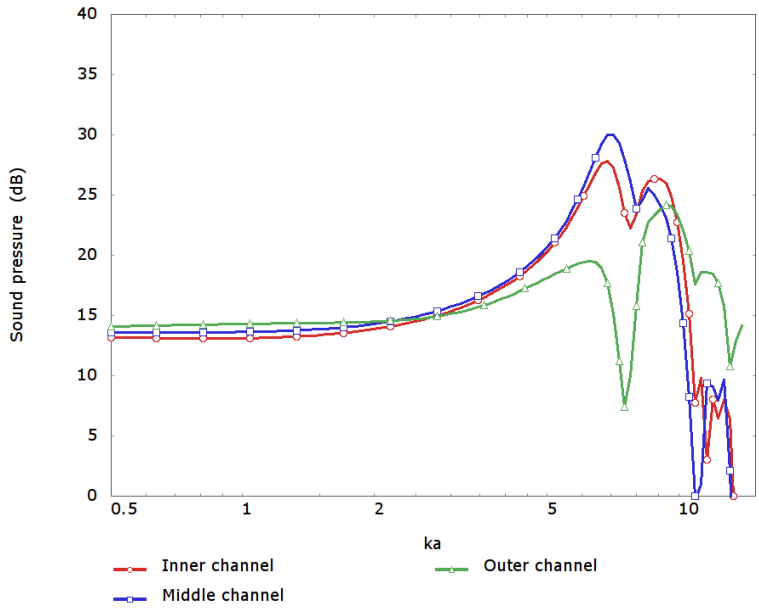

Figure 5.25. Normalised channel pressure-level response of FEM model of the CDX1.4 driver, shown in figure 5.24, with separated channels terminated with $\rho_0 c_0$ specifics acoustical impedance.

The compression cavity of the CDX1.4 is of a slightly larger physical volume than the idealised compression driver and this would be expected to result in a deteriorate in the modal suppression performance due to the assumption made in section 5.2.5 that the cavity compliance is negligible. Additionally, whereas with the idealised models the radiating diaphragm was constrained to move rigidly, in the real compression driver this is not the

case. Above 10kHz ($ka \approx 7$) the responses become more erratic as the dome behaves non-rigidly.

Figure 5.26 shows the FEM-modelled velocity at the centre of the radiating diaphragm in comparison to the drive point velocity at the voice coil. From this, it is clear that there is a mechanical resonance in the radiating parts at 10kHz ($ka \approx 7$). This resonance coincidences with the peaks in the pressure responses shown in figure 5.25 and also in the radiated pressure response shown in figure 5.23. The mechanical behaviour of the diaphragm is a limiting factor in the high frequency response of the driver. The idealised models of the compression drivers that were considered in the previous sections indicate that one would expect that the high-frequency limit of the driver because of acoustical effects to be around $ka \approx 8$, whereas, in this case, the response becomes erratic around $ka \approx 6.9$ close to the frequency when the dome begins to move non-rigidly. The case when the diaphragm is rigid was exclusively considered in the previous sections. These results highlight the need for more careful consideration of the radiating diaphragm motion. The CDX1.4 driver is a commercially available unit and it is currently widely used in the professional audio market.

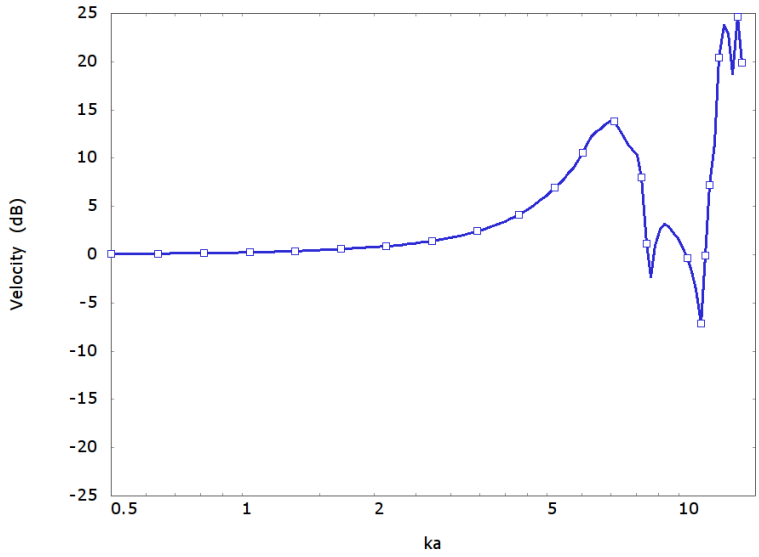

Figure 5.26. CDX1.4 velocity difference at centre of radiating diaphragm compared to drive point.

5.4 A generalised method

Two derivations have been presented to determine the optimal geometry for compression-driver annular-channel positions and areas in compression cavities of cylindrical and spherical-cap shape. In this section, a general approach for positioning and sizing of "narrow" phase-plug channels is described for a cavity with arbitrary shape. The method is generally applicable to any phase-plug design where the channel entrances are arranged so that they are narrow with respect to the effective cavity modes and can be considered to act on the cavity at a discrete location.

The acoustical pressure in an arbitrary compression cavity is described as the summation of the modal contributions as

$$p(\boldsymbol{x},\omega)=\sum_{n=0}^{\infty}\frac{j\omega\rho_0\Psi_n(\boldsymbol{x})}{V\left[k_n^2-k^2\right]}\int_S\Psi_n(\boldsymbol{y})\boldsymbol{u}(\boldsymbol{y}).\boldsymbol{n}\,dS \qquad 5.77.$$

It is assumed that the compression cavity is directly driven by a mechanical diaphragm that occupies some part of the cavity surface and that elsewhere on the cavity surface there are some exit channels through which the sound is radiated. All other locations on the compression cavity surface have zero normal velocity. The surface integral in equation 5.77 only need be performed over these two active regions

$$p(\boldsymbol{x},\omega)=\sum_{n=0}^{\infty}\frac{j\omega\rho_0\Psi_n(\boldsymbol{x})}{V\left[k_n^2-k^2\right]}\left[\int_{S_d}\Psi_n(\boldsymbol{y})\boldsymbol{u}_d(\boldsymbol{y}).\boldsymbol{n}\,dS+\int_{S_e}\Psi_n(\boldsymbol{y})u_e(\boldsymbol{y})\,dS\right] \qquad 5.78.$$

In this expression, S_d is the cavity surface occupied by the diaphragm, the function $\boldsymbol{u}_d(\boldsymbol{y})$ describes the velocity of the diaphragm. S_e is the cavity surface occupied by the various exit channels, and the function $u_e(\boldsymbol{y})$ describes the normal acoustical-particle velocity over this region.

The condition for the suppression of excitation for a particular mode, n, is clearly given by

$$\int_{S_d}\Psi_n(\boldsymbol{y})\boldsymbol{u}_d(\boldsymbol{y}).\boldsymbol{n}\,dS+\int_{S_e}\Psi_n(\boldsymbol{y})u_e(\boldsymbol{y})\,dS=0 \qquad 5.79.$$

As before, it is assumed that the channels are "narrow", acting upon the compression cavity at discrete locations, and the exit normal velocity function can be described accurately using N delta functions.

The surface integral over the channels in expression 5.79 can then be simply evaluated to

$$\int_{S_e} \Psi_n(\boldsymbol{y}) u_e(\boldsymbol{y}) dS = \sum_{i=1}^{N} \Psi_n(\boldsymbol{y}_i) A_i u_i \qquad 5.80.$$

where A_i is the area of the i-th channel entrance and u_i is the acoustical particle-velocity normal to the cavity surface at the entrance to the i-th channel. Using this expression 5.79 can be written as

$$\int_{S_d} \Psi_n(\boldsymbol{y}) \boldsymbol{u}_d(\boldsymbol{y}).\boldsymbol{n}\, dS + \sum_{i=1}^{N} \Psi_n(\boldsymbol{y}_i) A_i u_i = 0 \qquad 5.81.$$

In order to clarify the expressions a parameter, ζ_n^d, is introduced and defined as

$$\zeta_n^d = \int_{S_d} \Psi_n(\boldsymbol{y}) \boldsymbol{u}_d(\boldsymbol{y}).\boldsymbol{n}\, dS \qquad 5.82.$$

The reader will notice that this parameter is equivalent that used in section 5.2.5. ζ_n^d is a measure of how severely the motion of the diaphragm excites each cavity mode.

Assuming that it is desirable for the lumped cavity behaviour to be extended as high in frequency as possible, the phase plug should be designed to ensure that the first N modes meet the suppression condition above. While the compression driver is well behaved, the normal acoustical particle-velocity at the channel entrances, u_i, can be related to the diaphragm velocity function, $\boldsymbol{u}_d(\boldsymbol{y})$ by

$$\zeta_0^d + \sum_{i=1}^{N} A_i u_i = 0 \qquad 5.83.$$

i.e., the volume velocity entering the cavity is equal to the volume velocity leaving the cavity. Assuming that the acoustical impedances of the channel entrances are the same, this simplifies to

$$\zeta_0^d + A_T u_e = 0 \qquad 5.84.$$

where A_T is the total combined area of the exit channels. Note that the acoustical velocity, u_e, in each channel entrance is identical. Inserting equations 5.84 and 5.82 into 5.81, the condition for suppression of the nth mode is expressed as

$$A_T \frac{\zeta_n^d}{\zeta_0^d} - \sum_{i=1}^{N} \Psi_n(\boldsymbol{y}_i) A_i = 0 \qquad 5.85.$$

This can be written in matrix form for the first N modes of the compression cavity

$$\begin{bmatrix} \Psi_0(\boldsymbol{y}_1) & \Psi_0(\boldsymbol{y}_2) & \cdots & \Psi_0(\boldsymbol{y}_N) \\ \Psi_1(\boldsymbol{y}_1) & \Psi_1(\boldsymbol{y}_2) & \cdots & \Psi_1(\boldsymbol{y}_N) \\ \Psi_2(\boldsymbol{y}_1) & \Psi_2(\boldsymbol{y}_2) & \cdots & \Psi_2(\boldsymbol{y}_N) \\ \vdots & \vdots & \ddots & \vdots \\ \Psi_N(\boldsymbol{y}_1) & \Psi_N(\boldsymbol{y}_2) & \cdots & \Psi_N(\boldsymbol{y}_N) \end{bmatrix} \begin{bmatrix} A_1/A_T \\ A_2/A_T \\ \vdots \\ A_N/A_T \end{bmatrix} = \begin{bmatrix} \zeta_0^d/\zeta_0^d \\ \zeta_1^d/\zeta_0^d \\ \zeta_2^d/\zeta_0^d \\ \vdots \\ \zeta_N^d/\zeta_0^d \end{bmatrix} \qquad 5.86.$$

The values of $\boldsymbol{y}_i$ are set such that the bottom row of this matrix expression is trivial, one suitable condition to achieve this is

$$\Psi_N(\boldsymbol{y}_i) = \frac{\zeta_N^d}{\zeta_0^d} \qquad 5.87.$$

Alternative channel positioning approaches are possible, as was briefly discussed in section 5.2.6 on page 152. Irrespective of the positioning approach, the method is the same. A reduced set of equations defined with a square invertible matrix on the left-hand-side,

$$\begin{bmatrix} \Psi_0(\boldsymbol{y}_1) & \Psi_0(\boldsymbol{y}_2) & \cdots & \Psi_0(\boldsymbol{y}_N) \\ \Psi_1(\boldsymbol{y}_1) & \Psi_1(\boldsymbol{y}_2) & \cdots & \Psi_1(\boldsymbol{y}_N) \\ \Psi_2(\boldsymbol{y}_1) & \Psi_2(\boldsymbol{y}_2) & \cdots & \Psi_2(\boldsymbol{y}_N) \\ \vdots & \vdots & \ddots & \vdots \\ \Psi_{N-1}(\boldsymbol{y}_1) & \Psi_{N-1}(\boldsymbol{y}_2) & \cdots & \Psi_{N-1}(\boldsymbol{y}_N) \end{bmatrix} \begin{bmatrix} A_1/A_T \\ A_2/A_T \\ \vdots \\ A_N/A_T \end{bmatrix} = \begin{bmatrix} \zeta_0^d/\zeta_0^d \\ \zeta_1^d/\zeta_0^d \\ \zeta_2^d/\zeta_0^d \\ \vdots \\ \zeta_{N-1}^d/\zeta_0^d \end{bmatrix} \qquad 5.88.$$

From this expression the area ratios can be found by inversion of the matrix on the left-hand side. Comparison of this matrix expression with the two derived, firstly, for the Smith case (section 4.2.4 equation 4.50) and, secondly, for the spherical cavity representation (section 5.2.5 equation 5.62) clearly reveal that they are both more specific examples of this general approach. The general approach is a useful addition as it is derived independently from the geometry of the compression cavity. In this case no assumptions have been made about the geometry other than there are a number of narrow exit channels from the compression cavity and that the compression cavity a narrow shell of minimal volume. The matrix, $\boldsymbol{\Psi}$, on the left of expression 5.88 is composed of eigenfunction values. These may be determined using an FEM model of the cavity under consideration as described in 5.2.1. The vector, **A**, on the left of the expression is the unknown vector of channel area ratios which must be determined. The vector, ζ_{norm}^d, on the right of the expression contains the modal excitation factors that describe the extent to which the motion of the diaphragm excites each compression-cavity mode. These excitation factors, ζ_n^d defined in equation 5.82 are dependent upon the cavity eigenfunctions and the normal velocity of the diaphragm. So far

only the case when the diaphragm is rigid has been considered. In this situation the diaphragm normal velocity is easy to determine from the geometry of the diaphragm and may be defined in terms of the drive point velocity, U_0. As a general method, it is most straightforward to perform the integral in equation 5.82 numerically using the FEM modelled eigenfunctions.

5.4.1 An applied example of the generalised method

As discussed in section 5.2.5, it is important to keep the compression cavity volume to a minimum in order to both maximise the compression driver bandwidth and, secondly, to ensure that the modal suppression techniques, introduced in the preceding sections, work as well as possible.

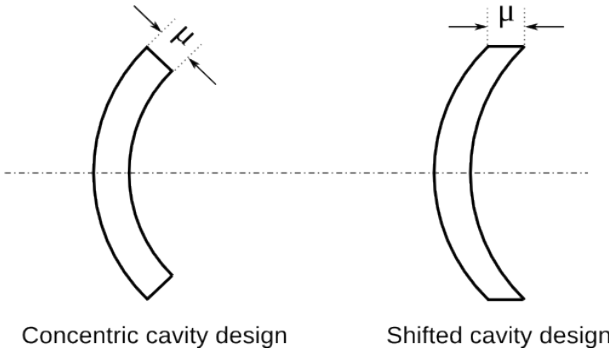

Figure 5.27. Schematic comparison of cavity cross section for concentric cavity design approach and shifted cavity design approach.

The most common geometry for the compression driver diaphragm is a thin foil spherical cap. In previous sections, a compression cavity with a constant thickness driven by this type of diaphragm was considered. Both the diaphragm and the exit side of the cavity are concentric and are easily described in terms of a spherical coordinate system. However, it is common for a slightly different geometry to be used where the exit surface is an axially shifted version of the input surface. This arrangement is preferred as it results in a smaller cavity volume for the same mechanical clearance, μ. The shifted cavity design volume is smaller than the concentric design by $1/\left(1+\tan\left(\phi_0/2\right)\right)$ for the same mechanical clearance. A schematic comparison between the two geometries is shown in figure 5.27.

An important difference between the two cavity designs is that, while the concentric cavity design that was previously considered may be described easily in a spherical coordinate system, the shifted cavity design does not readily fit into a simple coordinate system. Because of this, it is not easily possible to determine an analytical solution to the wave equation in the cavity. For this case, it is more straightforward to numerically apply the

generalised approach introduced above. This is achieved by firstly using a FEM model to determine the cavity eigenfrequencies and eigenfunctions. From this FEM model the coefficients of the matrix $\boldsymbol{\Psi}$ and vector ζ^d_{norm} in equation 5.88 are determined. In order to calculate the ζ^d_n coefficients, as defined in equation 5.82, a numerical integration is performed over the radiating diaphragm surface. This capability was implemented as a small extension to a Matlab-based FEM post-processing programme named Projector that has been developed by the author for other uses. For simplicity and generalisation, the process developed using Projector takes the diaphragm motion from a second FEM model. The steps to determine the channel geometry are as follows, firstly this secondary FEM model is loaded in Projector and a small routine is run that:

1. identifies solid element faces and nodes that are coupled to fluid element faces and nodes (denoted the set M);
2. calculates the surface-normal direction for each node identified ($\boldsymbol{n}_m$);
3. calculates the area of each structure-fluid coupling face and from this an effective area for each node in the identified set (a_m);
4. stores this information along with the FEM calculated nodal displacement ($\boldsymbol{x}_m$).

The modal analysis model, holding the calculated eigenfunctions and eigenfrequencies, is loaded in Projector at this stage. It is necessary for this mesh to have the same node locations as the model outlining the the diaphragm motion along the fluid-structure interface. Using the stored data, the ζ^d_n coefficients are approximately calculated using the summation

$$\zeta^d_n \approx \sum_{m \in M} \tilde{\Psi}_{n,m} a_m \boldsymbol{n}_m . \boldsymbol{x}_m \qquad 5.89.$$

where $\tilde{\Psi}_{n,m}$ is the value of the FEM calculated nth eigenfunction at the m-th node. Provided the FEM mesh is sufficiently fine, this expression converges with the integral in equation 5.82 for low values of n.

The channel positions are set by manually finding the nodal positions on the exit side of the compression cavity of the calculated Nth eigenfunction. Once the positions are set the matrix Ψ is formed using the FEM calculated eigenfunction values.

As a test of this implemented method, a FEM model of a compression cavity with a spherical cap geometry of a concentric type design was made and solved using PAFEC-FE. Additionally, a second model outlining a rigidly moving diaphragm occupying one face of the compression cavity was made and solved, again using PAFEC-FE. Geometric parameters

of $\mu=0.3\text{mm}$, $a=40\text{mm}$ and $\phi_0=55$ were used making this compression-cavity geometry directly comparable to that considered in section 5.2.5. The two FEM models were used, along with the tools developed for the Projector post-processing software, to calculate the values of ζ_n^d corresponding to this cavity and diaphragm arrangement. Table 5.8 shows a comparison of the two sets of derived values.

Analytical Values	Numerically Calculated Values	Analytical/Numerical Ratio
$\zeta_0^d/\zeta_0^d=1$	$\zeta_0^d/\zeta_0^d=1$	1.000000
$\zeta_1^d/\zeta_0^d=0.356271$	$\zeta_1^d/\zeta_0^d=0.354678$	1.004491
$\zeta_2^d/\zeta_0^d=-0.129868$	$\zeta_2^d/\zeta_0^d=-0.127144$	1.021425
$\zeta_3^d/\zeta_0^d=0.0727257$	$\zeta_3^d/\zeta_0^d=0.0735582$	0.988682

Table 5.8: Comparison of ζ_n^d/ζ_0^d calculated analytically in section 5.2.5 with values of calculated numerically using the method described above.

The third column of the table shows the ratio difference between the two methods, the agreement is good between the two methods. The channel areas calculated with the generalised method are given in table 5.9, the agreement with the analytical method is again very good.

	Analytical Values	Numerically Calculated Values	Analytical/Numerical Ratio
A_1/A_T	0.189356	0.188061	1.006886
A_2/A_T	0.381768	0.382330	0.998530
A_3/A_T	0.428875	0.429609	0.998291

Table 5.9: Comparison of the channel areas calculated analytically in section 5.2.5 with those calculated using the generalised method described above.

With some confidence in the approach, the case of the compression cavity with shifted geometry, as described on page 165, is considered. The approach is the same, two FEM models are created one to describe the diaphragm excitation the other in order to calculate the eigenfrequencies and eigenfunctions. Geometric parameters of $\mu=0.3\text{mm}$, $a=40\text{mm}$ and $\phi_0=55$ are again used. The calculated values of ζ_n^d for the shifted cavity design are shown in table 5.10 alongside those for the concentric cavity found above.

Concentric Cavity	Shifted Cavity
$\zeta_0^d/\zeta_0^d=1$	$\zeta_0^d/\zeta_0^d=1$
$\zeta_1^d/\zeta_0^d=0.354678$	$\zeta_1^d/\zeta_0^d=0.012463$
$\zeta_2^d/\zeta_0^d=-0.127144$	$\zeta_2^d/\zeta_0^d=0.013385$
$\zeta_3^d/\zeta_0^d=0.0735582$	$\zeta_3^d/\zeta_0^d=-0.015633$

Table 5.10: Comparison of values of ζ_n^d/ζ_0^d calculated numerically for a concentric compression cavity geometry and a shifted compression cavity geometry.

The channel area ratios calculated using the generalised method for the shifted cavity geometry are shown in table 5.11.

	Concentric Cavity	Shifted Cavity
A_1/A_T	0.189356	0.186524
A_2/A_T	0.381768	0.397768
A_3/A_T	0.428875	0.415707

Table 5.11: Comparison of the channel areas calculated numerically using the generalised method for the case of the concentric compression cavity and the shifted compression cavity.

There is a large difference between the two cavity geometries in the calculated values of ζ_n^d/ζ_0^d. For the shifted cavity design all are much lower except $n=0$ which is remains unity. However there is only a small difference in the computed values of the channel areas. The lower values of ζ_n^d/ζ_0^d implies that the excitation of the compression cavity modes other than $n=0$ is much lower for the shifted cavity than the concentric cavity. This should result in an improved cavity mode suppression performance compared to the concentric design because it is less necessary for the channel entrance velocities to compensate for the diaphragm velocity modal excitation. Consequently the problems associated with the compliance of the cavity, discussed on page 144, are greatly alleviated.

A simple FEM model was constructed to assess the performance of the generalised method for the shifted compression cavity case. The model is directly comparable to that used in section 5.2.5 and illustrated in figure 5.17. The channel geometry given in tables 5.11 and 5.10, above, was used with a compression ratio of 15 for the construction of the model. The other geometric parameters are the same as was used in the channel geometry derivation, $\mu=0.3\text{mm}$, $a=40\text{mm}$ and $\phi_0=55$.

Figure 5.28 shows the computed channel pressures for the shifted cavity case. The pressures are normalised by the specific acoustical impedance of a plane wave. Thus, at low frequencies, they have a value of 23.5dB corresponding to the compression ratio of 15. This result may be directly compared with figure 5.18 and 4.15 which show equivalent results for

the channel geometry derived analytically for the concentric spherical-cap cavity and the smith flat-disc cavity respectively. The three pressure responses are all very similar indeed, the result is much closer to the Smith disc case. As anticipated there is a distinct improvement compared to the concentric cavity design.

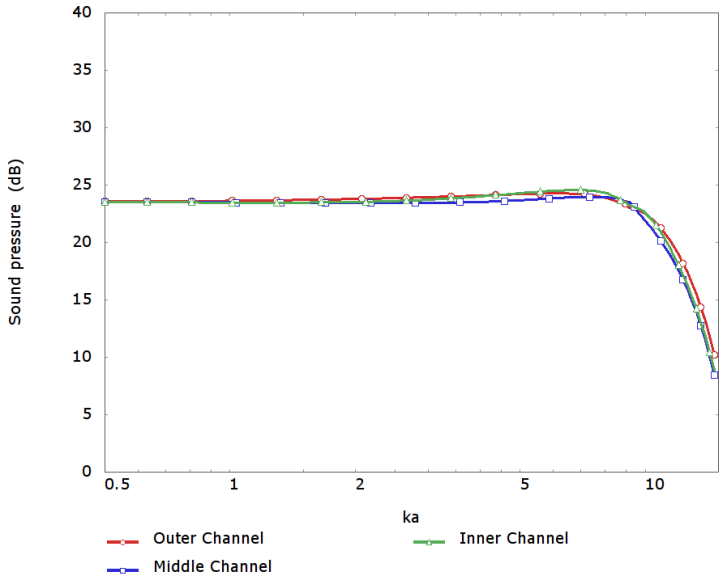

Figure 5.28. Normalised cavity-pressure level response for simple compression driver arrangement having a domed radiating diaphragm and a "shifted" compression cavity geometry using the generalised channel geometry design methodology.

This improvement is a result of the fact that, other than the zeroth mode, the diaphragm excites the compression cavity modes very little. The suppression condition can be more easily realised as it does not rely on the cavity width being vanishingly small. This is the same physical situation that was seen in the Smith channel-geometry derivation where the diaphragm excitation was only of the zeroth mode. The vector on the right-hand side of equation 4.48 is comparable to the vector ζ^d_{norm} in equation 5.88. It may be seen that there is only one non-zero entry in this vector, that which is equivalent to the ζ^d_0 term.

From the result outlined above, it is clear that in order for the compression-cavity modal-suppression techniques to work to their full potential it is very important that the shape of the compression cavity is carefully designed in order to minimise the values of ζ^d_n for $n > 0$. This is an exciting development. Initially, it was believed that the Smith result could not be replicated with a realistic diaphragm and compression-cavity geometry and that modal control to the extent shown in figure 5.18 was limit of what could be practically achieved. The results using the shifted compression cavity design have revealed that this is not the case

and that by control of the ζ_n^d parameters it appears that results approaching the performance of the ideal Smith case are achievable in practice. The following chapter discusses the reason that the combination of shifted cavity geometry and rigid axially moving dome result in low values of ζ_n^d for $n > 0$ and outlines a cavity design criterion by which this may be achieved for other diaphragm shapes.

5.5 Conclusions

In this chapter a more general approach to the positioning and sizing of the annular channels of compression driver phase-plug was outlined which builds upon the work of Smith. This allows the calculation of optimal channel geometries for arbitrary rigid diaphragm and compression cavity geometry, provided the geometry is axisymmetric and that the compression cavity closely follows the diaphragm surface. This is a useful extension upon the Smith method as the vast majority of real drivers are significantly different from the simple planar geometry used by Smith. It has been demonstrated that, for the case of the $45°$ spherical cap cavity, the new method results in improved performance. However, the method does not account for non-rigidly of the radiating diaphragm. Non-rigidity results in a reduction in the modal suppression performance. Clearly further work is required to tackle this problem. Additionally there is some variation in the resulting performance of different cavity and diaphragm geometries, this effect is considered in more detail in the next chapter.

6 Improved compression-driver modal suppression by cavity shaping

6.1 Introduction

In the previous chapter, the parameter ζ_n^d was introduced as a measure of the modal excitation by the compression driver radiating diaphragm. It is defined by the integral expression

$$\zeta_n^d = \int_{S_d} \Psi_n(\boldsymbol{y}) u_d(\boldsymbol{y}).\boldsymbol{n}\, dS \tag{6.1.}$$

It was also demonstrated that if the values of ζ_n^d/ζ_0^d are zero for all except the rigid body mode, i.e. ,

$$\int_{S_d} \Psi_n(\boldsymbol{y}) u_d(\boldsymbol{y}).\boldsymbol{n}\, dS = \delta_{0n} \tag{6.2.}$$

where δ_{nm} is the Kronecker delta function. Then optimal suppression of the cavity modes in the driven compression driver is achievable. It is relatively straightforward to outline guidelines for the compression cavity geometry in order to achieve this goal for a particular driving diaphragm by using the orthogonality of the compression-cavity modes. The compression-cavity modes form an orthonormal set, they obey the orthogonality relationship

$$\int_V \Psi_n(\boldsymbol{y}) \Psi_m(\boldsymbol{y})\, dV = V \delta_{nm} \tag{6.3.}$$

For maximum bandwidth of operation, it is necessary for the compression cavity volume to be kept to a minimum and, consequently, commonly the cavity follows the geometry of the radiating diaphragm closely and is a thin shell. In this case, it is useful to separate the volume integral into two as

$$\int_{S_d} \int_h \Psi_n(\boldsymbol{y}) \Psi_m(\boldsymbol{y})\, dh\, dS = V \delta_{nm} \tag{6.4.}$$

where the first integral is over the surface of the radiating diaphragm and the second is in the perpendicular direction through the cavity thickness at each point on the diaphragm. h is a geometric coordinate defining the position through the thickness of the cavity. Provided that the compression cavity is small in h, the cavity eigenfunctions $\Psi_n(\boldsymbol{y})$ are very nearly invariant to h and it is possible to make the approximation

$$\int_{S_d} \Psi_n(\boldsymbol{y}) \Psi_m(\boldsymbol{y}) \mu(\boldsymbol{y})\, dS \approx V \delta_{nm} \tag{6.5.}$$

where $\mu(\boldsymbol{y})$ is a function that describes the thickness of the cavity in a direction perpendicular to the diaphragm surface at the location $\boldsymbol{y}$. Setting $m=0$, recalling $\Psi_0(\boldsymbol{y})=1$, dividing both sides by V results in the expression

$$\int_{S_d} \Psi_n(\boldsymbol{y}) \frac{\mu(\boldsymbol{y})}{V} dS \approx \delta_{0n} \tag{6.6.}$$

Comparison of this with expression 6.2 shows that, in order for $\zeta_n^d/\zeta_0^d=\delta_{0n}$, then the cavity normal thickness function should be

$$\mu(\boldsymbol{y}) \propto u_d(\boldsymbol{y}).\boldsymbol{n} \tag{6.7.}$$

In other words, the thickness in the cavity-normal direction should be proportional to the normal velocity of the radiating diaphragm.

It is now clear exactly why the shifted cavity design considered in section 5.4.1 nearly had ideal values of ζ_n^d: the compression cavity geometry very nearly meets the criterion set in equation 6.7. The only reason that the condition is not perfectly met is that there is a very slight error at the outside diameter of the cavity when constructed by shifting the diaphragm in the axial direction.

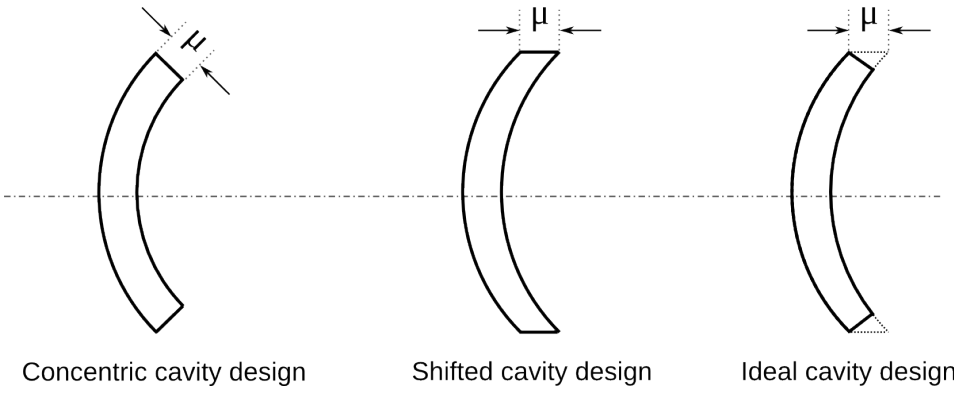

Figure 6.1. Illustration of cavity edge difference in section of i) concentric cavity design ii) shifted cavity design and iii) cavity design with cavity shaping method.

To demonstrate this, the FEM model used to numerically determine the values of ζ_n^d for the shifted cavity geometry, given in table 5.10, was adjusted at the outside diameter and re-solved. The calculated values of ζ_n^d, using the method described in section 5.4.1, for the new shaped cavity geometry are shown in table 6.1. It can be observed that this slight modification has resulted in values of ζ_n^d, which are indeed closer to the target of $\zeta_n^d/\zeta_0^d=\delta_{0n}$. The values of ζ_n^d/ζ_0^d for $n=1,2$ and 3 are very small and likely to be lower than the accuracy of the approximate integral used in their calculation, see section 5.4.1.

Shifted Cavity	Shaped Cavity
$\zeta_0^d/\zeta_0^d=1$	$\zeta_0^d/\zeta_0^d=1$
$\zeta_1^d/\zeta_0^d=0.012463$	$\zeta_1^d/\zeta_0^d=-0.002008$
$\zeta_2^d/\zeta_0^d=0.013385$	$\zeta_2^d/\zeta_0^d=0.000410$
$\zeta_3^d/\zeta_0^d=-0.015633$	$\zeta_3^d/\zeta_0^d=0.000404$

Table 6.1: Comparison of values of ζ_n^d/ζ_0^d calculated numerically for a shifted compression-cavity geometry and a shaped compression-cavity geometry as outlined above.

For completeness, the generalised channel-positioning method described in section 5.4 was used to determine the positions and areas of a three-channel phase plug for the new shaped cavity. A simple FEM model was constructed to assess the performance of the modal suppression. The resulting channel pressures are shown in figure 6.2. This is comparable to the result shown in figure 5.28 that provides the identical result for the shifted compression-cavity design. It is observed that there is a very slight improvement in the similarity of the pressures in each channel, as is anticipated by the slightly closer to ideal values of ζ_n^d/ζ_0^d.

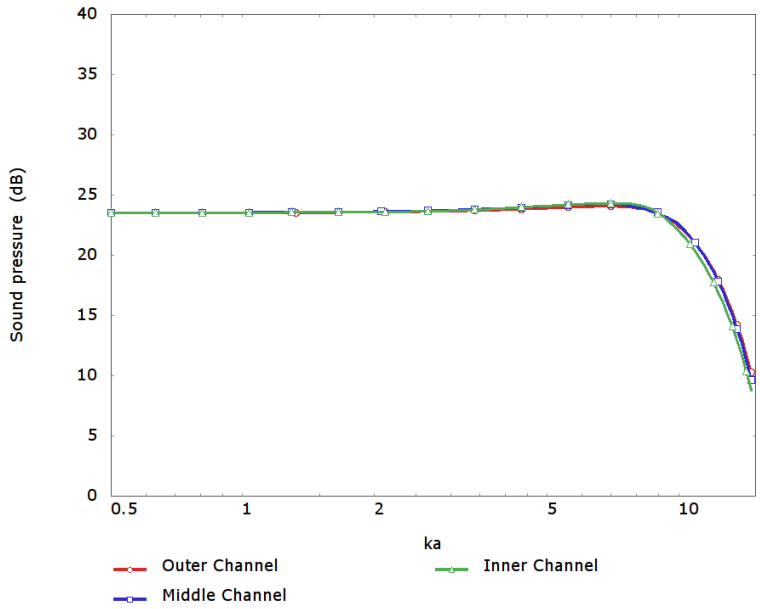

Figure 6.2. Normalised cavity-pressure level response for a simple compression-driver arrangement having a domed radiating-diaphragm and a "shaped" compression-cavity geometry using the generalised channel-geometry design methodology.

6.2 Practical considerations

In a practical design, there are additional constraints on the shape of the compression cavity arising because of the construction and assembly of the driver and/or due to the presence of

other supporting components such as the surround and voice coil gap. The ideal cavity shape introduced above is designed to meet the condition

$$\frac{\zeta_n^d}{\zeta_0^d} = \delta_{0n} \tag{6.8.}$$

To make this condition less restrictive, so that there is the possibility of approximately suppressing modal excitation from the diaphragm motion while still remaining within any practical constraints that might exist for a particular driver, the condition is only set for the first few cavity modes. This can be expressed as

$$\zeta_n^d = 0 \Big|_{(n>0)\wedge(n\leq N_c)} \tag{6.9.}$$

Provided that the eigenfrequency corresponding to N_c is above the operational bandwidth of the compression driver, it is anticipated that within the bandwidth of operation a similar improvement in the modal suppression will be seen.

In order to meet the condition in expression 6.9, the cavity shape must be adjusted to affect the eigenfunctions, $\Psi_n(\boldsymbol{y})$. It is assumed that the cavity entrance-surface S_e, which is either completely or partially occupied by the radiating diaphragm, is known and fixed. The radiating diaphragm does not occupy any other face of the cavity. The eigenfunctions may be altered by adjusting the thickness profile of the cavity, $\mu(\boldsymbol{y})$, to try to meet the condition for modal suppression, 6.9.

6.2.1 Calculation of the cavity eigenfunctions using a prototype cavity

To optimise the cavity thickness function $\mu(\boldsymbol{y})$, it is necessary to quickly and efficiently determine the eigenfunctions. In this section, it is demonstrated that the eigenfunctions of a thin compression cavity may be described using a prototype cavity. The prototype cavity is simply a narrow cavity that shares the same entrance geometry as the cavity for which the eigenfunctions and eigenfrequencies are being calculated (the subject cavity). It is approximated that the eigenfunctions of the prototype and subject cavity are only a function of the position on the entrance surface and that the eigenfunctions do not vary through the thickness of the compression cavity. For this approximation to be accurate, both the prototype and the subject cavity must be thin in the direction h. Geometrically, as the prototype and subject cavity share the same entrance surface, the two cavities only differ in their cavity thickness function, $\mu(\boldsymbol{y})$.

The prototype-cavity eigenfunctions have the orthogonality condition

$$\int_{V_p} \overset{p}{\Psi}_n(\boldsymbol{y})\,\overset{p}{\Psi}_m(\boldsymbol{y})\,dV = V_p\,\delta_{nm} \tag{6.10.}$$

where $\overset{p}{\Psi}_n(\boldsymbol{y})$ is the n-th eigenfunction of the prototype cavity at position $\boldsymbol{y}$. As the cavity is narrow in a direction perpendicular to the fixed entrance surface, this integral may be approximated as an integral over the entrance surface of the cavity, S_e,

$$\int_{S_e} \overset{p}{\Psi}_n(\boldsymbol{y})\,\overset{p}{\Psi}_m(\boldsymbol{y})\,\mu_p(\boldsymbol{y})\,dS_e \approx V_p\,\delta_{nm} \tag{6.11.}$$

The function $\mu_p(\boldsymbol{y})$ describes the thickness of the prototype cavity in the direction normal to the entrance surface as a function of position on the entrance surface $\boldsymbol{y}$. The eigenfunctions and eigenfrequencies of the prototype cavity are known, either by analytical or FEM calculation.

Using a Rayleigh-Ritz approach, as was outlined in section 3.6, the velocity potential in the subject cavity, $\phi(\boldsymbol{y})$, is described by the linear sum of a number of the pressure modes of the prototype cavity, $\overset{p}{\Psi}_n(\boldsymbol{y})$, such that

$$\phi(\boldsymbol{y}) = \sum_{i=0}^{N_\phi - 1} \overset{p}{\Psi}_i(\boldsymbol{y})\,\phi_i \tag{6.12.}$$

where ϕ_i are coefficients that indicate the proportions of each of the prototype cavity eigenfunctions. This can also be written as the multiplication of two vectors

$$\phi(\boldsymbol{y}) = \boldsymbol{\psi}_p(\boldsymbol{y})^T\boldsymbol{\phi} = \begin{bmatrix} \overset{p}{\Psi}_0(\boldsymbol{y}) & \overset{p}{\Psi}_1(\boldsymbol{y}) & \dots & \overset{p}{\Psi}_{N_\phi-1}(\boldsymbol{y}) \end{bmatrix} \begin{bmatrix} \phi_0 \\ \phi_1 \\ \vdots \\ \phi_{N_\phi-1} \end{bmatrix} \tag{6.13.}$$

The kinetic and potential energy densities for small-amplitude oscillations in fluids are given by the two expressions

$$\frac{T}{dV} = \frac{1}{2}\rho_0|u|^2 \qquad \text{and} \qquad \frac{U}{dV} = \frac{1}{2}\frac{1}{\rho_0 c_0^2}p^2 \tag{6.14.}$$

The system kinetic and potential energy can be found by integrating these densities over the volume of the cavity, resulting in the expressions

$$T = \frac{\rho_0}{2}\int_V |u(\boldsymbol{y})|^2\,dV \tag{6.15.}$$

and

$$U = \frac{1}{2\rho_0 c_0^2} \int_V p^2(\boldsymbol{y}) dV \tag{6.16.}$$

In terms of the velocity potential, these energies are

$$T = \frac{\rho_0}{2} \int_V \nabla^2 \phi(\boldsymbol{y}) dV \tag{6.17.}$$

and

$$U = \frac{\rho_0}{2c_0^2} \int_V \frac{\partial^2 \phi(\boldsymbol{y})}{\partial t^2} dV \tag{6.18.}$$

In terms of the matrix notation for $\phi(\boldsymbol{y})$ these energies can be written as

$$T = \frac{1}{2}\rho_0 \boldsymbol{\phi}^T \boldsymbol{H}\ \boldsymbol{\phi} \tag{6.19.}$$

and

$$U = \frac{1}{2}\rho_0 \dot{\boldsymbol{\phi}}^T \boldsymbol{Q}\ \dot{\boldsymbol{\phi}} \tag{6.20.}$$

where the elemental components of $\boldsymbol{H}$ and $\boldsymbol{Q}$ are

$$H_{i,j} = \int_V \nabla \overset{p}{\Psi}_{i-1}(\boldsymbol{y}) . \nabla \overset{p}{\Psi}_{j-1}(\boldsymbol{y}) dV \tag{6.21.}$$

and

$$Q_{i,j} = \frac{1}{c_0^2} \int_V \overset{p}{\Psi}_{i-1}(\boldsymbol{y}) \overset{p}{\Psi}_{j-1}(\boldsymbol{y}) dV \tag{6.22.}$$

Given the narrow compression-cavity geometry, these two volume integrals may be approximated using an integral over the cavity entrance surface.

$$H_{i,j} \approx \int_{S_e} \nabla \overset{p}{\Psi}_{i-1}(\boldsymbol{y}) . \nabla \overset{p}{\Psi}_{j-1}(\boldsymbol{y}) \mu(\boldsymbol{y}) dS_e \tag{6.23.}$$

and

$$Q_{i,j} \approx \frac{1}{c_0^2} \int_{S_e} \overset{p}{\Psi}_{i-1}(\boldsymbol{y}) \overset{p}{\Psi}_{j-1}(\boldsymbol{y}) \mu(\boldsymbol{y}) dS_e \tag{6.24.}$$

As is described in section 3.6, the $\boldsymbol{H}$ and $\boldsymbol{Q}$ matrices may be used to calculate the pressure eigenfrequencies and eigenfunctions of the subject cavity. This allows the eigenfunctions of the subject cavity to be calculated quickly from the prototype eigenfunctions and the cavity thickness function.

Example 1

To test this method of eigenfunction calculation, two FEM models were created (the meshed geometries are shown in figure 6.3). The first model is of a constant 0.5mm thickness disc cavity that serves as the prototype in this case. The second model has the same entrance (left) surface as the prototype cavity, but has a thickness defined by the function

$$\mu(r)=0.5\left(2-\frac{r}{a}\right) \qquad 6.25.$$

where a is the radius of the disc cavity, equal to 40mm. Both cavities are meshed with axisymmetric finite elements and PAFEC was used to calculate the first ten eigenfunctions and eigenfrequencies in each case.

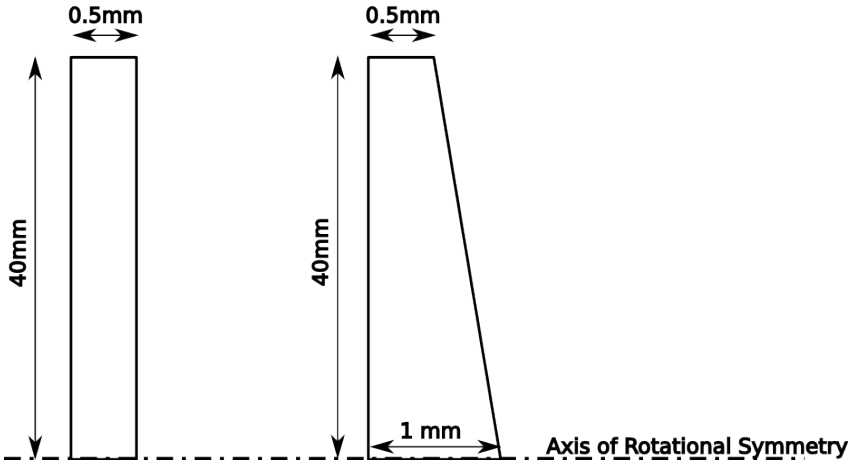

Figure 6.3. Illustration of the prototype cavity (left) and the subject cavity (right),the geometry is exaggerated for clarity. Both models are axisymmetric.

Using the eigenfunctions of the prototype cavity, along with the thickness profile for the subject cavity, the matrices $\boldsymbol{H}$ and $\boldsymbol{Q}$ were formed using the integrals given in expressions 6.23 and 6.24. The differential $\partial \overset{p}{\Psi}_m(r)/\partial r$ was computed numerically using the Matlab function “gradient” [54], which uses a three point difference calculation [47, p. 505]. The integrals in expressions 6.23 and 6.24 were computed numerically using the trapezium method [47, p.568]. The matrices were formed using the full ten computed eigenfunctions of the prototype cavity.

Prototype Cavity (FEM)	Subject Cavity (FEM)	Subject Cavity RR method	Subject cavity RR deviation from FEM
0.01 Hz	0.01 Hz	0.00 Hz	
5229.34 Hz	5172.30 Hz	5172.29 Hz	-0.0003%
9574.61 Hz	9529.85 Hz	9528.70 Hz	-0.012%
13884.47 Hz	13847.45 Hz	13842.97 Hz	-0.032%
18184.01 Hz	18152.19 Hz	18141.09 Hz	-0.061%
22479.27 Hz	22451.18 Hz	22429.10 Hz	-0.098%
26772.52 Hz	26747.24 Hz	26708.54 Hz	-0.145%
31064.92 Hz	31041.83 Hz	30980.14 Hz	-0.199%
35357.24 Hz	35335.91 Hz	35242.87 Hz	-0.263%
39650.17 Hz	39630.27 Hz	39512.26 Hz	-0.298%

Table 6.2: Comparison of the first ten eigenfrequencies for the FEM model of the prototype cavity, the FEM model of the profiled cavity and the Rayleigh-Ritz approximation to the profiled cavity.

The calculated eigenfrequencies for the FEM model of the prototype cavity, the FEM model of the subject cavity and the Rayleigh-Ritz approximation of the subject cavity using the FEM eigenfunctions of the prototype cavity are given in table 6.2. The Rayleigh-Ritz (RR) approximation using the prototype cavity eigenfunctions is a very good match with the FEM calculated results for all eigenfrequencies. However, it should be noted that, particularly for the high eigenfrequencies, the values are very similar for both cavity geometries. For the purposes of modal suppression, the predicted eigenfunctions are of more relevance as these appear directly in the modal suppression condition. The first six eigenfunctions for all three cavity models are shown in figure 6.4. It may be observed from these charts that the mode shapes in both cavities are similar in overall shape but have distinct differences in the detailed shape. For example, note that the anti-node magnitudes and the nodal positions are different. The RR approximation to the subject cavity performs extremely well providing a very good match with the FEM model of the subject cavity.

Example 2

As a second test of the method a more complex geometry was chosen with a more typical geometry for the compression cavity prototype. Figure 6.5 shows both the prototype cavity, with a constant thickness, and a subject cavity, which shares the same entrance surface geometry. The entrance surface of both cavities consists of a region that has a spherical-cap geometry connected to a cylindrical region at the outside diameter.

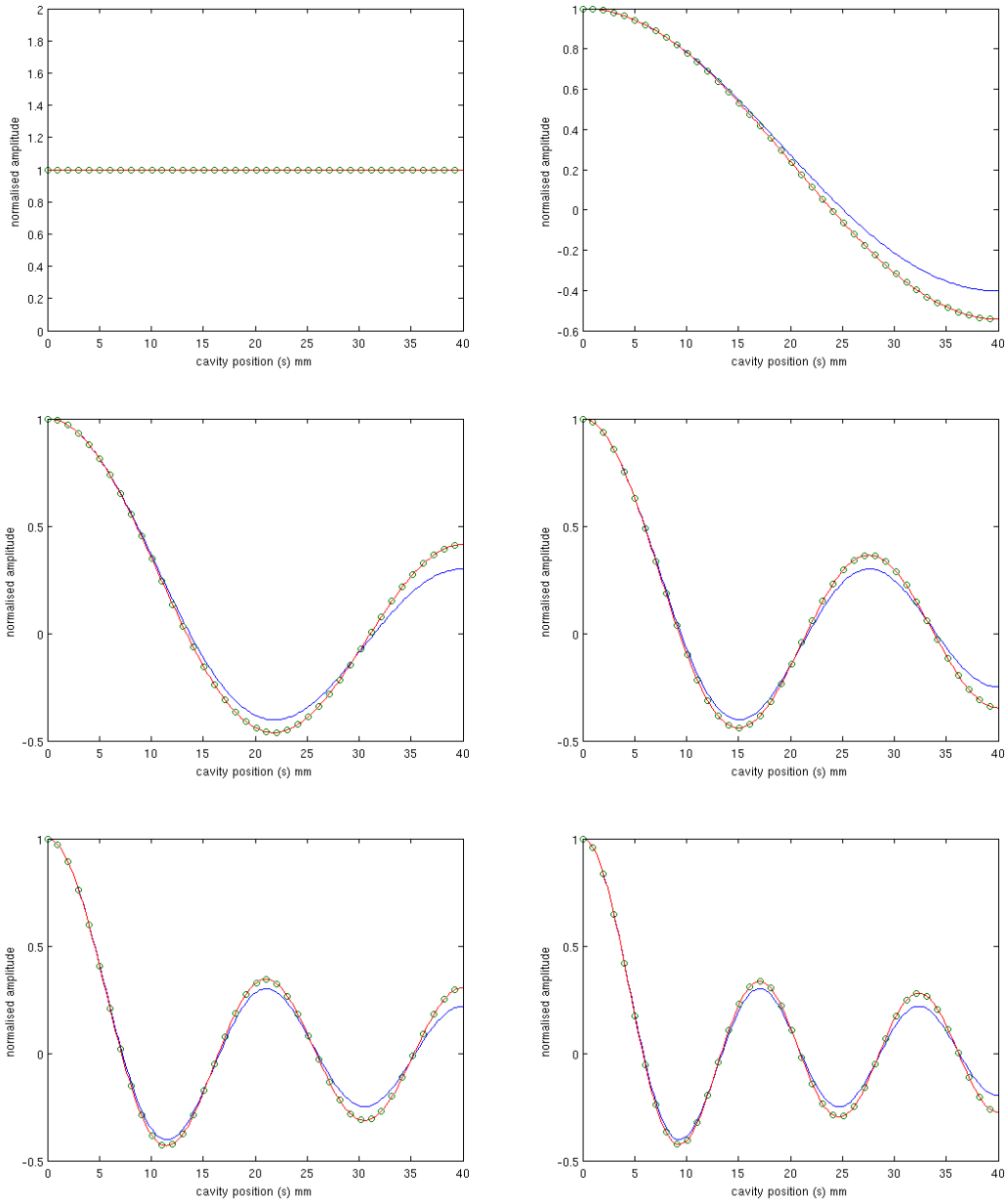

Figure 6.4. Comparison of the first six eigenfunctions for the FEM model of the prototype cavity (blue), the FEM model of the subject cavity (red) and the Rayleigh-Ritz approximation to the subject cavity from the eigenfunctions of the prototype cavity (green circles).

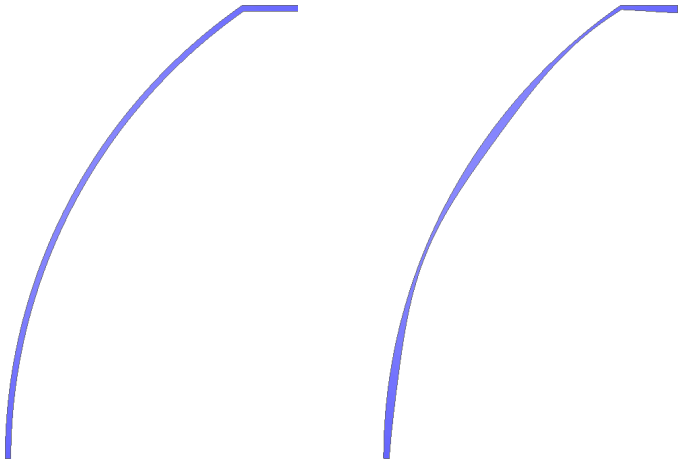

Figure 6.5. FEM mesh of prototype curved cavity (left) and subject curved cavity (right). Both models are axisymmetric, the axis of rotation is located at the bottom of the meshes in both instances.

The eigenfunctions of the subject cavity are approximated using the eigenfunctions of the prototype cavity, as outlined described above. These approximate eigenfunctions may be compared to the direct FEM model of the subject cavity. The thickness of the subject cavity is given by the expression

$$\mu(s)=0.5+0.25\sin\left(4\pi\frac{s}{s_e}\right) \tag{6.26.}$$

where s is a linear coordinate that is measured from the axis of rotation along the entrance surface profile. s_e is the value of the coordinate s at the intersection of the cylindrical and spherical cap regions. The matrices $\boldsymbol{H}$ and $\boldsymbol{Q}$ are formed using the integrals in s

$$H_{i,j}\approx 2\pi\int_{s=0}^{s_a}\frac{\partial\overset{p}{\Psi}_{i-1}(s)}{\partial s}\frac{\partial\overset{p}{\Psi}_{j-1}(s)}{\partial s}r(s)\mu(s)ds \tag{6.27.}$$

and

$$Q_{i,j}\approx\frac{2\pi}{c_0^2}\int_{s=0}^{s_a}\overset{p}{\Psi}_{i-1}(s)\overset{p}{\Psi}_{j-1}(s)r(s)\mu(s)ds \tag{6.28.}$$

where s_a is the value of the coordinate s at the extremity of the entrance surface.

Both cavities are analysed using FEM in order to determine the eigenfrequencies and eigenfunctions. Following this the subject cavity eigenfrequencies and eigenfunctions are approximated using the Rayleigh-Ritz-based approach using the first 10 eigenfunctions from the prototype cavity. This approximation can be compared to the FEM results for the subject compression cavity. Table 6.3 shows the eigenfrequencies and eigenfunctions for each of these solutions. The accuracy of the Rayleigh-Ritz approximation of the subject cavity is

reasonably good, although they appear a little less accurate than the simple cavity examined in example 1.

Prototype Cavity (FEM)	Subject Cavity (FEM)	Subject Cavity RR method	Subject cavity RR deviation from FEM
-0.02 Hz	-0.02 Hz	0.00 Hz	
4078.67 Hz	3865.97 Hz	3842.08 Hz	-0.618%
7462.71 Hz	5899.66 Hz	5859.35 Hz	-0.683%
10817.87 Hz	11239.39 Hz	11185.68 Hz	-0.478%
14162.02 Hz	14465.08 Hz	14388.36 Hz	-0.530%
17498.77 Hz	17790.24 Hz	17746.40 Hz	-0.246%
20829.57 Hz	21184.00 Hz	21129.44 Hz	-0.258%
24156.02 Hz	24344.56 Hz	24312.50 Hz	-0.132%
27480.52 Hz	27635.33 Hz	27563.64 Hz	-0.259%
30806.08 Hz	30963.63 Hz	30871.58 Hz	-0.297%

Table 6.3: Comparison of the first ten eigenfrequencies for the FEM model of the prototype cavity, the FEM model of the subject cavity and the Rayleigh-Ritz approximation to the subject cavity.

The FEM and Rayleigh-Ritz-based approximations of the cavity eigenfunctions are plotted in figure 6.6. As a result of the undulating cavity thickness, the eigenfunctions of the subject cavity have a slightly peculiar shape. The Rayleigh-Ritz-based approximation is a good match with the FEM model. However, as with the eigenfrequency approximation, it appears that the method is slightly less accurate for the first few modes with this more complex geometry compared to that considered in example 1. There are several possible causes of this slight drop in accuracy. Firstly, the integral over the cavity volume, required by the Rayleigh-Ritz method to determine the system kinetic and potential energies, is approximated with an integral over the entrance surface of the cavity multiplied by the thickness of the cavity. When the cavity is very thin these integrals converge with the required volume integrals. For this particular geometry, where the cavity curvature means that the right-hand surface of the compression cavity is of a smaller area than the left-hand surface, the integral approximations are less accurate than the disc cavity of example 1. Secondly, at the intersection between the spherical cap region and the cylindrical region the cavity-entrance surface is not smooth and it is difficult to determine the surface normal at this point. Consequently, it is also difficult to define the cavity thickness at this point. As a result of this, it is expected that the approximation to the volume integral is relatively poor. However, irrespective of these problems caused by a very challenging geometry, the predicted eigenfrequencies and eigenfunctions using the Rayleigh-Ritz-based method are reasonably accurate.

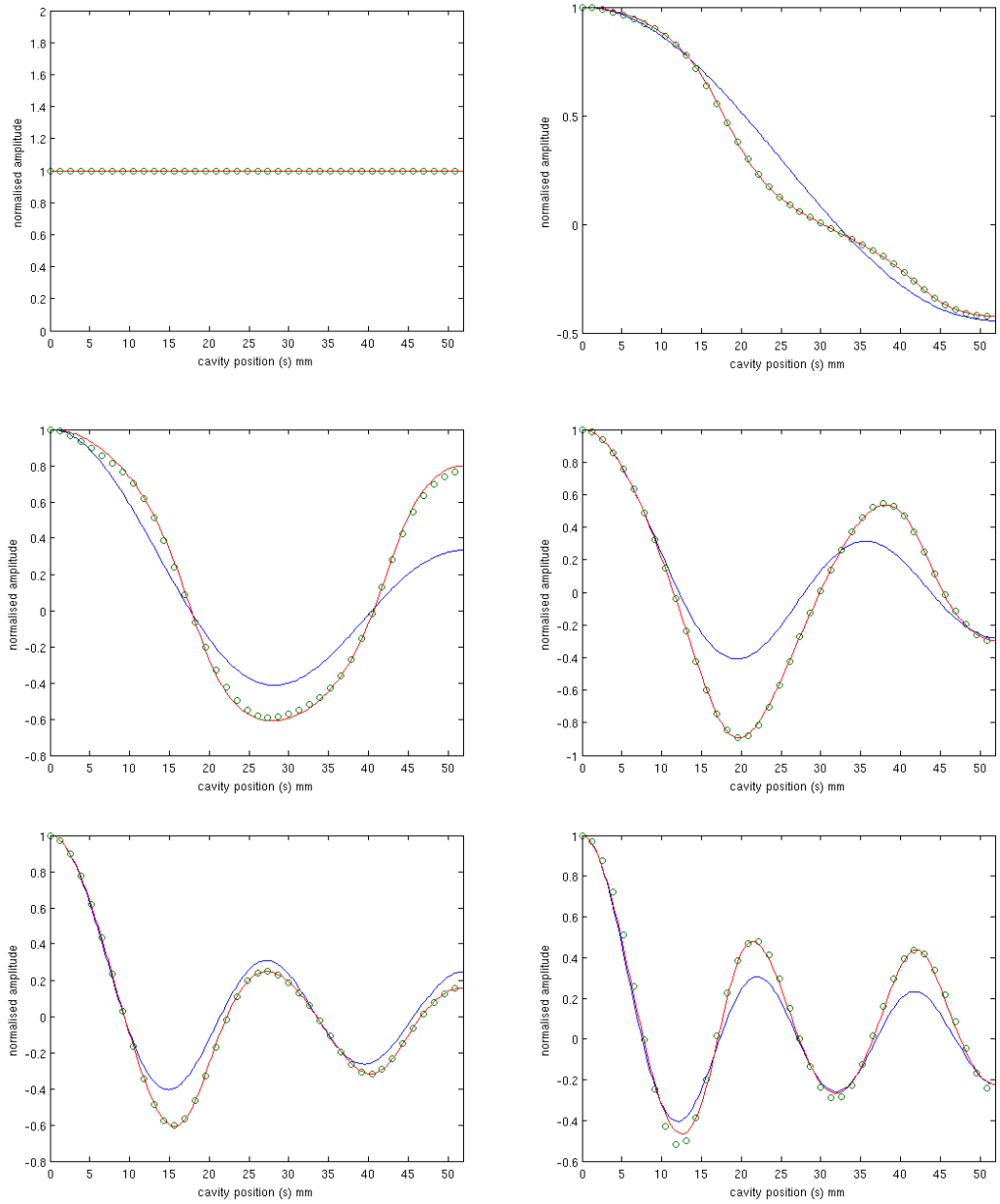

Figure 6.6. Comparison of the first six eigenfunctions for the FEM model of the prototype curved cavity (blue), the FEM model of the subject curved cavity (red) and the Rayleigh-Ritz approximation to the subject cavity from the first ten eigenfunctions of the prototype cavity (green circles).

6.2.2 Calculation of the driven cavity behaviour using a prototype cavity

The matrices $\boldsymbol{H}$ and $\boldsymbol{Q}$, calculated above to derive the eigenfunctions of the subject cavity from the eigenfunctions of the prototype cavity, may also be used to approximate the driven behaviour of the subject cavity by using the expression

$$[\boldsymbol{H}-\omega^2\boldsymbol{Q}]\boldsymbol{p}=j\omega\rho_0\boldsymbol{\zeta}^{dp} \qquad 6.29.$$

The vector $\boldsymbol{p}$ describes the cavity pressure in terms of the Rayleigh-Ritz prescribed functions, which are, in this case, the eigenfunctions of the prototype cavity. The complex pressure amplitude at a position $\boldsymbol{y}$ in the subject cavity is given by $p(\boldsymbol{y})=\psi_p(\boldsymbol{y})^T\boldsymbol{p}$. The vector $\boldsymbol{\zeta}^{dp}$ describes the excitation of the subject cavity due to the motion of the radiating diaphragm in terms of the eigenfunctions of the prototype cavity. The elemental coefficients are defined as

$$\zeta_i^{dp}=\int_{S_d}\overset{p}{\Psi}_{i-1}(\boldsymbol{y})\boldsymbol{u}_d(\boldsymbol{y}).\boldsymbol{n}\,dS \qquad 6.30.$$

For a given diaphragm velocity, it is possible to determine the subject cavity pressure response by inversion of the matrix on the left side of expression 6.29 resulting in

$$\boldsymbol{p}=j\omega\rho_0[\boldsymbol{H}-\omega^2\boldsymbol{Q}]^{-1}\boldsymbol{\zeta}^{dp} \qquad 6.31.$$

Example 1

To test this technique for approximating the driven response, the two cavities introduced in example 2 of section 6.2.1 were modelled directly using the Finite-Element Method (FEM). The driven cavity response to a rigid axially moving radiating diaphragm occupying the entirety of the entrance surface was calculated. These direct cavity-pressure response calculations may then be compared to the driven approximation of the subject compression-cavities using the Rayleigh-Ritz approach described above. For the Rayleigh-Ritz-based calculation, the first ten eigenfunctions of the prototype cavity are used. The pressure response at the outside extremity of the cavity is shown for each of the three cases in figure 6.7. It is obvious from these responses that the driven behaviour of the subject cavity is markedly different from the prototype cavity as a result of the different cavity-thickness profile and the resulting change to the eigenfunctions and eigenfrequencies. The Rayleigh-Ritz approximation of the subject-cavity driven response is a good match for the FEM model. On close inspection, there is a slight deviation in the frequencies of the maxima and minima. This inaccuracy results from the truncation of the Rayleigh-Ritz prescribed-function

set in addition to the simplification of the integrals discussed in the previous section. All three systems have no damping and, consequently, the response maxima and minima are extremely sharp. As a result of this, there is an apparent difference in the height of the peaks comparing the FEM and RR calculations, which is, in fact, due to the finite frequency resolution of the responses and the slight shift in the frequencies of the maxima and minima.

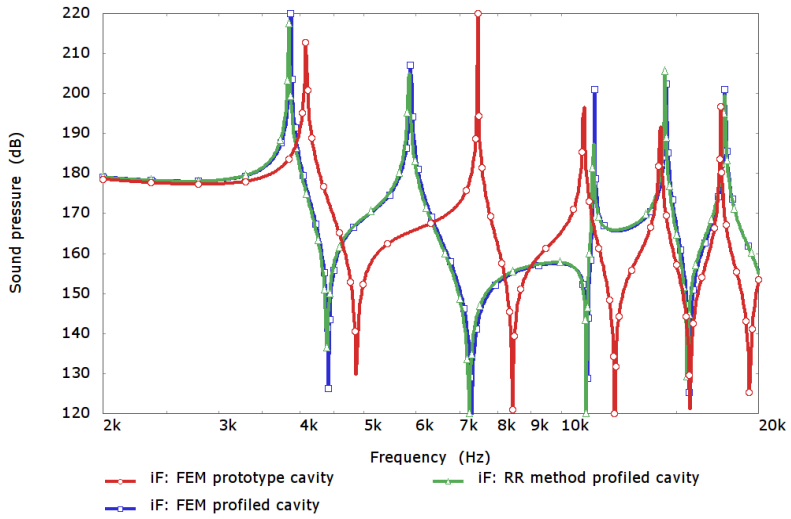

Figure 6.7. Rigid diaphragm driven cavity pressure response at the outside extremity for the prototype cavity FEM calculation (red), the subject cavity FEM calculation (blue) and the Rayleigh-Ritz based approximation to the subject cavity (green).

The accuracy of the Rayleigh-Ritz-based approximation to the subject-cavity response is impressive and is certainly accurate enough that it may be usefully applied to the problem of optimising the cavity thickness profile to minimise the modal excitation.

6.2.3 Suppression of modal excitation using cavity thickness shape functions

As discussed in the previous section, the driven behaviour of the profiled cavity can be approximated using the eigenfunctions of a prototype cavity by the expression

$$[\boldsymbol{H}-\omega^2\boldsymbol{Q}]\boldsymbol{p}=j\omega\rho_0\boldsymbol{\zeta}^{dp} \qquad 6.32.$$

where the vector $\boldsymbol{\zeta}^{dp}$ describes the cavity excitation in terms of the prototype eigenfunctions, with the elemental components given by the expression

$$\zeta_i^{dp}=\int_{S_d}\overset{p}{\Psi}_{i-1}(\boldsymbol{y})\boldsymbol{u}_d(\boldsymbol{y}).\boldsymbol{n}\,dS \qquad 6.33.$$

The function $\mu(\boldsymbol{y})$, which appears in the integrals defining the components of $\boldsymbol{H}$ and $\boldsymbol{Q}$, sets the thickness of the cavity profile. The intention is that this function is adjusted in order to

minimise the diaphragm excitation of the cavity modes. The thickness function is defined to be a linear combination of N_μ candidate functions such that

$$\mu(\boldsymbol{y}) = \sum_{n=1}^{N_\mu} b_n \mu_n(\boldsymbol{y}) \tag{6.34.}$$

where b_n are coefficients which describe the proportions of each candidate thickness function $\mu_n(\boldsymbol{y})$. This expression can also be written as as the multiplication of two vectors as

$$\mu(\boldsymbol{y}) = \boldsymbol{b}^T \boldsymbol{\mu}(\boldsymbol{y}) \tag{6.35.}$$

Using this definition of the thickness function, the matrix $\boldsymbol{H}$ may be expanded as the linear sum of N_μ matrices such that

$$\boldsymbol{H} = \sum_{n=1}^{N_\mu} b_n \boldsymbol{H}_n \tag{6.36.}$$

where the elemental components of $\boldsymbol{H}_n$ are approximated to be

$$H_{n,i,j} \approx \int_{S_e} \nabla \overset{p}{\Psi}_{i-1}(\boldsymbol{y}) . \nabla \overset{p}{\Psi}_{j-1}(\boldsymbol{y}) \mu_n(\boldsymbol{y}) dS_e \tag{6.37.}$$

Similarly, the matrix $\boldsymbol{Q}$ may be written as

$$\boldsymbol{Q} = \sum_{n=1}^{N_\mu} b_n \boldsymbol{Q}_n \tag{6.38.}$$

with the elements of $\boldsymbol{Q}_n$ approximated to be

$$Q_{n,i,j} \approx \frac{1}{c_0^2} \int_{S_e} \overset{p}{\Psi}_{i-1}(\boldsymbol{y}) \overset{p}{\Psi}_{j-1}(\boldsymbol{y}) \mu_n(\boldsymbol{y}) dS_e \tag{6.39.}$$

The driven cavity behaviour, in terms of these expanded $\boldsymbol{H}$ and $\boldsymbol{Q}$ matrices, is

$$\sum_{n=1}^{N_\mu} b_n \boldsymbol{H}_n \boldsymbol{p} - \omega^2 \sum_{n=1}^{N_\mu} b_n \boldsymbol{Q}_n \boldsymbol{p} = j\omega\rho_0 \boldsymbol{\zeta}^{dp} \tag{6.40.}$$

The target behaviour for the cavity is that only rigid-body pressure variation occurs in the bandwidth of the driver. Although the final eigenfunctions are as yet unknown, because the rigid-body eigenfunction is always unity, the target pressure in the resulting cavity can be set in terms of the prototype eigenfunctions to be

$$\boldsymbol{p}^T = \left[\frac{\rho_0 c_0^2 \zeta_0^{dp}}{j\omega V} \quad 0 \quad 0 \quad \dots \quad 0 \right] \tag{6.41.}$$

where V is the desired volume of the resulting compression cavity. Assuming that this target pressure is achieved, the system driven behaviour may be expressed as

$$\sum_{n=1}^{N_\mu} b_n \boldsymbol{h}_n - \omega^2 \sum_{n=1}^{N_\mu} b_n \boldsymbol{q}_n = \frac{-\omega^2 V}{c_0^2} \frac{\boldsymbol{\zeta}^{dp}}{\zeta_0^{dp}} \tag{6.42.}$$

where the vector $\boldsymbol{h}_n$ is the first column of $\boldsymbol{H}_n$ and the vector $\boldsymbol{q}_n$ is the first column of $\boldsymbol{Q}_n$. As a result of the $\nabla \overset{p}{\Psi}_{i-1}(\boldsymbol{y})$ term appearing in expression 6.37, the vector $\boldsymbol{h}_n$ is all-zero. This allows further simplification to

$$\sum_{n=1}^{N_\mu} b_n \boldsymbol{q}_n = \frac{V}{c_0^2} \frac{\boldsymbol{\zeta}^{dp}}{\zeta_0^{dp}} \tag{6.43.}$$

Introducing the matrix

$$\tilde{\boldsymbol{Q}} = \begin{bmatrix} \boldsymbol{q}_1 & \boldsymbol{q}_2 & \cdots & \boldsymbol{q}_{N_\mu} \end{bmatrix} \tag{6.44.}$$

with coefficients approximated from the integral

$$\tilde{Q}_{i,j} \approx \frac{1}{c_0^2} \int_{S_e} \overset{p}{\Psi}_{i-1}(\boldsymbol{y}) \mu_j(\boldsymbol{y}) \, dS_e \tag{6.45.}$$

and recalling the definition of $\boldsymbol{b}$, given in expression 6.35, the profiled cavity is described by the matrix equation

$$\tilde{\boldsymbol{Q}} \boldsymbol{b} = \frac{V}{c_0^2} \frac{\boldsymbol{\zeta}^{dp}}{\zeta_0^{dp}} \tag{6.46.}$$

From this expression, a set of coefficients $\boldsymbol{b}$ may be found that minimise the appearance of the prototype-cavity eigenfunctions in the pressure response of the profiled cavity. The number of prototype-cavity eigenfunctions included in the set of equations must be truncated in order to solve the system. Simply, in terms of the solubility of the problem, there are a number of possibilities. The most straightforward option is to truncate the number of prototype eigenfunctions to the first N_μ, in which case $\tilde{\boldsymbol{Q}}$ is square and invertible. In this case, unless the system is ill-conditioned, there is a single well-defined solution for $\boldsymbol{b}$. Alternatively, the number of eigenfunctions can be chosen to be greater than the number of candidate cavity thickness functions, N_μ, in which case the matrix $\tilde{\boldsymbol{Q}}$ has a greater number of rows than columns and the matrix equation is overdetermined. In this case, there is likely to be no exact solution to the set of equations, however it is possible to solve for $\boldsymbol{b}$ in a least squares sense. Finally the number of eigenfunctions may be chosen to be lower than N_μ, in

which case there are a greater number of columns than rows in $\tilde{\boldsymbol{Q}}$ and the system of equations is under-determined and, in general, there are an infinite number of possible solutions for $\boldsymbol{b}$. It is likely that the most interesting case is the first where N_μ eigenfunctions are considered.

The underlying method is based on the Rayleigh-Ritz approach. The more prototype eigenfunctions that are included, the better the underlying Rayleigh-Ritz approximation is able to describe the profiled cavity and the better the modal suppression is likely to be in the profiled cavity. However, at the same time, the greater the number of prototype eigenfunctions that are included, the greater the extent to which the cavity excitation is controlled. Including too many prototype eigenfunctions terms is likely to result in the solution converging on the ideal cavity shape. Clearly this is undesirable as the entire premise of the method is to try to find alternative cavity shapes. However, as was demonstrated in section 3.6, the accuracy of the Rayleigh-Ritz method is not dependent simply upon the number of prescribed functions, but also upon the ability of the prescribed functions to describe the solution. For example, if the eigenfunctions of the prototype cavity are very similar to the eigenfunctions of the profiled cavity then the Rayleigh-Ritz approximation will be very good even if only a few prototype eigenfunctions are considered in calculating $\boldsymbol{b}$. Additionally, if this is the case then the number of prototype eigenfunctions used in calculating $\boldsymbol{b}$ will be approximately equal to the number of modes controlled in the profiled cavity. Naturally, by implication this requires that the geometry of the prototype cavity is close to the geometry of the profiled cavity. However, as will be demonstrated below, it is possible to arrive at this situation by an iterative approach. The profiled cavity is first approximately calculated using an arbitrary prototype cavity, most likely a cavity with constant thickness. This approximate cavity may then be used as the prototype cavity to allow a more accurate calculation of the final cavity. These iteration steps may be repeated in order to improve the performance of the final cavity.

Example 1

To test this method for calculating the profiled cavity geometry, the same spherical cap cavity that was used at the start of the chapter is considered. An FEA model of the prototype cavity is shown in figure 6.8. This model was used to calculate the prototype cavity eigenfunctions required to determine the coefficients for the matrix $\tilde{\boldsymbol{Q}}$. The diameter of cavity is 80mm and the curvature of the cavity is 55 degrees measured from axis of rotation to cavity edge. It is assumed that the radiating diaphragm occupies the entire left hand side of the compression cavity and that it moves axially and rigidly.

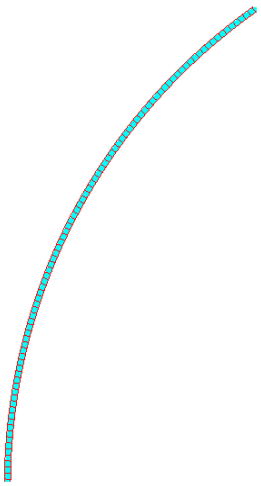

Figure 6.8. Mesh used for eigenfunction and eigenfrequencies FEA solution of spherical cap prototype cavity. The model is axisymmetric with the axis of rotational symmetry at the lower extent of the mesh.

In the first instance, the cavity thickness shape functions were chosen to be

$$\mu_n(s)=\cos\left[(n-1)\theta\right] \tag{6.47.}$$

The coefficients of the vector $\boldsymbol{\zeta}_p^d$ were found using the numerical method described in section 5.4.1. The coefficients of the matrix $\tilde{\boldsymbol{Q}}$ were found using the method described in section 6.2.1. The cavity was first considered using five shape functions from $n=1$ to $n=5$ and the first 5 eigenfunctions of the prototype cavity were used as prescribed functions. Resulting in a square matrix $\tilde{\boldsymbol{Q}}$ and a fully determined system of equations defining $\boldsymbol{b}$ uniquely. For this situation, the cavity thickness shape function coefficients, according to equation 6.46, were found to be

$$\boldsymbol{b}^T=\frac{V}{S_s}\left[3.869 \quad -5.107 \quad 3.492 \quad -1.165 \quad 0.182\right] \tag{6.48.}$$

where S_s is the area of the cavity entrance surface, given by the integral

$$S_s=2\pi\int_{s=0}^{s_a} r(s)ds \tag{6.49.}$$

From these coefficients, it is straightforward to calculate the profiled cavity-thickness function using the matrix expression $\mu(s)=\boldsymbol{b}^T\boldsymbol{\mu}(s)$. Inspection of this function reveals that the resulting cavity thickness is extremely close the ideal profiled cavity as described in the introduction to this chapter,

$$\mu(s)\frac{S_s}{V}=\left[1+\tan^2\left(\frac{\theta_0}{2}\right)\right]\cos(\theta(s)) \qquad 6.50.$$

Figure 6.9 shows both the ideal and the newly derived profiled cavity-thickness functions. The two profiles are extremely similar to one another.

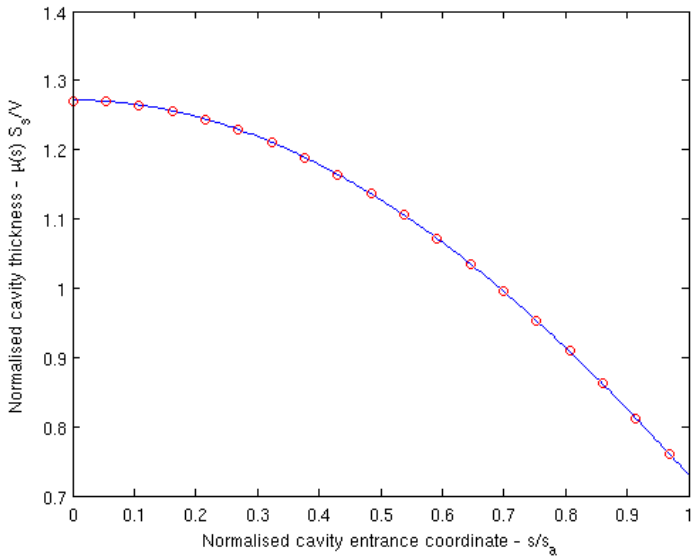

Figure 6.9. Comparison of derived profiled cavity thickness function using RR based method (solid line) with the ideal cavity profile (circles), function ordinate normalised by V/S_s, abscissa normalised by s_a.

It is interesting that the thickness function converges to the ideal solution with so few terms included in $\tilde{\boldsymbol{Q}}$. The calculated thickness function is highly dependent upon the selected thickness shape functions, $\mu_n(s)$. In this case, the shape functions are closely related to the ideal solution and the approximate Rayleigh-Ritz-based derivation quickly converges with the ideal solution.

A more interesting test of the method, which does not so quickly converge on the ideal solution, was devised using the shape functions

$$\mu_n(s)=\cos\left[(n-1)\frac{s}{s_a}\pi\right] \qquad 6.51.$$

Choosing these shape functions means that the thickness function of the profiled cavity is equivalent to a truncated Fourier-cosine-series with N_μ terms. Using these shape functions, the resulting profiled cavity shape was calculated from the same spherical cap prototype cavity for several different numbers of thickness functions N_μ. In each instance, the calculation is performed using the method described above, forming the matrix $\tilde{\boldsymbol{Q}}$ with N_μ

prototype cavity eigenfunctions resulting in a square matrix and a fully determined set of equations with a unique single solution of $\boldsymbol{b}$. A sinusoidally driven FEM model was constructed for each derived cavity-thickness profile in order to allow assesssment of the degree to which the cavity eigenfunctions are excited. The FEM models have a sinusoidally-driven spherical-cap rigid radiating-diaphragm located on the left side of the cavity. Otherwise, the cavity is completely closed without exit channels on the right-hand side. The radiating diaphragm moves sinusoidally with unit axial harmonic velocity. The pressure at the outside diameter of the cavity is used in order to assess how much the eigenfunctions are excited. Figure 6.10 shows the resulting profiled-cavity thickness function derived under these conditions for the case when there are 1, 2, 3 and 4 thickness functions. The pressure response of the corresponding driven FEM model is shown in each case. It is seen that as the number of thickness functions are increased, the solution converges on the ideal solution. Considering the pressure responses shown on the right-hand side, it is observed that as the number of thickness functions are increased the eigenfunction excitation is reduced, indicated by the large peaks on the response. In each instance the $(N_\mu - 1)$th eigenfunction is almost completely controlled.

The slight remaining “glitches” seen at the frequencies corresponding to the suppressed eigenfunctions are likely be due to the approximations in the profile derivation method and specifically because of inaccuracies in the approximation of the volume integral that was introduced in expression 6.11 in addition to the truncation of the Rayleigh-Ritz summation. These glitches are especially obvious because the system has no energy dissipation: at each suppressed eigenfunction, one can consider that, in terms of the Laplace transform of the system, the pole present as a result of the eigenfunction and corresponding eigenfrequency is covered by a zero. If the pole and the zero lie exactly upon one another, then the resonance is completely suppressed. However if there is even a minute difference in the position of the pole and the zero then perfect suppression does not occur. For the case when there is no dissipation in the system, the pole lies on the imaginary axis of the s-plane and even a vanishingly small offset of the zero results in a sharp frequency response glitch. The width of the glitch is very narrow especially if the pole/zero offset is small. With the addition of any energy dissipation into the system, the glitches very quickly disappear. This occurs because the pole and zero move away from the $j\omega$ axis into the negative real area of the plane. The offset of the pole and the zero is then much smaller than their distance to a point on the $j\omega$ axis. The behaviour of modal control in terms of Laplace pole and zero positions is discussed in some detail in [79].

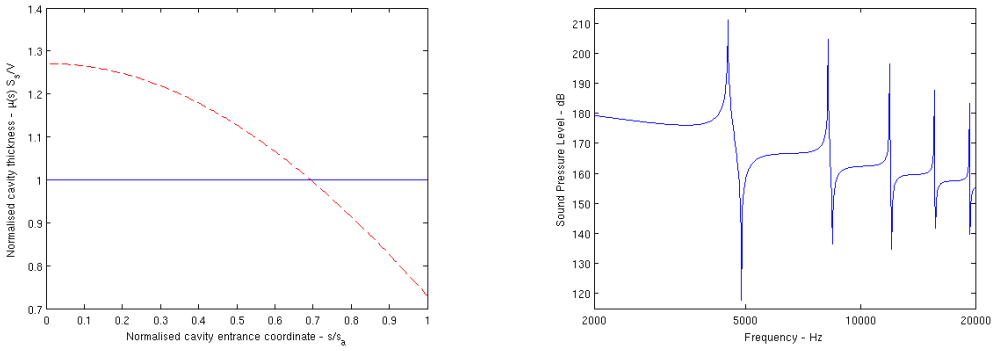

$N_\mu = 1$

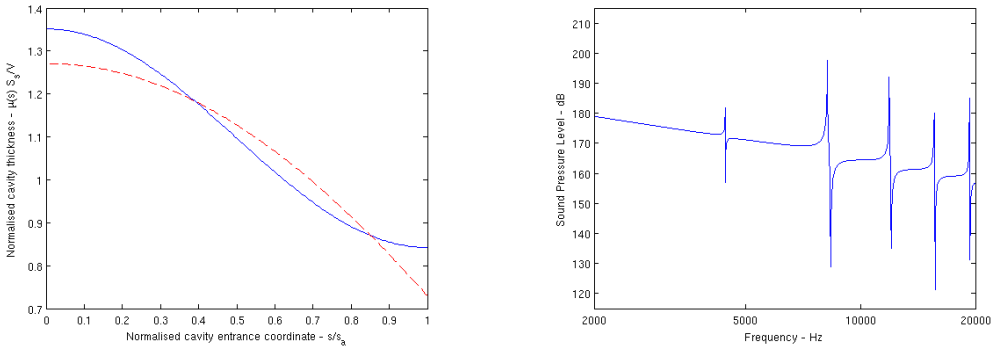

$N_\mu = 2$

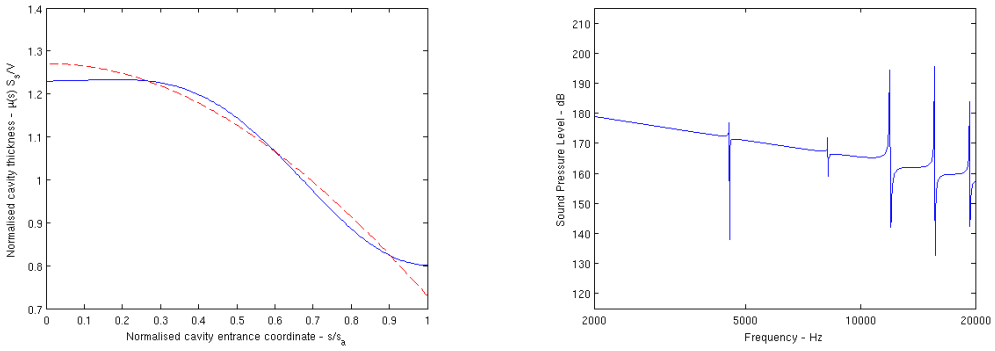

$N_\mu = 3$

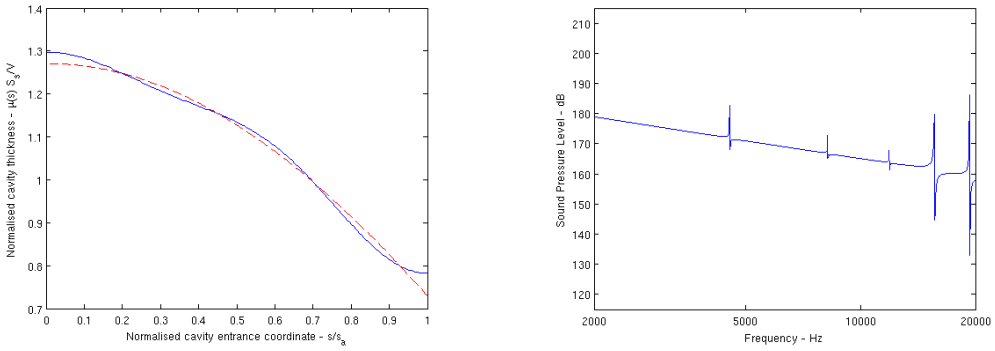

$N_\mu = 4$

Figure 6.10. Normalised derived profiled cavity thickness function, compared to the ideal profile (dashed red) and resulting diaphragm excited pressure response at outside diameter of cavity for different numbers of shape functions from 1 to 4.

Example 2

The geometry of the radiating diaphragm has a very significant effect on the mechanical performance of the driver. For drivers with metal radiating diaphragms, the upper limit of the usable bandwidth is usually set by the first mechanical eigenfrequency. Because there is very little loss in the mechanical structure, it is extremely difficult to usefully operate a metal radiating diaphragm once it has begun to "break up". The typical shape of the radiator used for high frequencies is a spherical cap or dome. This geometry is particularly suitable as even with a very thin material the "break-up" can be very high in frequency. The geometry of the edge of the dome is critical for optimum performance. The dome edge is usually the first part of the dome to bend in a conventional design. Anthony and Wright describe an elliptical section dome that they find is near optimal in terms of the first break-up mode [75]. Figure 6.11 shows the first break-up mode of their dome.

All the phase-plug analyses presented so far have made the assumption that the dome moves rigidly. Clearly, it is important that the shape of the diaphragm can be adjusted in order to maximise the rigidity of the diaphragm over the operating bandwidth. The elliptical shape is particularly difficult to handle in terms of the acoustical performance as the surface normal at the outside diameter of the diaphragm is perpendicular to the axis of motion. The result of this geometric problem is that if a constant thickness compression cavity is used, the excitation of the acoustical cavity modes resulting from axial motion of the diaphragm is very severe.

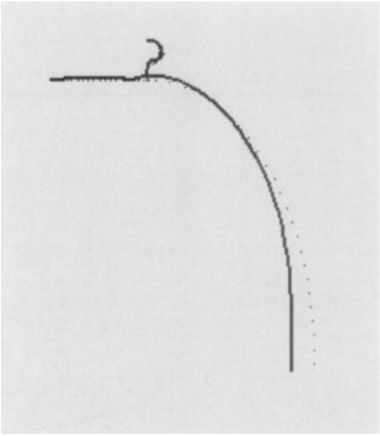

Figure 6.11. Reproduction of Wright and Anthony elliptical dome-shaped radiating-diaphragm modal analysis, "first break-up of elliptical dome, 31kHz", reproduced from [75].

To demonstrate this, an FEA model of a constant-thickness compression cavity with elliptical shape was constructed. The meshed geometry is shown in figure 6.12. The elliptical section

has a semi-major axis of 40mm and a semi-minor axis of 20.825mm. The cavity has a constant thickness of 0.3mm.

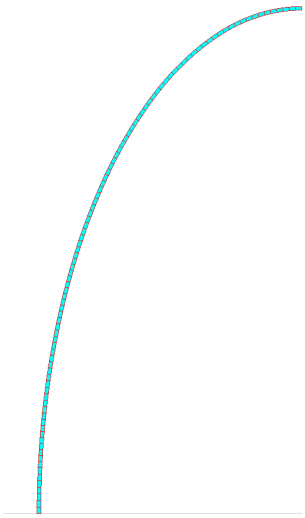

Figure 6.12. FEM mesh of elliptical compression driver cavity with constant thickness, axis of rotational symmetry is indicated with a grey line at the lower edge of the model.

Using this model, the generalised method, described in section 5.4, was used to compute the values of the parameter ζ_n^d for the case when the left-hand side of the elliptical section cavity is excited with a rigid axially-moving radiating diaphragm. These computed values are shown in table 6.4 in comparison to the values presented in section 5.4.1 for the simpler spherical-cap geometry. It may be observed for these results that, although the first compression cavity mode is excited slightly less strongly, the second and third mode are excited more strongly by the elliptical diaphragm than the spherical-cap cavity.

	Spherical Cap Cavity	Elliptical Section Cavity
ζ_0^d/ζ_0^d	1	1
ζ_1^d/ζ_0^d	0.354678	0.299834
ζ_2^d/ζ_0^d	-0.127144	-0.178592
ζ_3^d/ζ_0^d	0.0735582	0.112861

Table 6.4: Comparison of values of ζ_n^d/ζ_0^d calculated numerically for a spherical-cap concentric compression-cavity geometry and the elliptical section compression cavity geometry.

These values of ζ_n^d were then used to design a three channel compression driver, as described in section 5.4.1, the channels are positioned at the nodes of the third acoustical mode of the compression cavity, resulting in calculated channel areas of

$$\begin{bmatrix} A_1/A_T \\ A_2/A_T \\ A_3/A_T \end{bmatrix} = \begin{bmatrix} 0.205421 \\ 0.465484 \\ 0.329094 \end{bmatrix} \qquad 6.52.$$

where A_1 is the area of the inner of the three channels, A_2 is the area of the middle channel and A_3 is the area of the outer most channel. These areas can equivalently be written as channel width ratios as

$$\begin{bmatrix} w_2/w_1 \\ w_3/w_1 \end{bmatrix} = \begin{bmatrix} 1.0096 \\ 0.4919 \end{bmatrix} \qquad 6.53.$$

Comparison of these values with those for the spherical-cap compression cavity, that was originally considered in section 5.2.5, shows that the outer channel width is significantly lower in this case, whereas the middle channel width is slightly larger. This situation is indicative of the behaviour on the input side where the surface-normal velocity due to the motion of the radiating diaphragm is higher in the centre and much lower at the outside diameter compared to the spherical-cap geometry.

Using these geometric parameters, a simple compression-driver model was constructed using the same basic compression-cavity geometry as above. The model has a compression ratio of 15 and the three channels are terminated with a $\rho_0 c_0$ specific-acoustical-impedance boundary condition.

The FEM computed normalised pressures in the three channels are shown in figure 6.13. The results are directly comparable to those which were previously presented for the other simple compression driver models, such as those shown in figures 5.18, 5.28 and 6.2. Compared to the previously presented results, the performance of the elliptical-section cavity is very poor with a large difference in the pressure responses in each of the three channels. This poor performance is a direct result of the sub optimal ζ_n^d values presented earlier in this section.

The elliptical-section cavity presents a particular problem because the ideal cavity construction method, described at the start of this chapter, is totally unsuitable as the cavity entrance surface normal is perpendicular to the axis of symmetry at the outside edge. This results in a cavity with thickness that vanishes at this point.

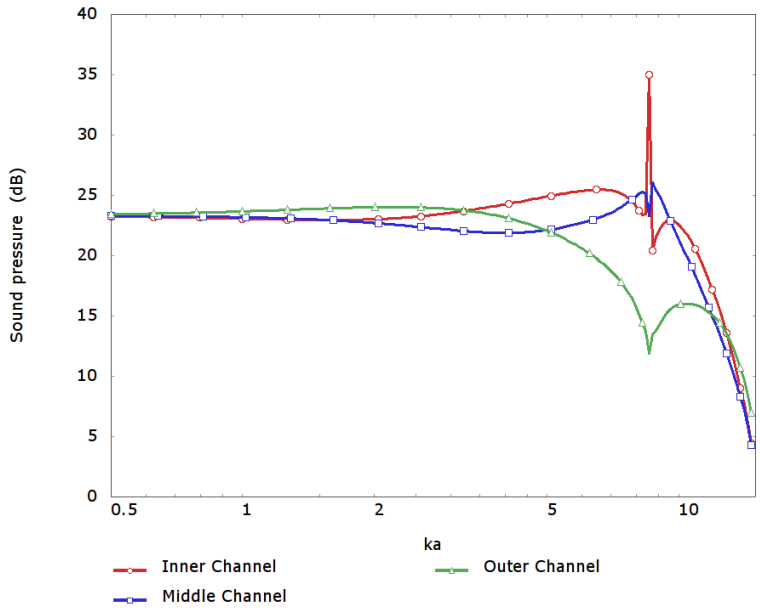

Figure 6.13. Normalised channel pressure level response for constant thickness elliptical-section compression-cavity with phase-plug geometry computed using the generalised method introduced in section 5.4.1.

The constant-thickness elliptical section cavity is now used as a prototype cavity for the shaping method described in this section in order to try to improve the performance of the resulting compression-driver channel arrangement while still maintaining a practical geometry. In an attempt to force the derived cavity thickness profile to have a non zero thickness at the outside diameter, the cavity thickness functions were chosen to be

$$\mu_n(s)=\cos\left[(n-1)\frac{s}{s_a}\pi\right] \qquad 6.54.$$

The resulting profiled compression cavity is to have a three-channel idealised phase plug attached to the exit surface. The three-channel design permits control of the cavity modes up to the third. To also consider the cavity modes up to the third it is necessary to use at least 4 thickness shape functions.

A profiled cavity shape using five thickness functions, with $n=1$ to 5, was calculated from constant-thickness elliptical-section prototype cavity. The calculation was performed over two iterations. The second iteration using the eigenfunctions of the profiled cavity resulting from the first iteration as the shape functions for the Rayleigh-Ritz approximation. For each iteration, the calculation is performed using the method described above forming the matrix $\tilde{\boldsymbol{G}}$ with N_μ prototype-cavity eigenfunctions, resulting in a square matrix and a fully determined set of equations with a unique single solution of $\boldsymbol{b}$. After each iteration, the

derived cavity-thickness function was used to construct a sinusoidally driven FEA model to assess the degree to which the pressure eigenfunctions are excited. The models have a sinusoidally-driven rigid radiating-diaphragm located on the left side of the cavity and are otherwise completely closed without exit channels on the right-hand side of the cavity. The radiating diaphragm moves sinusoidally with unit axial velocity. The pressure at the outside diameter of the cavity is used as a indicator of how much the eigenfunctions are excited.

Figure 6.14 shows the resulting cavity-thickness function derived with the conditions described above along with the pressure response of the corresponding FEA model. In this case, the excitation of the cavity modes is very severe in the constant-thickness cavity. After one iteration, the excitation of the first four cavity modes in the profiled cavity is significantly reduced. However, there is still significant irregularity present in the cavity pressure. This remaining irregularity indicates that the Rayleigh-Ritz approximation is poor in this instance and the four eigenfunctions of the prototype cavity are unable to accurately describe the solution in the profiled case. After a second iteration, using the profiled cavity from the first iteration as the prototype cavity, the excitation of the eigenfunctions of the profiled cavity is almost completely suppressed. This results from the fact that the eigenfunctions of the profiled cavity after the first iteration are better able to describe the solution to the profiled cavity and, consequently, the Rayleigh-Ritz-based approximation is more accurate.

Clearly, there are some conditions associated with the convergence of the iterative approach. If, for example, the first prototype cavity is very dissimilar from the final profiled cavity then one can conceive that the eigenfunctions of the profiled cavity after the first iteration may be no more suitable to describe the behaviour of the final profiled cavity than the original eigenfunctions of the first prototype. In this situation, it is possible that subsequent iterations do not converge to describe the final profiled result. However, the small number of cases that have been considered by the author have all converged to a well-performing profiled cavities after only one or two iterations. The criterion for convergence is not included in this thesis.

It should be noted that, as a result of the careful selection of the shape functions, the cavity width at the outside diameter is finite. However, in several areas the derived cavity is very narrow, notably at the centre. This is a significant problem; it is necessary to leave space between the diaphragm and the phase-plug so that the diaphragm may move during operation. To maintain the same clearance for the derived shape as the ideal cavity shape it would be necessary to increase the compression cavity volume significantly and, as discussed in section 2.4.1, this would reduce the bandwidth of the device.

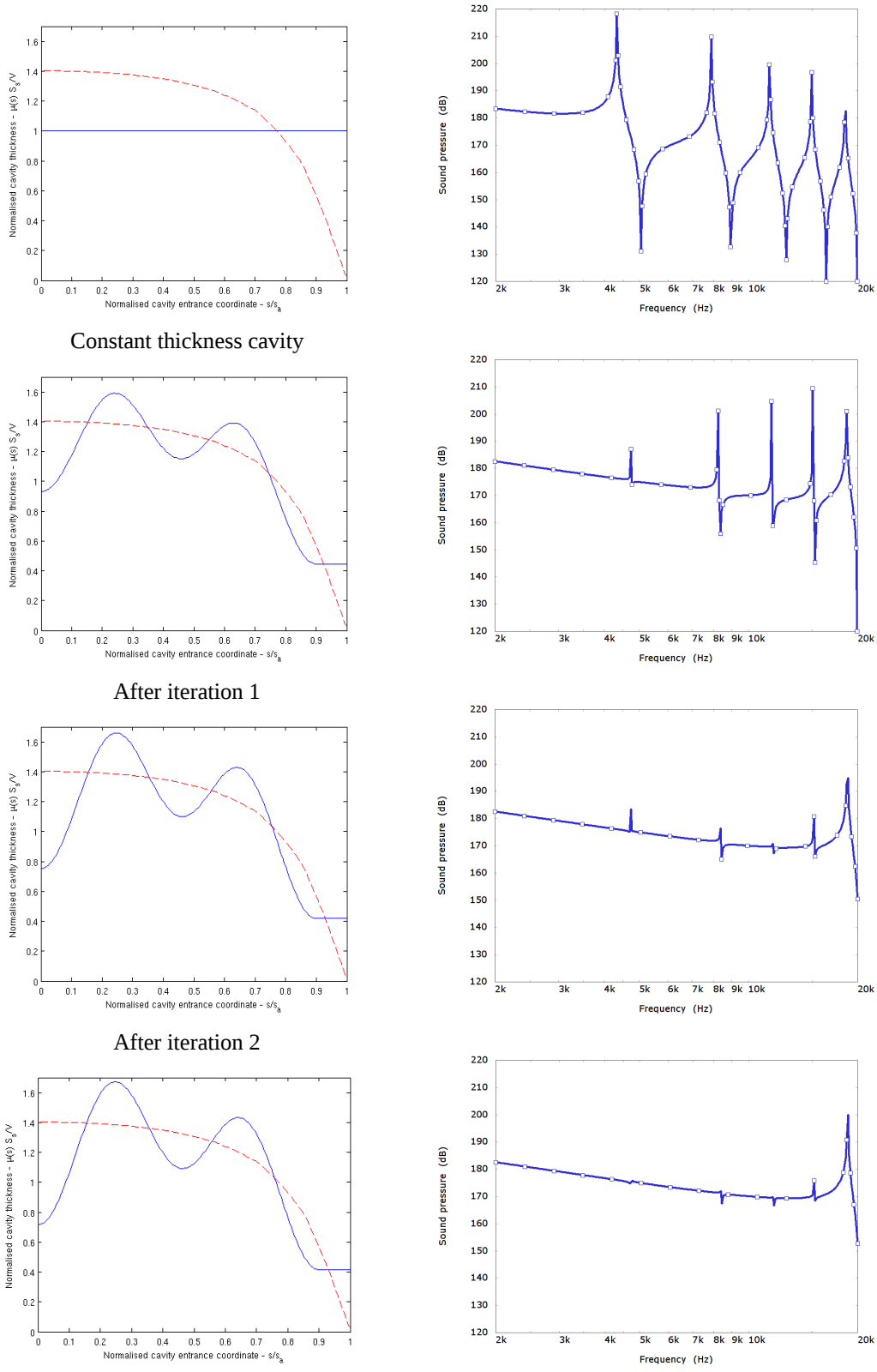

Figure 6.14. Normalised profiled cavity thickness function, compared to the ideal profile (dashed red) and resulting diaphragm excited pressure response at outside diameter of cavity for constant thickness prototype cavity, cavity after first iteration, cavity after second iteration and after third.

Using this derived cavity shape the generalised method was used to compute the values of the parameter ζ_n^d for the case when the left-hand side of the elliptical-section cavity is excited with a rigid axially-moving radiating diaphragm. These computed values are shown in table 6.5 in comparison to the values calculated previously for the prototype cavity. It is clear from these values that the profiled cavity has much more favourable values of ζ_n^d.

	Prototype Cavity	Final Cavity
ζ_0^d/ζ_0^d	1	1
ζ_1^d/ζ_0^d	0.299834	-0.000823
ζ_2^d/ζ_0^d	-0.178592	-0.000692
ζ_3^d/ζ_0^d	0.112861	0.000521

Table 6.5: Comparison of values of ζ_n^d/ζ_0^d calculated numerically for the prototype constant thickness elliptical compression cavity and the derived profiled compression cavity.

These values of ζ_n^d were then used to design a three-channel compression driver, as described in section 5.4.1. The channels are positioned at the nodes of the third acoustical mode of the profiled compression cavity resulting in calculated channel areas of

$$\begin{bmatrix} A_1/A_T \\ A_2/A_T \\ A_3/A_T \end{bmatrix} = \begin{bmatrix} 0.252270 \\ 0.459635 \\ 0.288095 \end{bmatrix} \qquad 6.55.$$

where A_1 is the area of the inner of the three channels, A_2 is the area of the middle channel and A_3 is the area of the outer most channel.

These areas can be equivalently written as channel width ratios,

$$\begin{bmatrix} w_2/w_1 \\ w_3/w_1 \end{bmatrix} = \begin{bmatrix} 0.853752 \\ 0.385079 \end{bmatrix} \qquad 6.56.$$

Using these geometric parameters, a simple compression-driver model was constructed using the same basic compression-cavity geometry as above. The model has a compression ratio of 15 and each channel is terminated with a $\rho_0 c_0$ specific acoustical impedance. The FEM-computed normalised pressures in the three channels are shown in figure 6.15.

This figure is directly comparable to the results shown in figure 6.3, which used the prototype constant-thickness compression cavity. In comparison the three channel pressures are much more even in the profiled cavity case. The three pressure responses are very similar up to a frequency of $ka = 5$ and, even above this frequency, they remain smooth individually despite diverging by around 5dB from one another.

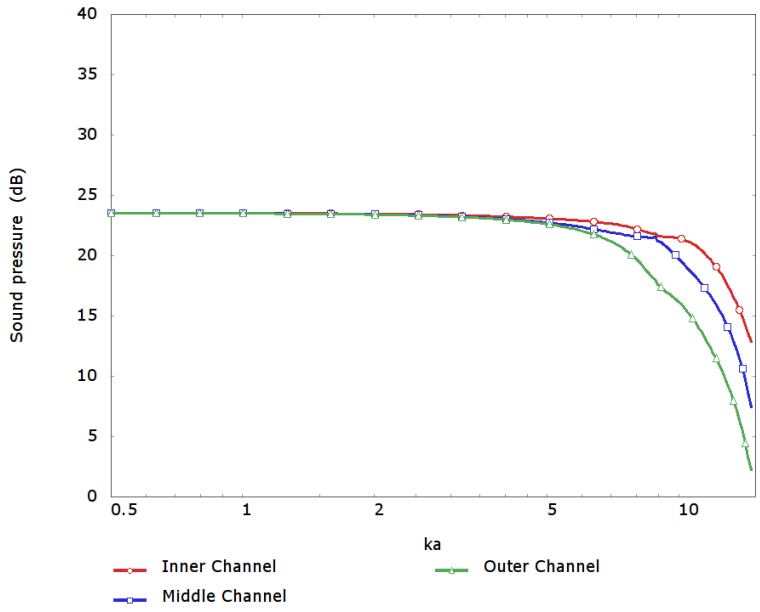

Figure 6.15. Normalised channel-pressure-level response for a profiled thickness elliptical-section compression cavity, as outlined above, with phase-plug geometry computed using the generalised method introduced in section 5.4.1.

6.3 Conclusions

Overall, the Rayleigh-Ritz based shaping method appears to have the potential to improve the compression-driver performance compared to the use of a constant thickness cavity. However, the results fall a little short of the performance seen with the ideal cavity construction method described at the start of the chapter. The main advantage of the method is that there is some degree of control over the shape of the final cavity and this provides the potential to overcome practical problems that can occur with the ideal cavity shaping method. There are a number of other considerations. If too many thickness functions are used in the calculation then the resulting cavity very quickly converges with the ideal shape. On the other hand if too few thickness functions are used then the suppression of modal excitation from the radiating diaphragm will not occur over the whole bandwidth of the compression driver and the full performance benefit will not be seen. It is also very hard to influence the shape of the final cavity. The only means of control are the number and choice of the thickness functions. Additionally, there is no guarantee that the derived profiled cavity shape is practical. For example, the derived profile may approach zero thickness or even a negative thickness.

In the final driver, there must be a practical clearance between the compression-driver diaphragm and the opposite face of the compression cavity. Inevitably, compared to a ideal

cavity design, the profiled cavity requires closer clearance in some places. It may be necessary to increase the volume of the compression cavity in order to maintain practical clearances. This is undesirable as it increases the volume of the compression cavity. It may be preferable to have a larger, but well controlled compression cavity, than a smaller, but poorly controlled compression cavity. However, the conventional wisdom, based on the lumped behaviour of the compression driver, is that a smaller compression cavity will provide a wider bandwidth.

An extension to the cavity shaping method presented above was also devised that allows the thickness of some regions of the compression cavity to be fixed. This method is outlined in Appendix XI. The intention is that the regions where the ideal-cavity approach results in a cavity thickness which is too small may be fixed and the surrounding regions adjusted to achieve the modal-suppression. Very similar issues were encountered using this approach: the final shape of the cavity is hard to control, the resulting cavity is not guaranteed to be practical and inevitably the acoustical volume of the cavity is larger than with the ideal cavity construction method, described at the beginning of the chapter.

The ideal cavity construction method is a very neat solution providing the optimal set of ζ_n^d/ζ_0^d for a given diaphragm and, additionally, the minimum possible cavity volume for a given mechanical clearance. The further shaping approaches that have been subsequently presented are very interesting, but, as has been highlighted, have practical and performance shortcomings compared to the ideal cavity construction method. In practice, the author feels that it is likely the best approach to attempt to design compression-driver diaphragms that permit the use of the ideal cavity construction method and avoid those that result in non-realisable cavities, such as the elliptical-section. The design of the compression-driver diaphragm itself for optimal performance is a subject that is considered in detail in chapter 8.

7 A new channel-positioning methodology for radial compression drivers

7.1 Introduction

An alternative arrangement for the phase plug was described by Blackburn [80] in his 1939 patent. In this embodiment, the channels between compression cavity and horn throat are arranged radially, extending from the centre of the diaphragm to the perimeter. One of the early cited advantages for this arrangement is that the phase plug may be constructed with a single cavity moulding tool, whereas the more common annular-plug design requires a number of annular parts to form the channels. The radial-channel phase plug is also subsequently the subject of other patents [81][82].

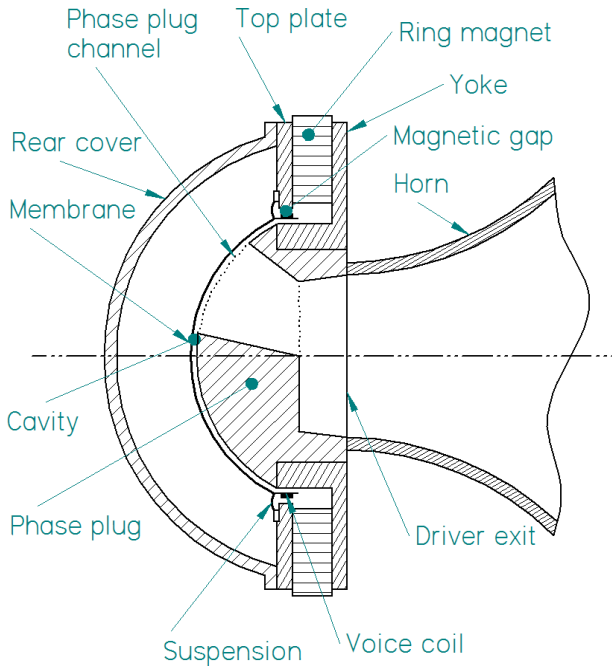

Figure 7.1. Schematic illustration of a radial-channel compression driver with a domed radiating diaphragm and compression cavity.

Surprisingly, the only published work on the acoustical behaviour is by Henricksen [71][70] in his two comparisons to annular phase plugs. However, the analysis of this arrangement presented in these papers uses an equivalent technique to the equal path-length approach, which was originally proposed by Wente [17] and superseded by Smith [35]. In this chapter, the design considerations for this type of compression driver are discussed and, as with the annular phase plug, a new methodology for optimal design of the channel entrances is described.

7.1.1 Comparison with the annular plug layout

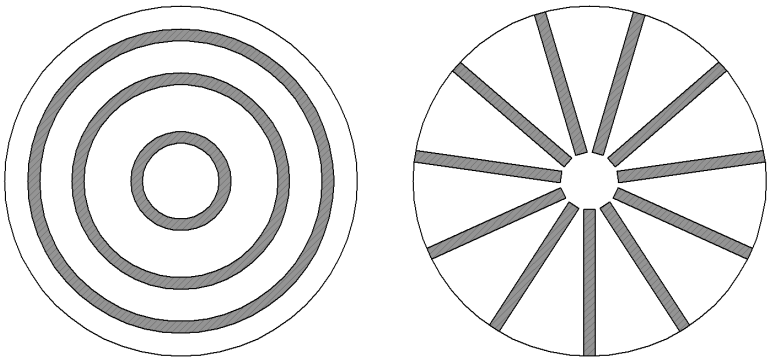

Figure 7.2. Comparison of annular channel arrangement (left) with radial channel arrangement (right) viewed from the diaphragm side of the phase plug. The channel entrances shown in grey.

The geometry of a radial-plug compression driver is similar to the annular layout, which was described in chapter 4. The driver has a rotationally symmetric radiating diaphragm that drives one face of a compression cavity and there are a number of exit channels on the opposite face that lead to a horn. These similarities make much of the approach applied to the annular case applicable to the radial geometry. However, there are significant differences that must be considered. The annular-channel phase-plug geometry is rotationally symmetrical, whereas the radial-channel phase plug has a geometry that is circumferentially periodic. When considering the annular design it was possible to discard the non-axisymmetric compression cavity modes (see section 4.2.1). As is demonstrated in the following sections, with the radial-channel design this cannot be assumed. A second difference is that with the annular design, irrespective of the detailed shape of the axisymmetric compression cavity, the geometry of each channel entrance is a narrow annular ring lying on a plane. It is obvious that if the entrance is extruded along the axis of the driver, an annular channel is created which, when pressure variation is constant over the entrance surface, carries a plane propagating-wave. Further to this, if the channel is constructed to gently curve and expand a little, while still remaining rotationally symmetrical, as was seen in section 5.3, this has a little impact on the wave propagation or the impedance of the channel at the entrance. Thus, the separate channels of the annular design can be routed as required to constructively sum at the horn throat. The radial-channel entrance geometry is more complex. For example, with a dome radiator and cavity, the channel entrances lie on a spherical surface, not a plane. Clearly, in this case, it is necessary for the channels to flare in order to allow spherical wave propagation in the channels. It is less obvious how the channels are to be routed to meet at the horn throat.

For the radial geometry, rather than try to use the routing of the phase-plug channels to provide the required pressure at the horn throat, it is much simpler to use a horn that is matched to the shape of the diaphragm. This would be done to create a situation where the wave-front shape carried by the channel is very close to the wave-front shape that the horn naturally carries. Then the channels can be gently blended into horn without the need for any routing to ensure correct summation. The most obvious case where this approach can be applied is to a dome-shaped radiating diaphragm. Dodd describes a driver that is composed of a dome radiator and matching horn, and reports extremely good response at high frequency when the dome angle and the horn throat angle are matched [83]. This type of driver is a perfect candidate for the radial-channel phase plug. The phase plug occupies part of the horn in front of the dome and does not try to adjust the wave front shape. If the phase plug is working correctly, a constant pressure over the channel entrance results in a spherically expanding wave that travels smoothly down the channels and into the horn, as depicted in figure 7.3.

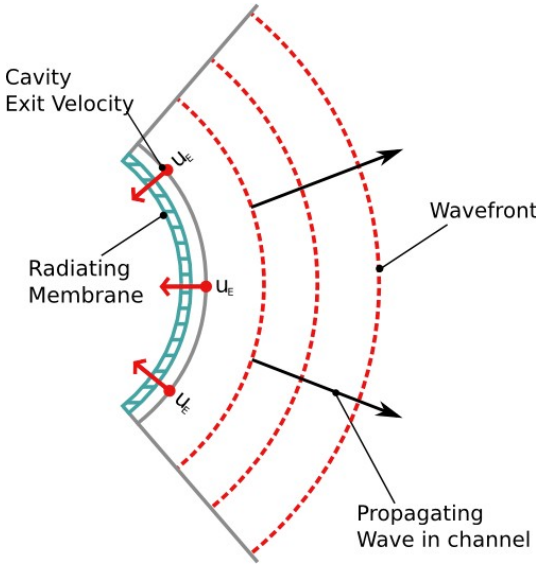

Figure 7.3. Schematic showing the section through the Dodd based driver arrangement with dome diaphragm, radial-channel phase plug, horn and indication of the direction of wave propagation.

7.1.2 Prior radial-channel geometries

Radial-channel phase plugs are much less common than their annular counterparts. However, there have been a number of attempts to use this phase-plug arrangement. Figures 7.4 and 7.5 are reproduced from the patents of Matsuoka [81] and Henricksen [82], respectively, and both outline relatively similar arrangements of the channels, diaphragm and the compression cavity. In both figures, the radial channels are of a constant width and do not extend all the way to the central driver axis. Henricksen also described an alternative arrangement with

channels entrances that narrow towards the central axis of the driver. Additionally, he outlines the importance of flaring the channels towards the throat of the horn. Neither of these two designs appear to consider the compression-cavity modal excitation and neither describe channel and horn arrangements that obviously allow wave propagation over the whole bandwidth of the driver.

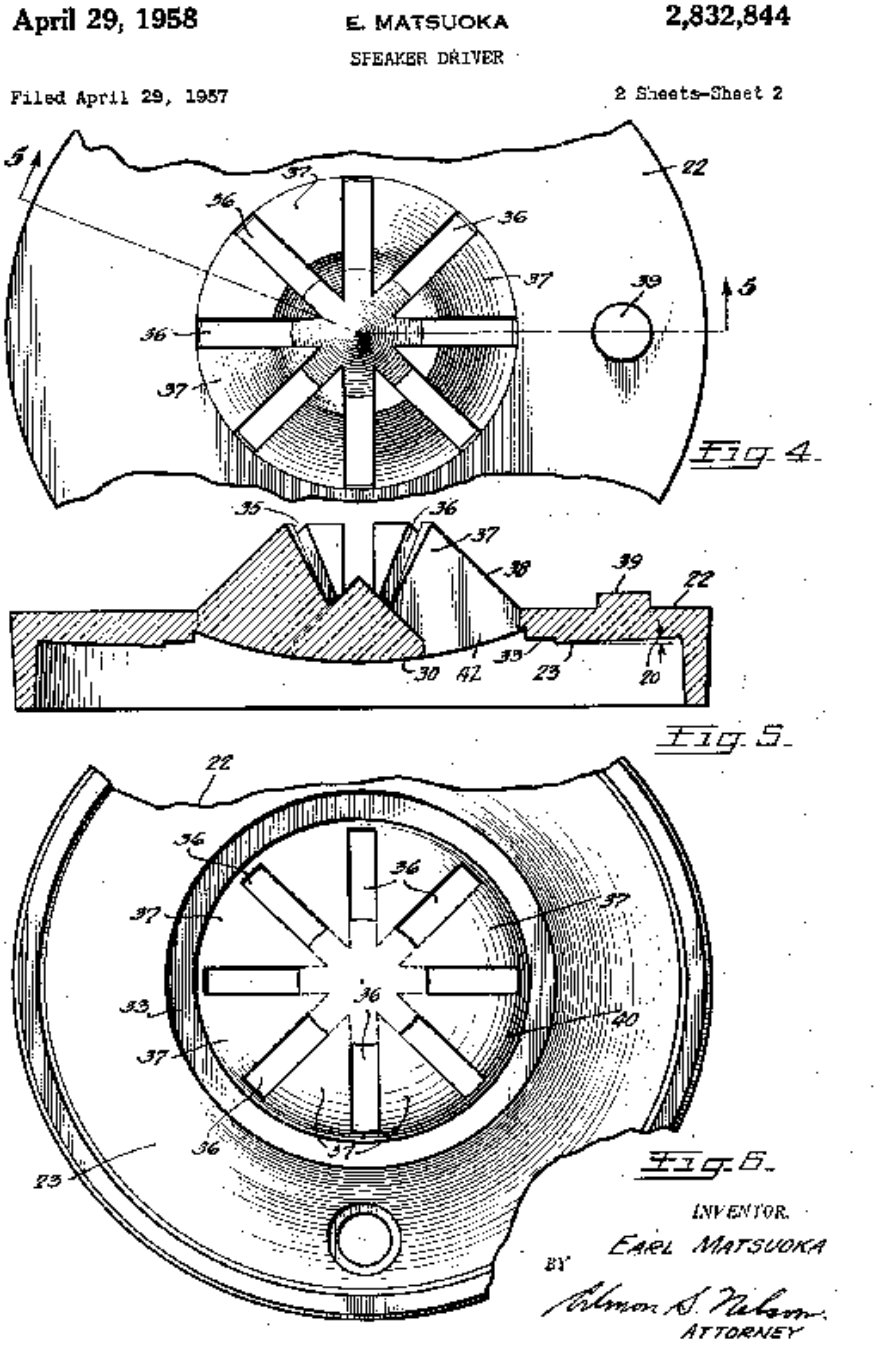

Figure 7.4. Figures taken from Matsuoka's radial phase-plug patent showing his channel entrance geometry.

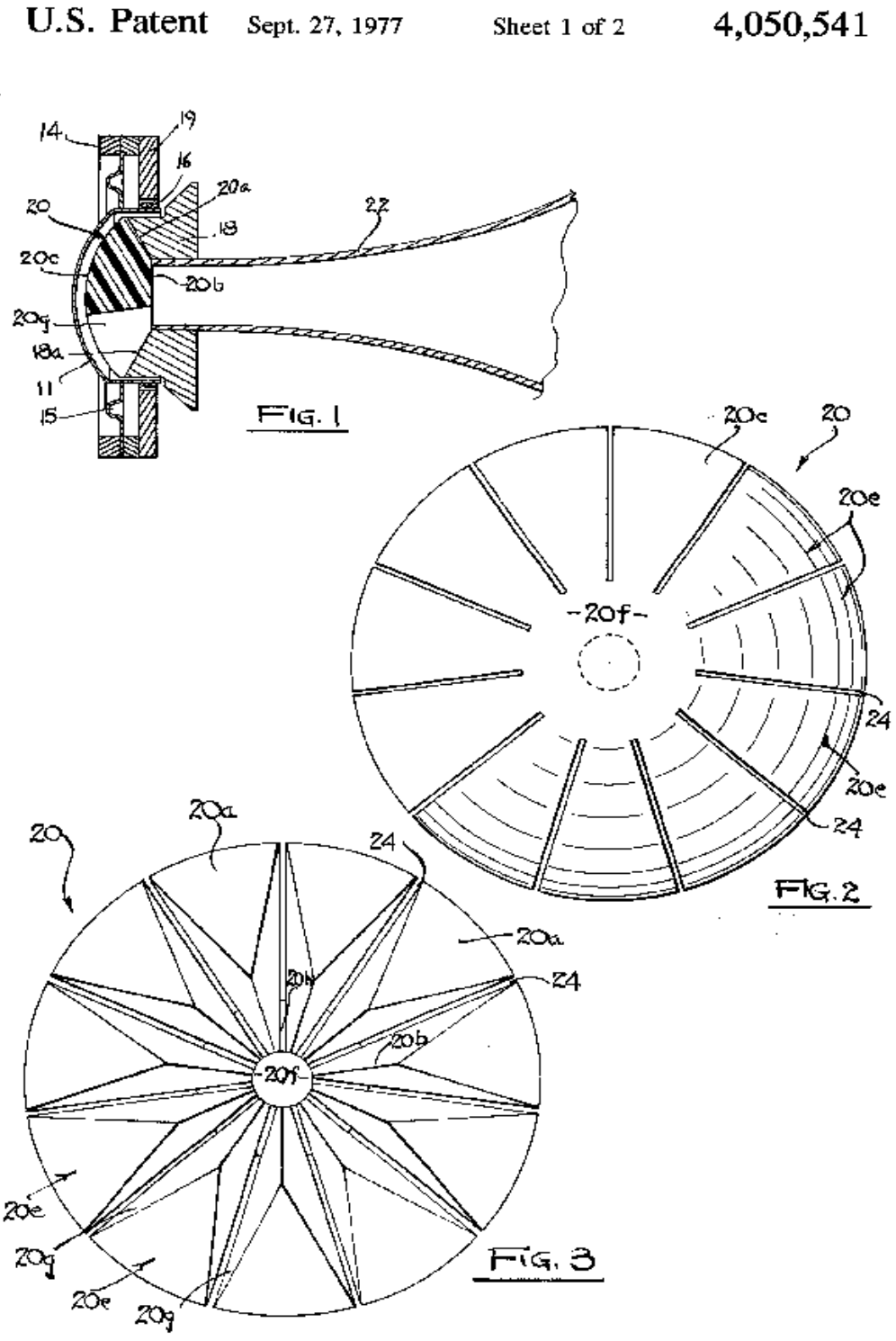

Figure 7.5. Figures taken from Henricksen's radial phase-plug patent showing his channel entrance geometry and flare in channel from cavity to horn throat.

7.1.3 Dodd's dome and horn geometry

The radial phase plug that is outlined in this chapter is based on the geometry described by Dodd for optimum performance of a dome radiating directly into a horn [83]. Dodd demonstrates that a dome of moderate angle placed at the throat of a horn behaves almost as a pulsating spherical source provided that the dome edge intersects the horn wall at a close to perpendicular angle. In order to demonstrate this effect, a simple FEM model was constructed, the mesh of which is shown in figure 7.6. The model is of a rigid 45 degree dome, meshed in axisymmetric shell of revolution elements and placed at the throat of an infinite conical horn. The infinite conical horn is created using a mesh of axisymmetric acoustical finite elements to model the first 100mm of the horn. This region is then coupled to a region of 100mm length meshed in axisymmetric wave-envelope elements [55]. The wave-envelope elements have a shape function that includes an oscillating decay along the long edge of the elements. In this way they are able to approximately model the effect of an infinite conical expansion.

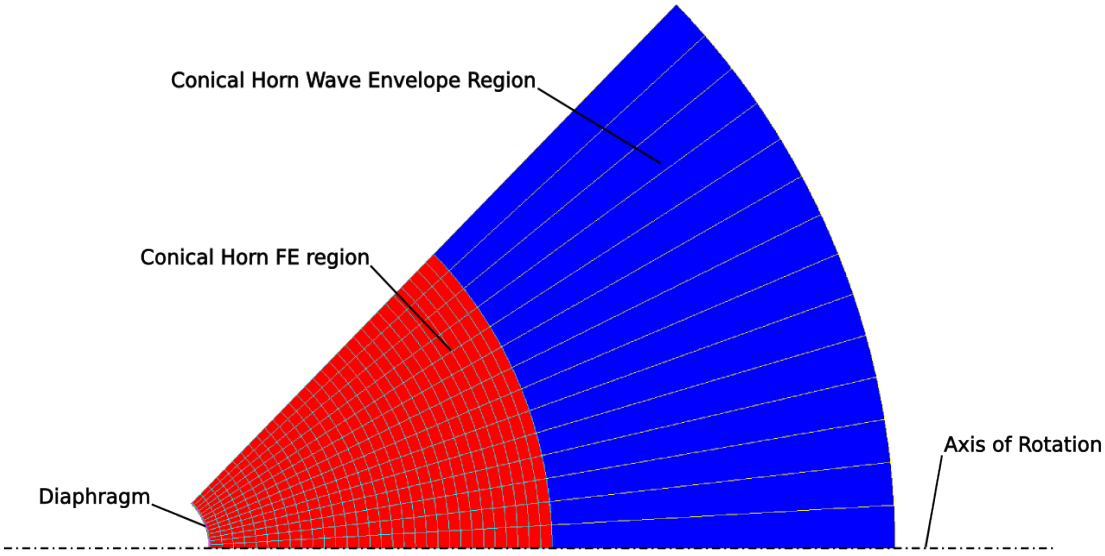

Figure 7.6. FEM mesh used to demonstrate Dodd dome and horn arrangement. The shell of revolution dome is located at the far left of the mesh at the horn throat. The red area is composed of axisymmetric acoustical finite elements. The blue region consists of axisymmetric wave-envelope elements to continue the conical flare infinitely.

The rigid-dome radiator is driven with harmonic velocity of unit amplitude. The pressure response at three points in the horn at the transition between the acoustical finite elements and the wave-envelope elements is shown in figure 7.7.

These pressures are normalised in magnitude by

$$z_{sph}\left[1+\tan^2\left(\frac{\Phi_0}{2}\right)\right]\frac{h_0}{h_{meas}} \qquad 7.1.$$

where Φ_0 is the angle of curvature of the dome, h_0 is the radius of curvature of the dome surface, h_{meas} is the radial distance at which the pressures are taken and z_{sph} is the specific acoustical impedance of a spherically spreading wave of curvature h_0 defined as [18, page 128]

$$z_{sph}=\rho_0 c_0\left(\frac{k^2h_0^2}{1+k^2h_0^2}+j\frac{k\,h_0}{1+k^2h_0^2}\right) \qquad 7.2.$$

The term in the square brackets of equation 7.1 is required because the effective radiating area of the axially moving rigid dome is smaller than that of a pulsating sphere, which would be the ideal source of spherically spreading waves.

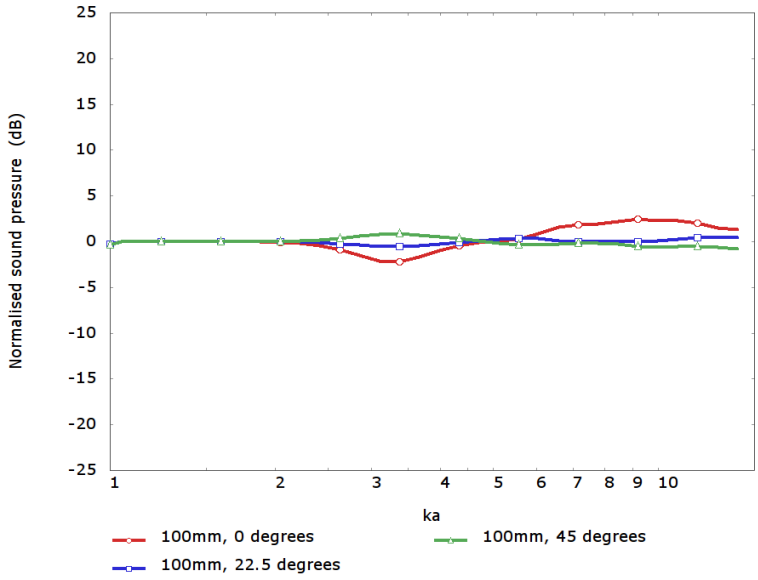

Figure 7.7. Normalised pressure response of a $\Phi_0=45$ degree dome driven infinite conical horn as described by Dodd, plotted versus normalised frequency for three sampling locations 100mm down the horn.

The acoustical pressure responses shown in figure 7.7 are reasonably similar. If a perfect spherically spreading wave were propagating in the horn, there would be no difference between the three pressure responses. At $ka=3.3$ there is a 3dB difference between the axial and horn wall pressure-responses.

7.1.4 Dodd's geometry with constant-angle radial-channel phase plug

Henricksen describes a radial-channel phase plug with channels of constant circumferential angle in his 1978 paper [71]. A FEM model was constructed to investigate the combination of this phase plug with the Dodd dome and horn arrangement. The model is based on the same geometry as that described above to demonstrate the Dodd dome and conical horn arrangement (shown in figure 7.6). The model is of a 10-degree segment of an idealised radial-channel compression driver. It is only necessary to model a 10-degree section of the full geometry because of the circumferential periodicity of the arrangement.

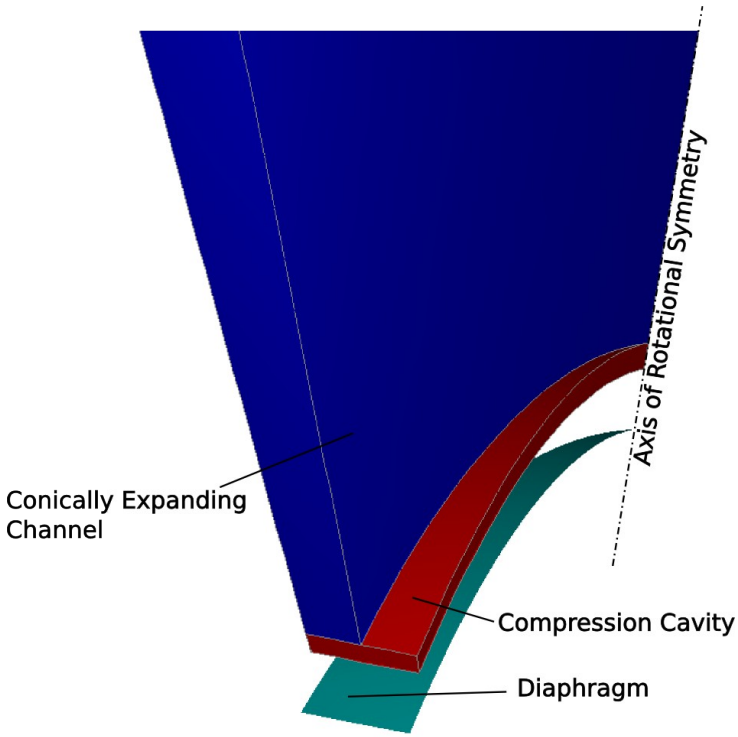

Figure 7.8. Detail from the idealised Henricksen-style constant-circumferential-angle radial-channel compression driver using the Dodd dome and horn arrangement.

In this model, a detail of which is shown in figure 7.8, a rigid axially moving dome radiator (turquoise) is coupled to a thin compression cavity (red). Both of these regions occupy the full 10-degree segment. The blue area is a channel that is coupled to the compression cavity, this region occupies only a 5-degree segment of the model. The channel is terminated with infinite wave-envelope elements such that it approximates a 5-degree segment from an infinite conical horn. In effect, this is a model of an idealised radial-channel compression driver with 18 radial channels of constant circumferential angle, a compression ratio of 1.7071 (as defined in Appendix X) and with a perfect termination to the channels.

The normalised pressure responses at a distance of 100mm down the conically expanding channel at three different angles across the channel are shown in figure 7.9. The pressures are again normalised by the expression given in equation 7.1. It may be observed that the responses are very similar indeed to those which were shown in figure 7.7. The level is increased by 6dB as a result of the compression effect. Once again, there is a region at approximately $ka = 3.3$ where the three pressures are dissimilar by approximately 3dB maximum.

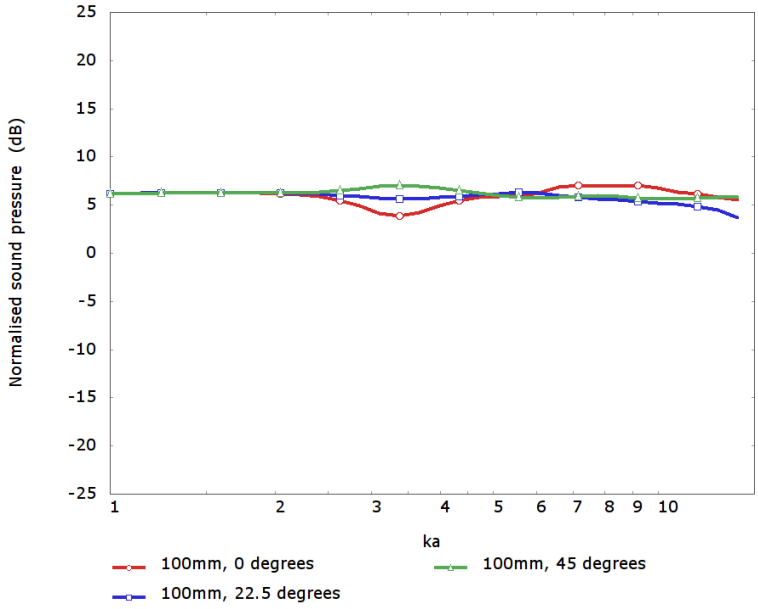

Figure 7.9. Normalised pressure response of an idealised Henricksen style constant circumferential angle channel radial compression driver using the Dodd dome and horn arrangement, plotted versus normalised frequency for three sampling locations 100mm down the horn.

The result is very interesting. The driver with the phase plug is almost identical to the performance without the plug, save for the 6 dB increase in pressure level.

7.2 Analysis of a radial-channel compression driver in spherical coordinates

The behaviour of the radial-channel case is now analysed in order to derive an improved channel geometry. As before, for the case of the annular-channel phase plug presented in section 5.2, initially an idealised compression driver that fits into a spherical coordinate system is considered. The compression cavity geometry is identical to that analysed for the annular channel compression driver.

The cavity eigenfrequencies and eigenfunctions are, from the derivation given on pages 132 to 134,

$$k_{nm}^2 = \frac{1}{h_0^2} l_{nm}\left(l_{nm} + 1\right) \tag{7.3.}$$

and

$$\Psi_{nm}(\phi,\theta) = A_{nm} P_{l_{nm}}^m(\cos\phi)\left(e^{-jm\theta} + e^{jm\theta}\right) \tag{7.4.}$$

As before, the normalisation term, A_{nm}, is chosen to satisfy the condition

$$\int_V \Psi_{nm}(\phi,\theta)^2 \, dV = V \tag{7.5.}$$

where V is the volume of the compression cavity.

7.2.1 Analysis of the driven behaviour of the cavity

The analysis continues in the same vein as that for the annular channel compression driver. The pressure in a lightly-damped acoustical cavity excited by motion of its walls can be described in terms of the rigid-walled eigenfunctions and eigenfrequencies.

$$p(\boldsymbol{x},\omega) = \sum_{n=0}^{\infty}\sum_{m=0}^{\infty} \frac{j\omega\rho_0\Psi_{nm}(\boldsymbol{x})}{V\left[k_{nm}^2 - k^2\right]} \int_s \Psi_{nm}(\boldsymbol{y})\boldsymbol{u}(\boldsymbol{y}).\boldsymbol{n}\,dS \tag{7.6.}$$

In this expression, $\boldsymbol{u}(\boldsymbol{y}).\boldsymbol{n}$ is the surface normal velocity of the cavity wall at vector position $\boldsymbol{y}$, and ρ_0 is the ambient fluid density. For this application, the integral on the right of this expression can be written as the sum of three integrals each over a separate part of the cavity surface, as shown in equation 7.7.

$$\begin{aligned}\int_s \Psi_{nm}(\boldsymbol{y})\boldsymbol{u}(\boldsymbol{y}).\boldsymbol{n}\,dS = &\int_{\phi=0}^{\phi_0}\int_{\theta=0}^{2\pi} \Psi_{nm}(\phi,\theta)u_d(\phi,\theta)h_0^2\sin\phi\,d\theta\,d\phi \\ &+ \int_{\phi=0}^{\phi_0}\int_{\theta=0}^{2\pi} \Psi_{nm}(\phi,\theta)u_e(\phi,\theta)\left(h_0+\mu\right)^2\sin\phi\,d\theta\,d\phi \\ &+ \int_{h=h_0}^{h_0+\mu}\int_{\theta=0}^{2\pi} \Psi_{nm}(\phi,\theta)u_h(h,\theta)h^2\sin\phi_0\,d\theta\,dh\end{aligned} \tag{7.7.}$$

The first double integral is performed over the diaphragm side of the compression-cavity surface, where the function $u_d(\phi,\theta)$ describes the normal velocity. The second double integral is performed over the exit side of the compression cavity surface, where the function $u_e(\phi,\theta)$ describes the normal velocity. Finally the third integral is performed over the small truncated-conical surface at the outside diameter of the compression cavity, where the function $u_h(h,\theta)$ describes the normal velocity.

For the annular-channel compression-driver analysis on page 139, it was possible to to reduce the set of relevant eigenfunctions because each of these three normal velocity functions were shown to be invariant to circumferential angle. It is a little more complex in this case. The diaphragm, $u_d(\phi,\theta)$, and edge velocity, $u_h(h,\theta)$, functions are once again invariant to circumferential position. However, the exit-side normal-velocity function, $u_e(\phi,\theta)$, is not circumferentially invariant, but rather circumferentially periodic, such that it follows the expression

$$u_e(\phi,\theta)=u_e(\phi,\theta+2\pi/N) \tag{7.8.}$$

where N is the number of radial channels in the phase plug. However, reduction of the eigenset is still possible and can be most easily demonstrated by writing the circumferential variation of the exit surface velocity using a Fourier series [47, p.692] as

$$u_e(\phi,\theta)=\sum_{m=0}^{\infty} U_{e,m}(\phi)e^{jm\theta} \tag{7.9.}$$

For a phase plug with N radial channels then clearly

$$U_{e,m}(\phi)=0 \;\Big|_{0<|m|<N} \tag{7.10.}$$

which allows the summation range in equation 7.9 to be reduced to

$$u_e(\phi,\theta)=U_{e,0}(\phi)+\sum_{m=N}^{\infty} U_{e,m}(\phi)e^{jm\theta} \tag{7.11.}$$

While it is a little trivial to do so, it should be noted the it is also possible to write the diaphragm or edge normal-velocities in this form with the same terms. The integral on the right of 7.6, over the exit surface, can be written as

$$\int_{S_e} \Psi_{nm}(\boldsymbol{y})\boldsymbol{u}(\boldsymbol{y}).\boldsymbol{n}\,dS=\int_{S_e} A_{nm}P_{l_{nm}}^{m}(\cos\phi)\left(e^{-jm\theta}+e^{jm\theta}\right)\sum_{m=0,\pm N}^{\pm\infty} U_{e,m}(\phi)e^{jm\theta}dS \tag{7.12.}$$

It is clear that, by the orthogonality of the set of functions $e^{jm\theta}\big|_{m\in z}$, the result is trivial when $0<|m|<N$. Thus, it is possible to use a reduced the set of eigenfrequencies and eigenfunctions excluding this range of m.

Indeed the strategy taken in this case is to set N to be high enough that the first circumferential eigenfunction has a corresponding eigenfrequency that is well above the desired bandwidth of the compression driver. Consequently, the same reduced set of eigenfrequencies and eigenfunctions with $m=0$ is used,

$$\Psi_n(\phi)=A_nP_{l_n}^{0}(\cos\phi) \tag{7.13.}$$

7.2.2 Suppression of modal excitation by channel geometry

For the case of the compression driver with radiating diaphragm occupying one spherical cap face of the cavity and with exit channels occupying the opposite spherical cap face, the integral on the right of expression 7.6 can be written as

$$2\pi h_0^2 \int_{\phi=0}^{\phi_0} \Psi_n(\phi) u_d(\phi) \sin\phi \, d\phi + 2\pi (h_0 + \mu)^2 \int_{\phi=0}^{\phi_0} \Psi_n(\phi) u_e(\phi) A(\phi) \sin\phi \, d\phi \qquad 7.14.$$

The first integral is over the diaphragm surface; the second is over the exit surface. The function $u_d(\phi)$ describes the normal velocity of the radiating diaphragm. The function $u_e(\phi)$ describes the acoustical velocity normal to the cavity surface in the channel openings. The function $A(\phi)$ describes the proportion of the circumference that is open to the channel entrances: this function determines the shape of the compression channels and, effectively, is proportional to the angular width of the compression cavity. In order to suppress the m-th compression cavity mode, it is clear that the sum of these two integrals must be zero.

If the radiating diaphragm is moving rigidly and axially, the normal velocity function $u_d(\phi)$ is given by the expression

$$u_d(\phi) = u_0 \cos\phi \qquad 7.15.$$

where u_0 is the axial velocity of the diaphragm. Provided that the following conditions are met:

- the compression cavity is small in volume;
- the channels leaving the compression cavity are of a geometry which allows wave propagation with wave-front shape coincident with the exit surface of the compression cavity;
- the modal behaviour of the compression cavity is suppressed;

then it may be assumed that within the bandwidth of the driver the channel entrance velocity function, $u_e(\phi)$, may be related to the volume velocity of the diaphragm radiator as

$$u_e \approx \frac{-\pi r_o^2}{A_T} u_O \qquad 7.16.$$

where A_T is the total open area of the channels on the output surface of the compression cavity, given by the expression

$$\int_{\phi=0}^{\phi_o} A(\phi)dS = A_T \tag{7.17.}$$

In other words, within the bandwidth of the compression driver, the compression cavity is incompressible and the input volume velocity is equal to the output volume velocity. Using these relationships, in order to avoid modal excitation in the compression cavity it is necessary for the condition

$$h_0^2 \int_{\phi=0}^{\phi_0} \Psi_n(\phi)\cos\phi\sin\phi\, d\phi - (h_0+\mu)^2 \frac{\pi r_o^2}{A_T} \int_{\phi=0}^{\phi_0} \Psi_n(\phi) A(\phi)\sin\phi\, d\phi = 0 \tag{7.18.}$$

to be met. From which it is obvious that the compression-channel-entrance area function $A(\phi)$ should be

$$A(\phi) = \frac{h_0^2}{(h_0+\mu)^2}\frac{A_T}{\pi r_o^2}\cos\phi \tag{7.19.}$$

Typically, $\mu \ll h_0$ and the approximation may be made that

$$A(\phi) \approx \frac{A_T}{\pi r_o^2}\cos\phi \tag{7.20.}$$

In any case, this approximation only introduces an inaccuracy in the compression ratio, not the derived channel shape. This indicates that the cavity exit channels should have a circumferential angular width that is proportional to the cosine of the polar angle. This results in more of the dome being covered at the outside edge compared to the centre. This is perhaps intuitive. The dome has a higher normal velocity at the centre compared to the outside edge. The channel exit velocity naturally acts upon the cavity modes in the opposite direction to the dome motion as while the dome moves into the cavity air flows out of the cavity in to the channels. The cosine weighting distributes this mirror velocity on the exit surface in exactly the same way that the normal velocity is arranged on the input surface.

In order to investigate this conclusion, an idealised compression-driver model was developed using the same construction and basic geometry as that introduced in section 7.1.4, shown in figure 7.8. The channel angular width is this time set according to equation 7.20. As before, the model is of a 10-degree section of an idealised radial-channel compression driver. It is only necessary to model a 10-degree section of the full geometry because of the circumferential periodicity of the arrangement. In this model, a detail of which is shown in

figure 7.10. A rigid axially moving dome radiator (turquoise) is coupled to a thin compression cavity (red). Both of these regions occupy the full 10-degree section. The blue area is a channel which is coupled to the compression cavity, this region has a circumferential angular width as outlined by equation 7.20. The channel is terminated with infinite wave-envelope elements such that it approximates a segment from an infinite conical horn. In effect, this is a model of an idealised radial-channel compression driver with 18 channels, a compression ratio of 1.7071 (as defined in Appendix X) and an perfect termination to the channels.

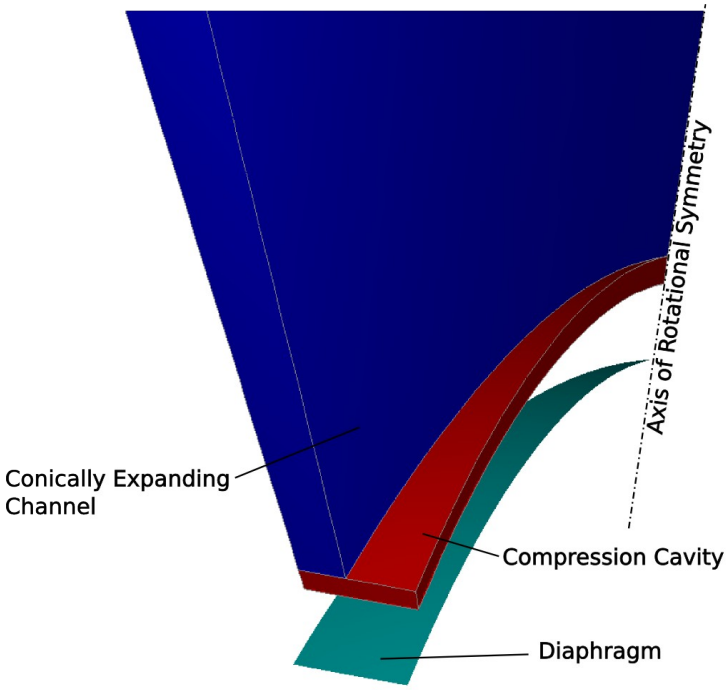

Figure 7.10. Detail from the idealised $\cos(\phi)$ *weighted channel style radial compression driver model using the Dodd dome and horn arrangement.*

Compared to the constant angular width version, shown in figure 7.8, it may be observed that the blue channel width is visibly narrower at the outside diameter of the model. The performance of the compression driver can be assesssed by looking at the pressure response in the channels of the driver to see how the pressure varies at different angles. If the channel is carrying a spherically spreading wave the pressure amplitude is constant at a given distance from the compression cavity. The pressures in the channel of the model are shown in figure 7.11 at comparable positions to those shown for the Dodd dome horn arrangement, (figure 7.7) and for the Henricksen-style constant circumferential-angle channel arrangement (figure 7.9). As before, the pressures have been normalised by the expression given in equation 7.1. The three pressures are within 1dB up to a frequency of $ka=4.2$. This is a significant improvement compared to the Henricksen style plug where the pressures are

within 1dB up to $ka = 2.58$. However, as was seen with the Henricksen and the unplugged Dodd case, at high frequencies the pressures become less consistent.

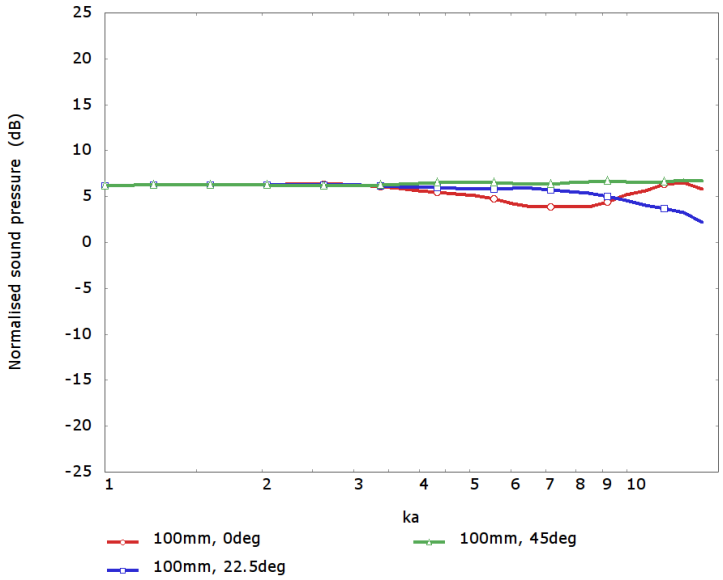

Figure 7.11. Normalised pressure response of an 18-channel idealised $\cos(\phi)$ *weighted channel style radial compression driver using the Dodd dome and horn arrangement, plotted versus normalised frequency for three sampling locations 100mm down the horn.*

7.2.3 A practical driver based on the cos-weighted radial-channel phase plug

The $\cos(\phi)$ weighted radial-channel approach was developed into a fully-working prototype in 2008. The prototype was part of a larger project to develop a coincident-source two-way mid- and high-frequency transducer [5]. This coincident source driver prototype was then subsequently used in the KEF Concept Blade loudspeaker, a one off prototype loudspeaker demonstrated at numerous events internationally [84].

A sectional drawing of the complete coincident source driver is shown in figure 7.12. The tweeter is located in the centre closest to the axis of rotational symmetry at the bottom edge of the half section. The tweeter dome is constructed from 25µm titanium and has an angle of curvature of approximately 35 degrees. The rigidity of the dome is increased by the use of a voice coil former, also in 25µm titanium, with an extended top edge that forms a triangular strut when assembled with the titanium dome as illustrated in 7.13. This arrangement of dome and former is described by Dodd in his 2005 patent [85]. Without the extended former the mechanical “breakup” mode occurs at 21.2kHz, while with the extended former the mechanical “breakup” mode occurs at 33.7kHz. This tweeter and former were originally designed for a direct radiating tweeter first introduced in 2006. The dome and former were chosen as the high frequency of the “break up” mode is ideal for our purposes given that the

theory outlined in the previous section assumes that the dome is perfectly rigid. The high break-up mode at least means that this is a reasonable assumption in the audio band.

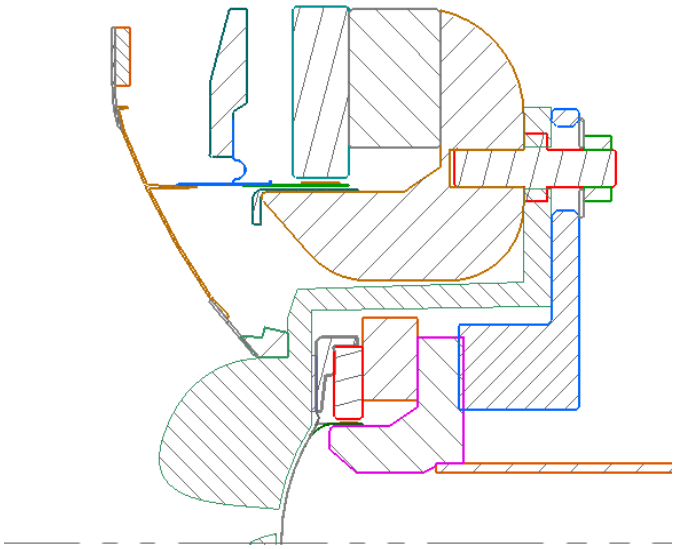

Figure 7.12. Half-sectional drawing of the complete prototype coincident source driver

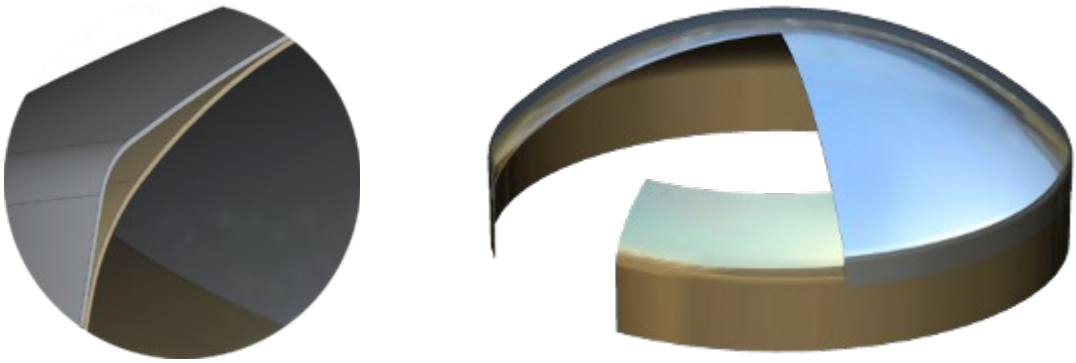

Figure 7.13. 3D CAD sectional views of the tweeter dome and extended former.

During the development of this driver, it was quickly realised that there is a practical difficulty with the new radial-channel phase-plug geometry. From the FEM modelling of this driver, it was determined that the minimum number of channels required to avoid circumferential pressure variation is twelve. As the twelve cosine-weighted channels approach the central axis of the phase plug, the distance between them becomes vanishingly small and results in a geometry that, in reality, is impossible construct. The most straightforward practical solution to this problem is to combine the channels at the centre of the plug into a single opening. However, FEM analysis of this approach highlighted severe performance degradation. Eventually, a solution was found. The number of radial channels

may be reduced at the very centre of the plug without any obvious problem because of circumferential pressure variation in the compression cavity. The resulting geometry is shown in figure 7.14. The outer diameters of the phase plug have 12 radial channels, while at the very centre the number of channels is reduced to 6. The $\cos(\phi)$ channel-weighting is still followed for both the 12-channel and 6-channel regions of the phase plug.

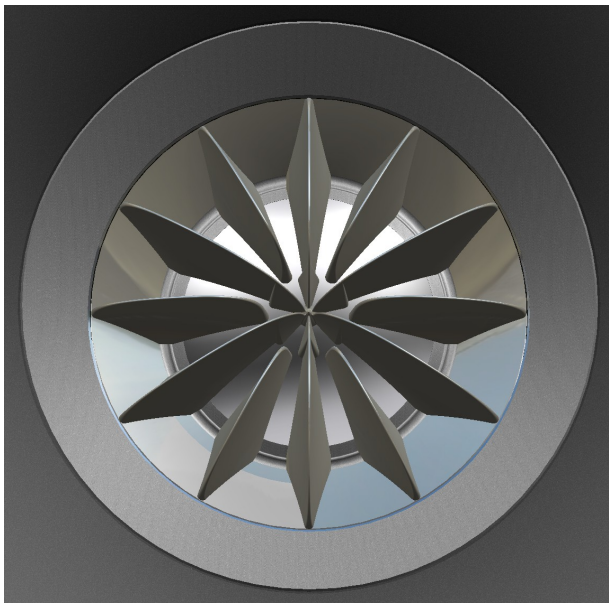

Figure 7.14. 3D CAD rendering of the practical implementation of the cos weighted radial-channel phase plug showing inner area with fewer radial channels.

The frequency response of the tweeter measured at 2.83 V rms in a large wall at 1m on axis with the driver is shown in figure 7.15 both with the radial-channel phase plug and with a smooth horn without a phase plug. On both measurements the large peak at approximately 33kHz corresponds to the breakup of the dome. Both responses are smooth. The gentle downward slope from 2kHz to 20kHz is a result of the horn loading of the diaphragm. The diaphragm itself moves with approximately constant acceleration amplitude in this frequency range. There are two encouraging observations about the version with the radial-channel phase plug in place. Firstly, the response is increased in level over a reasonably wide frequency band from 5.5kHz to 20kHz by a maximum of 4.5dB. Secondly, there appears to be a slight improvement of the smoothness of the response below 15kHz ($ka \approx 3.5$). However, the efficiency boost ends relatively abruptly at the top of the frequency response above 20kHz ($ka \approx 4.65$). This ties in very well with the idealised models shown in the previous chapters. Firstly, figure 7.9 shows irregularity occurring at $ka \approx 3$ for the idealised case of the Dodd dome and horn geometry. This is approximately the same frequency range area that appears to be smoother on the real driver with the radial-channel phase plug in

place. Secondly, figure 7.11 shows irregularity occurring above $ka \approx 4.5$ for the idealised model of the cos-weighted radial-channel compression driver. This is roughly the same frequency above which the increased efficiency is no longer seen in the real driver.

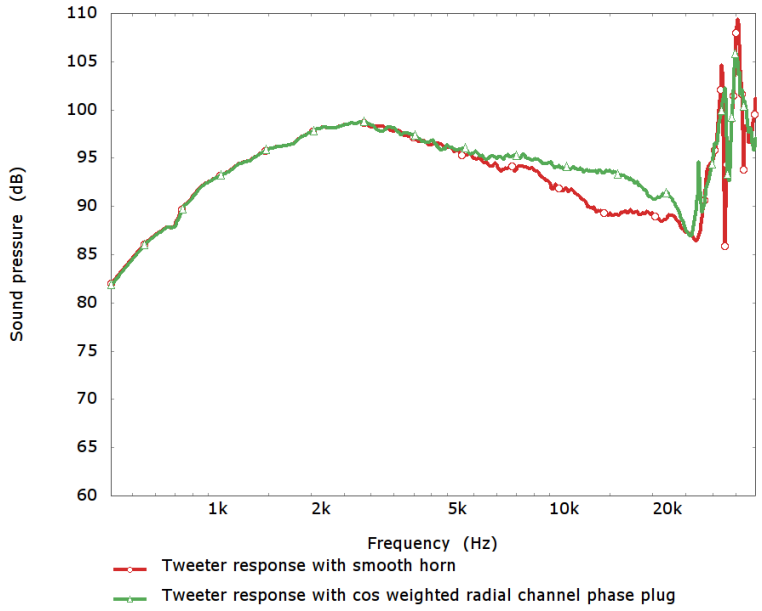

Figure 7.15. Measured tweeter performance of prototype loudspeaker with Dodd smooth horn geometry and cosine weighted phase plug.

The performance of the prototype driver was largely a success for the radial-channel phase plug concept. However, it does highlight that further work is required to maintain the efficiency increase to higher frequencies.

7.3 Improved modal suppression by cavity shaping for the radial-channel phase plug

The $\cos(\phi)$ channel weighting improved the behaviour of the idealised compression driver considered in section 7.2.2. However, there is clearly some progress still to be made at the top end of the response above $ka = 4$. The high-frequency limit is set by the lowest of either the circumferential periodicity becoming significant or the compliance of the compression cavity becoming significant. The reader may recall that the eigenset that was used when determining the $\cos(\phi)$ channel weighting was reduced by making the assumption that the circumferential periodicity of the geometry is sufficiently high that circumferential pressure variation would not occur in the bandwidth of the driver. The compliance of the compression cavity was assumed to be insignificant when it was approximated in equation 7.16 that the cavity input volume velocity was equal to the cavity output volume velocity.

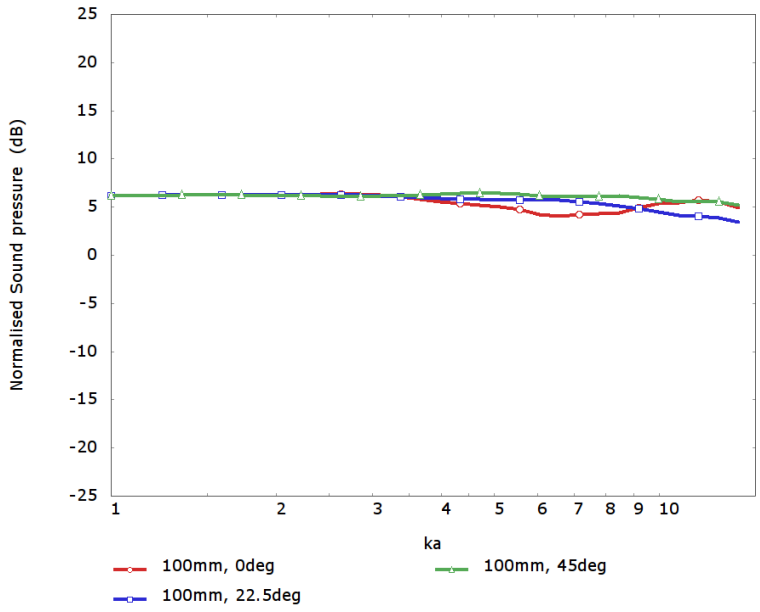

Figure 7.16. Normalised pressure response of a 24 channel idealised $\cos(\phi)$ *weighted channel style radial compression driver using the Dodd dome and horn arrangement, plotted versus normalised frequency for three sampling locations 100mm down the horn.*

The first of these possibilities is most easily eliminated by re-running the idealised compression-driver model with a different circumferential periodicity. The equivalent pressure results for a 7.5-degree segment model, corresponding to a 24 channel compression driver, are shown in figure 7.16. The results of the compression driver with higher circumferential periodicity are extremely close to the original 18 channel model up to a frequency of $ka=7$. Above this frequency the pressures from the 24 channel driver model are generally more consistent than the 18 channel model. This would seem to indicate that the variations in the pressure responses seen above $ka=4$ are not as a result of the periodicity effect and are likely to occur because of the compliance of the compression cavity.

It was found in chapter 6, for the case of the annular compression driver, that modal suppression performance could be greatly improved by shaping the cavity thickness such that the rigid body mode of the compression cavity is identical to the normal velocity profile of the radiating diaphragm. This adjustment makes the normal velocity function of the dome orthogonal to the higher-order eigenfunctions. The dome itself does not then excite these modes. Cavity shaping in this way greatly reduces the modal suppression deterioration at higher frequencies due to the compliance effect as it is no longer necessary that the cavity exit velocity modal excitation compensates for the diaphragm modal excitation.

The cavity shaping approach should be equally applicable to the radial case and would be expected to improve the modal suppression. In order to investigate this, a FEM model was

constructed using the cavity shape outlined on page 172. The required shape for the exit channels is unaffected by this change, the derivation of the $\cos(\phi)$ area weighting on page 213 does not make any assumption about the thickness-profile of the compression cavity other than that it is narrow in h.

The FEM model is again of an idealised compression driver with rigid axially moving dome diaphragm a 0.5mm cavity thickness, measured at the axis of rotation, and infinite conically expanding radial channels. The normalised pressure response at the same three positions in the horn are shown in figure 7.17 for the cavity shaped $\cos(\phi)$-weighted idealised radial-channel compression driver. The pressure responses are within 1dB up to $ka=8.5$. This is a significant improvement over the comparable responses without cavity shaping, which were shown in figure 7.16.

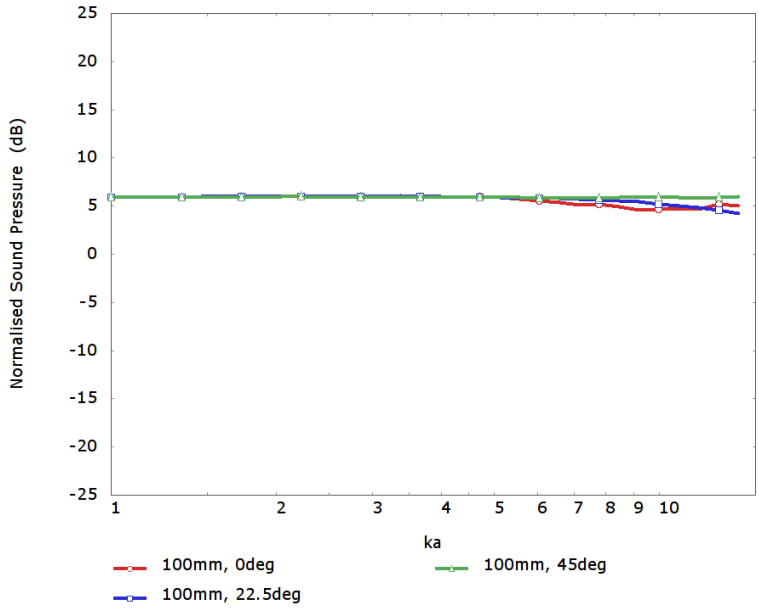

Figure 7.17. Normalised pressure response of a 24-channel idealised $\cos(\phi)$-weighted channel style radial compression driver using the Dodd dome and horn arrangement with $\cos(\phi)$ cavity thickness shaping, plotted versus normalised frequency for three sampling locations 100mm down the horn.

It took several attempts to find the horn and cavity arrangement that gave this response. The cavity width is arranged to be in proportion to the normal velocity of the rigidly moving dome. Thus, in this case, the width of the cavity, $\mu(y)$ is $\mu_0\cos(\phi)$, where μ_0 is the cavity width at the axis of rotation.

Geometrically, this means that the dome and exit surface have the same surface curvature radius, equal to $h_0=a/\sin(\phi_0)$, and are offset along the axis of rotation by μ_0. It was previously found that for the best results the edge of the compression cavity should be

perpendicular to the radiator surface (see page 172). This arrangement naturally results in the exit side of the compression cavity having a greater angle of curvature than the radiator. This is shown schematically in figure 7.18 and given the notation $\hat{\phi}_0$.

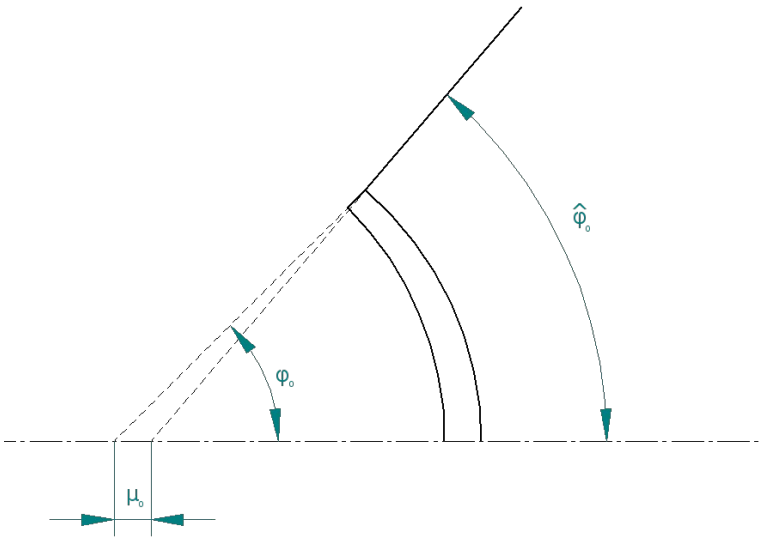

Figure 7.18. Schematic showing shaped compression cavity geometry.

The waveguide attached to the exit side must carry a wave which has wave-front coincident to the exit surface, thus the horn wall angle is equal to $\hat{\phi}_0$. The radial-channel area weighting, however, must be in terms of the entrance surface angle, not the exit surface angle, for the suppression to correctly function. On the other hand, it is important that the area weighting is constant for any given angle in the exit horn. For example, if the area weighting is defined in the spherical coordinate system centred at the focus of the entrance side of the compression cavity, this would result in an area weighting at the horn wall that would vary down the horn length. The solution is to arrange the weighting in a spherical coordinate system centred at the focus of the exit side and to map the horn angle, $\hat{\phi}$, to the equivalent radiator angle at the exit surface using the expression

$$\tan\phi = \frac{h_0 \sin\hat{\phi}}{h_0 \cos\hat{\phi} + \mu_0} \qquad 7.21.$$

This equivalent radiator angle should be used in the weighting function. Only after these fine adjustments to the geometry was it possible to obtain the performance seen in figure 7.17.

7.4 Practical problems with the radial-channel phase-plug geometry

The practical problems of the cosine-weighted radial-channel phase-plug geometry were discussed briefly in section 7.2.3. The derived radial-channel geometry requires that all channels extend to the very centre of the phase-plug cavity and meet at the axis of rotation, each covering an equal angular proportion of the dome. The width of the channels is vanishingly small at the axis of rotation. As the number of channels is increased, in order to counter the circumferential pressure variation problem, the angle that each channel covers in the centre of the phase plug becomes smaller and the vanishing channel width problem more severe. Ideally, the phase-plug geometry would permit either a small hole or a small post in the very centre of the construction to avoid the vanishing channel-width problem. However, there is no room for manoeuvre with the channel-geometry derivation as described. Rather than suppressing the excitation of all compression cavity modes, instead only the first N modes are suppressed. This allows alternative radial-channel geometries, which overcome these practical problems with the pure cosine geometry.

7.4.1 Alternative radial-channel geometries

In the same way as for the annular-channel phase plug, the cavity behaviour is described by a modal decomposition and the criterion for suppression of the cavity mode n is as before given by the expression

$$\int_{S_d} \Psi_n(\boldsymbol{y})\boldsymbol{u}_d(\boldsymbol{y}).\boldsymbol{n}\,dS + \int_{S_e} \Psi_n(\boldsymbol{y})u_e(\boldsymbol{y})\,dS = 0 \qquad 7.22.$$

where the first integral is over the diaphragm surface, S_d, and the second is over the open area of the cavity connecting to the phase-plug, S_e: the grey regions shown in figure 7.2.

In section 5.4, the parameter ζ_n^d was introduced to describe the cavity excitation from the diaphragm and is defined as

$$\zeta_n^d = \int_{S_d} \Psi_n(\boldsymbol{y})\boldsymbol{u}_d(\boldsymbol{y}).\boldsymbol{n}\,dS \qquad 7.23.$$

Assuming that modal suppression is working well, the cavity-exit normal velocity is constant over the open part of the compression cavity. Thus $u_e(\boldsymbol{z})$ is defined to be

$$u_e A(\boldsymbol{z}) \qquad 7.24.$$

where u_e is the constant channel entrance normal-velocity and $A(\boldsymbol{z})$ is an area weighting function that is unity at positions where the compression cavity is connected to the exit channels and zero at positions where the compression cavity is closed. It is assumed that the compression channels have a high order of periodicity in the circumferential direction. If this is true, modes with pressure variation in the circumferential direction can be ignored (as was outlined in section 7.2.1). The function $A(\boldsymbol{z})$ is defined to be composed of M functions, $A_m(\boldsymbol{z})$, whose linear combination in the proportions b_m describe the entrance area of the channels.

$$A(\boldsymbol{z}) = \sum_{m=1}^{M} b_m A_m(\boldsymbol{z}) \tag{7.25.}$$

To simplify the notation of the following expressions, the parameter ζ_{nm}^{e} is defined to be

$$\zeta_{nm}^{e} = \int_{S_e} \Psi_n(\boldsymbol{z})\, A_m(\boldsymbol{z})\, dS \tag{7.26.}$$

This parameter describes the modal excitation contribution of each of the functions $A_m(\boldsymbol{z})$. This allows the condition for the suppression of mode n to be written as

$$\zeta_n^d + u_e \sum_{m=1}^{M} b_m \zeta_{nm}^{e} = 0 \tag{7.27.}$$

While the compression driver is well behaved, the acoustical velocity u_e is related to the diaphragm velocity by

$$\zeta_0^d + u_e \sum_{m=1}^{M} b_m \zeta_{0\mathrm{m}}^{e} = 0 \tag{7.28.}$$

In other words, the volume velocity entering the cavity is equal to the volume velocity exiting the cavity. This is can be simplified to

$$\zeta_0^d + u_e A_T = 0 \tag{7.29.}$$

where A_T is the total exit channel area.

Inserting this into 7.28, the condition for the suppression of the nth mode can be written as

$$\frac{\zeta_n^d}{\zeta_0^d} - \sum_{m=1}^{M} \frac{b_m}{A_T} \zeta_{nm}^{e} = 0 \tag{7.30.}$$

In turn, this can be written in matrix form for the first N modes as

$$\begin{bmatrix} \zeta_{01}^{e} & \zeta_{02}^{e} & \cdots & \zeta_{0M}^{e} \\ \zeta_{11}^{e} & \zeta_{12}^{e} & \cdots & \zeta_{1M}^{e} \\ \zeta_{21}^{e} & \zeta_{22}^{e} & \cdots & \zeta_{2M}^{e} \\ \vdots & \vdots & \ddots & \vdots \\ \zeta_{N1}^{e} & \zeta_{N2}^{e} & \cdots & \zeta_{NM}^{e} \end{bmatrix} \begin{bmatrix} b_1/A_T \\ b_2/A_T \\ \vdots \\ b_M/A_T \end{bmatrix} = \begin{bmatrix} \zeta_0^d/\zeta_0^d \\ \zeta_1^d/\zeta_0^d \\ \zeta_2^d/\zeta_0^d \\ \vdots \\ \zeta_N^d/\zeta_0^d \end{bmatrix} \tag{7.31.}$$

Using this formulation, it is possible to construct phase-plug designs where the radial exit channels only cover part of the exit side of the compression cavity. This is easily achieved by choosing the area functions $A_m(\boldsymbol{z})$ so that they all exclude the area where the channels are not to be placed. Having determined these coefficients, the channel geometry may be calculated using the summation

$$A(\boldsymbol{z}) = \sum_{m=1}^{M} b_m A_m(\boldsymbol{z}) \tag{7.32.}$$

The exact shape of the phase plug which results from this derivation is dependent upon the choice of the functions $A_m(\boldsymbol{z})$. It should be noted that there is no guarantee that the phase-plug design that results from the process described above is either practical or physically possible. For example, the combined area profile calculated from the summation in 7.32 could give negative area results. So the designer must take care in order for the resulting design to be of practical use.

Radial-channel phase plug with part open area

Another option to make a more practical radial-channel phase plug is to only partially cover the radiating diaphragm and introduce an open hole to avoid the problematic central region. In this situation, the excitation of the compression cavity is considered to come from three separate volume velocities on the various parts of the surface of the cavity. S_d the radiating diaphragm surface, S_e the exit side of the compression cavity where the phase plug is located and S_h the part of the exit side that is totally open. In this case, the condition for the suppression of the cavity modes is

$$\int_{S_d} \Psi_n(\boldsymbol{y}) \boldsymbol{u}_d(\boldsymbol{y}) . \boldsymbol{n} \, dS + \int_{S_e} \Psi_n(\boldsymbol{y}) u_e(\boldsymbol{y}) dS + \int_{S_h} \Psi_n(\boldsymbol{y}) u_h(\boldsymbol{y}) \, dS = 0 \tag{7.33.}$$

The first of these three integrals is now very familiar and, once again, the parameter ζ_n^d is used to describe the excitation from the dome

$$\zeta_n^d = \int_{S_d} \Psi_n(\boldsymbol{y}) \boldsymbol{u}_d(\boldsymbol{y}).\boldsymbol{n}\, dS \tag{7.34.}$$

This parameter may be computed either analytically or numerically for a particular radiating diaphragm.

The second term is handled in exactly the same manner as for the complete radial-channel phase plug in the preceding section. The parameter ζ_{nm}^e is used to decompose the integral into a weighted summation of these determined integrals as

$$\int_{S_e} \Psi_n(\boldsymbol{y}) u_e(\boldsymbol{y}) dS = u_e \sum_{m=1}^{M} b_m \zeta_{nm}^e \tag{7.35.}$$

where

$$\zeta_{nm}^e = \int_{S_e} \Psi_n(\boldsymbol{z})\, A_m(\boldsymbol{z}) dS \tag{7.36.}$$

and u_e is the constant surface-normal acoustical velocity over the open parts of the compression-cavity exit surface.

Finally, the third integral may be directly evaluated as the velocity over this part of the surface should also be constant and equal to u_e when the compression driver is behaving well

$$\int_{S_h} \Psi_n(\boldsymbol{y}) u_h(\boldsymbol{y})\, dS = u_e \int_{S_h} \Psi_n(\boldsymbol{y}) dS = u_e \zeta_n^h \tag{7.37.}$$

The condition for the suppression of the nth mode in the compression cavity is now

$$\zeta_n^d + u_e \left(\zeta_n^h + \sum_{m=1}^{M} b_m \zeta_{nm}^e \right) = 0 \tag{7.38.}$$

While the compression driver is behaving well, the channel exit acoustical velocity is related to the volume velocity of the radiating diaphragm and the total open area of the exit side of the plug, A_T, as

$$\zeta_0^d + u_e A_T = 0 \tag{7.39.}$$

Using this expression to eliminate u_e the condition for suppression of the nth mode is

$$\frac{\zeta_n^d}{\zeta_0^d} - \frac{\zeta_n^h}{A_T} - \sum_{m=1}^{M} \frac{b_m}{A_T} \zeta_{nm}^e = 0 \tag{7.40.}$$

This can be written in matrix form for the first N modes as

$$\begin{bmatrix} \zeta_{01}^{e} & \zeta_{02}^{e} & \cdots & \zeta_{0M}^{e} \\ \zeta_{11}^{e} & \zeta_{12}^{e} & \cdots & \zeta_{1M}^{e} \\ \zeta_{21}^{e} & \zeta_{22}^{e} & \cdots & \zeta_{2M}^{e} \\ \vdots & \vdots & \ddots & \vdots \\ \zeta_{N1}^{e} & \zeta_{N2}^{e} & \cdots & \zeta_{NM}^{e} \end{bmatrix} \begin{bmatrix} b_1/A_T \\ b_2/A_T \\ \vdots \\ b_M/A_T \end{bmatrix} = \begin{bmatrix} \zeta_0^d/\zeta_0^d - \zeta_0^h/A_T \\ \zeta_1^d/\zeta_0^d - \zeta_1^h/A_T \\ \zeta_2^d/\zeta_0^d - \zeta_2^h/A_T \\ \vdots \\ \zeta_N^d/\zeta_0^d - \zeta_N^h/A_T \end{bmatrix} \quad 7.41.$$

This formulation can now be used to design radial-channel phase plugs with an alternative channel shape to the pure cosine weighting. The next section follows the design of a radial-channel phase plug in its entirety including use of both the alternative radial-channel phase-plug construction approaches. This section serves to highlight some of the considerations in applying these two new techniques.

7.5 The design of a radial-channel compression driver

This section outlines the design of a radial-channel compression driver from the FEM modelling stage through to prototyping. The driver in question is a 25mm dome tweeter designed for use in high-fidelity products. The basic tweeter driver assembly shown in figure 7.19. A full description of the driver is given in Appendix XII. The tweeter design is almost fully complete in this figure and, indeed, is a working design in this form. However, a radial-channel phase plug was added to increase the sensitivity and improve dispersion.

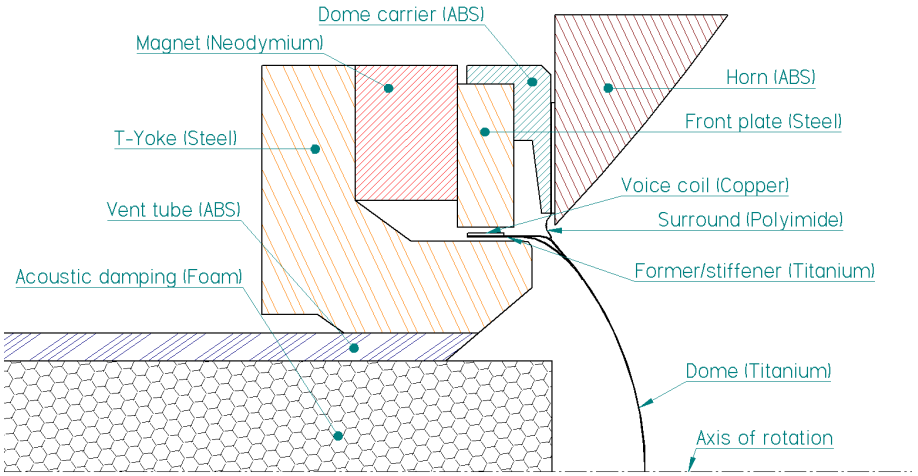

Figure 7.19. CAD drawing of the basic tweeter assembly before the design of the phase plug.

7.5.1 The design of the compression cavity

The normalised zeta parameters are critical to the performance of a compression driver. The closer these parameters are to the ideal of

$$\frac{\zeta_n^d}{\zeta_0^d} = \delta_{0n} \qquad 7.42.$$

the better the performance of the compression-cavity modal-suppression methods. With the compression driver design considered now, there is the added complication that, although it is very well behaved, the diaphragm is not perfectly rigidly moving. This makes it very difficult to directly apply the techniques of the previous chapter. The diaphragm velocity results that were calculated in the mechanoacoustical FEM model of the tweeter without the phase plug, presented in Appendix XII, were used to approximately calculate the zeta values of several different candidate compression-cavity designs. To perform this calculation, besides the velocity of the diaphragm, it is necessary to know the mode shapes of the cavity. These were computed using FEM models of the various candidate designs. As the dome moves non-rigidly, it is possible that the zeta parameters vary with frequency. To show this in the results, the zeta parameters were calculated for every solution frequency of the mechanoacoustical FEM model. This effectively redefines the zeta parameters to be functions of frequency

$$\zeta_n^d(\omega) = \int_{S_d} \Psi_n(\boldsymbol{y})\,\boldsymbol{u}_d(\boldsymbol{y},\omega).\boldsymbol{n}\,dS \qquad 7.43.$$

Four candidate compression cavities are shown in figure 7.20, given the labels J019, J020, J021 and J022.

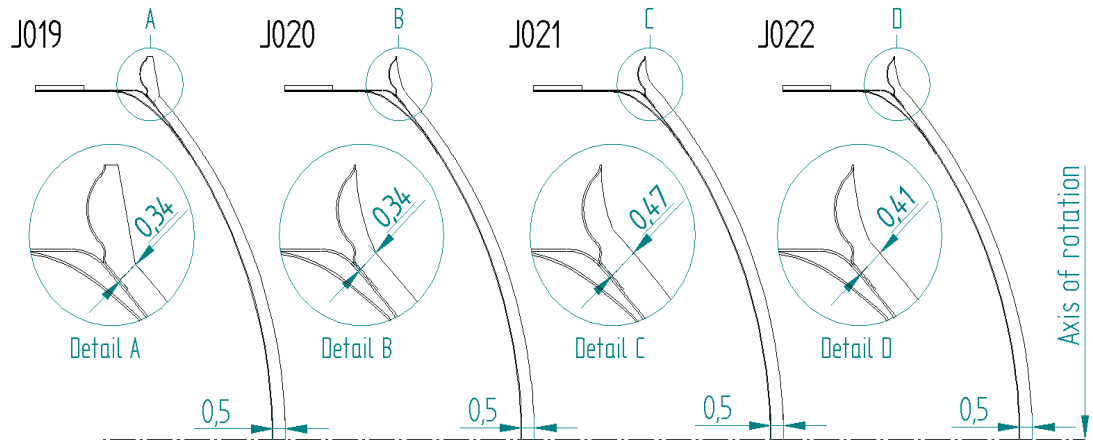

Figure 7.20. Four candidate compression-driver cavity geometries with subtle variations to the construction of the exit surface.

The first of the cavities, J019, is already a little way into the design process: the exit side of this cavity is constructed with a single radius that follows the shifted design approach being a 0.5mm axially displaced copy of the radius of the dome. The edge of this cavity, covering the surround, is relatively bluntly constructed with a straight join between the radius and the cavity outer diameter. J020 has the same basic construction as J019 with a refinement to the outer diameter of the cavity, which is constructed from a curve tangent to the main exit surface curve. Additionally, the width of the cavity fades to zero at the very outside diameter. The motivation for this change is to try to reduce the cavity volume over the surround. The basis for this is in chapter 6, that suggests that the cavity thickness should be proportional to the normal-velocity profile of the diaphragm. The normal velocity falls across the surround to zero at the clamped outer diameter and, consequently, it follows that the thickness profile should also fall to zero. Thirdly, J021 uses a cavity profile of a constant thickness. In other terms the exit surface of the cavity is constructed from a single arc that is concentric with the main arc of the dome. The edge construction is similar to J020. Finally, J022 is a blend of J020 and J021 with the single curve of the exit side neither purely concentric or shifted. The following four figures show the normalised zeta functions, $\zeta_n^d(\omega)/\zeta_0^d(\omega)$, calculated for each of these candidate geometries.

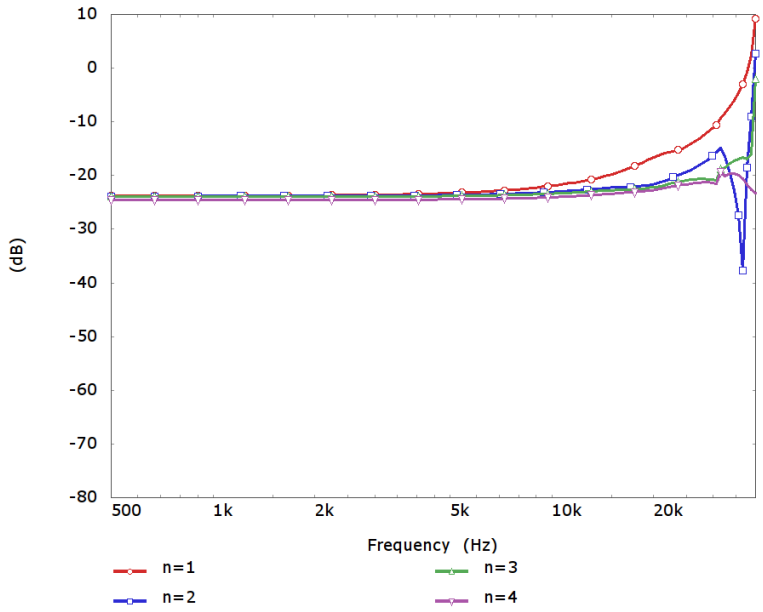

Figure 7.21. Computed $\zeta_n^d(\omega)/\zeta_0^d(\omega)$ functions for the candidate compression cavity geometry J019.

The four normalised zeta functions of the first cavity, J019, have approximately the same value at low frequencies. This is also the case over a wide range of the audio band up to

approximately 8kHz. The level of the functions increases quite dramatically at high frequencies.

The second cavity, J020, has completely different proportions of the functions at low frequencies, with the higher terms in particular at a much lower level than J019. In all four of the shown functions, there is a clear dip at high frequencies. The trend at the top of the computed range is quite similar to the previous result, with all four functions increasing dramatically.

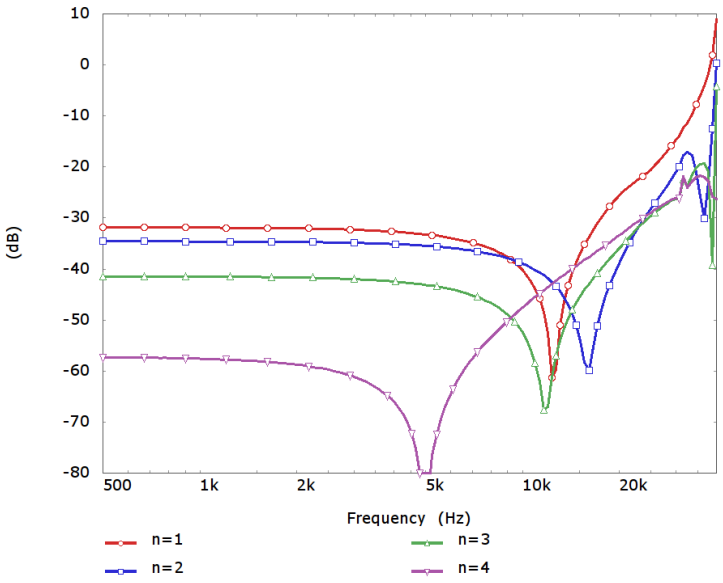

Figure 7.22. Computed $\zeta_n^d(\omega)/\zeta_0^d(\omega)$ functions for the candidate compression cavity geometry J020.

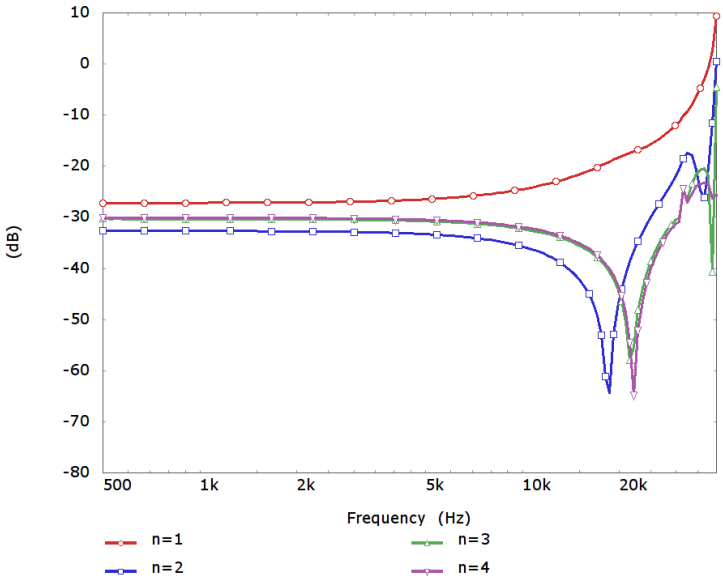

Figure 7.23. Computed $\zeta_n^d(\omega)/\zeta_0^d(\omega)$functions for the candidate compression cavity geometry J021.

The third geometry, J021, exhibits some features of each of the previous two: there is a clear dip in three of the four shown functions. However, no dip is seen in the function $n=1$. Again, the same upward trend is visible at high frequencies. At low frequencies, the functions are of quite a similar level to one another. Interestingly, the level is lower than J019: this is perhaps not what would have been expected given that J019 is based on a shifted cavity design, whereas J021 is a concentric design. This hints that the detail of the outside diameter of the cavity is very important, an area that was given little consideration in J019.

Finally, the functions computed for J022 are similar to J021, with three of the four shown functions having a dip in the response and the same upward trend at high frequencies. However, the levels of the functions are slightly different at low frequencies.

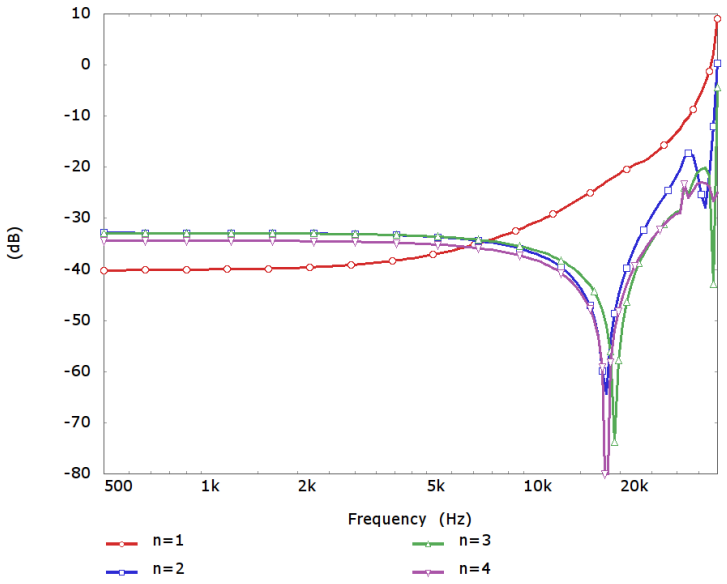

Figure 7.24. Computed $\zeta_n^d(\omega)/\zeta_0^d(\omega)$ functions for the candidate compression cavity geometry J022.

From visual inspection of the computed $\zeta_n^d(\omega)/\zeta_0^d(\omega)$ functions, design J020 was chosen as the most promising. The decision is not completely clear cut. However, there are some distinct reasons for selecting this option. Firstly, J020 has the lowest level of the $\zeta_n^d(\omega)/\zeta_0^d(\omega)$ functions at low frequencies. All four of the results show a general upward trend at high frequencies. This appears to be the influence of the first breakup mode of the dome on the functions, which is extremely undesirable from a modal control point of view as the modal suppression methods require that the relative excitation of the acoustical cavity modes does not vary with frequency. Given that it is not possible to find a cavity geometry that avoids this upward trend, then it is thought most sensible to choose the geometry with the lowest values of $\zeta_n^d(\omega)/\zeta_0^d(\omega)$ corresponding to the least excitation of the cavity modes

from the diaphragm motion. From this point of view the dips in some of the $\zeta_n^d(\omega)/\zeta_0^d(\omega)$ functions are quite helpful in lowering the responses at high frequencies. For geometry J020, the four $\zeta_n^d(\omega)/\zeta_0^d(\omega)$ functions remain below -20dB up to a frequency of 25.3kHz compared to 14.6kHz, 17.1kHz and 21.4kHz for geometries J019, J021 and J022, respectively.

7.5.2 The design of the compression-driver channel entrances

Having settled on a geometry for the compression cavity, the next stage in the design process is to find the shape of the phase-plug channel entrances. To separate this stage in the design from the next step, which is to work on the flaring and blending of the channels, rather than modelling the complete driver with the MF cone and infinite-baffle radiation, the tweeter assembly with full mechanical parts and rear acoustical arrangement was instead modelled with the radiation from the front of the dome coupled to an infinite conical region. This may be achieved using wave-envelope finite elements, as already introduced earlier in this chapter. For example, figure 7.25 shows the finite element axisymmetric mesh of the underlying tweeter design without phase plug and with the front radiation from the dome coupled to an infinite conical horn. The angle of the infinite conical horn is the same as the throat angle of the small horn indicated in figure 7.19.

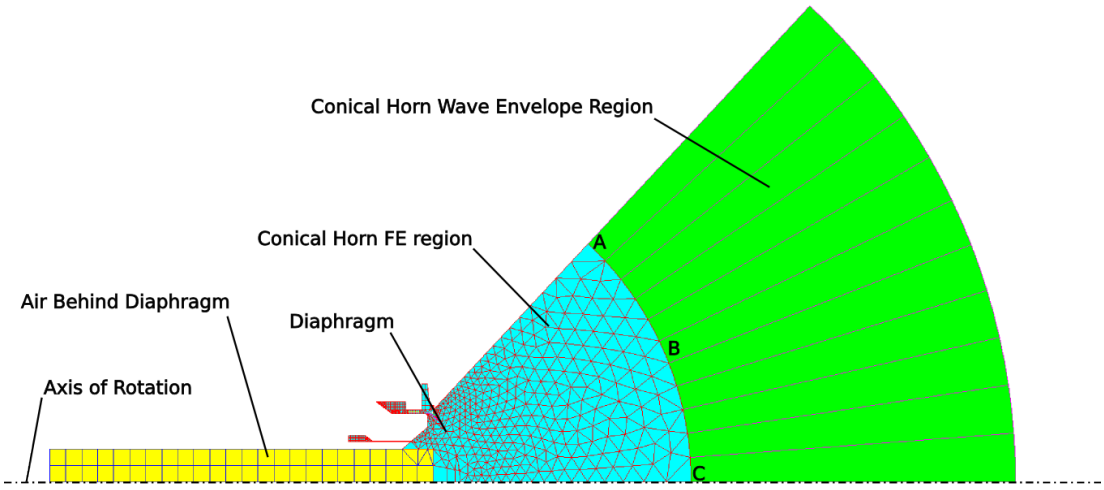

Figure 7.25. 2D axisymmetric mechanical and acoustical FEM model of the tweeter prior to phase-plug design coupled to an infinite conical horn.

The light-blue area of the model is a finite element mesh of acoustical elements with properties for air without any losses. The yellow region represents a region of acoustical absorption in the rear venting tube and is composed of acoustical finite elements having a complex bulk modulus and density in order approximate the lossy acoustical behaviour of foam. The green region at the front of the driver is a region of wave-envelope elements that

have the same acoustical properties as the blue region and model the infinite continuation of the conical horn.

The acoustical pressures at three positions in the infinite conical horn, for this 2D case without any phase plug, are shown in figure 7.26. These pressure responses are sampled at the intersection between the finite element and wave-envelope regions at the axis of rotation, the wall of the horn and a third position half-way between the other two sampling points. The mechanoacoustical model is driven with unit harmonic acceleration. The pressures at the three locations are similar to one another, within 1dB up to a frequency of 19kHz and within 3dB up to 25kHz, indicating that a close to ideal spherically spreading wave is propagating in the horn.

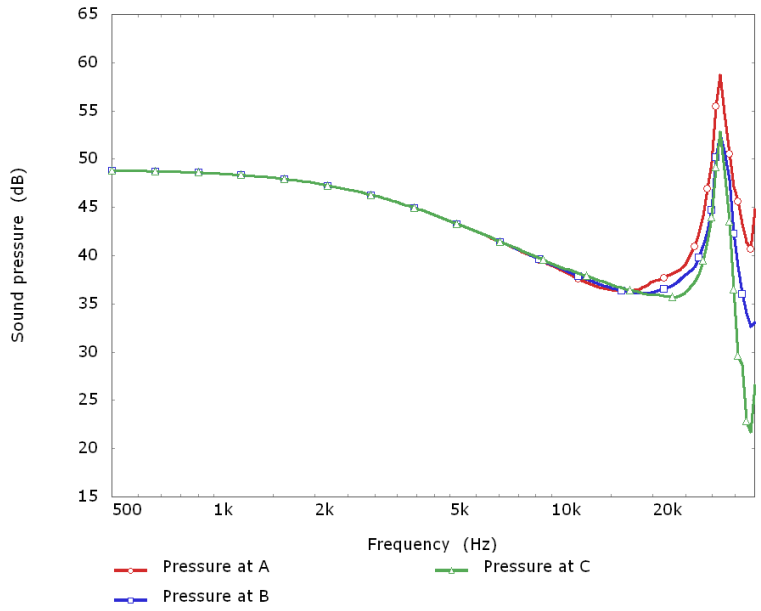

Figure 7.26. Acoustical pressure response at three positions in the infinite conical horn of the FEM model shown in figure 7.25 for unit axial harmonic acceleration of the voice coil region.

Modelling the tweeter in this manner allows various different geometries for the channel entrance to be examined independently from the effect of the channel flare and termination by simply expanding the channel-entrance geometry along the conical horn. The simplest channel geometry for the radial phase plug is a constant-angle design with each channel occupying a constant circumferential portion of the compression cavity exit surface. Figure 7.27 shows the geometry of an FEM model with infinite conically expanding channels, using the technique described above, with each channel occupying a constant-angle of the cavity exit surface. In this case, due to the symmetry of the situation, only a 20-degree segment of the tweeter is modelled, the angle of the region representing the channel is 9 degrees.

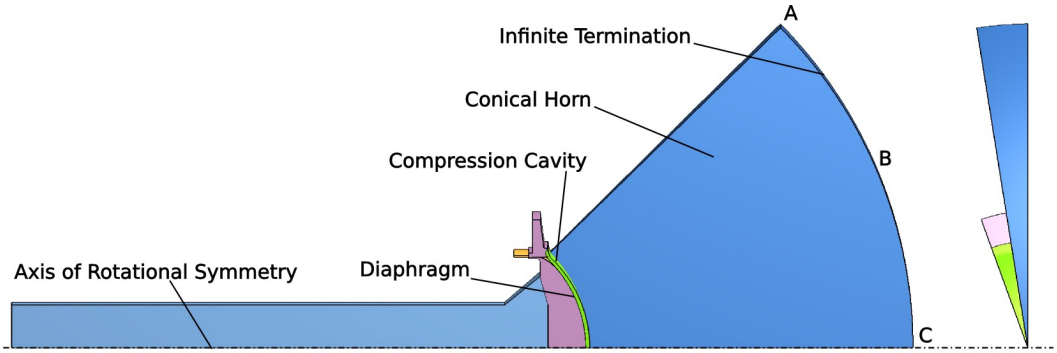

Figure 7.27. FEM model of tweeter with infinite conical termination and constant-angle radial phase-plug with 9 channels (wave-envelope region is not shown).

Figure 7.28 shows the pressure at three positions in the infinite conical channel at the intersection between the FEM and wave-envelope elements. Compared to the plots shown for the case without any phase plug, the level of the responses has increased as a result of the area reduction in the conical horn. There is also a degradation in the consistency of the pressures across the horn. For example, the pressure difference between the axis of rotation and the horn wall positions at 14kHz is 1.3dB on this model compared to 0.7dB on the case without the phase plug. There is also a large dip in the pressure at the axis of rotation which occurs at 26.9kHz.

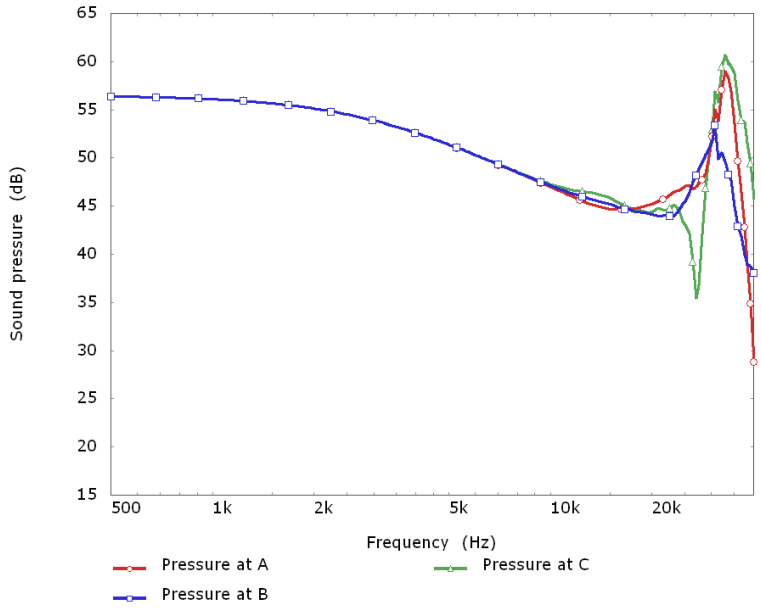

Figure 7.28. Acoustical pressure response at three positions in the infinite conical horn of the FEM model shown in figure 7.27 for unit axial harmonic-acceleration of the voice-coil region.

In section 7.2, the cosine weighting was demonstrated to be the ideal geometry for the radial channels when the diaphragm is a rigidly moving spherical cap. In this case, the domed

tweeter diaphragm is a relatively good approximation to this ideal. An infinite conical horn model of the tweeter was constructed with a cosine weighting applied to the radial channels. The geometry of this model is shown in figure 7.29. The channel pressure results are shown in figure 7.30 at the same three locations as for the previous infinite conical results.

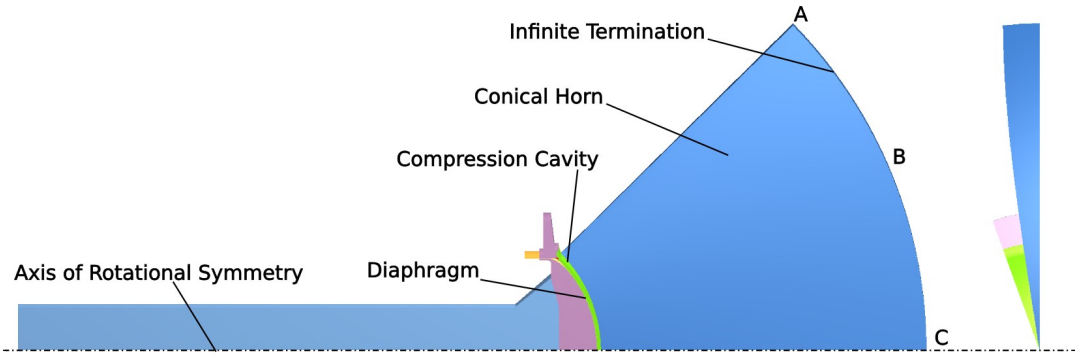

Figure 7.29. FEM model of tweeter with infinite conical termination and cosine weighted radial phase plug with 9 channels (wave-envelope region is not shown).

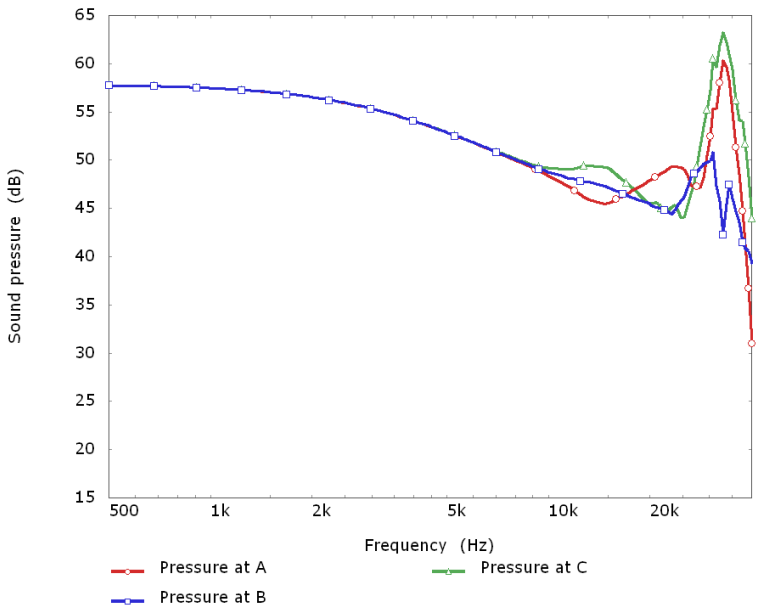

Figure 7.30. Acoustical pressure response at three positions in the infinite conical horn of the FEM model shown in figure 7.29 for unit axial harmonic acceleration of the voice coil region.

Interestingly, the pressures are significantly less consistent in this case, although the dip in the axial pressure response is avoided. The cosine weighting is correct for the case when the diaphragm is an axially-moving rigid spherical cap. In the previous models exemplary results were shown using this weighting. In this case, there is significant radiation from the diaphragm surround. In addition, the exit surface directly opposite the surround is completely covered and does not form part of the channel entrances. As the open area of the

channels mirrors the volume velocity profile of the radiating diaphragm, it seems natural that this extra radiation from the surround would require the channels to be wider towards the outside diameter of the cavity than the theoretical cosine weighting. This is perhaps the reason that the constant-angle cavity outperforms the cosine cavity in this case.

The final phase plug for the tweeter is to be incorporated into a small injection moulded horn positioned at the neck of the midrange cone and the combined part is to be manufactured in a single-piece injection moulding. It is vital that the geometry of the phase plug is manufacturable. This requires that the thickness of the mechanical parts be kept above a sensible minimum, that sudden changes in the wall thickness be avoided and, additionally, that the final complete part can be ejected from the moulding tool without any requirement for side actions. Neither the constant-angle design nor the cosine-weighted design are suitable for manufacture in this manner as the channel width tends to zero at the central axis of the driver.

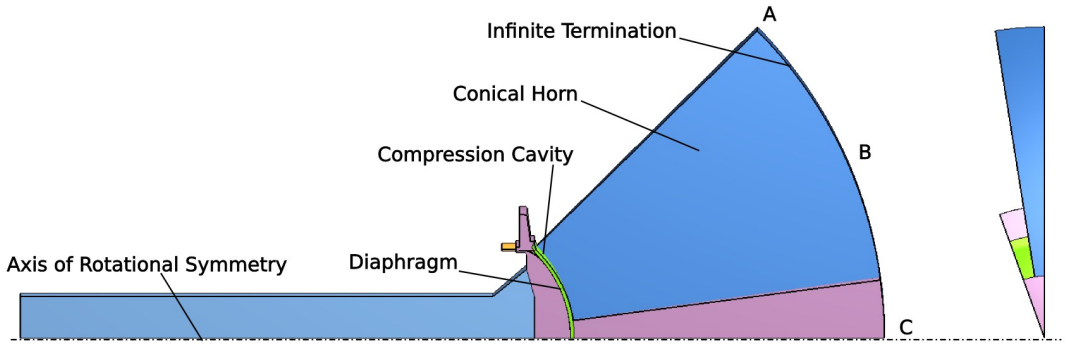

Figure 7.31. FEM model of tweeter with infinite conical termination and constant-angle radial phase plug with 9 channels with central 5mm diameter hole (wave-envelope region is not shown).

The most straightforward way to ensure a geometry that may be suitable for moulding is for a small region at the central axis of the driver to be excluded from the radial channels. This may be achieved either by a central open hole in the phase plug or a central peg in the phase plug. As an example of the effect of such a change, the FEM model shown in figure 7.27, with constant-angle infinitely-conically-expanding channels, was adapted to have a 5mm-diameter open hole in the centre of the geometry. The geometry of this model is shown in figure 7.31 and the corresponding channel pressure results in figure 7.32. Compared to the FEM model without the centre hole (figure 7.28) both the consistency of the pressure across the channels and also the severity of the dip in pressure at the central axis has severely deteriorated.

In section 7.4 of this chapter, two methods were outlined that allow the geometry of the radial channels to be derived in terms of a set of area-weighting functions in order to avoid the excitation of the first few compression cavity modes. The two approaches have significant advantages over the simple cosine-shaping method. Firstly, whereas the simple cosine shaping is only valid for the ideal situation when the radiating diaphragm is a rigidly moving spherical cap, the two new channel-geometry derivation techniques use the parameter zeta to characterise the excitation of the compression cavity by the radiating diaphragm. Secondly, by carefully choosing the area-weighting functions, the channel geometry may be controlled, to an extent. In particular, if all of the area-weighting functions are zero over a particular region of the exit surface, then the derived geometry is closed in that region. This is particularly helpful at the central axis of the driver where the channels inevitably become vanishingly narrow. Alternatively, a second technique was outlined that permits the calculation of radial-channel geometries with some part of the diaphragm not covered by the phase plug. Again this may be particularly helpful at the central axis of the driver.

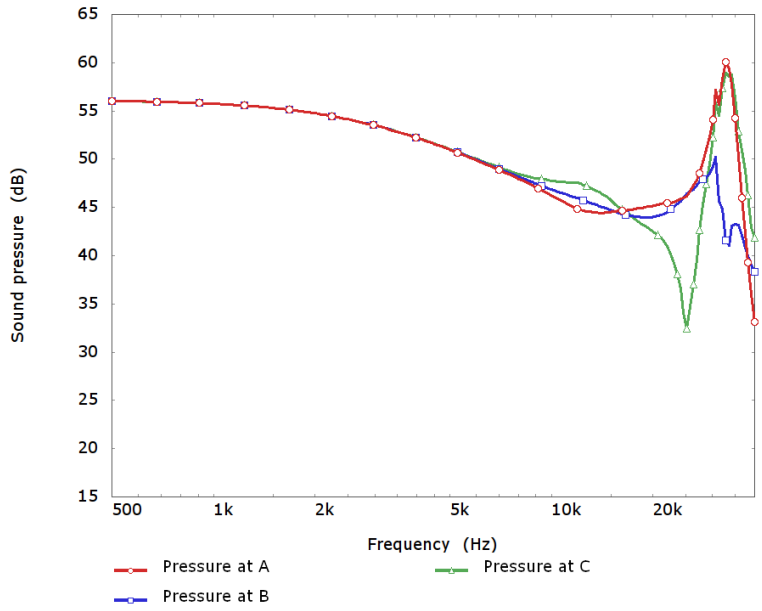

Figure 7.32. Acoustical pressure response at three positions in the infinite conical horn of the FEM model shown in figure 7.31 for unit axial harmonic-acceleration of the voice coil region.

Both of the techniques were attempted on the tweeter in question. The normalised zeta parameters, $\zeta_n^d(\omega)/\zeta_0^d(\omega)$, required for the geometry calculations were already approximated for this driver in section 7.5.1.

After some experimentation, the set of area weighting functions

$$A_m(\phi)=\cos(\phi(m-1)) \qquad 7.44.$$

was chosen, where ϕ is the the polar angular position on the channel entrance surface measured from the axis of rotation. Using these parameters for calculation, two geometries were constructed, one with a 5mm-diameter central hole in the compression driver and the other, with a central solid plug in the compression driver. The same infinite-channel FEM modelling approach was used so that the results are comparable to others in this section. Figure 7.33 shows the FEM model of the case with the 5mm central hole in the phase plug. Figure 7.34 shows the case with the 5mm central plug. Both geometries use five area weighting functions, have a compression ration of 1.8 and are of a 18-degree segment of the driver, equating to a 10-channel phase plug.

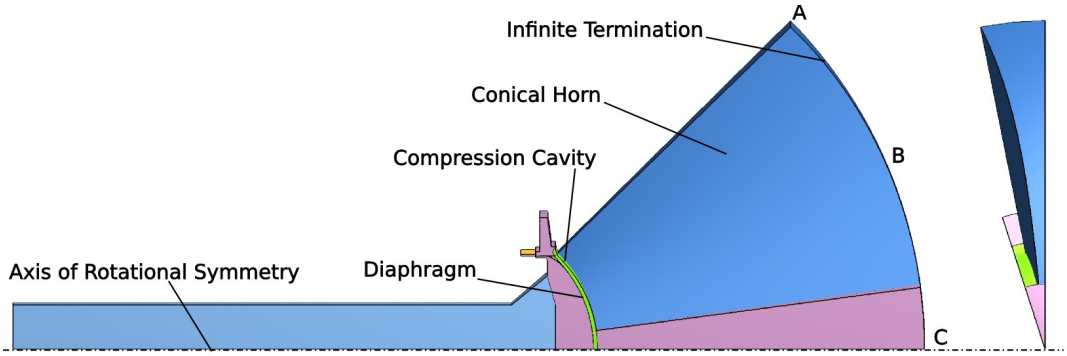

Figure 7.33. FEM model of tweeter with infinite conical termination and radial phase plug with central 5mm-diameter hole. Channel design method as described in section 7.4.1 (wave-envelope region is not shown).

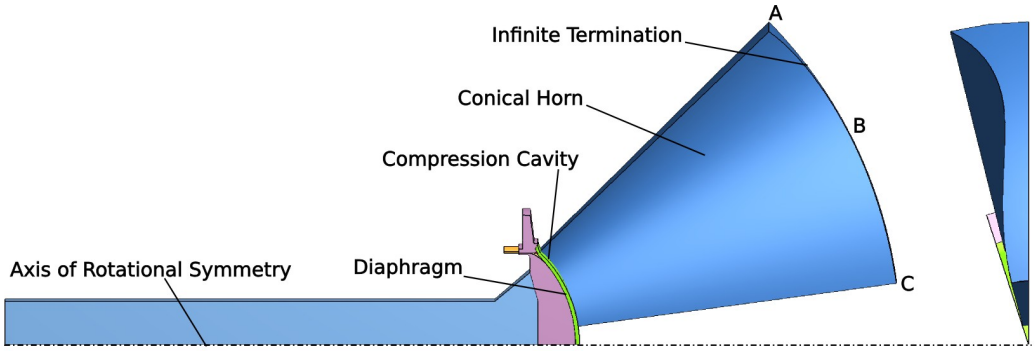

Figure 7.34. FEM model of tweeter with infinite conical termination and radial phase plug with central 5mm-diameter plug. Channel design method as described in section 7.4.1 (wave-envelope region is not shown).

With these parameters and area-weighting functions, both approaches result in realisable channel geometries. The geometry derived for the case with the central plug is particularly

interesting: adjacent to the horn wall, the channel width is much greater than on any of the previous geometries.

The corresponding channel pressure responses for the case with the central hole are shown in figure 7.35. The three channel pressures are similar to one another. All three pressures remain within 1dB of each other up to 20kHz and within 3dB of each other up to 23kHz. A slight dip is seen in the pressure response at the axis of rotation of the driver. Overall, this is a more consistent set of channel pressure results than any of the previously considered geometries.

Figure 7.36 shows the channel pressure results for the case with the central plug. The channel pressures are extremely close to one another and are within 1dB up to 24.5kHz. The three pressure responses are within 3dB up to a frequency of 30.5kHz. This result clearly outstrips the performance of any of the previous infinite conical horn models including the uncovered dome shown at the beginning of the section.

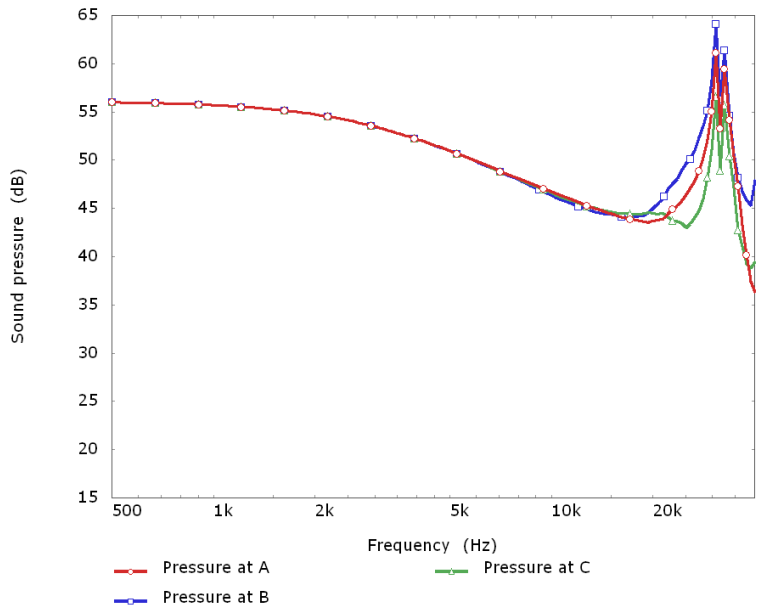

Figure 7.35. Acoustical pressure response at three positions in the infinite conical horn of the FEM model shown in figure 7.33 for unit axial harmonic acceleration of the voice coil region.

The results from applying the technique described in section 7.4 are very satisfying. However, it is interesting to ponder why the version with the open hole in the centre of the phase plug was still some way from the performance of the version with the central plug. Up to a frequency of 20kHz, the version with the central hole has equally good performance compare to the version with the central plug. It is in the frequency region 20kHz to 28kHz where the performance of the central hole version is poor. The main issue is seen at the axis

of rotation where there is a small dip in the pressure response at 25kHz. A similar dip was also seen on some of the previous models. It was observed that the depth of this dip is effected by the number of channels in the compression driver.

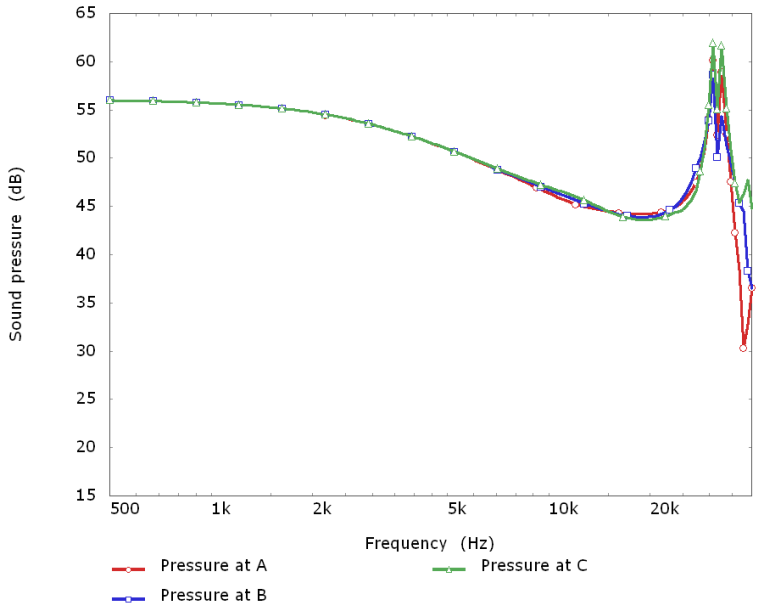

Figure 7.36. Acoustical pressure response at three positions in the infinite conical horn of the FEM model shown in figure 7.34 for unit axial harmonic acceleration of the voice coil region.

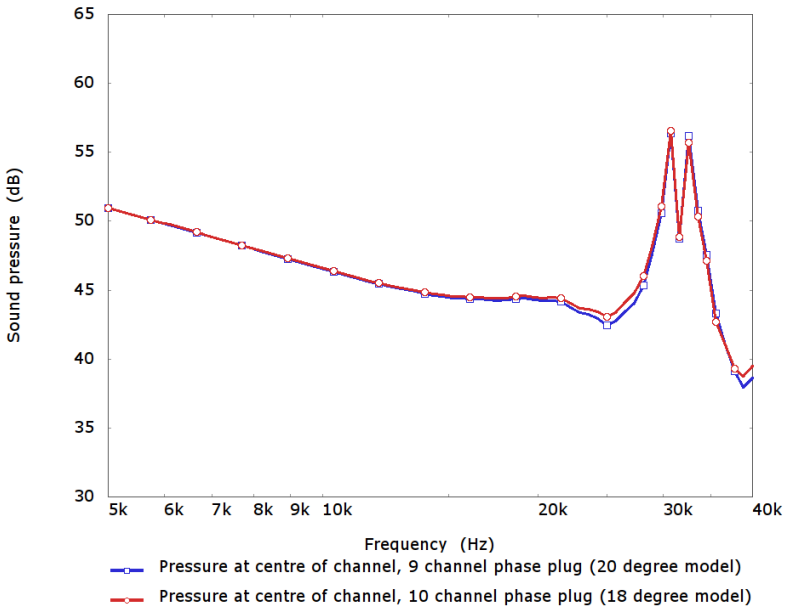

Figure 7.37. Comparison of the channel pressure at the axis of rotation of the FEM model shown in figure 7.33 for unit axial harmonic-acceleration of the voice-coil region with an equivalent mode having 9 radial channels.

Figure 7.37 shows a detailed comparison of the pressure a the central axis of the channels for a 9-channel and 10-channel design. Other than the change to the number of channels, the area weighting and compression ratio are kept identically the same. There is a small, but clear change in the magnitude of the 25kHz dip. This indicates that the performance loss in this region, for the design with the central hole, is largely due to circumferential pressure variation.

The reader may recall that early in the analysis of the radial-channel geometry, the assumption was made that the circumferential periodicity was sufficiently high that pressure variation in the circumferential direction could be ignored. This assumption was used in section 7.2 in order to reduce the set of modes that needed to be included in the driven analysis of the compression cavity. What is particularly interesting in this case is that for the geometry that has the central plug, this assumption appears to be valid to a higher frequency than the version with the central hole.

To understand why there is a difference it is helpful to visualise the first circumferential mode of the compression cavity in the periodic geometry. As discussed in section 7.2, the first circumferential mode that may be excited in the compression cavity has a circumferential order equal to the circumferential periodicity of the driver geometry. For simplicity, it is helpful to consider a thin cylindrical compression cavity geometry that was first discussed in section 4.2. The cavity modes in this case are given by the expression

$$\Psi_{mn}(r,\theta) = A_{nm} J_m(k_{mn} r)\left(e^{-jm\theta} + e^{jm\theta}\right) \qquad 7.45.$$

the values of k_{mn} found from the roots of the differentiated Bessel functions of the first kind

$$\frac{dJ_m(j_{mn})}{dr} = 0\Big|_{r=a} \qquad \text{where} \qquad k_{mn} = \frac{j_{mn}}{r_0} \qquad 7.46.$$

For the case of the 9-channel radial compression driver, the first excitable circumferential mode has a circumferential order of $m=9$. The lowest of these modes occurs when $n=1$, which results in $k_{mn}=10.711$.

Figure 7.38 shows this cavity mode with the two horizontal axis the spatial position in the cavity and the vertical axis denoting the normalised modal pressure. At the outer diameter of the cavity, the mode has 18 maxima oscillating circumferentially between positive and negative pressure. In a large section at the centre of the cavity, the mode is approximately zero.

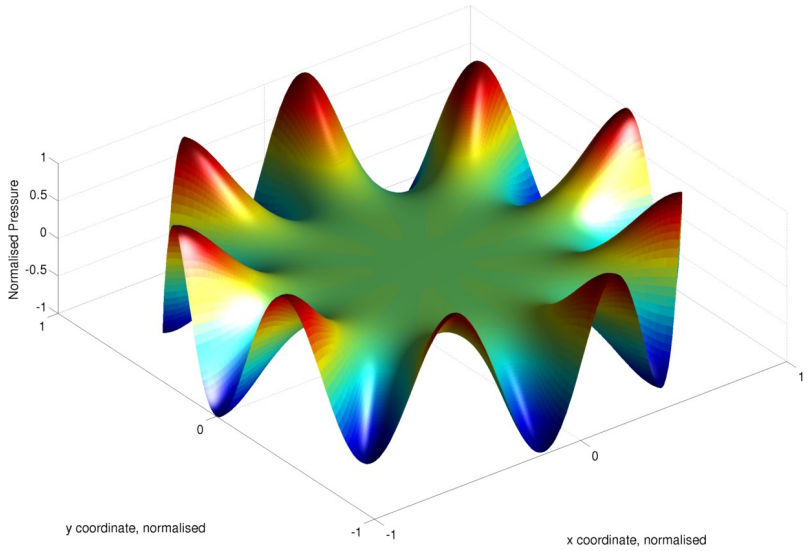

Figure 7.38. First excitable circumferential cavity mode of a thin cylindrical compression cavity when the driver has a periodicity of 9.

In terms of the phase-plug design, the extent to which such a mode is excited depends largely on the channel geometry at the very outside diameter. The modal excitation due to normal velocity at the enclosing surface of the compression cavity is found by the integral

$$\int_S \Psi_{nm}(\boldsymbol{y})\boldsymbol{u}(\boldsymbol{y}).\boldsymbol{n}\,dS \qquad 7.47.$$

When the radial compression driver is working well, the normal acoustical velocity over the open regions of the cavity exit surface is approximately constant. The worst-case situation for excitation of the cavity mode shown in figure 7.38 occurs when the channels at the outside diameter of the phase plug occupy half of the periodic circumferential angle. In this case, the circumferential mode is likely to be heavily excited. However, if the channels occupy more than half of the circumference, then the excitation of the circumferential mode is not as severe.

For the phase-plug design above with the central hole, at the outside diameter the channels occupy a 0.55 proportion of the circumferential segment. For the case with the central plug, the channels occupy 0.77 proportion of the circumferential segment. It seems highly likely that this is the reason for the better performance of the case with the central plug.

This interesting result raises the possibility of specifically designing channels that have a large open area at the outside diameter of the driver. However, this idea raises some practical difficulties: in this instance, for the phase plug and horn to be manufactured in a single part, it is necessary for there be sufficient material joining the central region, which forms the channels, with the horn walls. Additionally, a very wide open proportion at the outside

diameter makes avoiding undercuts difficult when flaring the channels into the horn. Given these difficulties, this idea has not been pursued further in this thesis.

Naturally, it is possible to improve the performance of the case with the hole if more channels are permitted in the phase-plug design. However, the fewer the channels the easier the geometry is to incorporate into a moulded part. As a consequence of these results, the radial-channel geometry with the central post was selected. In the next section, the design of the channel flare is described.

7.5.3 The design of the channel flare

The channels in the previous tweeter models expand in a conical coordinate system and are infinite in length. The final tweeter design sits at the centre of a mid-range driver and the cone of the mid-range driver acts as a horn for the tweeter. The currently separate and infinite channels must be expanded smoothly into this single horn flare without degradation to the smooth responses seen in the infinite channel models. The key to the final design working well lies in two key issues. Firstly, in the infinite channel case, a pressure change over the entrance surface of the channel causes a single parameter wave to travel down the infinite conical horn. Secondly, the specific acoustical impedance at the entrance to the channels is constant over the coupling surface. These two acoustical characteristics of the current infinite channels must be preserved in order for the cavity modal suppression to be effective and for a clean wide-band travelling wave to form in the horn.

The majority of the design of the channel flares was done using FEM models with the channel radiation coupled into an infinite conical horn. It would have equally been possible to perform this design work with the channel radiation coupled into the actual MF cone and then to use a BE region to model the full tweeter in an infinite baffle. However, this stage in the design of the tweeter is performed purely by manual iteration and manipulation of the geometry. Consequently it is vital that the solution time of the behavioural models is as short as possible. This allows relatively fast iterations of candidate designs, which makes the process much more manageable. The relatively small infinite conical-horn terminated models take between 10 and 15 minutes to run over a suitable frequency range, whereas a full BEM model of the tweeter takes at least one hour to run. This solution-time difference is extremely important. For example, with a 10-minute solution time, one can reasonably expect to iterate over roughly 30 designs in a working day. With a one hour solution time, only around five or six iterations at best can be made and, additionally, because of the

waiting time between solutions, it takes a much greater effort to maintain clarity of purpose in the task.

In the design of the channel flares, very careful attention must be paid to the manufacturability of the final design. Following the previous section, the channel entrance geometry has been determined. This final geometry is shown in figure 7.39. The white regions of this figure are solid parts that must be formed in the combined phase plug and horn moulding. Based purely on this entrance geometry, the most difficult part of the moulding is at the intersection between the central 5mm-diameter plug and the solid fins that form the walls of the channels. In this region the white solid part becomes very narrow.

The moulding is formed by injection moulding. In the process of injection moulding, a negative of the part to be constructed is cut into a steel mould tool. During production, hot molten plastic is injected into the tool cavity to form the part. Once the part has cooled slightly and is solid, it must be removed from the mould tool. To allow this, the tool is made in two parts that slide apart in a single line of draw. The surface where the two halves of the tool meet forms a “split-line”. In order for it to be possible to eject the part from the tool, it is necessary for the geometry of the part to monotonically decrease from the split line in the direction of the line of draw. If this is not the case, then this results in an undercut that prevents ejection and renders the tool useless. Under some circumstances, it is possible to design a tool with multiple sliding cores that allows undercuts to be moulded. However, the process is most robust and the tooling most cost effective when the part has no undercuts.

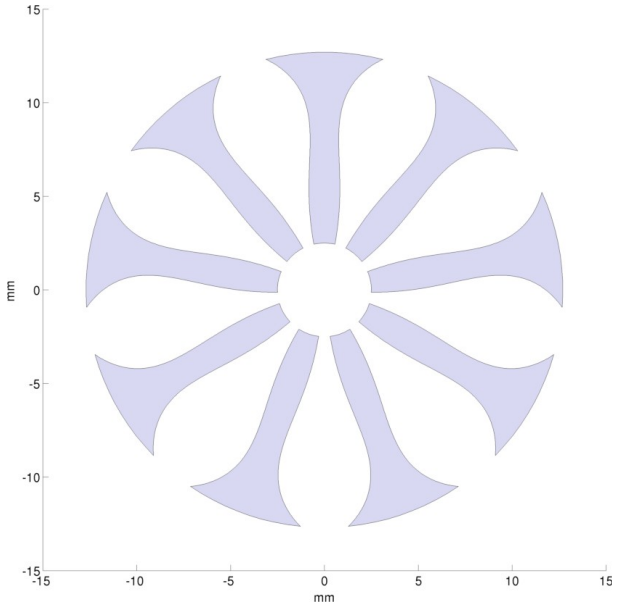

Figure 7.39. Plan view of the radial phase plug channel entrance geometry determined in section 7.5.2, the open regions are shaded, the white regions must be formed by the moulding.

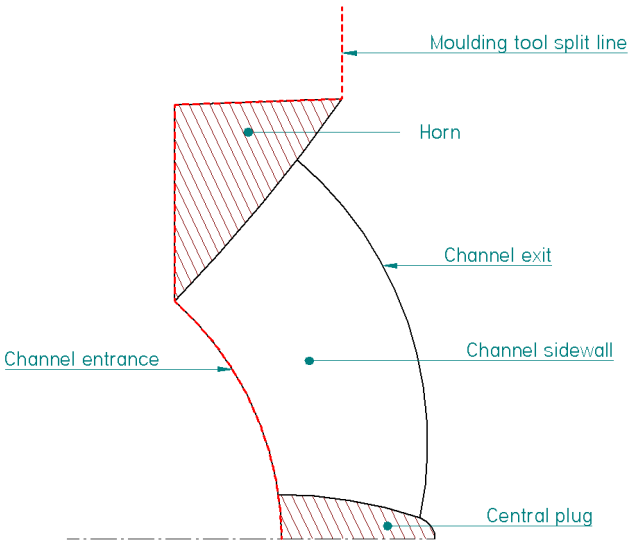

Figure 7.40. Illustration of the combined horn and phase-plug moulding.

Figure 7.40 shows an illustration of the layout of the horn and phase-plug moulding. The tooling split line is shown in red. Clearly, the geometry of the central plug and the horn wall are very easy to control to avoid an undercut. The side wall of the channel is much more difficult.

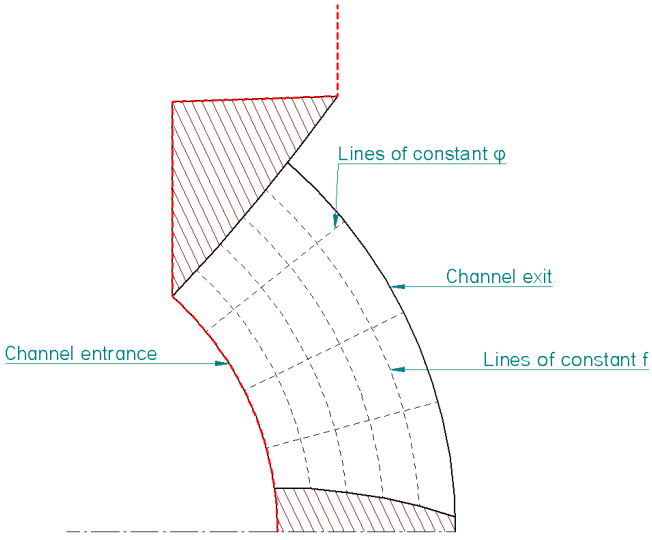

Figure 7.41. Illustration of the combined horn and phase-plug moulding showing first suggested side wall parametrisation coordinates.

From the starting geometry illustrated in figure 7.39, the channels must expand to fill the entire horn. Geometrically, this is quite tricky as the channel walls are curved at the entrance, but clearly at the exit each channel should occupy an equal full segment of the horn and the channel wall is effectively a straight radial edge. The most acoustically sympathetic way to

geometrically construct the channel flare is to parametrise the side wall into a coordinate system that approximately follows the natural path of the acoustical wave fronts in the channel.

Figure 7.41 illustrates this idea using the parameter coordinates ϕ, which is the polar angle in the dome coordinate system and f, which is a normalised radial coordinate system. The parameter f is normalised such that it has a value of 0 at the entrance surface and 1 at the exit surface. Using this approach, the geometry of the side wall may be parametrised by an expression of the form

$$A_{flare}(\phi, f) = \frac{2\pi}{N}\left[F(f) + A(\phi)\left[1 - F(f)\right]\right] \qquad 7.48.$$

where $A_{flare}(\phi, f)$ is the circumferential angular width of the channel, $A(\phi)$ is the channel entrance area function and N is the number of radial channels in the phase plug. The function $F(f)$ controls the flare of the side walls and must have a value of zero at the channel entrance surface and a value of unity at the channel-exit surface. Provided this is the case then at the entrance surface the circumferential angular width of the channel is $2\pi A(\phi)/N$ and at the exit surface the circumferential angular width of the channel is $2\pi/N$.

Unfortunately, although this parametrisation approach seems ideally suited from an acoustical point of view, it is extremely difficult to avoid undercuts in the side walls of the channels. For instance, with the area-weighting function that is the basis for figure 7.39, the channel is significantly wider at the outside diameter and, effectively, the side wall has a bulge approximately three quarters of the way from the central axis. Expanding this profile in a spherical coordinate system, as suggested by the above parametrisation, causes the bulge to propagate away from the central axis as the channel flares. Depending upon the flare function and the length of the plug, this is highly lightly to result in an undercut.

In order to better control the geometry and avoid undercuts in the side wall, the side wall parametrisation scheme was slightly adapted to force the lines of constant ϕ to be parallel to the tool draft as shown in figure 7.42. With the previous parametrisation, ϕ was equal to the polar coordinate in the channel-entrance spherical coordinate system. With the adjusted scheme ϕ is the given by

$$\phi = \sin^{-1}\left(\frac{r}{h_0}\right) \qquad 7.49.$$

where h_0 is the radius of curvature of the channel entrance surface and r is the radial distance from the centre of rotation. To ensure that ϕ remains in the defined range of the channel area

weighting function, $A(\phi)$, for $r > r_0$ the value $\sin^{-1}(r_0/h_0)$ is given, where $2r_0$ is the outside diameter of the channel entrance surface. The f coordinate varies linearly in the axial direction. On the entrance surface, f again has a value of zero, and, on the exit surface, f has a value of unity.

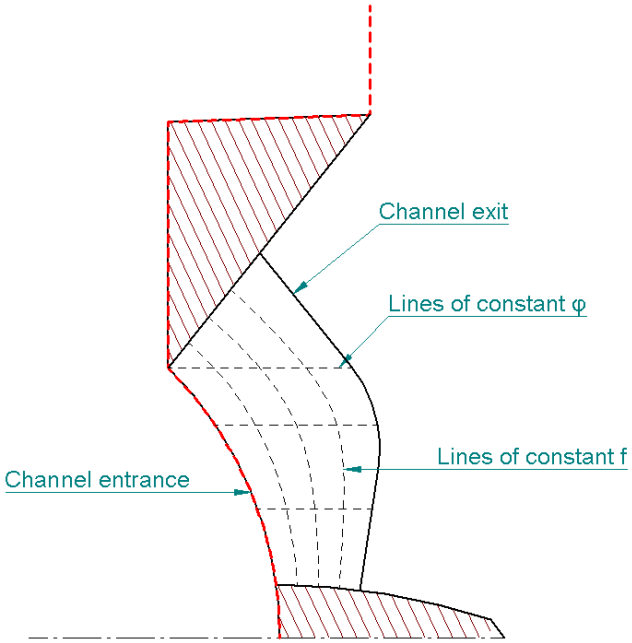

Figure 7.42. Illustration of the combined horn and phase-plug moulding showing alternative side wall parametrisation coordinates.

The same expression for the channel angular width, given in 7.48, may be used with the new parametrisation scheme. Using this approach the designer has three different means of adjusting the geometry at this stage: firstly, the location and shape of the channel exit surface; secondly, the geometry of the central plug; and, thirdly, the flare function $F(f)$.

The flare function must have a value of zero when $f = 0$ and a value of unity when $f = 1$, the family of functions

$$F(f) = f^a \qquad 7.50.$$

was used to investigate the effect of the flare on the tweeter response. The parameter a is a positive real valued coefficient that controls the shape of the flare as indicated in figure 7.43. Based on this flare function, numerous variations to the channel geometry were evaluated using FEM models. Approximately 80 different permutations of the channel flare were evaluated before a combination of central plug shape, exit surface and flare function were found that resulted in satisfactory performance.

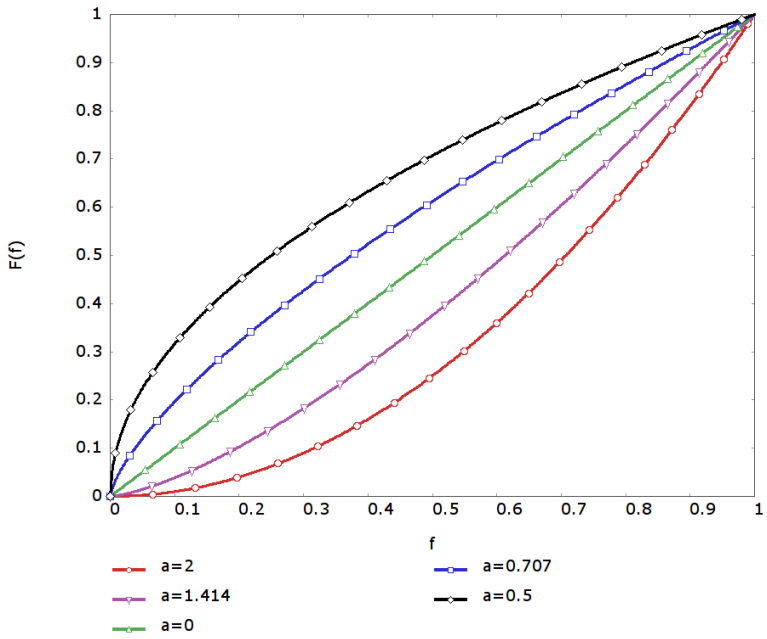

Figure 7.43. Channel flare function, given in equation 7.50, for various different values of a.

The geometry of the central plug and channel-exit surface of model J112 is shown in figure 7.44. The flare function, $F(f)$, in J112 is $f^{0.4}$, which results in a flare that expands quickly at the beginning of the channels and then more slowly towards the channel exit.

Figures 7.45 and 7.46 show the meshed geometry of model J112. This model is of a 20-degree segment from the tweeter corresponding to a phase plug with 9 radial channels. All regions of the model occupy the full 20-degree segment and are axisymmetric with the exception of the air in the radial channel, shown in detail in figure 7.46.

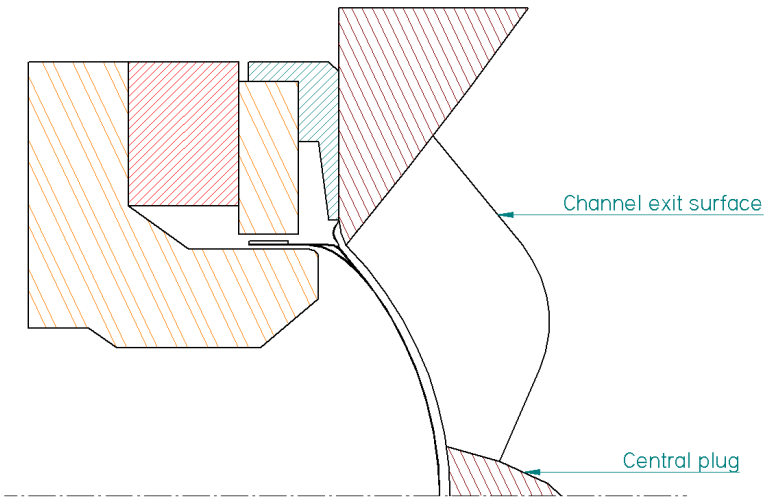

Figure 7.44. Geometry of the central plug and channel exit surface used in model J112.

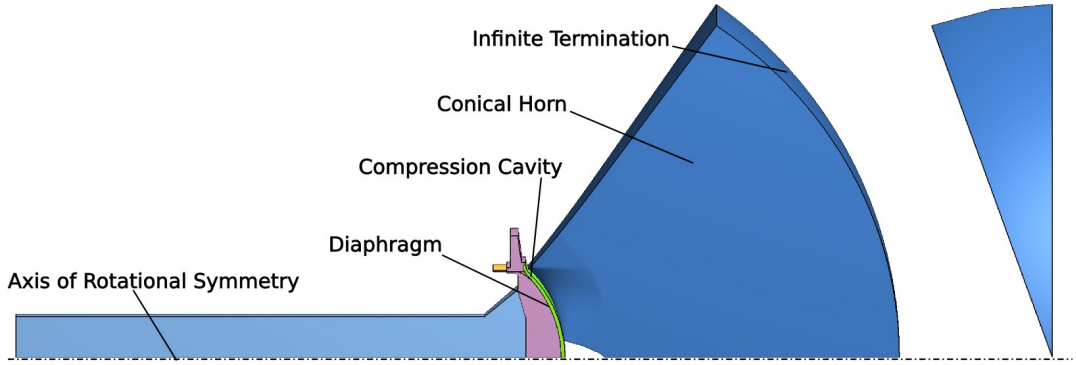

Figure 7.45. FEM model J112 of tweeter with 9 finite length radial channels terminating in an infinite conical horn (wave-envelope region is not shown).

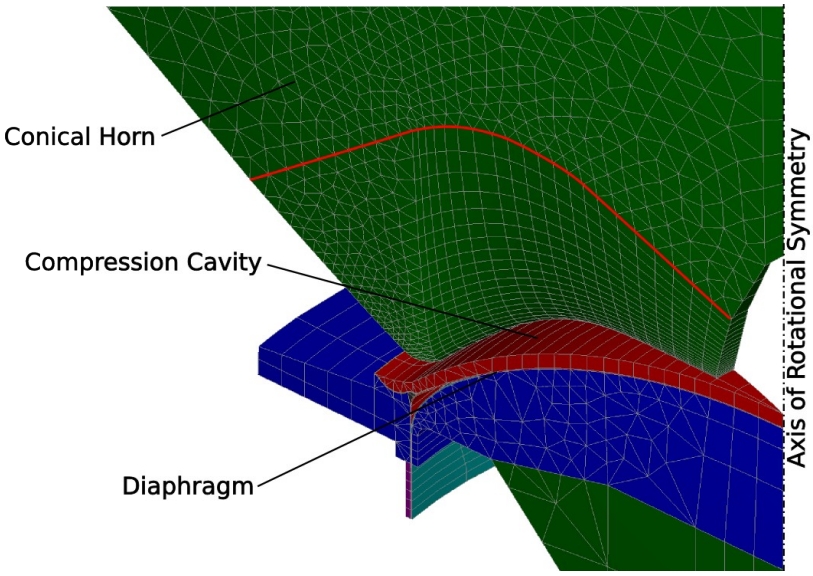

Figure 7.46. FEM model J112 of tweeter with 9 finite length radial channels terminating in an infinite conical horn. Detailed view of mesh in radial channel. Red stroked line indicates the exit of the channel, i.e., at this surface, the green air region occupies the full 20-degree sweep of the model.

The model is excited with unit axial harmonic acceleration applied to the voice-coil region. The performance of the this and the other candidate channel-flare geometries were evaluated by plotting the pressure responses at a number of positions in the conical-terminating horn at the beginning of the wave-envelope region.

Figure 7.47 shows the pressure response at 10-degree intervals in the conical horn. The responses at all positions are smooth with little ripple. The slight spreading of the responses, with the axial response a little stronger than the others, is due to the short horn region that is not a perfect cone but has a slight flare so that, when the tweeter is incorporated in the full driver, the flare rate is continuous between the small horn and the midrange cone.

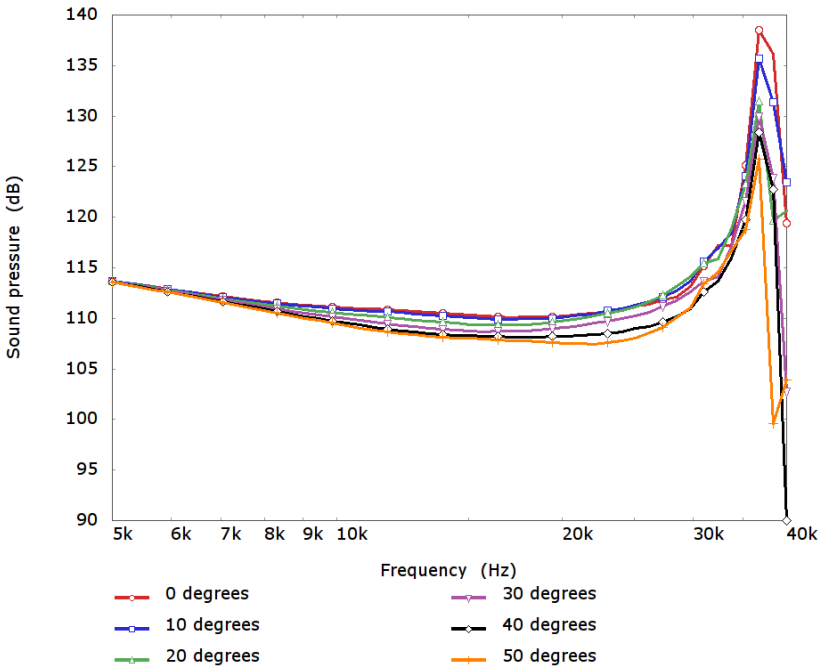

Figure 7.47. The pressure response at 10 degree intervals in the conical horn of model J112 at the intersection between the FE and wave-envelope regions.

Model J112 is almost a completed design for the phase plug. However, on close inspection, there are a couple of remaining manufacturability issues which need to be considered. Firstly, the horn flare function $f^{0.4}$ that was found to work acoustically very well is not ideal for manufacture as it results in a very thin region in the horn and phase-plug moulding at the beginning of the channels. Secondly, in J112 it has been assumed that the channel walls may flare to an infinitely fine edge at the end of the phase plug. This is not achievable in practice.

In order to deal with the first of these problems, a slightly adjusted horn-flare function was developed

$$F(f)=\frac{(f+c)^d-c^d}{(1+c)^d-c^d} \qquad 7.51.$$

with c and d real-valued coefficients that control the flare shape. With $c=0.1$ and $d=0.001$, the new flare function is similar in shape to $f^{0.4}$ for $0.5<f<1$, but has a much lower angle at the start of the flare, as seen in figure 7.48.

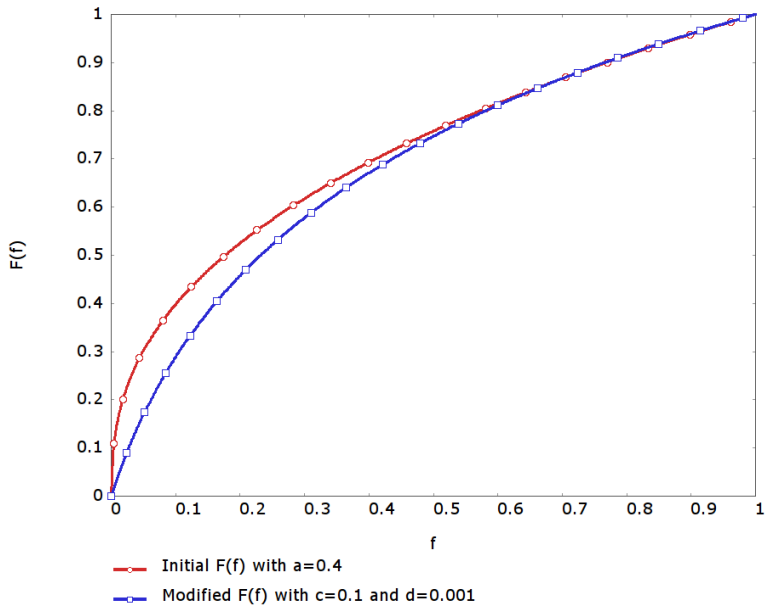

Figure 7.48. Comparison of modified flare function, which results in a lower flare start-angle, to the simple f^a flare that was originally used.

In order to address the second issue, that of the indefinitely fine edges created at the end of the channels, the expression for the circumferential channel angular width is augmented to include an additional term

$$A_{flare}(\phi, f) = \frac{2\pi}{N}\left[F(f) + A(\phi)\left(1 - F(f)\right)\right] - f\,\frac{w}{2r} \qquad 7.52.$$

where w is the finite width of the edge between neighbouring channels and r is the radial position on the channel side wall.

With these slight adjustments applied, another FEM model with an infinite conical horn termination was constructed. The geometry of the FEM model is shown in figure 7.49.

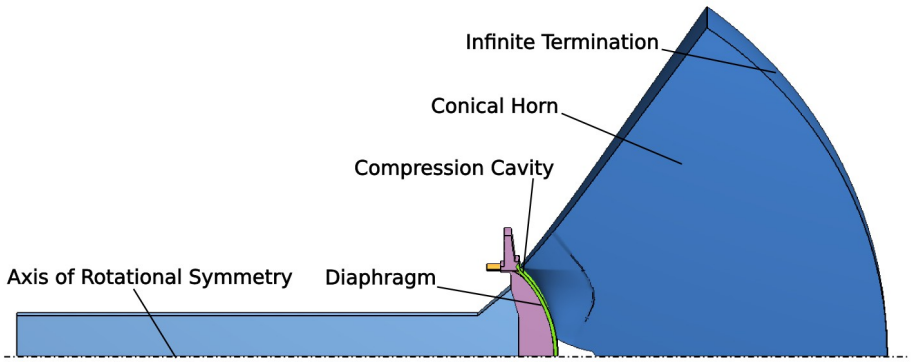

Figure 7.49. Adjusted version of J112 model incorporating alternative flare function and finite channel edges to make moulding possible.

The horn pressure responses in the same locations as were shown for model J112 are shown in figure 7.50. Compared to those demonstrated for J112 (figure 7.47) there is a slight deterioration, particularly in the axial response that now crosses over with the 10-, 20- and 30-degree responses in the region between 20kHz and 30kHz. However, this is, by quite a margin, the best performing practically realisable geometry that was found.

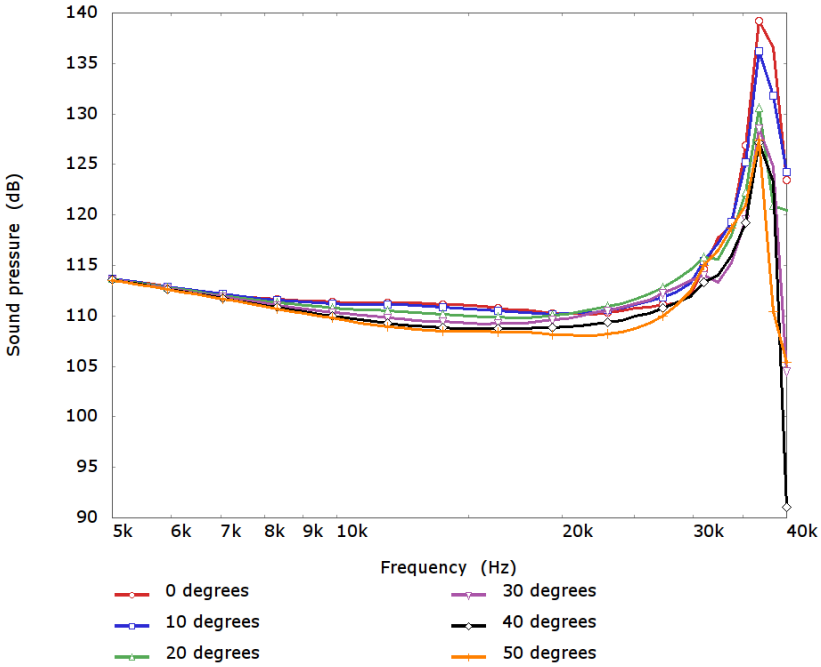

Figure 7.50. The pressure response at 10-degree intervals in the conical horn of the adjusted version of model J112 at the intersection between the FE and wave-envelope regions.

This design of phase plug was incorporated into a fully coupled FEM/BEM model of the tweeter with the full horn, incorporating the section that is formed from the midrange diaphragm, modelled in an infinite baffle. This model is directly comparable to that described at the end of Appendix XII for the tweeter without any phase plug. The geometry of the model is shown in figure 7.51. The voice-coil region is driven axially with unit harmonic force. The pressure radiated into the BEM region is shown in figure 7.52 at a distance of 1m from the infinite baffle and at a number of polar angles from the axis of the driver.

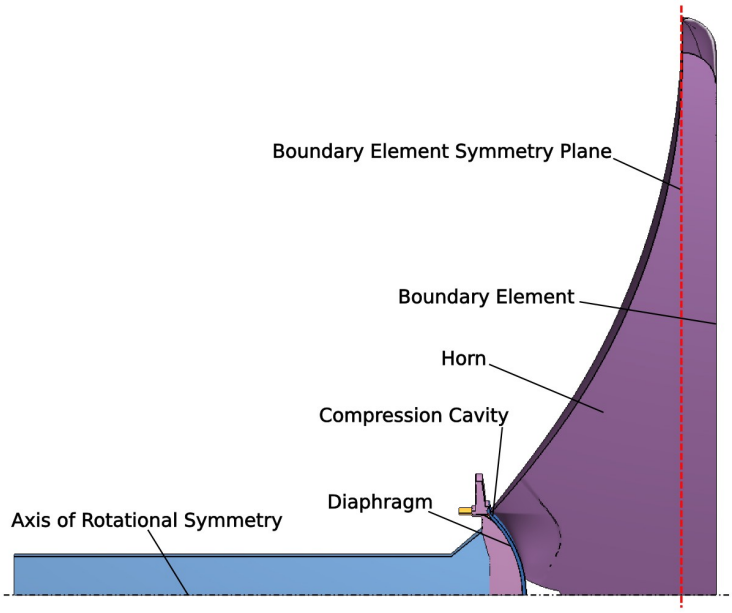

Figure 7.51. FEM/BEM model of the final tweeter design in the full MF cone horn mounted in an infinite baffle.

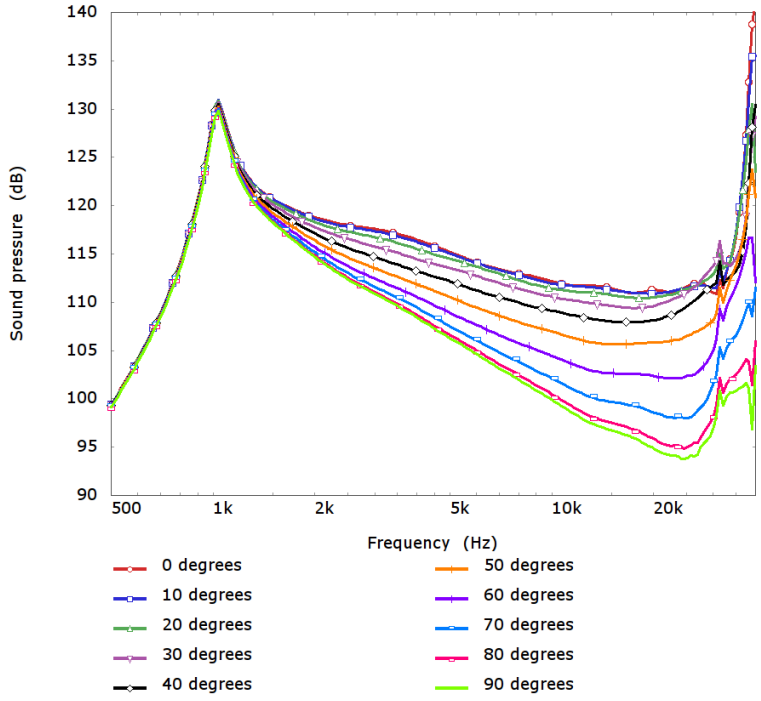

Figure 7.52. FEM/BEM simulated far field pressure of the final tweeter design in the full MF cone horn mounted in an infinite baffle at a distance of 1m from the baffle and at a number of polar angles.

Figure 7.53 shows the directivity index of the tweeter computed from this FEM/BEM model in comparison with the directivity index of the simulated tweeter without the phase plug. Up to a frequency of 20kHz, the directivity index is almost identical to the version without the phase plug. However, between 20 and 30kHz, the tweeter with the radial-channel phase plug

is less directional, although arguably the directivity index of the tweeter without the phase plug is slightly smoother.

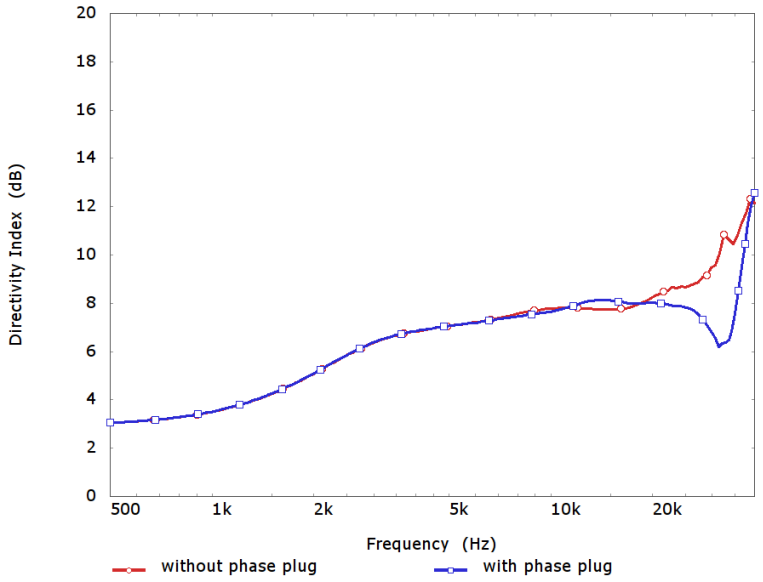

Figure 7.53. Comparison of the simulated directivity index of the tweeter with and without the radial-channel phase plug.

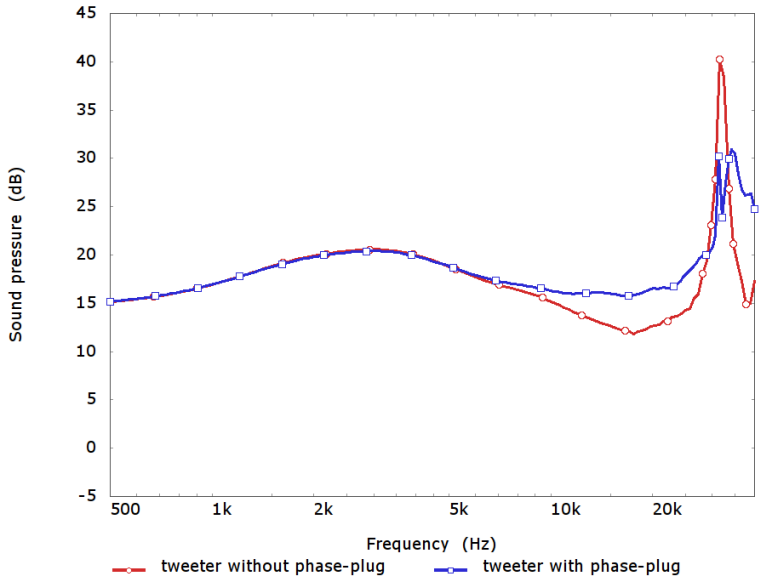

Figure 7.54. Simulated 1m axis pressure response of the tweeter when driven with a constant unit harmonic acceleration with and without phase plug.

Figure 7.54 shows the simulated 1m axial pressure response of the tweeter when the voice-coil region is driven with a constant amplitude harmonic acceleration compared to the simulated tweeter without the phase plug. Between 6kHz and 28kHz the pressure response of the tweeter with the phase plug is higher than the tweeter without the phase plug. The

maximum increase in the pressure level occurs at 20kHz where the tweeter with the phase plug is 3.8dB louder than the tweeter without the phase plug, over a wide frequency range, from 13kHz to 27.45kHz, the phase plug provides at least 3dB of gain in the pressure response. In addition the pressure response of the tweeter without the phase plug has a point of inflection at around 17.6kHz which is markedly improved on the tweeter with the phase plug.

7.5.4 The final tweeter design

At this stage of the design, the tweeter was developed into a working prototype. From the FEM models of the tweeter a full set of engineering drawings were generated by the KEF Audio research and development drawing-office engineers. Small adjustments were made to the basic geometry as necessary for manufacture, such as the addition of minimum radii: which are absolutely necessary on real parts but tricky to mesh on an FEM model. However, a great deal of care was taken to follow the FEM geometry as closely as possible, particularly on the horn and phase-plug moulding.

Figure 7.55 shows a photograph of the injection moulded combined horn and phase-plug part. This photograph shows the final moulded part. For the initial prototyping stages rapid prototype parts were made in SLA to test the design prior to tooling. The shape of the channel entrance is quite clearly seen, and is familiar from the illustration in figure 7.39.

Figure 7.55. Off-tool injection-moulded combined horn and phase plug of the tweeter.

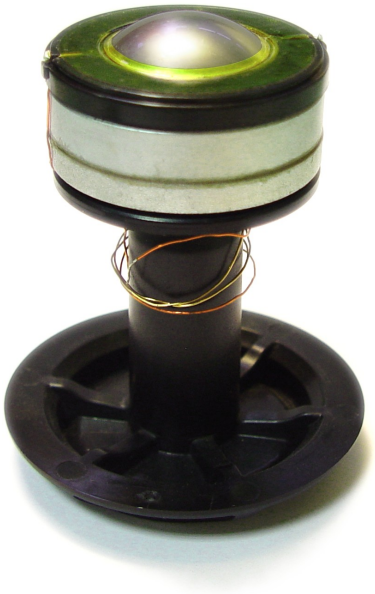

Figure 7.56. Main tweeter assembly with the phase plug removed.

Figure 7.56 shows a photograph of the main tweeter assembly with the phase plug removed. The rear-venting tube, which is manufactured as an ABS injection moulding, the metal work of the magnet system, the surround and the dome are clearly visible.

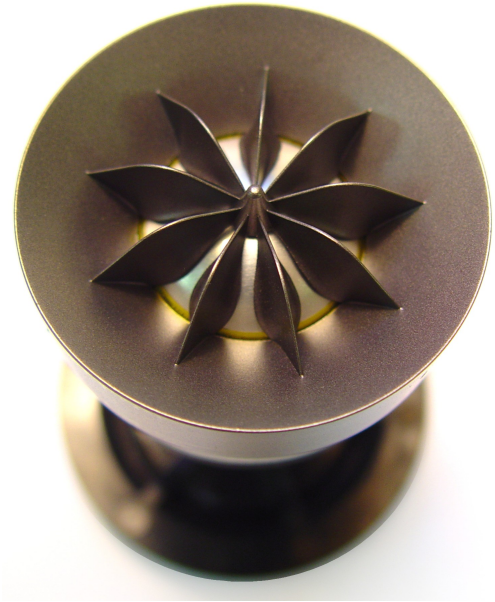

Figure 7.57. Horn and phase-plug moulding in position on the tweeter.

Figure 7.57 shows a photograph of the horn and phase-plug moulding in position on the tweeter, the yellow surround and silver dome are visible down the radial channels of the phase plug. In order to test the tweeter in exactly the same conditions that were modelled above, a CNC aluminium test horn was made and is shown in figure 7.58.

Figure 7.58. Tweeter placed in test horn.

To mimic the 2π steradians radiating space that was used in the FEM/BEM tweeter models, the test horn is mounted flush centrally into the wall of a large room (approx 20m square). This facility, at KEF Audio (UK) research and development centre, allows approximately free-field measurements to be taken by truncating the measured impulse response before the first acoustical reflection from the room boundaries. A photograph of this facility, called the "Transient Room", is shown in figure 7.61. Approximately 16ms of impulse response may be captured prior to the arrival of the first reflection. This provides a frequency-response resolution of 62.5Hz. Figure 7.59 shows the 1m-axial tweeter frequency-response measured in these conditions for a 2.83 RMS harmonic input voltage. The simulated frequency response at the same position is also shown. The voltage driven tweeter simulated frequency response is calculated from the FEM/BEM model of the final tweeter described above. This is done by incorporating the drive point mechanical impedance, derived from the FEM/BEM model, into a linear-circuit analysis program. The circuit used to calculate the voltage-drive response of the tweeter is shown in figure 7.60 and incorporates a simple lumped model of the blocked electrical impedance of the driver, Z_{eb} and the electromechanical transduction stage, with $BL = 1.54$. In addition, in order to obtain the best match between measured and simulated tweeter, it was necessary to add a mechanical damper to the drive point of the FEM/BEM model. This is quite common when comparing modelled and measured responses, as the model does not include any damping due of air flow in the narrow magnetic gap of the driver. In this case, the problem is exacerbated as the tweeter uses a magnetic fluid

to seal the gap. This adds significant damping which is not accounted in the FEM/BEM modelling.

The match between the measured and modelled results is extremely good, the tweeter appears to be working as intended.

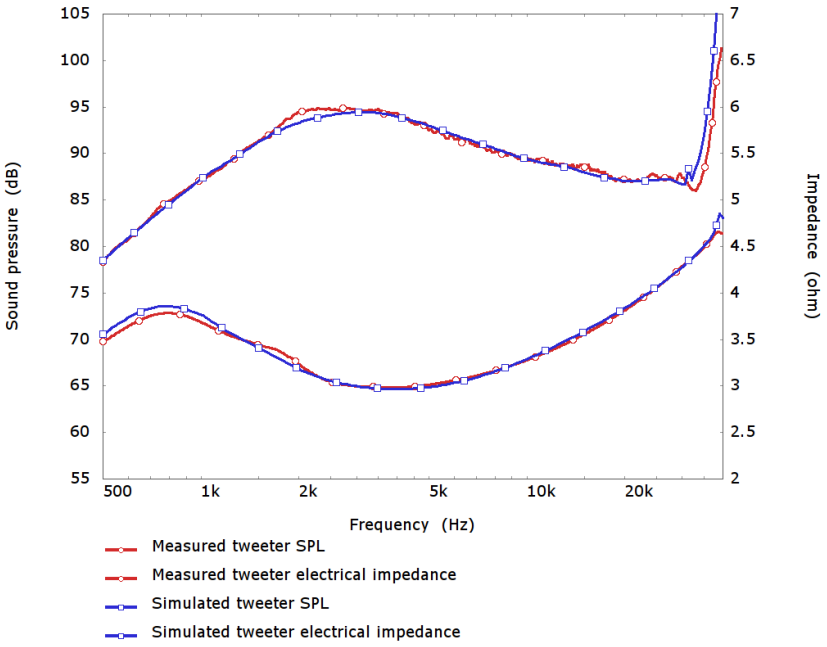

Figure 7.59. Measured 1m-axial response of the production driver in the test horn in comparison to the simulated frequency response and electrical impedance.

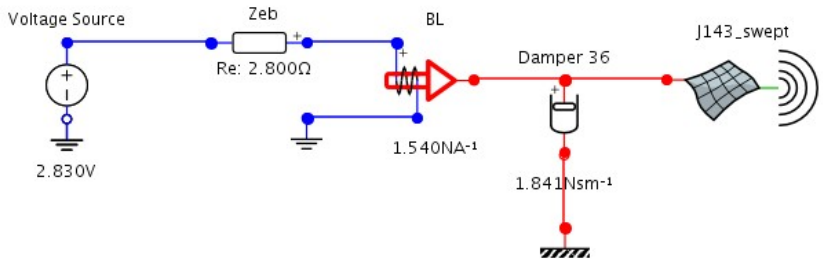

Figure 7.60. Circuit used for full simulation of the tweeter voltage response.

The phase-plug design described in this section was originally developed for the KEF Audio Q-series range of loudspeakers, which were launched in 2010. However, as a result of the performance of the phase-plug design, the same combined horn and phase-plug moulding has subsequently been used in a number of other products including the R-series range of loudspeakers and the Blade loudspeaker.

Figure 7.61. Photograph of the Transient Room measurement facility at the KEF Audio (UK) research and development centre. The room measures 20m in all directions. The test horn is visible in the centre of the wall opposite the camera. The microphone is positioned on the tall stand and located mid-way up the height of the room in order to ensure maximum possible window time.

7.6 Conclusions

The Smith type approach outlined in this chapter is shown to be equally effective in the radial arrangement as the more traditional annular compression driver arrangement. Indeed, the same parameters used for the annular case, such as ζ_n^d, are also used in the radial case and additionally the same cavity shaping approaches are applicable. From this chapter it is easy to appreciate how other channel arrangements, for example the pepper-pot style phase plug, could benefit from a Smith approach to the channel design. Compared to the annular case there are some additional considerations in the radial arrangement. Firstly, that the channels cannot be easily used to manipulate the wave path from compression cavity to horn throat. Secondly, due to the congestion which occurs at the centre of the radial geometry. However, it was demonstrated that these problems can be overcome for a particular diaphragm and horn arrangement based on a Dodd geometry and the resulting devices show significant improvements compared to the non phase-plugged situation.

8 Considerations for non-rigid radiating diaphragms

8.1 Introduction

Prior to this chapter, it has been assumed that the compression-driver diaphragm moves rigidly over the entire working bandwidth. This is a rather convenient assumption and has allowed a great deal of simplification in the analyses thus far. However, it is a poor assumption for the majority of real compression drivers. In a typical wide-band compression driver, the diaphragm moves approximately rigidly only at low frequencies, and the first structural modes of the diaphragm assembly are well within the compression-driver bandwidth. These modes are typically heavily excited and, at the upper end of the driver response, the diaphragm motion is far from rigid. It has been demonstrated in this thesis that, at the upper end of the compression-driver bandwidth, the cavity geometry is larger than an acoustical wavelength and it is in this region that the acoustical behaviour is hard to control. It is particularly inconvenient that in the same region the mechanical behaviour also deteriorates.

The displacement amplitude of a compression-driver diaphragm is extremely small and falls with increasing frequency at a rate of approximately 12dB per octave in the mass-controlled passband. Consequently, it is impossible to see the non-rigid behaviour of the diaphragm with the naked eye. However, there are a number of methods that allow the vibrational motion to be captured. Figure 8.1 shows a laser doppler vibrometer scan of a 76.2mm voice-coil diameter compression-driver diaphragm. The geometry of this compression driver diaphragm is a spherical cap, of angle 55 degrees measured from axis of rotation to diaphragm edge. The upper image shows the static geometry of the diaphragm for comparison with the scanned result. The lower image shows the same geometry with the measured surface velocity superimposed. The surface velocity was measured in the axial direction for a harmonic excitation of 2.83V RMS at a frequency of 12.8kHz. The velocity in the plot is shown for one instant in the input sine signal corresponding to a phase angle of 201 degrees. The amplitude of the displayed surface velocity is exaggerated to make it clearly visible. The laser scan was performed at KEF Audio using a laser scanner system developed in house. This particular scan was performed by, and reproduced with the kind permission of, George Perkins, KEF Research Engineer. The scan shows quite clearly the extent to which a real compression-driver diaphragm bends at the upper extent of the bandwidth. Some regions of the dome have a positive axial velocity at this instant, while others move in the opposite direction. Additionally, there is a relatively clear pattern of vibration at this frequency with three ring regions where little velocity is seen separating

annular regions that move in opposite directions. Clearly, the assumption that the diaphragm moves rigidly over the entire bandwidth is a very poor simplification in this case.

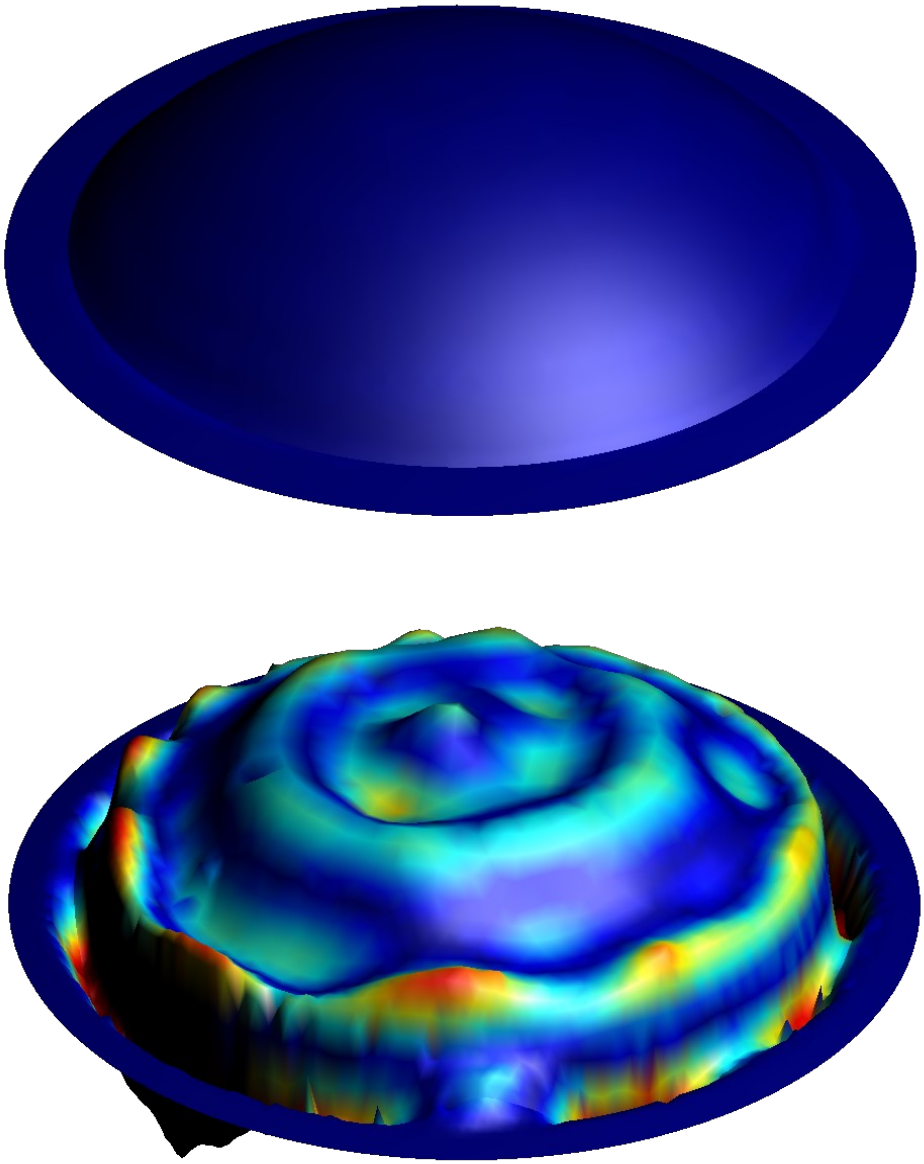

Figure 8.1. Laser Dopper vibrometer axial-velocity scan of a 76.2mm voice-coil diameter compression driver diaphragm at a frequency of 12.8kHz: upper image shows the static geometry for comparison, the lower image shows the measured axial velocity superimposed upon the static geometry.

In order to investigate the high-frequency diaphragm behaviour, and its impact upon the behaviour of the compression driver, a typical compression-driver diaphragm assembly, with a 30μm titanium dome diaphragm and a copper voice coil attached to the skirt of the diaphragm, was analysed using FEM. The geometry of the diaphragm assembly is shown in figure 8.2. The concave side of the diaphragm shares the same surface as the compression

cavity analysed in Appendix XI, in Example 1. The voice-coil region of the FE model is driven with a sinusoidally varying force of amplitude $j\omega$ such that, in the mass controlled region, the voice-coil velocity is of approximately constant aplitude. The model was solved at 400 frequencies beginning at 200Hz and increasing with an equal logarithmic spacing to 20kHz. This model is of the dome in isolation. There is no acoustic fluid adjacent to the diaphragm surface and consequently the motion calculated from this model differs from the fluid-loaded case. This difference is discussed in more detail later in this chapter.

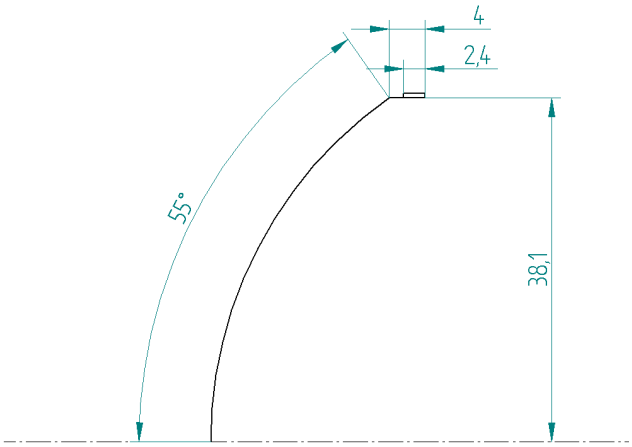

Figure 8.2. drawing of the compression-cavity diaphragm geometry used for the analysis, dimensions are in mm.

Figure 8.3 shows the calculated diaphragm displacement at an excitation frequency of 200Hz. At this frequency, the diaphragm assembly is rigid and simply translates along the axis of rotation.

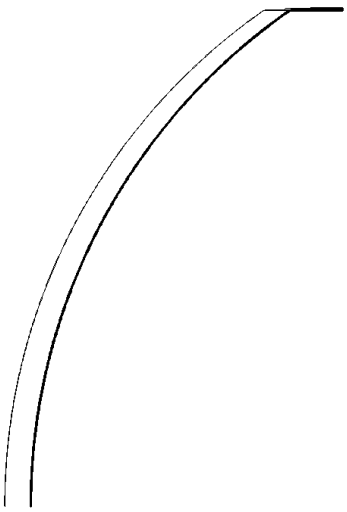

Figure 8.3. FEM calculated diaphragm displacement with 200Hz harmonic force applied to voice coil, results shown at input phase of 180 degrees. Undeformed geometry shown in light grey. The amplitude of the displacement is exaggerated to 2mm to clearly show the behaviour.

Figure 8.4 shows the FEM-calculated diaphragm displacement at 15kHz, at this frequency the diaphragm is bending severely. In particular, it is interesting to note that the outer part of the dome is displaced with the opposite phase to the inside part. In addition, the voice-coil region is displaced significantly in the radial direction.

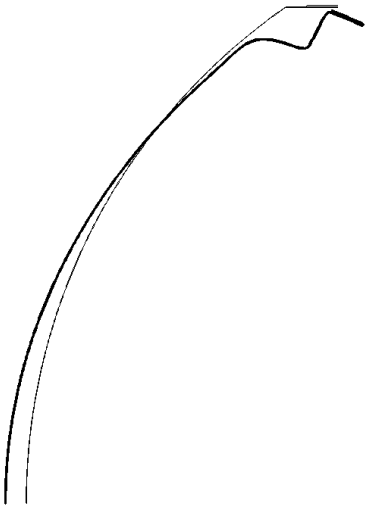

Figure 8.4. FEM calculated diaphragm displacement with 15000Hz harmonic force applied to voice coil, results shown at input phase of 180 degrees. Undeformed geometry shown in light grey. The maximum amplitude of the displacement is exaggerated to 2mm to clearly show the behaviour.

The importance of the diaphragm non-rigidity, in terms of the acoustical design of the compression driver, is the effect upon the parameter ζ_n^d, which describes the excitation of the cavity due to the motion of the diaphragm. The parameter ζ_n^d is calculated from the diaphragm velocity and the cavity eigenfunctions using the expression

$$\zeta_n^d = \int_{S_d} \Psi_n(\boldsymbol{y}) \boldsymbol{u}_d(\boldsymbol{y}).\boldsymbol{n}\, dS \qquad 8.1.$$

In the previous chapters, it has been assumed that the diaphragm velocity, $\boldsymbol{u}_d(\boldsymbol{y})$, is invariant to frequency. This effectively means that the diaphragm must move with the same shape of deformation over the entire bandwidth of the driver. Note that the analysis is still valid if the diaphragm velocity is dependent upon frequency, provided that the same transfer function applies to all points on the diaphragm surface. This can occur, for example, when there is some electrical filtering on the input of the driver or as a result of the mechanical impedance of the drive point. In the equations for modal suppression, the parameter ζ_n^d never appears in isolation, but always as the ratio ζ_n^d/ζ_0^d. Any overall response characteristic appears in both numerator and denominator.

For the non-rigid case, it is not possible to consider $\boldsymbol{u}_d(\boldsymbol{y})$ to be invariant to frequency. This is a problem in terms of the design of the compression driver because the cavity shaping and channel-positioning methods outlined in the preceding chapters are only valid for frequency invariant ζ_n^d/ζ_0^d.

To assess the level of non-rigid motion in terms of the modal excitation of the compression cavity, even though it is of no practical use in the modal suppression techniques, it is instructive to consider the parameter ζ_n^d as a function of frequency. The functions $\zeta_n^d(\omega)$ may be approximated using FEM-calculated in-vacuo diaphragm velocity results such as those presented at the start of this section. $\zeta_n^d(\omega)$ is defined by the expression

$$\zeta_n^d(\omega) = \int_{S_d} \Psi_n(\boldsymbol{y})\, \boldsymbol{u}_d(\boldsymbol{y}, \omega).\boldsymbol{n}\, dS \qquad 8.2.$$

which may be approximated by estimating the integral, using the same method as described in section 5.4.1, for each solved frequency in the mechanical FEM analysis of the diaphragm.

The approximated functions $\zeta_n^d(\omega)$ for the combination of the diaphragm shown in figure 8.2 and the constant-thickness cavity, shown in figure XI.1, are given in figure 8.5.

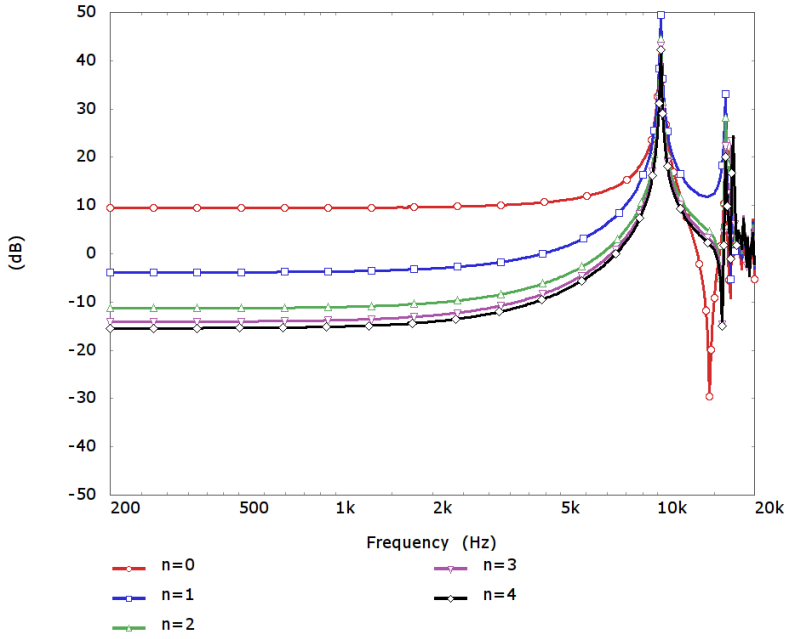

Figure 8.5. Decibel level of calculated functions $\zeta_n^d(\omega)$ for in-vacuo FEM-calculated non-rigid diaphragm and simple constant-thickness cavity described in figure XI.1.

The normalised functions $\zeta_n^d(\omega)/\zeta_0^d(\omega)$ are also shown in figure 8.6. It should be noted that these are complex response functions giventhat the diaphragm velocity is a complex function. At low frequencies, the values of $\zeta_n^d(\omega)$ are identical to those for a rigid diaphragm. At higher frequencies, where the diaphragm begins to flex, a large peak is seen in all the $\zeta_n^d(\omega)$ responses at 10kHz. Interestingly, on the figure showing the normalised zeta results, $\zeta_n^d(\omega)/\zeta_0^d(\omega)$, this peak disappears in the normalisation process and the more obvious irregularity is then the large peak at 14.5kHz. Comparing the two figures, it is clear that the peak at 14.5kHz on the normalised results corresponds to the large dip in the $\zeta_0^d(\omega)$ function.

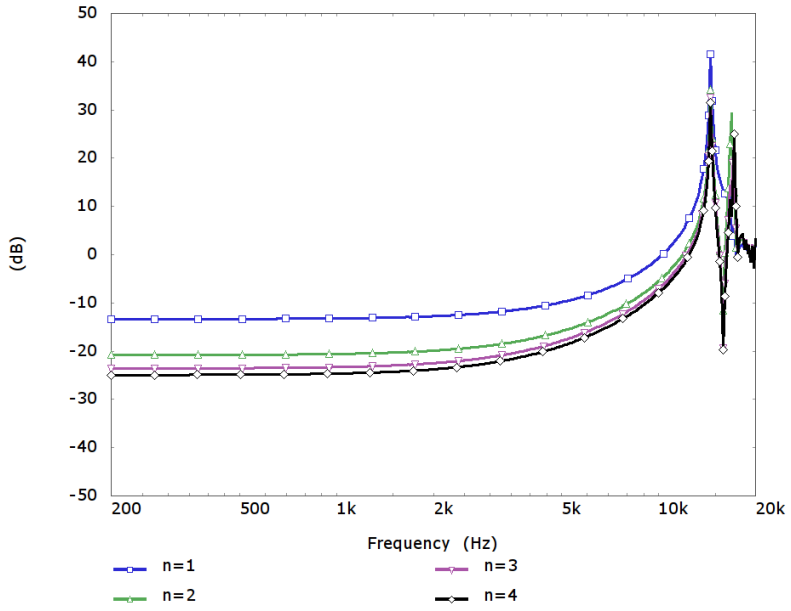

Figure 8.6. Decibel level of calculated functions $\zeta_n^d(\omega)/\zeta_0^d(\omega)$ for in-vacuo FEM-calculated non-rigid diaphragm and simple constant-thickness cavity described in figure XI.1.

Considering the normalised figure, the variation in the $\zeta_n^d(\omega)/\zeta_0^d(\omega)$ functions is severe, for example, the n=1 function varies by around 53dB over the calculated range.

The functions $\zeta_n^d(\omega)$ and $\zeta_n^d(\omega)/\zeta_0^d(\omega)$ may also be approximated for other cavity geometries using the same process described above. In chapter 6, a cavity geometry was derived that minimised the excitation of the first four cavity modes for the special case where the same driver diaphragm as shown in figure 8.2 was constrained to move rigidly. The resulting cavity geometry was shown in figure XI.2. Using the same in-vacuo FEM-computed diaphragm velocities, the approximated functions $\zeta_n^d(\omega)$ for this cavity are shown in figure 8.7, the functions $\zeta_n^d(\omega)/\zeta_0^d(\omega)$ are also given in figure 8.8.

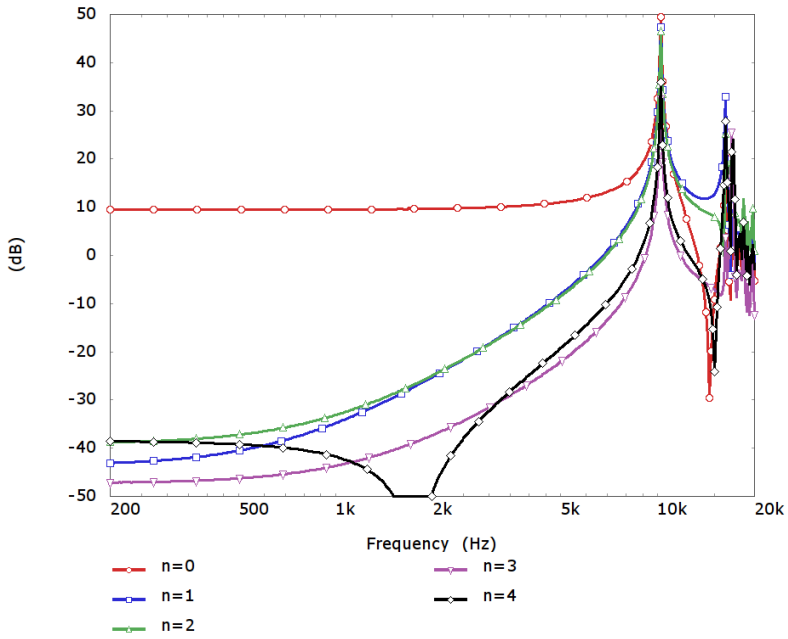

Figure 8.7. Decibel level of calculated functions $\zeta_n^d(\omega)$ for in-vacuo FEM-calculated non-rigid diaphragm and shaped cavity described in figure XI.2.

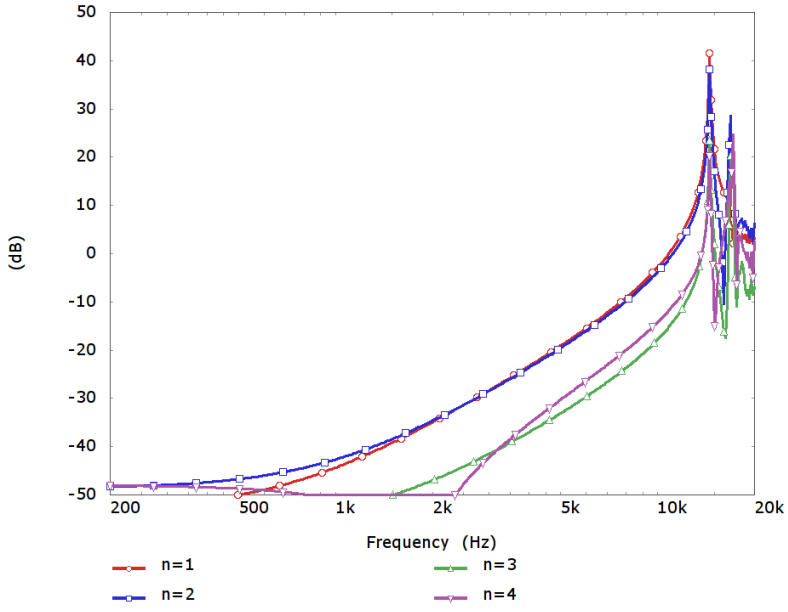

Figure 8.8. Decibel level of calculated functions $\zeta_n^d(\omega)/\zeta_0^d(\omega)$ for in-vacuo FEM-calculated non-rigid diaphragm and shaped cavity described in figure XI.2.

It is again interesting to note that there is a large peak in all of the $\zeta_n^d(\omega)$ functions at around 10kHz, which disappears in the normalised $\zeta_n^d(\omega)/\zeta_0^d(\omega)$ functions. The levels of the normalised functions $\zeta_n^d(\omega)/\zeta_0^d(\omega)$ tend to zero at low frequencies where the velocity of the

non-rigid diaphragm, used for this calculation, converges with the velocity of the rigid diaphragm which, was used for the cavity geometry derivation. Comparing the functions $\zeta_n^d(\omega)/\zeta_0^d(\omega)$ for this shaped cavity to the same results for the constant-thickness cavity, figure 8.6, the level of modal excitation is lower in the shaped case for the entire bandwidth below 14kHz and more than 3dB lower below 5kHz. At first consideration, this level of suppression is relatively impressive. However, in the high-frequency region, where the compression-driver and phase-plug acoustics are most difficult to control, the $\zeta_n^d(\omega)/\zeta_0^d(\omega)$ function are not improved compared to the constant thickness cavity.

With the rigid diaphragm, the excitation of the first few acoustical cavity modes can be almost completely suppressed when using the cavity-shaping approach (see figure XI.2). It is interesting to now take the derived shaped cavity and, rather than using a rigid diaphragm, to excite it using the FEM-calculated in-vacuo diaphragm velocities. This provides a useful illustration of how much deterioration can be expected when the diaphragm is not rigid. Figure 8.9 shows this result in comparison to the rigid diaphragm situation. The pressure at the outside diameter of the compression cavity is shown as an illustration of the extent of acoustical modal excitation.

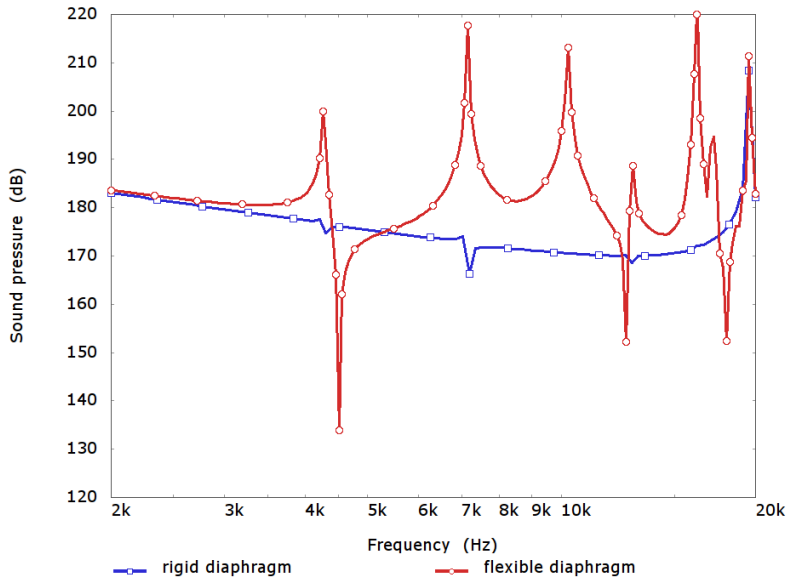

Figure 8.9. Diaphragm excited pressure response at the outside diameter of optimised compression cavity described in Appendix XI, example 1, for rigid diaphragm motion (as assumed in cavity shape derivation) and non-rigid diaphragm velocity approximated by in-vacuo FEM.

In both cases the diaphragm is driven with the same excitation force at the voice-coil region of the assembly. The extent of the deterioration in the modal suppression performance is

quite startling: the peaks in the pressure response are greater than those for the rigidly driven un-optimised cavity, which was shown in figure XI.2.

The first few acoustical eigenfunctions of the compression cavity occur at frequencies of 0Hz, 4279Hz, 7156Hz, 12859Hz and 16222Hz. Each of these, with the exception of the zeroth, may be seen on the rigid-diaphragm plot as a small excursion where the mode is not quite completely suppressed. For the non-rigid case, there are large peaks at each of these frequencies and, in addition, there are also peaks at approximately 10250Hz and 16200Hz. These two frequencies correspond quite neatly to the two peaks seen in figure 8.7. This confirms that, rather than being because of acoustical resonance in the cavity, these two peaks are a result of resonance of the mechanical assembly, which in turn results in a huge increase in the excitation of the acoustical system.

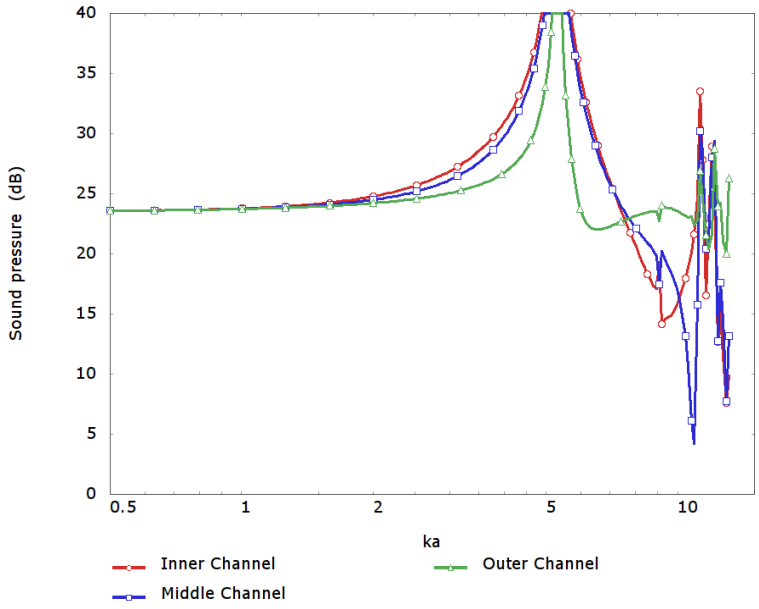

Figure 8.10. Normalised channel pressure level response of simplified compression driver previously shown in figure XI.3 for an ideal rigid diaphragm now driven by the computed in-vacuo response of the diaphragm described in figure 8.2.

In Appendix XI, the shaped cavity and rigid diaphragm are further developed into a simplified compression driver model. Figure XI.3 shows the calculated acoustical pressure responses in each of the three phase-plug channels. For comparison, this model was re-run using the in-vacuo diaphragm velocities to excite the compression cavity. The channel pressure responses are shown in figure 8.10 with the same axis limits as in figure XI.3. There is a clear and severe deterioration in the consistency and smoothness of the three channel responses.

The FEM model of the simplified compression driver was solved a third time and, in this instance, the mechanical structure and fluid regions were fully coupled. The channel pressure results for the fully coupled simplified compression driver are shown in figure 8.11. In this case, a similar deterioration is seen compared to the rigid diaphragm case. However, the difference between in-vacuo diaphragm-velocity excitation and the fully coupled case is large. It is clear that the fluid load on the mechanical structure is very significant and cannot be dismissed.

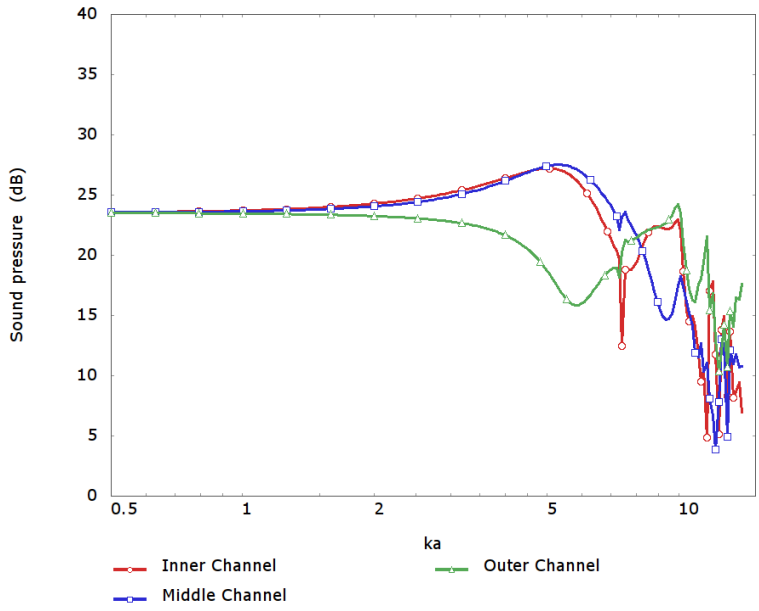

Figure 8.11. Normalised channel pressure level response of simplified compression driver previously shown in figure XI.3 for an ideal rigid diaphragm now driven by the diaphragm described in figure 8.2, note that the fluid and structural regions are fully coupled in this model.

In both the in-vacuo and fully coupled case, the amplitudes with which the acoustical modes of the cavity are excited by the diaphragm are completely different from the rigid case, and it is this which causes the deterioration in the compression driver performance compared to figure XI.3. In this chapter, the possibility of accounting for the non-rigid behaviour of the compression driver diaphragm is considered.

8.2 The diaphragm as a modal mechanical structure

The compression driver diaphragm has little mechanical damping and it is most convenient to use a modal description of its vibrational behaviour. The approach is extremely similar in concept to the modal approach to the driven behaviour of a lightly-damped acoustical enclosure that was introduced in 3.4. A full introduction to this approach is provided in Appendix XIII.

The mechanical structure has an infinite set of natural modes, or eigenfunctions, which are the solutions to the homogeneous wave equation in the structure, corresponding to each of these natural modes is a natural frequency, or eigenfrequency, which is the frequency for which the solution to the homogeneous wave equation is valid. The mechanical modes of the diaphragm structure, $\boldsymbol{\Phi}_n(\boldsymbol{x})$, are scaled to be orthonormal such that

$$\int_{V_d} \rho(\boldsymbol{x})\boldsymbol{\Phi}_n(\boldsymbol{x}).\boldsymbol{\Phi}_m(\boldsymbol{x})\,dV = \delta_{nm} \qquad 8.3.$$

where $\rho(\boldsymbol{x})$ is the density of the mechanical structure at the location $\boldsymbol{x}$, V_d is the volume occupied by the diaphragm mechanical structure, and δ_{nm} is the Kronecker delta [47, p.692], which has the property that

$$\delta_{nm} = \begin{cases} 0, & m \neq n \\ 1, & m = n \end{cases} \qquad 8.4.$$

The resulting harmonic velocity of the mechanical structure when driven by a harmonic force, $\boldsymbol{f}_i(\boldsymbol{y})$, may be expressed as a summation of contributions from each of the mechanical modes as

$$\boldsymbol{u}_d(\boldsymbol{x}) = \sum_{k=0}^{\infty} \frac{j\omega\boldsymbol{\Phi}_k(\boldsymbol{x})}{\omega_k^2 - \omega^2} \int_{V_d} \boldsymbol{\Phi}_k(\boldsymbol{y}).\boldsymbol{f}_i(\boldsymbol{y})\,dV \qquad 8.5.$$

where ω_k is the natural frequency corresponding to the nth mode and V_d is the volume of the mechanical structure. One important consideration in applying this technique is that the boundary conditions required for the driven case must be the same as the boundary conditions for the eigensolution.

Using PAFEC-FE, the modes and natural frequencies of the diaphragm structure described at the beginning of this section were analysed. The first twenty natural frequencies are given in table 8.1 below.

From this table, it is clear that nineteen of these modes lie in the audio bandwidth. The frequency distribution of the natural frequencies is interesting. The first three modes are widely spaced in frequency but the other seventeen are very densely packed. This is clearly shown if the natural frequency values are plotted against mode number, as shown in figure 8.12.

Mode Number	Frequency (Hz)
0	0
1	10225
2	15511
3	16230
4	16976
5	17188
6	17283
7	17344
8	17399
9	17460
10	17535
11	17633
12	17765
13	17940
14	18166
15	18452
16	18806
17	19236
18	19748
19	20349

Table 8.1: Lowest twenty mechanical natural frequencies computed using PAFEC-FE for the diaphragm structure shown in figure 8.2.

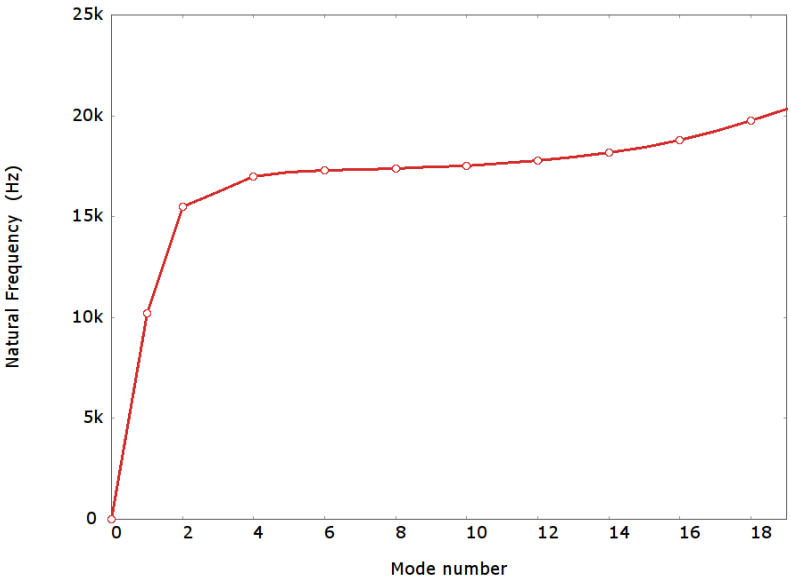

Figure 8.12. Lowest twenty mechanical natural frequencies computed using PAFEC-FE for the diaphragm structure shown in figure 8.2 plotted against mode number.

This modal distribution is typical of a thin shell like structure: because the material is very thin, there is little resistance to bending and the majority of the structural rigidity is derived from the in-plane stiffness of the shell. This shell stiffness is only effective where the curvature of the geometry is significant compared to a bending wavelength. As a result, the first modes are widely spaced as they derive a lot of stiffness from the curvature of the geometry. The higher modes ones are closely spaced as the curvature has little effect.

The modal summation approximation ignores damping. However light damping may be approximated by adding an additional imaginary term to the quadratic on the denominator in the summation, resulting in the expression

$$\boldsymbol{u}_d(\boldsymbol{x}) = \sum_{k=0}^{\infty} \frac{j\,\omega\,\boldsymbol{\Phi}_k(\boldsymbol{x})}{\left[\omega_k^2 + j\frac{\omega\,\omega_k}{Q_k} - \omega^2\right]} \int_{V_d} \boldsymbol{\Phi}_k(\boldsymbol{y}).\boldsymbol{f}_i(\boldsymbol{y})\,dV \qquad 8.6.$$

where Q_k is a quality factor coefficient that controls the degree of damping of each mode [46, page 95]. This damping approximation is only valid when the system under consideration is weakly damped.

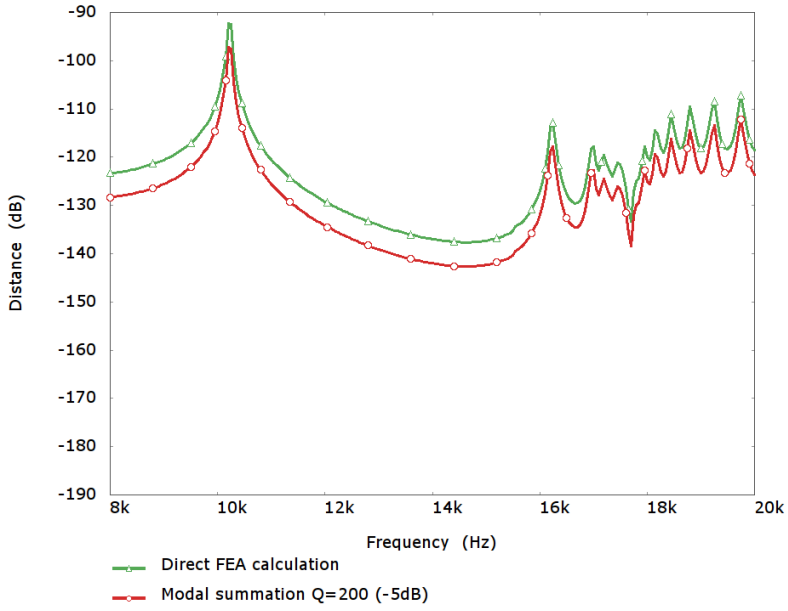

Figure 8.13. Axial displacement level at the axis of rotation of the dome diaphragm illustrated in figure 8.2 calculated using a summation of the FEM-calculated modes assuming a Q of 200 in comparison to the direct FEM-calculated acceleration a the same position

The in-vacuo axial displacement at the centre of the dome diaphragm was calculated using a summation of the FEM-calculated modes and natural frequencies, and is shown in figure 8.13 in comparison to the direct FEM calculated displacement at the same position. Damping

was approximated in the modal summation by using a quality factor of 200 for all modes in the summation. The agreement between the two methods is extremely good, the curves are separated by 5dB in the figure for clarity.

The parameter ζ_n^d has been widely used in the previous sections to quantify the degree to which the diaphragm motion excites the compression cavity acoustical modes, and in the previous section it was extended as a function of frequency defined as

$$\zeta_n^d(\omega) = \int_{S_d} \Psi_n(\boldsymbol{x}) \boldsymbol{u}_d(\boldsymbol{y}, \omega) . \boldsymbol{n} \, dS \qquad 8.7.$$

This extension made it possible to use the parameter to assess the level of diaphragm non-rigidity in terms of the cavity modal excitation. The function $\boldsymbol{u}_d(\boldsymbol{y}, \omega)$ is the complex harmonic diaphragm velocity at the point $\boldsymbol{y}$ and frequency ω. Substituting the modal description of the dome velocity, as given in equation 8.5, into the expression for ζ_n^d gives

$$\zeta_n^d(\omega) = \int_{S_d} \Psi_n(\boldsymbol{x}) \left\{ \sum_{k=0}^{\infty} \frac{j\omega \boldsymbol{\Phi}_k(\boldsymbol{x})}{\left[\omega_k^2 + j\frac{\omega \omega_k}{Q_k} - \omega^2 \right]} \int_{V_d} \boldsymbol{\Phi}_k(\boldsymbol{y}) . \boldsymbol{f}_i(\boldsymbol{y}) \, dV \right\} . \boldsymbol{n} \, dS \qquad 8.8.$$

where the symbol k is used to index the mechanical modes. Note that the volume integral is over the mechanical structure V_d, whereas the surface integral is over the part of the compression cavity surface which is occupied by the mechanical structure, S_d.

The volume integral over the mechanical mode shapes results in an scalar excitation amplitude for each mechanical mode. Additionally, it is only the acoustical mode shape function, $\Psi_n(\boldsymbol{x})$, and the first of the mechanical mode shape functions, $\boldsymbol{\Phi}_k(\boldsymbol{x})$, which are dependent upon the position on the surface S_d. The expression may be rearranged to give

$$\zeta_n^d(\omega) = \sum_{k=0}^{\infty} \frac{j\omega}{\left[\omega_k^2 + j\frac{\omega \omega_k}{Q_k} - \omega^2 \right]} \int_{S_d} \Psi_n(\boldsymbol{x}) \boldsymbol{\Phi}_k(\boldsymbol{x}) . \boldsymbol{n} \, dS \int_{V_d} \boldsymbol{\Phi}_k(\boldsymbol{y}) . \boldsymbol{f}_i(\boldsymbol{y}) \, dV \qquad 8.9.$$

This expression indicates that each of the $\zeta_n^d(\omega)$ functions may be described by a summation over the mechanical modes with each term in the summation a rational quadratic function of $j\omega$. The magnitude of each rational quadratic term is determined by the two integrals, the first integral characterises the coupling between the mechanical mode in question and the nth acoustical mode. The second integral calculates the mechanical excitation of the mechanical mode in question.

For clarity, the modal forcing parameter F_k is defined to be the result of the volume integral

$$F_k = \int_{V_d} \boldsymbol{\Phi}_k(\boldsymbol{y}).\boldsymbol{f}_i(\boldsymbol{y})\,dV \qquad 8.10.$$

F_k describes the forced excitation of each mechanical mode. Additionally, the modal coupling factor γ_{nk} is defined to be

$$\gamma_{nk} = \int_{S_d} \Psi_n(\boldsymbol{x})\boldsymbol{\Phi}_k(\boldsymbol{x}).\boldsymbol{n}\,dS \qquad 8.11.$$

γ_{nk} describes how effectively the nth acoustical mode couples to the kth mechanical mode. These two parameters allow the expression for $\zeta_n^d(\omega)$ to be written a little more concisely as

$$\zeta_n^d(\omega) = \sum_{k=0}^{\infty} \frac{j\omega F_k \gamma_{nk}}{\left[\omega_k^2 + j\frac{\omega\omega_k}{Q_k} - \omega^2\right]} \qquad 8.12.$$

8.3 Optimal diaphragm behaviour for acoustical modal suppression

In the previous section of this chapter, it was shown that ζ_n^d may be described in terms of the mechanical modes of the compression driver radiating diaphragm as outlined in expression 8.9. Using this expression, the normalised zeta parameters are

$$\frac{\zeta_n^d(\omega)}{\zeta_0^d(\omega)} = \frac{\sum_{k=0}^{\infty} \frac{F_k \gamma_{nk}}{\left[\omega_k^2 + j\frac{\omega\omega_k}{Q_k} - \omega^2\right]}}{\sum_{k=0}^{\infty} \frac{F_k \gamma_{0k}}{\left[\omega_k^2 + j\frac{\omega\omega_k}{Q_k} - \omega^2\right]}} \qquad 8.13.$$

Ideally, for optimal compression-driver behaviour, the parameters ζ_n^d/ζ_0^d are all zero except for $n=0$. For this to occur, the numerator of 8.13 must be zero when $n \neq 0$.

Excluding the case when the terms in the summation cancel one another, each term in the summation over k on the numerator must be zero. This may be achieved if for each term if either

$$F_k = 0 \qquad \text{or} \qquad \gamma_{nk} = 0 \qquad 8.14.$$

Additionally, once again considering 8.13, it is important that there is no frequency at which the denominator approaches zero. The reader may recall that this problem was encountered in the analysis at the start of this chapter: the $\zeta_0^d(\omega)$ function shown in figure 8.5 has a deep

dip at 14.5kHz, which subsequently appears as a large peak in all of the normalised $\zeta_n^d(\omega)/\zeta_0^d(\omega)$ functions in figure 8.6.

Concentrating first on the numerator, based on the natural frequencies computed in table 8.1, for control of the compression driver behaviour over the entire audio bandwidth it seems likely that it is necessary to control these parameters for at least $0<k<10$. This virtually rules out the possibility of using the F_k term to set the numerator to zero. Assuming that the compression driver diaphragm is driven approximately with a point force at a position $\boldsymbol{y}_d$ then the forcing term F_k may be simplified from equation 8.10 to

$$F_k \approx \boldsymbol{\Phi}_k(\boldsymbol{y}_d).\boldsymbol{f}_i(\boldsymbol{y}_d) \qquad 8.15.$$

In order for F_k to be zero, then $\boldsymbol{\Phi}_k(\boldsymbol{y}_d)$ must be zero, this implies that the position $\boldsymbol{y}_d$ is a node of vibration of the k^{th} mode. It is extremely rare for nodes of vibration to lie in the same positions for consecutive modes and, additionally, if F_k is zero for every ω_k in the audio bandwidth, except for $k=0$, this implies that the diaphragm moves rigidly, which has already seen to be a poor assumption for a realistic diaphragm.

Thus, in order to optimise the normalised zeta functions for optimal compression driver behaviour, it is necessary that

$$\gamma_{nk} = \int_{S_d} \Psi_n(\boldsymbol{x})\boldsymbol{\Phi}_k(\boldsymbol{x}).\boldsymbol{n}\,dS = A\,\delta_{0n}\delta_{0k} \qquad 8.16.$$

where A is the coupling factor between the zeroth acoustical and mechanical mode.

With the exception of the zeroth acoustical and mechanical mode, the acoustical cavity modes should be orthogonal to the mechanical modes over the radiating surface.

This orthogonality requirement appears in addition to the natural orthogonality of the acoustic and mechanical modes, which are, as previously stated,

$$\int_{V_d} \rho(\boldsymbol{x})\boldsymbol{\Phi}_n(\boldsymbol{x}).\boldsymbol{\Phi}_m(\boldsymbol{x})\,dV = \delta_{nm} \qquad 8.17.$$

and

$$\int_{S_d} \Psi_n(\boldsymbol{y})\Psi_m(\boldsymbol{y})\mu(\boldsymbol{y})\,dS \approx V\,\delta_{nm} \qquad 8.18.$$

These three orthogonality conditions are very similar to the definition of a biorthogonal system [47, p.286]. A set of functions, $g_n(x)$ and $h_n(x)$, is termed a complete biorthogonal system over the closed interval R if they meet the five conditions

$$\int_R g_m(x) g_n(x) dx = c_m \delta_{mn} \tag{8.19.}$$

$$\int_R h_m(x) h_n(x) dx = d_m \delta_{mn} \tag{8.20.}$$

$$\int_R g_m(x) h_n(x)\, dx = 0 \tag{8.21.}$$

$$\int_R g_m(x) dx = 0 \tag{8.22.}$$

and

$$\int_R h_m(x) dx = 0 \tag{8.23.}$$

The most common example of a bi-orthogonal set of functions are

$$g_m(x) = \sin(m x) \tag{8.24.}$$

and

$$h_m(x) = \cos(m x) \tag{8.25.}$$

with $0 < m < \infty$ and $R = [-\pi, \pi]$, which are recognisable as the basis functions of the Fourier Series [47, p.292].

Although this indicates that mathematically it is possible to find functions that simultaneously obey 8.16, 8.17 and 8.18, what is not immediately clear is whether it is possible to synthesise a cavity and diaphragm combination whose modes are able meet all three of these conditions at least for the first few values of k.

8.3.1 Fluid-structure coupling

The above analysis and discussion of the compression-driver diaphragm behaviour as a modal structure independent from the acoustical compression cavity is an oversimplification. The fluid and mechanical structure are coupled along the entire shared surface between the diaphragm and the compression cavity. Due to the compression loading arrangement, the mechanical impedance presented by the fluid on the radiating surface of the diaphragm, often called the radiation impedance, is much larger than on the direct radiating diaphragm discussed in section 2.3. In addition, to further complicate the situation, the exact fluid loading on the diaphragm may not be fully known at the time of diaphragm design as it is, to an extent, dependent upon the horn to which the compression driver is connected and also the arrangement of the phase-plug channels.

In section 8.2, a description of the diaphragm motion was outlined in terms of the natural frequencies and modes of the mechanical structure. For a lightly damped mechanical structure, the velocity may be accurately approximated with the summation

$$\boldsymbol{u}_d(\boldsymbol{x}) = \sum_{k=0}^{\infty} \frac{j\omega \boldsymbol{\Phi}_k(\boldsymbol{x})}{\left[\omega_k^2 + j\omega\frac{\omega_k}{Q_k} - \omega^2\right]} \int_{V_d} \boldsymbol{\Phi}_k(\boldsymbol{y}).\boldsymbol{f}_i(\boldsymbol{y})dV \qquad 8.26.$$

The integral in each term of the summation may be considered a forcing term that determines how severely each mechanical mode is excited. The acoustical pressure adjacent the diaphragm exerts a force on the diaphragm surface. Including this in addition to the direct forcing term gives an expression for the diaphragm velocity, which incorporates the fluid loading on the radiating face

$$\boldsymbol{u}_d(\boldsymbol{x}) = \sum_{k=0}^{\infty} \frac{j\omega \boldsymbol{\Phi}_k(\boldsymbol{x})}{\left[\omega_k^2 + j\omega\frac{\omega_k}{Q_k} - \omega^2\right]} \left[\int_{V_d} \boldsymbol{\Phi}_k(\boldsymbol{y}).\boldsymbol{f}_i(\boldsymbol{y})dV - \int_{S_d} \boldsymbol{\Phi}_k(\boldsymbol{y}).\boldsymbol{n}\, p(\boldsymbol{y})dS\right] \qquad 8.27.$$

Note that the negative is due to the fact that the force is exerted in the opposite direction to the face normal. Considering the situation when the diaphragm moves with velocity exactly equal to the m-th mechanical mode such that

$$\boldsymbol{u}_d(\boldsymbol{y}) = \frac{j\omega}{\left[\omega_m^2 + j\omega\frac{\omega_m}{Q_m} - \omega^2\right]} \boldsymbol{\Phi}_m(\boldsymbol{x}) \qquad 8.28.$$

In this case, in the absence of any other acoustical sources, the cavity pressure is

$$p_m(\boldsymbol{x}) = \frac{j\omega}{\left[\omega_m^2 + j\omega\frac{\omega_m}{Q_m} - \omega^2\right]} \sum_{n=0}^{\infty} \frac{j\omega\rho_0 \Psi_n(\boldsymbol{x})}{V\left[k_n^2 - k^2\right]} \int_{S_d} \Psi_n(\boldsymbol{y}) \boldsymbol{\Phi}_m(\boldsymbol{y}).\boldsymbol{n}\, dS \qquad 8.29.$$

or, using the definition of γ_{nk}

$$p_m(\boldsymbol{x}) = \frac{j\omega}{\left[\omega_m^2 + j\omega\frac{\omega_m}{Q_m} - \omega^2\right]} \sum_{n=0}^{\infty} \frac{j\omega\rho_0 \gamma_{nm} \Psi_n(\boldsymbol{x})}{V\left[k_n^2 - k^2\right]} \qquad 8.30.$$

The pressure $p_m(\boldsymbol{x})$ adjacent to the surface of the diaphragm exerts a force on the structure that excites the k-th mechanical mode with an excitation amplitude of

$$-\int_{S_d} \boldsymbol{\Phi}_k(\boldsymbol{x}).\boldsymbol{n}\, p_m(\boldsymbol{x})\, dS = \frac{-j\omega}{\left[\omega_m^2 + j\omega\frac{\omega_m}{Q_m} - \omega^2\right]} \int_{S_d} \boldsymbol{\Phi}_k(\boldsymbol{x}).\boldsymbol{n} \sum_{n=0}^{\infty} \frac{j\omega\rho_0 \gamma_{nm} \Psi_n(\boldsymbol{x})}{V\left[k_n^2 - k^2\right]} dS \qquad 8.31.$$

which, once again using the definition of γ_{nk}, is equivalent to

$$-\int_{S_d} \boldsymbol{\Phi}_k(\boldsymbol{x}).\boldsymbol{n}\, p_m(\boldsymbol{x})\, dS = \frac{-j\omega}{\left[\omega_m^2 + j\omega\frac{\omega_m}{Q_m} - \omega^2\right]} \sum_{n=0}^{\infty} \frac{j\omega\rho_0 \gamma_{nk} \gamma_{nm}}{V\left[k_n^2 - k^2\right]} \qquad 8.32.$$

Inserting the expression for the integral, 8.32, and the expression for the diaphragm velocity, 8.28, into the modal description of the mechanical velocity, expression 8.27, results in

$$\frac{j\omega \boldsymbol{\Phi}_m(\boldsymbol{x})}{\left[\omega_m^2 + j\omega\frac{\omega_m}{Q_m} - \omega^2\right]} =$$

8.33.

$$\sum_{k=0}^{\infty} \frac{j\omega \boldsymbol{\Phi}_k(\boldsymbol{x})}{\left[\omega_k^2 + j\omega\frac{\omega_k}{Q_k} - \omega^2\right]} \left[\int_{V_d} \boldsymbol{\Phi}_k(\boldsymbol{y}).\boldsymbol{f}_i(\boldsymbol{y})\, dV - \frac{j\omega}{\left[\omega_m^2 + j\omega\frac{\omega_m}{Q_m} - \omega^2\right]} \sum_{n=0}^{\infty} \frac{j\omega\rho_0 \gamma_{nk} \gamma_{nm}}{V\left[k_n^2 - k^2\right]} \right]$$

From this expression, it is clear that in order to excite the mechanical system in this manner it is necessary for the forcing integral to be

$$\int_{V_d} \boldsymbol{\Phi}_k(\boldsymbol{y}).\boldsymbol{f}_i(\boldsymbol{y})\, dV = \delta_{km} + \frac{j\omega}{\left[\omega_m^2 + j\omega\frac{\omega_m}{Q_m} - \omega^2\right]} \sum_{n=0}^{\infty} \frac{j\omega\rho_0 \gamma_{nk} \gamma_{nm}}{V\left[k_n^2 - k^2\right]} \qquad 8.34.$$

For comparison, when there is no fluid-loading the forcing integral required for the same diaphragm velocity, as given in expression 8.28, is

$$\int_{V_d} \boldsymbol{\Phi}_k(\boldsymbol{y}).\boldsymbol{f}_i(\boldsymbol{y})dV = \delta_{km} \qquad 8.35.$$

The interesting result from this exercise is that expression 8.34 indicates that as the modal coupling factors, γ_{nk}, are minimised the velocity of the fully-coupled diaphragm tends towards that of the in-vacuo diaphragm.

8.4 The search for the ideal compression-driver diaphragm

In the previous section, a criterion was outlined for the ideal compression driver diaphragm in terms of the mechanical mode shapes of the diaphragm structure. Unfortunately, there is no straightforward way to determine the ideal structure meeting this criterion. Indeed, it is entirely possible that no structure is exactly able to meet the required conditions. There are a great number of possible variations of geometry that may be considered as candidates. Thus, it makes sense prior to beginning an exhaustive search to first consider the most practical and likely options.

The prototypical example of a biorthogonal set of functions is $\sin(nx)$ and $\cos(nx)$. For a particular order n, where one of these functions is zero the other has a maxima. The acoustical modes of the compression cavity are subject to a rigid-walled boundary condition and, consequently, at the bounding surface the pressure gradient in the surface normal direction is zero. As a result, the acoustical modes of the cavity have maxima at both the centre and the outer diameter. Is likely that the ideal diaphragm is simply supported at the outside diameter such that the mechanical modes are zero at this location. Practically this is difficult to achieve and a fully clamped mechanical termination is a more practical option. Such a diaphragm would not have a rigid body mode and the net volume velocity providing acoustical output must come from the first mode of the structure. The natural frequency of this first mode would determine the natural frequency of the driver F_s.

This arrangement is quite convenient in some respects as it potentially allows the diaphragm to be directly connected to the phase-plug structure. This is a very nice mechanical situation in terms of controlling the relative positions of the diaphragm and the phase plug. Additionally, it is important that the compression cavity is completely closed in order for the channel-positioning methodology in sections 4.2 and 5 to be valid. With a conventional compression driver, this is often achieved by using a ferromagnetic fluid to seal the voice-coil gap (see figure 2.15). However, it is not always possible or desirable to use

ferromagnetic fluid in the gap. This is clearly not a problem if the diaphragm is directly connected to the phase plug.

For optimal compression-driver performance to high frequencies, it is vital that the volume of the compression cavity is minimised. The compression cavity always exhibits a rigid-body mode with unity magnitude. This allows the acoustical cavity shape required for a given diaphragm to be established in a deterministic manner by applying a similar logic to the analysis at the start of chapter 6 as follows.

Recalling that the acoustical cavity modes form an orthogonal set of functions and obey the orthonormal relationship

$$\int_V \Psi_n(\boldsymbol{y})\Psi_m(\boldsymbol{y})\,dV = V\delta_{nm} \tag{8.36.}$$

Provided that the compression cavity is a thin shell that closely follows the compression driver diaphragm, this integral may be approximated as

$$\int_{S_d}\int_h \Psi_n(\boldsymbol{y})\Psi_m(\boldsymbol{y})\,dh\,dS = V\delta_{nm} \tag{8.37.}$$

where the first integral is over the surface of the compression driver diaphragm, which must form one full face of the compression cavity, and the second integral is through the thickness of the compression cavity in a direction perpendicular to the driver diaphragm surface. Provided that the compression cavity is small in the direction h, the acoustical modes $\Psi_n(\boldsymbol{y})$ are very nearly invariant of h and it may be approximated that

$$\int_{S_d} \Psi_n(\boldsymbol{y})\Psi_m(\boldsymbol{y})\mu(\boldsymbol{y})\,dS \approx V\delta_{nm} \tag{8.38.}$$

where $\mu(\boldsymbol{y})$ is a function that describes the thickness of the cavity in a direction perpendicular to the diaphragm surface at the location $\boldsymbol{y}$.

Setting $m=0$, recalling $\Psi_0(\boldsymbol{y})=1$, dividing both sides by V results in the expression

$$\int_{S_d} \Psi_n(\boldsymbol{y})\frac{\mu(\boldsymbol{y})}{V}\,dS \approx \delta_{0n} \tag{8.39.}$$

The expression describing the condition for optimal compression driver diaphragm behaviour was given in 8.16 to be,

$$\gamma_{nk} = \int_{S_d} \Psi_n(\boldsymbol{x})\boldsymbol{\Phi}_k(\boldsymbol{x}).\boldsymbol{n}\,dS = A\,\delta_{n0}\delta_{0k} \tag{8.40.}$$

For the case $k=0$ this simplifies to

$$\int_{S_d} \Psi_n(\boldsymbol{x})\boldsymbol{\Phi}_0(\boldsymbol{x}).\boldsymbol{n}\,dS = A\,\delta_{n0} \qquad 8.41.$$

Comparison of 8.39 with 8.41 reveals that the compression-cavity thickness function should be proportional to the zeroth diaphragm eigenfunction in the direction normal to the compression cavity entrance surface.

$$\mu(\boldsymbol{y}) \propto \boldsymbol{\Phi}_0(\boldsymbol{y}).\boldsymbol{n} \qquad 8.42.$$

This is very convenient on two counts. Firstly, the low-frequency motion of the compression driver diaphragm is dominated by the rigid body mode and, consequently, using the first mechanical eigenfunction as the thickness-profile for the compression cavity generates an almost constant mechanical clearance over the entire diaphragm surface. This ensures that the acoustical volume of the compression cavity is minimised for a given mechanical clearance. Secondly, the search scope is greatly reduced as for each candidate compression-driver diaphragm there is a single unique cavity geometry.

Based on the discussion above, a global search approach was devised in order to try and find a compression-driver diaphragm that approximately meets the condition in expression 8.16. Each step of the global search consists of the following steps:

1. construct a PAFEC-FE mechanical modal analysis model of a candidate compression-driver diaphragm based on geometric parameters, such as the diaphragm curvature angle, which are under optimisation;
2. construct a PAFEC-FE acoustical modal analysis model of the complimentary compression cavity with geometry determined using the method outlined above along with the modal results from step 1;
3. approximately compute the integral γ_{nk} from the results of step 1, and 2, using the same method as was outlined in section 5.4.1 in order to approximate the integral;
4. calculate the value of an objective function based on the computed approximation to γ_{nk}.

The relationship between the geometric parameters and the objective function is complex and, as a consequence, a simple grid approach was used in order to search for optimal diaphragm geometries. An iterative minimisation approach is unlikely to find the global minimum: however, minimisation may be a useful approach to locally fine-tune the geometry once the global minimum has been located.

If one considers that the value of the zeroth modal coupling coefficients, γ_{00}, represents the desirable coupling between the acoustical and mechanical systems then it is helpful to express each coupling term in decibels as

$$\Gamma_{nk} = 20\log_{10}\left(\frac{\gamma_{nk}}{\gamma_{00}}\right) \qquad 8.43.$$

For each step of the search a single valued objective function must be calculated from the computed values of Γ_{nk}. The objective function used for the initial search was the maximum value of Γ_{nk} over the range $0 \le n \le 4$ and $0 \le k \le 3$ with the value for $n=0 \wedge k=0$ excluded. The acoustical cavity was created for each step with 1mm thickness at the axis of rotation. In order to ensure that modal model of the cavity is soluble, the minimum thickness was restricted to 0.025mm. It should be noted that this does not necessarily result in a practical cavity.

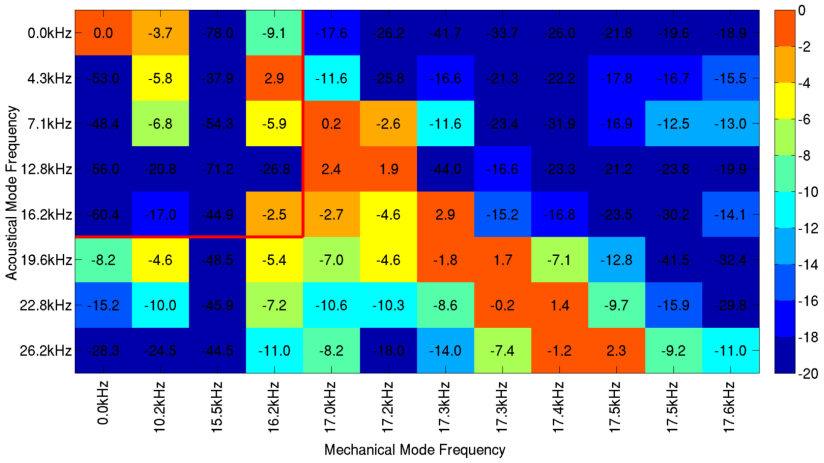

Figure 8.14. Computed values of Γ_{nk} for the compression driver diaphragm and cavity combination for which the driven cavity response was given in figure 8.9.

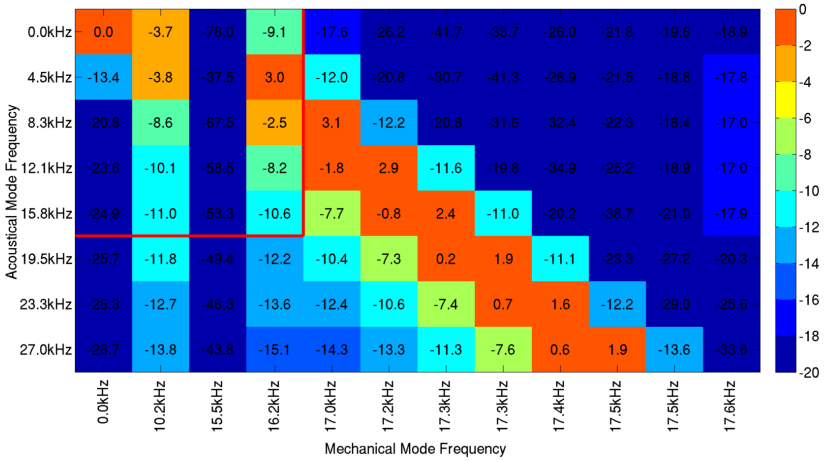

Figure 8.15. Computed values of Γ_{nk} for the compression-driver diaphragm and cavity combination for which the driven cavity response was given in figure 8.11.

For reference, figure 8.14 and 8.15 show the first few values of Γ_{nk} for the two example non-rigidly driven compression cavities, previously shown in figures 8.9 and 8.11, respectively. The red outlined region depicts the area to be controlled in the search. In both of the figures, some of the modes within the audio bandwidth couple almost as effectively as the desired zeroth mode coupling. Indeed, in the case shown in figure 8.15, one of the modal coupling factors in the audio band is 3dB more effective than the Γ_{00} factor.

In both of the examples, it can be seen that there is a clear diagonal band where the coupling between the acoustical and mechanical modes is most effective. It is also interesting to note that, in the case shown in figure 8.14 the values of Γ_{nk} are extremely low for the excitation of the first four acoustical modes by the rigid-body mechanical mode. This is because this particular cavity was designed using the cavity-shaping methodology, as described in Appendix XI, and was based on controlling the excitation of the first four acoustical modes for the case when this diaphragm is perfectly rigid.

8.4.1 Global search A

A first attempt to find a compression-driver diaphragm approximately meeting the condition on γ_{nk} using the global search approach was performed based on the geometry shown in figure 8.16. This geometry was chosen for a number of reasons. Firstly, the inverted roll at the outside diameter of the spherical cap section ensures that, in the first mode shape of the structure, the main body of the diaphragm translates along the axis of rotation and a useful net volume velocity is generated. Secondly, the diaphragm shape is very practical to form and is quite commonly used. The outside diameter of the diaphragm structure is fully restrained as if it is glued to a solid structure. The diaphragm geometry was modelled with a 25μm titanium construction and an outside diameter of 76.2mm.

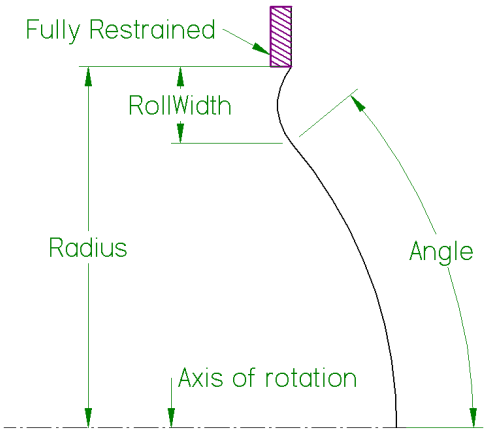

Figure 8.16. Spherical cap with inverted-roll surround compression-driver diaphragm geometry used for global search of γ_{nk}.

The global search was initially performed on a regular grid of the two geometrical parameters “angle” and “roll width”. The parameter “angle” was varied in increments of 2.5 degrees starting from 30 degree to a maximum of 70 degrees. The parameter “roll width” was varied in increments of 0.25mm starting from 2mm to a maximum of 20mm. In each step of the search, in addition to the maximum value of Γ_{nk} as discussed above, the diaphragm mass was also recorded.

Figure 8.17 graphically shows the values of Γ_{nk} in the global search space. There is a clear area of minimum Γ_{nk} for large dome angles and when the roll width is approximately 8.5mm.

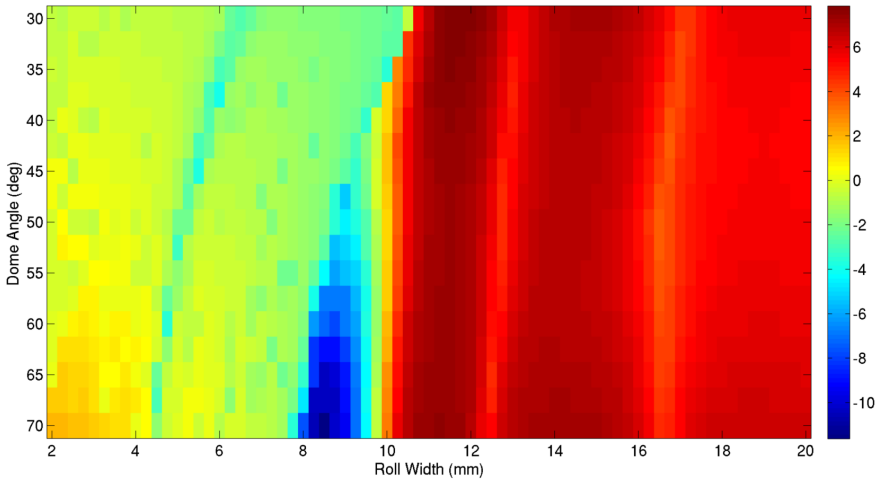

Figure 8.17. Objective function, Γ_{nk}, over first global optimisation parameter space.

Table 8.2 shows the ten geometries with the lowest objective function. The very lowest objective function found was -11.6dB, which indicates that the greatest coupling factor in the range $0 \leq n \leq 4$ and $0 \leq k \leq 3$ was 11.6dB lower than the coupling factor $n=0 \wedge k=0$. The coupling factors for this geometry, with angle 70 degrees and roll width 8.5mm, are shown graphically in figure 8.18. Comparison of this figure with those shown in figures 8.14 and 8.15 reveal that in the controlled region, outlined in red, the modal coupling parameter Γ_{nk} is much lower.

It is also interesting to note that just outside of the controlled region some of the coupling factors are extremely high. For example, for the mechanical mode $k=1$, the coupling factors with the acoustical modes $n=5$ and $n=6$ are 1.9dB and 5.2dB, respectively. The acoustical modes in this case lie right on the top end of the audio band. However, as they severely couple to the mechanical modes, the influence may be seen within the audio band.

Angle (deg)	Roll Width (mm)	Mass (g)	$max(\Gamma_{nk})$ (dB)
70.00	8.50	0.726369	-11.628800
70.00	8.25	0.727536	-10.507300
65.00	8.50	0.690432	-10.439400
67.50	8.75	0.706926	-10.358200
67.50	8.25	0.708705	-10.323500
67.50	8.50	0.707900	-10.269200
70.00	8.75	0.725597	-10.230100
65.00	8.75	0.689687	-9.977990
70.00	9.00	0.724598	-9.433200
67.50	9.00	0.706074	-9.030350

Table 8.2: Ten compression driver diaphragm geometries with the lowest objective function resulting from the global search, sorted in order of lowest objective function and then lowest mass.

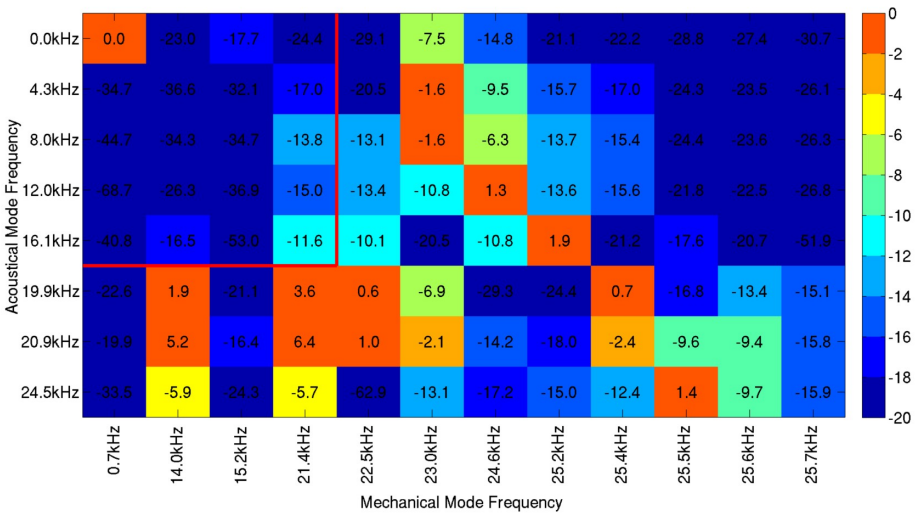

Figure 8.18. Computed values of Γ_{nk} for the compression driver diaphragm with geometry according to figure 8.16 with the geometric parameters angle=70, radius=76.2/2 and roll width=8.5.

To test the extent to which the acoustical modes are excited by the cavity, a sinusoidally driven FEM model was constructed to compute the approximate the in-vacuo mechanical velocities of this diaphragm. In this case, the diaphragm was driven axially at the intersection of the spherical cap and reverse roll region. However, it should be noted that this position is chosen arbitrarily. Indeed, there may be a more suitable location (see the discussion of F_k in section 8.2 for more detail). The diaphragm velocities computed in the in-vacuo mechanical FEM model were then used, along with the FEM modal acoustical analysis of the compression cavity, to calculate the functions $\zeta_n^d(\omega)/\zeta_0^d(\omega)$. The first four terms are shown in figure 8.19. These are intentionally placed on the same scale as figures 8.6 and 8.8 for

comparison. The computed values of $\zeta_n^d(\omega)/\zeta_0^d(\omega)$ seem quite encouraging as, comparing these with figures 8.6 and 8.8, there is a clear reduction in the level of the functions in the high-frequency region. However, at the top of the audio bandwidth the level is much higher.

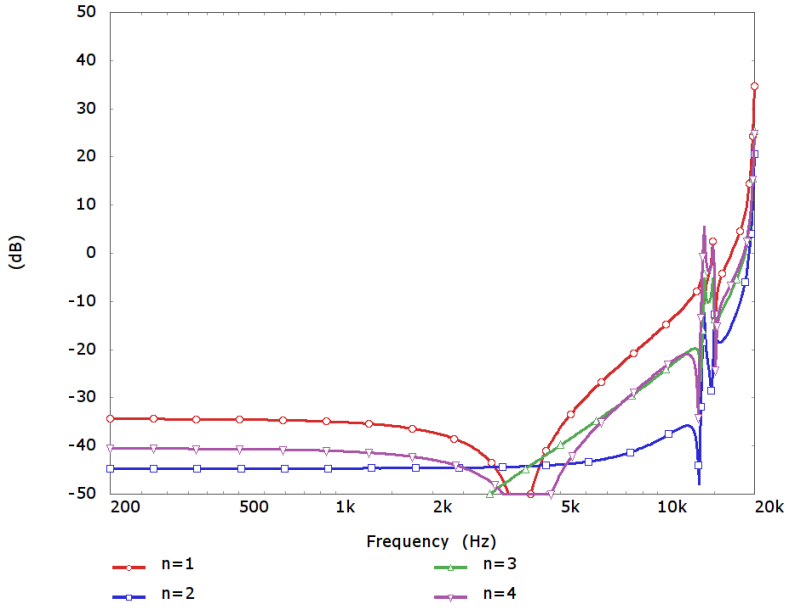

Figure 8.19. Decibel level of calculated functions $\zeta_n^d(\omega)/\zeta_0^d(\omega)$ for in vacuo FEM calculated non-rigid diaphragm and cavity found in first global search.

The in-vacuo diaphragm velocities were also used to drive an acoustical sinusoidal FEM model of the compression cavity with no exit channels in order to assess the level of acoustical modal excitation by looking at the pressure response in the cavity. The results are shown in figure 8.20. For comparison, the cavity pressure response previously shown in figure 8.9 for a diaphragm and cavity combination that made no attempt to account for the non-rigidity of the diaphragm is also shown (red). Below approximately 12kHz the optimised geometry is significantly better than the unoptimised. The three “glitches” on the response occurring at 4.3kHz, 8kHz and 12kHz correspond to the first three acoustical modes of the cavity, which are given in the axes labels of figure 8.18. These are relatively well suppressed. The peak in the pressure response at 14kHz and 15.2kHz correspond to the first two mechanical modes of the diaphragm.

Considering figure 8.19, the $\zeta_n^d(\omega)/\zeta_0^d(\omega)$ functions all clearly show glitches at these two frequencies that have the characteristic close peak and dip of a suppressed pole. The $\zeta_n^d(\omega)/\zeta_0^d(\omega)$ functions have an upward trend and the level of the functions is close to 0dB in the region of the glitches, seemingly due to the superposition on the upward trend. To further

improve the driven pressure performance it seems that it is necessary to extend the region of control of the γ_{nk} parameters to include the mechanical modes at the limit of the audio band.

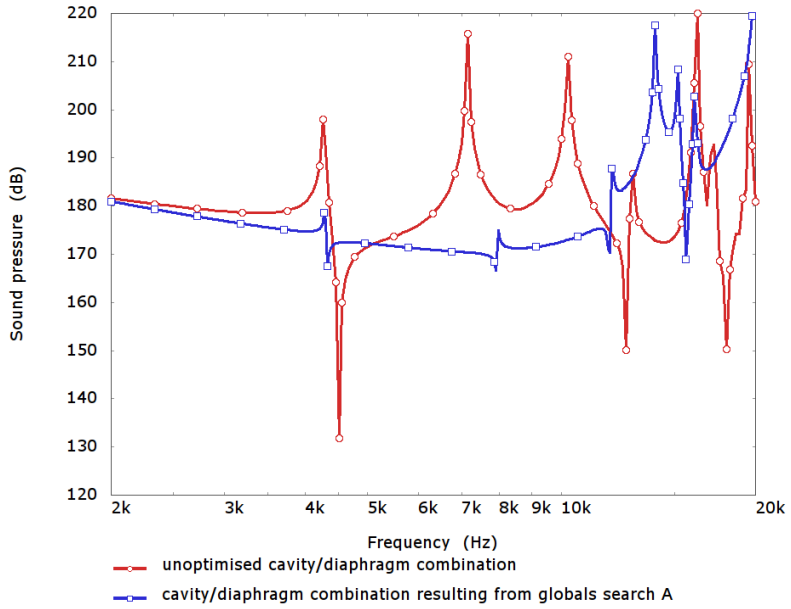

Figure 8.20. In-vacuo diaphragm velocity excited pressure response of an unoptimised compression driver diaphragm and cavity combination, previously described in figure 8.9, compared to the cavity and diaphragm combination resulting from global search A.

The performance of the diaphragm in a simple driver

To give an overall indication of the performance of this compression driver and cavity combination, a fully coupled FEM model was developed including a simple compression driver with channels terminated into ideal $\rho_0 c_0$ specific acoustical impedance conditions. As was highlighted previously, the compression-driver design method summarised in section 5.4 requires a single, frequency-invariant value for the normalised zeta parameters ζ_n^d/ζ_0^d. As figure 8.19 attests, the derived geometry does not provide frequency invariant values of ζ_n^d/ζ_0^d.

For an ideally behaving compression diaphragm and cavity, the ζ_n^d/ζ_0^d parameters are

$$\frac{\zeta_n^d(\omega)}{\zeta_0^d(\omega)} = \delta_{0n} \qquad 8.44.$$

The phase-plug was designed based on these ideal ζ_n^d/ζ_0^d parameters.

The three channels are placed in the nodal diameters of the third compression cavity mode resulting in the computed channel areas

$$\begin{bmatrix} A_1/A_T \\ A_2/A_T \\ A_3/A_T \end{bmatrix} = \begin{bmatrix} 0.2399 \\ 0.3797 \\ 0.3804 \end{bmatrix} \qquad 8.45.$$

where A_1 is the area of the inner of the three channels, A_2 is the area of the middle channel and A_3 is the area of the outer most channel. These areas can equivalently be written as channel width ratios as

$$\begin{bmatrix} w_2/w_1 \\ w_3/w_1 \end{bmatrix} = \begin{bmatrix} 0.7507 \\ 0.5673 \end{bmatrix} \qquad 8.46.$$

Using these geometric parameters, a simple compression-driver FEM model was constructed with a compression ratio of 15 and with the three channels terminated with a $\rho_0 c_0$ specific acoustical impedance. The diaphragm was driven at the same point as in the above calculation of the ζ_n^d/ζ_0^d functions. The FEM-computed pressures in the three channels are shown in figure 8.21. The pressure levels shown are normalised by the specific acoustical impedance of a tube,

$$L_{norm} = 20\log_{10}\left|\frac{p}{\rho_0 c_0}\right| \qquad 8.47.$$

At low frequencies all three channels have a normalised pressure level of 21.4dB. This is slightly lower than is seen on the preceding simple compression-driver models. This is because this compression-driver diaphragm does not radiate with a rigid-body mode, but rather the first bending mode and, consequently, the volume velocity for unit drive-point velocity is slightly lower.

The channel pressures are very similar indeed up to $ka = 2$. Above this they begin to diverge a little, but even at $ka = 6$ all three channels are within 3dB. Above $ka = 6$, there are distinct frequencies where the channel pressures are significantly different. For example, at $ka = 6.95$ and at $ka = 7.92$, there is a spread of 12.5dB and 9dB, respectively. However, the general shapes of the responses continue to follow the same pattern and between the glitches the pressures are relatively close. For example, at $ka = 7.5$ and at $ka = 8.8$ the spread is 3dB and 4dB, respectively.

The channel pressures in figure 8.21 are directly comparable to those which were previously shown in figure 8.11. Comparing these two figures, it is obvious that there is a clear

improvement in the performance in this case with the pressure difference between the channel responses much closer with this geometry. Additionally, it is interesting to observe that the channel pressures at the top end of the driver response are higher in this case.

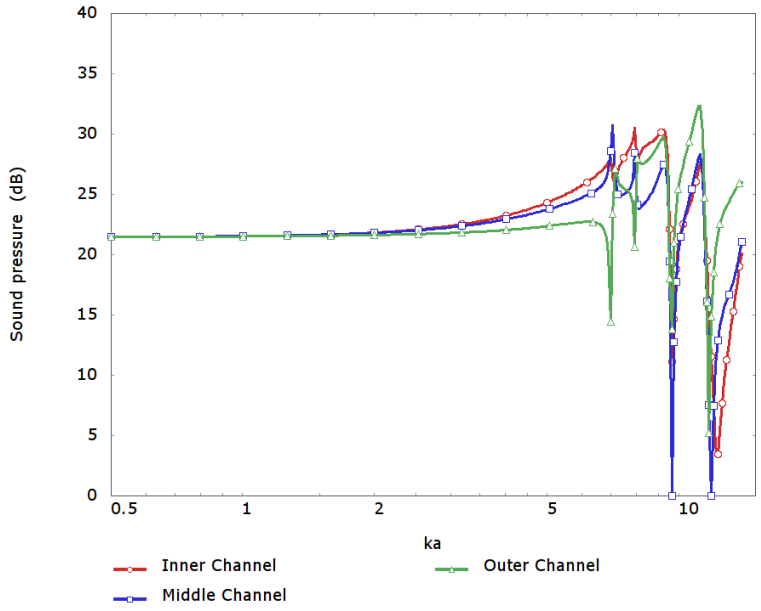

Figure 8.21.Normalised channel-pressure level response for diaphragm and cavity geometry found with global search A, with phase-plug geometry computed using the generalised method introduced in section 5.4.1, note that the fluid and structural regions are fully coupled.

8.4.2 Global search B & C

The geometry used in the first global search is composed only of a thin titanium membrane. There is no voice-coil region on this particular geometry. During the global search no assumptions were made about the location of the drive point and, additionally, the driven analyses were performed with an ideal point force applied arbitrarily to a point on the structure. In practice a voice-coil structure must be connected to some position on the diaphragm membrane. The mass and stiffness of the voice-coil assembly modifies the structural modes of the mechanical system. Consequently, it is not strictly accurate to leave the voice-coil structure from the mechanical system during the global search. In global search A the quality function was based only on the values of coupling parameters γ_{nk}. The definition of the normalised zeta functions, in terms of the mechanical modes, is

$$\frac{\zeta_n^d(\omega)}{\zeta_0^d(\omega)} = \frac{\sum_{k=0}^{\infty} \frac{F_k \gamma_{nk}}{\left[\omega_k^2 + j\omega\omega_k Q_k^{-1} - \omega^2\right]}}{\sum_{k=0}^{\infty} \frac{F_k \gamma_{0k}}{\left[\omega_k^2 + j\omega\omega_k Q_k^{-1} - \omega^2\right]}} \qquad 8.48.$$

If the drive location is known then the excitation amplitude of each mechanical mode, F_k, may be computed for each candidate geometry in the search. For the case when the structure is driven with a point force at a position $\boldsymbol{y}_d$, then the forcing term F_k may be simplified to

$$F_k = \boldsymbol{\Phi}_k(\boldsymbol{y}_d).\boldsymbol{f}_i \qquad 8.49.$$

where $\boldsymbol{f}_i$ is a point forcing vector. The parameter Γ^f_{nk} is defined to be

$$\Gamma^f_{nk} = 20\log_{10}\left(\frac{F_k\,\gamma_{nk}}{F_0\,\gamma_{00}}\right) \qquad 8.50.$$

and a quality function may then be based on the minimisation of the Γ^f_{nk} parameters for $n \neq 0 \wedge k \neq 0$. It is possible to plot the Γ^f_{nk} in the same way to the contours of Γ_{nk}. Figure 8.22 shows the Γ^f_{nk} coefficients for the optimal geometry found in search A for an axial point-force excitation at the junction between the spherical cap and half roll surround.

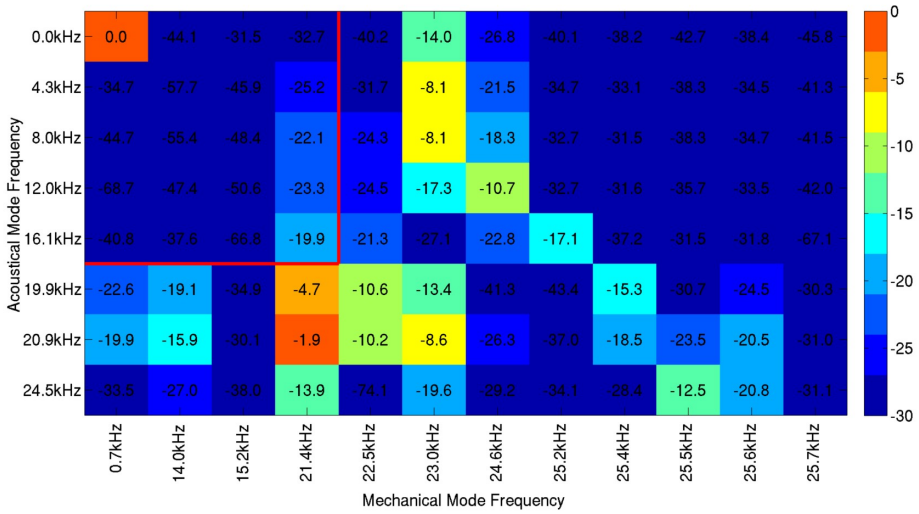

Figure 8.22. Computed values of Γ^f_{nk} for the compression driver diaphragm with geometry according to figure 8.16 with the geometric parameters angle=70, radius=76.2/2 and roll width=8.5, driven with an axial force at the junction between the spherical cap and the reverse roll regions.

Comparing this figure to 8.18, for this particular drive point generally, the level of the Γ^f_{nk} factors are reduced compared to the Γ_{nk} factors. It is also interesting to observe that some of the factors are now substantially lower, for example, the mechanical mode at 15.2kHz has extremely low values of Γ^f_{nk}. This indicates that for this particular drive point this mechanical mode is weakly excited.

For comparison figure 8.23 shows the values of Γ_{nk}^{f} for the situation when the diaphragm is driven at the centre on the axis of rotation. For this drive position, the values of Γ_{nk}^{f} are clearly much worse than for the drive position shown in figure 8.22.

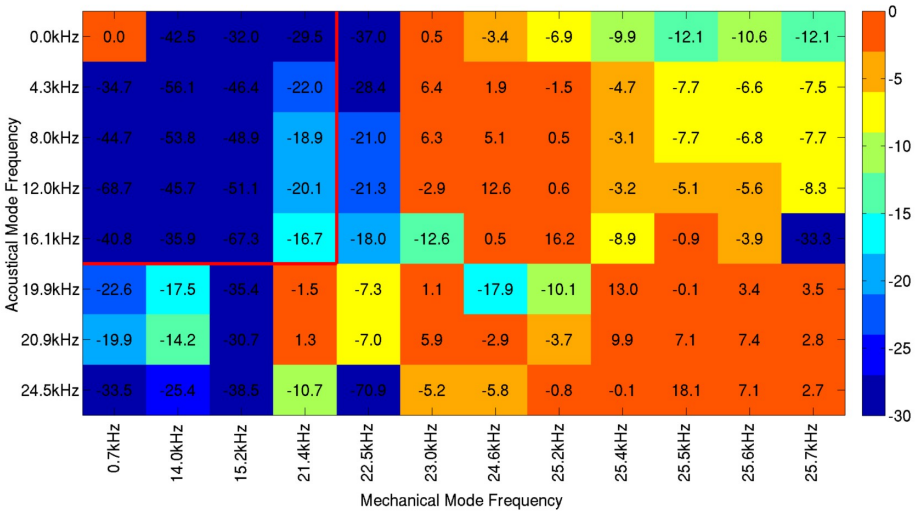

Figure 8.23. Computed values of Γ_{nk}^{f} for the compression driver diaphragm with geometry according to figure 8.16 with the geometric parameters angle=70, radius=76.2/2 and roll width=8.5, driven with an axial force centre of the geometry.

A global search based on the same diaphragm geometry described above with the addition of a voice coil region was performed using a objective function based on the forced parameters Γ_{nk}^{f}. Although the resulting diaphragm geometric parameters were slightly different from those found above, the performance of a simple compression driver using the diaphragm showed only moderate improvement compared to the results in figure 8.21. The full details are given in Appendix XIV.

8.4.3 Global search D

The diaphragm geometry used in global search A is fully restrained at the outer diameter. This configuration was chosen as the acoustical modes of the cavity had maxima at this location. It similarly seems logical that at the centre of the cavity, where the acoustical modes are also maxima, the diaphragm should also be fully restrained.

Figure 8.24 shows the geometry used in global search D. The voice-coil assembly is located between two annular radiating regions. Both the outer and the inner region are constructed of two tangential curves the ends of which are mechanically fully restrained. The geometry is controlled by numerous parameters that permit an extremely wide variation in the diaphragm geometry. In itself this presents a significant challenge: computation of the forced coupling factors $F_k \gamma_{nk}$ requires the solution of, firstly, a mechanical modal FEM model, then solution of the matching acoustical cavity FEM model, finally, the integrals are approximated in order to estimate $F_k \gamma_{nk}$. This process takes approximately 1 second on the solver machine[3].

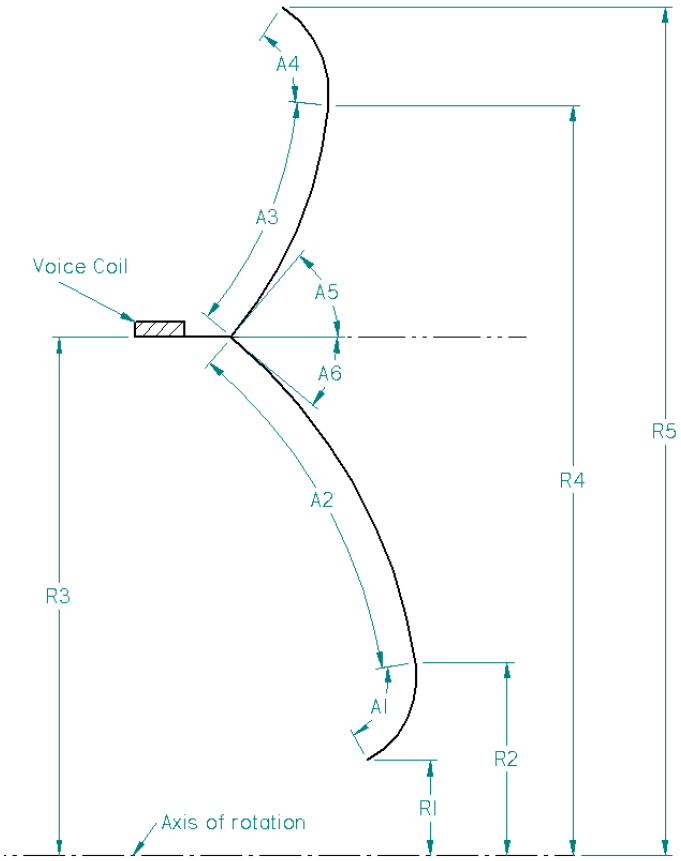

Figure 8.24. Compression-driver diaphragm geometry D used for global search of $F_k \gamma_{nk}$.

3 The solver computer has two Intel Xeon 5140 2.33GHz dual core processors and 8 GiB 667MHz synchronous RAM. PAFEC uses a single core for computation and the iterations were run serially.

Assuming that the diaphragm outside diameter is fixed, there are potentially 10 parameters for variation in the global search. If, for example, it is chosen to solve a full grid of these parameters with 10 variations of each, then this requires 10^{10} computations of the forced coupling factors $F_k \gamma_{nk}$. Given the 1-second solution time of the solver machine, then this full analysis would take approximately 317 years to complete. Clearly it is necessary, at least initially, to limit the search.

It was decided that the number of active parameters should be reduced to 5, for clarity given the notation p_1, p_2, p_3, p_4 and p_5. These search parameters are related to the geometric parameters shown in figure 8.24 by the expressions

$$R_1 = 5\,mm \tag{8.51.}$$

$$R_5 = \frac{76.2}{2}\ mm \tag{8.52.}$$

$$R_4 = R_5 - 2\ \ mm \tag{8.53.}$$

$$R_2 = R_1 + 2\ \ mm \tag{8.54.}$$

$$R_3 = R_2 + p_1(R_4 - R_2)\ \ mm \tag{8.55.}$$

$$A_5 = p_4\ \ deg \tag{8.56.}$$

$$A_6 = p_5\ \ deg \tag{8.57.}$$

$$A_1 = (135 - A_6)(1 - p_2)\ \ deg \tag{8.58.}$$

$$A_2 = (135 - A_6)(p_2)\ \ deg \tag{8.59.}$$

$$A_3 = (135 - A_5)(p_3)\ \ deg \tag{8.60.}$$

and

$$A_4 = (135 - A_5)(1 - p_3)\ \ deg \tag{8.61.}$$

The effect of this parametrisation is that the inner diameter and outer diameter of the diaphragm are fixed and in addition the radii R_2 and R_4 are fixed at 2mm from the inner and outer diameter, respectively. The angle of the diaphragm at the inner and outer diameter is fixed to be 45 degrees from the y-axis. The position of the voice coil is permitted to vary as are angles A_5 and A_6. The curvature of the inner and outer annular diaphragm regions may also vary with the radios p_2 and p_3, which control the amount of curvature in the inner regions, A_2 and A_3, compared to the outer regions, A_1 and A_4. The geometry of the voice

coil is fixed with a coil wind height of 3.5mm, a former length of 7mm and a winding thickness of 0.35mm.

Based on this parametrisation an initial global search of the geometry was run over the parameter values

$$p_1 = \begin{bmatrix} 0.35 & 0.40 & 0.45 & 0.50 & 0.55 & 0.60 & 0.65 \end{bmatrix} \quad 8.62.$$

$$p_2 = \begin{bmatrix} 0.1 & 0.2 & 0.3 & 0.4 & 0.5 & 0.6 & 0.7 & 0.8 & 0.9 \end{bmatrix} \quad 8.63.$$

$$p_3 = \begin{bmatrix} 0.1 & 0.2 & 0.3 & 0.4 & 0.5 & 0.6 & 0.7 & 0.8 & 0.9 \end{bmatrix} \quad 8.64.$$

$$p_4 = \begin{bmatrix} 30 & 40 & 50 & 60 & 70 \end{bmatrix} \quad 8.65.$$

$$p_4 = \begin{bmatrix} 30 & 40 & 50 & 60 & 70 \end{bmatrix} \quad 8.66.$$

A full grid search in of these parameter values results in 14175 permutations of the geometry, which is around a 4 hour solution time.

For this search, two objective functions were evaluated for each step, both are based on the forced coupling parameters Γ^f_{nk} which are defined to be

$$\Gamma^f_{nk} = 20\log_{10}\left(\frac{F_k \gamma_{nk}}{F_0 \gamma_{00}}\right) \quad 8.67.$$

Firstly, the maximum value of Γ^f_{nk} in the range $0 \le n \le 4$ and $0 \le k \le 3$ with the value for $n = 0 \wedge k = 0$ not included and secondly the maximum value of Γ^f_{nk} for all acoustical and mechanical modes with natural frequencies $< 30\text{kHz}$ with the value for $n = 0 \wedge k = 0$ not included. The reason for this change is that it was quickly found that the spacing of the mechanical modes for this geometry follows a slightly different pattern from the previous geometries with a greater number of modes occurring at low frequencies. The first objective function is included for comparison with the previous searches.

Tables 8.3 and 8.4 show the ten geometries found from this search with the lowest primary and secondary objective function, respectively. The primary objective function is directly comparable to those shown in tables XIV.1 and XIV.2 for geometry B and C. The primary objective function is significantly lower in all cases shown in both tables for this geometry. Interestingly the geometries that provide the lowest primary objective function are different from those that provide the lowest secondary objective function. The geometry that seems to be the best compromise between the two objective functions is the last shown in table 8.3.

p_1	p_2	p_3	p_4	p_5	**Mass(g)**	**Obj fun (dB)**	**Obj fun 2 (dB)**
0.45	0.3	0.1	40	70	1.16219962	-33.726749	-16.307957
0.45	0.3	0.2	40	70	1.12726545	-33.57473	-17.868168
0.4	0.3	0.3	30	70	1.11889648	-32.747311	-17.272783
0.45	0.3	0.3	40	70	1.10171556	-32.417145	-18.171526
0.5	0.3	0.1	50	70	1.13639247	-32.416424	-16.203581
0.5	0.4	0.2	30	60	1.22873569	-31.880079	-18.478706
0.4	0.3	0.2	30	70	1.16684115	-31.856867	-17.453962
0.5	0.3	0.2	50	70	1.11845601	-31.751837	-16.574821
0.6	0.4	0.1	50	60	1.20875919	-31.691792	-10.282484
0.5	0.4	0.3	30	60	1.186885	-31.36709	-19.10997

Table 8.3: Ten compression-driver diaphragm geometries with the lowest primary objective function resulting from the global search.

p_1	p_2	p_3	p_4	p_5	**Mass(g)**	**Obj fun (dB)**	**Obj fun 2 (dB)**
0.65	0.3	0.4	50	50	1.23387718	-21.812588	-21.812588
0.6	0.2	0.1	30	40	1.39049864	-20.905472	-20.905472
0.6	0.1	0.1	30	40	1.40781558	-20.898106	-20.898106
0.5	0.5	0.6	30	50	1.13147926	-22.716904	-20.535938
0.5	0.4	0.6	30	40	1.14957571	-21.007446	-20.501404
0.6	0.4	0.3	30	40	1.28177118	-20.899002	-20.462214
0.45	0.8	0.6	30	60	1.08826494	-20.927742	-20.404894
0.45	0.5	0.6	30	50	1.09397531	-22.205452	-20.36969
0.65	0.1	0.5	40	40	1.30630064	-20.362864	-20.362864
0.65	0.2	0.5	40	40	1.28679204	-20.332348	-20.332348

Table 8.4: Ten compression-driver diaphragm geometries with the lowest secondary objective function resulting from the global search.

Figure 8.25 and figure 8.26 show the forced coupling factors Γ_{nk}^{f} for the geometries with the lowest primary and secondary objective functions respectively. Both of the geometries show much improved attenuation of the coupling factors compared to previous results. The red box indicates the region over which the primary objective function is calculated, figure 8.25 shows extremely low coupling factors in this region. However the coupling factors for other mechanical modes, for example the one occurring at 16.2kHz, are significantly higher.

Figure 8.26 by contrast shows an extremely low level of coupling for high-frequency mechanical modes at the expense of the coupling factors over the first four mechanical modes. It is not immediately obvious from the Γ_{nk}^{f} values which of these is the better performing geometry.

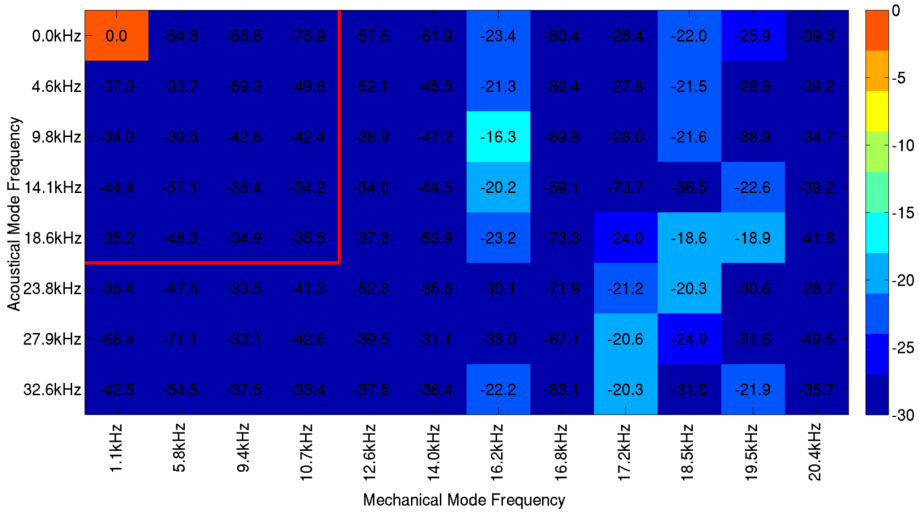

Figure 8.25. Computed values of Γ^{f}_{nk} for the compression-driver diaphragm with geometry according to figure 8.24 with the parameters $\boldsymbol{p}=\begin{bmatrix}0.45 & 0.3 & 0.1 & 40 & 70\end{bmatrix}$ corresponding to the lowest discovered primary objective function.

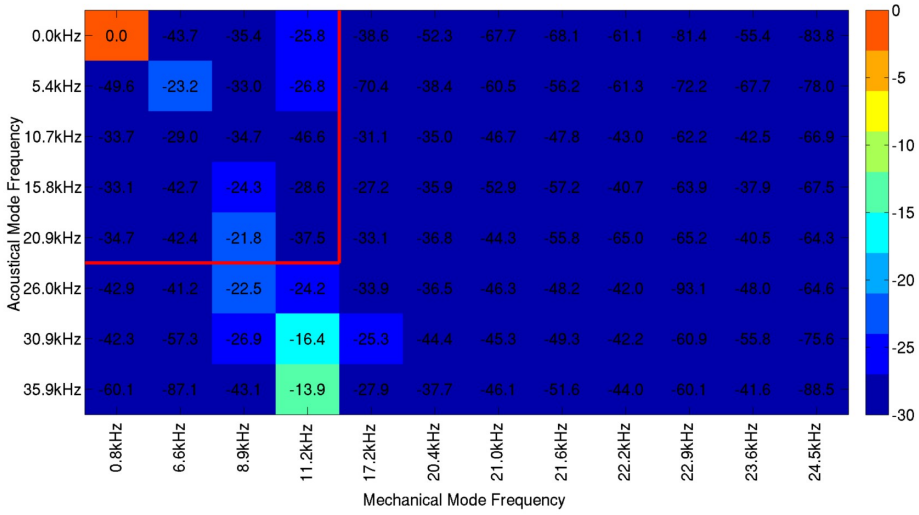

Figure 8.26. Computed values of Γ^{f}_{nk} for the compression driver diaphragm with geometry according to figure 8.24 with the parameters $\boldsymbol{p}=\begin{bmatrix}0.65 & 0.3 & 0.4 & 50 & 50\end{bmatrix}$ corresponding to the lowest discovered secondary objective function.

The normalised zeta functions for each of the geometries were approximated from the in-vacuo FEM-computed diaphragm velocities in combination with the FEM modal analyses of the compression cavity. The results are shown in figure 8.27 and figure 8.28 for the geometry with the lowest primary and secondary objective functions, respectively.

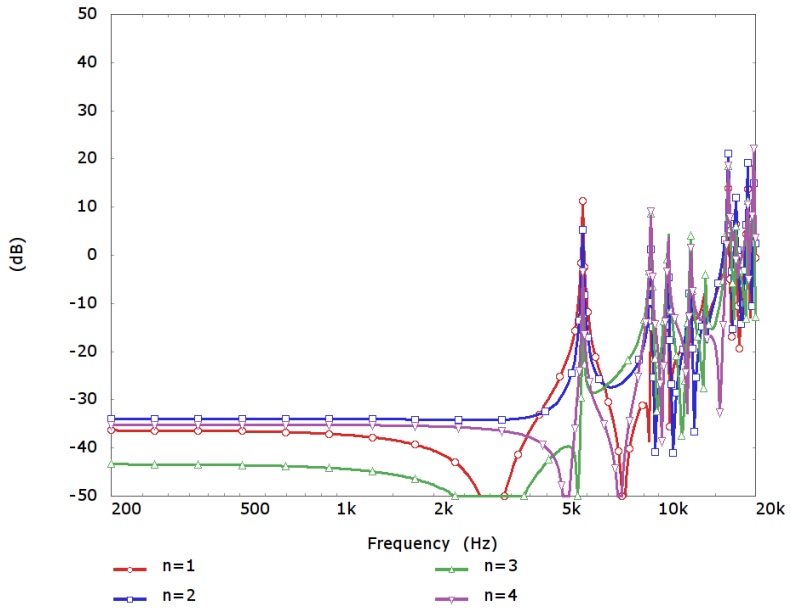

Figure 8.27. Decibel level of calculated functions $\zeta_n^d(\omega)/\zeta_0^d(\omega)$ for in-vacuo FEM-calculated non-rigid diaphragm and cavity found with geometry according to figure 8.24 with the parameters $\boldsymbol{p}=[0.45 \quad 0.3 \quad 0.1 \quad 40 \quad 70]$ *corresponding to the lowest discovered primary objective function.*

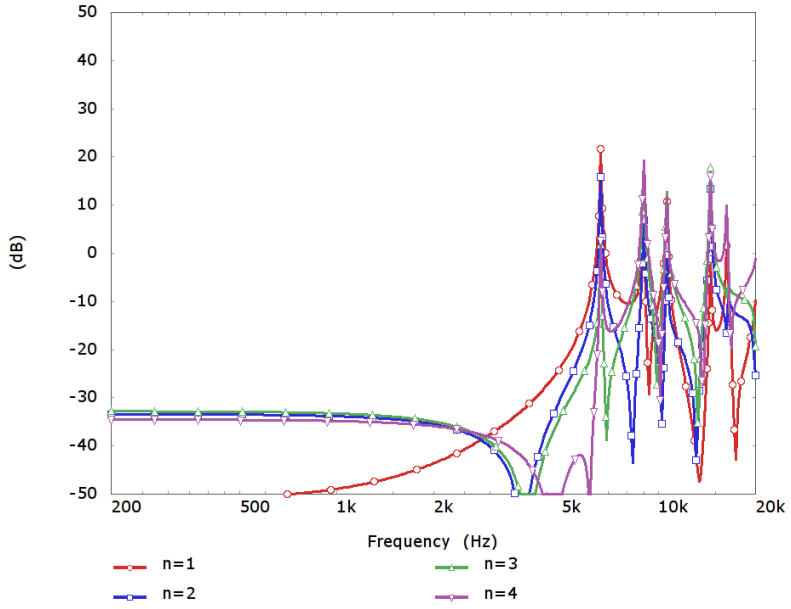

Figure 8.28. Decibel level of calculated functions $\zeta_n^d(\omega)/\zeta_0^d(\omega)$ for in-vacuo FEM-calculated non-rigid diaphragm and cavity found with geometry according to figure 8.24 with the parameters $\boldsymbol{p}=[0.65 \quad 0.3 \quad 0.4 \quad 50 \quad 50]$ *corresponding to the lowest discovered secondary objective function.*

Comparing these with one another the same pattern as was observed in the figures showing the forced coupling factors Γ_{nk}^f is seen. The geometry with the lowest primary objective function has lower levels of $\zeta_n^d(\omega)/\zeta_0^d(\omega)$ over the first four mechanical mode frequencies,

but high levels above this. Again, it is not immediately obvious from these figures which is the better performing geometry. The nature of the results is slightly different from those in the previous sections. In this case, the individual mechanical modes are clearly visible on each of the $\zeta_n^d(\omega)/\zeta_0^d(\omega)$ functions.

The two sets of results above are slightly contradictory as the forced coupling factors for the two geometries found from search D appear to be significantly improved compared to those previously presented. However, the $\zeta_n^d(\omega)/\zeta_0^d(\omega)$ are a little more difficult to interpret and do not show a clear improvement.

The performance of the diaphragm in a simple driver

To get a clear picture of the overall performance of the two new geometries, a three channel phase plug was designed and a fully-coupled FEM model of a simple compression driver with channels individually ideally terminated with a $\rho_0 c_0$ specific acoustical impedance condition was generated for each geometry. In the calculation of the channel positions and sizes, ideal values of $\zeta_n^d(\omega)/\zeta_0^d(\omega)=\delta_{0n}$ were assumed.

For the geometry with lowest primary objective function, this results in channel areas of

$$\begin{bmatrix} A_1/A_T \\ A_2/A_T \\ A_3/A_T \end{bmatrix} = \begin{bmatrix} 0.2690 \\ 0.2939 \\ 0.4371 \end{bmatrix} \tag{8.68.}$$

where A_1 is the area of the inner of the three channels, A_2 is the area of the middle channel and A_3 is the area of the outer most channel. These areas can equivalently be written as channel width ratios as

$$\begin{bmatrix} w_2/w_1 \\ w_3/w_1 \end{bmatrix} = \begin{bmatrix} 0.6576 \\ 0.7207 \end{bmatrix} \tag{8.69.}$$

For the geometry with lowest secondary objective function, this results in channel areas of

$$\begin{bmatrix} A_1/A_T \\ A_2/A_T \\ A_3/A_T \end{bmatrix} = \begin{bmatrix} 0.1920 \\ 0.3075 \\ 0.5005 \end{bmatrix} \tag{8.70.}$$

where A_1 is the area of the inner of the three channels, A_2 is the area of the middle channel and A_3 is the area of the outer most channel.

These areas can equivalently be written as channel width ratios as

$$\begin{bmatrix} w_2/w_1 \\ w_3/w_1 \end{bmatrix} = \begin{bmatrix} 0.9013 \\ 1.0377 \end{bmatrix} \quad 8.71.$$

The resulting normalised channel-pressure levels are shown for the primary objective function in figure 8.29 and for the secondary objective function in figure 8.30. The pressure levels shown are normalised by the specific acoustical impedance of a tube,

$$L_{norm} = 20\log_{10}\left|\frac{p}{\rho_0 c_0}\right| \quad 8.72.$$

From these figures, it is quite obvious that the geometry with the lowest primary objective function is clearly the better performer. Indeed, the performance of this geometry is extremely good and the channel pressures show a much greater consistency than the other similar results presented in this section with all three channel pressures within 5dB below $ka = 10$ (14.3kHz). There are clear "glitches" on the pressure responses at ka of 5.9, 7.0, 8.2 and 9.5 (8.45, 10, 11.7, and 13kHz). While these would seem to correspond to the mechanical modes of the diaphragm, it is interesting to note that the frequencies do not correlate with the in-vacuo natural frequencies of the diaphragm visible in figure 8.25.

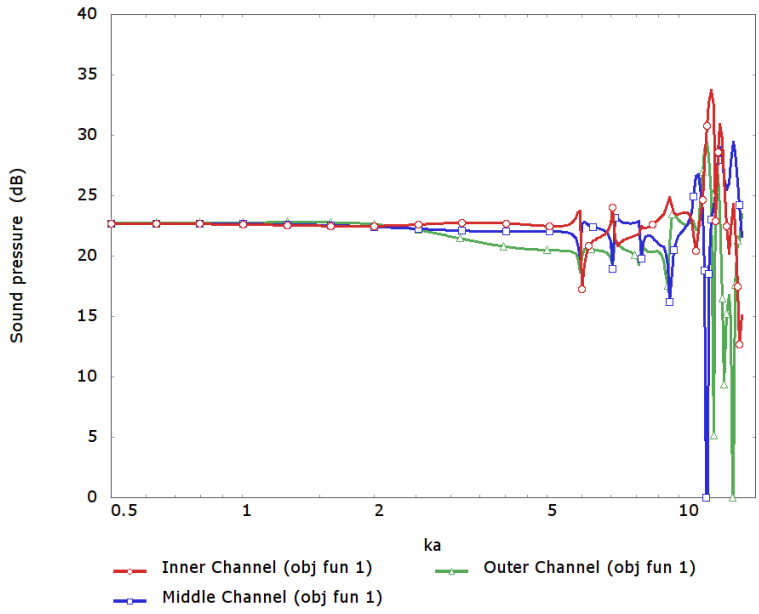

Figure 8.29. Normalised channel-pressure level response for diaphragm and cavity geometry found with global search D with lowest primary objective function, with phase-plug geometry computed using the generalised method introduced in section 5.4.1, note that the fluid and structural regions are fully coupled.

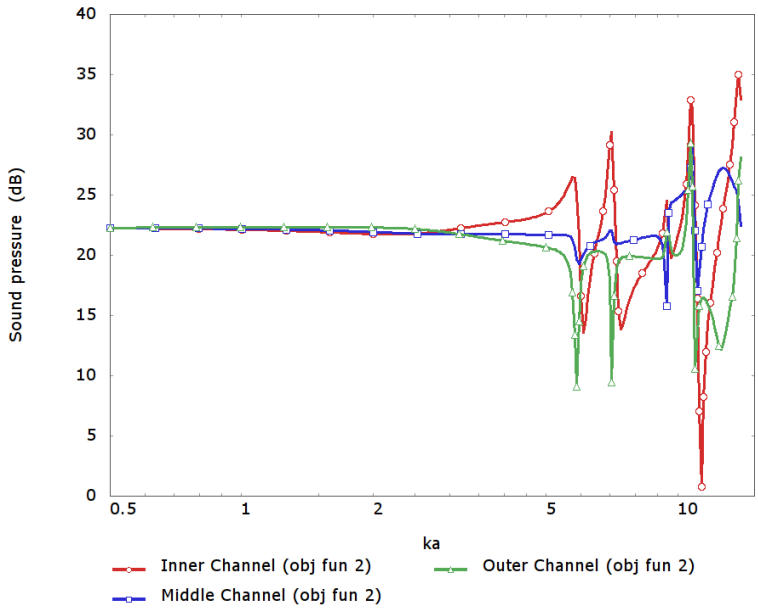

Figure 8.30. Normalised channel-pressure level response for diaphragm and cavity geometry found with global search D with lowest secondary objective function, phase-plug geometry computed using the method introduced in section 5.4.1, note that the fluid and structural regions are fully coupled.

The simplified compression driver results from this and the previous global searches are extremely encouraging as they suggest a direct correlation between low modal-coupling factors and increased compression driver performance. However, the correlation is not fully understood and the results above raise two clear points for further investigation. Firstly, further consideration is needed to determine the best way of forming an objective function from the coupling factors that more directly correlates to a well-performing diaphragm and cavity combinations. This would permit the geometric optimisation and search approaches to more quickly identify diaphragm and cavity combinations that correspond to good final driver performance. Secondly, the inconsistency between the calculated $\zeta_n^d(\omega)/\zeta_0^d(\omega)$ functions and the performance of the geometry in the simplified driver models. Improved understanding in this area may result in additional methods to improve driver performance.

8.5 Further consideration of the normalised zeta functions

The excitation of the cavity modes resulting from the diaphragm motion is characterised by the functions $\zeta_n^d(\omega)$. Optimal behaviour occurs when the normalised functions $\zeta_n^d(\omega)/\zeta_0^d(\omega)$ are minimised for $n\neq 0$. In the previous section, it was shown that this may be achieved if the modal coupling factors, γ_{nk}, are minimised for $n\neq 0 \wedge k\neq 0$. Additionally, using some basic analysis, it was demonstrated that if the coupling factors, γ_{nk}, are minimised, then the fluid-loading of the structure is also minimised. Based on this result, the in-vacuo mechanical velocities have been used in the computation of $\zeta_n^d(\omega)$ for the various examples above. However, it is instructive now to take the mechanical velocities from the final simplified compression-driver models given at the end of the previous section and recompute $\zeta_n^d(\omega)$ based on these. Figure 8.31 shows the functions $\zeta_n^d(\omega)$ for the geometry with the lowest primary objective function found in search D computed using the diaphragm velocity taken from the in-vacuo FEM analysis. This figure effectively shows the same information as figure 8.27, which demonstrated the normalised versions of the same functions $\zeta_n^d(\omega)/\zeta_0^d(\omega)$.

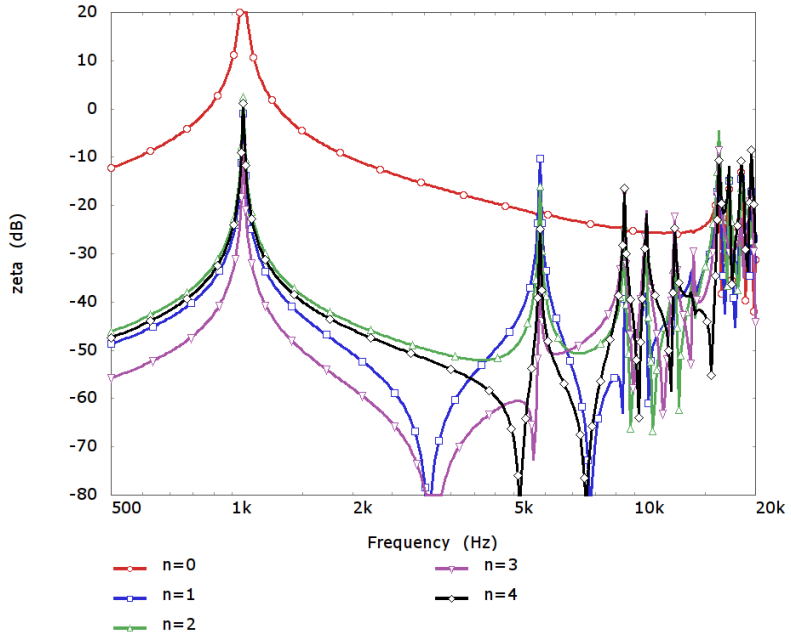

Figure 8.31. Decibel level of calculated functions $\zeta_n^d(\omega)$ for in vacuo FEM-calculated non-rigid diaphragm and cavity found with geometry according to figure 8.24 with the parameters $\boldsymbol{p}=[0.45 \quad 0.3 \quad 0.1 \quad 40 \quad 70]$ *corresponding to the lowest discovered primary objective function.*

Figure 8.32 shows the functions $\zeta_n^d(\omega)$ for the same diaphragm geometry computed using the mechanical velocities from in the fully-coupled simple compression driver model, the results of which were shown in figure 8.29.

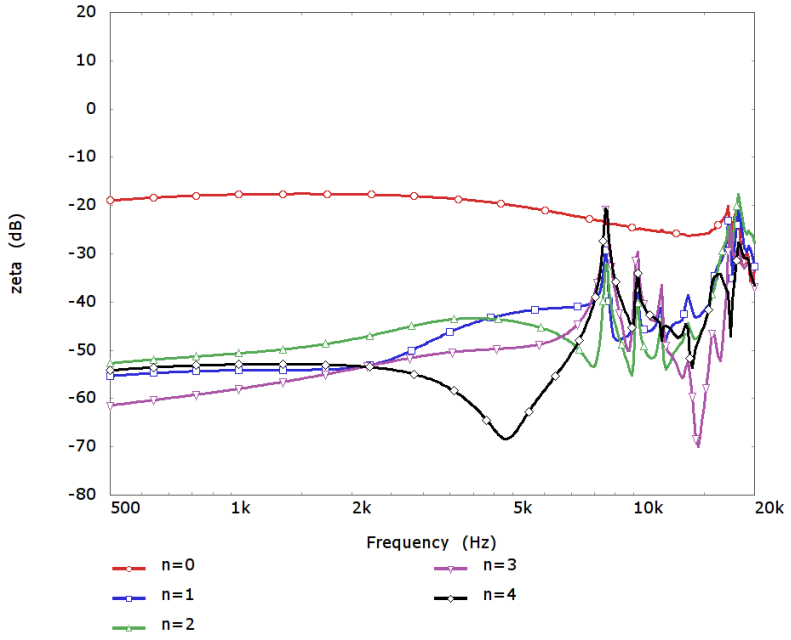

Figure 8.32. Decibel level of calculated functions $\zeta_n^d(\omega)$ for diaphragm and cavity found with geometry according to figure 8.24 with the parameters $\boldsymbol{p}=[0.45 \quad 0.3 \quad 0.1 \quad 40 \quad 70]$ corresponding to the lowest discovered primary objective function. In this case, the mechanical velocities for the diaphragm are taken from the fully-coupled simple compression driver model given in figure 8.29.

There is an obvious and large change in the level of the first mechanical mode. This mode provides the volume velocity from the radiator and, consequently, the modal coupling factor γ_{00} is not minimised in the global search. As a result, the first mechanical mode couples very effectively to the zeroth acoustical modal of the cavity and the fluid-structure coupling has a large effect. The phase-plug channels carry energy out of the system and this has the effect of dramatically increasing the apparent damping of the first mechanical mode. Less anticipated is that there is also a significant change to the zeta parameters for the other mechanical modes. The entire mechanical system behaves like there is significantly more damping than in the in-vacuo case. In addition, the frequency of some of the peaks in the zeta function is slightly different.

Figure 8.33 shows the functions $\zeta_n^d(\omega)$ for the geometry with the lowest secondary objective function found in search D computed using the in-vacuo calculated diaphragm velocity. Figure 8.34 shows the functions $\zeta_n^d(\omega)$ using the diaphragm velocity taken from the simple compression-driver model, the results of which were shown in figure 8.30.

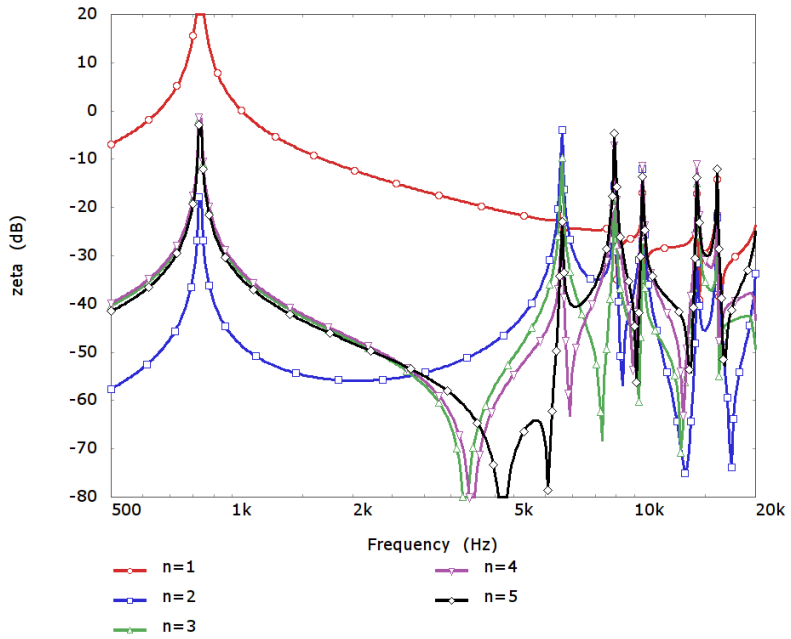

Figure 8.33. Decibel level of calculated functions $\zeta_n^d(\omega)$ for in vacuo FEM calculated non-rigid diaphragm and cavity found with geometry according to figure 8.24 with the parameters $\boldsymbol{p}=[0.65 \quad 0.3 \quad 0.4 \quad 50 \quad 50]$ corresponding to the lowest discovered secondary objective function.

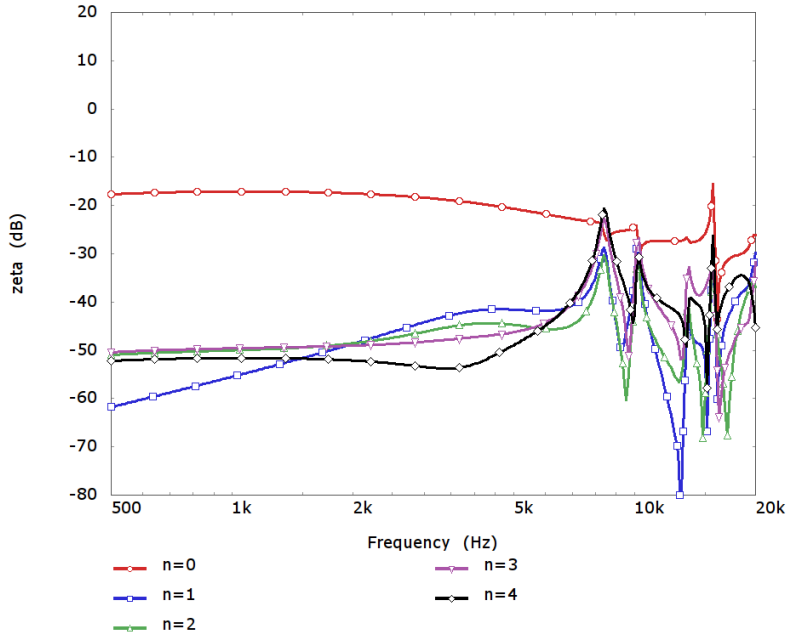

Figure 8.34. Decibel level of calculated functions $\zeta_n^d(\omega)$ for diaphragm and cavity found with geometry according to figure 8.24 with the parameters $\boldsymbol{p}=[0.65 \quad 0.3 \quad 0.4 \quad 50 \quad 50]$ corresponding to the lowest discovered secondary objective function. In this case, the mechanical velocities for the diaphragm are taken from the fully coupled simple compression driver model given in figure 8.30.

Again, the large increase in damping on the first mechanical mode is seen and, additionally, the higher mechanical modes also show an increased damping.

It is easier to correlate these fully-coupled $\zeta_n^d(\omega)$ results with the performances of the simple compression drivers given at the end of the previous section. One of the highlighted issues with the global search methods was the difficulty in correlating the γ_{nk} parameters with well-performing designs. Ideally, with approximation to the fully-coupled mechanical velocity, based purely on the mechanical and acoustical modes of the compression driver, it would be feasible to estimate the $\zeta_n^d(\omega)$ functions on each step of the search. An objective function could then be based upon the estimated $\zeta_n^d(\omega)$ functions, rather than the more abstract γ_{nk} parameters. The author has begun working on this approach. However, although the initial results are promising, the current approximation to the fluid-loaded mechanical velocity is poorer than is required as the basis of a reliable objective function.

8.5.1 The effect of mechanical damping upon the zeta functions

In section 8.2, a description of the zeta functions in terms of the modal coupling factors was outlined and described by

$$\zeta_n^d(\omega) = \sum_{m=0}^{\infty} \frac{j\,\omega\,F_m\,\gamma_{nm}}{\left[\omega_m^2 + j\,\frac{\omega\,\omega_m}{Q_m} - \omega^2\right]} \qquad 8.73.$$

The derivation of this expression does not include any fluid loading of the mechanical structure. Consequently, the summation is able to closely match the calculations of $\zeta_n^d(\omega)$ for the cases when in-vacuo driver-velocity FEM results were used. For example, figure 8.35 shows a comparison of the function $\zeta_1^d(\omega)$ calculated by integral approximation and using this expression.

As is discussed above, the in-vacuo zeta functions give a poor indication of the performance of the final driver so this approximation is of limited use. However, this expression highlights that if the mechanical damping of the diaphragm is increased, the Q_m parameters are reduced and then the $\zeta_n^d(\omega)$ functions become less erratic. In addition, in section 8.3.1 the fluid-loaded mechanical behaviour was briefly considered. The analysis in section 8.3.1 considered the applied force required on the diaphragm in order for the diaphragm to deform purely into a single in-vacuo mode. In summary, in order for the mechanical velocity of the diaphragm to be

$$\boldsymbol{u}_d(\boldsymbol{y}) = \frac{j\omega}{\left[\omega_k^2 + j\omega\frac{\omega_k}{Q_k} - \omega^2\right]}\boldsymbol{\Phi}_m(\boldsymbol{x}) \qquad 8.74.$$

it is necessary for the mechanical excitation of the dome to be

$$\int_{V_d} \boldsymbol{\Phi}_k(\boldsymbol{y}).\boldsymbol{f}_i(\boldsymbol{y})dV = \delta_{km} + \frac{j\omega}{\left[\omega_m^2 + j\omega\frac{\omega_m}{Q_m} - \omega^2\right]}\sum_{n=0}^{\infty}\frac{j\omega\rho_0\gamma_{nk}\gamma_{nm}}{V\left[k_n^2 - k^2\right]} \qquad 8.75.$$

At the frequency ω_m, the term preceding the summation on the right side of the expression simplifies to

$$\frac{Q_m}{\omega_m} \qquad 8.76.$$

If Q_m is large, then the fluid loading at the frequency ω_m may be significant, even if the γ_{nk} parameters have been minimised. Consequently, if the mechanical losses in the diaphragm are increased, the fluid-loading of the mechanical structure is reduced. This is advantageous as the the global search approaches, presented in the previous sections, attempt to find structures where the uncoupled mechanical and acoustical modes are approximately orthogonal.

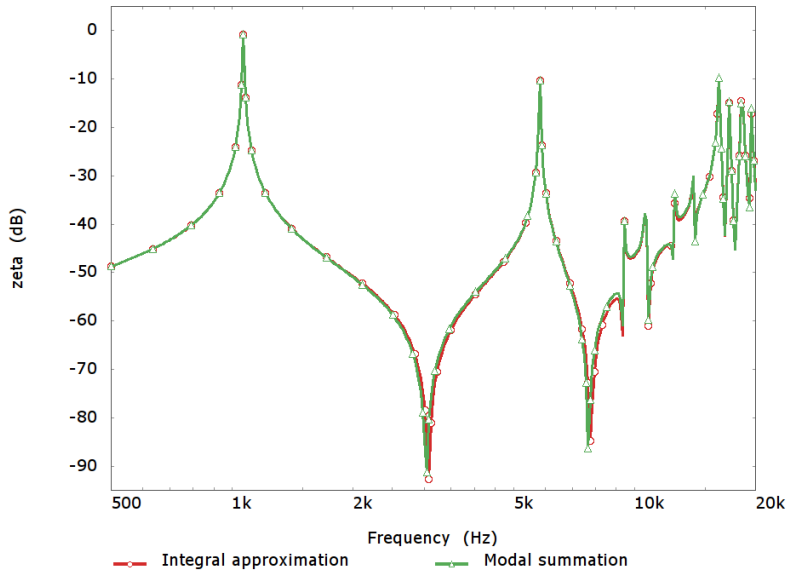

Figure 8.35. Comparison of the function $\zeta_1^d(\omega)$ calculated by approximation of the integral expression 8.59 using in-vacuo FEM-calculated non-rigid diaphragm velocities with the same function calculated using a modal summation approach as given in expression 8.73. In both cases, the geometry is of the compression driver as shown in figure 8.24 with the parameters $\boldsymbol{p} = [0.45 \quad 0.3 \quad 0.1 \quad 40 \quad 70]$, corresponding to the lowest discovered primary objective function.

If there is significant fluid-loading of the diaphragm, then the acoustical and mechanical modes will not remain approximately orthogonal. As a result, the performance of the compression driver will be reduced. It seems likely that an increase in the mechanical damping will have a very large performance benefit in terms of the overall compression-driver performance.

To test this hypothesis, the FEM model of the compression-driver design found with the lowest primary objective function from global search D, with results shown in figure 8.29, was remodelled with the mechanical damping coefficient of the diaphragm structure increased from $Q_m = 200$ to $Q_m = 20$. The resulting channel pressures are shown in figure 8.36. These results are very encouraging. The channel pressures are much more consistent than any of the previously presented non-rigid compression drivers. Figure 8.37 shows the accompanying geometry of the FEM model.

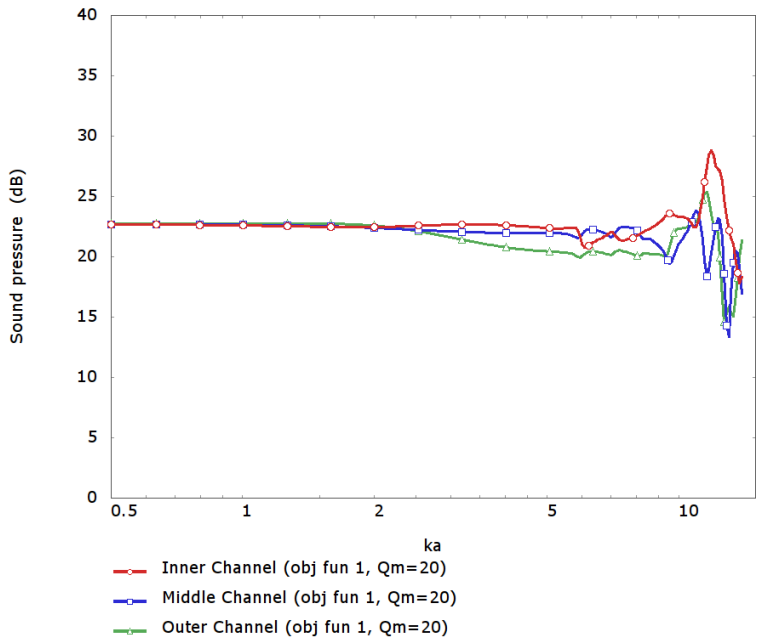

Figure 8.36. Normalised channel-pressure level response for diaphragm and cavity geometry found from global search D with lowest primary objective function, with phase-plug geometry computed using the generalised method introduced in section 5.4.1. Note that the fluid and structural regions are fully coupled. The diaphragm structure has a damping coefficient $Q_m = 20$ in this model.

The increase in the mechanical damping is quite significant, but not so drastic that it seems unachievable. High damping is desirable for mid-range direct-radiating loudspeaker diaphragms as they often operate in partial breakup at the upper end of the response. As a consequence, there are plenty of materials that are commonly used in loudspeaker diaphragms that have intentionality high damping. In addition, it was seen at the start of this

section that the acoustical coupling between the diaphragm and the compression cavity is effective enough to dramatically affect the diaphragm velocity. The effect, in this case, was to increase the apparent level of damping in the mechanical structure. This occurred because vibrational energy from the dome structure was radiated into the cavity and then through the phase-plug channels and out from the system. The diaphragm also radiates from the rear. It is conceivable that the mechanical structure of the compression driver may be effectively damped using the rear radiation. Most likely this approach would require some closely spaced acoustical absorbent material to be placed close to the rear of the dome. Naturally, this effect would have to be accounted for during the design of the diaphragm in order to ensure that the γ_{nk} parameters were correctly minimised. This would possibly also provide another means of adjusting the modes of the diaphragm, which may help this minimisation.

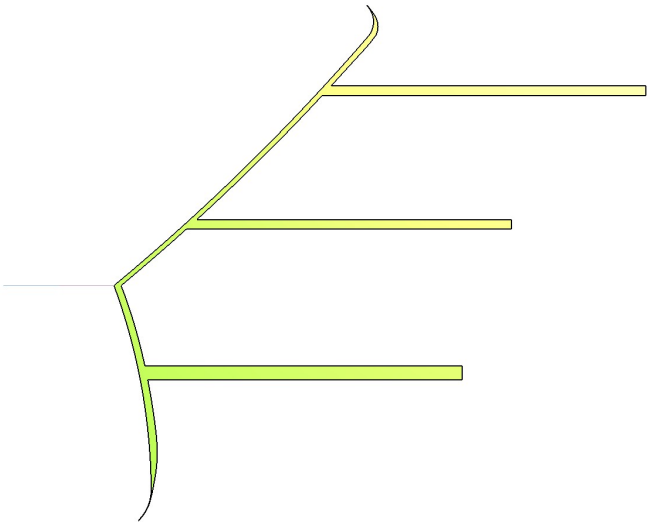

Figure 8.37.FEM model of a simple compression driver based on the diaphragm and cavity geometry found from global search D with lowest primary objective function. Axis of rotation is at the bottom of the figure.

8.6 Conclusions

In this chapter the problem of the non-rigid motion of the compression driver diaphragm has been considered. It was demonstrated that if the mechanical modes of the diaphragm are orthogonal to the acoustical modes of the cavity over the coupling surface then the overall acoustical output of the driver is not affected by the non-rigid motion. In addition several geometries were found, using an optimisation approach, which approximately meet this criterion. The resulting geometries show greatly improved performance in simple compression driver models when compared to designs which take no account of the non-

rigid behaviour. Increasing the mechanical damping of the diaphragm structure further improves the performance. This is a very exciting development in compression driver design and it merits further work to fully understand how to effectively search for suitable geometries and to identify suitable diaphragm arrangements.

9 Conclusions

The linear acoustical operation of compression drivers has been thoroughly analysed in this thesis. Several different aspects of the acoustical behaviour have been considered in detail.

Ideal targets for the acoustical behaviour were outlined with the aid of simplified models. It was demonstrated that, theoretically, the only additional fundamental linear-performance restriction on the arrangement, compared to other electromechanical loudspeaker types, is the volume of the compression cavity, which must be small in order to maintain a high bandwidth. However, in practice it is very challenging to design real devices that do not have frequency-response aberrations. This difficulty partly arises because many different aspects of the design are dependent upon one another working correctly so that the overall device performs well. In addition, while in theory it is easy to set particular targets for the compression-driver geometry, in practice these targets are hard to meet. For example, the target that the phase-plug channels are all of the same length is difficult to achieve in practice because the channels are of different areas, they begin and end in different locations, in most circumstances they must follow curved paths and they must fit in a finite space without intersecting one another. Consequently, this thesis is largely concerned with developing methods, and figures of merit, which may be used during the design of real devices to overcome these practical issues.

The compression-cavity behaviour was considered for annular-channel drivers and it was demonstrated that the conventional guidelines for the channel positioning and sizing, based on work by Smith [35], are not optimal with realistic compression-cavity geometries. As a first step towards establishing guidelines more suitable for practical compression-driver geometries, a similar analysis to that presented by Smith was outlined based on a spherical geometry. The spherical geometry is better suited as it more closely matches the geometry used by many real compression drivers. It was shown that this resulted in an improved performance compared to using Smith's guidelines for the spherical case.

A general design methodology was then presented for determining optimal annular-channel positions and sizes for compression drivers with arbitrary cavity geometry. This method is based upon numerical simulation techniques and, consequently, accounts for the exact geometry of any particular compression-driver design.

During these analyses it was observed that the detailed geometry of the compression cavity, and not just the channel positions and sizes, had a large impact upon the overall driver performance. Examination of this effect revealed that certain compression-cavity geometries result in better performance as a result of the manner in which the radiating diaphragm

excites the cavity modes. A parameter, ζ_n^d, was devised to quantify this effect and, using this parameter, a target was found for the ideal compression-cavity and diaphragm behaviour.

A method was presented that allows the compression-cavity geometry providing ideal values of ζ_n^d to be determined for drivers that have ideal rigidly moving radiating diaphragms. The resulting compression-driver geometries show extremely good performance. However, there is a one-to-one mapping between the rigid-body diaphragm and the cavity geometry. With some commonly used diaphragm geometries this results in cavities which are impractical. To overcome this issue, a method was presented for the design of compression cavities, again for rigidly moving radiating diaphragms, which approximately meet the target for ζ_n^d only within the bandwidth of operation. This method is able to generate alternative geometries for the compression cavity that also result in improved performance, but may be of more practical geometry. Unfortunately, as was discussed towards the end of chapter 6, this method has limitations because it is difficult to control the shape of the resulting cavity and also it inevitably requires a cavity of larger acoustical volume.

The channel geometry problem was also considered for compression drivers with a radial-channel arrangement. An optimal geometry for the radial-channel arrangement was presented using a Smith-type approach to the design. However, this optimal geometry suffers from practical issues that make the manufacture of such a device nearly impossible. Consequently, two methods were described allowing designs to be found that are optimal only over a the bandwidth within which the driver operates. These methods allow a greater flexibility in the final geometry of the radial-channel arrangement. As with the channel-shaping methods, there is some difficultly in controlling the resulting geometry. However, despite these challenges in applying the method, a working driver was developed based on one of the methods. The resulting device showed extremely good performance and is now used commercially in several loudspeaker designs.

Finally, the problem of non-rigid radiating diaphragms was considered. The analyses up to this stage in the thesis have ignored the issue of the diaphragm's non-rigid behaviour. It was demonstrated, with measured and modelled results, that the non-rigidity of the diaphragm is a significant issue for many compression drivers. Based on a modal analysis of the diaphragm structure, a target was outlined, based on a devised parameter γ_{nk} that quantifies the degree of orthogonality of the mechanical and acoustical modes, in order to give close to optimal values of the parameter ζ_n^d. If this target is achieved, then the non-rigidity of the diaphragm is not a limitation on the compression-driver performance. In addition, if the

target is achieved, the same generalised method for setting the annular-channel positions and sizes may be applied to the non-rigid case. Several different simple diaphragm geometries were found with favourable values of γ_{nk}. It was shown, using numerical models, that the performance of simple compression drivers based on these identified diaphragms demonstrated improved performance compared to other non-rigid cases.

To maximise the performance, many aspects of the compression-driver design must be correct. As a result of the work in this thesis, a clear framework has emerged that may be followed during the design process:

- a diaphragm geometry, and accompanying cavity geometry, is found that provides favourable values of γ_{nk};
- the channel-entrance geometry is computed, based on the parameters ζ_n^d for low-frequency diaphragm motion;
- a simple driver model, using separate and ideally terminated channels, may be used to assess the performance at this stage;
- assuming the performance is satisfactory, the channel paths are then designed to join the compression driver to the horn throat.

The framework is perhaps best illustrated in the example design described in section 7.5. It may be appreciated from this section that applying the framework is not simply a case of going through the stages. There is a great deal of engineering work to be done at each stage to ensure that the overall driver meets the particular required specification. However, it does allow the engineer to concentrate, at each stage, on the design of one particular aspect and not to end up chasing some particular effect whose source cannot be located. This is often a problem that is encountered with numerical modelling of complex light-weight radiating structures.

There is still a great deal of work to be done in order to fine-tune this framework into a really powerful design approach. Perhaps the most important of these is to find a method to estimate the fluid-loaded functions $\zeta_n^d(\omega)$ from the in-vacuo mechanical and acoustical modes of the diaphragm and cavity. This would allow the performance of candidate compression-driver diaphragms to be quickly and accurately assessed in terms of the overall driver performance. In addition to this, the presented targets for $\zeta_n^d(\omega)$ and γ_{nk} are absolute. It seems feasible to approximate the level of performance degradation in the final compression driver based on the values of these parameters. This would be a very useful addition, and allow the designer to make informed choices at each stage of the design.

References

[1] M. Dodd and J. Oclee-Brown, "A new methodology for the acoustic design of compression driver phase plugs with concentric annular channels," presented at the 123rd Convention of the AES, preprint 7258, Oct, 2007.

[2] M. Dodd and J. Oclee-Brown, "A new methodology for the acoustic design of compression driver phase plugs with concentric annular channels," presented at the Institute of Acoustics UK Conference, Reproduced Sound 24, Nov, 2008.

[3] M. Dodd and J. Oclee-Brown, "A new methodology for the acoustic design of compression driver phase plugs with radial channels," presented at the 125th Convention of the AES, preprint 7532, Oct, 2008.

[4] M. Dodd and J. Oclee-Brown, "New methodology for the acoustic design of compression driver phase plugs with concentric annular channels," *Journal of the Audio Engineering Society*, vol. 57, pp. 771-787, Oct 2009.

[5] M. Dodd and J. Oclee-Brown, "Design of a coincident source driver array with a radial channel phase-plug and novel rigid body diaphragms," presented at the 127th Convention of the AES, preprint 7846, Oct, 2009.

[6] L. L. Beranek, *Acoustics*. New York: McGraw-Hill, 1954.

[7] H. F. Olsen, *Acoustical engineering (reprint)*. Philadelphia, Pennsylvania: Professional Audio Journals Inc., 1991 (originally published in 1957).

[8] A. N. Thiele, "Loudspeakers in vented boxes: part 1," *Journal of the Audio Engineering Society*, vol. 19, pp. 382-392, May 1971.

[9] A. N. Thiele, "Loudspeakers in vented boxes: part 2," *Journal of the Audio Engineering Society*, vol. 19, pp. 471-483, Jun 1971.

[10] R. H. Small, "Direct radiator loudspeaker system analysis," *Journal of the Audio Engineering Society*, vol. 20, pp. 383-395, Jun 1972.

[11] R. H. Small, "Closed-box loudspeaker systems part i: analysis," *Journal of the Audio Engineering Society*, vol. 20, pp. 798-808, Dec 1972.

[12] R. H. Small, "Closed-box loudspeaker systems-part 2: synthesis," *Journal of the Audio Engineering Society*, vol. 21, pp. 11-18, Feb 1973.

[13] R. H. Small, "Vented-box loudspeaker systems-part 1: small-signal analysis," *Journal of the Audio Engineering Society*, vol. 21, pp. 363-372, Jun 1973.

[14] R. H. Small, "Vented-box loudspeaker systems-part 2: large-signal analysis," *Journal of the Audio Engineering Society*, vol. 21, pp. 438-444, Aug 1973.

[15] R. H. Small, "Vented-box loudspeaker systems-part 3: synthesis," *Journal of the Audio Engineering Society*, vol. 21, pp. 549-554, Sep 1973.

[16] R. H. Small, "Vented-box loudspeaker systems-part 4: appendices," *Journal of the Audio Engineering Society*, vol. 21, pp. 635-639, Oct 1973.

[17] E. Wente and A. Thuras, "A high-efficiency receiver for a horn-type loudspeaker of large power capacity (reprint)," *Journal of the Audio Engineering Society*, vol. 26, pp. 139-144, Mar 1978 (originally published 1928).

[18] L. E. Kinsler, A. R. Frey, A. B. Coppens and J. V. Sanders, *Fundamentals of acoustics*. New York: John Wiley & Sons, Inc., 4th edition: 2000.

[19] J. R. Wright, "An empirical model for loudspeaker motor impedance," *Journal of the Audio Engineering Society*, vol. 38, pp. 749-754, 1990.

[20] Leach, Jr., W. Marshall, "Loudspeaker voice-coil inductance losses: circuit models, parameter estimation, and effect on frequency response," *Journal of the Audio Engineering Society*, vol. 50, pp. 442-450, 2002.

[21] I. M. Dash, "An equivalent circuit model for the moving coil loudspeaker," M.Sc. Thesis, School of Electrical Engineering, University of Sydney, Sydney, Australia, 1982.

[22] M. Dodd, W. Klippel and J. Oclee-Brown, "Voice coil impedance as a function of frequency and displacement," presented at presented at the 117th Convention of the Audio Engineering Society, preprint 6178, Oct, 2004.

[23] P. Moon and D. E. Spencer, *Field theory handbook: including coordinate systems, differential equations and their solutions*. Berlin: Springer-Verlag, 1971.

[24] M. Abramowitz and I. A. Stegun, *Handbook of mathematical functions with formulas, graphs, and mathematical tables*. (electronic version): U.S. Department of Commerce, 2002.

[25] J. W. Strutt, *The theory of sound*. New York: Dover, 1945 (republished from original of 1896).

[26] J. W. Strutt, "On the theory of resonance," *Philosophical Transactions of the Royal Society of London*, vol. 161, pp. 77-118, 1871.

[27] S. Butterworth, "On the theory of filter amplifiers," *Experimental Wireless and the Wireless Engineer*, vol. 7, pp. 536-541, 1930.

[28] A. G. Webster, "Acoustical impedance, and the theory of horns and of the phonograph (reprint)," *Journal of the Audio Engineering Society*, vol. 25, pp. 24-28, Feb 1977 (originally published in 1919).

[29] C. R. Hanna and J. Slepian, "The function and design of horns for loudspeakers (reprint)," *Journal of the Audio Engineering Society*, vol. 25, pp. 573-585, Sep 1977 (originally published 1924).

[30] J. Borwick, K. Holland, J. Watkinson, P. J. Baxandall, G. Bank, L. Fincham, M. Colloms, J. Wright, G. Adams, P. Newell, P. Mapp, M. Gander, F. Toole, S. Olive, C. Poldy and J. Woodgate, *The loudspeaker and headphone handbook (third edition)*. Chichester: John Wiley & Sons, 2001.

[31] D. B. Keele, "Optimum horn mouth size," presented at the 46th Convention of the AES, preprint 933, Sep, 1973.

[32] D. J. Plach, "Design factors in horn-type speakers," *Journal of the Audio Engineering Society*, vol. 1, pp. 276-281, Oct 1953.

[33] D. B. Keele, "A loudspeaker horn that covers a flat rectangular area from an oblique angle," presented at the 74th Convention of the AES, preprint 2052, Oct, 1983.

[34] E. C. Wente, "Sound translating device," US patent US2037187, Apr, 1936.

[35] B. H. Smith, "An investigation of the air chamber of horn type loudspeakers," *The Journal of the Acoustical Society of America*, vol. 25, pp. 305-312, Mar 1953.

[36] F. M. Murray, "An application of bob smith's phasing plug," presented at the 61st Convention of the AES, preprint 1384, Oct, 1978.

[37] P. Robineau and R. Vaucher, "Analysis of nonlinearities in compression drivers and horns," presented at the 98th convention of the AES, preprint 3998, Feb, 1995.

[38] H. Schurer, A. P. Berkhoff, C. H. Slump and O. E. Hermann, "Modeling and compensation of nonlinear distortion in horn loudspeakers," presented at the 96th Convention of the AES, preprint 3819, Feb, 1994.

[39] A. Voishvillo, "Nonlinear versus parametric effects in compression drivers," presented at presented at the 115th Convention of the AES, preprint 5912, Oct, 2003.

[40] S. Kinoshita, T. Yoshimi, H. Hamada and B. N. Locanthi, "Design of 48mm beryllium diaphragm compression driver," presented at the 60th Convention of the AES, preprint 1364, May, 1978.

[41] E. Geddes and D. Clark, "Computer simulation of horn-loaded compression drivers," *J. Audio Eng. Soc*, vol. 35, pp. 556-566, 1987.

[42] M. Dodd, "The development of a forward radiating compression driver by the application of acoustic, magnetic and thermal finite element methods," presented at the 115th Convention of the AES, preprint 5886, Oct, 2003.

[43] C. Beltran, "Calculated response of a compression driver using a coupled field finite element analysis," presented at the 105th Convention of the AES, preprint 4787, Sep, 1998.

[44] P. A. Nelson and S. J. Elliot, *Active control of sound*. London: Academic Press, 1992.

[45] E. G. Williams, *Fourier acoustics - sound radiation and nearfield acoustical holography*. 24-28 Oval Road, London, NW1 7DX: Academic Press, 1999.

[46] F. Fahy and P. Gardonio, *Sound and structural vibration: radiation, transmission and response (2nd ed)*. Oxford: Academic Press, 2007.

[47] J. W. Harris and H. Stöcker, *Handbook of mathematics and computational science*. New York: Springer-Verlag, 1998.

[48] R. MacLaverty and D. J. Furlong, "Room acoustical simulation algorithms compared," presented at the 93rd Convention of the AES, preprint 3444, Oct, 1992.

[49] C. L. Morfey, *Dictionary of acoustics*. London: Academic Press, 2001.

[50] G. Gladwell and G. Zimmermann, "On energy and complementary energy formulations of acoustic and structural vibration problems," *Journal of Sound and Vibration*, vol. 3, pp. 233-241, 1966.

[51] L. Meirovitch, *Analytical methods in vibrations*. New York: Macmillan, 1967.

[52] J. N. Reddy, *An introduction to the finite element method*. New York: McGraw-Hill, 1984.

[53] F. W. Byron and R. W. Fuller, *Mathematics of classical and quantum physics*. New York: Dover Publications, Inc., 1992.

[54] The Mathworks Ltd., *Matlab*. Matrix House, Cambridge Business Park, Cambridge, CB4 0HH, United Kingdom: The MathWorks Ltd., 2009.

[55] PACSYS Ltd., *Pafec-fe*. Strelley Hall Nottingham NG8 6PE: PACSYS Ltd., 2008.

[56] P. Abbott, "Tricks of the trade: legendre–gauss quadrature," *The Mathematica Journal*, vol. 9, pp. 689-691, 2005.

[57] A. J. Burton and G. F. Miller, "The application of integral equation methods to the numerical solution of some exterior boundary-value problems," *Proceedings of the Royal Society of London. Series A, Mathematical and Physical Sciences*, vol. 323, p. pp. 201-210, 1971.

[58] H. A. Schenck, "Improved integral formulation for acoustic radiation problems," *The Journal of the Acoustical Society of America*, vol. 44, pp. 41-58, 1968.

[59] R. Penrose, "A generalized inverse for matrices.," *Proc. Cambridge Phil. Soc.*, vol. 51, pp. 406-413, Jul 1955.

[60] F. Holmström, "Structure-acoustic analysis using bem/fem; implementation in matlab," M.Sc. thesis, Lund University, Sweden, 2001.

[61] P. Morse and U. Ingard, *Theoretical acoustics*. New York: McGraw-Hill, 1968.

[62] G. W. Swenson and W. E. Johnson, "Radiation impedance of a rigid square piston in an infinite baffle," *The Journal of the Acoustical Society of America*, vol. 24, p. 84, Jan 1952.

[63] G. Bank and J. R. Wright, "Radiation impedance calculations for a rectangular piston," *Journal of the Audio Engineering Society*, vol. 38, pp. 350-354, May 1990.

[64] Yang Jun, Sha Kan, Gan Woon-Seng, Yan Yong-Hong and Tian Jing, "A simplified algorithm for impedance calculation of arbitrarily shaped radiators," *Chinese Physics Letters*, vol. 22, pp. 2459-2461, Oct 2005.

[65] Siemens PLM Software, *Nx*. 5800 Granite Parkway, Suite 600, Plano, TX 75024, USA: Siemens PLM Software, 2008.

[66] CIMNE, *Gid*. Edifici C-1, Campus Nord UPC, Gran Capitá, s/n, 08034, Barcelona, España: The International Center for Numerical Methods in Engineering, 2008.

[67] Altair Engineering, *Hypermesh*. 1820 Big Beaver Rd, Troy, MI 48083, USA : Altair Engineering, 2008.

[68] W. H. Beyer, *Standard mathematical tables and formulae, 28th edition (crc standard mathematical tables and formulae)*. Boca Raton, FL: CRC Press, 1973.

[69] D. A. McQuarrie, *Mathematical methods for scientists and engineers*. Sausalito, California: University Science Books, 2003.

[70] C. A. Henricksen, "Phase plug modelling and analysis: circumferential versus radial types," presented at the 55th Convention of the AES, preprint 1140, Oct, 1976.

[71] C. A. Henricksen, "Phase plug modelling and analysis: radial versus circumferential types," presented at the 59th Convention of the AES, preprint 1328, Feb, 1978.

[72] E. R. Geddes, "Compression driver plug," US patent US2006034475, Feb, 2006.

[73] CEDRAT GROUP, *Flux 2d*. 15, Chemin de Malacher - inovallée (ex-ZIRST), 38246, Meylan, Cedex, FRANCE : CEDRAT GROUP, 2008.

[74] R. Bücklein, "The audibility of frequency response irregularities (reprint)," *Journal of the Audio Engineering Society*, vol. 29, pp. 126-131, 1981 (originally published in 1962).

[75] P. Anthony and J. Wright, "Finite element analysis in the design of high-quality loudspeakers," presented at the 108th Convention of the AES, preprint 5162, Feb, 2000.

[76] M. Dodd, "The development of a forward radiating compression driver by the application of acoustic, magnetic and thermal finite element methods," presented at the 115th Convention of the AES, preprint 5886, Oct, 2003.

[77] D. Zwillinger, *Standard mathematical tables and formulae, 31st edition (crc standard mathematical tables and formulae)*. Boca Raton, FL: CRC Press, 2002.

[78] V. A. Hoersch, "Non-radial harmonic vibrations within a conical horn," *Physics Review*, vol. 25, pp. 218-224, Feb 1925.

[79] J. Oclee-Brown, "Pole-zero analysis of the soundfield in small rooms at low frequencies," presented at presented at the 121st Convention of the AES, preprint 6986, Oct, 2006.

[80] J. F. Blackburn, "Loudspeaker," U.S. patent 2 183 528, Dec, 1939.

[81] E. Matsuoka, "Speaker driver," U.S. Patent 2 832 844, Apr, 1958.

[82] C. A. Henricksen, "Acoustical transformer for horn-type loudspeaker," U.S. Patent 4 050 541, Aug, 1977.

[83] M. Dodd, "Optimum diaphragm and waveguide geometry for coincident source drive units," presented at the 121st Convention of the AES, preprint 6886, Oct, 2006.

[84] L. Greenhill, "Ces show report," *Stereophile*, vol. 33, p. available online (http://blog.stereophile.com/ces2010/kefs_special_blade/), Jan 2010.

[85] M. Dodd, "Loudspeaker," U.K. Patent 2 423 908 (B), Mar, 2005.

[86] M. Colloms, *High performance loudspeakers, 5th edition*. Chichester: John Wiley & Sons, 1997.

[87] R. M. Bews and M. J. Hawksford, "Application of the geometric theory of diffraction (gtd) to diffraction at the edges of loudspeaker baffles," *Journal of the Audio Engineering Society*, vol. 34, pp. 771-779, 1986.

[88] J. Vanderkooy, "A simple theory of cabinet edge diffraction," *Journal of the Audio Engineering Society*, vol. 39, pp. 923-933, 1991.

[89] J. R. Wright, "Fundamentals of diffraction," *Journal of the Audio Engineering Society*, vol. 45, pp. 347-356, 1997.

[90] M. Urban, C. Heil, C. Pignon, C. Combet and P. Bauman, "The distributed edge dipole (ded) model for cabinet diffraction effects," *Journal of the Audio Engineering Society*, vol. 52, pp. 1043-1059, 2004.

[91] L. Weinberg, *Network analysis and synthesis*. New York: McGraaw-Hill, 1962.

[92] R. M. Golden and J. F. Kaiser, "Root and delay parameters for normalized bessel and butterworth low-pass transfer functions," *IEEE Transactions on Audio Electro-Acoustics*, vol. AU-19, p. 64, Mar 1971.

[93] A. N. Thiele, "Filters with variable cut-off frequencies," *The Proceedings of the IREE (Australia)*, vol. 26, p. 284, Sep 1965.

[94] A. Budak and P. Aronhime, "Transitional butterworth-chebyshev filters, (correspondence)," *IEEE Transactions on Circuit Theory*, vol. CT-18, p. 413, May 1971.

[95] Y. Nomura, "An analysis of design conditions of a bass-reflex loudspeaker enclosure for fiat response," *Electronic Communications Japan*, vol. 52-A, p. 1, 1969.

[96] G. M. Jebsen and H. Medwin, "On the failure of the kirchhoff assumption in backscatter," *The Journal of the Acoustical Society of America*, vol. 72, pp. 1607-1611, 1982.

[97] L. R. Fincham, A. Jones and R. H. Small, "The influence of room acoustics on reproduced sound, part 2: design of wideband coincident-source loudspeakers," presented at the 87th Convention of the AES, 2877, Oct, 1989.

[98] F. Irgens, *Continuum mechanics*. Berlin: Springer-Verlag, 2008.

Appendix I Loudspeaker Enclosures

In this appendix the behaviour of enclosure-mounted direct-radiating loudspeakers is outlined.

The loudspeaker lumped circuits that were presented in section 2.2 only show mechanical to acoustical transduction on one side of the radiating diaphragm; however, in reality, both sides of the diaphragm radiate with equal and opposite volume velocity. In section 2.3, above, the direct-radiating loudspeaker was considered in an infinite baffle, which acted as a barrier between the two radiating sides, preventing the equal and opposite radiation from interfering. This “infinite baffle” arrangement is seldom found in reality, the exception being when a loudspeaker is mounted in the wall of a room with a very large acoustical volume on the rear side. It is much more common for a direct-radiating loudspeaker to be mounted in a loudspeaker enclosure to separate the rearward radiation. There are many different types of loudspeaker enclosure design. In this section the closed-box and vented-box types are introduced.

The lumped-circuit description of a loudspeaker including mechanoacoustical transduction from the rear of the diaphragm coupled to an enclosure of some kind is shown in figure I.1. In this figure the volume velocity at the rear of the diaphragm is equal to the volume velocity at the front, but with the polarity opposite and the acoustical impedance of the rear enclosure is Z_{ab}.

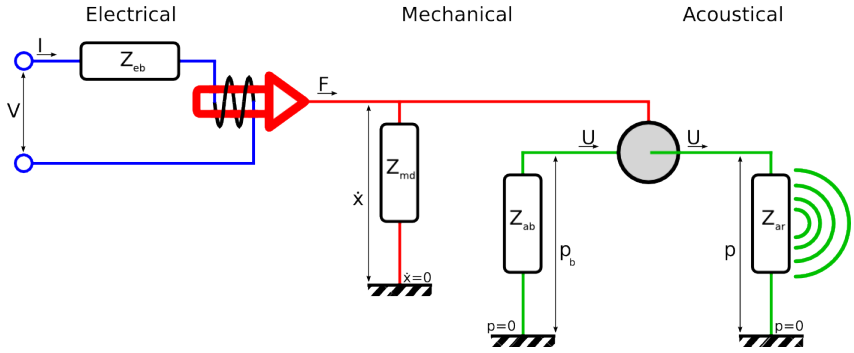

Figure I.1. Lumped-circuit representation of a generic electromagnetic loudspeaker including mechanoacoustical transduction from the rear of the diaphragm.

In the same way as the acoustical radiation impedance, Z_{ar}, is commonly described as a mechanical radiation impedance, Z_{mr} as defined in equation 2.4, it is also helpful to consider the effect of the box on the mechanical system directly by transferring the enclosure acoustical impedance Z_{ab} to the other side of the mechanoacoustical transduction step and define the enclosure mechanical impedance, Z_{mb}, to be

$$Z_{mb} = Z_{ab} S_d^2 \qquad \text{I.1.}$$

Overall, the enclosure-mounted lumped-system mechanical impedance, Z_{mc}, can be described as the sum of three mechanical impedances

$$Z_{mc} = Z_{md} + Z_{mr} + Z_{mb} \qquad \text{I.2.}$$

Using this definition, the enclosure-mounted loudspeaker behaviour may be analysed using the expressions outlined in section 2.2.

AI.i The effect of the enclosure on acoustical radiation

The direct-radiating loudspeaker analysed in section 2.3 was assumed to have a very specific radiating situation – that of a rigidly moving circular diaphragm mounted into an infinite baffle. Typically, a cabinet-mounted loudspeaker is not flush mounted into an infinite baffle, but is placed directly into the acoustical radiation environment. Acoustically, this is a somewhat more complex situation. The infinite baffle situation is commonly referred to as a 2π radiation environment because the solid angle into which the loudspeaker radiates is 2π steradians, when the cabinet-mounted loudspeaker is placed directly into the radiation environment the situation is commonly referred to as a 4π radiation environment. In the 4π situation, at high frequencies, where the acoustical wavelength is small compared to the size of the cabinet baffle into which the loudspeaker driver is mounted, there is little difference observed compared to the 2π situation. However, at low frequencies, when the wavelength is much larger than the cabinet dimensions, the loudspeaker cabinet is an insignificant barrier to the radiation, and the dispersion of the loudspeaker becomes omnidirectional. Compared to the 2π situation close to half the pressure magnitude is observed on the axis of the loudspeaker. In between these two extremes there is a transition region. In this region the detailed shape of the cabinet and the driver mounting position determines the shape of the response. This cabinet effect is commonly called the “diffraction” effect. Olsen studied this effect extensively and published axial-response measurements of the transition region for some common loudspeaker cabinet shapes [7, p.23], shown in figure I.2, these results are widely reproduced [30, p.318][86, p.347].

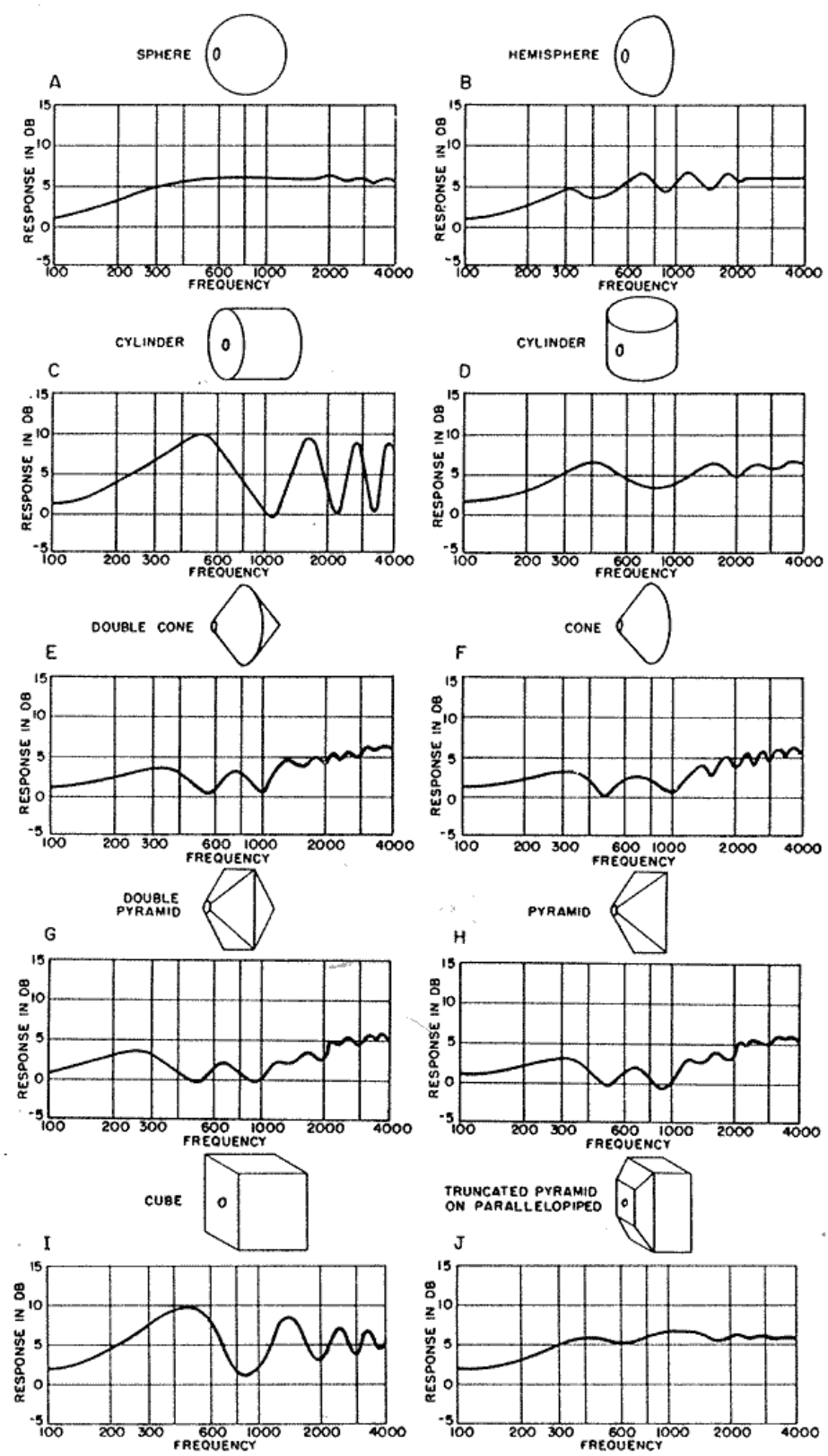

Figure I.2. Reproduction of Olsen's classic loudspeaker enclosure baffle-diffraction experiment..

The diffraction effect clearly also has an effect on the acoustical radiation impedance experienced by the diaphragm; however, this effect rarely considered in detail when simple lumped models are used. The reason for this that the commonly available models for diffraction, such as the edge source methods [87,88,89,90], are not suitable for predicting the pressure in the near field of the diaphragm and are hence also not ideally suited for the calculation of the effect of the diffraction upon the radiation impedance. Additionally, as was discussed in section 2.3, for a direct-radiating loudspeaker, the mechanical radiation impedance is very small compared to the mechanical impedance of the driver parts and the enclosure and thus very tolerant to approximation. It is common to assume that at low frequencies the mechanical radiation impedance is approximately half of that of the infinite-baffle mounted diaphragm, and can be approximated as

$$Z_{mr} \approx \frac{\rho_0 c \pi a^2}{2}\left[\frac{(ka)^2}{2} + j\frac{8ka}{3\pi}\right] \qquad \text{I.3.}$$

AI.ii The closed-box enclosure

The simplest type of loudspeaker enclosure is the closed-box design with the rear radiation from the loudspeaker completely enclosed by a solid cabinet. This arrangement is schematically shown in figure I.3. This type of loudspeaker enclosure was comprehensively analysed by Small [11].

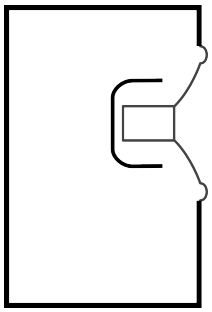

Figure I.3. Schematic of the closed-box enclosure showing a single loudspeaker driver with the rear radiation completely enclosed by the cabinet.

At low frequencies, when the dimensions of the cabinet are small compared to the acoustical wavelength, the behaviour of the cabinet is simple and, provided that the walls of the cabinet are sufficiently rigid, the volume of air trapped in the enclosure behaves like an acoustical compliance. It is common for the enclosure to be partially filled or lined with acoustical damping material, such as fibreglass wool, in order to reduce the magnitude of acoustical modes at higher frequencies. The result of this is, firstly, to introduce an acoustical resistance and, secondly, depending upon the quantity and type of material used for damping, to

slightly increase the apparent acoustical compliance. The additional resistance can also be used to mimic the effect of slight flexure of the cabinet walls. The acoustical impedance of the enclosure, Z_{ab}, can be written as

$$Z_{ab} = \frac{1}{j\omega C_{ab}} + R_{ab} \tag{I.4.}$$

where C_{ab} is the acoustical compliance of the enclosure and R_{ab} is the acoustical resistance of the loudspeaker enclosure. The acoustical compliance, C_{ab}, can be equivalently expressed as a volume, V_{ab}, using the relation

$$V_{ab} = \rho_0 c_0^2 C_{ab} \tag{I.5.}$$

If there is only a small amount of acoustical damping material, the apparent volume, V_{ab}, is approximately equal to the net internal physical volume of the enclosure, V_b. The term $\rho_0 c_0^2$ in this expression is known as the bulk modulus.

As discussed above, the enclosure acoustical impedance can be equivalently written as a mechanical impedance Z_{mb} defined as

$$Z_{mb} = \frac{K_{mb}}{j\omega} + R_{mb} \tag{I.6.}$$

where K_{mb} is the mechanical stiffness equivalent to the acoustical compliance C_{ab}, defined as

$$K_{mb} = \frac{S_d^2}{C_{ab}} \tag{I.7.}$$

and R_{mb} is the mechanical stiffness equivalent to the acoustical resistance R_{ab}, defined as

$$R_{mb} = S_d^2 R_{ab} \tag{I.8.}$$

The overall enclosure-mounted system mechanical impedance, Z_{mc}, is found by the sum of the enclosure impedance, Z_{mb}, and the driver mechanical impedance Z_{ms}. Overall, this can be written as

$$Z_{mc} = j\omega M_{mc} + R_{mc} + \frac{K_{mc}}{j\omega} \tag{I.9.}$$

In this case the system moving mass M_{mc} is the same as the infinite-baffle system,

$$M_{mc} = M_{md} + M_{mr} \tag{I.10.}$$

the system mechanical resistance R_{mc} is defined as

$$R_{mc} = R_{md} + R_{mr} + R_{mb} \quad \text{I.11.}$$

and the system mechanical stiffness K_{mc} is defined as

$$K_{mc} = K_{md} + K_{mb} \quad \text{I.12.}$$

The terms M_{md}, R_{md} and K_{md} are the effective mass, damping and stiffness of the mechanical parts of the loudspeaker driver, as was discussed in section 2.2.5. The terms M_{mr} and R_{mr} are the additional effective mass and damping due to radiation from the front side of the diaphragm and, as was discussed for the enclosure-mounted case at the beginning of this section, these are slightly different from the infinite-baffle case. Comparison with the system mechanical impedance for the infinite-baffle mounted direct-radiating loudspeaker, given in equation 2.31, reveals that the closed-box mechanical system has the same structure exactly. Because of this, the behaviour of the closed-box loudspeaker shares many characteristics with the infinite-baffle mounted case considered in section 2.3.

Introducing the parameter ω_c, the system natural frequency, defined as

$$\omega_c^2 = \frac{K_{mc}}{M_{mc}} \quad \text{I.13.}$$

and the parameter Q_{mc}, the mechanical system Q factor at ω_c defined as

$$Q_{mc} = \omega_c \frac{M_{mc}}{R_{mc}} \quad \text{I.14.}$$

the closed-box system mechanical impedance can be written as

$$Z_{mc} = \omega_c^2 M_{mc} \left[\frac{j\omega}{\omega_c^2} + \frac{1}{Q_{mc}\omega_c} + \frac{1}{j\omega} \right] \quad \text{I.15.}$$

It is common to define the cabinet losses as a Q factor independently from the driver, usually given the name Q_{mb} defined as

$$Q_{mb} = \omega_c \frac{M_{mc}}{R_{mb}} \quad \text{I.16.}$$

This is particularly common in enclosure design software primarily because it is easy for the designer to set the value, a typical loudspeaker enclosure with reasonably rigid and well-sealed walls has a Q_{mb} of between 7 and 15.

The low-frequency axial pressure response of the closed-box loudspeaker is

$$p_{ax}(r)=\frac{\rho_0}{4\pi r}\frac{S_d}{M_{mc}}\frac{BL}{R_e}\left[VG\left(\frac{j\omega}{\omega_c}\right)\right] \qquad \text{I.17.}$$

where the function $G(s)$ is defined to be

$$G(s)=\frac{s^2}{1+s/Q_{tc}+s^2} \qquad \text{I.18.}$$

and the Q-factor of the system, Q_{tc}, is found from the expression

$$Q_{tc}=\frac{Q_{ec}Q_{mc}}{Q_{ec}+Q_{mc}} \qquad \text{I.19.}$$

where Q_{ec} is the electrical Q-factor at the system natural frequency, defined as

$$Q_{ec}=\omega_c\frac{M_{mc}R_e}{B^2L^2} \qquad \text{I.20.}$$

In comparison to the infinite-baffle mounted piston, the nature of the response is identical except for the halving in the pressure output because of the 4π radiation conditions. The effect of the closed-box enclosure is to increase the system natural frequency by the square root ratio change in mechanical stiffness, because of the compliance of the air trapped in the cabinet,

$$\frac{\omega_c^2}{\omega_s^2}=\frac{K_{ms}+K_{mb}}{K_{ms}} \qquad \text{I.21.}$$

This shift in the system natural frequency also has an effect on the system Q-factor which increases in approximate proportion to the shift in natural frequency compared to the case without enclosure,

$$\frac{Q_{tc}}{Q_{ts}}\approx\frac{\omega_c}{\omega_s} \qquad \text{I.22.}$$

This expression is a good approximation unless the cabinet is heavily filled with absorbent materials, in which case the Q-factor contribution from the box is more significant and restricts this system Q increase.

The other figures of merit of the closed-box loudspeaker follow the same form as the direct-radiating loudspeaker in section 2.3 and are summarised below. Notice the change from 2π radiation conditions to 4π radiation conditions indicated in the denominator of many of these expressions.

The diaphragm excursion is given by the expression

$$x = \frac{1}{M_{mc}} \frac{BL}{R_e} \left[V \frac{G(j\omega/\omega_c)}{-\omega^2} \right] \qquad \text{I.23.}$$

The pressure sensitivity given by the expression

$$p_{sens} = \frac{\rho_0}{4\pi} \frac{S_d}{M_{mc}} \frac{BL}{R_e} \qquad \text{I.24.}$$

The low-frequency power sensitivity given by the expression

$$P_{sens} = \frac{\rho_0}{2c4\pi} \frac{S_d^2}{M_{mc}^2} \frac{B^2 L^2}{R_e^2} \qquad \text{I.25.}$$

The pass-band efficiency is given by the expression

$$\eta_{pass} = \frac{\rho_0}{4\pi c} \frac{S_d^2}{M_{mc}^2} \frac{B^2 L^2}{R_e} \qquad \text{I.26.}$$

AI.ii.i Maximum bandwidth

The expression for the pass-band efficiency, in expression I.5, may be equivalently written

$$\eta_{pass} = \frac{V_{ac}}{4\pi c^3} \frac{\omega_c^3}{Q_{ec}} \qquad \text{I.27.}$$

where V_{ac} is the volume of air having the same stiffness as the system mechanical stiffness K_{mc}, given by the expression

$$V_{ac} = \rho_0 c^2 \frac{S_d^2}{K_{mc}} \qquad \text{I.28.}$$

For minimum cabinet volume and maximum bandwidth and efficiency, the loudspeaker system is usually designed so that the driver suspension stiffness, K_{md}, is a small fraction of the overall system mechanical stiffness, K_{mc}. In this case, V_{ac} is approximately equal to the effective enclosure volume V_{ab} and the efficiency relationship becomes

$$\eta_{pass} \approx \frac{V_{ab}}{4\pi c^3} \frac{\omega_c^3}{Q_{ec}} \qquad \text{I.29.}$$

This expression neatly outlines the compromises that are present when designing a loudspeaker system. The electrical Q factor, Q_{ec}, should be minimised for maximum efficiency. Q_{ec} has a dominant effect on the shape of the system response so, in practice, it is

usual to try and minimise other losses in the system, such as the mechanical loss R_{md} and the acoustical cabinet loss R_{ab}, so that Q_{ec} can be as small as possible for the desired overall system Q-factor, Q_{tc}. The other parameters must be set by the loudspeaker designer for the best compromise between box volume, efficiency and low-frequency extension, for the particular application they are considering.

Figure I.4 shows the simulated 1m axial sound pressure level response of an example loudspeaker driver driven with an input voltage of 1v, radiating into a 2π environment. Both these simulations use the rigid planar circular piston radiation model, as was described in section 2.3. The response is shown for the situation when there is no rear loading on the diaphragm and when the rear surface of the diaphragm is attached to a lossless closed-box of 14L internal volume. The simulated driver has a purely resistive blocked electrical impedance with a voice coil resistance of R_e=3.2 Ohms. Measured in free air, the driver mechanical parameters are $\omega_s=2\pi 45$ rads^{-1}, Q_{ms}=12, Q_{ts}=0.38, BL=6 NA^{-1} and S_d=200 cm^2. The other mechanical parameters of the driver, such as the M_{ms}, can be calculated from these values.

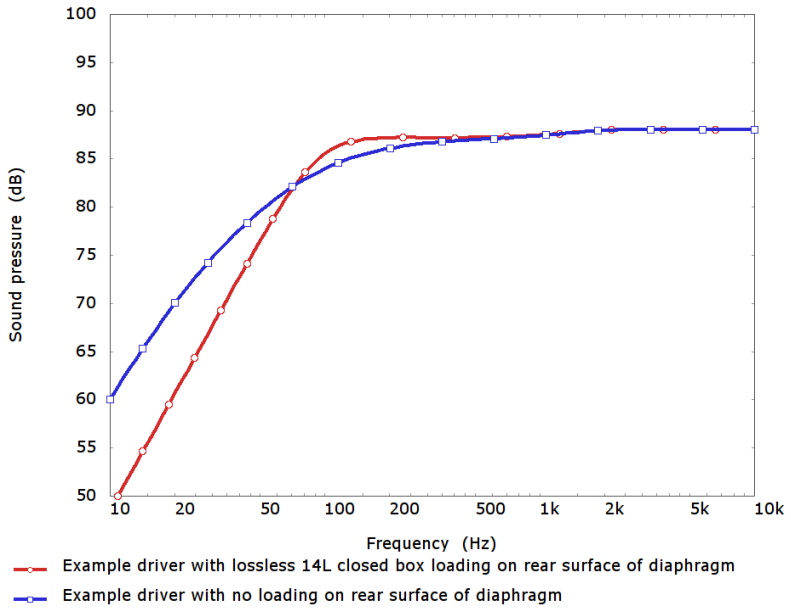

Figure I.4. Simulated sound pressure level response of a loudspeaker driver radiating into a 2pi environment for the situation when there is no read loading on the diaphragm (blue) and when the rear is loaded with a 14L lossless closed box.

Both responses are 2nd order high-pass functions, but there is a clear difference in the shape of the responses. The effect of the closed-box rear loading is to increase the system resonance frequency from 45 Hz to 92.3 Hz, and to increase the response Q factor from 0.38 to 0.779.

AI.iii The vented-box enclosure

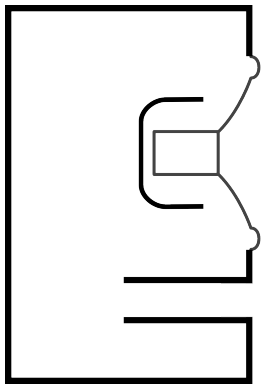

Figure I.5. Schematic of the vented-box enclosure showing a single loudspeaker driver with the rear radiation enclosed by a cabinet that has a single vent connecting the inside of the enclosure to the radiating environment.

The vented-box loudspeaker enclosure is very common. With this type of enclosure the driver is mounted in one face of a rigid-walled cabinet that is completely sealed with the exception of a vent – a narrow constriction that connects the inside of the loudspeaker enclosure to the radiating environment. This layout is depicted in figure I.5. This arrangement was first analysed by Thiele [8][9] and later by Small in a comprehensive series of papers [13][14][15][16]. The vent from the inside of the enclosure to the radiating environment behaves as a Helmholtz resonator [18, pp. 284-286].

The enclosure loads the radiating diaphragm with a mechanical impedance, Z_{mb}, given by the expression

$$Z_{mb} = R_{mb} + \frac{K_{mb}}{j\omega} - \frac{\left(R_{mb} + \frac{K_{mb}}{j\omega}\right)^2}{j\omega M_{mv} + R_{mb} + \frac{K_{mb}}{j\omega}} \qquad \text{I.30.}$$

The terms are familiar from the closed-box enclosure analysis with the exception of M_{mv}, which is the mechanical dual of the enclosure vent acoustical inertance. The loudspeaker system mechanical impedance at the drive point of the loudspeaker driver is given by the sum of the cabinet impedance with the impedance of the driver.

This results in the overall vented-box mechanical impedance given by the expression

$$Z_{mc} = j\omega M_{ms} + R_{ms} + \frac{K_{ms}}{j\omega} + R_{mb} + \frac{K_{mb}}{j\omega} - \frac{\left(R_{mb} + \frac{K_{mb}}{j\omega}\right)^2}{j\omega M_{mv} + R_{mb} + \frac{K_{mb}}{j\omega}} \qquad \text{I.31.}$$

where M_{ms}, R_{ms} and K_{ms} are the loudspeaker driver diaphragm mechanical part mass, resistance and stiffness respectively inclusive of acoustical loading on the front surface due to acoustical radiation. From this expression, the voltage driven diaphragm velocity may be found using the relation

$$\frac{\dot{x}_d}{V} = \frac{BL}{Z_{mc} Z_{eb} + B^2 L^2} \qquad \text{I.32.}$$

as was outlined in section 2.2.2, expression 2.11. The volume velocity at the exit of the vent can be expressed in terms of the diaphragm velocity as

$$\frac{U_p}{\dot{x}_d} = -S_d \frac{R_{mb} + \frac{K_{mb}}{j\omega}}{j\omega M_{mv} + R_{mb} + \frac{K_{mb}}{j\omega}} \qquad \text{I.33.}$$

Note the negative in front of the S_d term that occurs because forward motion of is considered positive and the enclosure is driven from the back of the radiating surface. For both of these radiating components, it is assumed that the pressure radiated may be found from the volume velocity using the low-frequency far-field approximation

$$p(r) = j\omega U \frac{\rho_0}{4\pi r} e^{-jkr} \qquad \text{I.34.}$$

Notice that this expression is for radiation into a 4π environment. Assuming that the vent and the diaphragm are located close to one another such that they can be considered to be at the same distance, r, from the listener, then the total pressure from the loudspeaker can be expressed in terms of the volume accelerations of the two radiators as,

$$p(r) = j\omega(U_d + U_v) \frac{\rho_0}{4\pi r} e^{-jkr} \qquad \text{I.35.}$$

After a little manipulation this can be written as

$$p(r) = \frac{\rho_0}{4\pi r} \frac{S_d}{M_{mc}} \frac{BL}{R_e} \left[VG\left(\frac{j\omega}{\omega_v}, \frac{j\omega}{\omega_s} \right) \right] \qquad \text{I.36.}$$

where the response function G is defined as

$$G(s_s, s_v) = \frac{s_v^2 s_s^2}{\left(s_v^2 + \frac{s_v}{Q_{av}} + 1\right)\left(s_s^2 + \frac{s_s}{Q_{ts}} + 1\right) + \alpha s_v^2 \left(\frac{s_v}{Q_{av}} + 1\right)} \quad \text{I.37.}$$

where ω_s is the natural frequency of the loudspeaker driver including the radiation load, defined as

$$\omega_s^2 = \frac{K_{ms}}{M_{ms}} \quad \text{I.38.}$$

ω_v is the natural frequency of the vent when the diaphragm is stationary, calculated as

$$\omega_v^2 = \frac{K_{mb}}{M_{mv}} \quad \text{I.39.}$$

The parameter Q_{av} is the Q-factor of the vent at ω_v, defined as

$$Q_{av} = \omega_v \frac{M_{mv}}{R_{mb}} \quad \text{I.40.}$$

the parameter Q_{ts} is the total Q-factor of the driver, including mechanical and electrical damping, at the natural frequency ω_s, as defined in equation 2.43.

The parameter α is the ratio of the stiffness of the box to the stiffness of the driver, defined as

$$\alpha = \frac{K_{mb}}{K_{ms}} \quad \text{I.41.}$$

Small shows that the response function G may be written in the form of a general fourth order high pass with filter coefficients a_1, a_2, and a_3 as

$$G(s) = \frac{s^4}{s^4 + a_1 s^3 + a_2 s^2 + a_3 s + 1} \quad \text{I.42.}$$

where the variable s is defined to be

$$s = \frac{j\omega}{\sqrt{\omega_s \omega_v}} \quad \text{I.43.}$$

The filter coefficients are found by comparison with the denominator of I.4 to be[4]

$$a_1 = \frac{hQ_{av} + (h^2 + \alpha)Q_{ts}}{h^{3/2}Q_{ts}Q_{av}} \quad \text{I.44.}$$

$$a_2 = \frac{h + (\alpha + 1 + h^2)Q_{ts}Q_{av}}{hQ_{ts}Q_{av}} \quad \text{I.45.}$$

and

$$a_3 = \frac{hQ_{av} + Q_{ts}}{h^{1/2}Q_{ts}Q_{av}} \quad \text{I.46.}$$

where the parameter h is the ratio of the two natural frequencies, $h = \omega_v / \omega_s$.

In this form, it is easy to see that, at low frequencies, the frequency response of the vented-box loudspeaker has a forth order high-pass characteristic, with an asymptotic roll-off of 24dB per octave. The parameters a_1, a_2 and a_3 are equivalent to the analogue filter coefficients used in signal processing theory [27], many different response shapes are possible with the 4th-order high-pass function each characterised by these coefficients. The breakthrough of Small [13] and Thiele [8] was to realise that it was possible to write the equations of motion for the enclosure mounted loudspeaker in a form that allows the loudspeaker designer to specify a response in terms of these well-known filter coefficients; such as those published describing the Butterworth response [91][92], the Tchebychev response [93] and less common filter types [94][95]; and then to quickly arrive at physical targets for the mechanical and acoustical parameters of the loudspeaker system to achieve that response. Figure I.6 shows a comparison of several of these high-pass alignments with x-axis normalised so that $\omega_s = 1$. For the Butterworth alignment, the two natural frequencies are equal, $\omega_v = \omega_s = 1$. For the alignments to the right of the Butterworth, the tuning frequency of the vent, ω_v is greater than the tuning frequency of the driver ω_s. For the alignments to the left of the Butterworth, the reverse is true and $\omega_v < \omega_s$. The choice of response shape is largely down to the preference of the designer, with smoothness of the response, low-frequency extension and the practicality of the required parameters important considerations.

4 Note that expression I.3 is slightly different from that published by Small [13]. This results from a term in the denominator his equation 13 that he has either neglected or omitted. The term in question, using Small's notation, is $s^3 \alpha T_v^3 / Q_L$. The effect of this term is very small if there is little acoustical damping – as was the case for much of Small's study.

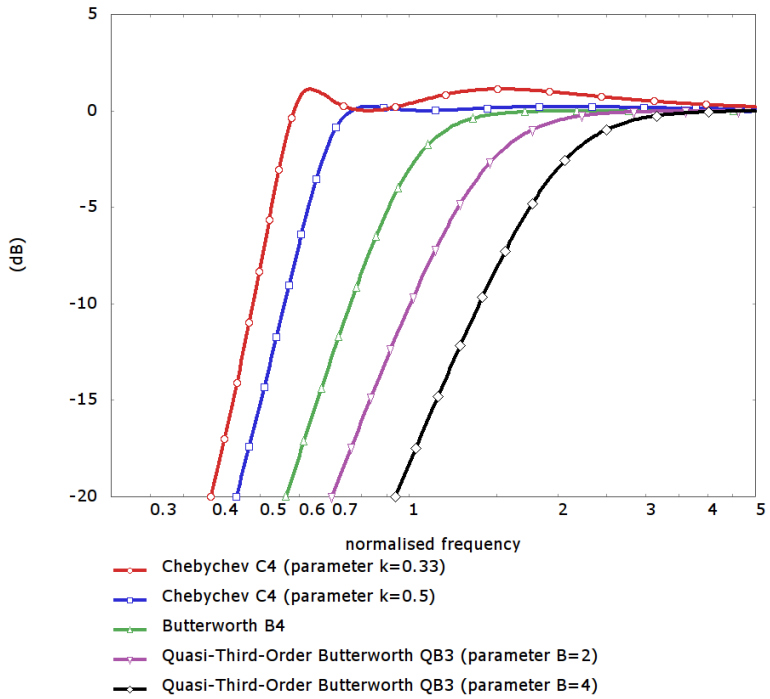

Figure I.6. Comparison of several possible vented-box high-pass alignments frequency normalised so that $\omega_s=1$.

Figure I.7 shows the normalised diaphragm displacement for a lossless vented enclosure in comparison to to a closed-box design having the same sensitivity, -3dB point and diaphragm area. At the natural frequency of the vent, ω_v, the excursion of the driver goes to zero and the excursion is reduced over a wide frequency region in comparison to the closed box.

An additional important difference between the closed and vented system is that, while the driver free air resonant frequency, ω_s, for a closed-box system must be at a lower frequency than the system cut-off frequency, for many alignments the free air resonance can be higher or equal to the system cut-off frequency. This is a much easier target for the driver designer.

Figure I.8 shows the normalised pressure output of a lossless 4^{th} order Butterworth (B4) vented-box enclosure design including the individual contributions from the vent and the diaphragm radiation. At the natural frequency of the vent, ω_v, the diaphragm radiation is zero and the entire loudspeaker output is from the vent. At frequencies below the vent tuning frequency, the system response falls off a 24dB per octave. The diaphragm and the port radiation both have a asymptotic roll off of 12dB per octave, the increased rate of the system compared to the vent and diaphragm is as a result of a π phase difference between the two radiations – at very low frequencies the volume velocity output from the vent is equal and opposite to the volume velocity output from the diaphragm.

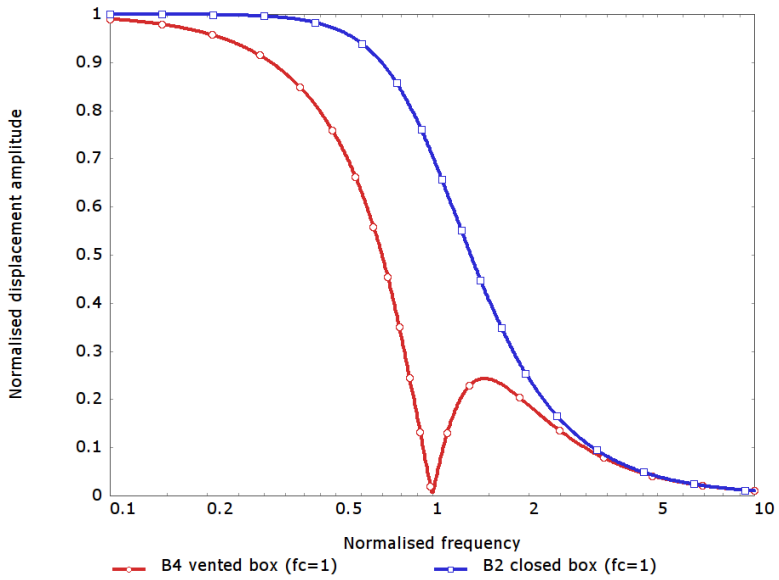

Figure I.7. Comparison of driver excursion of vented-box enclosure with a closed-box enclosure with the same -3dB frequency, sensitivity and diaphragm area. Frequency is normalised so that -3dB point is unity, amplitude is normalised so that pass-band acceleration amplitude is unity.

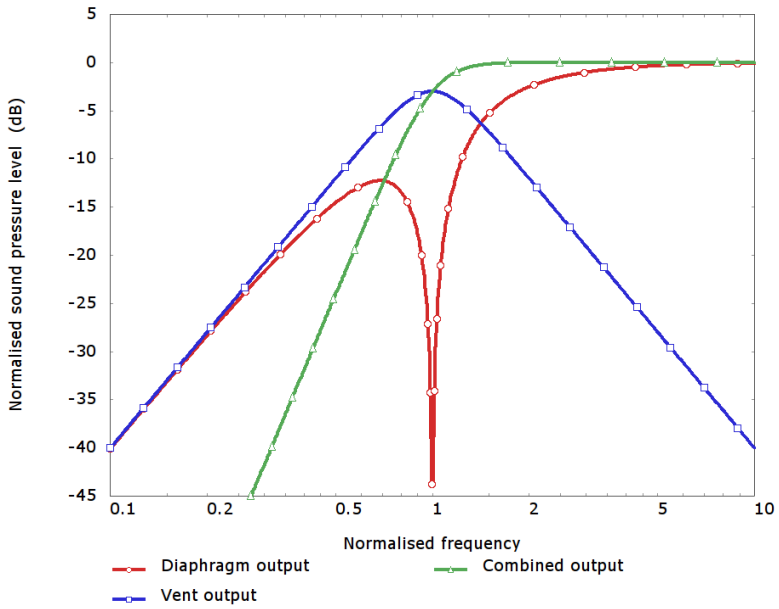

Figure I.8. Normalised sound pressure level amplitude dB versus normalised frequency, diaphragm radiation compared to vent radiation and overall combined radiation for a lossless B4 alignment.

AI.iii.i Maximum bandwidth

The bandwidth and efficiency of the vented box is dependent upon the target alignment and the level of acoustic losses in the system. A full discussion for lossy enclosures and arbitrary system response shapes is beyond the scope of this thesis (the interested reader is directed to

Small's first paper on vented enclosures [13]). The lossless B4 alignment is a useful case to consider in order to gain a comparison between the vented-box and the closed-box case, whose efficiency and bandwidth was surmised in equation I.2.

For the case of a lossless vented enclosure, as described by Thiele [8], the system parameters may be found in a straightforward manner from the three filter coefficients a_1, a_2 and a_3 in equation I.1, using the three relationships:

$$h = \frac{a_1}{a_3} \qquad \text{I.47.}$$

$$\alpha = a_2 h - h^2 - 1 \qquad \text{I.48.}$$

and

$$Q_{ts} = \frac{1}{\sqrt{a_1 a_3}} \qquad \text{I.49.}$$

For a B4 alignment this results in

$$h = 1 \qquad \text{I.50.}$$

$$\alpha = \sqrt{2} \qquad \text{I.51.}$$

$$Q_{ts} = \left(4 + 2\sqrt{2}\right)^{-1/2} \approx 0.382 \qquad \text{I.52.}$$

Assuming that the mechanical driver losses are negligible, the approximation may be made that

$$Q_{ts} \approx \omega_s \frac{M_{ms} R_e}{B^2 L^2} \qquad \text{I.53.}$$

After a little manipulation the expression for the system pass band efficiency, given in a basic form in equation 2.52, may be expressed as

$$\eta_{pass} \approx \alpha \frac{V_{ab}}{4 \pi c^3} \frac{\omega_s^3}{Q_{ts}} \qquad \text{I.54.}$$

where V_{ab} is the volume of air having the same stiffness as the enclosure stiffness K_{mb}, given by the expression

$$V_{ab} = \rho_0 c^2 \frac{S_d^2}{K_{mb}} \qquad \text{I.55.}$$

As the box has insignificant losses it is safe to assume that this volume is approximately the physical net volume of the air inside the loudspeaker cabinet.

In summary, the pass band efficiency of the lossless vented-box loudspeaker system with a B4 alignment has an efficiency that, compared to a lossless closed-enclosure with a Q of

$1/\sqrt{2}$ and with the same volume and -3dB frequency, is $1/0.382 = 2.6178 \equiv 4$dB higher. It should be emphasised that the B4 alignment is not the most efficient of the vented-enclosure alignments: the most efficient has a value of α of approximately 0.6. However, more efficient alignments have ripple in the pass band and are inferior to the B4 alignments in terms of the transient response, and so are infrequently used. Additionally, because the vented enclosure has a fundamental roll-off of 24dB per octave compared to the 12dB per octave of the closed-box, at frequencies below the -3dB point, the closed-box design is more sensitive than the vented-box design.

Appendix II Matlab Rayleigh-Ritz acoustical pipe model

The script below calculates the pressure eigenfunctions of a closed-closed pipe using the Rayleigh-Ritz method, it can be used to generate the result given in section 3.6.

AII.i RRpipe.m

```
% This script generates the Rayleigh-Ritz Example
L = 0.5; % the length of the pipe
A = pi*10e-3^2; % the area of the pipe
c0=343; % the sound speed
n=4; % the eigenfunction for plotting

N = 6; % the number of prescribed functions

[s,k]=meshgrid(0:N,(0:N)'); % create matrices of k and s

H = A*k.*s./(k+s-1).*((L/2).^(k+s-1) - (-L/2).^(k+s-1)); % calc matrix H
Q = A/c0^2./(k+s+1).*((L/2).^(k+s+1) - (-L/2).^(k+s+1)); % calc matrix Q

H(isnan(H))=0; % remove NAN (because x^0 has a zero differential in x)

[V,D] = eig(Q\H); % compute the eigen functions and freqs

[freqs,I]=sort(sqrt(diag(D))/2/pi); % sort the eigenfreqs and convert to freq
(Hz)
V=V(:,I); % sort the eigenfunctions in order of increasing eigenfreq

x = linspace(-L/2,L/2,200); % vector of positions in x to show the resulting
pressure

% calc the pressure eigenfunction
pRR = zeros(size(x));
for k=0:N
  pRR=pRR + V(k+1,n+1)*x.^k;
end
pRR=pRR/pRR(1); % normalise eigenfunction

% calc the exact solution for comparison
fExact=c0/L/2*(0:N-1);
pExact=cos((x+L/2)/L*pi*n);

% plot the results
plot(x,pRR,x,pExact);
```

Appendix III Matlab FEM acoustical pipe model

The two scripts in this appendix compute the eigenfrequencies and eigenfunctions of a straight closed-closed pipe using the FE method. The first script, FEMpip1.m, uses two noded linear elements. The second script, FEMpipe2.m uses three-noded quadratic elements. These two scripts can be used to recreate the results shown in section 3.7.

AIII.i FEMpipe1.m

```
L = 0.5; % the length of the pipe
A = pi*10e-3^2; % the area of the pipe
c0=343; % the sound speed
N = 21; % the number of nodes
i=2; % the mode to plot
x = linspace(-L/2,L/2,N); % the x location of the nodes
a = 0.5*L/(N-1); % half length of each element
He = A/a*[0.5 -0.5;-0.5 0.5]; % element stiffness matrix
Qe = A*a/c0^2*[2/3 1/3;1/3 2/3]; % element inertia matrix

% map the element matrices into the global matrices
H = zeros(N,N);
Q = zeros(N,N);
for n=1:N-1
  H((n-1)+(1:2),(n-1)+(1:2))=H((n-1)+(1:2),(n-1)+(1:2))+He;
  Q((n-1)+(1:2),(n-1)+(1:2))=Q((n-1)+(1:2),(n-1)+(1:2))+Qe;
end

% solve the eigen problem
[V,D] = eig(Q\H); % compute the eigen functions and freqs

[freqs,I]=sort(sqrt(diag(D))/2/pi); % sort the eigenfreqs and convert to freq
(Hz)
V=V(:,I); % sort the eigenfunctions in order of increasing eigenfreq

% calc the exact solution for comparison
xExact=linspace(-L/2,L/2,500);
fExact=c0/L/2*(0:N-1);
pExact=cos((xExact+L/2)/L*pi*i);

pRR=interp1(x,V(:,i+1)/V(1,i+1),xExact,'linear'); % normalise eigenfunctions
and interpolate nodal results.

plot(xExact,pExact,xExact,pRR)
```

AIII.ii FEMpipe2.m

```
L = 0.5; % the length of the pipe
A = pi*10e-3^2; % the area of the pipe
c0=343; % the sound speed
Ne = 10; % the number of elements
i = 2; % the mode to plot
N = 2*Ne+1; % the number of nodes
x = linspace(-L/2,L/2,N); % the x location of the nodes
a = L/(N-1); % half length of each element

He = A/a*[7/6 -4/3 1/6;-4/3 8/3 -4/3; 1/6 -4/3 7/6]; % element inertia matrix
Qe = A*a/c0^2*[4 2 -1;2 16 2;-1 2 4]/15; % element stiffness matrix

% map the element matrices into the global matrices
H = zeros(N,N);
Q = zeros(N,N);
for n=1:Ne
  I = 2*(n-1)+(1:3);
  H(I,I)=H(I,I)+He;
  Q(I,I)=Q(I,I)+Qe;
end
```

```
[V,D] = eig(Q\H); % compute the eigen functions and freqs
% calc the exact solution
xExact=linspace(-L/2,L/2,Ne*19+1);
fExact=c0/L/2*(0:N-1);
pExact=cos((xExact+L/2)/L*pi*i);

[freqs,I]=sort(sqrt(diag(D))/2/pi); % sort the eigenfreqs and convert to freq
(Hz)
V=V(:,I); % sort the eigenfunctions in order of increasing eigenfreq
pNodes=V(:,i+1)/V(1,i+1); % normalise he eigenfunctions
% interpolate the nodal pressure results using the element shape functions
pInterp=zeros(1,Ne*19+1);
for n=1:Ne
  I = 2*(n-1)+(1:3);
  Ix = (n-1)*19+(1:20);
  xElem = linspace(-1,1,20);
  pInterp(Ix) = pNodes(I(1))*xElem/2.*(xElem-1)...
      + pNodes(I(2))*(1-xElem.^2)...
      + pNodes(I(3))*xElem/2.*(xElem+1);
end
plot(xExact,pExact,xExact,pInterp)
```

Appendix IV PAFEC-FE: eigenanalysis of a rigid-walled pipe

```
CONTROL
c Every pafec dat file begins with a control module which defines job options
AXISYMMETRIC c Informs the solver that the geometry is axisymmetric
HARMONIC.NUMBER=0 c The Fourier axisymmetric elements should not model any
circumferential variation
CONTROL.END
PARAMETERS c The parameters module enables us to create some variables to use
in the dat file
'rho'=1.19 c Acoustic density
'c'=343 c Sound speed
'r' = 10e-3 c the diameter of the pipe
'L' = 0.5 c the length of the pipe
'N' = 10 c the number of elements along the length of the pipe
NODES
c The nodes module is used to directly define the position of nodes. For this
job we only need to define a few nodes at key positions
NODE X Y
1       0       0
2       0       <'r'/2>
3       'L'     0
4       'L'     <'r'/2>
MATERIALS
C the material for the pipe region is defined in this module
MATE RO       BULK
11   'rho'    <'c'*'c'*'rho'>
PAFBLOCKS
c PAFBLOCKS modules allow simple,easy definition of regularly shaped blocks of
nodes and elements. Each row defines a block. The shape of the block is defined
in the type column, the element type for the block defined in the Element
column. The group and properties for the elements is defined in the
corresponding columns. N1, N2 and N3 define mesh densities along edges of the
pafblock. Finally the topology of the block is defined in the last column,
these numbers refer to the nodes defined above.
TYPE    ELEMENT GROUP   PROPERIES       N1      N2      N3      TOPOLOGY
1       29220   1       11              'N'     1       0       1 3 2 4
MODES
c the modes module defines that we require 10 modes to be found starting with
the first.
MODES    START
10       1
END.OF.DATA
```

Appendix V Matlab BEM formulation

The following Matlab code outlines a simple BEM formulation with plane four noded straight edged patches using a Gauss integration of order 2 to form the patch matrices. The two scripts sphere.m and cube.m run the examples given in section 3.8. In order to run this code it is also necessary to include the vector routines provided in Appendix VI This code was developed with considerable reference to the Masters dissertation of Holmström [60].

AV.i sphere.m

```
% This script runs the BEM analysis on a pulsating sphere.
a = 100e-3; % radius of sphere
A = 4*pi*a^2; % area of sphere
% nodal coordinates
X=[1.0000         0         0
  0.9239    0.3827         0
  0.8534    0.3687    0.3687
  0.9239         0    0.3827
  0.6587    0.3727    0.6587
  0.7071         0    0.7071
  0.3687    0.3687    0.8534
  0.3827         0    0.9239
  0    0.3827    0.9239
  0         0    1.0000
  0.7071    0.7071         0
  0.6587    0.6587    0.3727
  0.5774    0.5774    0.5774
  0.3727    0.6587    0.6587
  0    0.7071    0.7071
  0.3827    0.9239         0
  0.3687    0.8534    0.3687
  0    1.0000         0
  0    0.9239    0.3827]*100e-3;
% patch topology
patches = [
  1     2     3     4
  2    11    12     3
  11    16    17    12
  16    18    19    17
  4     3     5     6
  3    12    13     5
  12    17    14    13
  17    19    15    14
  6     5     7     8
  5    13    14     7
  14    15     9     7
  8     7     9    10];
% symmetry definitions, each line defines a mirroring of the original
% geometry.
symmetry = [
  1  1  1
  1 -1  1
  -1  1  1
  -1 -1  1
  1  1  -1
  1 -1  -1
  -1  1  -1
  -1 -1  -1];
% prescribed unit vol velocity on the surface (unit volume velocity)
vNorm = ones(size(X,1),1)/A;
% additional points for collocation
Xcolloc=[0 0 0;0.2 0.1 0.8;0.7 0.4 0.2;0.1 0.6 0.1;]*100e-3;
% locations at which the pressure should be evaluated
Xeval=[0 0 1];
% frequencies for analysis
f = logspace(log10(20),log10(10000),300);
Nf=length(f);
```

```
% prepare vector to hold the pressure results at the eval point
pEval = zeros(Nf,1);
% loop over the BEM solver and solve for each frequency.
for n=1:length(f);
  fprintf(1,'freq: %0.2f\n',f(n))
  pEval(n) = BEMsolve(X,patches,symmetry,vNorm,Xcolloc,Xeval,f(n));
end
```

AV.ii cube.m

```
% This script runs the cube BEM example.
a = 200e-3; % side length of the cube
Na = 6; % the number of patches along each half edge
A=(a/Na/2)^2; % the area of a patch
% face 1 (front)
[x1,y1]=meshgrid(linspace(0,a/2,Na+1),linspace(0,a/2,Na+1));
z1=repmat(0,Na+1,Na+1);
patches1 = fliplr(repmat([(1:Na)' (2:Na+1)' Na+1+(2:Na+1)' Na+1+(1:Na)'],Na,1)+
(Na+1)*repmat(reshape(repmat(0:Na-1,Na,1),[],1,1),1,4));
% face 2 (right)
[z2,y2]=meshgrid(linspace(0,-a,2*Na+1),linspace(0,a/2,Na+1));
x2=repmat(a/2,2*Na+1,Na+1);
patches2 = max(patches1(:))+fliplr(repmat([(1:Na)' (2:Na+1)' Na+1+(2:Na+1)'
Na+1+(1:Na)'],2*Na,1)+(Na+1)*repmat(reshape(repmat(0:2*Na-1,Na,1),
[],1,1),1,4));
% face 3 (back)
[x3,y3]=meshgrid(linspace(a/2,0,Na+1),linspace(0,a/2,Na+1));
z3=repmat(-a,Na+1,Na+1);
patches3 = max(patches2(:))+fliplr(repmat([(1:Na)' (2:Na+1)' Na+1+(2:Na+1)'
Na+1+(1:Na)'],Na,1)+(Na+1)*repmat(reshape(repmat(0:Na-1,Na,1),[],1,1),1,4));
% face 4 (top)
[z4,x4]=meshgrid(linspace(0,-a,2*Na+1),linspace(0,a/2,Na+1));
y4=repmat(a/2,Na+1,2*Na+1);
patches4 = max(patches3(:))+repmat([(1:Na)' (2:Na+1)' Na+1+(2:Na+1)'
Na+1+(1:Na)'],2*Na,1)+(Na+1)*repmat(reshape(repmat(0:2*Na-1,Na,1),[],1,1),1,4);
% create global node list (note that this includes duplicates on every apex)
X = [x1(:),y1(:),z1(:);x2(:),y2(:),z2(:);x3(:),y3(:),z3(:);x4(:),y4(:),z4(:)];
patches = [patches1;patches2;patches3;patches4];
% collapse out coincident nodes
Nnodes=size(X,1);
for n=2:Nnodes;
  I=X(1:(n-1),1)==X(n,1)&X(1:(n-1),2)==X(n,2)&X(1:(n-1),3)==X(n,3);
  if any(I)
    replacement = find(I,1,'first');
    patches(patches==n)=replacement;
  end
end
% remove repetitions
[usedNodes]=unique(patches);
index(usedNodes)=1:length(usedNodes);
patches=index(patches);
X=X(usedNodes,:);
Nnodes=size(X,1);
% symmetry conditions
symmetry = [
  1  1  1
  1 -1  1
  -1  1  1
  -1 -1  1];
% prescribed velocity on the surface
vNorm = zeros(Nnodes,1);
% additional points for collocation
Xcolloc=a*[
  0 0 -0.5
  0.3 0.45 -0.9
  0.35 0.4 -0.3
  0.1 0.2 -0.6
  ];
% locations at which the pressure should be evaluated
Xeval=[0 0 1];
f = logspace(log10(100),log10(5000),100);
Nf=length(f);
```

```
pEval = zeros(Nf,1);
for n=1:length(f);
  w=2*pi*f(n);
  vNorm(1)=1./(1i*w*A);
  fprintf(1,'freq: %0.2f\n',f(n))
  pEval(n) = BEMsolve(X,patches,symmetry,vNorm,Xcolloc,Xeval,true,f(n));
end
```

AV.iii BEMsolve.m

```
function [pEval,pSurf] = BEMsolve(X,patches,symmetry,vNorm,Xcolloc,Xeval,f)
% function [pEval,pSurf] = BEMsolve(X,patches,symmetry,vNorm,Xcolloc,Xeval,f)
%
% Function to form the BEM matrices, find the BE surface pressure for a
% given node normal velocity field and to evaluate the pressure at points
% in the modelled fluid region.
%
% Inputs:
%   X - node coordinates, Nnx3
%   patches - patch definitions Npx4
%   symmetry - mirror definitions for jobs with symmetry Nsx3
%   vNrom - normal velocity at each node on the BE, Nnx1
%   Xcolloc - additional points for collocation for CHIEF method Ncx3
%   Xeval - points in the modelled region for eval of pressures Npx3
%   f - frequency in Hz for analysis
%
% Outputs:
%   pEval - the computed pressures at the points Xeval, Npx1
%   pSurf - the computed pressures at the points X, Nnx1

% acoustical properties
rho0=1.19;
c0=343;
omega=2*pi*f;
const=[omega c0 rho0];
Nsymmetry=size(symmetry,1);
Npatches = size(patches,1);
Nnodes = size(X,1);
Ncolloc = size(Xcolloc,1);
Neval = size(Xeval,1);
% total number of iterations required to form the equations
Ntot = (Nnodes+Ncolloc)*Nsymmetry*Npatches;
count = 0 ;
lastStat=-1;
tic;
% construct the behavioural matricies
H=zeros(Ncolloc+Nnodes,Nnodes);
G=zeros(Ncolloc+Nnodes,Nnodes);
for n=1:Nnodes % loop over colloc points
  for s=1:Nsymmetry % loop over symmetries
    for p=1:Npatches % loop over patches
      if toc-lastStat>0.5
        fprintf(1,repmat(char(8),1,count));
        count=fprintf(1,'%0.2f%%',...
          100*((n-1)*Nsymmetry*Npatches+(s-1)*Npatches+p)/Ntot);
        lastStat=toc;
      end
      [He,Ge]=calcPatchHG(X(n,:),...
       repmat(symmetry(s,:),4,1).*X(patches(p,:),:),...
       const,...
       isodd(sum(symmetry(s,:)==-1)));
      H(n,patches(p,:))=H(n,patches(p,:))+He;
      G(n,patches(p,:))=G(n,patches(p,:))+Ge;
    end
  end
end
% add the additional CHIEF collocation points
for n=1:Ncolloc
  for s=1:Nsymmetry % loop over symmetries
    for p=1:Npatches % loop over patches
      if toc-lastStat>0.5
        fprintf(1,repmat(char(8),1,count));
```

```
        count=fprintf(1,'%0.2f%%',...
          100*(Nnodes*Nsymmetry*Npatches+(n-1)*Nsymmetry*Npatches+(s-
1)*Npatches+p)/Ntot);
        lastStat=toc;
      end
      [He,Ge]=calcPatchHG(Xcolloc(n,:),...
        repmat(symmetry(s,:),4,1).*X(patches(p,:),:),...
        const,isodd(sum(symmetry(s,:)==-1)));
      H(Nnodes+n,patches(p,:))=H(Nnodes+n,patches(p,:))+He;
      G(Nnodes+n,patches(p,:))=G(Nnodes+n,patches(p,:))+Ge;
    end
  end
end
fprintf(1,repmat(char(8),1,count));
fprintf(1,'100%%\n');
% calculate the coefficients C for each node
C = zeros(Ncolloc+Nnodes,Nnodes);
c = calcC(X,patches,symmetry);
C(1:Nnodes,1:Nnodes) = diag(c);
% calculate the pressure on the surface
pSurf = (C-H)\(1i*rho0*omega*G*vNorm);
% construct the matrices for the eval points
Heval=zeros(Neval,Nnodes);
Geval=zeros(Neval,Nnodes);
for n=1:Neval
  for s=1:Nsymmetry % loop over symmetries
    for p=1:Npatches % loop over patches
      [He,Ge]=calcPatchHG(Xeval(n,:),...
        repmat(symmetry(s,:),4,1).*X(patches(p,:),:),...
        const,isodd(sum(symmetry(s,:)==-1)));
      Heval(n,patches(p,:))=Heval(n,patches(p,:))+He;
      Geval(n,patches(p,:))=Geval(n,patches(p,:))+Ge;
    end
  end
end
% calculate the pressure at the eval points
pEval = Heval*pSurf+1i*rho0*omega*Geval*vNorm;
end
```

AV.iv isodd.m

```
function o=isodd(x)
% function o=isodd(x)
%
% Returns true if x is odd
o=2*round(x/2)~=x;
end
```

AV.v calcC.m

```
function C = calcC(X,patches,symmetry)
% C = calcC(X,patches,symmetry)
%
% This function calculates the pressure weighting coefficients C for each
% node on the boundary element. A geometrical method is used to calculate
% the solid angle in the fluid at each nodal position. This calculation is
% performed on the full mirrored geometry, with symmetry removed, to ensure
% that the correct values are found. The process is simple:
% 1. The node normal is found as the average of the face normals to which
%    it is attached.
% 2. For each patch attached to the node the edges which use the node in
%    question are found and two edge vectors pointing away from the node
%    along the patch edges are found.
% 3. The solid angle contained by these three vectors is found using the
%    solid angle calculation for the apex of a trapezium.
% 4. The solid angles from all attached patches are summed to give the
%    total.
%
% inputs:
%    X - Cartesian coordinate vectors for all nodes in the unmirrored
%        system , Nnodesx3
```

```
%    patches - the node index forming the patch faces, Npatchesx4.
%    symmetry - a matrix defining all reflections required to construct the
%               full geometry.
Nnodes=size(X,1);
% get the full geom including the symmetric mesh (reduced so no repeated nodes)
[fullX,fullPatches] = mirrorGeom(X,patches,symmetry);
% calc face norms for all patches
faceNorms = vunit(vcross(fullX(fullPatches(:,1),:)-
fullX(fullPatches(:,2),:),...
  fullX(fullPatches(:,4),:)-fullX(fullPatches(:,1),:)));
C=zeros(Nnodes,1);
for n=1:Nnodes
  % find all patches which share this node.
  [i,j]=find(fullPatches==n);
  % the average face normal is the surface normal at this node.
  normal = vunit(mean(faceNorms(i,:),1));
  attachedPatches=fullPatches(i,:);
  % shift so that the node is at the start.
  for m=1:length(j)
    p=circshift(attachedPatches(m,:),[1 -j(m)+1]);
    edge1 = vunit(fullX(p(2),:)-fullX(n,:));
    edge2 = vunit(fullX(p(4),:)-fullX(n,:));
    C(n) = C(n) - tetrahedronAngle(-normal,edge1,edge2)/4/pi;
  end
end
  function angle=tetrahedronAngle(a,b,c)
    det = abs(vdot(a,vcross(b,c)));
    div = 1 + vdot(a,b) + vdot(a,c) + vdot(b,c);
    at = atan2(det,div);
    if at<0
      at = at + pi;
    end
    angle = 2*at;
  end
end
```

AV.vi mirrorGeom.m

```
function [fullX,fullPatches,X2fullX] = mirrorGeom(X,patches,symmetry)
% [fullX,fullPatches,X2fullX] = mirrorGeom(X,patches,symmetry)
%
% Function to return the full mirrored geometry given the node and patch
% definitions of the segment of the geometry for modelling and a matrix
% defining the symmetry conditions.
%
% Inputs:
%          X - matrix of node coordinates, Nnx3
%          patches - matrix of patch definitions, Npx4
%          symmetry - matrix of symmetries, Nsx3
%
% Outputs:
%          fullX - matrix of nodes supplimented with additional nodes
%          required to define the full geometry.
%          fullPatches - matrix of patches suplimented with additional
%          patches as required to define the full geometry.
%          X2fullX - vector of length size(fullX,1) showing mapping X to
%          fullX, this can be used to map the results onto the full
%          geometry.

% find the sizes of the inputs
Nnodes=size(X,1);
Npatches=size(patches,1);
Nsymmetry=size(symmetry,1);
% prepare the outputs
fullX = zeros(Nnodes*Nsymmetry,3);
fullPatches = zeros(Npatches*Nsymmetry,4);
X2fullX = zeros(Nnodes*Nsymmetry,1);
% mirror the geometry
for n=1:Nsymmetry
  fullX((n-1)*Nnodes+(1:Nnodes),:) = repmat(symmetry(n,:),Nnodes,1).*X;
  X2fullX((n-1)*Nnodes+(1:Nnodes),:) = 1:Nnodes;
  if isodd(sum(symmetry(n,:)==-1)) % correct the face direction
```

```
    fullPatches((n-1)*Npatches+(1:Npatches),:) = fliplr(patches)+(n-1)*Nnodes;
  else
    fullPatches((n-1)*Npatches+(1:Npatches),:) = patches+(n-1)*Nnodes;
  end
end
% remove repetitions from fullX.
for n=Nnodes+1:Nsymmetry*Nnodes;
  X = fullX(n,:);
  I=fullX(1:(n-1),1)==X(1,1)&fullX(1:(n-1),2)==X(1,2)&fullX(1:(n-1),3)==X(1,3);
  if any(I)
    replacement = find(I,1,'first');
    fullPatches(fullPatches==n)=replacement;
  end
end
% adjust fullPatches to index the reduced fullX set
[usedNodes]=unique(fullPatches);
index(usedNodes)=1:length(usedNodes);
fullPatches=index(fullPatches);
fullX=fullX(usedNodes,:);
X2fullX=X2fullX(usedNodes,:);
end
```

AV.vii calcPatchHG.m

```
function [He,Ge]=calcPatchHG(Xe,Xn,const,normFlip)
% [He,Ge]=calcPatchHG(Xe,Xn,const,n)
%
% This function calculates the patch He and Ge vectors for a single patch
% for a given pressure evaluation point. The normal to the patch face is
% calculated within this function, there is the option to flip the
% calculated normal which can be very handy particularly when using
% geometries with symmetry.
%
% Xe - pressure evaluation point, cartesian vector 1x3
% Xn - patch node positiongs, cartesian vectors 4x3
% const - vector of acoustical constants [omega, c0, rho0]
% normFlip - boolean to flag if the normal of this patch requires inverting

% calc the wavenumber
k=const(1)/const(2);
%% calc face normal
n = vunit(vcross(Xn(1,:)-Xn(2,:),Xn(4,:)-Xn(1,:)));
if normFlip;
  n = -n;
end
% use the helper function to find the coefficients for the Gauss integration
[Bg,A]=gaussHelper(Xn);
% calc global coords of the gauss points
Xg=Bg*Xn;
Xge = repmat(Xe,4,1)-Xg; % vectors from gauss points to eval point
r = vabs(Xge); % distance from gauss points to eval point
% make Ge vector
g = exp(-1i*k*r)./(4*pi*r);
Ge = zeros(1,4);
Ge(:) = Bg*(A.*g);
% make He vector
h = vdot(Xge,n).*(1i*k+1./r).*exp(-1i*k*r)./(4*pi*r.^2);
He = zeros(1,4);
He(:) = Bg*(A.*h);
end
```

AV.viii gaussHelper.m

```
function [Bg,A]=gaussHelper(Xn)
% function [Bg,A]=gaussHelper(Xn)
%
% This function provides the shape functions and area weightings at the
% Gauss points which allows integration to be quickly performed. In this
% case the Gaussian Quadrature has order N=2 for both the integral in the
% local patch coordinate system.
%
```

```
% Inputs
%   Xn: cartesian coordinate vector with patch node positions 4x3
%
% Outputs
%   Bg: shape function coefficients for each gauss point 4x4
%       rows - gauss point
%       columns - shape function coefficient
%
%   A: area weightings for each gauss point (equal if pathc is rectangular)

%% Calc weightings and areas for quadrature
% gauss points in normalised coords (a=xi1,b=xi2)
a=[-1; 1; 1;-1]./sqrt(3);
b=[-1;-1; 1; 1]./sqrt(3);
% shape function values at gauss points
Bg=zeros(4,3);
Bg(:,1)=(1-a).*(1-b)/4;
Bg(:,2)=(1+a).*(1-b)/4;
Bg(:,3)=(1+a).*(1+b)/4;
Bg(:,4)=(1-a).*(1+b)/4;
% differential of shape function wrt local coord a at each gauss point
dBda=zeros(4,3);
dBda(:,1)= (b-1)/4;
dBda(:,2)= (1-b)/4;
dBda(:,3)= (1+b)/4;
dBda(:,4)=-(1+b)/4;
% differential of shape function wrt local coord b at each gauss point
dBdb=zeros(4,3);
dBdb(:,1)=-(1-a)/4;
dBdb(:,2)=-(1+a)/4;
dBdb(:,3)= (1+a)/4;
dBdb(:,4)= (1-a)/4;
% convert to differentials of global coords wrt local coords
dXda=dBda*Xn;
dXdb=dBdb*Xn;
% area weightings for each shape function
A=vabs(vcross(dXda,dXdb));
end
```

Appendix VI Matlab vector utility functions

In this appendix four Matlab utility functions are outlined which perform simple common manipulations to vectors. These functions are required by the code for the BEM formulation in Appendix V

AVI.i vabs.m

```
function o=vabs(s)
% function o=vabs(s)
% Compute the absolute value of a vector
%
% Inputs:
%          s - array of vectors Nx3
% Outputs:
%          o - column vector of absolute values Nx1
if isempty(s)
  o=[];
else
  if size(s,2) ~= 3
    error('Incompatible dimensions.');
  end
  o=sqrt(sum(real(conj(s).*s),2));
end
end
```

AVI.ii vcross.m

```
function o=vcross(s,t)
% function o=vcross(s,t)
% Compute the cross product of two vectors
%
% Inputs:
%          s - array of vectors Nx3
%          t - array of vectors Nx3
% Outputs:
%          o - array of vectors Nx3
%
% s and t can be arrays with multiple vectors provided that hold the same
% number of vectors.
if isempty(s) || isempty(t)
  o=[];
else
  if size(s,2)~=3 || size(t,2)~=3 || size(s,1)~=size(t,1)
    error('Incompatible dimensions.');
  end
  o=[s(:,2).*t(:,3)-s(:,3).*t(:,2)...
       s(:,3).*t(:,1)-s(:,1).*t(:,3)...
       s(:,1).*t(:,2)-s(:,2).*t(:,1)];
end
end
```

AVI.iii vdot.m

```
function o=vdot(s,t)
% function o=vdot(s)
% Compute the dot product of two vectors
%
% Inputs:
%          s - array of vectors Nx3 or 1x3
%          t - array of vectors Nx3 or 1x3
% Outputs:
%          o - vector of dot proucts Nx1
%
% s and t can be arrays with multiple vectors provided that hold the same
% number of vectors. Alternatively if one of the inputs is an array of
% vectors and the other is a single vector then the dot product of the
```

```
% single vector with each entry in the array is returned.
if isempty(s) || isempty(t)
  o=[];
else
  if size(s,2) ~= 3 || size(t,2) ~= 3
    error('Incompatible dimensions.');
  end
  if numel(s) == 3
    d=size(t,1);
    o=sum(repmat(conj(s),d,1).*t,2);
  elseif numel(t) == 3
    d=size(s,1);
    o=sum(conj(s).*repmat(t,d,1),2);
  elseif size(s,1)~=size(t,1)
    error('Incompatible dimensions.');
  else
    o=sum(conj(s).*t,2);
  end
end
end
```

AVI.iv vunit.m

```
function o=vunit(s)
% function o=vunit(s)
% Compute the equivalent unit vector
%
% Inputs:
%          s - array of vectors Nx3
% Outputs:
%          o - array of vectors Nx3
if isempty(s)
  o=[];
else
  if size(s,2) ~= 3
    error('Incompatible dimensions.');
  end
  a=vabs(s);
  o=zeros(size(s));
  o(a~=0,:) = s(a~=0,:)./repmat(a(a~=0),1,3);
end
end
```

Appendix VII A second BEM example

In this appendix a second example of the BEM is presented: that of a simple acoustical volume velocity source, U_s, located in the centre of one the face of a cube, of side length a, as illustrated in figure VII.1. Unlike the pulsating sphere in section 3.8, an analytical solution is not known for this geometry.

The BEM mesh used to approximate the geometry is shown in figure VII.2.

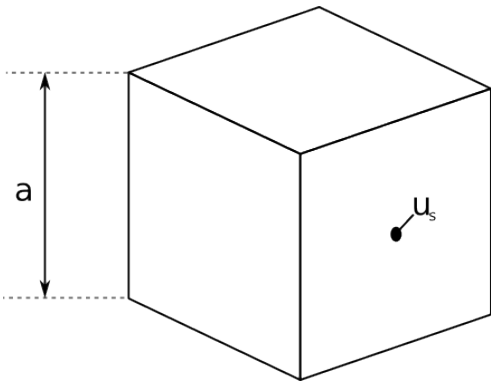

Figure VII.1. Illustration of the acoustical problem to be solved using the Boundary-Element Method.

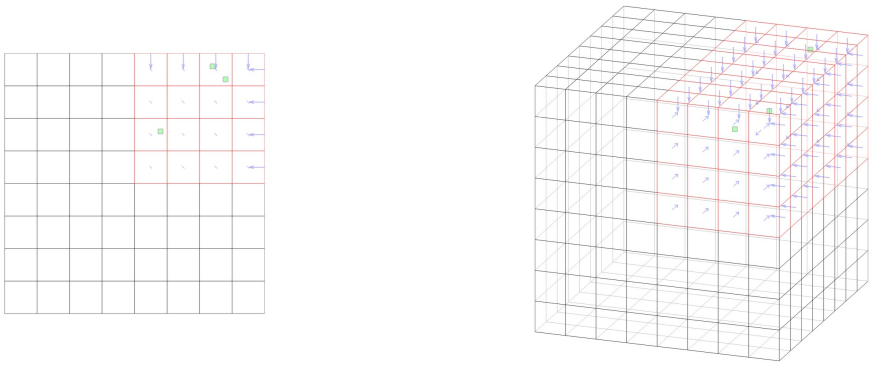

Figure VII.2. BEM mesh with 384 patches used to approximate the rigid cube.

As with the sphere example, the symmetry of the problem can be used to reduce the size of the matrices to be solved. The area shown in red is the region over which the behavioural matrices are constructed. The normal velocity at all the nodes, with the exception of a single node at the centre of the closest face to the view shown in figure VII.2.a, is zero. At the driven node the normal velocity is set to $1/j\omega A_p$, where A_p is the area of a patch. In this way, due to the linear shape functions, the driven node has an imposed volume acceleration of unity. The cube edge dimension is set as 200mm.

In appendix AI.i, the effect of the enclosure on loudspeaker radiation is discussed including the effect of the finite baffle size on the the axial pressure radiation. There are a number of methods described that approximate the cabinet diffraction effect by placing secondary sources along the edges of the front face of the loudspeaker enclosure [87,88,89,90]. The most recent of these methods is that described by Urban et al. [90] who show that the baffle-diffraction problem may be simulated with increased accuracy if the secondary sources placed on the edges of the front face have a dipole directivity characteristic. The dipole null must be arranged to be in the plane of the baffle and the negative polarity lobe directed away from the enclosure perpendicular to the front face.

The rationale for the Urban diffraction model is based on an approximate solution to the Kirchoff Helmholtz integral equation. The approximation is thus: the front surface of the box is considered as a thin, rigid, acoustical baffle in isolation without the presence of the remainder of the enclosure. It is assumed that only the pressure on the front of the baffle is significant and that it is only necessary to perform the integrals of the Kirchoff Helmholtz equation over the front surface. This is an assumption that has been previously shown to be valid when the observation point is in front of the baffle [96]. It further is assumed that the pressure on the surface of the baffle is accurately approximated as the pressure at the same position on an infinite baffle. It is assumed that this infinite-baffle pressure is known, either by measurement of a loudspeaker driver in 2π conditions or by the use of a model such as the rigid piston model outlined in section 2.3. These assumptions provide a known pressure field and normal velocity field on the surface of the baffle and the far-field pressure is approximated using the Kirchoff Helmholtz integral over the front surface. For the case when the baffle is a finite circular disc and the source is a point source, Urban et al. show that, by geometric approximation for a point in the far field that lies close to an axis perpendicular to the baffle passing through the source, the pressure can be approximately described as the sum of two pressures. The first is a direct pressure term equal to the pressure radiated to the same observation point by the infinite-baffle case modified by an additional cardioid directivity term. The second is a diffracted pressure term from a dipole line source along the edge of the baffle with strength proportional to the same directivity modified infinite-baffle pressure. This can be written as

$$p_{far}(\boldsymbol{x}) \approx p_{drive}(\boldsymbol{x}) - \frac{\boldsymbol{n}\cdot\boldsymbol{x}}{|\boldsymbol{x}|}\frac{2\pi}{L}\int_{edge} p_{drive}(\boldsymbol{y})\frac{e^{-jk|\boldsymbol{x}-\boldsymbol{y}|}}{2\pi|\boldsymbol{x}-\boldsymbol{y}|}d\boldsymbol{y} \qquad \text{VII.1.}$$

where the function $p_{drive}(\boldsymbol{x})$ is defined to be

$$p_{drive}(\boldsymbol{x}) = p_{inf}(\boldsymbol{x})\left[\frac{1}{2} + \frac{\boldsymbol{n}\cdot\boldsymbol{x}}{2|\boldsymbol{x}|}\right] \qquad \text{VII.2.}$$

$p_{inf}(\boldsymbol{x})$ is the pressure at position $\boldsymbol{x}$ generated by the same source placed in an infinite baffle, $\boldsymbol{n}$ is the unit normal pointing out of the front baffle, L is the total length of the baffle edges. Note that the term $\boldsymbol{n}\cdot\boldsymbol{x}/|\boldsymbol{x}|$ returns the cosine of the angle between the vector $\boldsymbol{x}$ and unit vector $\boldsymbol{n}$ and, consequently, defines that the edge line source has a dipole directivity. While the approximation is only strictly valid for points in the far field directly in front of the baffle, Urban shows with experimental results that the predicted pressure accuracy is good even when the observation point is behind the plane of the front baffle.

In the absence of an analytical solution to the problem of a point source on the face of a cube, it is interesting to compare the BEM results to simulations using the Urban method. For the Urban simulation, the infinite-baffle pressure from a point source located on the baffle is given by

$$p_{inf}(\boldsymbol{x}) = \frac{e^{-jk|\boldsymbol{x}|}}{2\pi|\boldsymbol{x}|} \qquad \text{VII.3.}$$

The line integral in expression VII.1 was approximately performed by discretisation of the four edges into 40 edge dipole sources.

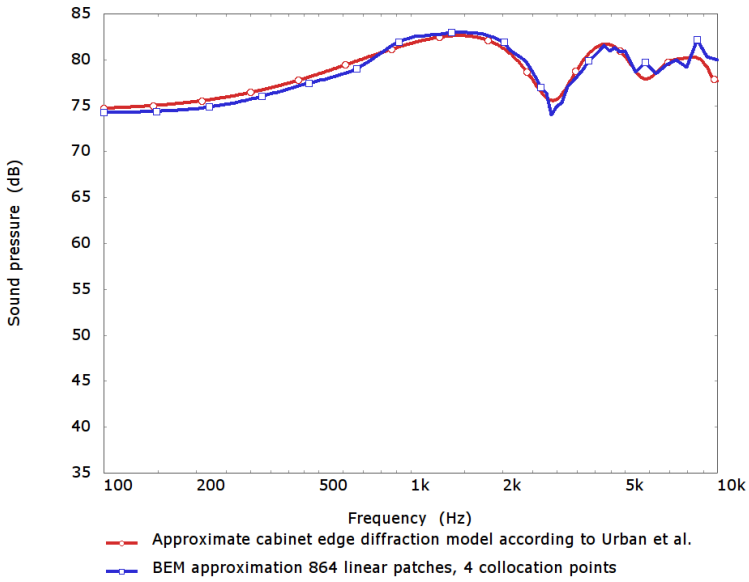

Figure VII.3. Unit volume-acceleration source located on in the centre of the front surface of a 200mm cube pressure response at 1m on axis, approximate calculation using the edge-source method described by Urban et al. [90] (red), BEM calculation using 864 linear patches in full geometry (blue).

The approximated pressure response magnitude at 1m directly in front of the face that holds the point source is shown in figure VII.3 for both the Urban method and the BEM approximation described above. The agreement between the two methods is remarkable, particularly considering the rudimentary nature of the Urban model.

Appendix VIII PAFEC-FE: piston in an Infinite Baffle

```
CONTROL
c Every pafec dat file begins with a control module which defines job options
AXISYMMETRIC c Informs the solver that the geometry is axisymmetric
HARMONIC.NUMBER=0 c The Fourier axisymmetruc elements should not model any
circumferential variation
FRONTAL.SINUSOIDAL.SOLUTION c The solve type that we require – direct solution
of the equations of motion in the frequency domain
CONTROL.END
PARAMETERS c The parameters module enables us to create some variables to use
in the dat file
'rho'=1.19 c Acoustic density
'c'=343 c Sound speed
'a'=38.2e-3 c Piston radius
'Fmin'=20 c Lowest frequency for analysis
'Fmax'=20000 c Highest frequency for analysis
'Nf'=200 c Number of frequencies for analysis
'elemSize'=<'c'/(6*'Fmax')> c Element size (6 elements per wavelength at Fmax)
'Nelem'=INT <'a'/'elemSize'+1> c Number of elements across the piston
NODES
c The nodes module is used to directly define the position of nodes. For this
job we only need to define a few nodes at key positions
NODE                  X             Y
1                     0             0
2                     0             'a'
3                     'elemSize'    0
4                     'elemSize'    'a'
5                     0             <'a'+'elemSize'>
10                    0             <'a'+'elemSize'>
<10+2>                'elemSize'    'a'
<10+2+'Nelem'*2>      'elemSize'    0
PAFBLOCKS
c PAFBLOCKS modules allow simple,easy definition of regularly shaped blocks of
nodes and elements. Each row defines a block. The shape of the block is defined
in the type column, the element type for the block defined in the Element
column. The group and properties for the elements is defined in the
corresponding columns. N1, N2 and N3 refer to entries in the MESH module which
defines mesh densities along edges of the pafblock. Finally the topology of the
block is defined in the last column, these numbers refer to the nodes defined
above.
TYPE    ELEMENT GROUP   PROPERIES     N1     N2     N3     TOPOLOGY
1       29220   1       11            1      2      0      1 2 3 4 c FE
acoustic 2D elements (block A)
2       29210   1       11            2      2      2      2 5 4   c FE acoustic
2D elements (block B)
6       42130   2       1             1      0      0      1 2     c FE acoustic
1D elements (block C)
LINE.NODES
c LINE.NODES is used to position nodes on a straight line. The position of the
start and end node must be defined elsewhere, the nodes between are created
along the line in equally spaced locations. A shorthand notation is used “X,-
1,Y” is a list beginning at X and incrementing by 1 until Y is reached.
LIST
10,-1,<10+2>
<10+2>,-1,<10+'Nelem'*2+2>
ELEMENTS
c The elements of the BE are created directly using a single entry in the
elements module. The number column sets the element number, the group column
the element group. The Topology entry defines the nodes which are used by this
element using the same list shorthand as seen in LIST.NODES
NUMBER  GROUP   PROPERTY      ELEMENT        TOPOLOGY
1       3       11      23610          10,-1,<10+'Nelem'*2+2>
MESH
c The MESH module is used by the PAFBLOCKS module to define the mesh density
for pafblock edges
REFERENCE SPACING
1       'Nelem'
2       1
COLLAPSE
c The nodes of the BE, the acoustical FE and the structural FE must have
distinct separate nodes. The collapse module is normally used to merge nodes
but in this case, with couplingtype=3 it will separate any common nodes shared
between the groups GR1 and GR2. Here the structural FE, group 1, is separated
```

```
from the acoustical FE, group 2, and also the BE, group 3. New nodes are
created on GR2 the acoustical FE and BE.
COUPLINGTYPE=3
GR1     GR2
1       2
1       3
PLATES.AND.SHELLS
c The plates.and.shells module is used by 2D and 1D structural FE elements to
define thickness and associate the elements with a material definition. Plate
refers to the properties setting of the elements, mate to the material number
used in the material modules. In this case we have one entry for the structural
FE thin shell of revolution elements used to model the rigid piston.
PLATE MATE THICKNESS
 1      1      0.01
RESTRAINTS
c The nodes of the structural FE are constrained so that the piston can only
move axially. This is done by selecting all the nodes on a plane of constant x
passing through node 1, at the centre of the piston. The nodes are restrained
in directions 2,3 and 6: y motion, x motion and rotation about the x axis.
NODE    PLANE   DIRE
 1      1       236
REPEATED.FREEDOMS
c The nodes of the structural FE are constrained to move rigidly in the x
direction. This is done by selecting all the nodes on a plane of constant x
passing through node 1, at the centre of the piston. The nodes have their
“freedoms” repeated in direction 1, the x direction.
N1      PLANE   DIRE
1       1       1
MATERIALS
c This module defines the material characteristics of the acoustical regions.
The material number is refered to by the element properties setting.
MATE    RO      BULK
 11     'rho'   <'c'*'c'*'rho'>
ENFORCED.HARMONIC.MOTION
c Motion is defined on the piston. Type 1 defines velocity, node 1 at the
centre of the piston will have motion enforced, the rest of the piston will
follow due to the repeated.freedoms module. Direction 1 is the x-direction. The
variation of the velocity with frequency is defined in table 1, below.
TYPE    NODE    DIRE    TABLE
2       1       1       1
TABLES
c This module holds a table of piston velocity variation with frequency.
TABLE=1
BASIS   VALUE
'Fmin'  1       0
'Fmax'  1       0
MASTERS
c The driven node and direction must be defined as a master. Masters are
freedoms which are retained in the solution and not eliminated during the
reduction of the equations of motion.
NODE    DIRE
1       1
MODES
c By default PAFEC will calculate eigenvalues and vectors for the discretised
system. We do not wish to use a modal decomposition method, this module
instructs PAFEC not to calculate any modes nor to assign any automatic masters.
MODES   AUTO
0       0
RESPONSE
c Response type 0 defines a sinusoidal response with no damping
TYPE
0
FREQUENCIES.FOR.ANALYSIS
c Here we define the frequencies for analysis, type 3 sets logarithmically
spaced frequency points
TYPE    START   FINISH  NUMBER
3       'Fmin'  'Fmax'  'Nf'
ACOUSTICS
c The acoustics module defines the type of solution used for the boundary
element module. Solution type 3, by  default, defines a pure surface Helmholtz
formulation which does suffer from the characteristic frequency problem.
However for this geometry and frequency range defined in the parameters module,
```

```
the first eigenvalue of the internal acoustical space defined by the BE
geometry is sufficiently above the highest frequency range of interest.
SOLUTION.TYPE  ELEMENT
3              1
SYMMETRY
c The infinite baffle in which the piston is mounted is defined by applying a
symmetry condition on the boundary element formulation.
ELEMENT AXIS   SYMMETRY
1       1      1
END.OF.DATA
```

Appendix IX PAFEC-FE: eigenanalysis of a rigid-walled cavity

```
C The mesh for this FEM analysis was generated in Flux, the PAFEC dat file was
created
C using an automated mesh translation program from PACSYS called Mesh2paf.
C
C File name J001.DAT
C Converted from J001.TRA
C by MESH2PAF version 1.6
C at 14:21 on  19th June 2009
C
C  Group    Name           Number of elements
C
C      1    AIR                          40
CONTROL
c Every pafec dat file begins with a control module which defines job options
TRACE.LEVEL=2
TIME.STAGES
COMPUTE.RADIUS
AXISYMMETRIC c Informs the solver that the geometry is axisymmetric
HARMONIC.NUMBER=0 c The Fourier axisymmetric elements should not model any
circumferential variation. This is equivalent to m=0 in the analysis of section
5.2.1
SKIP.COLLAPSE c skip any collapsing of nodes – flux has already done this
SKIP.CHECK c skip any checking of the geometry – flux has already done this.
PHASE=1
TOLERANCE=10E-4
BASE=4000000
PHASE=2
BASE=20000000
PHASE=4
BASE=20000000
PHASE=7
CLEAR.FILES
BASE=20000000
CONTROL.END

MATERIALS C the acoustics elements are given the properties of air by this
module.
MATE RO BULK
101 1.19    <343*343*1.19>

NAMES C this is a useful utility module to associate groups of element with
names.
TYPE=1
NUMBER NAME
     1 "AIR"

ELEMENTS c the elements converted from the flux mesh.
PROPERTY=   101
NUMBER GROUP ELEMENT TOPOLOGY
     1     1 29220       2      4      8      6      1      7      3      5
     2     1 29220       8      6     13     11      5     12      9     10
     3     1 29220      13     11     18     16     10     17     14     15
     4     1 29220      18     16     23     21     15     22     19     20
     5     1 29220      23     21     28     26     20     27     24     25
..... continues for 35 more elements

NODES c the nodes converted from the flux mesh
NODE X Y Z
     1  0.2500000E-03   0.000000       0.000000
     2   0.000000       0.000000       0.000000
     3  0.5000000E-03  0.5000000E-03   0.000000
     4  0.5000000E-03   0.000000       0.000000
     5  0.2500000E-03  0.1000000E-02   0.000000
     6  0.5000000E-03  0.1000000E-02   0.000000
     7   0.000000      0.5000000E-03   0.000000
     8   0.000000      0.1000000E-02   0.000000
     9  0.5000000E-03  0.1500000E-02   0.000000
    10  0.2500000E-03  0.2000000E-02   0.000000
..... continues for 193 more nodes
```

```
MODES.AND.FREQUENCIES c defines which modes (eigenfunctions and frequencies) to
evaluate
MODES AUTO
  20     200

END.OF.DATA
```

Appendix X On the definition of compression ratio

The common definition of compression ratio is the ratio of the radiating diaphragm area, A_m, to the summed area of the phase-plug channel entrances, A_T,

$$\alpha = \frac{A_m}{A_T} \qquad \text{X.1.}$$

Although simple, this is not a sufficiently precise definition and it is open to be misinterpreted. Under normal operation, the volume velocity entering the compression cavity is equal to the volume velocity leaving the compression cavity. The actual acoustical velocity at the channel entrance is dependent upon the area of the channel entrances: as the area is decreased, the acoustical velocity is increased. It is this increase in acoustical velocity that facilitates the increased acoustical loading experienced by the radiating diaphragm and hence leads to higher efficiencies. The increase in loading experienced by the diaphragm is proportional to the ratio of the channel-entrance acoustical velocity, u_E, to the diaphragm drive velocity, u_m, and this is equal to the compression ratio,

$$\alpha = \frac{-u_E}{u_m} \qquad \text{X.2.}$$

The negative sign occurs because the polarity of both velocities is defined to be positive toward the interior of the compression cavity.

Much of the analysis work on compression drivers uses a simplified planar diaphragm. However, most real drivers do not have planar diaphragms. Clearly, with a non-planar diaphragm the volume velocity generated for a given axial vibration is the same as a planar diaphragm of the same diameter. Because the diaphragm velocity is constrained to be axial, in our original definition, the diaphragm area, A_m, should not refer to the surface area, but rather the projected area in the direction of vibration.

The channel-entrance acoustical velocity, unlike the diaphragm velocity, is not constrained to be axial. The channel-entrance velocity direction is dependent upon the channel in question. In general, the channel carries the acoustical wave away from the compression cavity in a direction perpendicular to the cavity surface, and so this is the relevant direction. Thus, the compression ratio is precisely defined to be the diaphragm area projected in the direction of vibration to the open area of the exit surface of the compression cavity,

$$\alpha = \frac{\pi a^2}{A_T} \qquad \text{X.3.}$$

This definition of compression ratio is assumed throughout this thesis.

Appendix XI Suppression of modal excitation using range-limited cavity-thickness shape functions

In chapter 6, it was shown that using a Rayleigh-Ritz approximation, along with eigenfunctions from a prototype compression cavity, it is possible to describe the driven acoustical behaviour of a subject compression-cavity with arbitrary thickness profile. Using this approximate description of the compression cavity, along with a set of thickness-profile candidate functions, it was demonstrated that it is possible to derive geometries that suppress the diaphragm excitation of the first few cavity modes. However, one of the problems encountered with this approach is that there is very little control over the shape of the final compression cavity. This is of great importance when designing a compression driver as there are typically some regions of the cavity that, due to practical constraints, must have a fixed pre-determined geometry. The most obvious example of such a region is the area at the outside diameter of the compression driver where the cavity is formed by part of the magnetic gap. This region not only forms a section of the enclosing surface of the cavity, but must also be of the correct geometry to function as part of the magnetic circuit from which the the driving force on the diaphragm is generated.

The Rayleigh-Ritz approximation describes the compression cavity in terms of two matrices, $\boldsymbol{H}$ and $\boldsymbol{Q}$. Given the narrow compression-cavity geometry, these two matrices are approximately constructed using the expressions

$$H_{i,j} \approx \int_{S_e} \nabla \overset{p}{\Psi}_{i-1}(\boldsymbol{y}) . \nabla \overset{p}{\Psi}_{j-1}(\boldsymbol{y}) \mu(\boldsymbol{y}) \, dS_e \qquad \text{XI.1.}$$

and

$$Q_{i,j} \approx \frac{1}{c_0^2} \int_{S_e} \overset{p}{\Psi}_{i-1}(\boldsymbol{y}) \overset{p}{\Psi}_{j-1}(\boldsymbol{y}) \mu(\boldsymbol{y}) dS_e \qquad \text{XI.2.}$$

The driven behaviour is then given by the expression

$$[\boldsymbol{H} - \omega^2 \boldsymbol{Q}] \boldsymbol{p} = j \omega \rho_0 \boldsymbol{\zeta}^{dp} \qquad \text{XI.3.}$$

To accommodate an area of the compression cavity geometry that is known and fixed, the matrices $\boldsymbol{H}$ and $\boldsymbol{Q}$ are each described as the sum of two matrices: one governing the behaviour in the fixed region and, the other, in the region which may vary:

$$\boldsymbol{H} = \boldsymbol{H}^{fix} + \boldsymbol{H}^{var} \qquad \text{XI.4.}$$

and

$$\boldsymbol{Q} = \boldsymbol{Q}^{fix} + \boldsymbol{Q}^{var} \qquad \text{XI.5.}$$

The entrance surface of the compression cavity, S_e, is correspondingly split into two regions, one over which the geometry is fixed, S_e^{fix}, and the other, over which the geometry is permitted to vary S_e^{var}. The union of these two surfaces must form the complete entrance surface of the compression cavity

$$S_e = S_e^{fix} \cup S_e^{var} \tag{XI.6.}$$

The elemental component of the matrices $\boldsymbol{H}^{fix}$, $\boldsymbol{H}^{var}$, $\boldsymbol{Q}^{fix}$ and $\boldsymbol{Q}^{var}$ are given by the integral expressions

$$H_{i,j}^{fix} \approx \int_{S_e^{fix}} \nabla \overset{p}{\Psi}_{i-1}(\boldsymbol{y}).\nabla \overset{p}{\Psi}_{j-1}(\boldsymbol{y}) \mu^{fix}(\boldsymbol{y}) dS_e^{fix} \tag{XI.7.}$$

$$H_{i,j}^{var} \approx \int_{S_e^{var}} \nabla \overset{p}{\Psi}_{i-1}(\boldsymbol{y}).\nabla \overset{p}{\Psi}_{j-1}(\boldsymbol{y}) \mu^{var}(\boldsymbol{y}) dS_e^{var} \tag{XI.8.}$$

$$Q_{i,j}^{fix} \approx \frac{1}{c_0^2} \int_{S_e^{fix}} \overset{p}{\Psi}_{i-1}(\boldsymbol{y}) \overset{p}{\Psi}_{j-1}(\boldsymbol{y}) \mu^{fix}(\boldsymbol{y}) dS_e^{fix} \tag{XI.9.}$$

and

$$Q_{i,j}^{var} \approx \frac{1}{c_0^2} \int_{S_e^{var}} \overset{p}{\Psi}_{i-1}(\boldsymbol{y}) \overset{p}{\Psi}_{j-1}(\boldsymbol{y}) \mu^{var}(\boldsymbol{y}) dS_e^{var} \tag{XI.10.}$$

Where the function $\mu^{fix}(\boldsymbol{y})$ describes the thickness of the cavity in the fixed region and the function $\mu^{var}(\boldsymbol{y})$ describes the thickness of the cavity in the region which may vary.

The driven behaviour of the cavity is now given by the expression

$$\left[\boldsymbol{H}^{fix} + \boldsymbol{H}^{var} - \omega^2 \left(\boldsymbol{Q}^{fix} + \boldsymbol{Q}^{var}\right)\right] \boldsymbol{p} = j\omega\rho_0 \boldsymbol{\zeta}^{dp} \tag{XI.11.}$$

In the same manner as was outlined in section 6.2.3, the cavity-thickness function in the part of the cavity permitted to vary, $\mu^{var}(\boldsymbol{y})$, is defined to be the linear combination of N_μ candidate functions such that

$$\mu^{var}(\boldsymbol{y}) = \sum_{n=1}^{N_\mu} b_n \mu_n^{var}(\boldsymbol{y}) \tag{XI.12.}$$

where b_n are coefficients that describe the proportions of each candidate thickness function $\mu_n^{var}(\boldsymbol{y})$. This expression can also be written as as the multiplication of two vectors as

$$\mu^{var}(\boldsymbol{y}) = \boldsymbol{b}^T \boldsymbol{\mu}^{var}(\boldsymbol{y}) \tag{XI.13.}$$

The matrix $\boldsymbol{H}^{var}$ may be expanded as the linear sum of N_μ matrices such that

$$\boldsymbol{H}^{var} = \sum_{n=1}^{N_\mu} b_n \boldsymbol{H}_n^{var} \qquad \text{XI.14.}$$

where the elemental components of $\boldsymbol{H}_n^{var}$ are approximated to be

$$H_{n,i,j}^{var} \approx \int_{S_e} \nabla \overset{p}{\Psi}_{i-1}(\boldsymbol{y}).\nabla \overset{p}{\Psi}_{j-1}(\boldsymbol{y}) \mu_n^{var}(\boldsymbol{y}) dS_e^{var} \qquad \text{XI.15.}$$

Similarly the matrix $\boldsymbol{Q}^{var}$ may be written as

$$\boldsymbol{Q}^{var} = \sum_{n=1}^{N_\mu} b_n \boldsymbol{Q}_n^{var} \qquad \text{XI.16.}$$

with the elements of $\boldsymbol{Q}_n^{var}$ approximated to be

$$Q_{n,i,j}^{var} \approx \frac{1}{c_0^2} \int_{S_e} \overset{p}{\Psi}_{i-1}(\boldsymbol{y}) \overset{p}{\Psi}_{j-1}(\boldsymbol{y}) \mu_n^{var}(\boldsymbol{y}) dS_e^{var} \qquad \text{XI.17.}$$

The driven cavity behaviour, in terms of these expanded $\boldsymbol{H}^{var}$ and $\boldsymbol{Q}^{var}$ matrices, is

$$\boldsymbol{H}^{fix}\boldsymbol{p} + \sum_{n=1}^{N_\mu} b_n \boldsymbol{H}_n^{var}\boldsymbol{p} - \omega^2 \left(\boldsymbol{Q}^{fix}\boldsymbol{p} + \sum_{n=1}^{N_\mu} b_n \boldsymbol{Q}_n^{var}\boldsymbol{p} \right) = j\omega\rho_0 \boldsymbol{\zeta}^{dp} \qquad \text{XI.18.}$$

The target behaviour for the cavity is that only rigid-body eigenfunction excitation occurs in the bandwidth of the driver. Although the final eigenfunctions are as yet unknown, because the rigid-body eigenfunction is always unity, the target pressure in the resulting cavity can be set in terms of the prototype eigenfunctions to be

$$\boldsymbol{p}^T = \left[\frac{\rho_0 c_0^2 \zeta_0^{dp}}{j\omega V} \quad 0 \quad 0 \quad \ldots \quad 0 \right] \qquad \text{XI.19.}$$

where V is the desired volume of the resulting compression cavity. Assuming that this target pressure is achieved, the system driven behaviour may be expressed as

$$\boldsymbol{h}^{fix} + \sum_{n=1}^{N_\mu} b_n \boldsymbol{h}_n^{var} - \omega^2 \left(\boldsymbol{q}^{fix} + \sum_{n=1}^{N_\mu} b_n \boldsymbol{q}_n^{var} \right) = \frac{-\omega^2 V}{c_0^2} \frac{\boldsymbol{\zeta}^{dp}}{\zeta_0^{dp}} \qquad \text{XI.20.}$$

where the vector $\boldsymbol{h}^{fix}$ is the first column of $\boldsymbol{H}^{fix}$, the vector $\boldsymbol{h}_n^{var}$ is the first column of $\boldsymbol{H}_n^{var}$, the vector $\boldsymbol{q}^{fix}$ is the first column of $\boldsymbol{Q}^{fix}$, and the vector $\boldsymbol{q}_n$ is the first column of $\boldsymbol{Q}_n$.

From expressions XI.7 and XI.8, it is obvious that, as $\overset{p}{\Psi}_0(\boldsymbol{y}) = 1$ and, correspondingly, $\nabla \overset{p}{\Psi}_0(\boldsymbol{y}) = 0$, the vectors $\boldsymbol{h}^{fix}$ and $\boldsymbol{h}_n^{var}$ contain only zeros. Equation XI.20 may be simply written as

$$\boldsymbol{q}^{fix} + \sum_{n=1}^{N_\mu} b_n \boldsymbol{q}_n^{var} = \frac{V}{c_0^2} \frac{\zeta^{dp}}{\zeta_0^{dp}} \qquad \text{XI.21.}$$

Introducing the matrix

$$\tilde{\boldsymbol{Q}}^{var} = \left[\boldsymbol{q}_1^{var} \quad \boldsymbol{q}_2^{var} \quad \cdots \quad \boldsymbol{q}_{N_\mu}^{var} \right] \qquad \text{XI.22.}$$

with coefficients approximated from the integral

$$\tilde{Q}_{i,j}^{var} \approx \frac{1}{c_0^2} \int_{S_e} \overset{p}{\Psi}_{i-1}(\boldsymbol{y}) \mu_j^{var}(\boldsymbol{y}) dS_e \qquad \text{XI.23.}$$

and recalling the definition of $\boldsymbol{b}$, given in expression XI.13, the profiled cavity is described by the matrix equation

$$\tilde{\boldsymbol{Q}}^{var} \boldsymbol{b} = \frac{V}{c_0^2} \frac{\zeta^{dp}}{\zeta_0^{dp}} - \boldsymbol{q}^{fix} \qquad \text{XI.24.}$$

From this expression, a set of coefficients $\boldsymbol{b}$ may be found that minimise the appearance of the prototype cavity eigenfunctions in the pressure response of the profiled cavity. This expression is very similar to 6.46, derived in the previous section for the situation where the entire compression cavity thickness was permitted to vary. The only difference being the addition of the term $\boldsymbol{q}^{fix}$ that represents the region where the cavity profile is fixed. Clearly, if the region where the cavity is fixed is reduced to nothing then the $\boldsymbol{q}^{fix}$ term disappears from the expression and it simplifies to 6.46.

Solution of 6.46 is performed in the same manner as is discussed for 6.46 on page 186. However, there is a significant difference; previously, it was possible to solve for $\boldsymbol{b} S_s / V$ where S_s is the area of the cavity entrance surface, given by the integral

$$S_s = 2\pi \int_{s=0}^{s_a} r(s) ds \qquad \text{XI.25.}$$

In other words, rather than a single, absolutely defined solution for the cavity-thickness profile, expression 6.46 provides the shape of the cavity thickness profile. The overall cavity volume is not prescribed. For the new expression where part of the cavity has a fixed thickness profile, because of the additional $\boldsymbol{q}^{fix}$ term, this is not possible and solution of expression XI.24 results in a single absolutely-defined solution for the cavity-thickness profile.

Example 1

Figure XI.1 shows an FEM mesh of the geometry chosen to demonstrate the technique. The compression cavity in this case consists of two regions: a small cylindrical annulus at the outside diameter of the geometry and a spherical cap region. The cylindrical annulus is typical of the the magnetic gap region of a compression cavity. The length of the cylinder is 1.5mm and the outside diameter is 76.2mm. The spherical cap region has a angle of curvature of 55 degrees from axis of rotation to outside edge. The thickness of the cavity is 0.3mm. This prototype cavity mesh was analysed using PAFEC-FE in order to approximately calculate the eigenfrequencies and eigenfunctions. An additional PAFEC-FE model was constructed having a rigid piston region occupying the left hand side of the compression cavity as an indicator of the extent to which the pressure modes are excited without any cavity shaping.

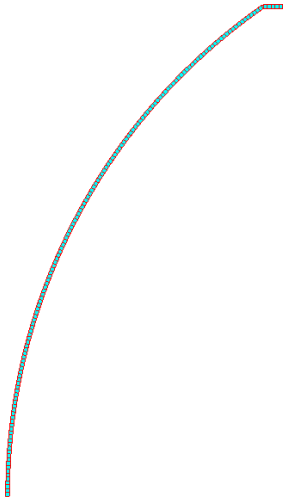

Figure XI.1. Mesh used for eigenfunction and eigenfrequencies FEA solution of prototype cavity. The model is axisymmetric with the axis of rotational symmetry at the lower extent of the mesh.

The very outer diameter of the geometry, at diameter 72.6mm or greater, is not permitted to vary in the the calculation of the cavity-thickness shaping. Five cavity-thickness shape functions were used in the calculations. In this case, the thickness functions are chosen to be a number of rectangular functions defined as

$$\mu_n^{var}(s)=\begin{cases}1 & w_s(n-1)\le s< w_s n\\ 0 & otherwise\end{cases} \qquad \text{XI.26.}$$

where the variable w_s is the width of the rectangular regions, s is the linear coordinate along the entrance surface of the compression cavity. The value of w_s is set to be s_t/N_μ, where s_t is the value of s corresponding to a diameter of 72.6mm above which the cavity thickness is

fixed. Five thickness shape functions were used for the calculation of the cavity shape. To maximise the performance of the cavity shaping, several iterations were performed as was described in section 6.2.3.

The resulting cavity shapes are shown in figure XI.2. The calculated thickness profile is quite different from that presented in the previous section. This is a result of the choice of rectangular functions as the candidate thickness functions. After each iteration a model of the driven cavity was created and the pressure at the outer diameter is shown alongside the thickness profiles as a measure of the extent of modal excitation. It is interesting that, in this case, after only one iteration there is already a significant reduction in the irregularity of the pressure response in the cavity and the subsequent iterations make only small further improvements. It is not clear if this fast convergence is due to the thickness candidate functions chosen or as a result of the entrance surface geometry. In all three iterations the calculated thickness profile is the same in the region $0.9 < s/s_a < 1$, which corresponds to the region that was designated to remain fixed.

This example illustrates that the method outlined in this section to only adjust part of the compression-cavity geometry appears to work successfully for a realistic cavity geometry. However, in common with the previous, unconstrained, method there is no guarantee that the calculated thickness profile is achievable. For instance, it is very easy to derive thickness profiles with negative regions. Clearly, these cannot be practically used. Additionally, there remains the issue that by profiling the compression cavity, it is inevitable that, in order to maintain a reasonable minimum thickness of cavity, the overall volume of the compression cavity is larger than an unprofiled cavity. This is significant as in order to maximise the bandwidth of the compression driver, the cavity volume must be minimised. Nonetheless it is reiterated that this volume/bandwidth relation is based on a simple lumped description of the compression driver and, hence, is only valid when the compression cavity is behaving simply as a basic acoustical compliance. This is clearly not the case in the constant thickness model shown in figure XI.2.

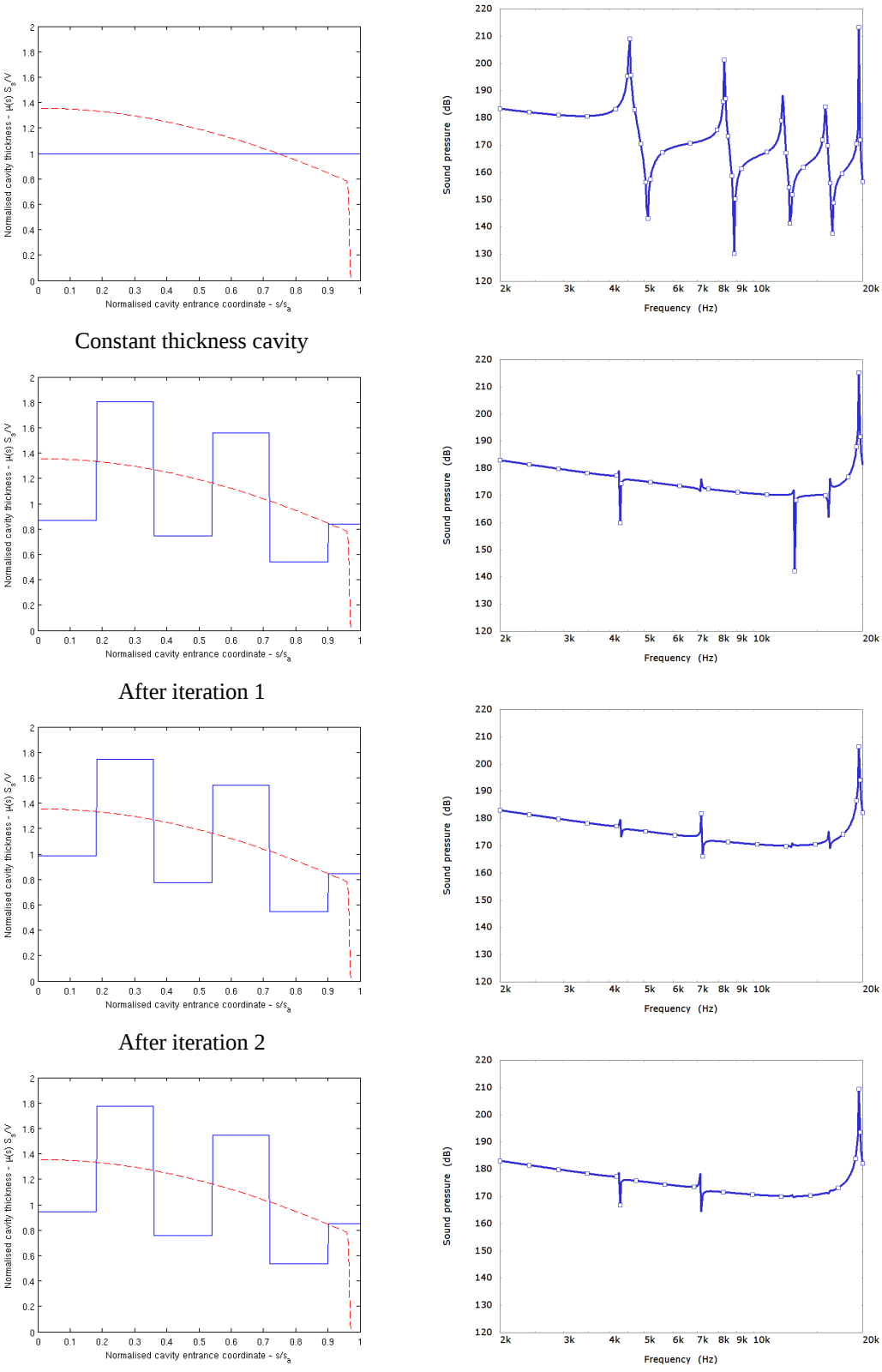

Figure XI.2. Normalised derived profiled cavity-thickness function, compared to the ideal profile (dashed red) and resulting diaphragm-excited pressure-response at outside diameter of cavity for constant-thickness prototype cavity, cavity after first iteration, cavity after second iteration and after third.

For completeness, a three-channel phase plug was designed for the derived profiled cavity. The computed values of ζ_n^d/ζ_0^d, using the generalised method described in section 5.4, are given in table XI.1.

ζ_0^d/ζ_0^d	1
ζ_1^d/ζ_0^d	0.354678
ζ_2^d/ζ_0^d	-0.127144
ζ_3^d/ζ_0^d	0.0735582

Table XI.1: Values of ζ_n^d/ζ_0^d calculated numerically for the profiled cavity given in figure XI.2 when driven with a rigid axially-moving diaphragm on the left hand side of the cavity.

The three channels are placed in the nodal diameters of the third compression cavity mode resulting in the computed channel areas

$$\begin{bmatrix} A_1/A_T \\ A_2/A_T \\ A_3/A_T \end{bmatrix} = \begin{bmatrix} 0.247353 \\ 0.450323 \\ 0.302324 \end{bmatrix} \qquad \text{XI.27.}$$

where A_1 is the area of the inner of the three channels, A_2 is the area of the middle channel and A_3 is the area of the outer most channel. These areas can equivalently be written as channel width ratios as

$$\begin{bmatrix} w_2/w_1 \\ w_3/w_1 \end{bmatrix} = \begin{bmatrix} 0.818646 \\ 0.390653 \end{bmatrix}. \qquad \text{XI.28.}$$

Using these geometric parameters, a simple compression driver FEM model was constructed using the same basic compression-driver diaphragm and cavity geometry, a compression ratio of 15 and with the three channels terminated with a $\rho_0 c_0$ specific acoustical-impedance. The FEM-computed pressures in the three channels are shown in figure XI.3. The pressure levels shown are, once again, normalised by the specific acoustical impedance of a tube.

The pressures in the inner two channels are very similar to one another. The outer channel is also very close to a frequency of $ka=5$, corresponding to 7.16kHz in this case. Above this point, the pressure in the outer channel is a little lower than the other two channels. If the values of ζ_n^d/ζ_0^d were absolutely ideal, i.e. $\zeta_n^d/\zeta_0^d=\delta_{n0}$, then the phase-plug channel-design methods would be expected to work perfectly. The fact that there is some pressure difference in the outer channel indicates that in this instance it is necessary to control the ζ_n^d/ζ_0^d to a greater extent if the final result is to be improved. This could be achieved by including more

shape functions in the calculation of the cavity profile in order to meet the ideal ζ_n^d/ζ_0^d parameters for mode cavity modes. However, as more terms are included then the derived cavity shape either converges with the ideal cavity solution or, if the controlled areas prevent this, then it is likely that a non-physical thickness functions result (with zero or negative thickness over some part of the cavity).

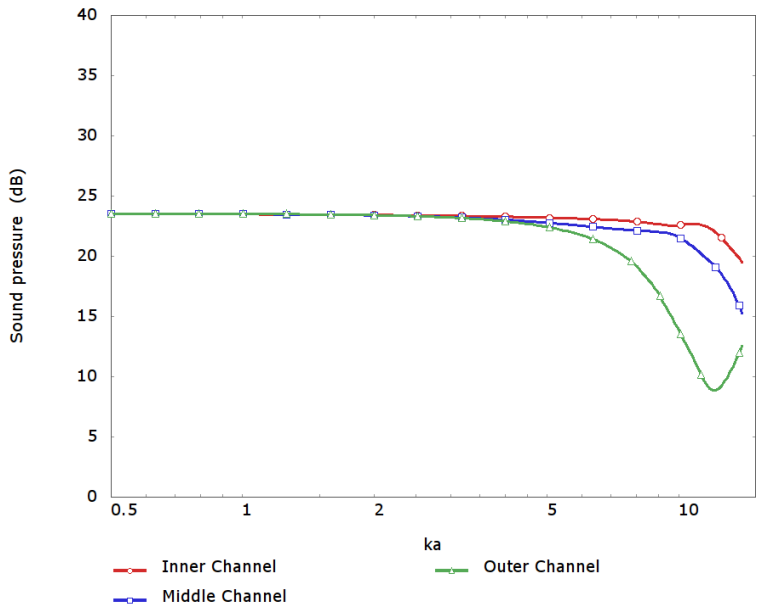

Figure XI.3. Normalised channel pressure-level response for shaped-cavity compression driver with fixed cavity outer geometry with phase-plug geometry computed using the generalised method introduced in section 5.4.1.

Appendix XII Outline of the basic tweeter design

Prior to the design of the phase plug, the other parts of the tweeter were designed using FEM modelling resulting in the basic tweeter driver assembly shown in figure XII.1. This design work was carried out by the author as part of his role as an engineer working for KEF Audio (UK) Ltd.

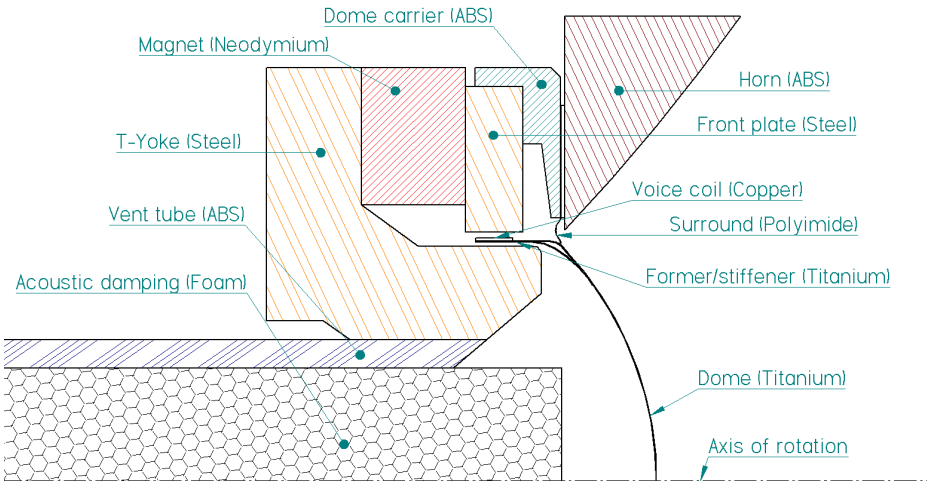

Figure XII.1. CAD drawing of the basic tweeter assembly before the design of the phase plug.

The geometry shown in figure XII.1 was arrived at as a result of several modelling stages. The motor system is designed with the aid of magneto static FEM simulation using CEDRAT Flux2D. The simulated flux in the final model of the motor system is shown in figure XII.2. As the tweeter uses a neodymium magnet, the magnetic flux in the steel parts is high. This helps to improve the linearity of the motor system by reducing modulation of the static magnetic field by the dynamic magnetic field generated by the voice coil.

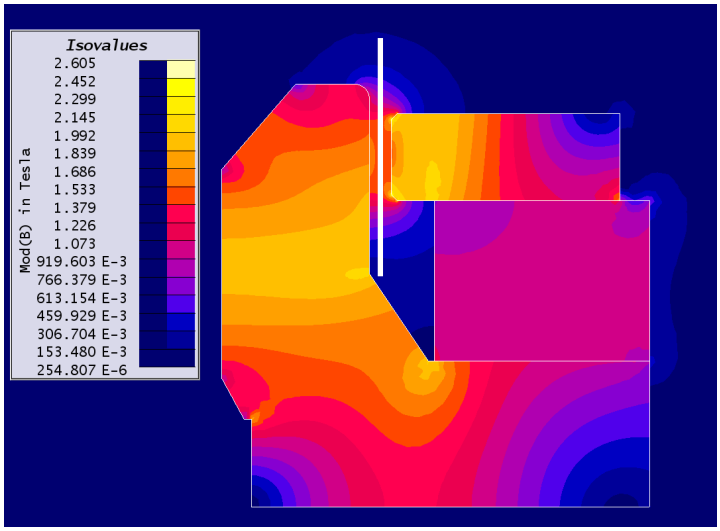

Figure XII.2. FEM computed magnetic flux magnitude in the tweeter motor system parts. The motor orientation is at 90 degrees compared with figure XII.1. The white line is in the centre of the magnetic gap. The axis of rotation is at the left hand extent of the figure.

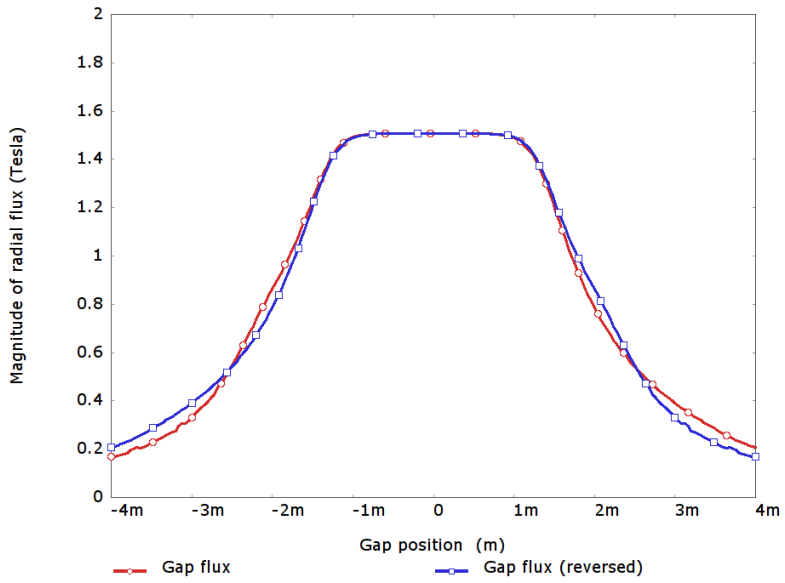

Figure XII.3. FEM computed radial magnetic flux magnitude in the centre of the motor system gap.

The computed radial magnetic flux along a line in the centre of the magnet gap is shown in figure XII.3. The radial magnetic flux is approximately 1.5 Tesla over a 2mm region at the centre of the gap. The same radial flux plot is also shown with the abscissa reversed, indicating that the radial flux profile is very symmetrical in the region close to the gap.

Using the FEM computed radial magnetic flux, it is possible to approximate the $BL(x)$ of the tweeter using the integral

$$BL(x)=\int_{y} B(y)L(x)\,dy \qquad \text{XII.1.}$$

where the function $B(x)$ is the computed gap radial-flux profile as shown in figure XII.3, and $L(x)$ is the wire-length density profile, in meters of wire per gap length. The wire density is approximated using the a voice-coil winding calculator that simply uses the geometrical wire data from the manufacturer to approximate the physical parameters of the voice coil, such as the number of turns, the height of the windings and the mass of the wire. The estimated parameters of the voice coil are shown in table XII.1.

Total length of wire	1.04m
Number of turns in coil	13.05
Winding height	1.835mm
Mass of wire	0.08g

Table XII.1: Approximated tweeter voice-coil parameters.

Using the assumption that the wire-length density, $L(x)$, is constant over the winding height of the voice coil, the $BL(x)$ is calculated as shown in figure XII.4. The BL when the voice

coil is in the centre of the motor-system gap is predicted to be $1.54\,NA^{-1}$. The BL drops by approximately 10% when the voice coil is displaced by 1mm from the centre of the gap.

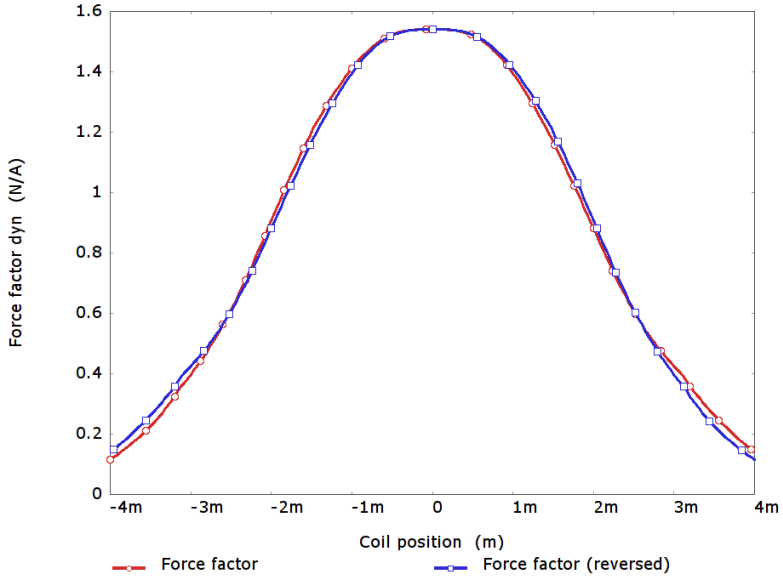

Figure XII.4. Computed tweeter BL using FEM approximated gap flux.

The diaphragm of the tweeter is designed in 30µm titanium and has the basic structure of a spherical cap, as required by the Dodd diaphragm and horn geometry. The former is also designed in 30µm titanium and, instead of the more usual straight cylinder, it has a elliptical profile at the top such that a triangular strut is formed at the junction with the dome. This arrangement of dome and former is described by Dodd in his 2005 patent [85]. Compared to an unsupported spherical cap dome of the same angle and diameter this arrangement results in a substantial increase in the first natural frequency of the diaphragm structure. The surround is thermoformed from a thin polyimide film, which provides a low stiffness with a small radial width: the minimisation of the surround width is very important for optimal performance of the Dodd dome and horn geometry. The rear radiation from the diaphragm is coupled into a large diameter venting tube that passess through the centre of the magnet system. The purpose of this tube is to increase the acoustical volume behind the tweeter and avoid large acoustical pressures on the rear face of the diaphragm. This is an important aspect of the design. If only the volume between the diaphragm and the magnet system is used to load the rear of the diaphragm then the acoustical pressure in the rear cavity is high enough for acoustical non-linearities to be significant during normal use. The acoustical configuration of the front surface of the diaphragm and the adjacent horn follows the guidelines of Dodd [83] with the horn approximately perpendicular to the dome. The tweeter

is designed to be placed at the centre of a midrange cone driver, with the midrange cone tangential to, and forming a continuation of, the horn.

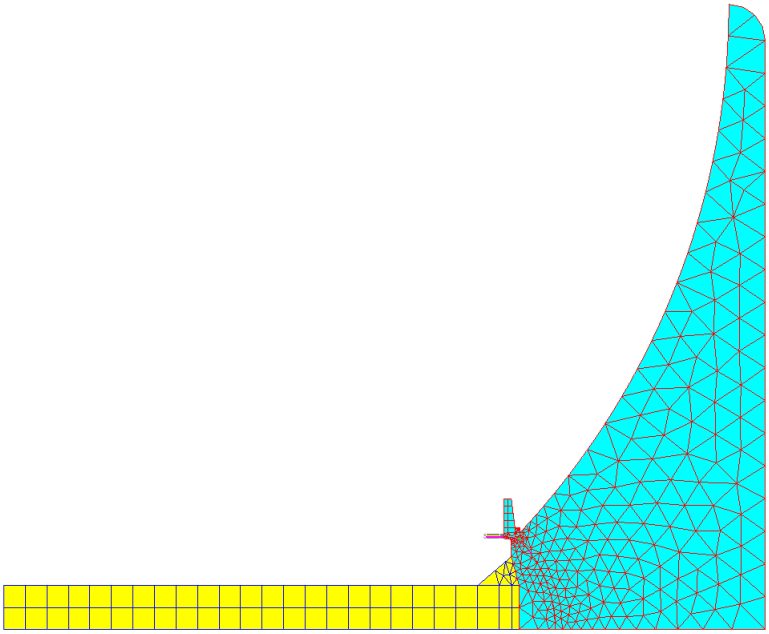

Figure XII.5. 2D axisymmetric mechanical and acoustical FEM and BEM model of the tweeter prior to phase-plug design.

The spherical cap dome is significantly deeper than is typically used on this type of tweeter. In the Dodd arrangement this has the advantage of wide dispersion at high frequencies. However, the penalty for this deep diaphragm structure, and for the complex former arrangement, is that the moving mass of the mechanical parts is high. As a result, at this stage the performance of the tweeter is very good, but the sensitivity is a little lower than required between 10 and 20kHz. The acoustical design of the tweeter to this state has been performed with FEM and BEM modelling using PAFEC-FE. As all the parts described above are rotationally symmetric, axisymmetric acoustical models were used to predict the performance. The FEM mesh of the final 2D axisymmetric model prior to the start of the phase-plug design is shown in figure XII.5.

The yellow region on the left of the figure is the rear-venting tube that is filled with an acoustical absorbent material to prevent standing waves forming in the tube. The blue region to the right of the figure is the air in front of the tweeter diaphragm. The shape of the horn and cone are clearly visible. The tweeter is modelling in a 2π steradians radiation space with the end of the horn flare terminated in a flat infinite baffle. This infinite baffle and radiation into the 2π space is modelled using a BEM region that is fully coupled to the FEM region shown in the figure. The voice-coil FEM region is driven with a harmonic axial force of unit

amplitude. The axial pressure response at 1m from infinite baffle in the region modelled using the BEM is shown in figure XII.6.

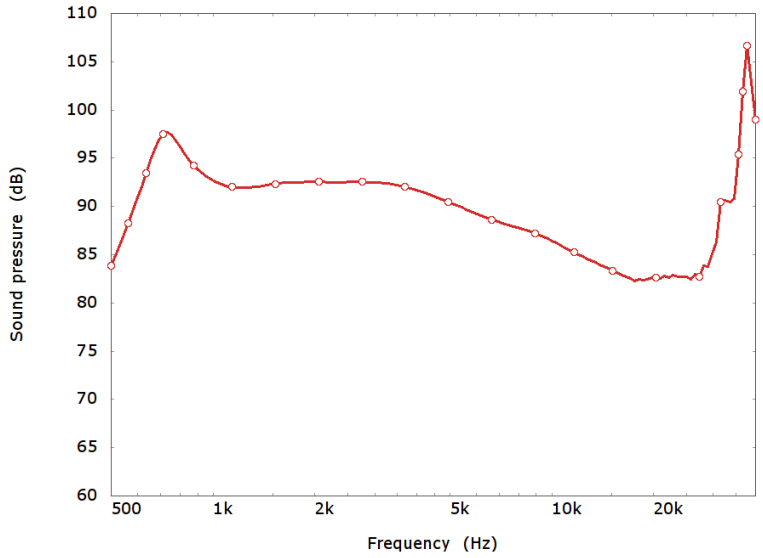

Figure XII.6. The axial pressure response of the mechanoacoustical FEM/BEM model of the infinite-baffle-mounted tweeter prior to phase-plug design at 1m from the baffle when the voice coil is driven with harmonic force of 1N RMS.

This response plot gives some indication of the frequency response of the design. In the real tweeter, the voice coil is not driven directly with a force, but instead with a voltage signal. In order to take this into account, the drive point mechanical impedance of the FEM/BEM model was calculated from the drive point axial velocity. This mechanical impedance is a very good approximation for the driver mechanical impedance Z_{ms}, which was outlined in detail in chapter 2. Having calculated the driver mechanical impedance it is possible to include the FEM/BEM model in a lumped-circuit model and to approximate the effect of voltage drive with the motor system described above. As part of his work at KEF Audio, the author has, for several years, been developing software that is dedicated to this combined FEM/BEM and lumped-modelling approach. With this software, the FEM/BEM model of the mechanical and acoustical parts are driven using an actuator component, which follows the transduction rule for a electromagnetic motor system as outlined in chapter 2. This actuator component is connected to a voltage source in series with a passive electrical component that models the blocked electrical impedance, Z_{eb}, using the LR2 model [22]. The full circuit layout is shown in figure XII.7.

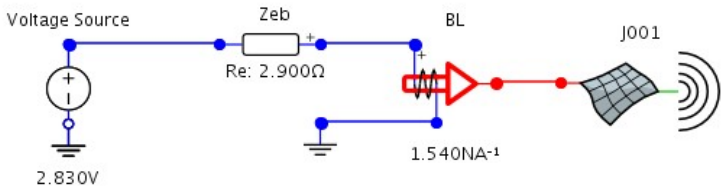

Figure XII.7. Schematic of the lumped circuit used in order to approximate the voltage-driven response of the tweeter from the FEM/BEM model of the mechanical and acoustical parts.

In the circuit simulation, the tweeter's voice-coil is driven with a harmonic voltage of 2.83V RMS. The resulting 1m axial pressure is shown in figure XII.8 along with the electrical input impedance of the driver as predicted by the circuit simulation.

This result is much easier to interpret, as it shows exactly the same data that can be readily measured from a real loudspeaker. Comparison of this figure with XII.6 clearly shows the damping effect that occurs when the loudspeaker diaphragm is excited with a voltage driven electrodynamic motor system. The large peak at 730Hz is completely controlled in the voltage drive case. Note that the large peak in the electrical impedance at this frequency is as a result of the reflection of the driver mechanical impedance to the electrical side of the electromagnetic transduction.

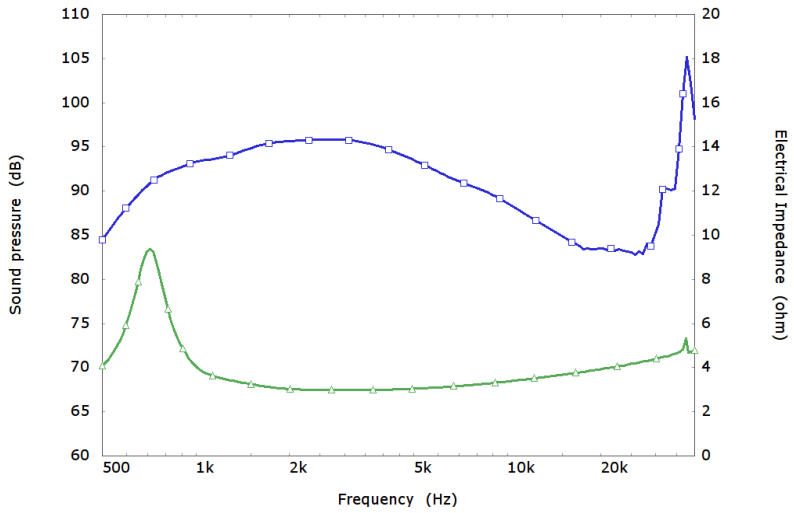

Figure XII.8. The simulated 1m axial pressure response (blue upper curve) and electrical input impedance(green lower curve) of the tweeter for a harmonic drive voltage of 2.83V RMS.

The response of the tweeter is very smooth over a wide range. The efficiency of the tweeter is extremely high at the lower end of its range. This is a result of acoustical loading of the diaphragm: the gentle and continuous flare of the horn and midrange cone are sufficient to provide a useful horn-loading effect that begins at approximately 1.5kHz. As a consequence

of this horn loading, and the corresponding approximately constant radiation resistance, the driver response falls gently between 3kHz and 20kHz. When this tweeter is used in a loudspeaker system, the response characteristic is compensated in the system crossover to create a flat passband between approximately 2kHz and 20kHz. At the very top of the modelled frequency response, a large peak is seen, at approximately 37.7kHz. This peak corresponds to the first natural frequency of the tweeter diaphragm, which has very little mechanical damping due to its construction in titanium. The peak frequency is sufficiently above the audio band that it is of little concern, moreover it is high enough that one would expect the diaphragm motion to be approximately rigid over the entire audio bandwidth. This is a prerequisite for the radial-channel design methods outlined at the start of this chapter.

An additional effect of the horn and midrange cone is the control of the directivity of the tweeter. The Uni-Q driver arrangement [97], with the tweeter placed at the apex of the midrange cone, is motivated by the desire to unify both the position and directivity of the tweeter and the midrange driver. In chapter 3, the directivity of a rigidly moving circular piston was discussed and it was demonstrated that above $ka=1$ the directivity of such a radiator begins to narrow. The rigid piston is a good approximation to the radiating behaviour of a loudspeaker diaphragm. The tweeter is, by necessity (see chapter 2), smaller than the midrange driver and as a consequence, if both are simple direct-radiating transducers, they have badly miss-matched directivity at the crossover frequency. At crossover, the tweeter directivity is typically close to omnidirectional whereas the midrange driver directivity is significantly narrower. The horn and adjacent cone in the tweeter described above are designed to control the directivity of the tweeter so that it is matched to the midrange driver directivity at the crossover point and well controlled and consistent up to the top of the audio band. Figure XII.9 shows the simulated voltage-driven frequency response at 1m from the baffle in 15 degree intervals from on-axis with the driver round to the plane of the baffle. From this figure, it may be seen that the off-axis response of the tweeter is very smooth and consistent without any nulls as were seen on the rigid-piston directivity plot shown in chapter 2 (figure 2.9).

The directivity index (DI) of the tweeter was also computed and is shown in figure XII.10 in comparison to a rigid circular piston of the same size. At low frequencies both radiators have a directivity index of 3dB indicating that they are radiating omnidirectionally into 2π-steradian space. However, while the rigid piston remains omnidirectional up to approximately 4.5kHz and then narrows rapidly, the simulated tweeter is moderately directional at around the crossover frequency of 2kHz and then narrows very slowly above

this. Above 12kHz, the rigid piston is more directional than the horn- and cone-loaded tweeter.

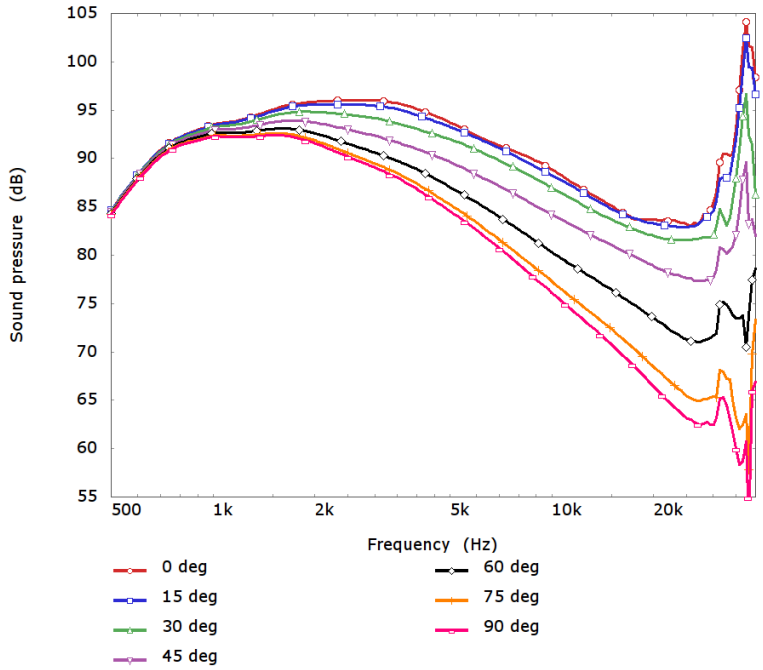

Figure XII.9. The simulated 1m pressure response of the tweeter for a harmonic drive voltage of 2.83V RMS at 15 degree polar integrals.

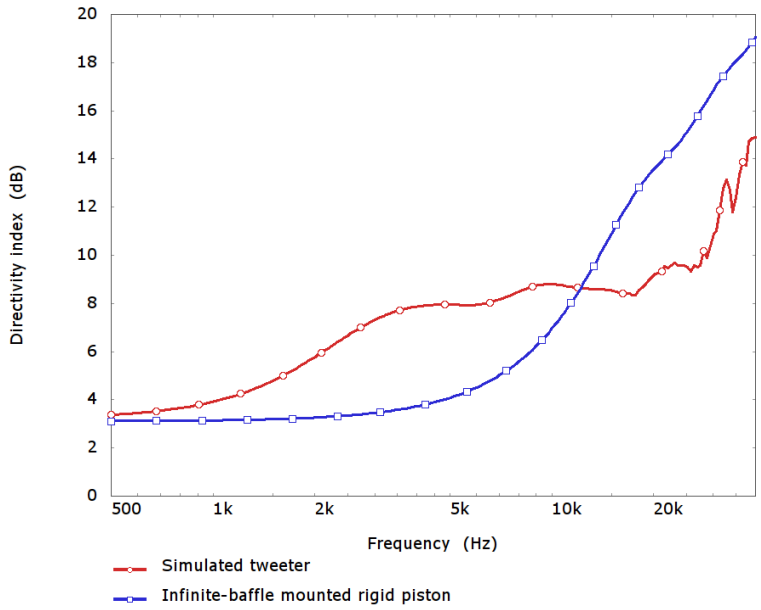

Figure XII.10. Comparison of the simulated DI of the tweeter described above and a infinite baffle mounted piston of the same diameter.

In summary, the tweeter prior to the design of the phase plug is relatively complete and exhibits a well controlled frequency response and dispersion. The high peak frequency of the dome breakup is also a positive sign that the diaphragm is likely to be approximately rigid in the audio band. The main issue with the tweeter at this stage is that the voltage sensitivity is a little lower than ideal at the upper end of the response, above 10kHz. Unfortunately this is not an easy problem to solve by conventional means. A reduction in the mass is not possible without compromising the high rigidity of the diaphragm arrangement. An increase in *BL* requires additional magnet material that would add extra cost to the design. In the next section, the process of designing a radial-channel phase plug is outlined in order to increase the sensitivity at high frequencies.

Appendix XIII Forced vibration of a lightly damped continuous mechanical system

The forced vibrational behaviour of a lightly-damped mechanical structure may be approached in a similar manner to that described for an acoustical enclosure in section 3.4: by considering that the forced structural displacement is a linear sum of the structural eigenfunctions. The behavioural equations for a general continuous mechanical body are outlined with reference to Irgens [98].

The fundamental laws of motion for any body of continuous material are given by the Cauchy equations of motion which may be expressed as [98, §3.2.5]

$$\nabla . \boldsymbol{T}(\boldsymbol{x}) + \boldsymbol{f}(\boldsymbol{x}) = \rho \frac{\partial^2 \boldsymbol{h}(\boldsymbol{x})}{\partial t^2} \qquad \text{XIII.1.}$$

$\boldsymbol{x}$ is the vector position in the body, $\boldsymbol{f}(\boldsymbol{x})$ is the vector field of external force per unit volume applied to the body, ρ is the mass density of the body and $\boldsymbol{h}(\boldsymbol{x})$ is the displacement vector field. $\boldsymbol{T}(\boldsymbol{x})$ is the stress tensor field, for example in Cartesian coordinates

$$\boldsymbol{T}(\boldsymbol{x}) = \begin{bmatrix} \sigma_{xx}(\boldsymbol{x}) & \sigma_{xy}(\boldsymbol{x}) & \sigma_{xz}(\boldsymbol{x}) \\ \sigma_{yx}(\boldsymbol{x}) & \sigma_{yy}(\boldsymbol{x}) & \sigma_{yz}(\boldsymbol{x}) \\ \sigma_{zx}(\boldsymbol{x}) & \sigma_{zy}(\boldsymbol{x}) & \sigma_{zz}(\boldsymbol{x}) \end{bmatrix} \qquad \text{XIII.2.}$$

where $\sigma_{xx}(\boldsymbol{x})$, $\sigma_{yy}(\boldsymbol{x})$ and $\sigma_{zz}(\boldsymbol{x})$ are normal stresses and $\sigma_{xy}(\boldsymbol{x})$, $\sigma_{xz}(\boldsymbol{x})$ and $\sigma_{yz}(\boldsymbol{x})$ are shear stresses (note that $\boldsymbol{T}(\boldsymbol{x}) = \boldsymbol{T}(\boldsymbol{x})^T$). $\nabla .$ is the divergence operator [98, §4.4.2], for example in Cartesian coordinates with a second order tensor field $\boldsymbol{S}$

$$\nabla . \boldsymbol{S} = \begin{bmatrix} \frac{\partial s_{xx}}{\partial x} + \frac{\partial s_{yx}}{\partial y} + \frac{\partial s_{zx}}{\partial z} \\ \frac{\partial s_{xy}}{\partial x} + \frac{\partial s_{yy}}{\partial y} + \frac{\partial s_{zy}}{\partial z} \\ \frac{\partial s_{xz}}{\partial x} + \frac{\partial s_{yz}}{\partial y} + \frac{\partial s_{zz}}{\partial z} \end{bmatrix} \qquad \text{XIII.3.}$$

Considering the small amplitude vibrational behaviour of the body, harmonic time dependence is assumed and the mechanical displacement, $\boldsymbol{h}(\boldsymbol{x})$, and stress tensor, $\boldsymbol{T}(\boldsymbol{x})$, are complex valued amplitudes.

For linear elastic materials, the stress tensor is linearly related to the strain tensor, $\boldsymbol{E}(\boldsymbol{x})$, by

$$\boldsymbol{T}(\boldsymbol{x}) = \boldsymbol{S} : \boldsymbol{E}(\boldsymbol{x}) \qquad \text{XIII.4.}$$

$\boldsymbol{S}$ is the elasticity tensor [98, §7.2.1] which is a 4th order tensor, the symbol ":" denotes the tensor contraction operation. In this case the tensor contraction operation is equivalently expressed as

$$T_{ij}=\sum_{k=1}^{3}\sum_{l=1}^{3} S_{ijkl}E_{kl} \qquad \text{XIII.5.}$$

The linear elastic behaviour of the material is defined by the tensor $\boldsymbol{S}$ which contains 81 elastic coefficients. However, due to the symmetry of the stress, strain and elasticity tensor only a maximum of 21 of these coefficients are independent. Indeed, for many materials models there are even fewer independent coefficients. For example, using the more compact Voigt notation in place of the stress and strain tensors, the Hookean relationship for an isotropic material, with Young's modulus E and Piosson's ratio ν, in Cartesian coordinates is

$$\begin{bmatrix}\sigma_{xx}\\ \sigma_{yy}\\ \sigma_{zz}\\ \sigma_{yz}\\ \sigma_{zx}\\ \sigma_{xy}\end{bmatrix}=\frac{E}{(1+\nu)(1-2\nu)}\begin{bmatrix}1-\nu & \nu & \nu & 0 & 0 & 0\\ \nu & 1-\nu & \nu & 0 & 0 & 0\\ \nu & \nu & 1-\nu & 0 & 0 & 0\\ 0 & 0 & 0 & 1-2\nu & 0 & 0\\ 0 & 0 & 0 & 0 & 1-2\nu & 0\\ 0 & 0 & 0 & 0 & 0 & 1-2\nu\end{bmatrix}\begin{bmatrix}\epsilon_{xx}\\ \epsilon_{yy}\\ \epsilon_{zz}\\ \epsilon_{yz}\\ \epsilon_{zx}\\ \epsilon_{xy}\end{bmatrix} \qquad \text{XIII.6.}$$

where ϵ_{ij} are the Cartesian components of the strain tensor, $\boldsymbol{E}(\boldsymbol{x})$.

For infinitesimal deformations, the strain tensor is related to the mechanical displacement gradient, $\boldsymbol{H}=\nabla\boldsymbol{h}(\boldsymbol{x})$, by the expression [98, §5.3.2]

$$\boldsymbol{E}=\frac{1}{2}\left[\boldsymbol{H}+\boldsymbol{H}^{T}\right] \qquad \text{XIII.7.}$$

∇ is the gradient operator [98, §2.4], for example in Cartesian coordinates

$$\nabla\boldsymbol{h}(\boldsymbol{x})=\begin{bmatrix}\frac{\partial h_x(\boldsymbol{x})}{\partial x} & \frac{\partial h_x(\boldsymbol{x})}{\partial y} & \frac{\partial h_x(\boldsymbol{x})}{\partial z}\\ \frac{\partial h_y(\boldsymbol{x})}{\partial x} & \frac{\partial h_y(\boldsymbol{x})}{\partial y} & \frac{\partial h_y(\boldsymbol{x})}{\partial z}\\ \frac{\partial h_z(\boldsymbol{x})}{\partial x} & \frac{\partial h_z(\boldsymbol{x})}{\partial y} & \frac{\partial h_z(\boldsymbol{x})}{\partial z}\end{bmatrix} \qquad \text{XIII.8.}$$

The stress tensor, $\boldsymbol{T}(\boldsymbol{x})$, is in effect a linear function of the mechanical displacement. Consequently the equations of motion for the vibration of the system are a linear partial differential equation in $\boldsymbol{h}(\boldsymbol{x})$ and, when there are no external forces, may be written

$$\nabla.\boldsymbol{T}(\boldsymbol{h}(\boldsymbol{x}))+\rho\omega^{2}\boldsymbol{h}(\boldsymbol{x})=0 \qquad \text{XIII.9.}$$

In addition, the mechanical structure may also be subject to boundary conditions which frequently restrain the mechanical displacement or velocity over some regions of the structure.

There are various different approaches to the solution of equation XIII.9. For some geometries it is possible to solve directly by separation of variables, for more complex structures it is frequently the case that no analytical solution is possible and a numerical approximate approach must be used such as the finite element method (FEM).

In general, for the homogeneous case there are an infinite set of functions which are solutions to XIII.9

$$\boldsymbol{h}(\boldsymbol{x}) = \boldsymbol{\Phi}_n(\boldsymbol{x}) \qquad \text{XIII.10.}$$

The vector functions $\boldsymbol{\Phi}_n(\boldsymbol{x})$ are the eigenfunctions of the mechanical system. Each of these eigenfunctions is associated with a corresponding eigenfrequency, ω_n, which is the frequency at which the solution is valid

$$\nabla . \boldsymbol{T}(\boldsymbol{\Phi}_n(\boldsymbol{x})) + \rho\,\omega_n^2 \boldsymbol{\Phi}_n(\boldsymbol{x}) = 0 \qquad \text{XIII.11.}$$

As with the acoustical eigenfunctions introduced in section 3.2, the scale of the mechanical eigenfunctions is arbitrary. Additionally, the mechanical eigenfunctions form an orthogonal set. A common scheme for normalisation of the eigenfunctions is summarised by the orthonormal integral expression

$$\int_V \rho\, \boldsymbol{\Phi}_n(\boldsymbol{x}) . \boldsymbol{\Phi}_m(\boldsymbol{x})\, dV = \delta_{nm} \qquad \text{XIII.12.}$$

where V is the volume occupied by the mechanical body and δ_{nm} is the Kronecker delta [47, p.692], which has the property that

$$\delta_{nm} = \begin{cases} 0, & m \neq n \\ 1, & m = n \end{cases} \qquad \text{XIII.13.}$$

AXIII.i General solution to the forced case

The inhomogeneous equation of motion of the mechanical structure is given by

$$\nabla . \boldsymbol{T}(\boldsymbol{h}(\boldsymbol{x})) + \rho\,\omega^2 \boldsymbol{h}(\boldsymbol{x}) = -\boldsymbol{f}(\boldsymbol{x}) \qquad \text{XIII.14.}$$

where $\boldsymbol{f}(\boldsymbol{x})$ is a complex vector field which defines the amplitude of external harmonic forces applied to the system.

To outline a general solution for $\boldsymbol{h}(\boldsymbol{x})$ it is helpful to first consider the particular situation when the system is driven with a unit point force at position $\boldsymbol{y}$ in direction $\hat{\boldsymbol{u}}_f$. In this case

$$\boldsymbol{f}(\boldsymbol{x}) = \delta(\boldsymbol{x}-\boldsymbol{y})\hat{\boldsymbol{u}}_f \qquad \text{XIII.15.}$$

The structure mechanical displacement to this excitation force, $\boldsymbol{h}_f(\boldsymbol{x})$, may be described as a linear combination of the eigenfunctions

$$\boldsymbol{h}_f(\boldsymbol{x}) = \sum_{m=0}^{\infty} b_m \boldsymbol{\Phi}_m(\boldsymbol{x}) \qquad \text{XIII.16.}$$

To determine the complex coefficients, b_m, this expression is first substituted into expression XIII.14

$$\sum_{m=0}^{\infty} b_m \left[\nabla . \boldsymbol{T}(\boldsymbol{\Phi}_m(\boldsymbol{x})) + \rho\omega^2 \boldsymbol{\Phi}_m(\boldsymbol{x})\right] = -\delta(\boldsymbol{x}-\boldsymbol{y})\hat{\boldsymbol{u}}_f \qquad \text{XIII.17.}$$

Using the eigensolution to the homogeneous equation, expression XIII.11, the stress tensor term may be eliminated leaving

$$\sum_{m=0}^{\infty} \rho b_m \boldsymbol{\Phi}_m(\boldsymbol{x})\left[\omega_m^2 - \omega^2\right] = \delta(\boldsymbol{x}-\boldsymbol{y})\hat{\boldsymbol{u}}_f \qquad \text{XIII.18.}$$

Taking the dot product of both sides by $\boldsymbol{\Phi}_n(\boldsymbol{x})$ and integrating over the volume results in

$$\sum_{m=0}^{\infty} b_m \left[\omega_m^2 - \omega^2\right] \int_V \rho \boldsymbol{\Phi}_n(\boldsymbol{x}).\boldsymbol{\Phi}_m(\boldsymbol{x}) dV = \int_V \delta(\boldsymbol{x}-\boldsymbol{y})\boldsymbol{\Phi}_n(\boldsymbol{x}).\hat{\boldsymbol{u}}_f dV \qquad \text{XIII.19.}$$

The shifting property of the dirac delta allows the right hand side integral to be easily evaluated. In addition, comparison of the left hand side with expression XIII.12 allows further simplification resulting in

$$\sum_{m=0}^{\infty} b_m \left[\omega_m^2 - \omega^2\right] \delta_{nm} = \boldsymbol{\Phi}_n(\boldsymbol{y}).\hat{\boldsymbol{u}}_f \qquad \text{XIII.20.}$$

from which it is clear that the complex amplitude coefficients are given by

$$b_n = \frac{\boldsymbol{\Phi}_n(\boldsymbol{y}).\hat{\boldsymbol{u}}_f}{\omega_n^2 - \omega^2} \qquad \text{XIII.21.}$$

and the mechanical displacement is

$$\boldsymbol{h}_f(\boldsymbol{x}) = \sum_{m=0}^{\infty} \frac{\boldsymbol{\Phi}_m(\boldsymbol{x})}{\omega_m^2 - \omega^2} \boldsymbol{\Phi}_m(\boldsymbol{y}).\hat{\boldsymbol{u}}_f \qquad \text{XIII.22.}$$

The solution for am arbitrary harmonic force applied the structure may be easily inferred from this special case by considering any applied force density distribution, $\boldsymbol{f}(\boldsymbol{x})$, as a

continuum of point forces. The mechanical displacement is the linear superposition of the response from each point force, this is calculated by integrating over the volume of the structure which results in the concise expression

$$\boldsymbol{h}(\boldsymbol{x}) = \sum_{m=0}^{\infty} \frac{\boldsymbol{\Phi}_m(\boldsymbol{x})}{\omega_m^2 - \omega^2} \int_V \boldsymbol{\Phi}_m(\boldsymbol{y}).\boldsymbol{f}(\boldsymbol{x}) dV \qquad \text{XIII.23.}$$

Appendix XIV Global search B & C

In an attempt to incorporate both the effect of the voice-coil region on the mechanical modes and also to account for the difference between the raw coupling parameters γ_{nk} and the forced coupling parameters $F_k\gamma_{nk}$ during the global search, the diaphragm geometry used for the first global search was augmented to include a voice-coil region. Based on the results shown in figure 8.22 and 8.23, the voice-coil region is located approximately at the junction between the spherical cap and the roll surround.

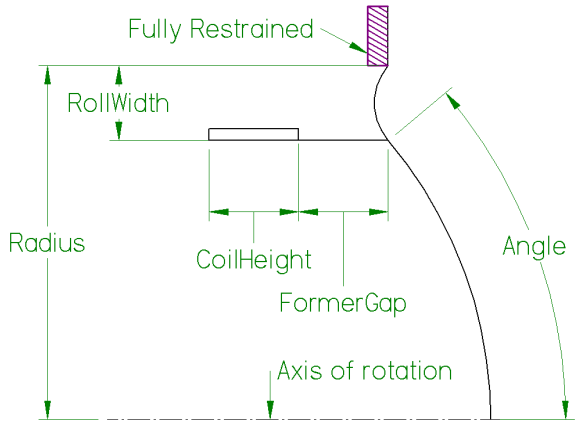

Figure XIV.1. Compression-driver diaphragm geometry B composed of a spherical cap with inverted roll surround, driving voice coil and former assembly as used for global search B of $F_k\gamma_{nk}$.

The geometry for the second global search is shown in figure XIV.1. The geometry of the front surface of the compression driver diaphragm is the same as was used for the initial geometry search with the addition of a voice coil and former assembly added at the junction between the roll and the spherical cap region. The coil height and former gap parameters are both fixed during the search at 3.5mm.

In addition to this quite conventional diaphragm and voice-coil arrangement, a third global search was also performed on a slightly different diaphragm geometry, figure XIV.2 shows the geometry used for global search C.

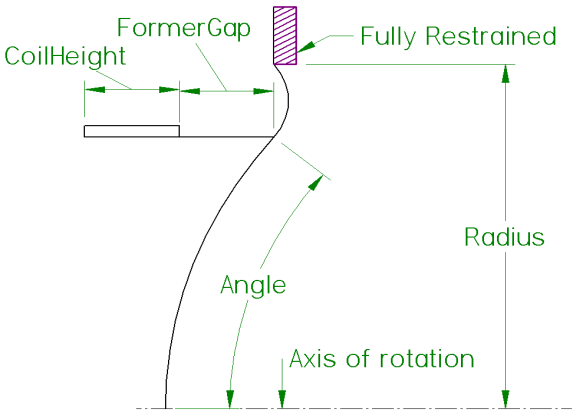

Figure XIV.2. Compression-driver diaphragm geometry B composed of a spherical cap with inverted roll surround, driving voice coil and former assembly connected for radiation from concave side as used for global search C of $F_k \gamma_{nk}$.

Geometry C is quite similar to B with the exception that the acoustical radiation is taken from the concave side of the compression-driver diaphragm. This is of some advantage as it permits more space for the phase plug and, as typically the phase-plug channels must join at a small-diameter horn throat, it is generally easier to route the phase-plug channels from the concave side in such a way that they have the same effective length to the horn throat.

Both geometry C and geometry B were subject to a global search over the geometric parameters “angle” and “roll width” using the same parameter ranges as global search A. In the mechanical FEM models, the voice-coil region is given material properties of aluminium and the voice-coil former material properties of 25μm titanium.

The objective function used for search B and C was the maximum value of Γ_{nk}^{f} over the range $0 \le n \le 4$ and $0 \le k \le 3$ with the value for $n=0 \wedge k=0$ not included. In addition to this objective function, a second objective function was also computed as the maximum value of Γ_{nk}^{f} over the range $0 \le n \le 5$ and $0 \le k \le 11$ to try to determine if it is feasible to control Γ_{nk}^{f} over a wider range of modes.

The results of global searches B and C are presented in figure XIV.3, figure XIV.4, table XIV.1 and table XIV.2. There are a number of interesting observations. Firstly it seems that geometry B performs slightly better that geometry C. However, the practical advantage of geometry C may still prove this to be the better choice.

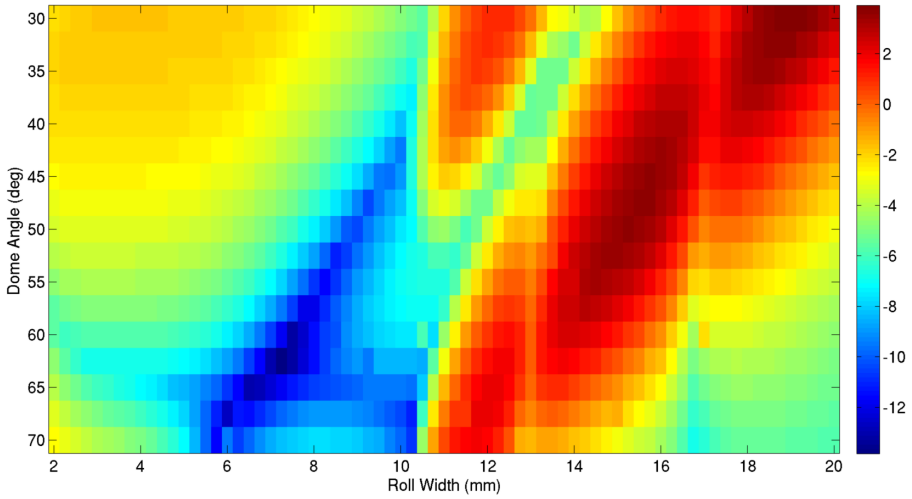

Figure XIV.3. Objective function over global optimisation B parameter space.

Angle (deg)	Roll Width (mm)	Mass (g)	Obj fun (dB)	Obj fun 2 (dB)
62.5	7.25	1.5405	-13.8344	-13.8344
62.5	7.50	1.5323	-13.2635	-13.2635
60.0	7.50	1.5184	-13.1758	-13.1758
62.5	7.00	1.5487	-13.0187	-13.0187
65.0	6.50	1.5807	-12.9622	-12.9622
65.0	6.75	1.5723	-12.8296	-12.8296
67.5	6.00	1.6146	-12.7620	-12.7620
60.0	7.75	1.5102	-12.5074	-12.5074
65.0	7.00	1.5640	-12.2825	-12.2825
62.5	7.75	1.5240	-12.2613	-12.2613

Table XIV.1: Ten compression-driver diaphragm geometries with the lowest objective function resulting from the global search B, sorted in order of lowest objective function.

Secondly, the geometries found with the lowest objective function for both B and C have identical values of the additionally computed objective function. This implies that the worst values of Γ_{nk}^{f} occur in the range $0 \leq n \leq 4$ and $0 \leq k \leq 3$. It is also interesting as one of the conclusions from the analysis of the resulting geometry from global search A was that it is necessary to control the modal coupling parameter over a wider frequency range. The third interesting difference in the returned results is that the optimum geometrical parameters are slightly different from A. The reason for this comes from both the change in the mechanical modes resulting from the addition of the voice coil and former to the mechanical structure and also because the objective function is slightly different in this instance as it is based on Γ_{nk}^{f} rather than Γ_{nk}.

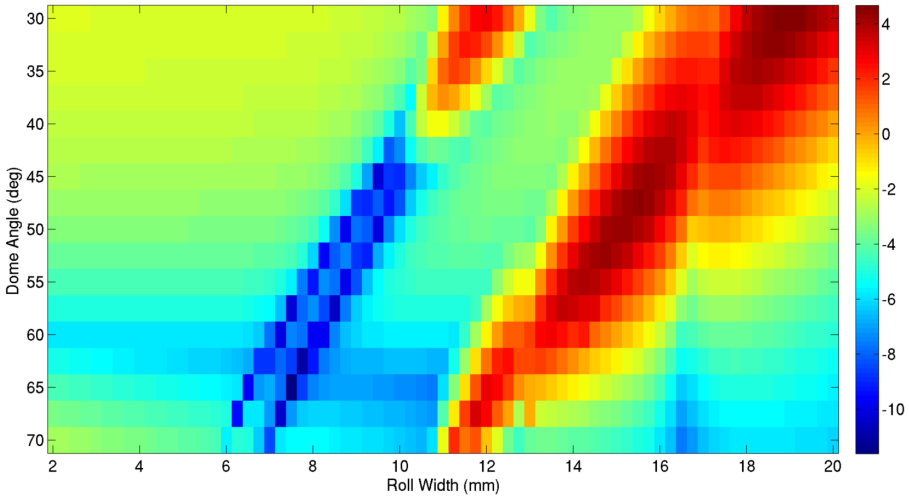

Figure XIV.4. Objective function over global optimisation C parameter space.

Angle (deg)	Roll Width (mm)	Mass (g)	Obj fun (dB)	Obj fun 2 (dB)
65	7.5	1.51371	-11.634	-11.634
62.5	7.75	1.48681	-11.0715	-11.0715
57.5	8.5	1.42923	-10.6381	-10.6381
67.5	7.25	1.54212	-10.4611	-10.4611
57.5	7.5	1.46004	-10.3061	-10.3061
45	9.5	1.32995	-10.2363	2.00809
60	7.25	1.48461	-10.1158	-10.1158
50	9.5	1.35522	-10.0076	-2.64182
55	8.75	1.40604	-9.86877	-7.78871
60	8.25	1.45344	-9.79548	-9.79548

Table XIV.2: Ten compression-driver diaphragm geometries with the lowest objective function resulting from the global search C, sorted in order of lowest objective function.

Figure XIV.5 and figure XIV.6 show the forced coupling factors Γ^{f}_{nk} for the optimal geometries resulting from search B and C, respectively. These are directly comparable to the coupling factors shown in figure 8.22 for the optimal geometry from search A. The difference between the coupling factors for geometry A and geometries B and C are interesting as the coupling factors of A are lower in the controlled range $0 \leq n \leq 4$ and $0 \leq k \leq 3$; however, B and C are substantially lower for higher mechanical modes.

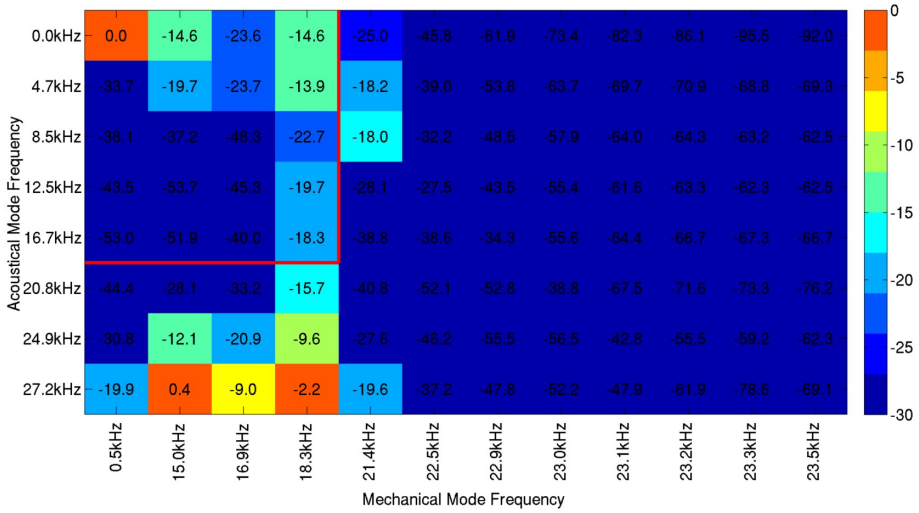

Figure XIV.5. Computed values of Γ_{nk}^{f} for the compression driver-diaphragm with geometry according to figure XIV.1 with the geometric parameters angle=62.5deg, radius=76.2/2mm and roll width=7.25mm.

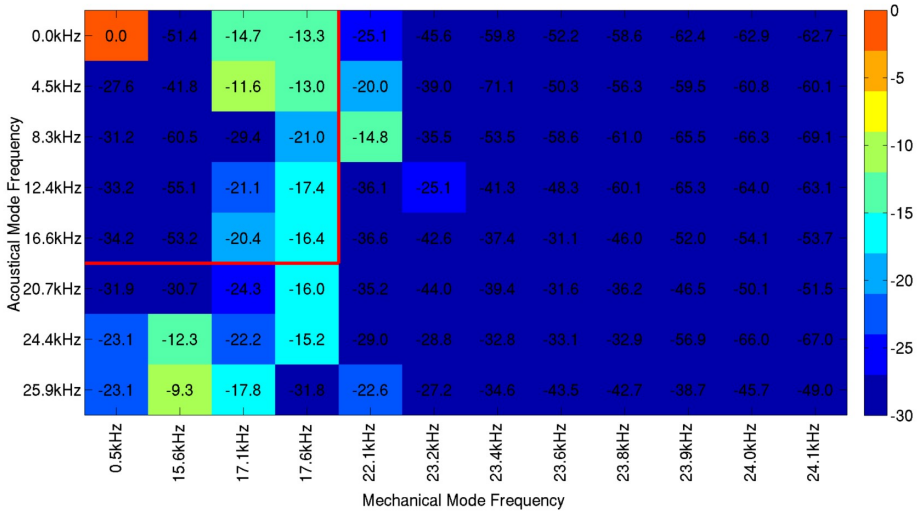

Figure XIV.6. Computed values of Γ_{nk}^{f} for the compression-driver diaphragm with geometry according to figure XIV.2 with the geometric parameters angle=65, radius=76.2/2 and roll width=7.5.

The normalised zeta functions for each of the geometries were approximated from the in-vacuo FEM-computed diaphragm velocities in combination with the FEM modal analyses of the compression cavity. The results are shown for geometry B in figure XIV.7 and for geometry C in figure XIV.8. In comparison with figure 8.19, which shows the same calculation for the geometry found in global search A, the most obvious difference is that the level of the functions is reduced at 20kHz. There is also a slight reduction in the level of the functions at approximately 10kHz. The results for geometry C are particularly interesting as

the glitches at 15kHz and 17kHz, corresponding to the first mechanical modes of the diaphragm, are significantly smaller than on both geometry A and geometry B.

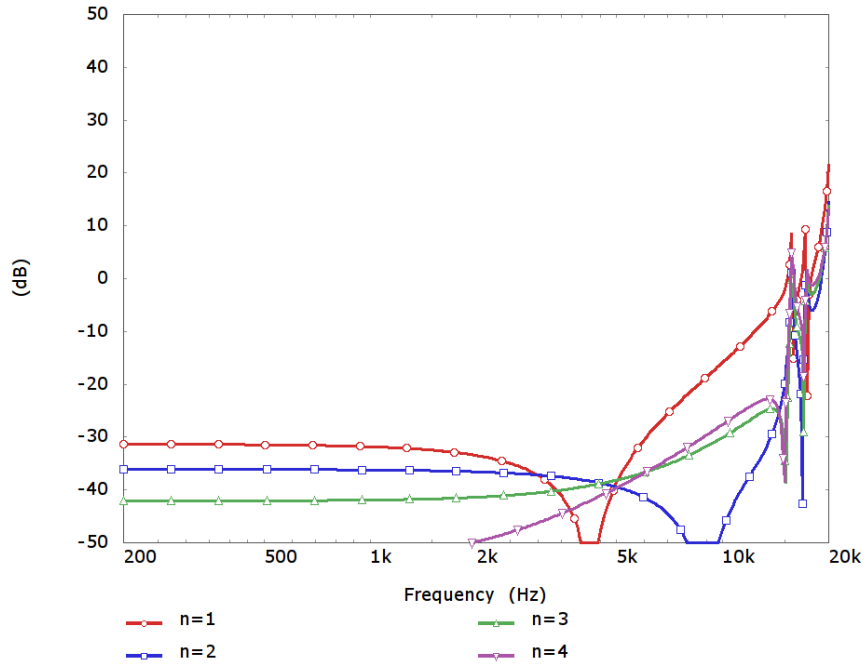

Figure XIV.7. Decibel level of calculated functions $\zeta_n^d(\omega)/\zeta_0^d(\omega)$ for in-vacuo FEM-calculated non-rigid diaphragm and cavity found in global search B.

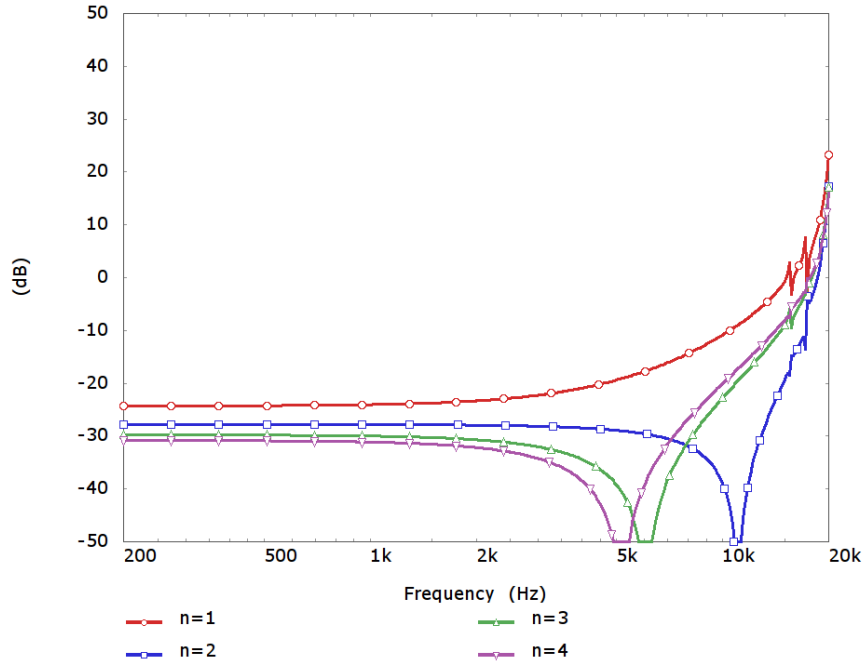

Figure XIV.8. Decibel level of calculated functions $\zeta_n^d(\omega)/\zeta_0^d(\omega)$ for in-vacuo FEM-calculated non-rigid diaphragm and cavity found in global search B.

It is interesting to now see if these seemingly improved zeta functions result in improved performance for a fully coupled compression driver. For both geometry B and geometry C, a simple phase plug was designed and in the same was as was done for geometry A, in the calculation of the channel positions and sizes ideal values of $\zeta_n^d(\omega)/\zeta_0^d(\omega)=\delta_{0n}$ were assumed. For the geometry found in global search B this results in channel areas of

$$\begin{bmatrix} A_1/A_T \\ A_2/A_T \\ A_3/A_T \end{bmatrix} = \begin{bmatrix} 0.2091 \\ 0.3874 \\ 0.4035 \end{bmatrix} \quad \text{XIV.1.}$$

where A_1 is the area of the inner of the three channels, A_2 is the area of the middle channel and A_3 is the area of the outer most channel. These areas can equivalently be written as channel width ratios as

$$\begin{bmatrix} w_2/w_1 \\ w_3/w_1 \end{bmatrix} = \begin{bmatrix} 0.8421 \\ 0.6303 \end{bmatrix} \quad \text{XIV.2.}$$

For the geometry found in global search C, this results in channel areas of

$$\begin{bmatrix} A_1/A_T \\ A_2/A_T \\ A_3/A_T \end{bmatrix} = \begin{bmatrix} 0.2247 \\ 0.3879 \\ 0.3874 \end{bmatrix} \quad \text{XIV.3.}$$

where A_1 is the area of the inner of the three channels, A_2 is the area of the middle channel and A_3 is the area of the outer most channel. These areas can equivalently be written as channel width ratios as

$$\begin{bmatrix} w_2/w_1 \\ w_3/w_1 \end{bmatrix} = \begin{bmatrix} 0.7922 \\ 0.5790 \end{bmatrix} \quad \text{XIV.4.}$$

The resulting normalised channel-pressure levels are shown for geometry B in figure XIV.9 and for geometry C in figure XIV.10. The pressure levels shown are normalised by the specific acoustical impedance of a tube,

$$L_{norm} = 20\log_{10}\left|\frac{p}{\rho_0 c_0}\right| \quad \text{XIV.5.}$$

Compared to figure 8.20, which shows the equivalent pressure level responses for geometry A, the two pressure response figures are very similar and show a similar level of uniformity between the three channels. From these results, it can be seen that geometry B performs slightly better in the region $5 < ka < 8$, whereas the channel pressures of geometry C are more similar in the region above $ka = 10$. The differences are, however, relatively small and the

overall trend in the channel-pressure levels in geometry A, B and C are similar. For a significant improvement in the compression driver performance, it seems that it is necessary to consider less conventional compression-driver diaphragm geometries.

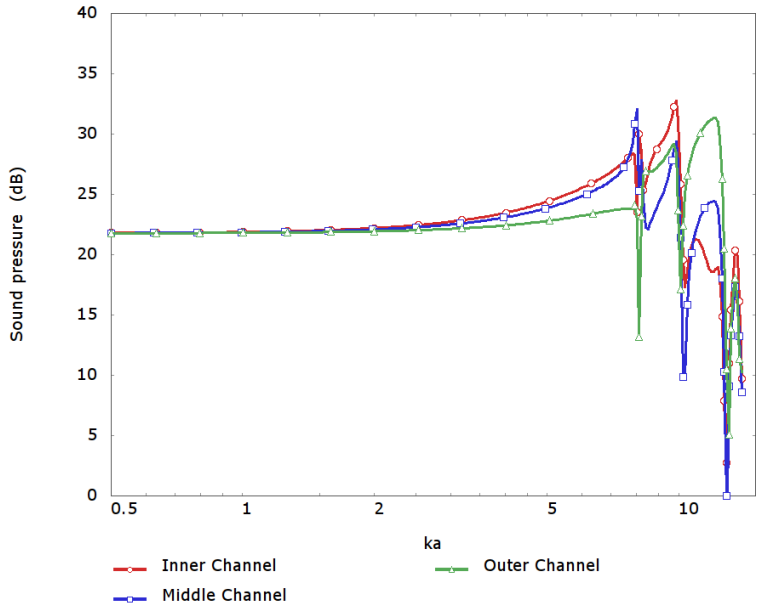

Figure XIV.9. Normalised channel-pressure level response for diaphragm and cavity geometry found with global search B, with phase-plug geometry computed using the generalised method introduced in section 5.4.1, note that the fluid and structural regions are fully coupled.

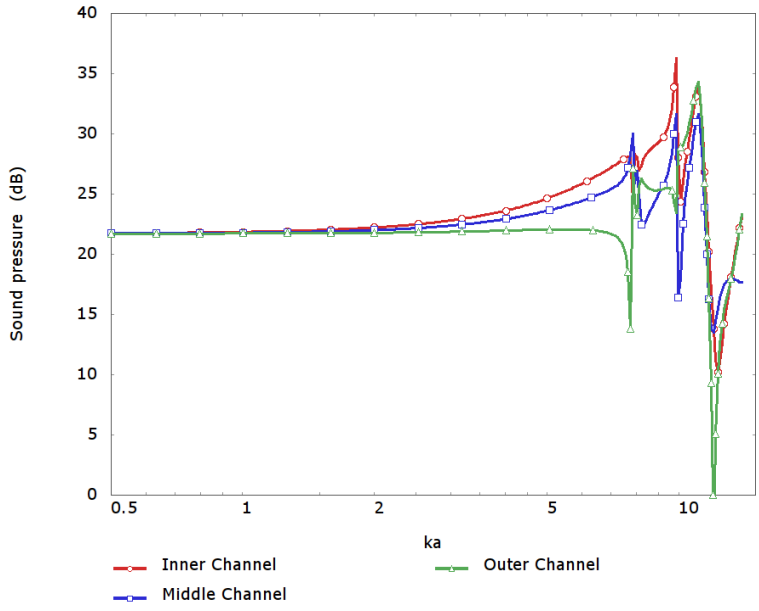

Figure XIV.10. Normalised channel-pressure level response for diaphragm and cavity geometry found with global search C, with phase-plug geometry computed using the generalised method introduced in section 5.4.1, note that the fluid and structural regions are fully coupled.